

Neuroscience Bulletin

The Official Journal of the Chinese Neuroscience Society

神经科学通报

Volume 39
Number 6
June 2023



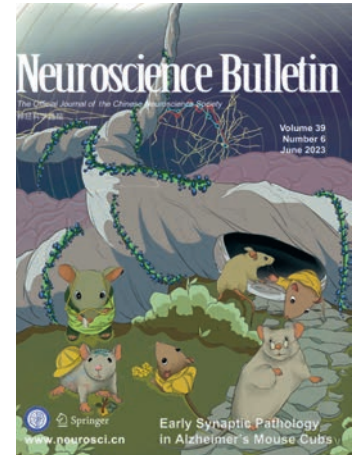
Springer

www.neurosci.cn

Early Synaptic Pathology
in Alzheimer's Mouse Cubs

About the Cover

The overexpression of transgenic mutant forms of APP/PS1 in 5XFAD mice results in early developmental defects of synaptic function, which could potentially contribute to age-dependent synaptic pathology and neurodegeneration later in life. As a result, while Alzheimer's disease is typically considered a condition that arises in old age, subtle neurological defects caused by genetic mutations or risk factors may emerge during the early stages of development. The cover illustrates the subtle neurological dysfunctions and defects in synaptic development in the 5XFAD mouse at an early post-weaning age, using a gray mouse cub in the lower left corner. These changes in neuronal function may initiate a lifelong process, depicted by the gray adult mouse in the lower right corner that cannot find its way back to its tree-hole home. See pages 881–892. (Cover provided by Chang Chen)

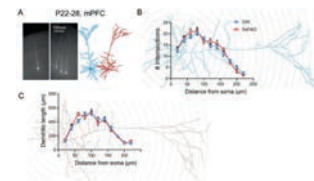


Volume 39 Number 6
June 2023

Original Articles

881 Disrupted Maturation of Prefrontal Layer 5 Neuronal Circuits in an Alzheimer's Mouse Model of Amyloid Deposition

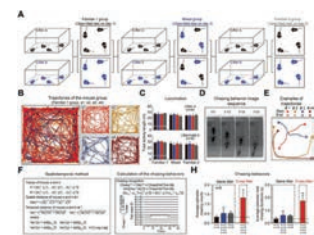
Chang Chen · Jing Wei · Xiaokuang Ma · Baomei Xia · Neha Shakir · Jessica K. Zhang · Le Zhang · Yuehua Cui · Deveroux Ferguson · Shenfeng Qiu · Feng Bai



p 888

893 Noninvasive Tracking of Every Individual in Unmarked Mouse Groups Using Multi-Camera Fusion and Deep Learning

Feng Su · Yangzhen Wang · Mengping Wei · Chong Wang · Shaoli Wang · Lei Yang · Jianmin Li · Peijiang Yuan · Dong-Gen Luo · Chen Zhang



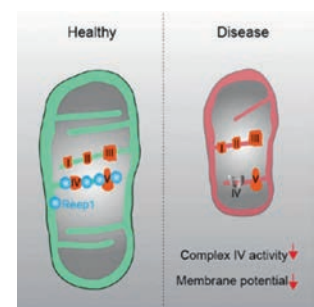
p 907

911 Leaky Gut Plays a Critical Role in the Pathophysiology of Autism in Mice by Activating the Lipopolysaccharide-Mediated Toll-Like Receptor 4–Myeloid Differentiation Factor 88–Nuclear Factor Kappa B Signaling Pathway

Fang Li · Haoran Ke · Siqi Wang · Wei Mao · Cexiong Fu · Xi Chen · Qingqing Fu · Xiaori Qin · Yonghua Huang · Bidan Li · Shibing Li · Jingying Xing · Minhui Wang · Wenlin Deng

929 REEP1 Preserves Motor Function in SOD1^{G93A} Mice by Improving Mitochondrial Function via Interaction with NDUFA4

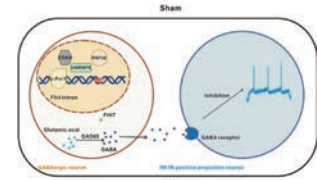
Siyue Qin · Pan You · Hui Yu · Bo Su



p 943

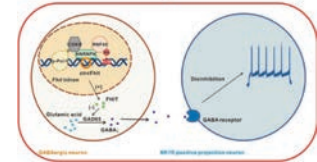
947 CircFhit Modulates GABAergic Synaptic Transmission via Regulating the Parental Gene *Fhit* Expression in the Spinal Dorsal Horn in a Rat Model of Neuropathic Pain

Ting Xu · Zhen-Yu Li · Meng Liu · Su-Bo Zhang · Huan-Huan Ding · Jia-Yan Wu · Su-Yan Lin · Jun Liu · Jia-You Wei · Xue-Qin Zhang · Wen-Jun Xin



962 Corticostriatal Neurons in the Anterior Auditory Field Regulate Frequency Discrimination Behavior

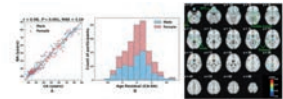
Zhao-Qun Wang · Hui-Zhong Wen · Tian-Tian Luo · Peng-Hui Chen · Yan-Dong Zhao · Guang-Yan Wu · Ying Xiong



p 959

973 The Emotion-Regulation Benefits of Implicit Reappraisal in Clinical Depression: Behavioral and Electrophysiological Evidence

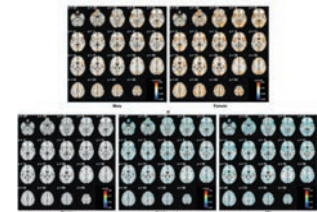
Jiajin Yuan · Yueyao Zhang · Yanli Zhao · Kexiang Gao · Shuping Tan · Dandan Zhang



Letters to the Editor

984 Different Regional Patterns in Gray Matter-based Age Prediction

Nianming Zuo · Tianyu Hu · Hao Liu · Jing Sui · Yong Liu · Tianzi Jiang



p 987

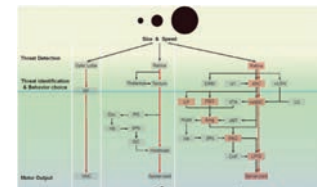
989 TRPM7 Kinase Domain is Part of the Rac1-SSH2-cofilin Complex Regulating F-actin in the Mouse Nervous System

Junzhuang Chang · Cui Chen · Wei Li · Nashat Abumaria

Reviews

994 Neural Circuit Mechanisms Involved in Animals' Detection of and Response to Visual Threats

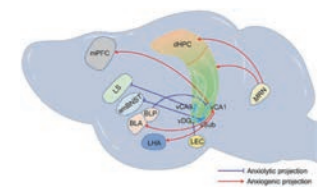
Qiwen Wu · Yifeng Zhang



p 1002

1009 Hippocampus: Molecular, Cellular, and Circuit Features in Anxiety

Hu-Jiang Shi · Shuang Wang · Xin-Ping Wang · Rui-Xin Zhang · Li-Juan Zhu



p 1018

Research Highlights

1027 Neuronal Mechanisms Govern Glioblastoma Cell Invasion

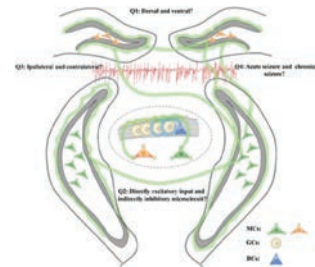
Xiaowu Lin · Zhihui Huang · Yongjie Wang

1031 Double-Edged Mossy Cells in Temporal Lobe Epilepsy: Evil in the Early Stage Through a BDNF-Dependent Strengthening Dentate Gyrus Circuit

Heming Cheng · Qiuwen Lou · Yi Wang · Zhong Chen

1034 One Small Step for Neurotechnology, One Giant Leap for an In-Depth Understanding of the Brain

Xiaoyun Qiu · Minjuan Sun · Cenglin Xu · Yingying Tang · Zhong Chen

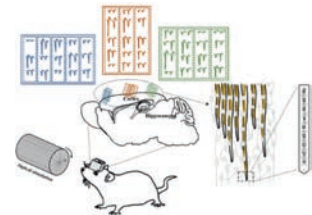


p 1032

Retraction

1037 Retraction Note to: Gray Matter-Based Age Prediction Characterizes Different Regional Patterns

Nianming Zuo · Tianyu Hu · Hao Liu · Jing Sui · Yong Liu · Tianzi Jiang



p 1035

Disrupted Maturation of Prefrontal Layer 5 Neuronal Circuits in an Alzheimer's Mouse Model of Amyloid Deposition

Chang Chen^{1,2}  · Jing Wei² · Xiaokuang Ma² · Baomei Xia² · Neha Shakir² · Jessica K. Zhang² · Le Zhang² · Yuehua Cui² · Deveroux Ferguson² · Shenfeng Qiu² · Feng Bai¹

Received: 26 April 2022 / Accepted: 18 June 2022 / Published online: 24 September 2022

© Center for Excellence in Brain Science and Intelligence Technology, Chinese Academy of Sciences 2022

Abstract Mutations in genes encoding amyloid precursor protein (APP) and presenilins (PSs) cause familial forms of Alzheimer's disease (AD), a neurodegenerative disorder strongly associated with aging. It is currently unknown whether and how AD risks affect early brain development, and to what extent subtle synaptic pathology may occur prior to overt hallmark AD pathology. Transgenic mutant APP/PS1 over-expression mouse lines are key tools for studying the molecular mechanisms of AD pathogenesis. Among these lines, the 5XFAD mice rapidly develop key features of AD pathology and have proven utility in studying amyloid plaque formation and amyloid β ($A\beta$)-induced neurodegeneration. We reasoned that transgenic mutant APP/PS1 over-expression in 5XFAD mice may lead to neurodevelopmental defects in early cortical neurons, and performed detailed synaptic physiological characterization of layer 5 (L5) neurons from the prefrontal cortex (PFC) of 5XFAD and wild-type littermate controls. L5 PFC neurons from 5XFAD mice show early APP/ $A\beta$ immunolabeling. Whole-cell patch-clamp recording at an early post-weaning age (P22–30) revealed functional impairments; although 5XFAD PFC-L5 neurons exhibited similar membrane properties, they were intrinsically less excitable. In addition, these neurons received smaller amplitude and frequency of miniature excitatory synaptic inputs. These functional

disturbances were further corroborated by decreased dendritic spine density and spine head volumes that indicated impaired synapse maturation. Slice biotinylation followed by Western blot analysis of PFC-L5 tissue revealed that 5XFAD mice showed reduced synaptic AMPA receptor subunit GluA1 and decreased synaptic NMDA receptor subunit GluN2A. Consistent with this, patch-clamp recording of the evoked L23>L5 synaptic responses revealed a reduced AMPA/NMDA receptor current ratio, and an increased level of AMPAR-lacking silent synapses. These results suggest that transgenic mutant forms of APP/PS1 overexpression in 5XFAD mice leads to early developmental defects of cortical circuits, which could contribute to the age-dependent synaptic pathology and neurodegeneration later in life.

Keywords Alzheimer's disease · Mouse model · Synaptic plasticity · Long-term potentiation · Cortical circuit · Electrophysiology · Learning and memory

Introduction

Alzheimer's disease (AD) is the most frequent form of dementia. A hallmark pathology of the AD brain is the degenerating cortical neurons overloaded with neurofibrillary tangles and amyloid plaques [1]. At the cellular and functional levels, early AD brain pathology is characterized by impaired synaptic function and synapse loss, manifested as disrupted synaptic plasticity, learning, memory, and cognition [2–4]. Transgenic mice that overexpress mutated human amyloid precursor protein (APP), presenilin, and tau genes reproduce many aspects of AD pathology such as amyloid β ($A\beta$) plaques, neurofibrillary tangles, reactive gliosis, and synaptic and neuronal loss, which are consistent with behavioral changes such as progressive age-dependent memory impairments [5, 6]. As such, these

✉ Shenfeng Qiu
sqiu@arizona.edu

✉ Feng Bai
baifeng515@126.com

¹ Department of Neurology, Affiliated Drum Tower Hospital, Medical School of Nanjing University, Nanjing 210008, China

² Basic Medical Sciences, University of Arizona College of Medicine-Phoenix, Phoenix, AZ 85004, USA

mouse lines are useful to inform the molecular and cellular changes associated with AD.

The 5XFAD mouse line, which co-overexpresses human APP and presenilin 1 (PS1) harboring five familial AD mutations manifest very early-onset and aggressive amyloid deposition [7, 8]. These mice start to develop amyloid plaques as early as ~2 months of age, when they show dramatically accelerated intraneuronal A β 42 production. Pathologically, A β deposition emerges in the hippocampal subiculum and in layer 5 (L5) principal neurons of the neocortex, and rapidly increases in affected brain regions [7, 9]. Synaptic failure reportedly takes place prior to overt plaque formation; for example, hippocampal basal synaptic transmission and theta burst stimulus-induced LTP are impaired at 6 months, but not prior to 4 months [10]. In addition, synaptic failure manifests at multiple levels, ranging from functional alterations to structural disturbances [11]. Synaptic failure of L5 neurons in 5XFAD mice reportedly long precedes the physical loss of synapses, which occurs by 12 months of age [11].

Although AD is considered to be an aging-related neurodegenerative disorder, mutant forms of APP/PS1 are expressed throughout the life span. How transgenic over-expression of these mutant forms affects the developing neural circuits remain an outstanding question. The 5XFAD mouse line, in which the thy1 promoter is used to drive very early transgenic APP/PS1 expression in the brain, offers a unique opportunity to study neurodevelopmental effects of mutant APP/PS1 over-loading in the affected neuron populations [7]. Despite a large literature exploring the mechanisms of neurodegeneration in 5XFAD mice [12–15], no study has explored the potential developmental sequelae of mutant APP/PS1 early on in vulnerable cortical circuits. As the thy1-promotor-driven expression of mutated forms of APP/PS1 is expected to predominantly affect L5 neurons [11, 16, 17], we reasoned that these mutated forms may have a detrimental effect at an early developmental time point, thus impairing the normal trajectory of synapse function and connectivity. In this study, we provide electrophysiology evidence of altered intrinsic excitability and impaired synaptic activity, as well as disrupted synaptic glutamate receptor content and functional glutamatergic synapses in L5 PFC neurons at an early post-weaning age (P22–28). To the best of our knowledge, this study reveals some of the earliest synaptic functional alterations, and suggests negative neurodevelopmental sequelae as an underappreciated neuropathology in this prominent AD mouse model.

Materials and Methods

Animals and Disease Model

The 5XFAD mice used in this study were purchased from the Jackson Laboratory (catalog #34848-JAX). This line

overexpresses both the human amyloid precursor protein (*APP*) gene with K670N/M671L, V717I, and I716V mutations and the human *PS1* M146L and L286V mutations under the Thy1 promoter [7]. Mice were genotyped according to the JAX protocol using three primers (mutant, AAG CTA GCT GCA GTA ACG CCA TTT; wild type, ACC TGC ATG TGA ACC CAG TAT TCT ATC; and common, CTA CAG CCC CTC TCC AAG GTT TAT AG). Mice were weaned at P21 and used for experiments on postnatal days 22–28. All experimental procedures conformed to NIH guidelines and were approved by the Institutional Animal Care and Use Committee of the University of Arizona and the Animal Care and Use Committee of the Model Animal Research Center, Nanjing University.

Immunohistochemistry/Immunofluorescence

Mice were anesthetized with 4% isoflurane and transcardially perfused with 0.01 mol/L PBS, followed by cold 4% paraformaldehyde (PFA) formulated in 0.1 mol/L phosphate buffer (pH 7.4). Brains were post-fixed in cold 4% PFA overnight at 4°C, and cryoprotected in 30% sucrose for 2 days. The brains were then embedded in OCT, and cut into 40- μ m frozen sections on a sliding microtome (Leica SR-2000). The sections were washed three times in 0.01 mol/L PBS, and permeabilized in PBS-0.2% Triton. For APP/A β staining, free-floating sections were blocked in primary antibody dilution solution (0.2% Triton, 5% normal goat serum, and 1% bovine serum albumin in 0.01 mol/L PBS) for 2 h, and incubated with anti-APP/A β primary antibody (clone 6E10, Biolegend, Cat# SIG-39320. Antibody Registry ID: AB_662798. 1:500 dilution) for 24 h, followed by Alexa 555-conjugated goat anti-mouse antibody. For APP/A β , Iba1, and Thio-S triple staining, sections were similarly blocked in primary antibody dilution solution, and incubated with anti-APP/A β (6E10) and anti-Iba1 (#019-19741, Wako, 1:500 dilution) primary antibodies for 24 h. After incubation with A555-conjugated goat anti-mouse and A488-conjugated goat anti-rabbit antibodies for 24 h, sections were extensively washed in 0.01 mol/L PBS, and further stained with 0.025% Thio-S (prepared in 50% ethanol–50% PBS) for 10 min. These sections were mounted on SuperFrost Plus slides (VWR Scientific, West Chester, PA) using DAPI-containing Vectashield mounting medium (H-1200, Vector Laboratories). Images were captured on an LSM 710 confocal microscope (Zeiss GmbH, Germany) with appropriate laser lines and filters.

Whole-Cell Patch-Clamp Recording in Brain Slices

Whole-cell recordings were made in L5 pyramidal neurons in parasagittal PFC slices. Mice of desired genotypes were

anesthetized using 3%–5% isoflurane. To improve slice viability, intra-cardiac perfusion of ice-cold choline solution (in mmol/L: 110 choline chloride, 25 NaHCO₃, 2.5 KCl, 1.25 NaH₂PO₄, 0.5 CaCl₂, 7 MgSO₄, 25 D-glucose, 11.6 sodium ascorbate, and 3.1 sodium pyruvate, saturated with 95% O₂ / 5% CO₂) was perfused before mice were decapitated and brains quickly dissected out. To prepare PFC slices (350 μm thick), we used parasagittal sections, which allows better preservation of intracortical synaptic connectivity [18]. Slices were cut in ice-cold choline solution on a vibratome (VT-1200S, Leica). PFC slices were kept in artificial cerebrospinal fluid (ACSF, containing in mmol/L: 126 NaCl, 2.5 KCl, 26 NaHCO₃, 2 CaCl₂, 2 MgCl₂, 1.25 NaH₂PO₄, and 10 D-glucose; saturated with 95% O₂ / 5% CO₂) for 30 min at 35°C, and then maintained at 24°C (room temperature) until recording.

The brain slices were transferred to a customized submerged chamber and perfused with ACSF saturated with 95% O₂ / 5% CO₂. Slices were visualized under a 4× objective (Olympus UPlanApo, NA = 0.16) to locate the cytoarchitectural landmarks of layer 5. To minimize neurite cutoffs, only L5 pyramidal neurons with a soma at least 50 μm below the slice surface were selected for whole-cell recordings. Neuronal somas were identified and targeted using a 60× objective (NA = 0.9) under IR illumination (Olympus BX-51 WI microscope). Neuronal signals were amplified using a MultiClamp 700B amplifier (Molecular Devices, Foster City, CA), low-pass filtered at 1 kHz (voltage clamp) or 10 kHz (current clamp), and digitized at 20 kHz using a Digidata 1440A interface controlled by pClamp 10.6 (Molecular Devices). Neuronal membrane properties (input resistance and capacitance) were measured as current responses to +/- 5mV voltage steps. Intrinsic excitability was quantified as the number of action potentials elicited by current injection (-100 to 500 pA in 50-pA steps). To record mEPSCs, D-AP5 (50 μmol/L, Tocris) and tetrodotoxin (TTX, 1 μmol/L, Tocris) were added to the circulating ACSF. The electrode internal solution contained (in mmol/L): 130 K-gluconate, 10 HEPES, 4 KCl, 4 ATP-Mg, 0.3 GTP-Na, 2 NaCl, 1 EGTA, and 14 phosphocreatine (pH 7.2, 295–300 mOsm). To record miniature inhibitory postsynaptic currents (mIPSCs), the ACSF contained 1 μmol/L TTX and 10 μmol/L CNQX, and the electrode internal solution consisted (in mmol/L): 125 KCl, 2.8 NaCl, 2 MgCl₂, 0.3 Na₃GTP, 2 Mg²⁺-ATP, 1 EGTA, 10 HEPES, and 10 phosphocreatine (pH 7.25, ~300 mOsm). In some mEPSC/mIPSC recording experiments, 0.15% biocytin (W/V) was included in the recording electrode to reveal neuronal morphology. During the recordings, series resistance (R_s, <25 MΩ) was constantly monitored and neurons with >20% variations in R_s were excluded from analyses.

To measure the AMPA/NMDA receptor current ratio (A:N) in L5 PFC neurons, a bipolar stimulating electrode

(FHC, Bowdoin, ME) was placed in L2/3 of the PFC. A Cs⁺-based internal solution (containing in mmol/L, 125 Cs-gluconate, 5 TEA-Cl, 10 HEPES, 2.5 CsCl, 8 NaCl, 5 QX314-HCl, 4 Mg²⁺-ATP, 0.3 Na₃GTP, 1 EGTA and 10 phosphocreatine, pH 7.25) was used. Evoked monosynaptic responses were obtained when neurons were sequentially voltage-clamped at -70 mV (for AMPAR-mediated synaptic currents) and +40 mV (AMPA+NMDAR currents). The A:N ratio was quantified using the peak of EPSC amplitude at -70 mV (AMPA current), and +40 mV (NMDAR current, which was measured at 75 ms after stimulus onset [19]).

To estimate the proportion of silent synapses in the L2/3 to L5 mPFC circuit, we used a minimum stimulation protocol to activate a small number of axons (release sites) by placing a theta glass electrode in L2/3. L5 neurons were first voltage-clamped at -70 mV using the Cs-based internal solution described above. A minimum stimulus intensity that produced interleaved success and failure of AMPAR EPSCs at -70 mV was applied and kept constant. After collecting 200 trials (inter-trial interval, 2 s), neurons were voltage-clamped at +40 mV to collect 200 more trials. The percentage of NMDAR-only silent synapses was calculated from the difference in failure rates of AMPAR-EPSCs (-70 mV) and compound-EPSCs (+40 mV) [20–22].

Surface Protein Biotinylation and Western Blot Analysis

To assess total glutamate receptor protein levels and their membrane-bound fractions at synaptic sites, P25–28 acute PFC slices were treated with 0.25 mg/mL sulfo-NHS-S-S-biotin for 30 min at 4°C, using a PierceTM cell surface protein isolation kit (ThermoFisher Scientific, cat# 89881), similar to that described previously for biotinylation in slices [21, 23]. Micro-dissected PFC-L5 tissue (pooled from 2–3 mice) was homogenized on ice in buffer (containing 320 mmol/L sucrose, 4 mmol/L HEPES, and 1:50 protease inhibitor mixture; P8340, Sigma-Aldrich). The homogenates were centrifuged at 1500× *g* for 10 min, after which the supernatant was collected and centrifuged at 16,000× *g* for 20 min to pellet the crude synaptosome fraction, which was further equally divided into two aliquots. One aliquot was used to assess total synaptosomal proteins, while the other was lysed and re-suspended in ice-cold water supplemented with the protease inhibitor mixture (P8340, Sigma-Aldrich). NeutraAvidin beads (ThermoFisher) were then added to capture biotinylated synaptic proteins by rotation of the sample for 2 h at 4°C. The beads were washed three times in RIPA buffer, and the biotinylated synaptic membrane proteins were eluted with 2× Laemmli buffer (supplemented with 50 μmol/L DTT). The biotinylated proteins were separated

by SDS-PAGE, and subjected to Western blot analysis using specific antibodies against glutamate receptor subunits.

A standard Western blot protocol was applied to quantify proteins. Total synaptic protein or synaptic surface protein samples were mixed with an equal amount of 2× Laemmli loading buffer and boiled for 5 min, then separated on 4%–15% SDS-polyacrylamide gels. Proteins were then transferred to PVDF membranes (Immobilon-P, Sigma-Aldrich), incubated overnight at 4°C with antibodies against several glutamate receptor subunits that were diluted in 5% nonfat dry milk. The PVDF membranes were then washed three times in 0.01 mol/L PBS-Tween 20, followed by a 2-h incubation with HRP-conjugated secondary antibodies (Jackson ImmunoResearch). Protein signals were developed using an enhanced chemiluminescence method (SignalFire, Cell Signaling Technology), and captured on ECL Hyperfilm (Amersham). The antibodies used in this study were, rabbit anti-GluA1 (AB5849) from Millipore/Chemicon and rabbit anti-GluN2A (#4205), rabbit anti-GluN2B (#14544), rabbit anti-GAPDH (#5174), and rabbit anti-GluN1 (#5704) from Cell Signaling Technology. The final dilution of antibodies was between 1:1000 and 1:2000. The optical density of protein signal bands on Hyperfilm was quantified by densitometry using ImageJ/FIJI.

Neuronal Morphology

Recorded PFC-L5 neuronal morphology, including dendritic arborization and spine morphometric measures, were analyzed as described previously [21, 24]. After completion of whole-cell recording, neurons were injected with 500 pA current to facilitate biocytin diffusion into the neurite processes. The slices were then fixed in 4% PFA overnight, blocked with 1% BSA/0.01 mol/L PBS, and permeabilized with 0.2% Triton X-100. Slices were further incubated with avidin-Alexa 488 for 24 h and mounted on glass slides with a pair of ~350- μ m spacers to prevent tissue crushing. Neuronal dendritic arbors were reconstructed after collecting Z-stack images on a confocal microscope (Zeiss LSM 710). The maximal projection images were then imported into FIJI/ImageJ, and neurite arborization and Sholl analysis [25] were done using the Simple Neurite Tracer plugin [26]. This allows quantification of morphometric features such as dendritic arbor, length, and number of intersections as a function of distances from soma. To analyze spines, Z stacks of spines from the apical dendrites (200–450 μ m from the soma, secondary branches) were collected with a 63× objective (Plan-Apochromat, NA 1.4). Each Z stack was collected at 512 × 512 pixels, with 4× digital zoom and 0.2- μ m Z step size. Imaris software (V8.02, Bitplane, South Windsor, CT) was used to measure spine length, density, and head volume, as we described previously [21, 24].

Statistical Analyses

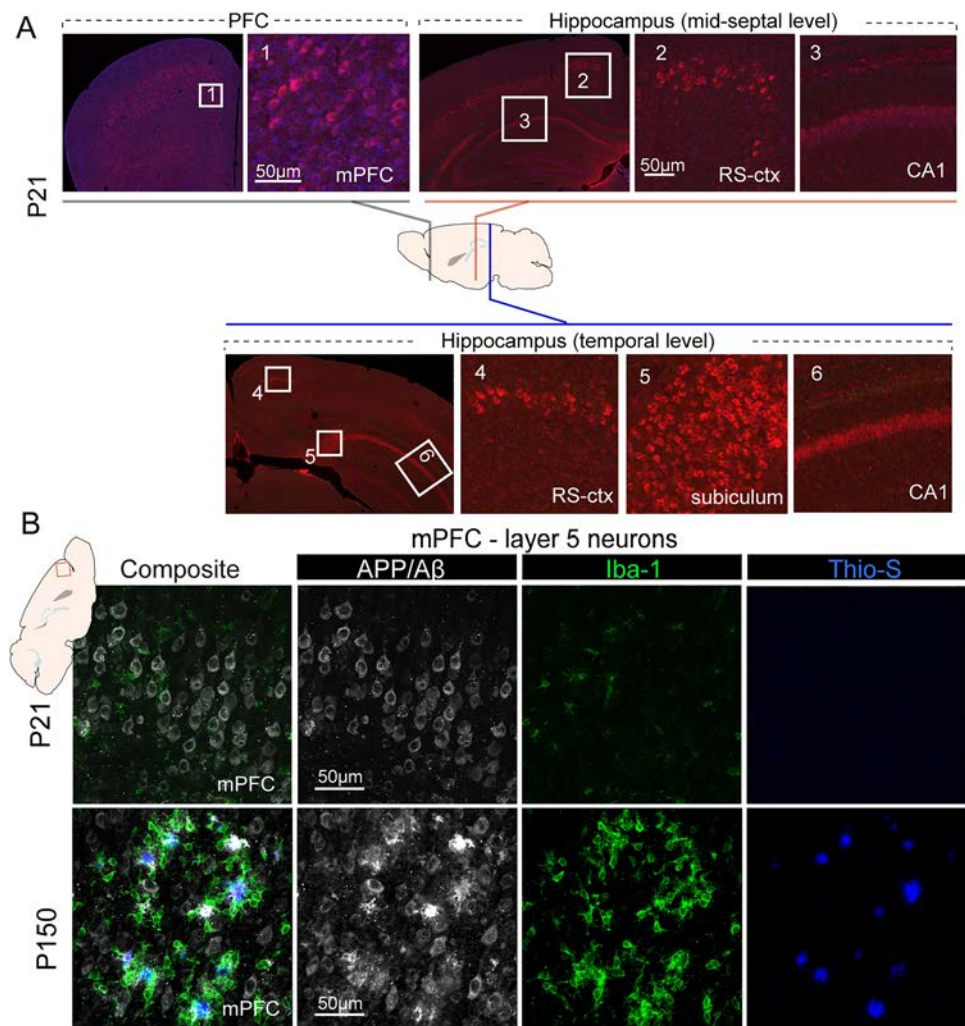
All results are reported as the mean \pm SEM. (standard error of the mean). The experimenters were blinded to genotypes/grouping during data collection and analyses. Sample sizes and numbers of independent experiments were estimated by power analyses using an R script ('pwr' package in CRAN) that takes pre-specified effect size, and type I and II errors as input arguments. Sex-segregated data were first analyzed for potential sex-specific effects, and pooled together for grouped analyses. The Shapiro–Wilk test and *F* test were first applied to test normality and equal variance. For normally-distributed/equal-variance data, Student's *t* test or one/two-way analysis of variation was used; for non-normally distributed/ordinal data types, the nonparametric Mann-Whitney U test or Kolmogorov–Smirnov (K-S) test was used. The K-S test was used to compare the cumulative distributions of mEPSC amplitudes. Statistical analyses and graphing were applied using GraphPad Prism 8.0, Microsoft Excel and MATLAB. Figures were prepared using Adobe Creative Cloud. *P* < 0.05 was considered statistically significant for all tests.

Results

APP/A β Overload in PFC L5 Neurons During Early Postnatal Development

It has been shown that 5XFAD mice exhibit robust A β pathology with onset of extracellular plaque pathology at ~2 months of age, and manifest abundant intraneuronal and plaque-associated changes as early as 3 months of age [7]. Because thy1 promoter-driven transgenic APP/PS1 expression is enriched in cortical L5 neurons and occurs across life span [16, 17], we asked whether the intraneuronal APP/A β load can be detected in cortical L5 neurons at very early developmental stages. We applied IHC staining to detect APP/A β (6E10 antibody) [27], and found that at postnatal day P21, in most cortical regions including the PFC and retrosplenial cortex, L5 neurons showed APP/A β immunoreactivity, which was stronger than in CA1 neurons (Fig. 1A). In addition, we observed strong APP/A β immunoreactivity in the subiculum region in the temporal levels of the hippocampus, consistent with reports that the subiculum is one of earliest structure to show APP/A β deposition [7]. APP/A β overloading in L5 neuron at this early age was associated with a small number of Iba1-positive activated microglia (Fig. 1B). Importantly, at this early age, no extracellular amyloid plaques or Thio-S+ insoluble fibrillar dense core A β deposits were observed. In contrast, PFC L5 neurons in 5-month-old (P150) 5XFAD mice showed extensive APP/A β immunoreactivity, substantial A β plaque deposition that

Fig. 1 Age-dependent transgenic APP/A β overloading and pathology in the PFC. **A** IHC using 6E10 antibody reveals extensive L5 intraneuronal labeling of APP/A β in prefrontal cortex (left) and to a lesser extent, in the retrosplenium cortex (RS-ctx). CA1 neurons also show relatively weaker APP/A β immunoreactivity. In comparison, hippocampal subiculum and CA1 neurons at the temporal levels along the septo-temporal axis show stronger APP/A β immunoreactivity. **B** Triple IHC staining of APP/A β , Iba1, and Thio-S to label amyloid deposition, reactive microglia, and dense-core fibrillar amyloid plaques. L5 neurons of P21 PFC show strong intracellular APP/A β labeling, with minimum reactive microglia and no Thio-S+ plaque deposition. In contrast, L5 neurons from P150 mPFC show strong extracellular amyloid deposition with dense Thio-S+ fibrillar A β cores that are surrounded by large numbers of Iba1+ reactive microglia.



was surrounded by clustered Iba-1+ reactive microglia, and profound Thio-S-labeled dense-core fibrillar amyloid deposits (Fig. 1B). Notably, the APP/A β intracellular overloading in PFC-L5 neurons was also seen at earlier ages (P11 and P14, data not shown), indicating that transgenic expression of mutant APP/PS1 is a continuous process that spans early cortical development.

Decreased Intrinsic Excitability in PFC-L5 Neurons

The early APP/A β overloading in PFC-L5 neurons justified investigation on the functional alterations in these affected neurons. We conducted whole-cell patch-clamp recording in PFC-L5 pyramidal neurons to probe potential functional alterations. Parasagittal brain slices containing the PFC were prepared from P22–28 5XFAD mice and their WT littermate controls. We first measured the membrane properties of L5 neurons (Fig. 2A), and found that 5XFAD neurons had similar input resistance (WT, 280.5 ± 20.4 M Ω ; 5XFAD, 310.3 ± 19.6 M Ω , $t_{16} = 1.03$, $P = 0.32$) and membrane capacitance

(WT, 66.6 ± 3.2 pF; 5XFAD, 66.9 ± 3.6 pF, $t_{16} = 0.05$, $P = 0.96$). 5XFAD PFC-L5 neurons did not show a change in action potential (AP) spike frequency adaptation (Fig. 2B. WT, 0.82 ± 0.03 ; 5XFAD, 0.81 ± 0.02 , $t_{13} = 0.23$, $P = 0.83$). In addition, neurons from both groups exhibited a similar AP half-width (Fig. 2C. WT, 1.34 ± 0.04 ms; 5XFAD, 1.38 ± 0.04 ms, $t_{14} = 0.69$, $P = 0.50$), and the slope of AP depolarization/repolarization, as evidenced by the overlapping 95% confidence intervals of the phase plot (dV/dt vs Vm).

PFC-L5 neurons from 5XFAD and WT brain slices were next injected with current steps from -100 to 500 pA in 50 -pA increment to test their intrinsic excitability. Fig. 2D shows two representative AP firing responses from WT and 5XFAD neurons in response to each current step injection. Comparing the responses from all neurons (WT, $n = 4$; 5XFAD, $n = 4$) revealed that 5XFAD neurons were intrinsically less excitable, with a smaller number of AP responses to current steps (Fig. 2E. Repeated measures two-way ANOVA, genotype effects: $F_{(1,6)} = 10.9$, $P = 0.016$). For both 5XFAD and WT control neurons, a representative

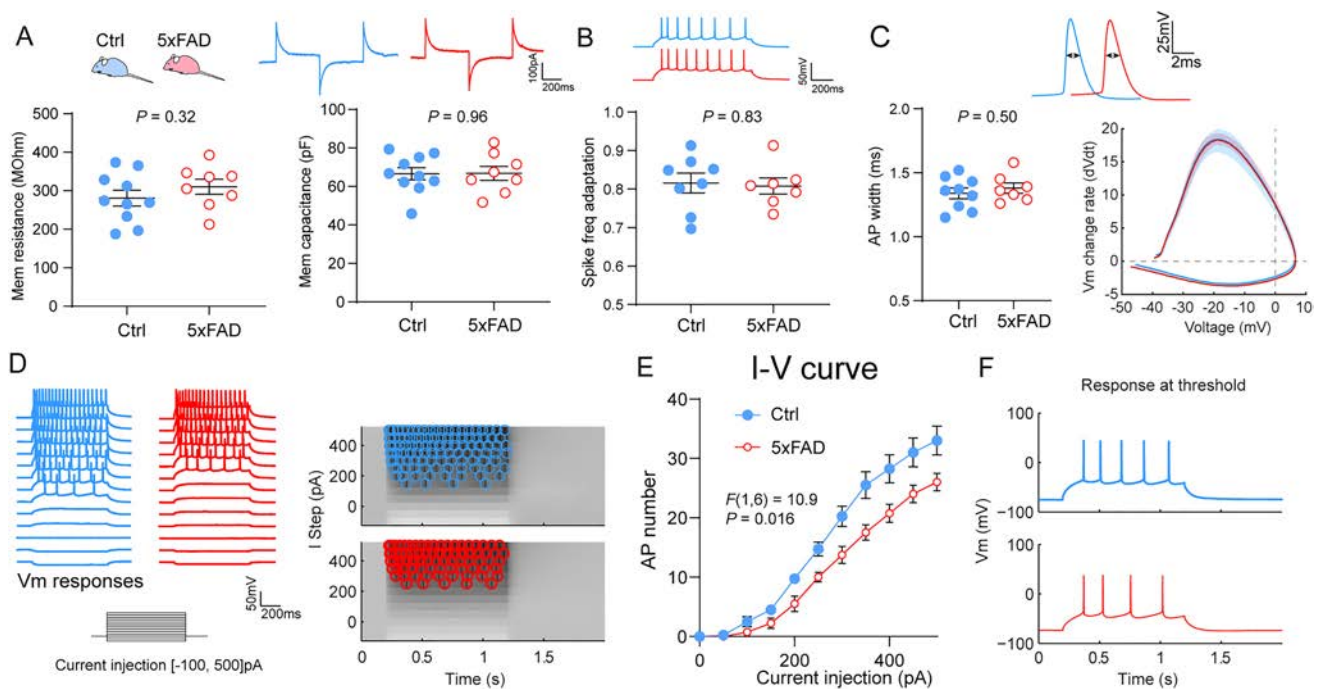


Fig. 2 PFC-L5 neurons in 5XFAD mice exhibit reduced intrinsic excitability. **A** Compared with control littermate neurons, PFC-L5 neurons from 5XFAD brain slices show similar membrane input resistance ($t_{16} = 1.03$, $P = 0.32$) and membrane capacitance ($t_{16} = 0.05$, $P = 0.96$). Representative current responses to voltage steps are shown above, based on which membrane properties were calculated. **B** 5XFAD PFC-L5 neurons exhibit similar spike frequency adaptation ($t_{13} = 0.23$, $P = 0.83$). **C** 5XFAD neurons show similar action potential half-width ($t_{14} = 0.69$, $P = 0.50$), and the slope of AP depo-

larization/repolarization, as evidenced by the overlapping 95% confidence intervals of the phase plot (dV/dt vs Vm). **D** Representative intrinsic excitability responses and AP density plot from control and 5XFAD neurons in response to current-step injections (-100 to 500 pA) at 50-pA increments. **E** Pooled data demonstrate that 5XFAD neurons show significantly lower firing rates (genotype effects: $F(1,6) = 10.9$, $P = 0.016$. Repeated measures two-way ANOVA). **F** Representative AP firing responses to threshold current step injection in control and 5XFAD neurons.

AP firing response to threshold current step injection is presented in Fig. 2F. These data indicate that PFC-L5 neurons in 5XFAD slices are intrinsically less excitable as a result of developmental transgenic overexpression of mutant APP/PS1.

Reduced Excitatory Synaptic Transmission in PFC-L5 Neurons at 3–4 Weeks Age

We next asked whether developmental intracellular APP/A β overloading changes the synaptic activity of PFC-L5 neurons at an early post-weaning age. Whole-cell patch-clamp recording was used to first measure miniature excitatory postsynaptic currents (mEPSC) in slices prepared from P22–28 5XFAD and WT littermate mice. Representative mEPSC traces from both groups are shown in Fig. 3A, which also revealed a decreased averaged mEPSC amplitude in 5XFAD neurons. Pooled responses showed that 5XFAD neurons exhibited an overall lower amplitude of mEPSC (Fig. 3B), evidenced by both percentage distribution of the varying mEPSC amplitude bins, and the normalized cumulative distribution curve (number of

mEPSC events: WT, $n = 1244/12$ cells/6 mice; 5XFAD, $n = 1165/10$ cells/5 mice. K-S test, $D = 0.14$, $P < 0.0001$). In addition, 5XFAD neurons showed a significantly lower mEPSC frequency (Fig. 3C. Events/sec: WT, 3.72 ± 0.38 ; 5XFAD, 2.48 ± 0.28 , $P = 0.018$). We next recorded miniature inhibitory postsynaptic currents (mIPSCs) in a different set of PFC slices, and found that mIPSC amplitude was largely unaltered in 5XFAD (Fig. 3D), as shown by the percentage and cumulative distribution across varying mIPSC amplitude bins (Fig. 3E. Number of mIPSCs analyzed: WT, $n = 1244/7$ cells/4 mice; 5XFAD, $n = 1657/9$ cells/5 mice. K-S test on cumulative distribution: $D = 0.05$, $P = 0.79$). Interestingly, we found a significant reduction of mIPSC frequency (Fig. 3F. Events/s: WT, 3.44 ± 0.32 ; 5XFAD, 2.23 ± 0.36 . $t_{18} = 2.54$, $P = 0.02$). These data indicate alteration of both excitatory and inhibitory inputs onto PFC-L5 neurons in 5XFAD mice at an early post-weaning age.

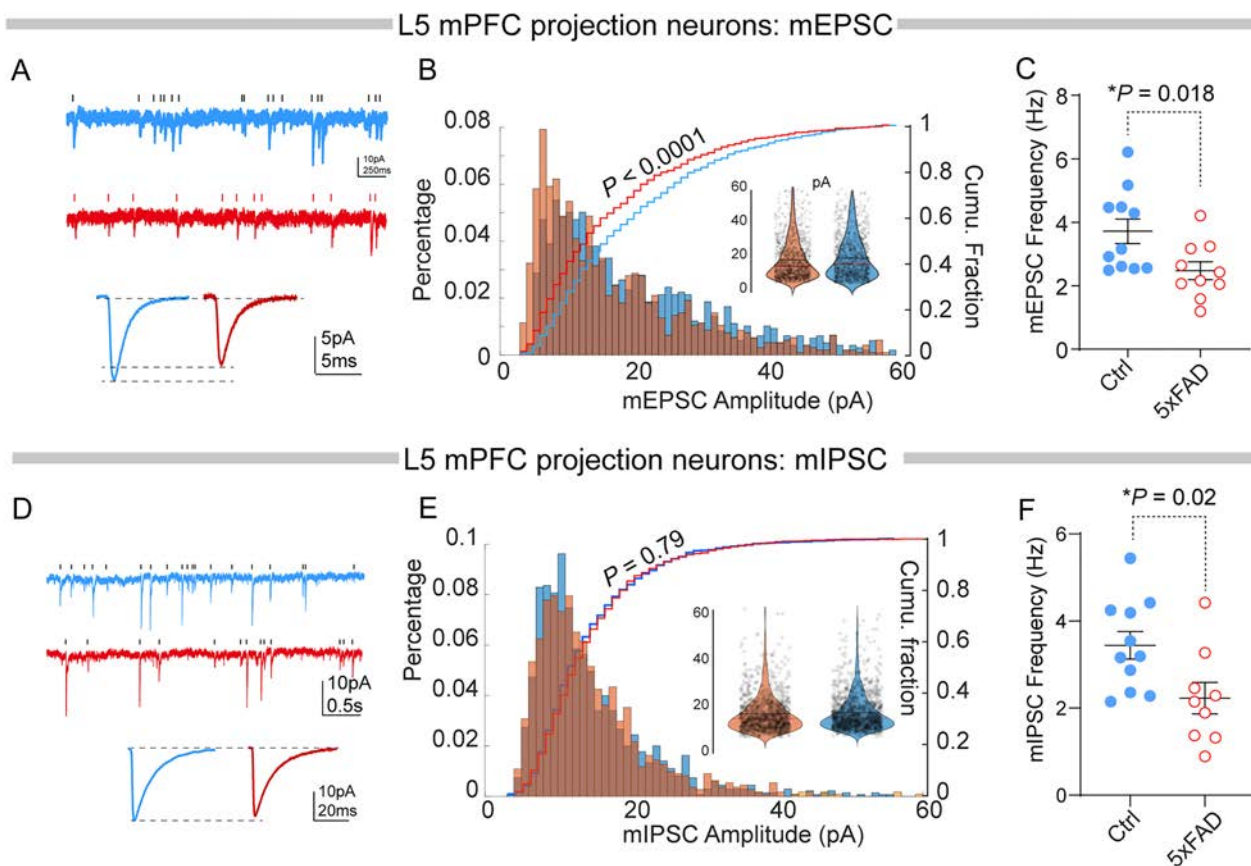


Fig. 3 Altered spontaneous synaptic mEPSC and mIPSC responses in PFC-L5 neurons at an early post-weaning age. **A** Representative whole-cell patch-clamp recording of spontaneous mEPSCs from 5XFAD and control neurons. **B** Quantification of all recorded mEPSC events. mEPSC amplitudes from 5XFAD neurons are distributed more to the smaller amplitude bins. There was also a significant difference between the cumulative distribution curves (K-S test, $D = 0.14$, $***P < 0.0001$). Inset, violin plot of pooled mEPSC

amplitudes from both groups. **C** mEPSC frequency in 5XFAD PFC-L5 neurons is significantly reduced ($*P = 0.018$). **D** Representative traces of spontaneous mIPSCs from 5XFAD and control neurons. **E** 5XFAD and control neurons show a similar percentage distribution and cumulative distribution of all analyzed mIPSC amplitudes. No significant difference in the cumulative distribution curves was found (K-S test, $P = 0.79$). **F** 5XFAD neurons show a significant reduction in mIPSC frequency ($t_{18} = 2.54$, $P = 0.02$).

Decreased Dendritic Spine Size and Density in mPFC-L5 Neurons

We next asked whether the changes in synaptic responses have a morphological correlate. We analyzed anatomical changes of the dendritic structure and spines in PFC-L5 neurons from both WT and 5XFAD mice at P22–28. L5 neuron morphology was revealed by biocytin injection during whole-cell recording (Fig. 4A), followed by imaging of the dendritic structure and confocal Z-stack images of spines. Sholl analysis of dendritic arborization revealed that 5XFAD did not affect the number of dendritic intersections as a function of distance from the soma (Fig. 4B. Main group effect: $F_{(1, 15)} = 2.93$, $P = 0.11$, two-way ANOVA), nor did it affect the dendritic length distribution (Fig. 4C. Main group effect: $F_{(1, 15)} = 0.033$, $P = 0.86$, two-way ANOVA). However, 5XFAD neurons exhibited a reduced dendritic spine density (Fig. 4D, E. Number of spines/10 μm : WT, $12.52 \pm$

0.45 ; 5XFAD, 10.8 ± 0.37 . $t_{21} = 2.89$, $P = 0.008$). In comparison, the spine length of 5XFAD neurons did not differ (Fig. 4F. Average length in μm : WT, 2.06 ± 0.13 ; 5XFAD, 2.20 ± 0.17 . $t_{21} = 0.69$, $P = 0.49$). We next quantified the spine head volume and found that 5XFAD neurons showed a significant reduction (Fig. 4G. WT, $n = 274$ spines/6 neurons/6 mice; 5XFAD, $n = 258$ spines/7 neurons/5 mice. $D = 0.286$, $P < 0.0001$, K-S test). These data were consistent with the decreased mEPSC amplitude and frequency, and further suggest impaired synaptic function in the PFC at a very early development age.

Altered Synaptic Glutamate Receptor Content in PFC-L5 Neurons

Considering that dendritic spine size and geometry are known to be correlated with glutamate receptor content and functional maturity [28], we asked whether PFC-L5 neurons

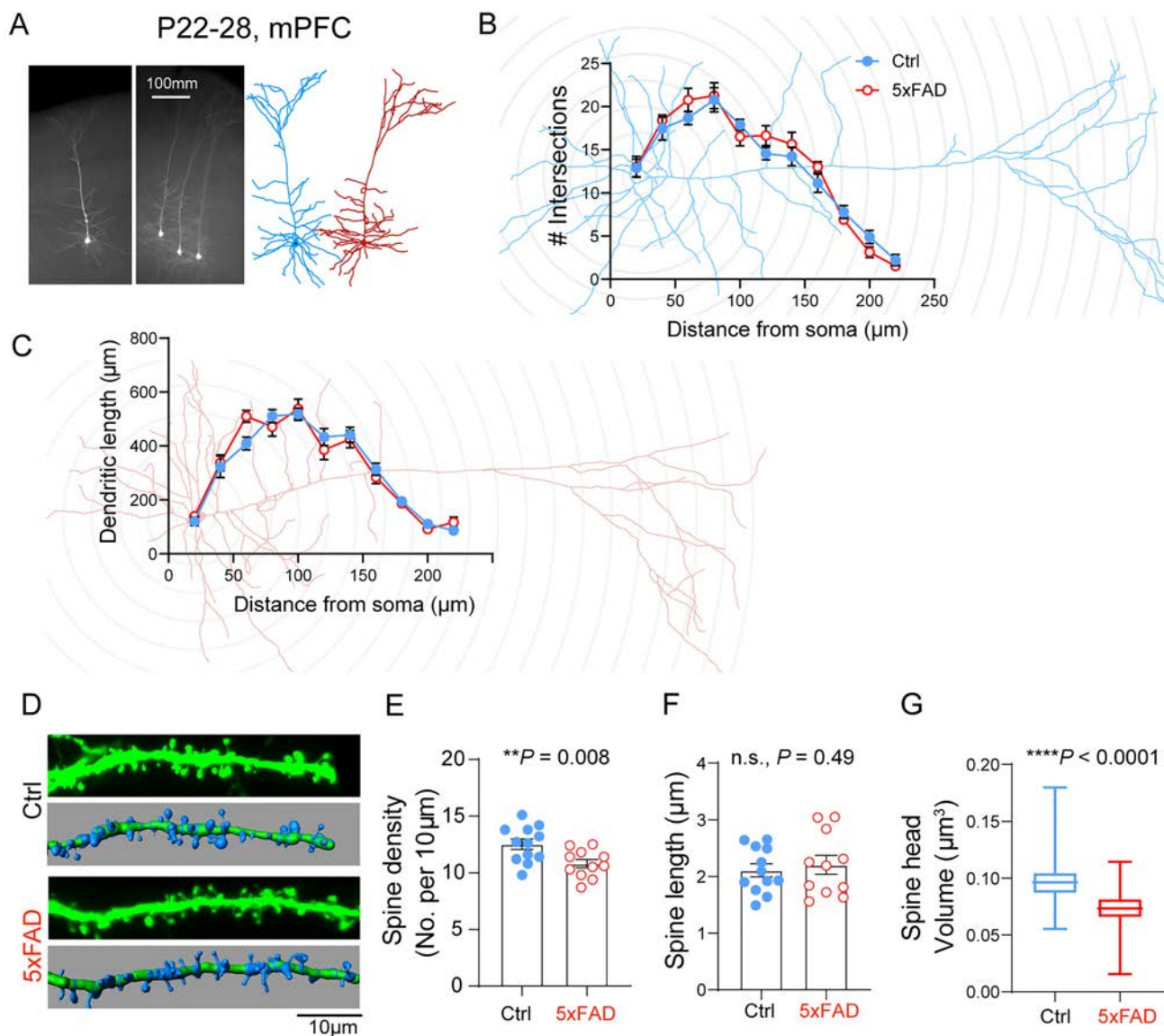


Fig. 4 Reduced dendritic spine size and density in PFC-L5 neurons in the early post-weaning period. **A** Dendritic morphology in L5 PFC neurons using avidin-Alexa 488 following whole-cell patch-clamp recordings. **B** Sholl analyses of the number of intersections of the PFC-L5 neuron dendritic arbors in control and 5XFAD neurons. No statistically significant differences if genotype were found ($P = 0.107$, two-way ANOVA). Note distal arbors are not included for analysis due to cutoff of some neurons. **C** Sholl analyses of dendritic length distribution. No significant difference was found for the dendritic length as

a function of distance from soma between control and 5XFAD neurons ($F(1, 15) = 0.033$; $P = 0.86$ for main group effects). **D** Representative dendritic spines from control and 5XFAD PFC-L5 pyramidal neuron apical dendrites. **E** 5XFAD neurons show decreased spine density ($**P = 0.008$). **F** 5XFAD neurons do not differ in spine length ($P = 0.49$). **G** Cumulative distribution of spine head volume. Spine head volume from 5XFAD neurons is significantly reduced ($****P < 0.0001$, K-S test).

show changes of synaptic glutamate receptors. We first biotinylated the surface protein in parasagittal PFC slices, as described previously [29], then prepared crude synaptosome fractions using the biotinylated slices. Neutravidin beads were used to pull down the synaptic surface proteins. Total proteins were also probed using the crude synaptosome fraction without neutravidin pulldown (Fig. 5A). We found a significant reduction of AMPAR subunit GluA1 and the NMDA

receptor subunit GluN2A. In comparison, the NMDA receptor subunit GluN2B was slightly increased. None of these changes, however, was observed using total synaptosome proteins (Fig. 5B). Quantification of these Western blot results (Fig. 5C) confirmed statistically significant decreases in GluA1 ($t_6 = 4.8$, $P = 0.003$) and GluN2A ($t_6 = 4.1$, $P = 0.007$). There was no statistical change in GluN1 ($t_6 = 0.41$, $P = 0.69$), but a marginal increase in GluN2B ($t_6 = 1.8$, P

= 0.12). These biochemical measures of synaptic glutamate receptor content further support the hypothesis that dendritic spine maturation is impaired at this age.

Impaired Functional Maturation of the PFC L2/3>L5 Circuits in 5XFAD Mice

Based on the changes in synaptic glutamate receptor content, we made whole-cell patch-clamp recordings to measure several parameters related to excitatory synapse maturation. PFC-L5 pyramidal neurons were first voltage-clamped at -70 mV, and monosynaptic responses to L23 stimulation were recorded. Neurons were then clamped at $+40$ mV to record compound AMPA/NMDA receptor responses. Quantification of pooled recordings revealed a significantly reduced AMPA/NMDA receptor current ratio (Fig. 6A. WT, 1.43 ± 0.06 ; 5XFAD, 1.16 ± 0.07 . $t_{18} = 2.97$, $P = 0.008$), indicating impairment of synaptic transmission or synapse maturation. Cortical excitatory synapse maturation often entails activity-dependent AMPA receptor acquisition at synaptic sites that initially contain only NMDARs (silent synapses) [20, 30, 31] so that these synapses can be rendered functional. Impaired maturation can thus manifest as an increased number of silent synapses. Using a minimum stimulation protocol, we tested the proportions of silent synapses in WT and 5XFAD PFC-L5 neurons. A representative response to minimum stimulation from both groups of neurons at -70 mV and $+40$ mV holding potential is shown in Fig. 6B. Pooled data from multiple trials revealed that both WT and 5XFAD neurons showed an increased success rate of transmission (i.e., reduction in failure rate) at $+40$ mV compared to -70 mV (Fig. 6C). When failure rates were compared from all recorded neurons, it was found that

5XFAD neurons exhibited a larger difference in failure rates between the two holding potentials (Fig. 6D. WT, 17.5 ± 1.7 ; 5XFAD, 25.3 ± 2.9 . $t_{14} = 2.26$, $P = 0.03$), confirming a higher proportion of immature silent synapses on 5XFAD PFC-L5 neurons.

Discussion

In this study, we present evidence on synaptic deficits in 5XFAD mice in the early post-weaning period that indicates altered intrinsic excitability, excitatory and inhibitory synaptic inputs, functional synapse maturation, and morphological perturbations in PFC projection neurons. Collectively, our data suggest the transgenic mutant APP/PS1 expression in a commonly studied AD mouse model [7, 32] perturbs the early developmental trajectory of the cortical circuit. The main focus was not to exhaustively pursue age-dependent pathological or electrophysiological changes, but rather to focus on L5 PFC neurons at a very early age and uncover potential circuit impairment using sensitive physiological and morphological measures. To the best of our knowledge, this study reports the earliest synaptic function and connectivity changes in 5XFAD mice in a major PFC projection neuron population. Our data demonstrate that mutant forms of APP/PS1 and likely the associated A β production [33] could have neurodevelopmental sequelae featuring disrupted early synapse development and maturation.

Our study also has a few limitations: first, only an early post-weaning age was examined, based on the early APP/A β overloading in the vulnerable L5 neuron population. It is unclear whether the synaptic pathology is transient, or persist and progress into adulthood. Second, the study focuses

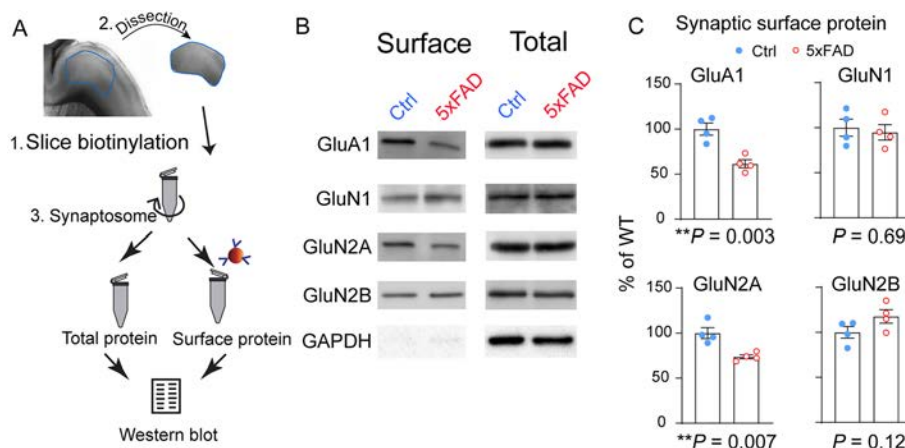
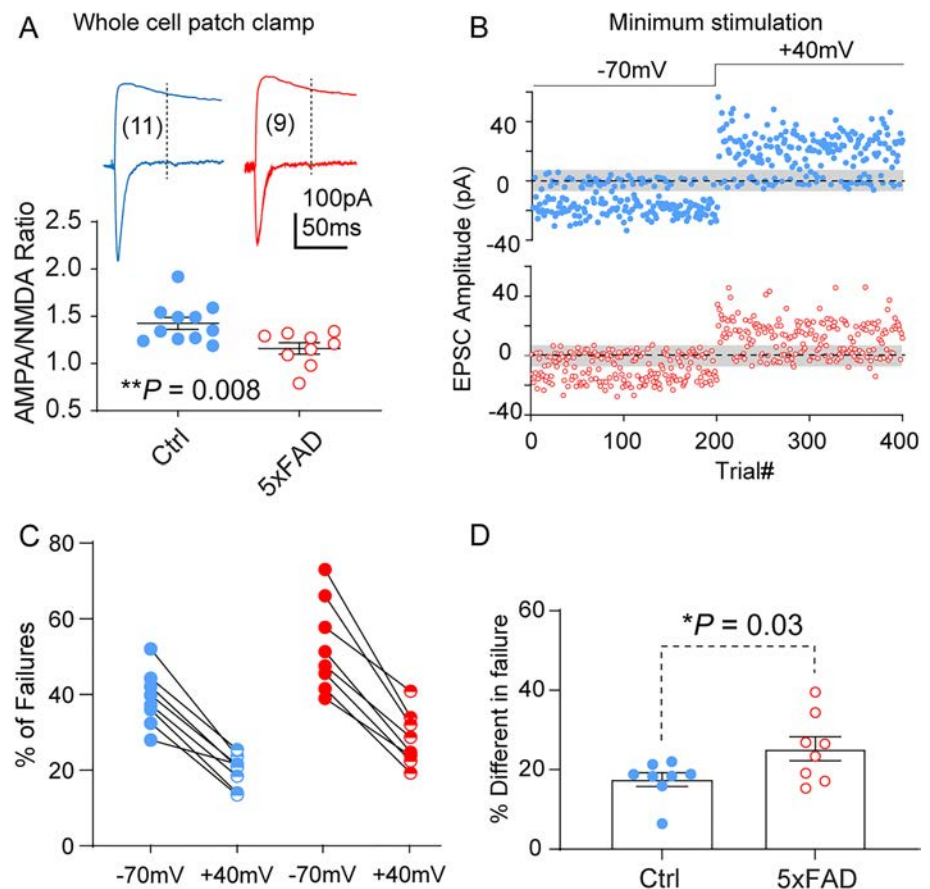


Fig. 5 Altered synaptic glutamate receptor content in 5XFAD L5 neurons (P22–28). **A** Schematic of dissecting PFC tissue after slice biotinylation, followed by crude synaptosome fraction preparation and synaptic surface protein isolation. **B** Representative Western blot results of synaptic surface and total synaptosome glutamate receptors:

GluA1, GluN1, GluN2A, and GluN2B. **C** Quantification of Western blot results. 5XFAD PFC-L5 tissue shows reduced synaptic surface GluA1 (** $P = 0.003$) and GluN2A (** $P = 0.007$). There is a slight but non-significant increase in GluN2B ($P = 0.12$) and no difference in GluN1 ($P = 0.69$).

Fig. 6 5XFAD PFC-L5 neurons show a decreased AMPA/NMDA current ratio and increased number of silent synapses at P22–28. **A** AMPA/NMDA receptor current ratio is significantly reduced in 5XFAD neurons ($t_{18} = 2.97$, $**P = 0.008$). **B** Representative responses of 5XFAD and control L5 neurons to consecutive trials in response to minimum stimulation of L2/3. Shaded patch centered on 0pA indicates RMS noise. Neurons had 200 trials at -70 mV holding potential followed by 200 trials at $+40$ mV. **C** Quantification of failure rates at -70 mV and $+40$ mV holding potentials in control and 5XFAD neurons. **D** 5XFAD neurons exhibit a larger difference in failure rates between the two holding potentials ($*P = 0.03$).



on one neuronal type and brain region, i.e., L5 neurons in the PFC. It is unclear how other neuronal types, the broader network activity, and even early behavior may be affected. Third, the implication of these findings on *adult* circuit function and age-dependent pathology remain to be studied. Nevertheless, our data indicate that certain circuit- and behavior-level deficits in adult and aging mice [7, 9, 34, 35] involve potential developmental perturbations in vulnerable neuronal populations, such as the L5 neurons across cortical regions.

Using immunohistochemical staining, we have shown that PFC-L5 neurons exhibit increased intracellular APP/A β loading at P21 (and earlier at P11–14, data not shown). Similarly, another vulnerable cortical population in terms of APP/A β overloading is the subiculum neurons of the temporal hippocampus, in which functional changes remain to be investigated at this age. Because the 6E10 antibody does not distinguish between APP and A β [36, 37], we cannot attribute these synaptic and circuit connectivity changes to APP or to intracellular A β production, which may be present at this age [33, 38]. Yet, our IHC staining revealed minimum microglial activation at P21, and there was no extracellular amyloid or dense-core fibrillar A β plaques in extracellular space. It is therefore less likely that physical loss of L5 neurons or synapses occurs at this early age. It has

been reported that cortical L5 neurons are among the first neuronal populations that develop synaptic pathology [7, 9, 11], which is consistent with our recordings of decreased spontaneous mEPSC frequency and amplitude, a higher threshold for firing of APs, altered chemical composition of glutamate receptors, and increased silent synapses indicating less maturation at this early post-weaning age.

It is unclear how mutant APP/PS1 over-expression affects synaptic function in the developing brain and how the detrimental effects evolve with age. APP family members are posited to be involved in nervous system development, synaptogenesis, axon guidance and growth, formation of the neuromuscular junction, and establishing dendritic complexity and spines. They also contribute to synaptic functions, including synaptic plasticity, and learning and memory [39–42]. However, neurophysiological data exploring the effects of transgenic APP/PS1 on PFC circuit function are rather limited. Yet, the PFC is a primary and early target that develops AD pathology [43–45]. Transgenic mutant APP/PS1 in the developing cortical circuits may disrupt a myriad of physiological functions in neurons, including endo-lysosomal trafficking [46, 47], intracellular cargo transport [48], molecular signaling [49, 50], or neurotransmitter release [51] that collectively contribute to failure of synapse development and activity-dependent maturation.

In summary, our study revealed that synaptic function changes occur at an early post-weaning age in the 5XFAD mouse model. Our work supports the prevailing view of early intervention in AD at the cellular and circuit levels [52]. We provide detailed physiological characterization of PFC-L5 neurons, which is among the earliest affected cell types as a result of mutant APP/PS1. These functional disruptions suggest that transgenic mutant APP/PS1 overexpression has a profound effect on developing cortical circuits, and changes in neuronal function may instigate a life-long process that impacts neuronal degeneration at later ages. Therefore, although AD is considered a disease of old age, subtle neurological defects conferred by genetic mutations or risk factors may emerge early in life. This thought-provoking hypothesis justifies further studies to extend the limited scope of the current work.

Acknowledgements This work was supported by institutional startup funding from the University of Arizona (to SQ).

Data Availability The data used to support the findings of this study are available from the corresponding author upon reasonable request.

Conflict of interest The authors declare no conflict of interests.

References

- De-Paula VJ, Radanovic M, Diniz BS, Forlenza OV. Alzheimer's disease. *Subcell Biochem* 2012, 65: 329–352.
- Gómez-Isla T, Frosch MP. Lesions without symptoms: Understanding resilience to Alzheimer disease neuropathological changes. *Nat Rev Neurol* 2022, 18: 323–332.
- Soria Lopez JA, González HM, Léger GC. Alzheimer's disease. *Handb Clin Neurol* 2019, 167: 231–255.
- Ying Y, Wang JZ. Illuminating neural circuits in Alzheimer's disease. *Neurosci Bull* 2021, 37: 1203–1217.
- Duyckaerts C, Potier MC, Delatour B. Alzheimer disease models and human neuropathology: Similarities and differences. *Acta Neuropathol* 2008, 115: 5–38.
- Long X, Tao Y, Chen XC, Deng B, Cai J, Zhang SJ. Getting lost: Place cells and grid cells in rodent models of Alzheimer's disease. *Neurosci Bull* 2021, 37: 894–897.
- Oakley H, Cole SL, Logan S, Maus E, Shao P, Craft J. Intraneuronal beta-amyloid aggregates, neurodegeneration, and neuron loss in transgenic mice with five familial Alzheimer's disease mutations: Potential factors in amyloid plaque formation. *J Neurosci* 2006, 26: 10129–10140.
- Oh SJ, Lee HJ, Kang KJ, Han SJ, Lee YJ, Lee KC, *et al.* Early detection of A β deposition in the 5xFAD mouse by amyloid PET. *Contrast Media Mol Imaging* 2018, 2018: 5272014.
- Richard BC, Kurdakova A, Baches S, Bayer TA, Weggen S, Wirths O. Gene dosage dependent aggravation of the neurological phenotype in the 5XFAD mouse model of Alzheimer's disease. *J Alzheimers Dis* 2015, 45: 1223–1236.
- Kimura R, Ohno M. Impairments in remote memory stabilization precede hippocampal synaptic and cognitive failures in 5XFAD Alzheimer mouse model. *Neurobiol Dis* 2009, 33: 229–235.
- Buskila Y, Crowe SE, Ellis-Davies GCR. Synaptic deficits in layer 5 neurons precede overt structural decay in 5xFAD mice. *Neuroscience* 2013, 254: 152–159.
- Tible M, Mouton Liger F, Schmitt J, Giralt A, Farid K, Thomasseau S, *et al.* PKR knockout in the 5xFAD model of Alzheimer's disease reveals beneficial effects on spatial memory and brain lesions. *PKR knockout in the 5xFAD model of Alzheimer's disease reveals beneficial effects on spatial memory and brain lesions*. *Aging Cell* 2019, 18: e12887
- Angel A, Volkman R, Royal TG, Offen D. Caspase-6 knockout in the 5xFAD model of Alzheimer's disease reveals favorable outcome on memory and neurological hallmarks. *Int J Mol Sci* 2020, 21: 1144.
- Martorell AJ, Paulson AL, Suk HJ, Abdurrob F, Drummond GT, Guan W, *et al.* Multi-sensory gamma stimulation ameliorates Alzheimer's-associated pathology and improves cognition. *Cell* 2019, 177: 256–271.e22.
- Seo J, Giusti-Rodríguez P, Zhou Y, Rudenko A, Cho S, Ota KT, *et al.* Activity-dependent p25 generation regulates synaptic plasticity and β -induced cognitive impairment. *Cell* 2014, 157: 486–498.
- Feng G, Mellor RH, Bernstein M, Keller-Peck C, Nguyen QT, Wallace M, *et al.* Imaging neuronal subsets in transgenic mice expressing multiple spectral variants of GFP. *Neuron* 2000, 28: 41–51.
- Bradley JE, Ramirez G, Hagood JS. Roles and regulation of Thy-1, a context-dependent modulator of cell phenotype. *Biofactors* 2009, 35: 258–265.
- Qiu S, Anderson CT, Levitt P, Shepherd GMG. Circuit-specific intracortical hyperconnectivity in mice with deletion of the autism-associated Met receptor tyrosine kinase. *J Neurosci* 2011, 31: 5855–5864.
- Terashima A, Pelkey KA, Rah JC, Suh YH, Roche KW, Collingridge GL, *et al.* An essential role for PICK1 in NMDA receptor-dependent bidirectional synaptic plasticity. *Neuron* 2008, 57: 872–882.
- Liao D, Hessler NA, Malinow R. Activation of postsynaptically silent synapses during pairing-induced LTP in CA1 region of hippocampal slice. *Nature* 1995, 375: 400–404.
- Qiu S, Lu Z, Levitt P. MET receptor tyrosine kinase controls dendritic complexity, spine morphogenesis, and glutamatergic synapse maturation in the hippocampus. *J Neurosci* 2014, 34: 16166–16179.
- Qiu S, Weeber EJ. Reelin signaling facilitates maturation of CA1 glutamatergic synapses. *J Neurophysiol* 2007, 97: 2312–2321.
- Qiu S, Zhao LF, Korwek KM, Weeber EJ. Differential reelin-induced enhancement of NMDA and AMPA receptor activity in the adult hippocampus. *J Neurosci* 2006, 26: 12943–12955.
- Peng Y, Lu Z, Li G, Piechowicz M, Anderson M, Uddin Y, *et al.* The autism-associated MET receptor tyrosine kinase engages early neuronal growth mechanism and controls glutamatergic circuits development in the forebrain. *Mol Psychiatry* 2016, 21: 925–935.
- Sholl DA. Dendritic organization in the neurons of the visual and motor cortices of the cat. *J Anat* 1953, 87: 387–406.
- Longair MH, Baker DA, Armstrong JD. Simple Neurite Tracer: Open source software for reconstruction, visualization and analysis of neuronal processes. *Bioinformatics* 2011, 27: 2453–2454.
- Herzig MC, Winkler DT, Burgermeister P, Pfeifer M, Kohler E, Schmidt SD, *et al.* A β is targeted to the vasculature in a mouse model of hereditary cerebral hemorrhage with amyloidosis. *Nat Neurosci* 2004, 7: 954–960.
- Matsuzaki M, Ellis-Davies GCR, Nemoto T, Miyashita Y, Iino M, Kasai H. Dendritic spine geometry is critical for AMPA receptor expression in hippocampal CA1 pyramidal neurons. *Nat Neurosci* 2001, 4: 1086–1092.

29. Qiu S, Korwek KM, Pratt-Davis AR, Peters M, Bergman MY, Weeber EJ. Cognitive disruption and altered hippocampus synaptic function in Reelin haploinsufficient mice. *Neurobiol Learn Mem* 2006, 85: 228–242.
30. Huang YH, Lin Y, Mu P, Lee BR, Brown TE, Wayman G, *et al.* *In vivo* cocaine experience generates silent synapses. *Neuron* 2009, 63: 40–47.
31. Isaac JTR, Nicoll RA, Malenka RC. Evidence for silent synapses: Implications for the expression of LTP. *Neuron* 1995, 15: 427–434.
32. Holcomb L, Gordon MN, McGowan E, Yu X, Benkovic S, Jantzen P, *et al.* Accelerated Alzheimer-type phenotype in transgenic mice carrying both mutant amyloid precursor protein and presenilin 1 transgenes. *Nat Med* 1998, 4: 97–100.
33. William CM, Andermann ML, Goldey GJ, Roumis DK, Reid RC, Shatz CJ, *et al.* Synaptic plasticity defect following visual deprivation in Alzheimer's disease model transgenic mice. *J Neurosci* 2012, 32: 8004–8011.
34. Forner S, Kawauchi S, Balderrama-Gutierrez G, Kramár EA, Matheos DP, Phan J, *et al.* Systematic phenotyping and characterization of the 5xFAD mouse model of Alzheimer's disease. *Sci Data* 2021, 8: 270.
35. Oblak AL, Lin PB, Kotredes KP, Pandey RS, Garceau D, Williams HM, *et al.* Comprehensive evaluation of the 5XFAD mouse model for preclinical testing applications: A MODEL-AD study. *Front Aging Neurosci* 2021, 13: 713726.
36. Huwait EA, Baghallab IM, Glabe CG, Abulnaja KO, Kumosani TA, Moselhy SS. Identification of amyloid antibodies for Alzheimer disease-immunotherapy. *Arch Physiol Biochem* 2020, <https://doi.org/10.1080/13813455.2020.1767147>.
37. Droste P, Frenzel A, Steinwand M, Pelat T, Thullier P, Hust M, *et al.* Structural differences of amyloid- β fibrils revealed by antibodies from phage display. *BMC Biotechnol* 2015, 15: 57.
38. William CM, Stern MA, Pei X, Saqran L, Ramani M, Frosch MP, *et al.* Impairment of visual cortical plasticity by amyloid-beta species. *Neurobiol Dis* 2021, 154: 105344.
39. Benitez DP, Jiang S, Wood J, Wang R, Hall CM, Peerboom C, *et al.* Knock-in models related to Alzheimer's disease: Synaptic transmission, plaques and the role of microglia. *Mol Neurodegener* 2021, 16: 47.
40. Müller UC, Deller T, Korte M. Not just amyloid: Physiological functions of the amyloid precursor protein family. *Nat Rev Neurosci* 2017, 18: 281–298.
41. Probst S, Krüger M, Kägi L, Thöni S, Schuppli D, Nitsch RM, *et al.* Fe65 is the sole member of its family that mediates transcription regulated by the amyloid precursor protein. *J Cell Sci* 2020, 133: jcs242917.
42. Steubler V, Erdinger S, Back MK, Ludewig S, Fässler D, Richter M, *et al.* Loss of all three APP family members during development impairs synaptic function and plasticity, disrupts learning, and causes an autism-like phenotype. *EMBO J* 2021, 40: e107471.
43. Xu P, Chen A, Li Y, Xing X, Lu H. Medial prefrontal cortex in neurological diseases. *Physiol Genomics* 2019, 51: 432–442.
44. Bazzigaluppi P, Beckett TL, Koletar MM, Lai AY, Joo IL, Brown ME, *et al.* Early-stage attenuation of phase-amplitude coupling in the hippocampus and medial prefrontal cortex in a transgenic rat model of Alzheimer's disease. *J Neurochem* 2018, 144: 669–679.
45. Har-Paz I, Roisman N, Michaelson DM, Moran A. Extra-hippocampal learning deficits in young apolipoprotein E4 mice and their synaptic underpinning. *J Alzheimers Dis* 2019, 72: 71–82.
46. Kepp KP. Alzheimer's disease due to loss of function: A new synthesis of the available data. *Prog Neurobiol* 2016, 143: 36–60.
47. Maulik M, Peake K, Chung J, Wang Y, Vance JE, Kar S. APP overexpression in the absence of NPC1 exacerbates metabolism of amyloidogenic proteins of Alzheimer's disease. *Hum Mol Genet* 2015, 24: 7132–7150.
48. Bhalla A, Vetanovetz CP, Morel E, Chamoun Z, di Paolo G, Small SA. The location and trafficking routes of the neuronal retromer and its role in amyloid precursor protein transport. *Neurobiol Dis* 2012, 47: 126–134.
49. Xie CW. Calcium-regulated signaling pathways: Role in amyloid beta-induced synaptic dysfunction. *Neuromolecular Med* 2004, 6: 53–64.
50. Woods NK, Padmanabhan J. Neuronal calcium signaling and Alzheimer's disease. *Adv Exp Med Biol* 2012, 740: 1193–1217.
51. Ari C, Borysov SI, Wu J, Padmanabhan J, Potter H. Alzheimer amyloid beta inhibition of Eg5/kinesin 5 reduces neurotrophin and/or transmitter receptor function. *Neurobiol Aging* 2014, 35: 1839–1849.
52. Fan DY, Wang YJ. Early intervention in Alzheimer's disease: How early is early enough? *Neurosci Bull* 2020, 36: 195–197.

Springer Nature or its licensor holds exclusive rights to this article under a publishing agreement with the author(s) or other rightsholder(s); author self-archiving of the accepted manuscript version of this article is solely governed by the terms of such publishing agreement and applicable law.

Noninvasive Tracking of Every Individual in Unmarked Mouse Groups Using Multi-Camera Fusion and Deep Learning

Feng Su^{1,2,3,4} · Yangzhen Wang⁵ · Mengping Wei¹ · Chong Wang⁶ · Shaoli Wang⁷ · Lei Yang¹ · Jianmin Li⁸ · Peijiang Yuan⁹ · Dong-Gen Luo⁴ · Chen Zhang^{1,2,3}

Received: 14 May 2022 / Accepted: 29 August 2022 / Published online: 26 December 2022

© Center for Excellence in Brain Science and Intelligence Technology, Chinese Academy of Sciences 2022

Abstract Accurate and efficient methods for identifying and tracking each animal in a group are needed to study complex behaviors and social interactions. Traditional tracking methods (e.g., marking each animal with dye or surgically implanting microchips) can be invasive and may have an impact on the social behavior being measured. To overcome these shortcomings, video-based methods for tracking unmarked animals, such as fruit flies and zebrafish, have been developed. However, tracking individual mice in a group remains a challenging problem because of their flexible body and complicated interaction patterns. In this study, we report the development of a multi-object tracker

for mice that uses the Faster region-based convolutional neural network (R-CNN) deep learning algorithm with geometric transformations in combination with multi-camera/multi-image fusion technology. The system successfully tracked every individual in groups of unmarked mice and was applied to investigate chasing behavior. The proposed system constitutes a step forward in the noninvasive tracking of individual mice engaged in social behavior.

Keywords Noninvasive tracking · Deep learning · Multi-camera · Mouse group · Social interaction

Feng Su, Yangzhen Wang, Mengping Wei, and Chong Wang contributed equally to this work.

Supplementary Information The online version contains supplementary material available at <https://doi.org/10.1007/s12264-022-00988-6>.

✉ Peijiang Yuan
itr@buaa.edu.cn

✉ Dong-Gen Luo
dgluo@pku.edu.cn

✉ Chen Zhang
czhang@188.com

¹ Department of Neurobiology, School of Basic Medical Sciences, Beijing Key Laboratory of Neural Regeneration and Repair, Capital Medical University, Beijing 100069, China

² Chinese Institute for Brain Research, Beijing 102206, China

³ State Key Laboratory of Translational Medicine and Innovative Drug Development, Nanjing 210000, China

⁴ Peking-Tsinghua Center for Life Sciences, Academy for Advanced Interdisciplinary Studies, Peking University, Beijing 100871, China

⁵ School of Life Sciences, Tsinghua University, Beijing 100084, China

⁶ School of Biological Science and Medical Engineering, Beihang University, Beijing 100191, China

⁷ The Key Laboratory of Developmental Genes and Human Disease, Institute of Life Sciences, Southeast University, Nanjing 210096, Jiangsu, China

⁸ Institute for Artificial Intelligence, the State Key Laboratory of Intelligence Technology and Systems, Beijing National Research Center for Information Science and Technology, Department of Computer Science and Technology, Tsinghua University, Beijing 100084, China

⁹ School of Mechanical Engineering and Automation, Beihang University, Beijing 100191, China

and social groups [1–3]. In addition to these behavioral patterns, which include maternal [4, 5], aggressive [6, 7], and reproductive behavior [8, 9], social interactions are known to be relevant in many psychiatric disorders [10, 11] (e.g., autism [12, 13], schizophrenia [14], depression [15], substance abuse [16], and anxiety [17]) in humans and modeled in non-human animals. To examine these patterns, animals are typically kept in controlled environments that restrict their movements and behaviors, such as the three-chamber test [18–20] and the tube test [21, 22], and these environmental restrictions usually alter or limit the behaviors being studied or result in artificial or contrived behaviors that are not necessarily related to natural behaviors [23, 24]. However, despite the growing literature evaluating behavioral and social interactions [25–30], accurately identifying and tracking an individual animal in a group has remained a major challenge because of the complexity of animal interaction patterns, including occlusion, crossing, and huddling [30, 31].

Video-based tracking systems play an important role in monitoring and tracking the behavior of individual animals and contribute positively to biology and neuroscience studies [32, 33]. Initially, thresholding and binarization techniques were widely used to track individuals [34, 35], and the methods used to track multiple individuals typically involved differentiating them based on physical differences (size or color or the presence of dyes of various colors). For example, marking mice by bleaching different patterns into their fur achieved a 99.4% recognition accuracy for a group of four mice [36]. Marking mice with composite dyes that emit different colors under ultraviolet light resulted in an identification accuracy of 99.6% for a group of four mice in 500 randomly-selected images taken by one color-sensitive camera [37]. Using a similar method, the trajectories of four mice using color markings for 12 h showed stable differences between individuals that were interpreted as representing different personalities [33]. Nevertheless, color markings are usually not permanent, and the gradually-fading color features would increase the risk of error when tracking multiple individuals.

The ability of video-based tracking to detect complex behaviors in animals can be enhanced through combination with other technologies. For instance, a video-based tracking model was implemented that incorporates radio-frequency identification (RFID) to monitor individual rodent behavior in complicated social settings [38]. RFID technology contributed to location-related (rather than trajectory-related) information on 40 mice in a large enriched environment; this approach was able to quantify the behavioral characteristics of individual mice [39]. Meanwhile, a combination of RFID and a camera achieved a tracking accuracy of 97.27% in a group of five mice in a semi-natural environment and was applied to the quantitative analysis of social levels within

mouse populations [40]. However, implanted chip technology requires specific surgical skills, and invasive operations can affect animal recognition and behavior [41–43].

Non-invasive tracking of unmarked animals has been greatly aided by the development of machine learning algorithms. Using a foreground pixel-clustering and identity-matching algorithm, the trajectories of 50 individual fruit flies have been tracked, allowing differences in behavior to be identified at the individual level [44]. Subsequently, the MiceProfiler system used computer vision and an *a priori* geometrical constraints algorithm that permits tracking and quantitative evaluation of social interactions between two unlabeled mice by calculating mouse-body geometric characteristics [45]. Later, Hong *et al.* used depth-sensing technologies to track two mice with different fur colors and applied video-based tracking approaches to detect social behaviors such as mating and fighting in mice [29]. In 2014, Pérez-Escudero *et al.* established the idTracker system based on a color correlogram transformation that extracts data fingerprints, enabling it to differentiate among individual animals throughout the study; this method has been used to track unmarked animals and achieved recognition accuracy of 99.5% for five zebrafish and 99.3% for four mice [30]. In 2019, Romero-Ferrero *et al.* established the idTracker.ai system based on a convolutional neural network (CNN) and achieved recognition accuracy of >99.9% for groups of >60 zebrafish or fruit flies [25]. Besides, the idTracker.ai system is also able to track a group of mice, and we have compared it with our proposed system in the following study. Overall, video-based tracking methods have proven highly effective at detecting movements and social interactions even in large, unmarked groups, including zebrafish and flies. However, tracking groups of mice, the most widely-used experimental animals, is still challenging compared with zebrafish and flies. The motion patterns among rodents are more complicated due to their flexible bodies, and the tracked shape or size of the animal is usually continuously changing. The features of the same mouse in different behaviors (e.g., curled up in a ball or rearing) can vary greatly, making it difficult to extract efficient and stable data fingerprints to differentiate unmarked individuals. The study of mouse tracking is still challenging in identifying individual mice, especially when faced with crossing, huddling, and occlusion.

Driven by big data and high computing power, deep learning (DL) has achieved great performance in many challenging animal behavior tasks, such as pose estimation [32, 46–48], whole-body 3D-kinematic analysis [49–51], and chimpanzee face recognition [52]. In object-tracking problems, multi-camera systems have been widely used to increase tracking accuracy and robustness [53, 54]. Here, we established a multi-object tracker for mice (MOT-Mice) powered by multi-camera acquisition and a deep learning algorithm for the marker-free tracking of individuals within

a group of up to six mice. Using the MOT-Mice system, we found that unfamiliar wild-type C57BL/6 male mice exhibited significantly more chasing (following) behavior, a typical social interaction behavior in mouse groups [36, 55, 56], than familiar mice. Our experimental results established that the MOT-Mice system is able to track a group of mice even though there were crossings, occlusions, and huddling.

Materials and Methods

Multi-Camera System Configuration

The multi-camera system included one experimental box without a lid, 4 cameras (Hikvision Digital Technology Co., Ltd., Hangzhou, China), and a set of multi-camera synchronization recording software programs (iVMS-4200, Hikvision Digital Technology Co., Ltd., Hangzhou, China) (Fig. S1). The resolution of the camera was 1280 pixels \times 720 pixels. The cameras had a lens focal length of 4 mm and an aperture of F2.0. The experimental box was made of transparent acrylic panels and its dimensions were 60 \times 60 \times 50 cm³. The primary camera was placed above the experimental box, while the three auxiliary cameras were distributed on three sides of the box. The computer with the synchronous recording software was connected to the 4 cameras through a 4-port Ethernet switch to implement video recording and to set camera parameters. The videos recorded by the cameras were temporally corrected to ensure that the videos acquired by all the cameras were completely synchronized (Fig. S2). In the positive control experiment, the videos included a timer display such that the same frame in the 4 videos all showed the same time, indicating that they were synchronized.

Single-Camera Modeling

Cameras were calibrated with the MatLab R2019b Computation Vision Toolbox (The MathWorks, Inc., Massachusetts, USA), including both single-camera modeling and multi-camera registration. We used checkerboard feature detection for calibration. The definitions and descriptions of the checkerboard feature extractor are shown in Fig. S3. The size of the checkerboard pattern used in this experiment was 16 \times 17 squares (height \times width), and the size of each square was 30 \times 30 mm². For camera calibration in three dimensions, the checkerboard-pattern board was placed inside the experimental box at 15 different angles, and each of the cameras took one picture at each placement. The 15 checkerboard images were used to establish a single-camera pinhole imaging model. A point was projected from the world coordinate system ($[X Y Z 1]$) to the pixel coordinate system of a camera ($[x y 1]$).

$$m \cdot [x y 1] = [X Y Z 1] \cdot P,$$

$$P = Q \cdot K,$$

$$Q = \begin{bmatrix} R \\ T \end{bmatrix},$$

$$K = \begin{bmatrix} f_x & 0 & 0 \\ s & f_y & 0 \\ c_x & c_y & 1 \end{bmatrix},$$

$$R = \begin{bmatrix} a & d & g \\ b & e & h \\ c & f & i \end{bmatrix},$$

$$T = [j \ k \ l],$$

where P denotes the camera matrix, m denotes the scale factor, Q and K denote the extrinsic and intrinsic parameters, respectively, and R and T denote the rotation matrix and translation vector, respectively. The extrinsic parameters of the single-camera model represent a spatial transformation between the world coordinate system and the camera coordinate system (Fig. S4).

Then, the single-camera model was used to remove distortion in the checkerboard images and recorded videos caused by the lenses using the lens distortion model. The straight-line features in the world coordinate system were curved in the distorted images. The image correction operation corrected the points in pixel coordinates to recover the real features. Zooming out on the image to a proper scale ensured that the experimental region did not lie outside the edges of the images after correction.

Multi-Camera Registration

After detecting the feature points (the corners of squares in the checkerboard image) in the undistorted checkerboard image, we transformed the feature points of the top-view and side-view cameras to the same coordinate system. The multi-camera registration was based on a general projective geometric transformation model. We projected each point in the original camera coordinate system ($[u v 1]$) to a unified coordinate system ($[x y 1]$).

$$[x y 1] = [u v 1] \cdot Tr,$$

$$Tr = \begin{bmatrix} A & D & G \\ B & E & H \\ C & F & 1 \end{bmatrix},$$

where Tr is the transformation matrix. Then,

$$\begin{cases} x = (Au + Bv + C)/(Gu + Hv + 1) \\ y = (Du + Ev + F)/(Gu + Hv + 1) \end{cases}$$

$$\begin{cases} x = Au + Bv + C - Gux - Hvx \\ y = Du + Ev + F - Guy - Hvy \end{cases}$$

$$\begin{bmatrix} x \\ y \end{bmatrix} = \begin{bmatrix} u & v & 1 & 0 & 0 & 0 & -ux & -vx \\ 0 & 0 & 0 & u & v & 1 & -uy & -vy \end{bmatrix} \cdot Tvec,$$

$$Tvec = [A B C D E F G H]^T.$$

We solved $Tvec$, which consists of all the parameters in transformation matrix Tr , based on the checkerboard image pattern for the k^{th} feature point pair, the original point $P_k = [u_k \ v_k \ 1]$, and the projected point $Q_k = [x_k \ y_k \ 1]$.

The mathematical relationships for all the feature pairs are as follows:

$$\begin{bmatrix} x_1 \\ \dots \\ x_k \\ y_1 \\ \dots \\ y_k \end{bmatrix} = \begin{bmatrix} u_1 & v_1 & 1 & 0 & 0 & 0 & -u_1x_1 & -v_1x_1 \\ & & & & & & \dots & \\ & & & & & & & \\ u_k & v_k & 1 & 0 & 0 & 0 & -u_kx_k & -v_kx_k \\ 0 & 0 & 0 & u_1 & v_1 & 1 & -u_1y_1 & -v_1y_1 \\ & & & & & & \dots & \\ & & & & & & & \\ 0 & 0 & 0 & u_k & v_k & 1 & -u_ky_k & -v_ky_k \end{bmatrix} \cdot Tvec.$$

The above matrix equations can be rewritten as:

$$X = U \cdot Tvec,$$

$$Tvec = U \setminus X.$$

The unified coordinate system was generated by fine-tuning the feature points of the top-view camera; then, all the feature points of the side-view cameras were projected to the unified coordinate system (Fig. S5). Although the registration errors of the auxiliary cameras [Camera 2 error: 0.347 ± 0.028 mm; Camera 3 error: 0.635 ± 0.040 mm; Camera 4 error: 0.175 ± 0.008 mm; $n = 240$ (15×14 checkerboard points)] were higher than the main camera error (Camera 1 error: 0.106 ± 0.005 mm) because the content in the side-view cameras had greater deformation (Fig. S6), all the multi-camera registration errors were very small compared to the average mouse body width (30.35 ± 0.45 mm; $n = 15$).

Mouse Detection by the Faster R-CNN Model

The MOT-Mice system, a mouse multi-object tracker, uses a Faster region-based CNN (R-CNN) model to detect all the individual mice in each image by marking them with bounding boxes. We constructed the Faster R-CNN model based on a pre-trained ResNet-18 model using transfer learning. During the model training process, data augmentation techniques based on various image transformation methods were used to improve model generalizability and avoid overfitting. These image transformation operations comprised image flipping (horizontal and vertical), image translation, saturation and brightness adjustment, and noise addition (Figs S7, S8). The image augmentation parameters were set as follows: random horizontal and vertical flipping with 50% probability, horizontal and vertical translation range $[-40, 40]$ pixels, random saturation modification range $[-0.2, 0.2]$, random brightness modification range $[-0.2, 0.2]$, and the addition of salt and pepper noise with a variance of 0.02 to each channel of the image. The deep learning architectures and experiments were implemented on a computer with MatLab R2019b software and configured with an NVIDIA GeForce GTX 1080 Ti GPU with 11 GB memory (NVIDIA Corp., Santa Clara, USA).

Evaluation of Mouse Detection Performance

Two criteria were used to evaluate the mouse detection performance: frame-based accuracy and individual-based accuracy. For an image with n mice and annotated bounding boxes (Bbox- n), the MOT-Mice system detected m mice and calculated their bounding boxes (Bbox- m). We determined the number of correct detections (K) by calculating the pairwise intersection over union (IoU) between Bbox- n and Bbox- m . A correct mouse detection meant that the IoU between Bbox- n and Bbox- m exceeded a threshold of 0.5. Then, the individual-based accuracy for this image was calculated as K/n . The average individual-based accuracy of $>1,500$ testing images for each group size (1, 2, 3, 4, 5, 6, 10, and 15) was used to evaluate the mouse detection performance. The original image size was 1280 pixels \times 720 pixels. The distribution of the diagonal length of all the bounding boxes in the training and testing datasets is shown in Fig. S9A {diagonal length (pixels): median [interquartile range (IQR) Q1–Q3], 70.01 [IQR 79.76–98.86]}. The frame-based accuracy denotes the percentage of images with 100% individual-based accuracy (Fig. S9).

Comparison of Mouse Detection Performance Across Multiple Deep Learning Algorithms

We constructed Faster R-CNN models based on several excellent deep neural networks (SqueezeNet, GoogLeNet, and ResNet-18) to find the most appropriate model for the mouse detection task (Fig. S9). SqueezeNet is a compact 18-layer CNN architecture that has 50 \times fewer parameters than AlexNet but maintains AlexNet-level accuracy on the ImageNet dataset. GoogLeNet is a 22-layer CNN architecture designed with the Hebbian principle and the concept of multiscale processing to improve its computational efficiency. GoogLeNet consists of a repeated “Inception module” that moves from fully-connected to sparsely-connected architectures. Residual neural network (ResNet) uses identity mapping for all shortcuts and zero-padding to increase the dimensions without increasing the parameters. ResNet-18 is an 18-layer residual learning framework.

We constructed R-CNN, Fast R-CNN, and Faster R-CNN models based on ResNet-18 and compared their run-times for mouse detection (Fig. S10). All three models are gradually-optimized deep-learning algorithms [57]. The Faster R-CNN model achieved the best performance (the highest accuracy and lowest time consumption). The R-CNN model consists of three modules that generate region proposals and crop images, classify the cropped images, and refine the region proposal bounding boxes. Unlike the R-CNN model, the Fast R-CNN processes the entire image and then pools the CNN features to each region proposal for further classification. Fast R-CNN accelerates algorithm execution by

sharing the computations for overlapping regions. Faster R-CNN is more efficient than the other models because its implemented region proposal network generates region proposals faster and more accurately.

To compare the performance of developed mouse detection models effectively, all the models used the same parameter settings: maximum number of strongest region proposals of 128, detection score threshold of 0.65, processing batch size of 16, and GPU execution environment.

Generating Tracklets From the Detection Results

The MOT-Mice system tracks individual mice detected by the Faster R-CNN model using a multi-object tracking algorithm, and it generates tracklets for each detected animal. In most cases, the mouse movements recorded by the camera (at a sampling frequency of 25 Hz) had smooth trajectories. As a result, the bounding boxes corresponding to the same mouse largely overlapped in two adjacent frames, while the bounding boxes corresponding to different mice had no or only small overlaps.

For two adjacent frames, we assumed that all the mice detected in the first frame have determined identities, while the mice in the next frame have only the detection results indicated by the bounding boxes but no identities. Then the core function of multi-object tracking is to assign identities to support the detection results of the next frame, or in mathematical terms, to identify the pairing method that maximizes the total IoU. We paired the bounding boxes in the two adjacent images and calculated the IoU matrix of these boxes. An IoU of 0 indicates that the two boxes do not overlap, while an IoU of 1 indicates that the two boxes overlap perfectly. We solved the identity assignment problem using the Munkres global nearest-neighbor assignment algorithm based on the pairwise IoU matrix.

To improve the tracking accuracy, the identity assignment operations were further optimized by setting two criteria according to the IoU. For the k^{th} target bounding box (Bbox) in the previous frame (BboxPre $_k$), the IoU between BboxPre $_k$ and each Bbox in the next frame (BboxNext $_i$) is denoted as v_{ki} , where $i = 1, 2, \dots, n$. The largest and second-largest v_{ki} values are denoted as v_{km} and v_{kn} , respectively, denoting that the BboxNext $_m$ and BboxNext $_n$ in the next frame are the two Bboxes that overlap most with the BboxPre $_k$ in the previous frame. BboxPre $_k$ and BboxNext $_m$ are paired and considered to denote the same object when the following two criteria (IoU $_{\text{Thre}}$ and IoUDiff $_{\text{Thre}}$; Thre means threshold) are satisfied: (1) IoU value criterion: $v_{km} \geq \text{IoU}_{\text{Thre}}$; (2) IoU difference criterion: $v_{km} - v_{kn} \geq \text{IoUDiff}_{\text{Thre}}$. Furthermore, we implemented a parameter optimization test on the parameters IoU $_{\text{Thre}}$ and IoUDiff $_{\text{Thre}}$. Our experimental results suggested that the optimal parameter settings are IoU $_{\text{Thre}} = 0.20$ and IoUDiff $_{\text{Thre}} = 0.15$.

When no matching detection result occurred between the bounding boxes in the previous frame and the next frame, the corresponding trajectory segment in the previous frame was terminated. When a detection result occurred in the next frame and no matching bounding box could be found in the previous frame, a new trajectory segment was generated. This process was repeated iteratively until the entire video was analyzed and the tracklets of all the animals were obtained.

Mathematical Definitions of the Tracklets

Tracklets are the intermediate results of the multi-object tracking process. We fused the shorter tracklets to obtain longer trajectory segments until a complete trajectory was obtained. We used a 2D trace plot and a Gantt chart to describe the spatial and temporal information, respectively, contained in the tracklets (Fig. S11).

The mathematical definition of a tracklet is $Z = [z_M, z_{M+1}, \dots, z_N]$, $z_n = (z\text{bbox}_n, z_{x_n}, z_{y_n}, z_{t_n})$, where Z denotes a tracklet and z_n denotes a point in the Z tracklet. For a point z_n , $z\text{bbox}_n$ denotes the current bounding box, (z_{x_n}, z_{y_n}) denotes the center of $z\text{bbox}_n$, and z_{t_n} denotes the current frame, which is usually the video frame index. The duration of tracklet Z denotes the number of frames or the number of points it covers and is calculated as $\text{Duration}(Z) = N - M$. Tracklet Z is a continuous trajectory when $\text{Duration}(Z)$ is equal to the total number of frames in the video.

Tracklet Evaluation

Before conducting the trajectory segment evaluation, the ground-truth trajectories were obtained by manually clicking the centers of the targeted mouse frame by frame for each mouse. The evaluation metrics for tracklets focus on two aspects: accuracy and completeness. We adopted the following four metrics based on the most popular multi-object tracking challenge (MOT challenge) to evaluate the validity and reliability of the system: (1) the number of identity switches (IDS) in a tracked trajectory that differs from its matched ground-truth identity, (2) the total number of times a trajectory is fragmented (Frag) during tracking, (3) mostly lost targets (ML) represent the ratio of ground-truth trajectories that are covered by a track hypothesis for at most 20% of their respective life spans; and (4) mostly tracked targets (MT) represent the ratio of ground-truth trajectories that are covered by a track hypothesis for at least 80% of their respective life spans. The perfect values for IDS, Frag, ML, and MT are 0, 0, 0, and 100%, respectively. In the subsequent steps, we tried to decrease the values of IDS, Frag, and ML, and increase the value of MT by tracklet assembly.

Matchability of Tracklet Pairs

To ensure tracking accuracy, we set strict thresholds for generating tracklets from the detection results. As a result, the initial tracking results were almost free of identity switch errors but consisted of several fragments. To obtain the complete trajectory for each animal, we needed to fuse the tracklets belonging to the same animal. We calculated the matchability of two tracklet fragments to judge whether two tracklets belong to the same mouse and should be fused. For two tracklets P and Q ,

$$P = [p_A, p_{A+1}, \dots, p_B], p_b = (pbbox_b, px_b, py_b, pt_b)$$

$$Q = [q_C, q_{C+1}, \dots, q_D], q_d = (qbbox_d, qx_d, qy_d, qt_d)$$

The matchability of tracklets P and Q [$\text{Match}(P, Q)$] was determined based on both temporal and spatial criteria. First, we characterized the temporal relationship between tracklets P and Q . Assume P is prior to Q so that $pt_A < qt_C$ and $pt_B < qt_D$. In other words, the endpoints of p_B and q_C are temporal neighbors, and tracklet assembly would occur between p_B and q_C if tracklets P and Q refer to the same animal. The tracklets P and Q temporally overlap when $pt_B \geq qt_C$ and do not overlap when $pt_B < qt_C$. The temporal distance between p_B and q_C is $\text{Temp}(p_B, q_C) = |pt_B - qt_C|$. If the temporal distance between p_B and q_C is larger than the threshold [$\text{Temp}(p_B, q_C) > \text{Temp}_{\text{Thre}}$], then $\text{Match}(P, Q) = 0$ (Fig. S12).

For each tracklet pair that satisfied the temporal criterion, we then calculated $\text{Match}(P, Q)$ based on spatial and temporal information. When the tracklets P and Q are separate, only their endpoints (p_B and q_C) are counted, i.e., $\text{Match}(P, Q) = \text{SpatialFunc}(p_B, q_C)$, where $\text{SpatialFunc}(\cdot)$ denotes the function used to calculate the spatial relationship between two Bboxes.

If tracklets P and Q temporally overlap, $\text{Match}(P, Q)$ is the average matchability value of all the overlapping segments:

$$\text{Match}(P, Q) = 1/\text{Temp}(p_B, q_C) \cdot \sum_{k=C}^B \text{SpatialFunc}(p_k, q_k)$$

Two kinds of $\text{SpatialFunc}(\cdot)$ were used in this study: distance-dominated and IoU-dominated functions. The distance-dominated $\text{SpatialFunc}(\cdot)$ uses the distance between the centers of two Bboxes to characterize matchability. A higher $\text{SpatialFuncDist}(\cdot)$ value denotes lower matchability between tracklets:

$$\text{SpatialFuncDist}(p_k, q_k) = \left| \left| (px_k - qx_k, py_k - qy_k) \right| \right|$$

The IoU-dominated $\text{SpatialFunc}(\cdot)$ uses the IoU between two Bboxes to characterize matchability. A higher $\text{SpatialFuncIoU}(\cdot)$ value denotes higher matchability between tracklets:

$$\text{SpatialFuncIoU}(p_k, q_k) = \text{IoU}(pbbox_B, qbbox_C)$$

Here we determined the definition and calculation of tracklet pair matchability, then we used it to guide the tracklet assembly operations.

Tracklet Assembly by Spatial Information

Next, spatial information-based tracklet assembly operations were used to calculate the spatial information between a target tracklet Q and multiple tracklets that may be fused $\{P_k\}$ and identify pairs of tracklets belonging to the same individual that can be fused. $\{P_k\}$ denotes the set of tracklet P , and the definition and calculation of $\text{Match}(P_k, Q)$ is the same as $\text{Match}(P, Q)$. The matchability of a tracklet pair Q and P_k , $\text{Match}(P_k, Q)$, is denoted v_k .

Distance-dominated tracklet assembly calculates tracklet pair matchability by $\text{SpatialFuncDist}(p_k, q_k)$. The smallest and the second-smallest v_k are denoted v_m and v_n , respectively. Then, tracklets Q and P_m denote the same animal and can be fused when the following two criteria are satisfied: (1) a distance value criterion: $v_m \leq \text{Dist}_{\text{Thre}}$; and (2) a distance difference criterion: $v_m - v_n \geq \text{DistDiff}_{\text{Thre}}$.

IoU-dominated tracklet assembly calculates tracklet pair matchability by $\text{SpatialFuncIoU}(p_k, q_k)$. The largest and second-largest v_k are denoted v_x and v_y , respectively. Tracklets Q and P_x denote the same animal and can be fused when the following two criteria are satisfied: (1) the tracklet IoU value criterion: $v_x \geq \text{TrackletIoU}_{\text{Thre}}$; and (2) the tracklet IoU difference criterion: $v_x - v_y \geq \text{TrackletIoUDiff}_{\text{Thre}}$.

Parameter Optimization Test for Tracklet Assembly

The parameter optimization test assesses system performance under different parameter settings by changing the values of a single key parameter or combinations of the values of multiple key parameters. The goal of this test is to find the relationship between parameter values and system performance and to provide a reference basis for the parameter settings. Here, we implemented a parameter optimization test for three operations: generating tracklets from the detection results, distance-dominated tracklet assembly, and IoU-dominated tracklet assembly. All three operations had two key parameters. We conducted parameter optimization tests by setting different combinations of values for these key parameters. During the parameter optimization test, the parameters are optimized based on the conditions that the multi-object tracking performance is improved insofar as possible while satisfying the fundamental no-identity-switch principle. To generate tracklets from the detection results, eight parameter sets were tested for $(\text{IoU}_{\text{Thre}}, \text{IoUDiff}_{\text{Thre}})$: (0.02, 0.01), (0.05, 0.05), (0.15, 0.10), (0.20, 0.10), (0.20, 0.15), (0.25, 0.15), and (0.30, 0.20). For distance-dominated tracklet assembly, six gradually increasingly strict parameter sets were tested $(\text{Dist}_{\text{Thre}}, \text{DistDiff}_{\text{Thre}})$: (50, 5), (45, 5), (40,

5), (40, 10), (30, 10), and (30, 15). For IoU-dominated tracklet assembly, 6 gradually increasingly strict parameter sets were tested (TrackletIoU_{Thre}, TrackletIoUDiff_{Thre}): (0.05, 0.05), (0.15, 0.15), (0.25, 0.25), (0.30, 0.25), (0.30, 0.30), and (0.35, 0.30).

Tracklet Assembly by Trace Prediction

At the trajectory breakpoints, we used a cascade-forward artificial neural network (C-ANN) for trace prediction, tracklet length extension, and trajectory segment assembly. We constructed the C-ANN model to predict the position of the next point from K ($K = 24$) consecutive trajectory points. The C-ANN model contains an input layer, a hidden layer, and an output layer. The nodes in each layer were fully connected in the forward direction with the nodes in surrounding other layers. In addition, there were direct connections between the input layer and the output layer. The input layer had 48 nodes and accepted the position coordinates (x, y) of the K consecutive trajectory points. The hidden layer had 32 nodes with a tansig transfer function: $\text{tansig}(x) = 2/[1 + \exp(-2x)] - 1$. The output layer had 2 nodes with a linear transfer function that output the predicted position of the next point.

During C-ANN model training, the training and testing datasets were automatically generated based on the tracking results. Although most of the tracklets were still not the final complete trajectories, many had extended durations and could be used to train the C-ANN model. The tracklets were divided into standard segments of length $K + P$, where P is the number of points that needed to be predicted. In addition, we used the trace similarity (TraceSimi) algorithm based on Euclidean distance to evaluate the trace prediction accuracy.

For two traces, Trace_A and Trace_B , with N points that were temporally fully overlapped,

$$\begin{aligned} \text{Trace}_A &= \{p_t^A\}, p_t^A = [x_t^A, y_t^A], \\ \text{Trace}_B &= \{p_t^B\}, p_t^B = [x_t^B, y_t^B], \end{aligned}$$

where $t = 1, 2, \dots, N$.

The traces Trace_A and Trace_B were normalized as follows:

$$\begin{aligned} \text{Trace}_{A\text{-norm}} &= \{P_t^A\} = \{p_t^A - (p_1^A + p_1^B)/2\}, P_t^A = [X_t^A, Y_t^A], \\ \text{Trace}_{B\text{-norm}} &= \{P_t^B\} = \{p_t^B - (p_1^A + p_1^B)/2\}, P_t^B = [X_t^B, Y_t^B], \\ \text{TraceDist} &= \|\text{Trace}_{A\text{-norm}} - \text{Trace}_{B\text{-norm}}\|, \end{aligned}$$

$$\text{TraceDist} = \frac{1}{N} \sum_{t=1}^N \sqrt{(X_t^A - X_t^B)^2 + (Y_t^A - Y_t^B)^2},$$

$\text{Dist} \in [0 \infty)$,

and $\text{TraceSimi} = e^{-\text{TraceDist}}$, where $\text{TraceSimi} \in (0, 1]$.

When the number of predicted points was 2, 4, 6, 8, or 10, the trace prediction accuracy (the similarity between the observed and predicted traces) was 0.9727, 0.9627, 0.9535, 0.9449, and 0.9368, respectively. To ensure the reliability of trace prediction, we set 0.95 as the trace similarity threshold

and predicted a maximum of 6 points for the subsequent tracklet assembly process by trace prediction.

The prerequisite for tracklet Z to use the C-ANN was set to $\text{Duration}(Z) \geq 24$, $Z = [z_M, z_{M+1}, \dots, z_N]$. For the last K points of tracklet Z , we obtained the forward tracklet prediction Z_{Forward} by iteratively repeating the C-ANN P times ($P = 6$):

$$Z_{\text{Forward}} = [z_M, z_{M+1}, \dots, z_N, z_{N+1}, \dots, z_{N+P}].$$

We input the first K points of tracklet Z into the C-ANN in reverse and obtained the backward predicted tracklet Z_{Backward} by iteratively repeating the C-ANN process P times:

$$Z_{\text{Backward}} = [z_{M-P}, \dots, z_{M-1}, z_M, z_{M+1}, \dots, z_N].$$

Trace prediction was carried out both forward and backward for all the tracklets after the initial assembly; then, the operations described above were conducted on the tracklets. For the tracklets that still could not be fused after trace prediction, the trajectory predictions were deleted, and the original tracklets were retained.

Tracklet Assembly from Multiple Camera Recordings

During the process of tracklet assembly from multiple camera images, the tracklets from the top-view camera dominate the process, while the side-view camera recordings are used to assist in tracklet assembly in conjunction with the main camera recordings. We applied the same operations for the videos from the side-view cameras as were described previously for the top-view camera, including mouse detection, multi-object tracking, initial tracklet assembly, and tracklet assembly by trace prediction. Notably, due to the imaging angle, the fields of view of the side-view cameras had sensitive regions that were defined as one-third of the area farthest from the camera. In the sensitive regions, the mouse individuals were relatively small and often occluded by other mice. In addition, objects in the sensitive region of the images were substantially deformed after camera registration. Therefore, we deleted the detection results in the sensitive region before conducting multi-object tracking for the side-view cameras. For the side-view cameras, mouse detection and tracking were achieved before image registration, and tracklets were generated after image registration.

We used the distance matrices between the tracklets of the top-view camera and the side-view cameras to achieve multi-camera fusion (Fig. S13). The distance between a tracklet P from the top-view camera and a tracklet Q from a side-view camera was determined by the $\text{TrackDist}(P, Q)$ function:

$$\begin{aligned} P &= [p_A, p_{A+1}, \dots, p_B], p_b = (p\text{bbox}_b, px_b, py_b, pt_b), \\ Q &= [q_C, q_{C+1}, \dots, q_D], q_d = (q\text{bbox}_d, qx_d, qy_d, qt_d), \end{aligned}$$

$$\text{TrackDist}(P, Q) = \frac{1}{\Omega} \sum_{b=A}^B \sum_{d=C}^D D(p_b, q_d) \cdot S(p_b, q_d),$$

$$D(p_b, q_d) = \sqrt{(px_b - qx_d)^2 + (py_b - qy_d)^2},$$

$$S(p_b, q_d) = \begin{cases} 1, & \text{if } pt_b = qt_d, \\ 0, & \text{else} \end{cases}$$

$$\Omega = \sum_{b=A}^B \sum_{d=C}^D S(p_b, q_d),$$

where $D(p_b, q_d)$ denotes the spatial distance, $S(p_b, q_d)$ is a temporal indicator and a value of 1 means that p_b and q_d refer to the same time point. The symbol Ω denotes the length of the temporally overlapped segment between tracklets P and Q . When two tracklets P and Q do not overlap ($\Omega = 0$), the distance $\text{TrackDist}(P, Q)$ is infinite.

The implementation of tracklet assembly by multiple cameras consists of two steps. First, a set of tracklets Φ , defined from the top-view camera, with small distances between the same tracklets identified by a side-view camera is found:

$$\Phi = \{P_k\},$$

$$\text{TrackDist}(P, Q) < \text{DistThre},$$

where the tracklets P_k are from the top-view camera and tracklet Q is from a side-view camera; DistThre denotes the distance threshold for tracklet assembly by multiple cameras, and is usually set to the average mouse body width. Then, the output tracklet set Φ belongs to the same mouse and should therefore be fused into a single tracklet.

Post-processing by Manual Checking and Correction

In rare cases, we identified some tracklets that could not be fused or for which the identities of the mice associated with the trajectories switched. The MOT-Mice system post-processes the tracking results through the MOT checking and correction (MOT-CC) module.

For the trajectory breakpoints that could not be automatically fused by the algorithm, the MOT-Mice system achieves manual fusion by artificially inputting the indexes of the paired tracklets. Then, the MOT-CC module automatically calculates a risk factor (high risk usually refers to close interaction scenarios) for each frame of the video based on the tracking results. If the distance between the two nearest mice is less than the risk distance ($\text{RiskDist} = \text{average body width}$), the frame was automatically marked as a risk frame; then, the segment of risky tracking results was replayed to an investigator to determine whether an identity error existed. For the trajectories with identity switches, the misaligned trajectories were broken by manually marking the trajectory index and the frame index. Then, the broken trajectories were fused by manually pairing the tracklets belonging to the same individual. Finally, the correct trajectories of all the individual mice were obtained.

Comparison of Tracking Multiple Mice Between Three Methods

idTracker.ai is the most recently reported model and is the state-of-the-art CNN-based system for tracking unmarked animal groups. We applied both the idTracker.ai and MOT-Mice systems to process two videos (2 min) with five unmarked mice. The trajectory of each mouse in these videos was manually tracked by iteratively clicking the center of each mouse in each frame. During the manual tracking process, the trajectories of the five mice were extracted individually; then, these trajectories were used as ground truth to evaluate the performances of the idTracker.ai and MOT-Mice systems. A qualitative criterion was used to evaluate the identity error of the trajectories. If an identity error exists in a tracker's tracking result (either idTracker.ai or MOT-Mice), some mice would be mismatched between the 2D trace plot of the tracker and the manual tracking results (Fig. S14); otherwise, the 2D trace plots of the tracker and the manual tracking results should overlap almost exactly.

Animals and Experimental Settings

All procedures were approved by the Animal Care and Use Committee of the Capital Medical University and were performed according to the National Institutes of Health Guide for the Care and Use of Laboratory Animals. All the mice used in this study were specific pathogen-free wild-type C57BL/6J male mice aged 8–9 weeks purchased from Vital River (Vital River Lab Animal Technology Co., Ltd., Beijing, China). The temperature of the colony room was maintained at 20–26°C, and the humidity at 40%–70% with light and darkness alternating every 12 h. The mice were habituated to the testing room for 1 h before the tests. We cleaned the apparatus with 70% ethanol after each experiment and conducted the next experiment after a 10-min interval.

In social experiments involving familiar and unfamiliar groups, two litters of mice were used in each experiment. Four mice in each litter had marked tails: Litter a (a1, a2, a3, and a4) and Litter b (b1, b2, b3, and b4). On the first day of the test, open-field experiments were conducted with the two litters (Familiar-1 group), and the activity of the familiar group was recorded for 10 min. Then, the mice were returned to their home cages. On the third day of the test, the two litters were regrouped to obtain a mixed group. Mice a1, a2, b3, and b4 constituted one group, and mice b1, b2, a3, and a4 constituted the other group. The activity of the mixed mouse groups in an open-field environment was recorded for 10 min; then, the mice were returned to their home cages. On day 5 of the test, the activity of the 2 familiar mouse groups in the open-field environment was again recorded for 10 min (Familiar-2 group).

Definition and Recognition of Chasing Behavior

Chasing is a typical social behavior in mice. Mice not only chase each other for play but also during fights. Chasing is associated with a specific spatiotemporal relationship between the movements of two mice and can be recognized *via* mouse trajectories. An analysis of chasing demonstrated the effectiveness and potential application of the MOT-Mice system. We defined and calculated chasing behavior from two trajectories using the spatiotemporal method. The chasing was directional for each pair of mice. We used three criteria to recognize chasing. First, the distance between two mice should be relatively small (ChaseDistThre). Second, neither mouse can be standing still, and both mice should exhibit real-time location changes (i.e., their location variations within a short time window [$-\text{Lag}$ Lag] should be relatively large (ChaseVarThre)). Third, one mouse must be behind the other during the chasing process. Notably, crossing behavior (two mice quickly cross over in a head-to-head manner) usually satisfies these three criteria but has a very short duration. To increase the reliability of chasing recognition, only events that satisfied these three criteria and lasted for >0.75 s were counted as chasing behaviors.

Statistical Analyses

All the statistical analyses were performed using GraphPad Prism 7.0 software (GraphPad Software Inc., San Diego, USA). The data are presented as the mean \pm SEM. Differences were considered statistically significant at $*P < 0.05$.

Code Availability

The associated codes in this study are available online. The source code is available at <https://github.com/ZhangChenLab/Multi-Object-Tracker-for-Mice-V1.2>.

Results

Establishment of the MOT-Mice System

The MOT-Mice system performs the following four steps (Fig. 1A): (1) registering images taken from the primary (individual top-view) camera and auxiliary (multiple side-view) cameras and projecting the images onto a normalized coordinate system, (2) using a deep learning-based algorithm to detect multiple animals in every image, (3) generating tracklets, a trajectory segment without interruptions, that include mouse identity using a multi-object tracking algorithm based on the mouse detection results, and (4) generating the trajectories of all the individual mice by tracklet assembly. When animal aggregation or

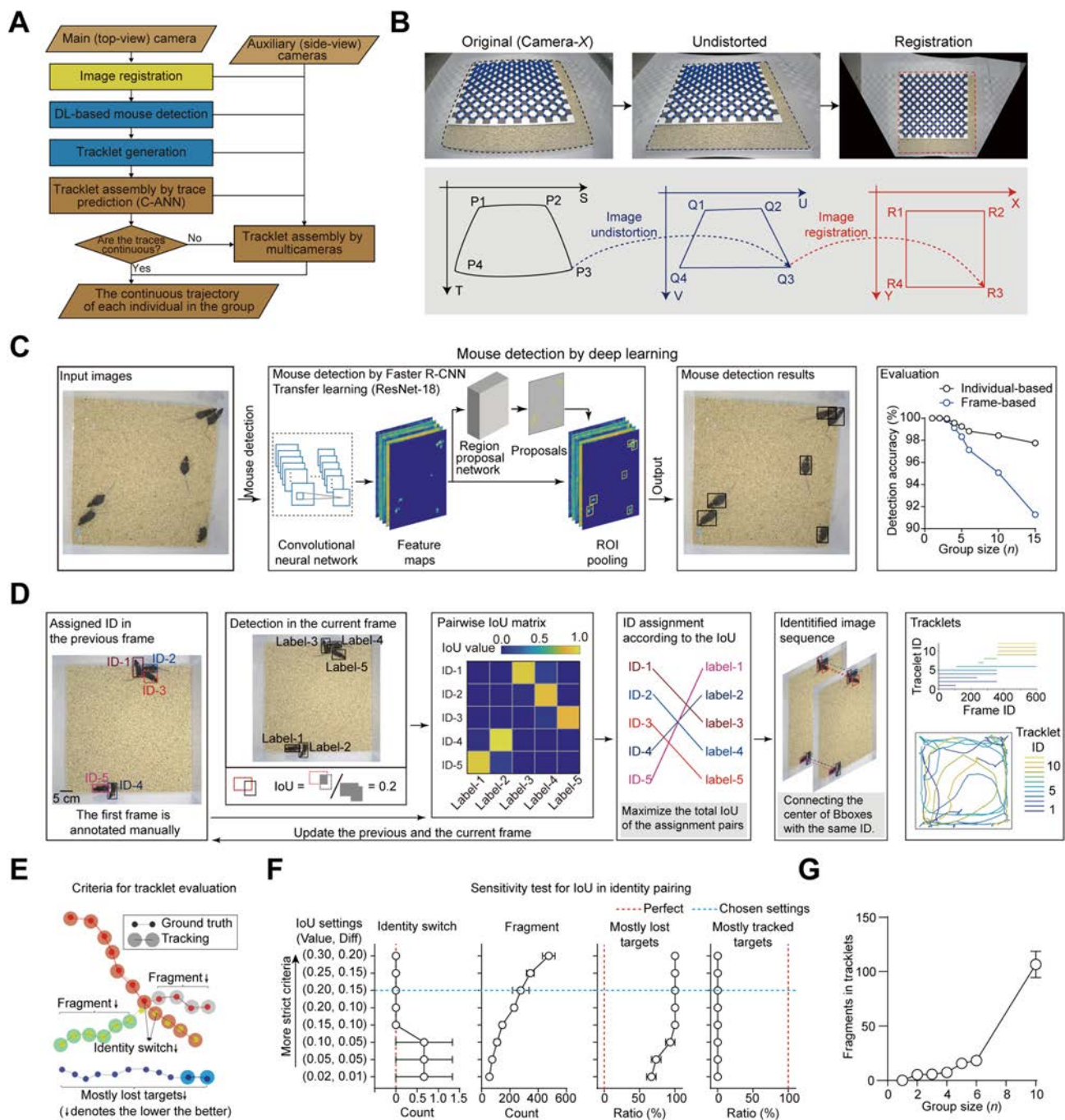
trajectory breakpoints (the time points at which the identity of a mouse is lost) were encountered, trace prediction was used for tracklet assembly. For the breakpoints that could not be solved by the primary camera during the tracking process, the MOT-Mice system used images taken by the auxiliary side cameras to reconstruct the tracklets and obtain a continuous trajectory.

Projecting Multiple Cameras onto the Same Coordinate System

Since the MOT-Mice system incorporates images from different cameras and the images are usually distorted [especially when those from multiple cameras (Figs S1, S2) are processed together], each image needs to be calibrated to generate a normalized image. As such, we calibrated and normalized the images using a checkerboard feature-based spatial geometric transformation method (Figs 1B and S3–S6). Image distortion caused by the camera lens was first removed through image correction by a pinhole camera model and a radial distortion algorithm. Then, the images from different cameras were aligned by projection onto a single target coordinate system (Fig. 1B). In this manner, the image calibration module transformed the images from multiple cameras into a unified framework, providing a basis for the subsequent mouse detection process.

Detecting All Mouse Individuals in Each Frame

To detect individual mice in each frame, the MOT-Mice system uses deep learning object detection methods [i.e., the MOT-Mice object detection (MOT-OD) module] to detect the bounding boxes, the smallest rectangles enclosing each mouse (Fig. 1C). To train the MOT-OD model, we first established a large mouse image dataset. We assigned each mouse to a training or testing set before recording the videos (Fig. S7). For recorded videos with 1, 2, 3, 4, 5, 6, 10, and 15 mice, we extracted frames at 2-s intervals. The images were then annotated with bounding boxes using MatLab; the training dataset consisted of 12,244 labeled original images with a total of 67,096 annotations, and the test dataset included 1,000 labeled images with a total of 5,324 annotations. The MOT-OD module used the Faster R-CNN model to detect the mice; a pre-trained deep learning network (ResNet-18) was used as the basis of the Faster R-CNN model. We used transfer learning and data augmentation techniques (Fig. S8) to fine-tune the model parameters. After training, the MOT-OD module achieved an average accuracy of 99.8% with transfer learning and 97.6% without transfer learning on the test dataset. We evaluated the accuracy of the MOT-OD module with transfer learning using an individual-based accuracy criterion (where the error reflects incorrect mouse detections) and a frame-based



accuracy criterion (where the error reflects an image exhibiting incorrect mouse detection). The MOT-OD module analyzed 1,500 images under each experimental setting, namely, the presence of 1, 2, 3, 4, 5, 6, 10, and 15 mice, and achieved gradually decreased individual-based accuracy (from 100% down to 97.75%) and frame-based accuracy (from 100% down to 91.27%) with increased group size (Fig. S9). We compared the three most popular and widely-used CNNs (ResNet-18, GoogLeNet, and SqueezeNet) and found that

the ResNet-18 model achieved the highest mouse detection accuracy. We further compared the time consumption of R-CNN, Fast R-CNN, and Faster R-CNN. The Faster R-CNN model used a region proposal network to search for features and dramatically improved the mouse detection speed [the average detection times for each image by the R-CNN, Fast R-CNN, and Faster R-CNN models were 1.86, 0.53, and 0.18 s (10.39:2.94:1), respectively; Fig. S10]. The MOT-OD module achieved highly accurate performance in detecting

Fig. 1 Multi-object tracker for mice (MOT-Mice) powered by multi-camera acquisition and a deep learning (DL) algorithm extracts the tracklets of unmarked mice in a group. **A** Flowchart of the MOT-Mice system. **B** Image registration using a checkerboard pattern (Fig. S3). Left to right: original distorted checkerboard image of camera-X and its corresponding pixel coordinate system; image with distortion removed by single-camera modeling using a pinhole imaging model and a radial distortion model (Fig. S4); image registration by projective geometric transformation. All images from all cameras are projected to a normalized coordinate system (Figs S5, S6). **C** DL-based mouse detection. Left to right: implementation of the Faster R-CNN model for mouse detection (Figs S7–S10); mouse detection accuracy *versus* group size. **D** Pre-tracking of multiple mice by a single camera based on spatiotemporal information. The mice in the previous frame are labeled by bounding boxes (Bboxes) with a specific color and assigned an identity (ID-*x*); then, the mice detected in the current frame are labeled (label-*y*). The intersection over union (IoU) value reflects the spatial relationship between the Bbox for ID-*x* and label-*y*. The solutions to the identity assignment problem are indicated by the connecting lines. The algorithm is repeated iteratively to obtain the tracking results as tracklets, which are shown as a Gantt chart (temporal information) and a 2D trace plot (spatial information) (Fig. S11). **E** Criteria for tracklet evaluations. The criteria for identity switches, fragments, and mostly lost targets are illustrated. Dotted line and small circle, the ground truth of trajectory. Solid line and large circle, the tracking results. **F** Parameter optimization test for IoU in identity pairing. The plot shows IoU settings *versus* tracklet evaluation criteria. Dotted red line, the perfect value for each criterion. Blue dotted line, the chosen parameter settings. The optimization tests were conducted using videos recorded with five mice. **G** Plot of tracklet fragments *versus* animal group size.

all mouse individuals in each image and provided a sound basis for subsequently generating tracklets.

Tracklet Generation Based on Mouse Detection Results

To obtain a tracklet (Fig. S11), the same animal in two adjacent images was recognized by comparing the bounding boxes using the MOT-Mice identity pairing (MOT-IP) module. The mice detected in the two images (images A and B) were assigned identities (A-Mouse_{*i*} and B-Mouse_{*j*}). The pairing of IDs between two adjacent images was determined by the Munkres global nearest neighbor algorithm [58, 59], which solved the identity assignment problem by maximizing the total IoU between pairs (Fig. 1D).

Arguably, the most significant difficulty in multi-animal tracking is reflected in identity switches and fragments of varying lengths in the tracked trajectories. This phenomenon can occur when one mouse is occluded by another. The uncorrected and unsuccessful matches found by the MOT-IP module resulted in identity switches and tracklet fragments, respectively.

Trajectory accuracy, which is represented by identity switching, and trajectory completeness, which is represented by the numbers of tracklet fragments, mostly lost targets, and mostly tracked targets, are two important types of evaluation metrics in multi-object tracking (Fig. 1E).

The parameter optimization test for IoU in identity pairing reflected the relationship between the performance of the MOT-IP module and the value of the key parameter pair (IoU_{Thre} , $\text{IoUDiff}_{\text{Thre}}$). We set the optimized value of (IoU_{Thre} , $\text{IoUDiff}_{\text{Thre}}$) to (0.20, 0.15) to ensure no identity switch and as few fragments as possible (Fig. 1F). By analyzing 3 sets of 5-min videos containing 1, 2, 3, 4, 5, 6, or 10 animals (for a total of 21 videos) and validating the MOT-IP module, we found that on average, there were $0, 5.33 \pm 0.58, 5.67 \pm 1.53, 7.33 \pm 1.53, 15.67 \pm 4.04, 18.33 \pm 2.08,$ and 106.67 ± 20.82 fragments in the 5-min videos containing 1, 2, 3, 4, 5, 6, and 10 animals, respectively (Fig. 1G). To ensure tracking accuracy, we set strict rules for the MOT-IP process that led to no identity switches but resulted in several fragments. The MOT-IP module achieved relatively few tracklet fragments for the videos containing 1–6 mice and had great potential to be further assembled to obtain complete trajectories for each individual.

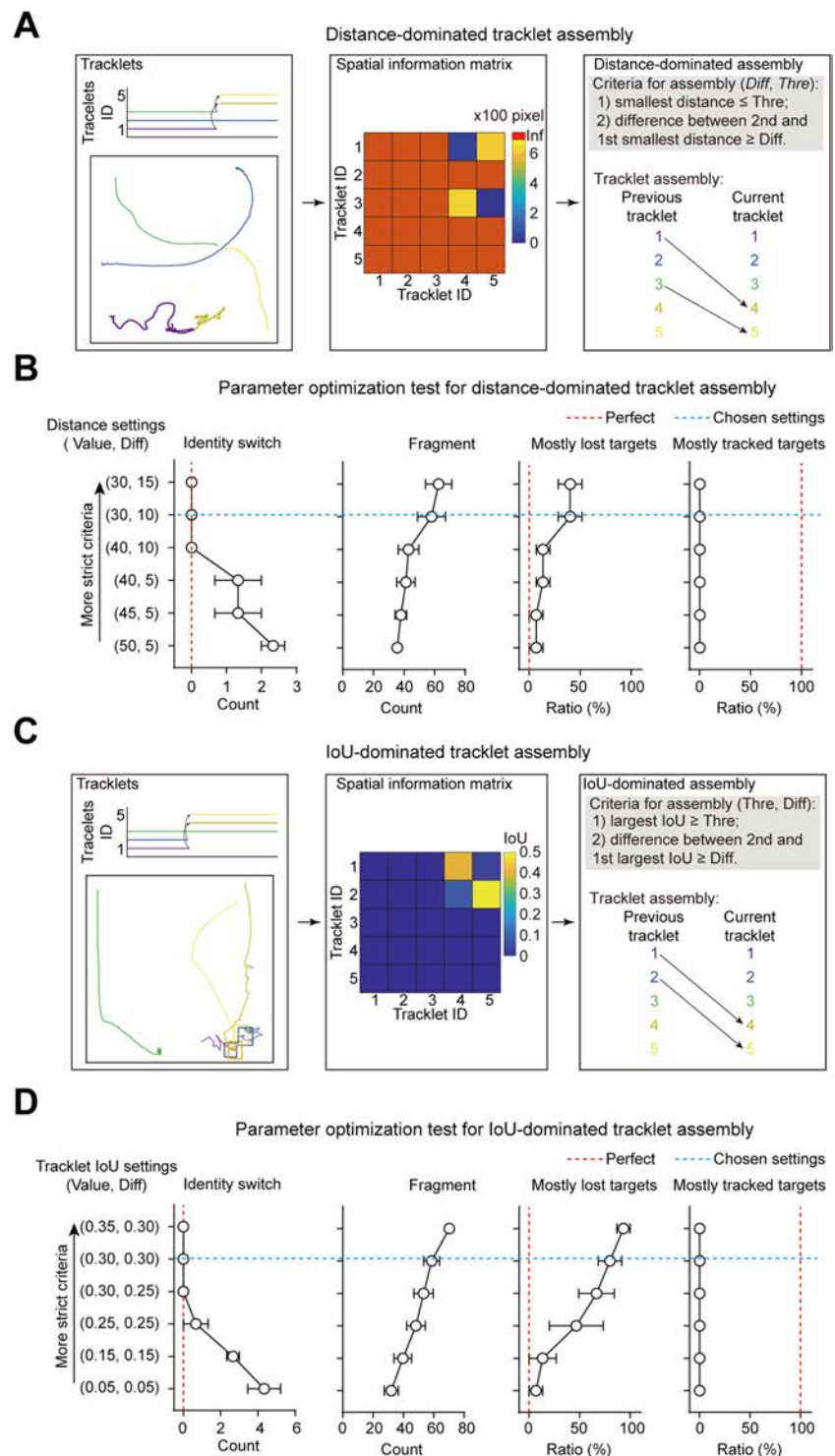
Parameter Optimization Test for Tracklet Assembly Using Spatial Information

We further explored trajectory completeness by tracklet assembly using spatial information that did not lead to a loss of trajectory accuracy (Figs 2 and S12). Both distance-dominated (Fig. 2A, B) and IoU-dominated (Fig. 2C, D) tracklet assemblies were adopted in this study, and a parameter optimization test was applied using the recorded videos with five mice. We tested two sets of gradually strict parameters for distance-dominated and IoU-dominated tracklet assemblies to find the optimized parameter settings. The optimized value of the key parameter pair ($\text{Dist}_{\text{Thre}}$, $\text{DistDiff}_{\text{Thre}}$) for distance-dominated tracklet assembly was set to (30, 10) pixels to ensure that no identity switches occurred and to result in as few fragments as possible (Fig. 2B). The optimized value of the key parameter pair ($\text{TrackletIoU}_{\text{Thre}}$, $\text{TrackletIoUDiff}_{\text{Thre}}$) for IoU-dominated tracklet assembly was set to (0.30, 0.30) (Fig. 2D). We optimized the key parameters for distance-dominated and IoU-dominated tracklet assembly algorithms to increase the trajectory completeness without the loss of trajectory accuracy.

Trajectory Generation by Tracklet Assembly

The main problem in tracklet assembly is to find the tracklet that belongs to the same individual on both sides of a breakpoint. The MOT-Mice system uses two steps to solve this problem. First, it uses a trace prediction module (the MOT-TP module) to extend the tracklet at the breakpoint for both the overhead and auxiliary cameras (Fig. 3A). The MOT-TP module is a cascade-forward artificial neural network (C-ANN) trained to predict extended trajectory points

Fig. 2 Parameter optimization test to achieve optimal performance in tracklet assembly by spatial information. **A** Processes of distance-dominated tracklet assembly. Left to right: Gantt chart and a 2D trace plot of six tracklets; a calculated distance-based spatial information matrix; the rule and results of distance-dominated tracklet assembly. Inf, infinite distance. **B** Parameter optimization test for distance-dominated tracklet assembly. The plots show distance settings *versus* the tracklet evaluation criteria. Dotted red line, the perfect value for each criterion. Blue dotted line, the selected parameter settings. The parameter optimization tests were conducted using recorded videos with five mice. **C** IoU-dominated tracklet assembly. From left to right: Gantt chart and a 2D trace plot of six tracklets; calculated IoU-based spatial information matrix; the rule and results of IoU-dominated tracklet assembly. **D** Parameter optimization test for IoU-dominated tracklet assembly. The plots show tracklet IoU settings *versus* the tracklet evaluation criteria. Dotted red line, the perfect value for each criterion. Blue dotted line, the selected parameter settings.



in both the forward and backward directions through 24 consecutive trajectory points. After training the MOT-TP module with 7,838 automatically-generated training and testing tracklets, the trace prediction accuracy of the MOT-TP module (i.e., the similarity between the original and predicted traces) significantly improved. As the prediction

length increased from 1 to 10 based on 24 consecutive points, the prediction accuracy gradually decreased. The accuracy for a prediction length of 6 points was $19.17\% \pm 3.09\%$ in pre-training and $95.68\% \pm 0.25\%$ in post-training. We then used the MOT-TP module to process 18 5-min videos containing 2, 3, 4, 5, 6, and 10 animals. The MOT-TP

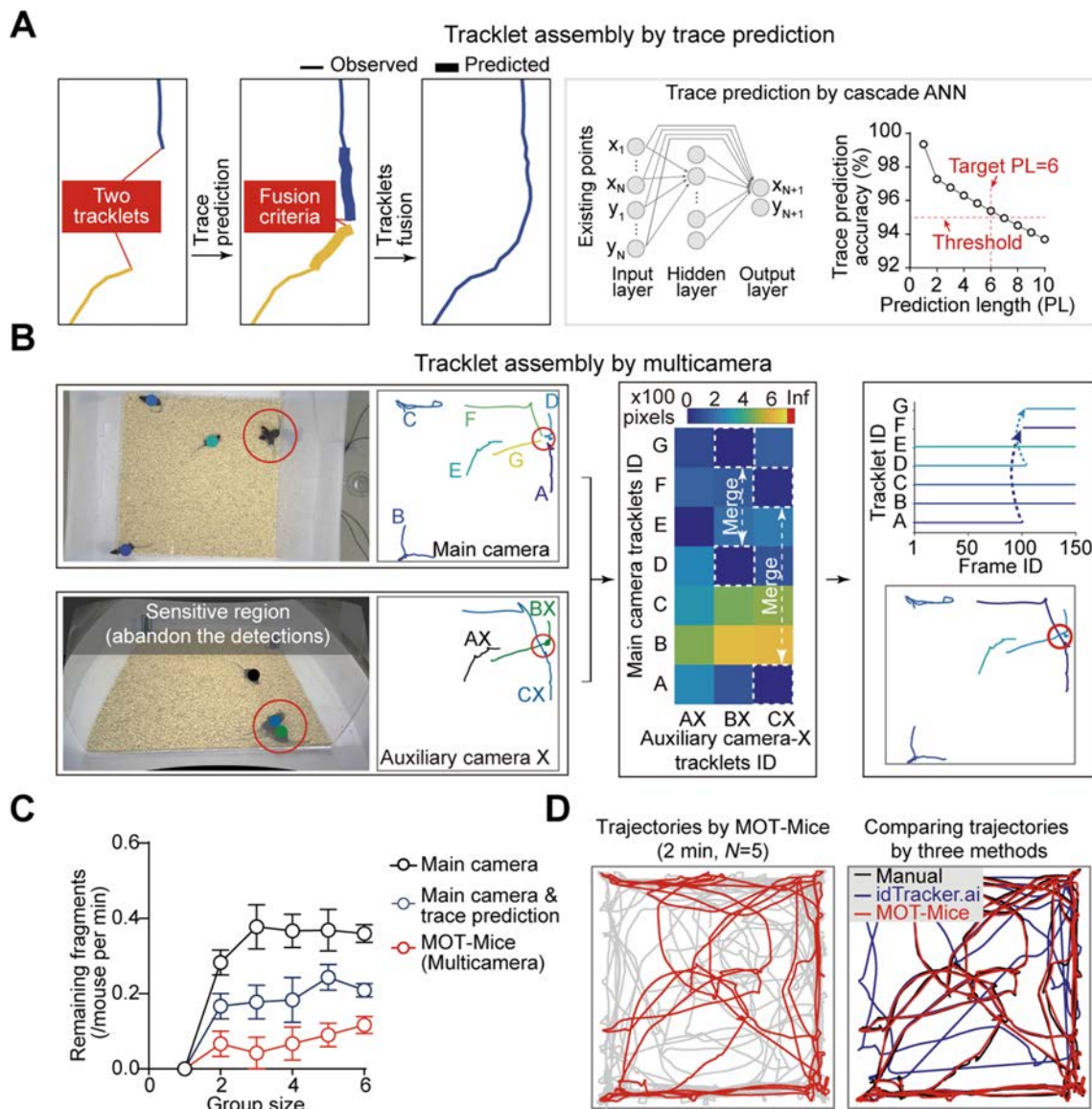
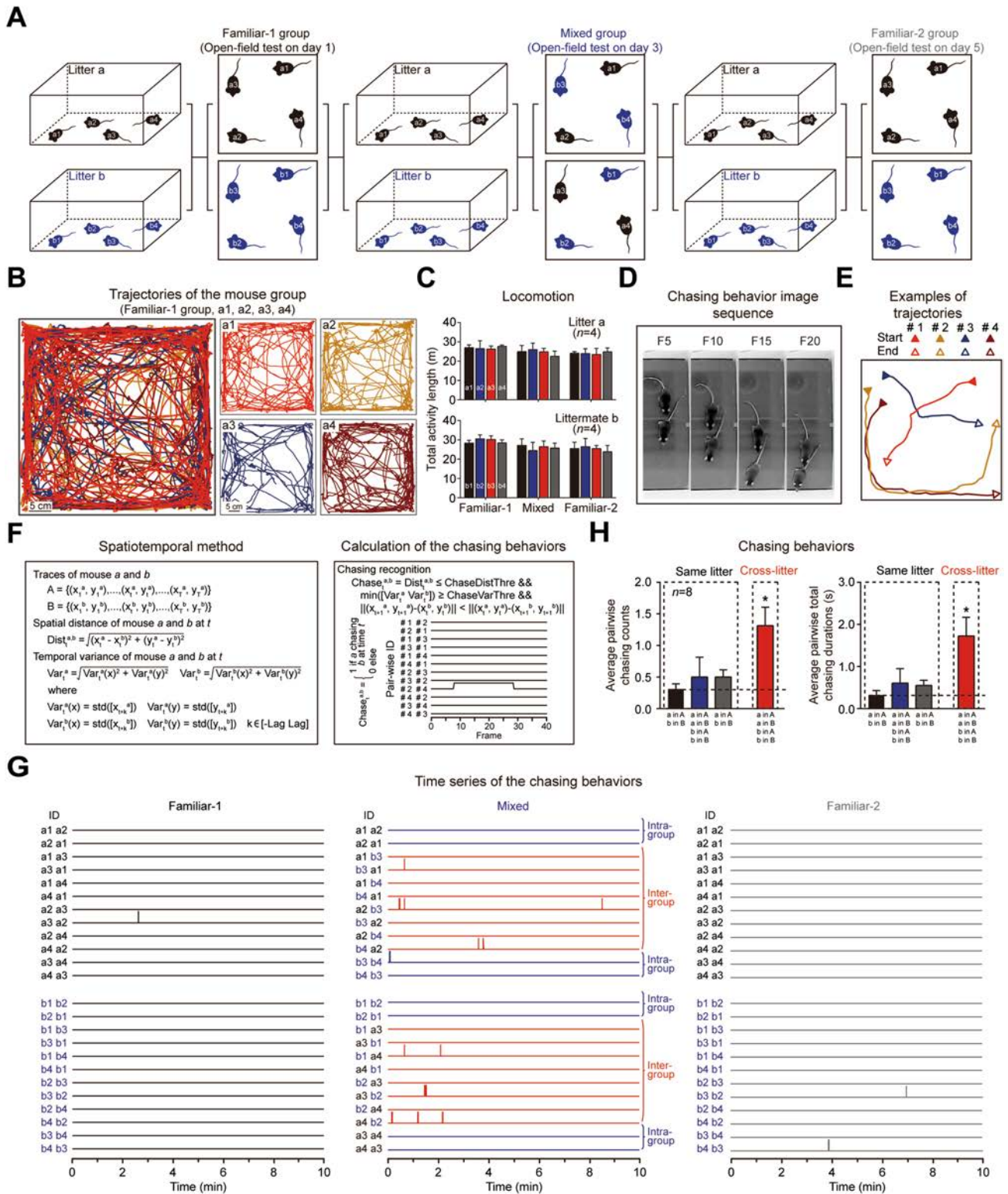


Fig. 3 Tracklet assembly by trace prediction and multi-camera fusion. **A** Single-camera tracklet assembly obtained by trace prediction using a cascade-artificial forward neural network (C-ANN). Left to right: two non-continuous tracklets are extended by the C-ANN and fused; C-ANN architecture and a trace prediction accuracy *versus* prediction length (PL) plot. **B** Multi-camera tracklet merging. Left: non-continuous tracklets from the top-view camera and simultaneously continuous tracklets from the side-view Camera X; seven tracklets (A to G) extracted from the video fragment from the top-view camera, and three tracklets (AX, BX, and CX) extracted from the video fragment from the side-view Camera X (for the side-view cameras, mouse detection and tracking were achieved before image registration, and the tracklets were generated after image registration). Middle: pairwise tracklet distances between the top-view camera and side-view Camera X; tracklets A and F in the top-view camera

belong to the same mouse, while tracklets D and G belong to a different mouse. Right: in the Gantt chart, the connecting arrows indicate that tracklets A and F and tracklets D and G should be connected; the mathematical model of tracklet merging by multiple cameras. The details regarding the two other side-view cameras in the same video segment are shown in Fig. S13. **C** Performance of the MOT-Mice system: remaining fragments *versus* the mouse group size. Black, only the main camera was used. Blue, the tracklet was generated by the main camera and fused by trace prediction. Red, the MOT-Mice multi-camera system was used. **D** Mouse group trajectories. Left: trajectories tracked by MOT-Mice. The trajectory of one mouse is highlighted in red, while the trajectories of the other four mice are denoted in gray. Right: comparison of the three tracking methods (black, manual tracking; blue, idTracker.ai; red, MOT-Mice; Fig. S14).

module successfully connected $68.89\% \pm 10.18\%$, $53.17\% \pm 12.22\%$, $54.23\% \pm 30.66\%$, $32.78\% \pm 15.12\%$, $41.95\% \pm 1.88\%$, and $13.22\% \pm 3.28\%$ of the fragmented tracklets

by identifying that they are attributed to the same mouse, but the performance degraded as the number of animals increased.



Next, to fix the remaining tracklets that could not be fixed by the MOT-TP methods, the MOT-Mice system used images collected by the auxiliary cameras to fuse the tracklets (Figs 3B and S13). For those images, the tracklets are obtained and processed in the same way as the images

collected by the main camera. Specifically, the MOT-Match module aligns the broken trajectory with a trajectory obtained from auxiliary camera images. If the trajectory from the main camera at both ends of the breakpoint can be aligned with a continuous trajectory from an auxiliary

Fig. 4 Analysis of the chasing behavior between two litters. **A** Experimental protocol. The experimental animals comprise two litters, each with 4 mice. The behaviors of the familiar-1, mixed, and familiar-2 groups were recorded for 10 min in the open field on days 1, 3, and 5. **B** Trajectories of the familiar-1 mouse group in the open field (10 min). Scale bar, 5 cm. **C** Summary graph of the total activity length for the mice in the familiar-1, mixed, and familiar-2 groups. **D** Image sequence of chasing behavior. FX, the X^{th} frame. **E** Sample trajectories from the mouse groups with 4 mice in the open field. The solid triangles indicate the start point for each mouse and the empty triangles indicate the endpoints for each mouse. **F** Mathematical definitions of the spatiotemporal method and the calculation of chasing behavior. Mathematical implementation of chasing behavior recognition and the time series of pairwise chasing behaviors for the trajectories in panel **E**. **G** Time series of the pairwise chasing behaviors for the familiar-1, mixed, and familiar-2 groups. Two sessions are shown for each group. Each session contains 12 pairwise directed chasing behavior of four mice. Each horizontal line denotes the chasing behavior of a mouse pair. The vertical lines denote the occurrence of chasing behavior. **H** Statistics of the chasing behaviors between the same-litter and cross-litter mice in the familiar-1, mixed, and familiar-2 groups. Left: average pairwise chasing counts. Right: average pairwise total chasing durations. Black, Familiar-1 group; Blue, Mixed group; Gray, Familiar-2 group; Red, Mixed group. Student's *t*-test, $n = 8$, $*P < 0.05$. Horizontal black dashed line, baseline of chasing behaviors in the Familiar-1 group.

camera, these two broken trajectories can be regarded as trajectories from the same animal. The data showed that the ability to repair breakpoints was significantly improved using the three auxiliary cameras relative to the repair ability using the main camera alone (Fig. 3C). The remaining trajectory breakpoints that could not be adequately resolved/fused for the 18 5-min videos containing 2, 3, 4, 5, 6, and 10 animals were $0.67\% \pm 0.58\%$, $0.33\% \pm 1.53\%$, $3.33\% \pm 1.53\%$, $4.67\% \pm 2.31\%$, $5.00\% \pm 1.00\%$, and $23.52\% \pm 5.27\%$, respectively, and we determined that the breakpoint-fixing performance depended on the number of animals and the number of cameras. In a 5-min video with 6 animals, the MOT-Mice system was able to track nearly complete trajectories of all the animals; only 0.117 breakpoints/(mouse per min) remained (3.51 remaining breakpoints in the 5-min video of 6 animals) (Fig. 3C).

The MOT-Mice system post-processed the tracking results through the semiautomatic checking and correction (MOT-CC) module. The MOT-CC module fuses the remaining trajectory breakpoints by human intervention and automatically finds the high-risk video segments in which two or more mice are very close to allow manual verification of whether an identity switch occurred. In an experiment tracking five mice, the trajectories generated by idTracker.ai exhibited identity errors, while all the trajectories generated by the MOT-Mice system without manual correction maintained correct identities (Figs 3D and S14). Hence, the MOT-Mice system achieved noninvasive tracking of every individual in unmarked mouse groups.

Application of the MOT-Mice System to Social Behavior (Chasing)

Finally, as proof of principle, we used the MOT-Mice system to investigate chasing behavior, which is a typical social interaction behavior in mouse populations (Fig. 4). Four mice were placed in an open field; then their chasing behavior over a 10-min period was investigated using the MOT-Mice system (Fig. 4A–D). Chasing behavior typically involves one mouse following directly behind another and was defined as the trajectories of two animals with a concomitant relationship. The accompanying relationship satisfies a distance and time threshold (in this study, these thresholds were defined as a distance between the two mice < 30 mm that lasted for > 0.75 s; Fig. 4E, F). We found that animals that had been housed together since birth rarely chased each other during the recording on the first day (rate: 0.3125 ± 0.0799 times/mouse pair, duration: 0.3264 ± 0.1013 s/mouse pair; Fig. 4G, H); however, when 4 mice from two different litters were put into the open field together, the cross-litter chasing count was significantly higher than the same-litter chasing count (rate: 1.3125 ± 0.2941 times/mouse pair, $P < 0.05$; duration: 1.7238 ± 0.4460 s/mouse pair, $P < 0.05$). This result demonstrated a social preference of mice for chasing novel peers. Thus, the MOT-Mice system provides a reliable and precise method for simultaneously tracking the movement trajectories of multiple mice that can facilitate the study of social behavior in mice.

Discussion

To overcome challenging problems in tracking unmarked mice in groups (such as the flexible bodies of rodents and close interactions), we established the noninvasive MOT-Mice tracking system based on artificial intelligence and multi-camera image fusion technology. The MOT-Mice system accurately detects unmarked individual mice using a deep CNN algorithm, and it also applies both multi-camera fusion and C-ANN technologies to assemble the fragmented tracklets and obtain complete trajectories.

Tracklet fragments are common in multi-object tracking. The MOT-Mice system used the MOT-TP module to assemble tracklets of the main camera first, then used multi-camera fusion technology to assemble the tracklets when the MOT-TP method failed. In the idTracker.ai system, animal crossing and occlusion scenarios are detected and abandoned; abandonment leads to the loss of critical information during social interaction and a high risk of misidentification [25]. The MOT-Mice system solved these problems directly by continuously detecting and tracking animals even when they engaged in close interactions such as crossing and huddling. This approach is more robust than single-camera tracking

systems and can be applied to scenarios of different complexities (different arena sizes and numbers of animals, and environmental enrichment) and excellent scalability can be achieved by increasing or decreasing the number of monitoring cameras. Besides, this approach has the potential to fuse information from different kinds of cameras, such as infrared and regular cameras.

Many existing tracking systems detect animals using traditional image-processing methods such as image binarization based on thresholding algorithms. However, the existing systems have major limitations for use in experimental environments because their traditional image-processing methods are susceptible to the contrast between animals and environments. The MOT-Mice system applies the state-of-the-art Faster R-CNN model, which has won numerous competitions such as the ImageNet Large Scale Visual Recognition Challenge (ILSVRC) and Common Objects in Context (COCO) [57], to achieve mouse detection. Furthermore, the ResNet-18 model [60] used to extract features has proven to be powerful in many complex tasks, such as natural image and medical image recognition [61, 62]. As a result, the MOT-Mice system can detect animals even from images with low contrast between the fur color and background (such as detecting black mice against a black background panel), as well as detecting individual mice in enriched environments (Fig. S15). The incorporation of deep learning techniques greatly extends the application potential of the MOT-Mice system.

There are also several reported DL-based solutions for animal pose estimation [32, 46–48], and animal whole-body 3D kinematic analysis [49–51]. DeepLabCut [46] and LEAP (LEAP estimates animal pose) [32] are powerful DL-based animal pose estimation tools, both of which require only a few data annotations and achieved high-performance prediction of animal body parts. In addition, the successors of the two tools, Multi-animal DeepLabCut (maDLC) [63] and social LEAP (SLEAP) [48], achieve multi-animal pose tracking. Both maDLC and SLEAP tools adopt a bottom-up approach to identify key body points and then assign them to individuals [64]. Although these tools (DeepLabCut, LEAP, maDLC, and SLEAP) have proven to be powerful and are widely used, they still lack detailed 3D behavioral descriptions of animal bodies. The CAPTURE (Continuous Appendicular and Postural Tracking Using Retroreflector Embedding) tool achieves week-long timescale tracking of the 3D kinematics of a rat's head, trunk, and limbs [49]. The MouseVenue3D tool provides a hierarchical 3D-motion learning framework to acquire a markerless animal skeleton with tens of body parts [50, 51]. Notably, both the CAPTURE and MouseVenue3D tools applied multi-camera techniques and were designed for the individual animal. The MOT-Mice system was developed to track multiple animals using multi-camera fusion and deep learning techniques, and

it may work cooperatively with these reported solutions to achieve a more sophisticated analysis of animal behavior.

There are two main limitations in this study. First, like the reported maDLC and SLEAP tools, the MOT-Mice system lacks an identity maintenance approach for animal identification [64]. When the number of animals increases and the animals interact closely and more frequently, the probability of identity-switch errors increases, leading to additional manual correction tasks. A possible solution is to use invasive RFID technology to ensure identity maintenance in the long-term tracking of multiple animals. Although the non-invasive MOT-Mice system has shown stronger adaptability to the experimental environment than traditional RFID-based solutions [38, 40], the combination of DL and RFID may enhance the system's applicability for hours and even days of multi-animal behavioral video recording.

Another limitation of the MOT-Mice system lies in its inability to automatically mine complex interactions. In applying the MOT-Mice system to chasing behavior, it was necessary to define the chasing behavior before exploring the differences between same- and cross-litter chasing behaviors. There are many other important fine social behaviors, such as mating, fighting, and sniffing. However, when analyzing various fine behaviors, centroid-based metrics may not be accurate enough because of the lack of information. Combining the MOT-Mice system with pose estimation [48], whole-body 3D kinematics [50, 51], and visual features from original videos [65] would be more efficient for fine behavior analysis. Most importantly, advanced DL-based animal behavior analysis systems can recognize complex individual behaviors and social interactions from video recordings, and have great potential to facilitate research on psychiatric disorders, such as autism, schizophrenia, depression, substance abuse, and anxiety. In a study that analyzed spontaneous behavior, although the whole-body 3D kinematics approach analyzed individual animals' behavior, it achieved accurate identification of behavioral phenotypes for transgenic animal models that showed autistic-like behaviors [50]. The animal group analysis systems have the advantages that they can provide more complicated features for social interaction, and it will be compelling to extend the technology to psychiatric disorders research.

In summary, the MOT-Mice system is strongly generalizable to different experimental environments, such as a large arena with occlusions or several chambers connected by a corridor that need multiple cameras to monitor the activities of animals all the time. The system provides a step forward in the noninvasive tracking of unmarked individual animals within groups and has great potential for providing insights into the patterns and mechanisms of animal social interactions.

Acknowledgments This work was supported by grants from the National Key R&D Program of China (2017YFA0105201); the National Natural Science Foundation of China (81925011, 92149304, 31900698, 32170954, and 32100763); the Key-Area Research and Development Program of Guangdong Province (2019B030335001); The Youth Beijing Scholars Program (015), Support Project of High-level Teachers in Beijing Municipal Universities (CIT&TCD20190334); Beijing Advanced Innovation Center for Big Data-based Precision Medicine, Capital Medical University, Beijing, China (PXM2021_014226_000026).

Conflict of interest The authors declare that there are no conflicts of interest.

References

- Dunbar RI, Shultz S. Evolution in the social brain. *Science* 2007, 317: 1344–1347.
- Sallet J, Mars RB, Noonan M, Andersson JL, O'Reilly J, Jbabdi S. Social network size affects neural circuits in macaques. *Science* 2011, 334: 697–700.
- Ben-Ami Bartal I, Decety J, Mason P. Empathy and pro-social behavior in rats. *Science* 2011, 334: 1427–1430.
- Keller M, Vandenberg LN, Charlier TD. The parental brain and behavior: A target for endocrine disruption. *Front Neuroendocrinol* 2019, 54: 100765.
- Bridges RS. Neuroendocrine regulation of maternal behavior. *Front Neuroendocrinol* 2015, 36: 178–196.
- Jager A, Maas DA, Fricke K, de Vries RB, Poelmans G, Glennon JC. Aggressive behavior in transgenic animal models: A systematic review. *Neurosci Biobehav Rev* 2018, 91: 198–217.
- Manchia M, Carpiniello B, Valtorta F, Comai S. Serotonin dysfunction, aggressive behavior, and mental illness: Exploring the link using a dimensional approach. *ACS Chem Neurosci* 2017, 8: 961–972.
- Safran RJ, Levin II, Fosdick BK, McDermott MT, Semenov GA, Hund AK, *et al.* Using networks to connect individual-level reproductive behavior to population patterns. *Trends Ecol Evol* 2019, 34: 497–501.
- Port M, Schülke O, Ostner J. Reproductive tolerance in male primates: Old paradigms and new evidence. *Evol Anthropol* 2018, 27: 107–120.
- Bass C, Halligan PW. Illness related deception: Social or psychiatric problem? *J R Soc Med* 2007, 100: 81–84.
- Greene RW, Biederman J, Zerwas S, Monuteaux MC, Goring JC, Faraone SV. Psychiatric comorbidity, family dysfunction, and social impairment in referred youth with oppositional defiant disorder. *Am J Psychiatry* 2002, 159: 1214–1224.
- Shultz S, Klin A, Jones W. Neonatal transitions in social behavior and their implications for autism. *Trends Cogn Sci* 2018, 22: 452–469.
- Yu B, Yuan B, Dai JK, Cheng TL, Xia SN, He LJ, *et al.* Reversal of social recognition deficit in adult mice with MECP2 duplication *via* normalization of MeCP2 in the medial prefrontal cortex. *Neurosci Bull* 2020, 36: 570–584.
- Green MF, Horan WP, Lee J, McCleery A, Reddy LF, Wynn JK. Social disconnection in schizophrenia and the general community. *Schizophr Bull* 2018, 44: 242–249.
- Fernández-Theoduloz G, Paz V, Nicolaisen-Sobesky E, Pérez A, Buunk AP, Cabana Á, *et al.* Social avoidance in depression: A study using a social decision-making task. *J Abnorm Psychol* 2019, 128: 234–244.
- Lemyre A, Gauthier-Légaré A, Bélanger RE. Shyness, social anxiety, social anxiety disorder, and substance use among normative adolescent populations: A systematic review. *Am J Drug Alcohol Abuse* 2019, 45: 230–247.
- Romano M, Moscovitch DA, Ma RF, Huppert JD. Social problem solving in social anxiety disorder. *J Anxiety Disord* 2019, 68: 102152.
- Rein B, Ma KJ, Yan Z. A standardized social preference protocol for measuring social deficits in mouse models of autism. *Nat Protoc* 2020, 15: 3464–3477.
- Ariyasiri K, Choi TI, Kim OH, Hong TI, Gerlai R, Kim CH. Pharmacological (ethanol) and mutation (Sam2 KO) induced impairment of novelty preference in zebrafish quantified using a new three-chamber social choice task. *Prog Neuropsychopharmacol Biol Psychiatry* 2019, 88: 53–65.
- Zheng J, Tian Y, Xu H, Gu L, Xu H. A standardized protocol for the induction of specific social fear in mice. *Neurosci Bull* 2021, 37: 1708–1712.
- Fan Z, Zhu H, Zhou T, Wang S, Wu Y, Hu H. Using the tube test to measure social hierarchy in mice. *Nat Protoc* 2019, 14: 819–831.
- Zhou T, Zhu H, Fan Z, Wang F, Chen Y, Liang H, *et al.* History of winning remodels thalamo-PFC circuit to reinforce social dominance. *Science* 2017, 357: 162–168.
- Gomez-Marin A, Paton JJ, Kampff AR, Costa RM, Mainen ZF. Big behavioral data: Psychology, ethology and the foundations of neuroscience. *Nat Neurosci* 2014, 17: 1455–1462.
- Crabbe JC, Morris RG. Festina lente: Late-night thoughts on high-throughput screening of mouse behavior. *Nat Neurosci* 2004, 7: 1175–1179.
- Romero-Ferrero F, Bergomi MG, Hinz RC, Heras FJH, de Polavieja GG. Idtracker ai Tracking all individuals in small or large collectives of unmarked animals. *Nat Methods* 2019, 16: 179–182.
- Bai YX, Zhang SH, Fan Z, Liu XY, Zhao X, Feng XZ, *et al.* Automatic multiple zebrafish tracking based on improved HOG features. *Sci Rep* 2018, 8: 10884.
- Orger MB, de Polavieja GG. Zebrafish behavior: Opportunities and challenges. *Annu Rev Neurosci* 2017, 40: 125–147.
- Egnor SE, Branson K. Computational analysis of behavior. *Annu Rev Neurosci* 2016, 39: 217–236.
- Hong W, Kennedy A, Burgos-Artizzu XP, Zelikowsky M, Navonne SG, Perona P, *et al.* Automated measurement of mouse social behaviors using depth sensing, video tracking, and machine learning. *Proc Natl Acad Sci U S A* 2015, 112: E5351–E5360.
- Pérez-Escudero A, Vicente-Page J, Hinz RC, Arganda S, de Polavieja GG. idTracker: Tracking individuals in a group by automatic identification of unmarked animals. *Nat Methods* 2014, 11: 743–748.
- Dolado R, Gimeno E, Beltran FS, Quera V, Pertusa JF. A method for resolving occlusions when multitasking individuals in a shoal. *Behav Res Methods* 2015, 47: 1032–1043.
- Pereira TD, Aldarondo DE, Willmore L, Kislin M, Wang SS, Murthy M, *et al.* Fast animal pose estimation using deep neural networks. *Nat Methods* 2019, 16: 117–125.
- Forkosh O, Karamihalev S, Roeh S, Alon U, Anpilov S, Touma C, *et al.* Identity domains capture individual differences from across the behavioral repertoire. *Nat Neurosci* 2019, 22: 2023–2028.
- Noldus LP, Spink AJ, Tegelenbosch RA. EthoVision: A versatile video tracking system for automation of behavioral experiments. *Behav Res Methods Instrum Comput* 2001, 33: 398–414.
- Spink A, Tegelenbosch R, Buma M, Noldus L. The EthoVision video tracking system—a tool for behavioral phenotyping of transgenic mice. *Physiol Behav* 2001, 73: 731–744.
- Ohayon S, Avni O, Taylor AL, Perona P, Egnor SR. Automated multi-day tracking of marked mice for the analysis of social behaviour. *J Neurosci Methods* 2013, 219: 10–19.

37. Shemesh Y, Sztainberg Y, Forkosh O, Shlapobersky T, Chen A, Schneidman E. High-order social interactions in groups of mice. *eLife* 2013, 2: e00759.
38. Howerton CL, Garner JP, Mench JA. A system utilizing radio frequency identification (RFID) technology to monitor individual rodent behavior in complex social settings. *J Neurosci Methods* 2012, 209: 74–78.
39. Freund J, Brandmaier AM, Lewejohann L, Kirste I, Kritzler M, Krüger A, *et al.* Emergence of individuality in genetically identical mice. *Science* 2013, 340: 756–759.
40. Weissbrod A, Shapiro A, Vasserman G, Edry L, Dayan M, Yitzhaky A, *et al.* Automated long-term tracking and social behavioural phenotyping of animal colonies within a semi-natural environment. *Nat Commun* 2018, 2013: 4.
41. Pavković Ž, Potrebić M, Kanazir S, Pešić V. Motivation, risk-taking and sensation seeking behavior in propofol anesthesia exposed peripubertal rats. *Prog Neuro Psychopharmacol Biol Psychiatry* 2020, 96: 109733.
42. Jin X, Ji L, Chen Q, Sheng R, Ji F, Yang J. Anesthesia plus surgery in neonatal period impairs preference for social novelty in mice at the juvenile age. *Biochem Biophys Res Commun* 2020, 530: 603–608.
43. Stratmann G, Lee J, Sall JW, Lee BH, Alvi RS, Shih J, *et al.* Effect of general anesthesia in infancy on long-term recognition memory in humans and rats. *Neuropsychopharmacology* 2014, 39: 2275–2287.
44. Branson K, Robie AA, Bender J, Perona P, Dickinson MH. High-throughput ethomics in large groups of *Drosophila*. *Nat Methods* 2009, 6: 451–457.
45. de Chaumont F, Coura RD, Serreau P, Cressant A, Chabout J, Granon S, *et al.* Computerized video analysis of social interactions in mice. *Nat Methods* 2012, 9: 410–417.
46. Mathis A, Mamidanna P, Cury KM, Abe T, Murthy VN, Mathis MW, *et al.* DeepLabCut: Markerless pose estimation of user-defined body parts with deep learning. *Nat Neurosci* 2018, 21: 1281–1289.
47. Bala PC, Eisenreich BR, Yoo SBM, Hayden BY, Park HS, Zimmermann J. Automated markerless pose estimation in freely moving macaques with OpenMonkeyStudio. *Nat Commun* 2020, 11: 4560.
48. Pereira TD, Tabris N, Matsliah A, Turner DM, Li J, Ravindranath S, *et al.* SLEAP: A deep learning system for multi-animal pose tracking. *Nat Methods* 2022, 19: 486–495.
49. Marshall JD, Aldarondo DE, Dunn TW, Wang WL, Berman GJ, Ölveczky BP. Continuous whole-body 3D kinematic recordings across the rodent behavioral repertoire. *Neuron* 2021, 109: 420–437.e8.
50. Huang K, Han Y, Chen K, Pan H, Zhao G, Yi W, *et al.* A hierarchical 3D-motion learning framework for animal spontaneous behavior mapping. *Nat Commun* 2021, 12: 2784.
51. Han Y, Huang K, Chen K, Pan H, Ju F, Long Y, *et al.* MouseVenue3D: A markerless three-dimension behavioral tracking system for matching two-photon brain imaging in free-moving mice. *Neurosci Bull* 2022, 38: 303–317.
52. Schofield D, Nagrani A, Zisserman A, Hayashi M, Matsuzawa T, Biro D, *et al.* Chimpanzee face recognition from videos in the wild using deep learning. *Sci Adv* 2019, 5: 0736.
53. Liu WQ, Camps O, Szaier M. Multi-camera multi-object tracking. 2017: arXiv: 1709.07065. doi: <https://doi.org/10.48550/arXiv.1709.07065>.
54. Wang X. Intelligent multi-camera video surveillance: A review. *Pattern Recognit Lett* 2013, 34: 3–19.
55. Thanos PK, Restif C, O'Rourke JR, Lam CY, Metaxas D. Mouse Social Interaction Test (MoST): A quantitative computer automated analysis of behavior. *J Neural Transm* 2017, 124: 3–11.
56. Peters SM, Pinter IJ, Pothuizen HH, de Heer RC, van der Harst JE, Spruijt BM. Novel approach to automatically classify rat social behavior using a video tracking system. *J Neurosci Methods* 2016, 268: 163–170.
57. Ren S, He K, Girshick R, Sun J. Faster R-CNN: Towards real-time object detection with region proposal networks. *IEEE Trans Pattern Anal Mach Intell* 2017, 39: 1137–1149.
58. Blackman S, Popoli R (1999) *Design and Analysis of Modern Tracking Systems*. Artech House Publishers, Norwood.
59. Zhu H, Liu D, Zhang S, Zhu Y, Teng L, Teng S. Solving the Many to Many assignment problem by improving the Kuhn-Munkres algorithm with backtracking. *Theor Comput Sci* 2016, 618: 30–41.
60. He K, Zhang X, Ren S, Sun J. Deep residual learning for image recognition. *IEEE Conference on Computer Vision and Pattern Recognition (CVPR)* 2016, 2016: 770–778.
61. Szegedy C, Ioffe S, Vanhoucke V, Alemi A. Inception-v4, inception-ResNet and the impact of residual connections on learning. *Proc AAAI Conf Artif Intell* 2017, <https://doi.org/10.48550/arXiv.1602.07261>.
62. Su F, Sun Y, Hu Y, Yuan P, Wang X, Wang Q, *et al.* Development and validation of a deep learning system for ascites cytopathology interpretation. *Gastric Cancer* 2020, 23: 1041–1050.
63. Lauer J, Zhou M, Ye S, Menegas W, Schneider S, Nath T, *et al.* Multi-animal pose estimation, identification and tracking with DeepLabCut. *Nat Methods* 2022, 19: 496–504.
64. Agezo S, Berman GJ. Tracking together: Estimating social poses. *Nat Methods* 2022, 19: 410–411.
65. Jia Y, Li S, Guo X, Lei B, Hu J, Xu XH, *et al.* Self-supervised features extraction of animal behaviors. *eLife* 2022, 11: e76218.

Springer Nature or its licensor (e.g. a society or other partner) holds exclusive rights to this article under a publishing agreement with the author(s) or other rightsholder(s); author self-archiving of the accepted manuscript version of this article is solely governed by the terms of such publishing agreement and applicable law.

Leaky Gut Plays a Critical Role in the Pathophysiology of Autism in Mice by Activating the Lipopolysaccharide-Mediated Toll-Like Receptor 4–Myeloid Differentiation Factor 88–Nuclear Factor Kappa B Signaling Pathway

Fang Li¹ · Haoran Ke² · Siqi Wang³ · Wei Mao¹ · Cexiong Fu⁴ · Xi Chen⁵ ·
Qingqing Fu⁶ · Xiaori Qin¹ · Yonghua Huang¹ · Bidan Li⁴ · Shibing Li⁷ ·
Jingying Xing⁸ · Minhui Wang⁹ · Wenlin Deng¹⁰

Received: 14 April 2022 / Accepted: 9 August 2022 / Published online: 18 December 2022
© The Author(s) 2022

Abstract Increased intestinal barrier permeability, leaky gut, has been reported in patients with autism. However, its contribution to the development of autism has not been determined. We selected dextran sulfate sodium (DSS) to disrupt and metformin to repair the intestinal barrier in BTBR T⁺tf/J autistic mice to test this hypothesis. DSS treatment resulted in a decreased affinity for social proximity; however, autistic behaviors in mice were improved after the administration of metformin. We found an increased affinity

for social proximity/social memory and decreased repetitive and anxiety-related behaviors. The concentration of lipopolysaccharides in blood decreased after the administration of metformin. The expression levels of the key molecules in the toll-like receptor 4 (TLR4)–myeloid differentiation factor 88 (MyD88)–nuclear factor kappa B (NF-κB) pathway and their downstream inflammatory cytokines in the cerebral cortex were both repressed. Thus, “leaky gut” could be a trigger for the development of autism *via* activation of the lipopolysaccharide-mediated TLR4–MyD88–NF-κB pathway.

Fang Li, Haoran Ke, Siqi Wang, Wei Mao and Cexiong Fu have contributed equally to this work.

Supplementary Information The online version contains supplementary material available at <https://doi.org/10.1007/s12264-022-00993-9>.

✉ Wenlin Deng
dengwl3@mail.sysu.edu.cn

¹ Department of Gastroenterology, Gastroenterology Endoscopy Center, Hainan General Hospital, Hainan Affiliated Hospital of Hainan Medical University, Haikou 570311, China

² Hepatology Unit, Department of Infectious Diseases, Nanfang Hospital, Southern Medical University, Guangzhou 510515, China

³ Department of Gastroenterology, First Affiliated Hospital of Guangzhou Medical University, Guangzhou Medical University, Guangzhou 510120, China

⁴ Department of Hepatopancreatobiliary Surgery, Hainan General Hospital, Hainan Affiliated Hospital of Hainan Medical University, Haikou 570311, China

⁵ Otolaryngology-Head and Neck Surgery, Hospital of Hainan Province, Department of Otorhinolaryngology, Head and Neck Surgery, Hainan General Hospital, Hainan Affiliated Hospital of Hainan Medical University, Haikou 570311, China

Keywords Autism · Gut · Lipopolysaccharide · Toll-like receptor 4 · Metformin

⁶ Department of Radiology, Hainan General Hospital, Hainan Affiliated Hospital of Hainan Medical University, Haikou 570311, China

⁷ Department of Pediatric Surgery, Hainan General Hospital, Hainan Affiliated Hospital of Hainan Medical University, Haikou 570311, China

⁸ Department of Gastroenterology, Hainan General Hospital, Hainan Affiliated Hospital of Hainan Medical University, Haikou 570311, China

⁹ Department of Nephrology, Department of Nephrology, Hainan Affiliated Hospital of Hainan Medical College, Hainan General Hospital, Haikou 570311, China

¹⁰ Department of Pediatrics, The Sixth Affiliated Hospital, Sun Yat-sen University, Guangzhou 510655, China

Introduction

Autism falls under autism spectrum disorder and is characterized by repetitive behaviors and difficulties with social communication [1] that can affect multiple systems in the body, including the nervous system, immune system, and gastrointestinal tract [2]. The prevalence of autism has dramatically increased during the past few decades [3], but its causes are largely unknown. There is currently no effective way to treat the core symptoms of autism.

In addition to the aforementioned features, individuals with autism spectrum disorder (ASD) often suffer from gastrointestinal problems [4]. Studies over the past decade have demonstrated that autistic children experience gastrointestinal symptoms 4.4 times more often than neurotypical children; this mainly includes constipation, diarrhea, and abdominal pain [5]. A large meta-analysis comparing autism cases with healthy controls from 1980 to 2012 and a multicenter study with >14,000 ASD individuals both reported this phenotype [6]. Furthermore, GI symptoms tend to be strongly correlated with the severity of autism and with increased irritability, anxiety, and social withdrawal [7]. The frequency of gastrointestinal problems was associated with greater social withdrawal, stereotypy, irritability, and hyperactivity in an examination of 960 children from the Childhood Autism Risks from Genetics and Environment (CHARGE) study [8]. Thus, scientists have reached a consensus that gastrointestinal problems may potentiate autistic behavioral issues [9–11]. This evidence suggests that gut dysfunction may be a major promotor of the behavioral symptoms of autism. This conclusion is consistent with the concept of the "gut–brain" axis proposed in recent years [12–14].

The 'gut–brain' axis describes the bidirectional physiological connection that helps information exchange between the gut and the brain [12]. For instance, studies have reported that lipopolysaccharides (LPS), metabolites of gram-negative bacteria, can pass through the damaged intestinal barrier into the brain and induce a pro-inflammatory environment that can affect brain function [12, 15]. The gastrointestinal mucosa forms a barrier between the body and the luminal environment *via* intestinal epithelial cells connected through tight junctions (TJs) and a mucus layer, which separates trillions of microorganisms from the body. The exclusionary properties of the gastrointestinal mucosa are referred to as the gastrointestinal barrier, which is considered to be the core link between the gut and the brain in the gut–brain axis [16]. Dysbiosis of microbiota has not only been reported in gut-related diseases such as inflammatory bowel disease and irritable bowel syndrome, but also in neurological and mental disorders, like stress, depression, Alzheimer's disease, Parkinson's disease, and ASD. In addition to dysbiosis, the integrity of intestinal barrier composition is

also important to health. Dysfunction of the intestinal barrier has been reported in patients with autism and even in first-degree relatives of affected individuals; a high percentage of abnormal intestinal permeability values, measured by calculating the lactulose/mannitol ratio, has been found in patients with autism and their relatives when compared with healthy controls [17]. D' Eufemia *et al.* also found damage to TJs of the gut in autistic children and indicated that in some patients with infantile autism, damage to these junctions occurs in the absence of gastrointestinal disorders [18]. However, another recent study showed no abnormal intestinal permeability in autistic children compared with healthy siblings and unrelated controls [19]. Increased intestinal permeability has also been found in some close non-autistic relatives of autistic individuals, suggesting that intestinal integrity is not a consequence of ASD [20]. Thus, it is unclear whether the disruption of the intestinal barrier is a cause or a consequence of autism.

Our results confirmed that increased intestinal barrier permeability, referred to as 'leaky gut', does occur in BTBR T⁺tf/J mice that have been used as an animal model of autism [21]. Behavioral manifestations of these autistic mice were significantly relieved after the administration of metformin to repair the intestinal barrier. These results showed that the 'leaky gut' may indeed contribute to the development of autism. Moreover, we elucidated the potential mechanism by which gut-originated LPS may pass through the damaged intestinal barrier into the brain to activate the TLR4-mediated myeloid differentiation primary response protein 88-dependent nuclear factor-kappa B (TLR4/MyD88/NF- κ B) pathway, resulting in a pro-inflammatory micro-environment, which seems to be an important contributor of autism. The down-regulated expression levels of the key molecules and inflammatory cytokines of the TLR4 signaling pathway in the cerebral cortex, after the intestinal barrier was repaired, support our point.

Few studies have been designed to determine the role of abnormal gut permeability in the neuropsychiatric manifestations of ASD. In this study, we aimed to elucidate the effect of a 'leaky gut' on the various autistic behavioral phenotypes, using BTBR mice (an autism model). In addition, we sought to further understand the underlying mechanisms that increase the permeability of the intestinal barrier contributing to autism.

Materials and Methods

Animals

All animal experiments were performed according to protocols approved by the Animal Care Committee of Hainan General Hospital and were conducted in accordance with

the US National Institutes of Health Guide for the Care and Use of Laboratory Animals (NIH Publication 85–23, revised 2011). Male BTBR T⁺tf/J (BTBR, Jackson Laboratory, Bar Harbor, ME, USA) and C57BL/6 (B6, Southern Medical University, Guangzhou, China) mice, aged 7–8 weeks, and weighing 20–25 g were maintained under controlled light conditions (12:12 light-dark cycle) with a normal chow diet and water provided *ad libitum*.

Treatment Protocol

To explore the effects of intestinal barrier changes on autistic behavior, all animals were divided into four groups as follows (Fig. 1):

- (1) NS (normal distilled water) group: BTBR and B6 mice both received distilled water only (BTBR *vs* B6);
- (2) DSS group: 2% DSS treatment was administered to BTBR mice daily for one week. Matched, mice of the same strain were administered distilled water daily for the same time (DSS *vs* Distilled water);
- (3) Metformin group: metformin was administered to BTBR mice by lavage for two weeks. Matched mice of the same strain were administered distilled water daily for the same time (Met *vs* Distilled water);

(4) Metformin plus DSS group: 2% DSS was administered to BTBR mice in the first week, followed by metformin treatment or distilled water for the next week (DSS+Met *vs* DSS+Distilled water).

During the observation period, the body weight of each mouse was monitored every two days. All the animals were anesthetized and then sacrificed by cervical dislocation by the end of the experiment. The cerebral cortex was carefully removed and immediately frozen in liquid nitrogen for further analysis. Colon tissue was removed and cut into two pieces. One piece was immediately frozen in liquid nitrogen for further analysis. The other piece was fixed in 10% formaldehyde for histopathological study.

Drugs

Metformin (Sigma-Aldrich, Cat No. 317240) and Dextran Sulfate Sodium Salt (DSS) (Sigma-Aldrich, Cat No. 67578) were from Sigma-Aldrich (St. Louis, Missouri, USA). Metformin was dissolved in H₂O and stored at –20°C. Mice were dosed with a metformin compound formulation of 400 mg/kg once per day by oral gavage.

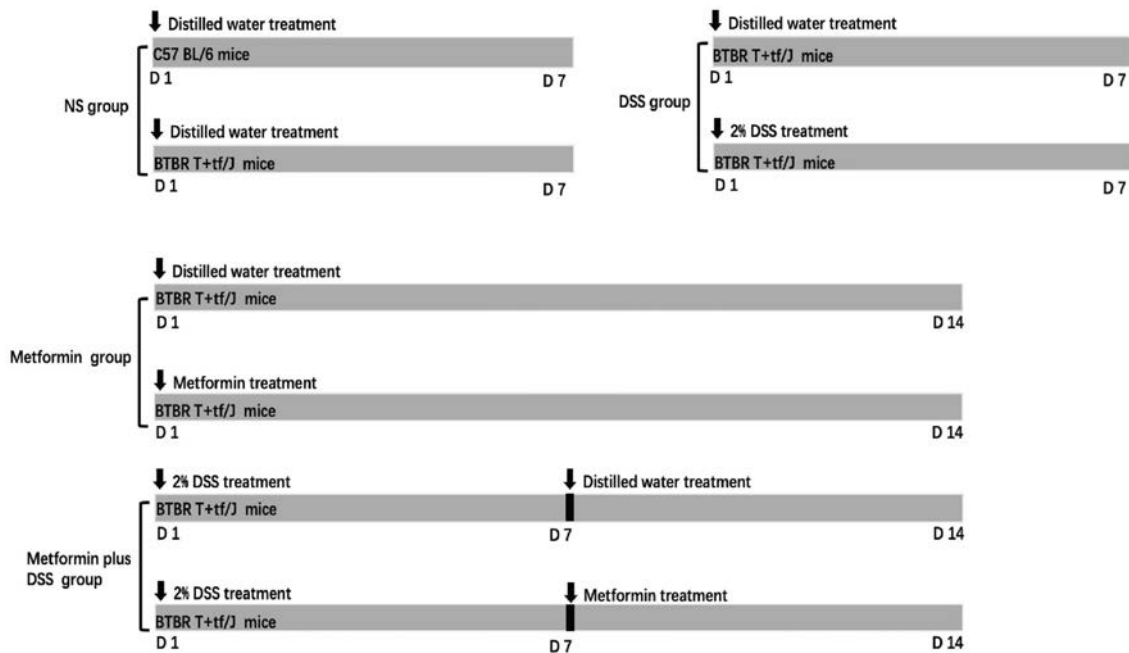


Fig. 1 Design of the mouse experiment. The experiments were performed on four groups each composed of 9–13 male C57BL/6J and BTBR T⁺tf/J mice: (1) NS (normal saline) group – BTBR T⁺tf/J and C57 BL/6 mice both received distilled water; (2) DSS group – BTBR T⁺tf/J mice received 2% DSS treatment or distilled water; (3) metformin group – metformin or distilled water was applied to BTBR T⁺tf/J mice by lavage for two weeks; (4) metformin plus DSS group

– BTBR T⁺tf/J mice received 2% DSS in the first week followed by metformin treatment or distilled water for the next week. To test our hypothesis, we applied a number of tests on these groups: IHC and RT-PCR, an intestinal barrier permeability test, and behavioral analysis (5 mice per treatment for IHC analysis, 6–8 mice per treatment for FITC dextran testing, 8–13 mice per treatment for behavioral analysis, and 4–8 mice per treatment for RT-PCR analysis).

Total RNA Extraction and Real-Time Quantitative Polymerase Chain Reaction (RT-PCR)

Total RNA was extracted using TRIzol reagent (Invitrogen™, Waltham, Massachusetts, USA; Cat No. 15596-026). A total of 1 µg of RNA was reverse-transcribed using the PrimeScript RT Master Mix (Takara Bio Inc., Shiga, Japan; Cat No. RR036A) to produce cDNA. The levels of mRNA expression were measured by RT-PCR assays with TB Green PCR Master Mix (Takara, Cat No. 639676, TB Green Advantage qPCR Premix) on a Bio-Rad Real-Time PCR instrument (Bio-Rad, Hercules, CA, USA) using the forward and reverse primers listed in Table S1. Data were analyzed using the $\Delta\Delta C_t$ method with β -actin as the reference marker.

Immunohistochemistry (IHC) Analyses

IHC was applied to paraffin-embedded sections as described in our previous study [9]. Briefly, the sections were dewaxed in xylene, rehydrated in graded ethanols, and immersed in 3% H₂O₂ for 10 min to block endogenous peroxidase activity. Antigen retrieval was achieved by immersing the slides in the ethylenediaminetetraacetic acid buffer for 15 min. Non-specific signals were blocked with goat serum for 30 min. Sections were stained with primary antibodies (listed in Table S2) overnight at 4°C in a humid chamber, followed by incubation with HRP-conjugated Streptavidin (R&D Systems, Minneapolis, MN, USA, Cat No. DY998) for 30 min. Finally, a positive signal was generated by incubation with 3,3-diaminobenzidine free base (DAB) (Sigma, Cat No. D5637) for 10 s. The tissue sections were imaged under a fluorescence microscope (BX53, Olympus Corp., Center Valley, PA, USA).

Quantitative Analyses of Stained Tissue Sections

Fiji software, an open-source image-processing package based on ImageJ (Media Cybernetics, Inc., Rockville, MD, USA), was used to measure the fractional area and integrated optical density (IOD) of the stained slides as reported in our previous study [22]. To summarize, first, the microscopic image of each tissue stained with IHC was transformed into an 8-bit grayscale. Then we created a ‘threshold’ binary image by selecting ‘Image > Adjust > Threshold’ and used the slider to adjust the threshold to match the positive areas. Finally, we called ‘Analyze > Measure’ for the results popup menu with fractional area to get the automatic percentage-stained area value. The OD was obtained using the formula: $OD = \log(250/\text{Pixel value})$ under the calibration procedure performed on the 8-bit grayscale images. After processing the threshold of the image as described above, the IOD was measured by clicking ‘Analyze > Measure’ for the integrated

density value. DAB staining intensity was determined by mean IOD (mean IOD = IOD/area). The protein levels of each section are represented as an average IOD.

Quantitative Analyses of Endotoxin Concentration in Plasma

Endotoxin concentrations in plasma were determined using the Bioendo™ End point Chromogenic Endotoxin Test Kit (EC64405S). The data are presented in terms of endotoxin unit (EU) per milliliter.

Intestinal Barrier Permeability Test

Intestinal epithelial barrier permeability was analyzed by the oral administration of the permeability marker, fluorescein isothiocyanate-dextran (FITC-dextran), 40 kDa (Chondrex, Redmond-Woodinville, Washington, USA; Cat No. 4009). Briefly, 7- to 8-week-old mice were fasted for 4 h and then 40 kDa FITC-dextran was administered by gavage at 20 mL/kg. The mice were then allowed to remain in the cages for 1 h followed by anesthesia. Blood was withdrawn to isolate plasma. Standards were obtained by diluting the FITC-dextran stock solution in phosphate-buffered saline (PBS). Plasma was diluted in an equal volume of PBS (pH 7.4) for analysis and FITC dextran concentrations in plasma were calculated with the help of standard concentrations prepared in PBS at 0.2 µg/mL, 0.4 µg/mL, 0.8 µg/mL, 1.6 µg/mL, 3.1 µg/mL, 6.2 µg/mL, and 12.5 µg/mL. Measurement of the FITC-dextran concentration was carried out on a Cary Eclipse fluorescence spectrophotometer (Agilent, Santa Clara, CA, USA; excitation, 490 nm, emission, 520 nm). Emission signals in mice treated with 40 kDa dextran were excluded from blank values (33% normal mouse plasma in PBS).

Autistic Behavior Analysis

Marble-Burying Test

Repetitive digging behavior was assessed by counting the number of marbles buried for 30 min after placing the BTBR mice in a plastic container [23, 24]. A marble was considered buried when more than 2/3 of its volume was covered by shaved aspen bedding [24]. After the test, the marbles were thoroughly cleaned, and new bedding was used for each mouse.

Self-grooming

The self-grooming test was applied as an assay to evaluate repetitive behaviors as previously described [24]. Each mouse was placed in a standard mouse cage. After a 5-min

habituation period, each mouse was blindly scored by independent observers for 10 min for the time spent grooming all of its body parts. Full-body grooming or face-wiping, and scratching/rubbing of the head and ears were all defined as self-grooming behaviors. The areas of the cage were cleaned with water followed by 70% ethanol after each test.

Open-Field Task (OFT)

The OFT was used to assess psychomotor outcomes and exploratory behaviors [25]. Each animal was individually placed in the central zone of the open field and video-recorded for 20 min with an overhead camera. Distance moved and time spent in the central zone were analyzed by TSE systems (VideoMot2, Germany). A 70% alcohol disinfection was used each time before initiating a new test.

Elevated Plus Maze (EPM)

The elevated maze is widely used for testing anxiety behaviors [25, 26]. The specific process was consistent with that reported in most studies [27]. The mouse was placed in the center with the nose pointing at one open arm and was allowed to move freely about the maze for 10 min. The time spent in the open arms was recorded by a video camera attached to a computer and these measurements served as an index of anxiety-like behavior. Finally, the results were calculated by the Image EP program. After each trial, all arms and the central area were cleaned with alcohol to prevent a bias based on olfactory cues.

Three-Chamber Test

The three-chamber test was applied to evaluate social preference in the form of general sociability and interest in social novelty in rodent models of autism disorders [28, 29]. As previously described [30], a mouse was habituated to the central chamber of a clear box, which was divided into a three-chamber apparatus, for 5 min, and was allowed to freely explore the chambers for another 10 min.

In the sociability test, a social stimulus (an age- and sex-matched unfamiliar mouse, ‘stranger 1’) was introduced into one cup of the box; the non-social stimulus was referred to as the empty cup.

In the social novelty preference test, a second unfamiliar mouse (‘stranger 2’), was placed in the empty cup located opposite the social stimulus, as in the previous test. The time spent interacting with each cup was recorded by two independent observers. The three-chambered apparatus was cleaned with water followed by 70% ethanol after each test.

Statistical Analysis

All data are presented as the mean \pm SD for each group. Statistically significant differences between groups were analyzed using GraphPad Prism 7 software version (GraphPad, San Diego, CA). Pearson’s correlation was applied to assess relationships between autistic behaviors and intestinal barrier permeability. Student’s two-tailed unpaired *t*-test was used to determine statistically significant differences between experimental groups. *P* values <0.05 were considered to be statistically significant.

Results

BTBR Mice Have Gut Barrier Dysfunction Compared to B6 Mice

Similar to humans suffering from autism [31], BTBR mice (autism model) also have a “leaky” intestinal epithelium (Fig. 2). To characterize epithelial permeability in the intestine, we measured the efficacy of macromolecular diffusion across the epithelium *in vivo* (40 kDa FITC flux) and found a dramatic increase in epithelial permeability in BTBR mice (Fig. 2A). The FITC flux concentration in plasma of BTBR mice was more than double that in controls at the 60-min time point. The macromolecular permeability of intestinal epithelium is largely dependent on the proper function of TJs and the mucus layer. Despite an increase in FITC flux, we failed to find substantial alterations in the expression levels of TJ proteins [zonula occludens-1 (ZO-1) and occludin] (Fig. 2B). Interestingly, the expression of Muc2, a gene encoding mucin 2, which is the major constituent of the mucus layer, was down-regulated in the large intestine of BTBR mice (Fig. 2C), which is consistent with the finding of Golubeva *et al.* [32].

2% DSS Induces Gut Leakage in BTBR Mice

Gut leakage was induced in male BTBR mice by the addition of 2% DSS to the drinking water for 7 days. To avoid affecting the normal behavior of the mice, care was taken not to introduce sustained diarrhea and rectal bleeding owing to the treatment. The maximum weight loss did not exceed 7% of the total body weight after DSS treatment (Fig. 3A; the shift from the lowest average weight on the seventh day to baseline was 6.13%). Histological analysis revealed differences in intestinal barrier permeability in mice of the DSS group, and damage of intestinal epithelium was seen in DSS-treated BTBR mice. An *in vivo* permeability assay, using 40 kDa FITC-dextran, revealed that the intestinal barrier permeability was much higher in DSS-treated BTBR mice than in distilled water-treated

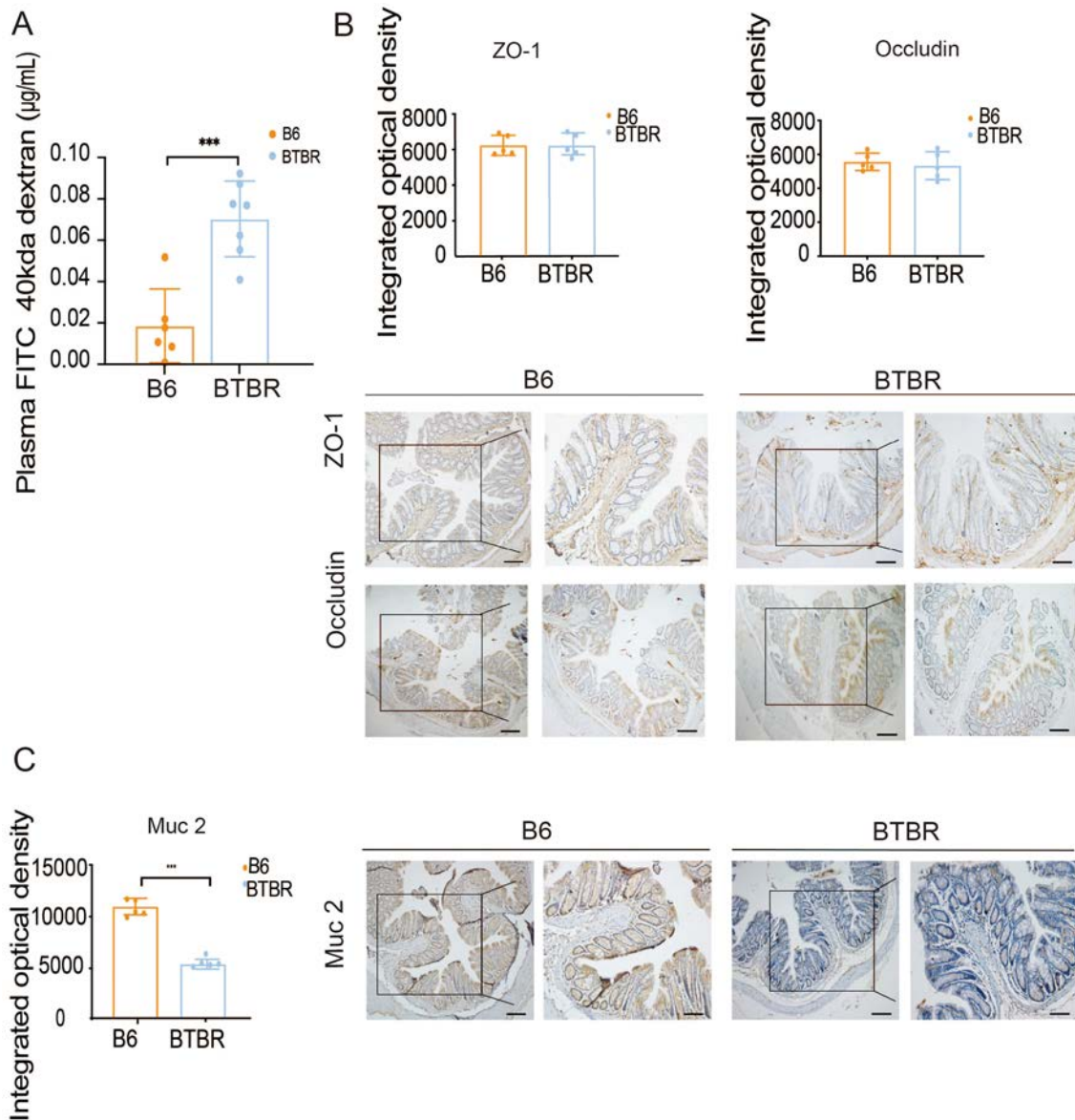


Fig. 2 Intestinal barrier dysfunction in BTBR $T^{+tf/J}$ mice. **A** FITC-dextran plasma concentrations in C57BL/6 (B6) and BTBR $T^{+tf/J}$ (BTBR) mice ($n = 6-7$ per treatment). **B**, **C** Immunohistochemical staining and RT-qPCR analysis of tight junction- and mucus layer-related genes of the intestinal barrier from B6 and BTBR mice ($n = 5$ per treatment). Data are shown as the mean \pm SEM and were analyzed by two-tailed unpaired Student's t test. * $P < 0.05$, ** $P < 0.01$,

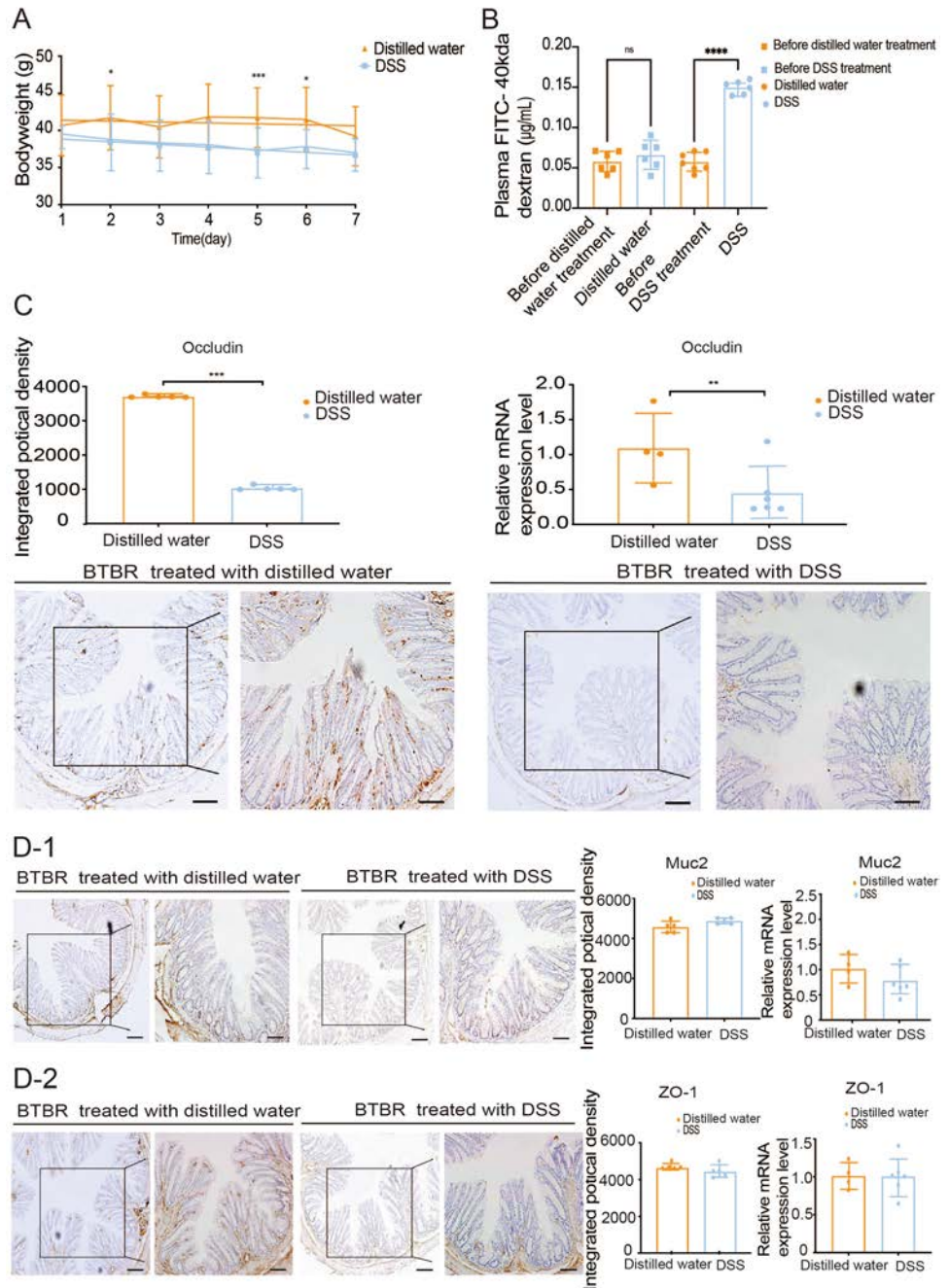
*** $P < 0.001$. Images were captured by confocal microscopy. Scale bars, 40 μm (left graph) and 20 μm (the inset of the left graph). The immunostaining analyses compare the gene expression levels. B6, C57BL/6 mice; BTBR, BTBR $T^{+tf/J}$ mice; ZO-1, zonula occludens 1; Muc 2, Mucin 2. RT-qPCR, reverse transcription-quantitative polymerase chain reaction.

mice (Fig. 3B), with increased concentration of dextran in plasma. An altered expression of TJs and mucus proteins that are closely associated with epithelial barrier integrity [17] explains this phenomenon. Compared with distilled water-treated BTBR mice, DSS-treated mice demonstrated decreased expression of occludin in the colon samples, as shown by IHC and RT-PCR data (Fig. 3C, D).

Increased Gut Barrier Permeability Aggravates Autistic Behavior in BTBR Mice

There was an apparent effect of intestinal permeability on the time spent by the mice investigating sociability and novelty. Compared to DSS-treated mice, distilled water-treated mice spent more time interacting with the

Fig. 3 Administration of DSS specifically induces epithelial barrier dysfunction in BTBR mice. **A** Body weights of mice from day 0 to day 7 ($n = 12-13$ per treatment) and recorded every two days. **B** FITC-dextran levels in the plasma of BTBR mice receiving DSS treatment or distilled water ($n = 6-7$ per treatment). **C, D** Tight junction- and mucus layer-related gene expression in the colon. ZO-1, Occludin, and Muc 2 were analyzed with immunohistochemistry staining ($n = 5$ per treatment) and RT-qPCR ($n = 4$ for distilled water, $n = 6$ for DSS treatment). Images captured by confocal microscopy. Scale bars, 40 μm (left graph) and 20 μm (the inset of the left graph). Immunostaining analyses compare the gene expression levels. DSS, DSS-treated BTBR mice; Distilled water, distilled water-treated BTBR mice. Data are shown as the mean \pm SEM. * $P < 0.05$, ** $P < 0.01$, *** $P < 0.001$, two-tailed unpaired Student's t test. ZO-1, zonula occludens 1; Muc 2, Mucin 2. RT-qPCR, reverse transcription-quantitative polymerase chain reaction.



‘stranger 1’ mouse than the empty object; this finding was notwithstanding the difference in time spent between ‘stranger 1’ and ‘stranger 2’ (Fig. 4A-1, A-2). These results indicate that increased intestinal barrier permeability causes less preference for social proximity. But there was no interaction between gut permeability and repetitive (Fig. 4B) or anxiety (Fig. 4C, D) behaviors. There were no significant differences between DSS and distilled water-treated mice regarding the number of marbles buried (Fig. 4B-1). Furthermore, the self-grooming

test demonstrated that the leaky gut did not have a major effect on repetitive behavior (Fig. 4B-2). In addition, increased intestinal permeability had no effect on the amount of time spent in the open arms (Fig. 4C). Distance or time traveled in the open field was also measured in the open-field task test (Fig. 4D). It was interesting to note that DSS-treated BTBR mice traveled no further than their controls. Furthermore, no significant differences were found in the time spent in the central area between DSS- and distilled water-treated BTBR mice.

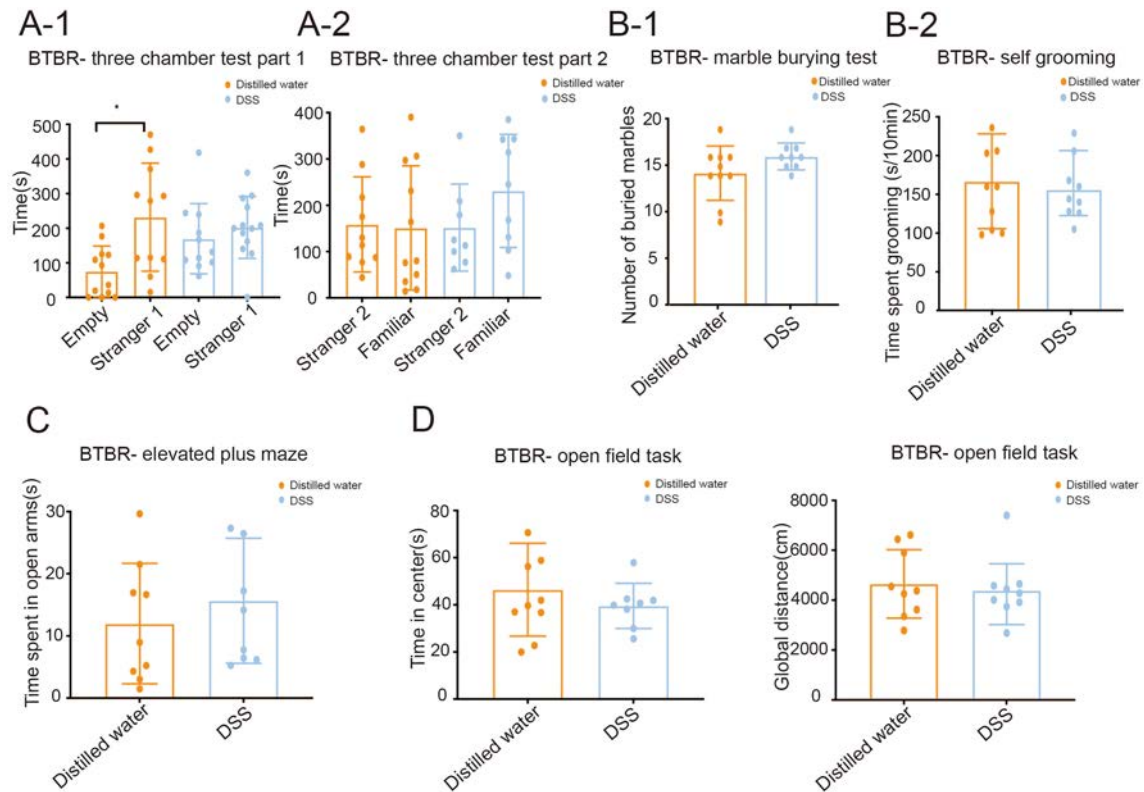


Fig. 4 Effects of DSS on the behavioral performance of BTBR mice. In three-chamber tests, mice given distilled water spend significantly more time in the ‘stranger 1’ chamber and indicate more social proximity (A). DSS treatment does not change repetitive behaviors (B)

or anxiety (C, D) behaviors. DSS, DSS-treated BTBR mice; Distilled water, distilled water-treated BTBR mice; Data are shown as the mean \pm SEM. * $P < 0.05$, ** $P < 0.01$, *** $P < 0.001$, two-tailed unpaired Student’s t test ($n = 8$ –13 per treatment).

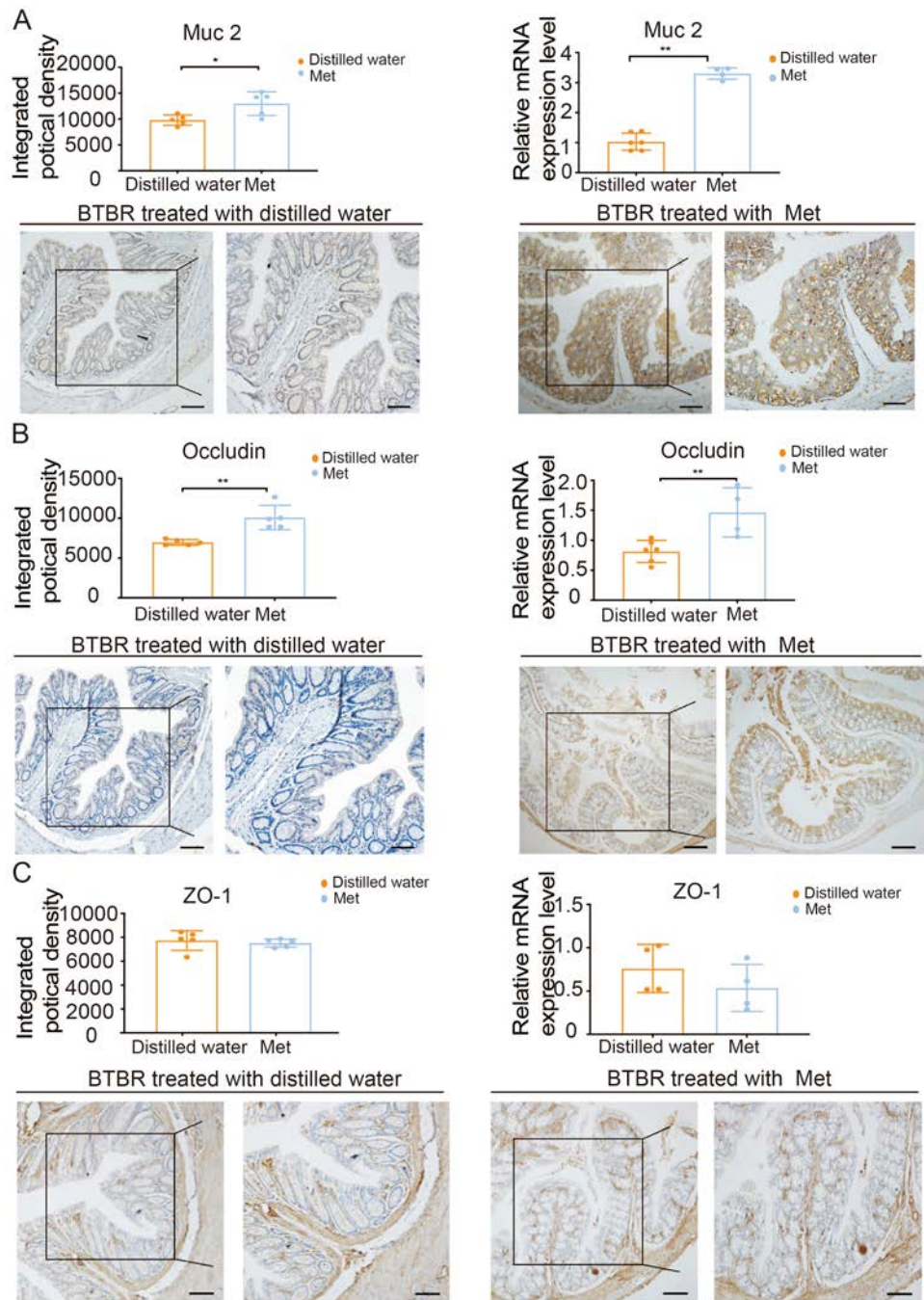
Metformin Improves Intestine Barrier Dysfunction via Increasing Expression of Mucin 2

Metformin, with a favorable safety profile, is one of the most frequently prescribed drugs worldwide due to the high prevalence of type 2 diabetes (T2D) [33]. First marketed for T2D in 1957, metformin has commanded a significant market share in the ensuing decades and is a mainstay of treatment, with a current prescription rate of 77% in T2D patients [34]. Metformin is now considered to have multiple beneficial effects in humans, other than its use as an anti-diabetic drug [35–37]. Our team previously demonstrated that metformin protects against intestinal barrier dysfunction through its effects on intestinal permeability [38]. We chose metformin as a positive stimulant not only because of its protective barrier effect but also because it has no negative effects on the anatomy of the brain and does not activate intracranial TLR4/MyD88/NF- κ B signaling pathways resulting in an increase of pro-inflammatory factors (Fig. S1). This is consistent with the conclusion that metformin has a potential neuroprotective effect in neurodegenerative disease reported in the literature [39–41].

It has been previously demonstrated that the phenomenon of leaky gut exists in BTBR mice with downregulation of mucin 2 expression levels (Fig. 2C). It is surprising that not only was the decrease in the expression levels of mucus protein—Muc 2 reversed (Fig. 5A), but occludin expression also significantly increased, when mice were administered metformin (400 mg/kg) by oral gavage (Fig. 5B). However, there were no significant differences in the TJs (ZO-1) between metformin-treated and distilled water-treated BTBR mice (Fig. 5C).

To further confirm our hypothesis, we administered 400 mg/kg of metformin to BTBR mice for another 7 days after DSS treatment to confirm its role in intestinal barrier protection. As we expected, metformin treatment after DSS administration restored the loss in body weight (Fig. 6A) and significantly reduced the increased 40-kDa FITC-dextran concentration in plasma (Fig. 6B). Metformin induced significant changes in barrier function, owing to the dramatic increase in the Mu2 expression levels (Fig. 6C) after metformin exposure in DSS treated-BTBR mice regardless of Occludin and ZO-1 levels (Fig. 6D, E). Based on this evidence, metformin might be capable of reducing gut

Fig. 5 Protective effects of metformin on intestinal barrier dysfunction in Metformin group mice. After 14 days of metformin treatment, immunohistochemistry ($n = 5$) and RT-qPCR ($n = 4-6$) were used to evaluate Muc 2 (A), Occludin (B), and ZO-1 (C) expression. The images were captured by confocal microscopy. Scale bars, 40 μm (left graph) and 20 μm (the inset of the left graph). Data are shown as the mean \pm SEM. * $P < 0.05$, ** $P < 0.01$, *** $P < 0.001$, two-tailed unpaired Student's t test. Met, metformin-treated BTBR mice; Distilled water, distilled water-treated BTBR mice; ZO-1, zonula occludens 1; Muc 2, Mucin 2. RT-qPCR, reverse transcription-quantitative polymerase chain reaction.



permeability *via* increased expression of Muc 2 or both occludin proteins.

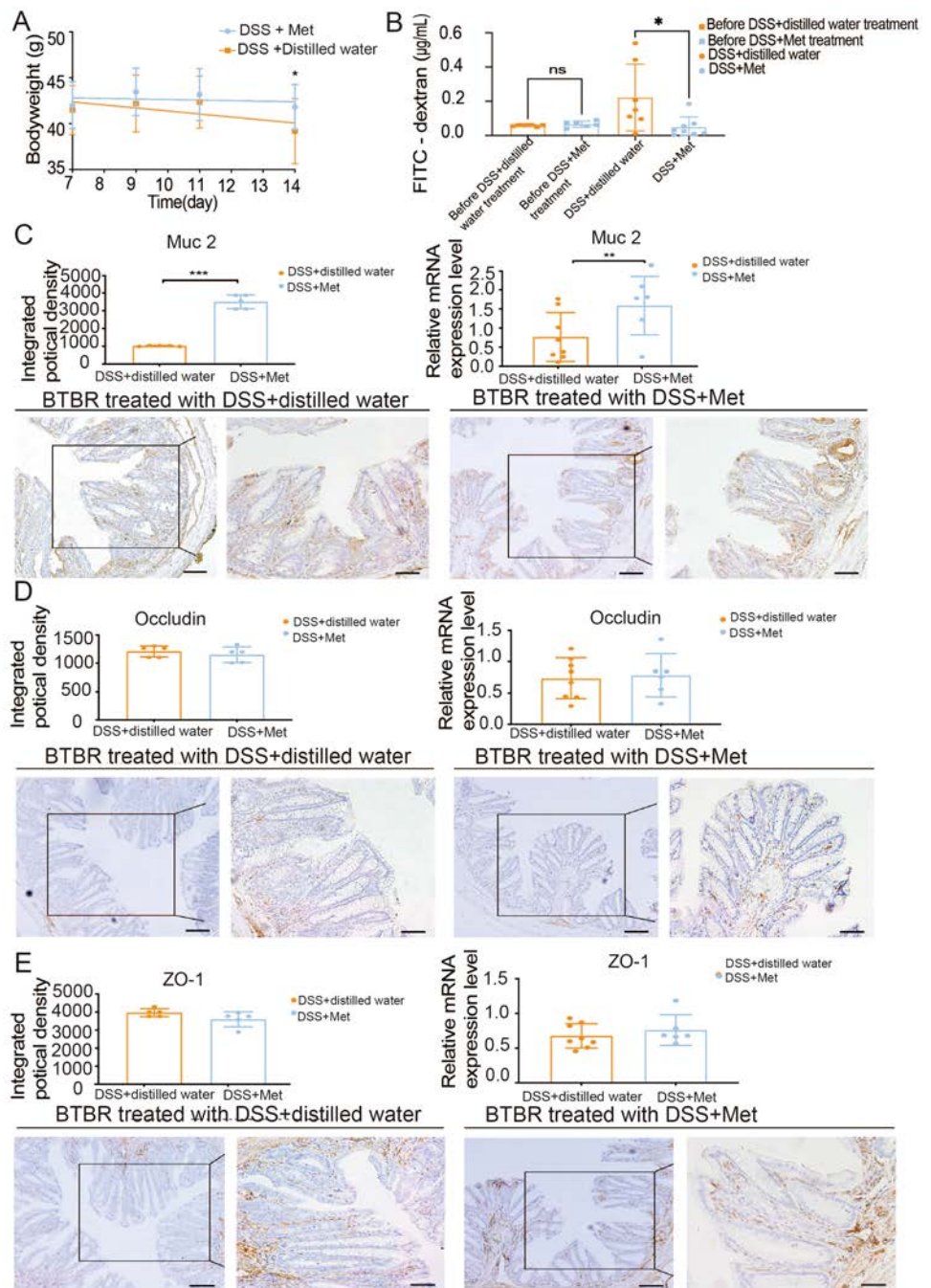
Decreased Gut Permeability Alleviates Symptoms of Autism

We have shown that aggravating the disruption of the intestinal barrier can aggravate the social behaviors of autistic mice. To provide a more complete chain of evidence, we demonstrated that reversing intestinal barrier disruption

with metformin significantly alleviated repetitive and social behaviors in BTBR autistic mice.

The EPM and OFT tests were used to investigate whether high levels of anxiety-like responses were present [25–27]. Fig. 7A shows the time spent on the open arms of the plus-maze in the metformin group. In the EPM test, we noted that metformin in autistic animals did not have a significant effect on the time spent in the open arms compared to that spent by distilled water-treated mice. The OFT is another method widely used to measure anxiety-related behaviors

Fig. 6 Protective effects of metformin on intestinal barrier dysfunction in Metformin plus DSS group mice. (A) and (B), changes in body weight during 7 days ($n = 10–13$ per treatment) and plasma FITC-40 kDa dextran concentration ($n = 6–8$ per treatment) are shown in the Metformin plus DSS group. Muc 2 (C), Occludin (D), and ZO-1 (E) mRNA expression and protein levels in the colonic mucosa of the Metformin plus DSS group ($n = 6–8$ per treatment for RT-PCR, $n = 5$ per treatment for immunohistochemistry). The images were captured by confocal microscopy. Scale bars, 40 μm (left graph) and 20 μm (the inset of the left graph). Data are shown as the mean \pm SEM. * $P < 0.05$, ** $P < 0.01$, *** $P < 0.001$, two-tailed unpaired Student's t test. BTBR mice received 2% DSS in the first week followed by metformin or distilled water treatment for the next week (DSS+Distilled water and DSS +Met mice, respectively). ZO-1, zonula occludens 1; Muc 2, Mucin 2. RT-qPCR, reverse transcription-quantitative polymerase chain reaction.



[42]. Although metformin did not considerably increase the total distance traveled in 30 min, it significantly increased the time spent in the center by BTBR mice compared with that spent by distilled water-treated mice (Fig. 7B). These results suggest that metformin improves autistic anxiety behavior in the OFT *via* repairing the gut barrier to a physiological state.

Repetitive behaviors were assessed by marble-burying and self-grooming tests, which reflect ethologically normal, stereotypical behaviors in rodents [43]. After metformin

treatment in BTBR mice, the number of buried marbles was lower than in distilled water-treated mice (Fig. 7C). But self-grooming behavior did not significantly differ between the metformin- and distilled water-treated mice (Fig. 7D). This indicates that metformin improves repetitive behaviors, as assessed using the marble-burying test.

Finally, we conducted social behavioral tests (Fig. 7E, F). With respect to sociability, metformin-treated BTBR mice spent more time exploring the chamber with the 'stranger' mouse than they spent in the empty

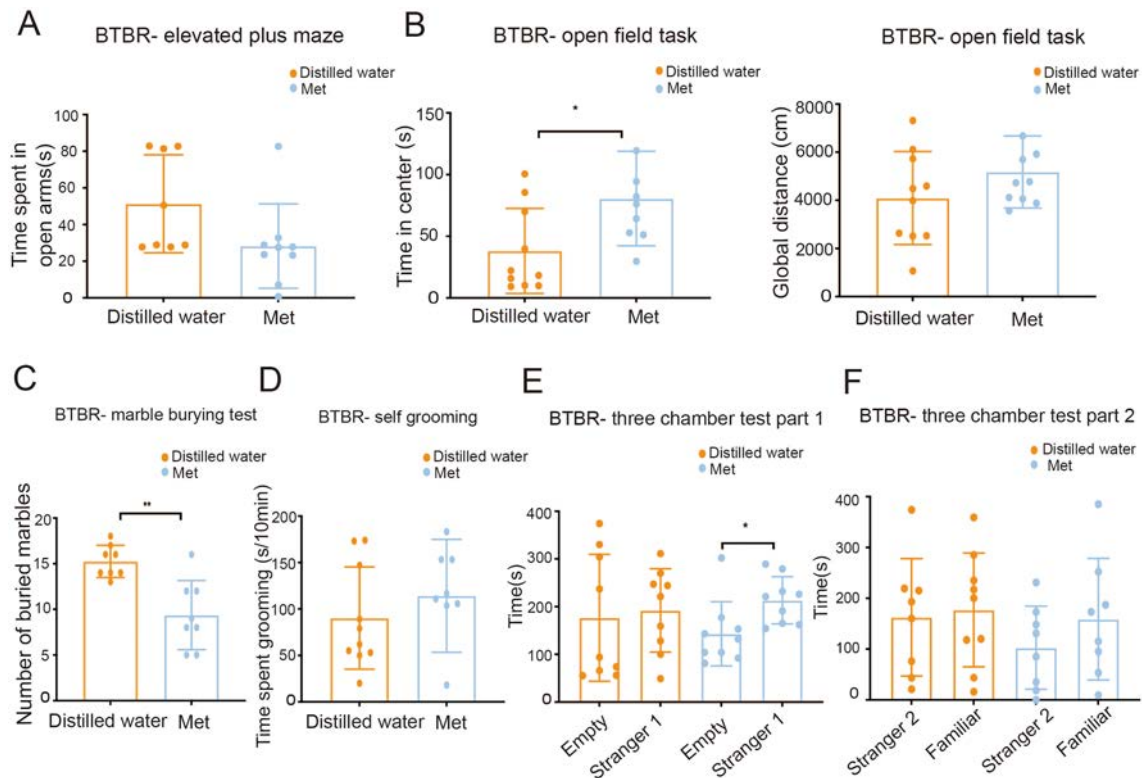


Fig. 7 Effects of metformin on the behavioral performance of mice in the Metformin group. In BTBR mice, metformin therapy increases the time spent in the center in the open field test (B) but does not affect anxiety-linked behavior in the elevated plus maze test (A). Metformin consumption reduces marble burying (C) but does not affect self-grooming (D). In the three-chamber test, metformin treatment in

BTBR mice spend significantly more time in the ‘stranger 1’ chamber and indicate more proximity (E). Met, metformin-treated BTBR mice; Distilled water, distilled water-treated BTBR mice. Data are shown as the mean \pm SEM. * $P < 0.05$, ** $P < 0.01$, *** $P < 0.001$, two-tailed unpaired Student’s *t* test ($n = 8$ –10 per treatment).

chamber when compared to the distilled water-treated mice (Fig. 7E); metformin administration in BTBR mice increased the social proximity behavior. Furthermore, animals in the metformin group did not show any particular preference for social novelty behavior (Fig. 7F). Metformin management in BTBR exhibited a similar time spent between familiar and ‘stranger 2’ mice.

Although the same behavioral pattern cannot be ascribed to the autistic mice in the metformin plus DSS group (Fig. 8A–F), an overall trend of improvement in autistic behavior was consistently seen. Although metformin intervention after DSS treatment did not affect anxiety-related behavior (Fig. 8A, B) and social proximity (Fig. 8E) or social novelty performance (Fig. 8F), it caused a significant decrease in the number of buried marbles (Fig. 8C) and an increase in time spent exploring the familiar mouse chamber (Fig. 8F), which indicated that these mice demonstrated fewer repetitive and more social memory behaviors than the BTBR mice that received DSS and distilled water treatment.

The TLR4–MyD88–NF- κ B Signaling Pathway May Play a Key Role in Aggravating Autistic Behavior

Endotoxin, a type of LPS, is elevated in patients with autism [28, 44]. The central pathway by which LPS leads to an inflammatory environment in the brain causing neurodegeneration in patients with autism is as follows: gut endotoxins may enter the blood due to a leaky gut and subsequently enter the brain tissue by crossing the blood-brain barrier and cause brain inflammation *via* activation of the TLR4–MyD88–NF- κ B transcriptional pathway in macrophages to induce pro-inflammatory cytokines, such as tumor necrosis factor α (TNF- α), monocyte chemoattractant protein-1 (MCP-1), interleukin-1 (IL-1), IL-6, and IL-1 β [28, 45, 46]. The LPS levels in plasma were higher after intestinal barrier damage as exhibited in DSS-treated BTBR mice (Fig. 9A). To investigate whether downstream cytokines are regulated by the TLR4–MyD88–NF- κ B signaling pathway in macrophages stimulated by gut-derived LPS, we measured the primary macrophage marker F4/80 and key

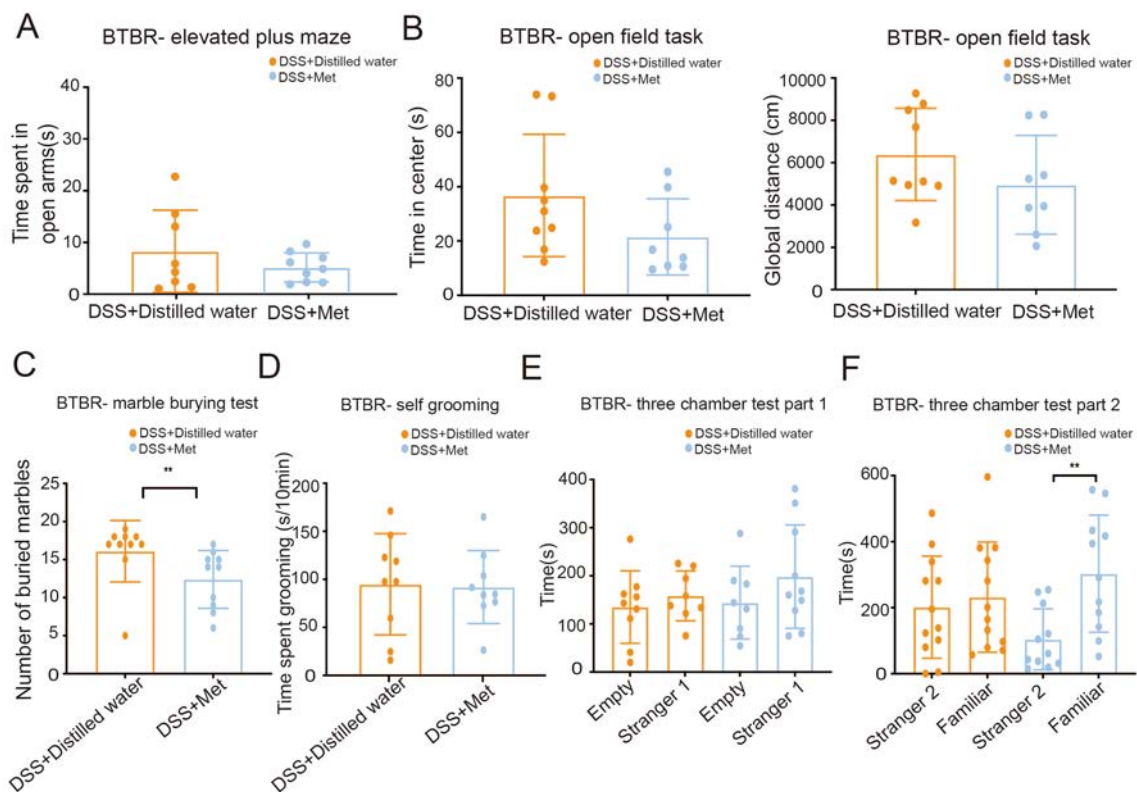


Fig. 8 Effects of metformin on the behavioral performance of mice in the Metformin plus DSS group. The BTBR mice receiving metformin management after DSS treatment show an increased preference for the familiar mouse chamber (F), indicating more social memory. BTBR mice received 2% DSS in the first week fol-

lowed by metformin or distilled water treatment for the next week (DSS+Distilled water and DSS +Met mice). Data are shown as the mean \pm SEM. * $P < 0.05$, ** $P < 0.01$, *** $P < 0.001$, two-tailed unpaired Student's t test ($n = 8$ –12 per treatment).

molecules for the signaling pathway (TLR4, MyD88, and NF- κ B) in brain tissue. We noted that the LPS challenge significantly increased the expression of F4/80 and NF- κ B in DSS-treated BTBR mice (Fig. 9B, D). Moreover, the expression of the downstream pro-inflammatory factor TNF- α was also increased correspondingly (Fig. 9C). Although there was no statistical difference in the expression of MyD88 and TLR4 between the two different treatments, DSS-treated BTBR mice showed an increasing trend of NF- κ B compared to distilled water-treated mice (Fig. 9D).

Metformin administration in DSS-treated BTBR mice repressed macrophages (Fig. 9E) and excessive release of inflammatory factors (MCP-1, IL-1 β , and TNF α) (Fig. 9F). It also resulted in infiltration of the cerebral cortex by these inflammatory factors, which was partly attributable to inhibition of the TLR4–MyD88–NF- κ B signaling pathway as demonstrated by the downregulation of expression of all three key molecules: TLR4, MyD88, and NF- κ B (Fig. 9G).

To establish the specific brain areas where these important pro-inflammatory cytokines are expressed, we added immunohistochemical studies (Fig. S2). Our findings revealed that these essential inflammatory factors were

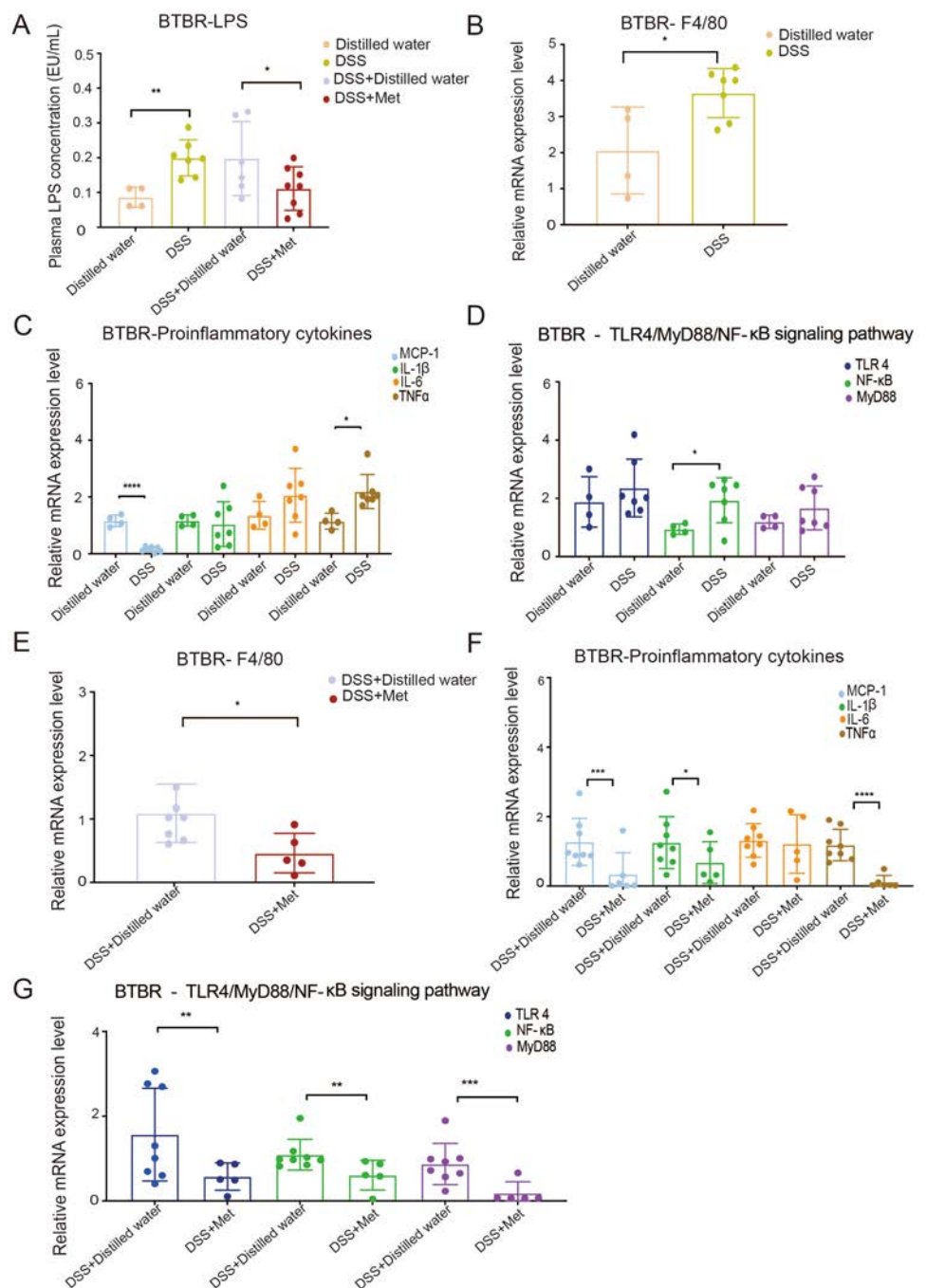
expressed in the dorsomedial cerebral cortex and the CA1 substructure of the hippocampus and that changes in protein levels measured by IHC corresponded to the changes in mRNA levels measured by RT-PCR.

Discussion

Few studies have been performed that determine the role of abnormal gut permeability in the neuropsychiatric manifestations of ASD. In this study, we aimed to clarify the effect of “leaky gut” on the various autistic behavioral phenotypes using BTBR mice (an autism model). Our study provided evidence that increased intestinal barrier permeability may make a vital contribution to the pathological changes in autism; it induces a gut-derived endotoxin to transfer to the brain and create a pro-inflammatory environment *via* activation of the TLR4–MyD88–NF- κ B signaling pathway. Listed below are the main findings of the study:

(1) Administration of metformin to BTBR mice caused a dramatic decrease in repetitive behaviors measured by

Fig. 9 Metformin regulates intracranial inflammation through TLR 4/NF-κB/MyD88 signaling *in vitro*. Metformin lowers endotoxin levels in plasma (A) and suppresses activation of the TLR 4/NF-κB/MyD88 signaling pathway (G) in the brain of BTBR mice treated with DSS; the mRNA levels of the major macrophage marker F4/80 (B, E), signaling pathway components TLR4, MyD88, and NF-κB (D, G), and downstream pro-inflammatory cytokines TNFα, MCP-1, IL-6, and IL-1β (C, F) measured by RT-qPCR. DSS, DSS-treated BTBR mice; Distilled water, distilled water-treated BTBR mice; BTBR mice received 2% DSS in the first week followed by metformin treatment or distilled water for the next week (DSS+Distilled water and DSS+Met mice). RT-qPCR, reverse transcription-quantitative polymerase chain reaction. Data are shown as the mean ± SEM (*n* = 4 for the mice receiving distilled water; *n* = 7 for the mice receiving DSS treatment; *n* = 5–8 or 6–8 for mice receiving metformin treatment or distilled water after DSS consumption). **P* < 0.05, ***P* < 0.01, ****P* < 0.001, two-tailed unpaired Student's *t* test.



marble burying, which may be a consequence of intestinal barrier impairment;

(2) Loss of function of the intestinal barrier caused a decreased tendency for social proximity in autistic mice; administration of metformin reversed this phenomenon;

(3) LPS levels in plasma were higher in DSS-treated autistic mice than in mice receiving metformin treatment;

(4) The expression levels of the pro-inflammatory cytokines MCP-1, IL-1β, and TNFα and the degree of macrophage infiltration declined after metformin treatment, and

expression of the upstream regulatory molecules TLR4, MyD88, and NF-κB also decreased.

Consequently, we postulate that restoring the gut barrier with metformin could be an effective method to improve autistic behavior in adult mice with autism.

ASD refers to a broad range of conditions characterized by cognitive disabilities, repetitive behavior patterns, and restricted social interaction and communication [1]. Gastrointestinal disorders are the most common problems in patients with ASD. Despite their prevalence, they are often

overlooked [47]. Leo Kanner, a Boston physician, who first described autism, reported in an article published in 1943 that most of the children with autism had more difficulty in eating or feeding at a young age, i.e., they had issues with food selectivity, food refusal, and poor oral intake compared to healthy children, which supported the connection between autism and the gut, thereby affecting the pathophysiology of ASD [48]. Extensive studies have identified the dynamic and bidirectional interaction between the gut and brain along the “gut–brain axis”. Different metabolites of intestinal origin have been reported in the blood and brain of autistic children, such as short-chain fatty acids, indoles, LPS, and serotonin [49–51]. This explains how the leakage of intestinal metabolites into the brain may trigger autistic behavioral responses. Thus, damage to the gut barrier may act as a key bridge in the development of autism.

Impairment of intestinal the barrier in autism has been reported [52]. Several investigations have found that people with autism have a damaged intestinal barrier: D’Eufemia *et al.* reported that an altered intestinal permeability was found in 9 of 21 (43%) autistic patients based on the most traditional method for ascertaining gut permeability, the lactulose: mannitol test (comprising two different sugars given orally and output measured in urine), but in none of the 40 controls [18], and this was among the first evidence for a leaky gut in autism. Magistris *et al.* in 2010 reported on the presence of abnormal intestinal permeability (leaky gut) in over a third of a cohort of children diagnosed with autism (36.7%) [17]. More than that, the studies on leaky gut and autism do not stop there. Previous studies found decreased intestinal TJ claudin in ASD patients [16, 53]. In Esnafoglu’s study, serum zonulin, a measure of increased intestinal permeability, was considerably higher in autistic children than in healthy controls [54]. These are consistent with our results. The efficacy of macromolecular diffusion across the epithelium *in vivo* (40-kDa FITC flux) was measured to characterize the differences in intestinal epithelial permeability between BTBR and B6 mice. As previously reported [32], increased intestinal permeability in BTBR mice caused a much higher FITC flux than in B6 mice. Consistent with this, we found molecular dysfunction of the intestinal barrier. Despite failing to find alterations in TJs (ZO-1, occludin), the expression of Muc2, a constituent of the main epithelial mucus layer in BTBR mice, was significantly lower. These findings strongly suggested that the intestinal barrier may play an irreplaceable role in the development of autistic behavior.

Many studies have indicated that metformin might have a beneficial effect on neurodegenerative diseases. Chronic treatment with metformin for 24 weeks significantly improves the cognitive and depressed performance in depressed patients with T2DM [55]; Metformin treatment rescues spatial memory impairment and neuronal death in

the hippocampus and promotes hippocampal neurogenesis in a mouse model of Alzheimer’s disease [56]; Metformin treatment *in vitro* increases the neuronal activation of partitioning defective 1, a family of Ser/Thr kinases playing a key role in synaptic plasticity and neuroinflammation in functional recovery from traumatic brain injury [57]. There is no doubt that metformin has the potential to improve the cognitive and behavioral deficits shown in ASD models. Although metformin has been reported to improve autistic behavior in mouse pups [58], we are the first to report the influence of metformin in adult mice in alleviating autistic behavioral phenotypes by protecting the integrity of the intestinal barrier; this offers the hope of a cure for autism in adults. To confirm our hypothesis, we applied positive and negative tests to explore the alteration in intestinal barrier permeability and its impact on autistic behavior by further disrupting and repairing the intestinal barrier. To avoid excessive intestinal inflammation that could have affected the normal activities of mice, 2% DSS was administered only for a week, resulting in a minimal loss in weight (7% of the total body weight, Max weight = 38.25 ± 4.781 g; Min weight = 35.07 ± 4.728 g) and no blood in stool; however, diarrhea was observed. The expression of occludin in the intestinal epithelial decreased and the concentration of dextran in plasma increased correspondingly, which indicated that the addition of DSS serves as a negative regulator of gut permeability. As a positive stimulus, metformin was chosen to restore the “leaky gut”; as it has been demonstrated to protect against intestinal barrier dysfunction in previous studies [51] and it does not contribute to the development of an inflammatory environment in the brain. Our results demonstrated that metformin not only had a beneficial effect in preserving the intestinal barrier integrity of BTBR mice *via* upregulating the expression of the main TJ, occludin, and the mucus barrier molecule, Muc 2, in a physiological state, but it also protected mice from the intestinal barrier damage caused by 2% DSS. Administrating metformin to DSS-treated BTBR mice showed a significantly reduced loss in body weight compared to those treated with DSS only. Consistent with these findings, immunohistochemical examination showed higher protein Muc 2 expression in DSS+Met mice; in addition, RT-PCR results provided strong evidence to support this finding.

It is noteworthy that the permeability of the intestinal barrier changed along with the autistic behavior of BTBR mice. Repetitive behaviors are considered to be a core diagnostic feature of autism [59]. Repetitive behaviors in patients with autism are characterized by jumping, spinning, head tilting, nodding, and arm or hand flapping [35]. In rodents, one way of assessing such behaviors is through marble-burying and self-grooming tests, as these reflect ethologically normal and stereotypical behaviors in rodents [43]. Although the damage to the intestinal barrier with DSS showed no

differences in the number of buried marbles, administration of metformin to BTBR mice or DSS-treated BTBR mice, dramatically decreased the number of marbles buried compared to those buried by distilled water-treated BTBR mice or both DSS and distilled water-treated BTBR mice. However, changes in the integrity of the intestinal barrier had no effect on self-grooming behavior. These results suggested that repetitive behaviors measured by marble burying may be a consequence of intestinal barrier impairments.

The EPM and OFT are routinely used to study anxiety-related behavior in mice [28]. When anxiety-related behavior was analyzed, the increased intestinal barrier permeability induced by DSS had no effect on the EPM and OFT tests. Metformin was administered to BTBR and DSS-treated BTBR mice and these mice neither showed a significant increase in the time spent in open arms compared to distilled water-treated and both DSS and distilled water-treated BTBR mice in the EPM test. As another method to measure anxiety in animals, similar levels of locomotor activity in the OFT test were exhibited in the metformin group and the metformin plus DSS group. However, the exploratory behaviors were improved in BTBR mice after receiving metformin; they spent much more time in the center than the BTBR mice that received distilled water.

Our study demonstrated that loss of intestinal barrier function might cause a deficit in social interaction and recognition. Unlike DSS-treated BTBR mice, distilled water-treated mice displayed a greater preference for the ‘stranger 1’ mouse. This result indicated that an increased intestinal barrier permeability results in a reduced preference for social proximity. As expected, restoring the gut barrier function using metformin in BTBR mice reversed this phenomenon, and consequently, mice showed more interest in interaction with the ‘stranger 1’ than with the empty chamber.

Repair of intestinal barrier permeability by metformin did not have any apparent effect on the social novelty behavior of autistic mice; however, metformin-treated BTBR mice after DSS intervention did demonstrate more interest in communicating with familiar mice. Therefore, the repair of intestinal barrier permeability tended to increase social memory, which has the potential to improve a vital behavioral defect in autistic mice, as seen by the absence of a time delay for recognizing the familiar mouse [60].

As a result, alterations in the intestinal barrier appear to be linked to autistic behavioral changes in BTBR mice. To assess the causal association between alleviating autism-like behaviors and repairing the intestinal barrier, we conducted a correlation study on significantly improved autistic behaviors and changes in intestinal barrier permeability following intervention (Fig. S3). In the three-chamber test, BTBR mice spent less time with ‘stranger 1’ as their gut barrier permeability increased (Fig. S3A) and more time with ‘stranger 1’ after the permeability decreased with metformin treatment

(Fig. S3B3). This shows that social deficit behaviors in autism can be improved by lowering intestinal barrier permeability. And as intestinal barrier permeability declined, the number of marbles buried declined as well (Fig. S3B1), correlating with an increase in time spent in the center of the OFT (Fig. S3B2), which shows that reduced intestinal barrier permeability may improve repetitive stereotypical and anxiety-related behaviors in autistic mice. All these results suggested that gut leakage might be the etiology of autism and improvement in intestinal barrier dysfunction may be a potential target for relieving the symptoms of ASDs.

Finally, we sought to further understand the underlying mechanisms that increased the permeability of the intestinal barrier contributing to autism. Studies have shown evidence of increased gut metabolites and serum endotoxin levels in patients with ASD, and this offers a mechanism by which a ‘leaky gut’ could play a role in this neurodevelopmental disease [10, 61, 62]. Among the potential mechanisms by which absorption of LPS from the gut lumen affects autistic behaviors, activation of the innate immune system in the brain owing to circulating pro-inflammatory cytokines has been demonstrated in many studies [63]. LPS can act upon TLR4 to activate systemic inflammation which affects the central nervous system through the extracellular medium (mediated by LPS-binding protein, the cluster of differentiation 14, and myeloid differentiation factor 2 [MD-2]) and intracellularly (TLR4/MyD88/NF- κ B and TLR4/TRIF/IRF3 pathways) [64]. The first MyD88-dependent pathway starts from the LPS/MD-2/TLR4 complex located on the plasma membrane, and the second TLR4/TRIF transduction begins in early endosomes after endocytosis of the receptor. The MyD88-dependent pathway is responsible for pro-inflammatory cytokine production; TLR4 recognizes LPS through the accessory molecule MD2, and the intracellular TIR region of TLR4 binds to the carboxyl terminus of MyD88, while the terminus of MyD88 recruits IL-1 receptor-associated kinase-4 (IRAK4), IRAK1, and IRAK2 through homotypic interactions. The activated IRAK4, IRAK1, and IRAK2 are phosphorylated, detach from the MyD88/IRAK complex, and bind to TNF receptor-associated factor 6 (TRAF6). Subsequently, TRAF6 activates the transforming growth factor B-activated kinase (TAK1) complex. Upon activation, TAK1 activates the downstream I κ B kinase (IKK), which is made up of two kinases (IKK α and IKK β), which in turn phosphorylates the NF- κ B inhibitor I κ B α , leading to NF- κ B activation. Finally, free NF- κ B is translocated to the nucleus and activates the transcription of inflammatory cytokines such as IL-1, IL-6, and TNF- α [65].

Growing evidence indicates that ASD pathogenesis may involve brain inflammation associated with increased inflammatory biomarkers, such as IL-6 and TNF- α [63, 66, 67]. The protein expression levels of TLR4, phospho-NF κ B, p65, and pro-inflammatory cytokines, such as TNF α are

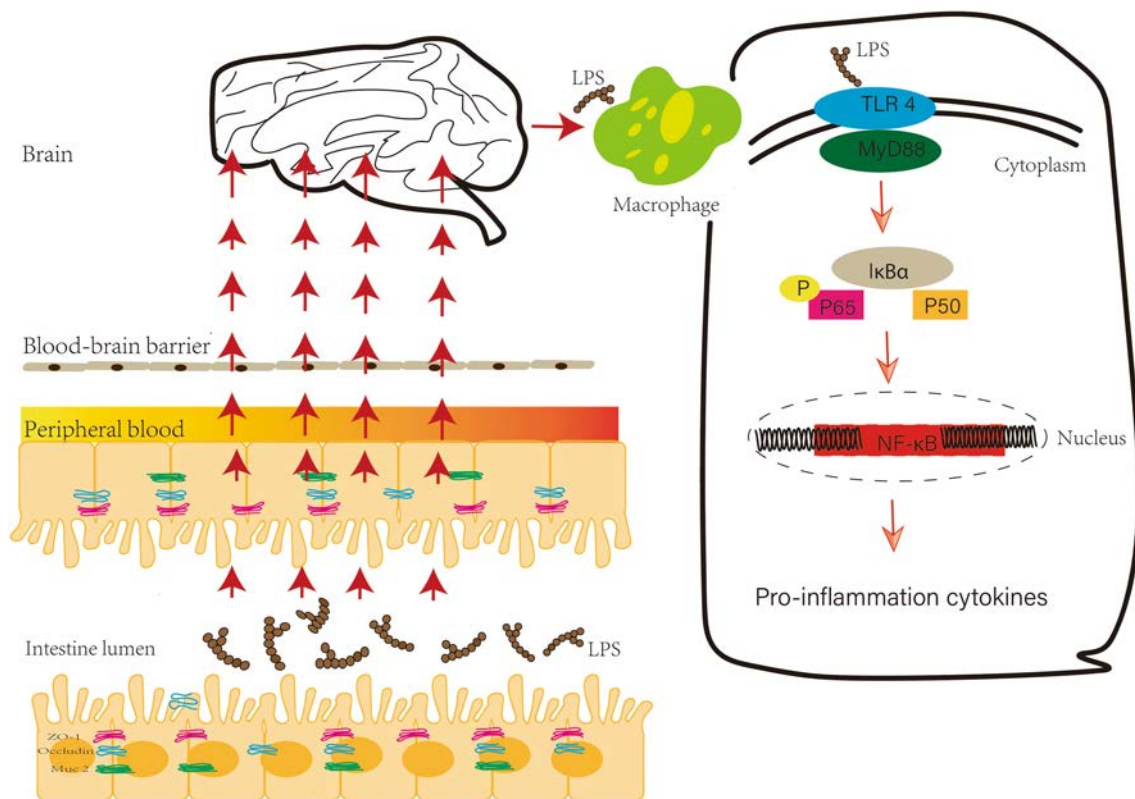


Fig. 10 The central pathway of how endotoxin leads to autism spectrum disorder. The leaky gut allows gut endotoxin (LPS) to enter brain tissue. The TLR4/MyD88/NF- κ B inflammatory signaling path-

way in macrophages promotes brain inflammation and neurodegeneration, contributing to autistic symptoms.

dramatically increased in the brain of fetal mice by activating TLR4 signaling in microglia through maternal LPS treatment; these offspring show ASD-like behavior with less social behavior and increased anxiety and repetitive behaviors. However, maternal LPS exposure has no effect on TLR4-knockout mice [64]. The published data support the hypothesis that there may exist a link between TLR-4 activation and NOX-2/ROS upregulation in ASD patients. Activation of TLR-4 by LPS on T-cells *in vitro* leads to enhanced generation of NOX-2-derived ROS *via* the NF- κ B pathway, which perhaps plays a pathogenic role under the condition of central nervous system inflammation [68].

Thus, we examined the link in the gut–brain axis to clarify whether gut-derived endotoxins, induced by a “leaky gut”, could be the cause of autism. Our results are in agreement with the findings of the published data [16–19, 45]. LPS levels in plasma were higher in BTBR mice and DSS-treated autistic mice than in metformin-treated BTBR mice. LPS was found in the cell wall of gram-negative bacteria in the gut and high LPS levels reflect an increased intestinal barrier permeability [52]. The expression levels of the pro-inflammatory cytokines MCP-1, IL-1 β , and TNF- α and the degree of macrophage infiltration were reduced after metformin treatment. Furthermore, the expression of the

upstream regulatory molecules TLR4, MyD88, and NF- κ B also decreased. Our previously published articles and other studies also supported this phenomenon [11, 60, 63, 69]. Activated immune cells produce high levels of NF- κ B and pro-inflammatory cytokines linked to autism [10]. Children with ASD and BTBR mice have dramatically elevated NF- κ B signaling in the brain and periphery [52, 53]. Deng *et al.* reported that metformin alleviates neuroinflammation by decreasing pro-inflammatory cytokines (NF- κ B and IL-6) in the hippocampus and rescues the autism-linked behaviors in BTBR mice [69].

These data supported the hypothesis that increased barrier permeability in autistic mice may transfer LPS to brain tissue to activate the TLR 4/MyD88/NF- κ B pathway and further promote the development of the pro-inflammatory environment in the brain leading to neurodegeneration (Fig. 10). Last but not least, the results of our study provided evidence that neuroinflammation may be the main driver behind autism, as already demonstrated by a large number of studies [70–72].

Acknowledgements This work was supported by the National Natural Science Foundation of China (82100609) and the Hainan Provincial Natural Science Foundation of China (821QN0982).

Conflict of interest The authors declare that they have no competing interests.

Open Access This article is licensed under a Creative Commons Attribution 4.0 International License, which permits use, sharing, adaptation, distribution and reproduction in any medium or format, as long as you give appropriate credit to the original author(s) and the source, provide a link to the Creative Commons licence, and indicate if changes were made. The images or other third party material in this article are included in the article's Creative Commons licence, unless indicated otherwise in a credit line to the material. If material is not included in the article's Creative Commons licence and your intended use is not permitted by statutory regulation or exceeds the permitted use, you will need to obtain permission directly from the copyright holder. To view a copy of this licence, visit <http://creativecommons.org/licenses/by/4.0/>.

References

- Waye MMY, Cheng HY. Genetics and epigenetics of autism: A review. *Psychiatry Clin Neurosci* 2018, 72: 228–244.
- Masi A, DeMayo MM, Glozier N, Guastella AJ. An overview of autism spectrum disorder, heterogeneity and treatment options. *Neurosci Bull* 2017, 33: 183–193.
- Matson JL, Kozlowski AM. The increasing prevalence of autism spectrum disorders. *Res Autism Spectr Disord* 2011, 5: 418–425.
- Madra M, Ringel R, Margolis KG. Gastrointestinal issues and autism spectrum disorder. *Child Adolesc Psychiatr Clin N Am* 2020, 29: 501–513.
- Vuong HE, Hsiao EY. Emerging roles for the gut microbiome in autism spectrum disorder. *Biol Psychiatry* 2017, 81: 411–423.
- Kohane IS, McMurry A, Weber G, MacFadden D, Rappaport L, Kunkel L. The co-morbidity burden of children and young adults with autism spectrum disorders. *PLoS One* 2012, 7: e33224.
- Gorrindo P, Williams KC, Lee EB, Walker LS, McGrew SG, Levitt P. Gastrointestinal dysfunction in autism: Parental report, clinical evaluation, and associated factors. *Autism Res* 2012, 5: 101–108.
- Chaidez V, Hansen RL, Hertz-Picciotto I. Gastrointestinal problems in children with autism, developmental delays or typical development. *J Autism Dev Disord* 2014, 44: 1117–1127.
- Yu Y, Zhao FQ. Microbiota-gut-brain axis in autism spectrum disorder. *J Genet Genomics* 2021, 48: 755–762.
- Morais LH, Schreiber HL 4th, Mazmanian SK. The gut microbiota-brain axis in behaviour and brain disorders. *Nat Rev Microbiol* 2021, 19: 241–255.
- Chidambaram SB, Tuladhar S, Bhat A, Mahalakshmi AM, Ray B, Essa MM, *et al.* Autism and gut-brain axis: Role of probiotics. *Adv Neurobiol* 2020, 24: 587–600.
- Srikantha P, Mohajeri MH. The possible role of the microbiota-gut-brain-axis in autism spectrum disorder. *Int J Mol Sci* 2019, 20: E2115.
- Clapp M, Aurora N, Herrera L, Bhatia M, Wilen E, Wakefield S. Gut microbiota's effect on mental health: The gut-brain axis. *Clin Pract* 2017, 7: 987.
- Lasheras I, Seral P, Latorre E, Barroso E, Gracia-García P, Santabárbara J. Microbiota and gut-brain axis dysfunction in autism spectrum disorder: Evidence for functional gastrointestinal disorders. *Asian J Psychiatr* 2020, 47: 101874.
- Kim HS, Kim S, Shin SJ, Park YH, Nam Y, Kim CW, *et al.* Gram-negative bacteria and their lipopolysaccharides in Alzheimer's disease: Pathologic roles and therapeutic implications. *Transl Neurodegener* 2021, 10: 49.
- Fiorentino M, Sapone A, Senger S, Camhi SS, Kadzielski SM, Buie TM, *et al.* Blood-brain barrier and intestinal epithelial barrier alterations in autism spectrum disorders. *Mol Autism* 2016, 7: 49.
- de Magistris L, Familiari V, Pascotto A, Sapone A, Frolli A, Iardino P, *et al.* Alterations of the intestinal barrier in patients with autism spectrum disorders and in their first-degree relatives. *J Pediatr Gastroenterol Nutr* 2010, 51: 418–424.
- D'Eufemia P, Celli M, Finocchiaro R, Pacifico L, Viozzi L, Zaccagnini M, *et al.* Abnormal intestinal permeability in children with autism. *Acta Paediatr* 1996, 85: 1076–1079.
- Horvath K, Papadimitriou JC, Rabsztyn A, Drachenberg C, Tildon JT. Gastrointestinal abnormalities in children with autistic disorder. *J Pediatr* 1999, 135: 559–563.
- Fond G, Boukouaci W, Chevalier G, Regnault A, Eberl G, Hamdani N, *et al.* The “psychomicrobiotic”: Targeting microbiota in major psychiatric disorders: A systematic review. *Pathologiebiologie* 2015, 63: 35–42.
- Amodeo DA, Jones JH, Sweeney JA, Ragozzino ME. Differences in BTBR T+ tf/J and C57BL/6J mice on probabilistic reversal learning and stereotyped behaviors. *Behav Brain Res* 2012, 227: 64–72.
- Li F, Xu RJ, Lin CL, Low BE, Cai L, Li S, *et al.* Maternal and fetal alkaline ceramidase 2 is required for placental vascular integrity in mice. *FASEB J* 2020, 34: 15252–15268.
- Angoa-Pérez M, Kane MJ, Briggs DI, Francescutti DM, Kuhn DM. Marble burying and nestlet shredding as tests of repetitive, compulsive-like behaviors in mice. *J Vis Exp* 2013: 50978.
- Chang YC, Cole TB, Costa LG. Behavioral phenotyping for autism spectrum disorders in mice. *Curr Protoc Toxicol* 2017, 72: 11.22.1–11.22.21.
- Silverman JL, Tolu SS, Barkan CL, Crawley JN. Repetitive self-grooming behavior in the BTBR mouse model of autism is blocked by the mGluR5 antagonist MPEP. *Neuropsychopharmacology* 2010, 35: 976–989.
- Faraji J, Karimi M, Lawrence C, Mohajerani MH, Metz GAS. Non-diagnostic symptoms in a mouse model of autism in relation to neuroanatomy: The BTBR strain reinvestigated. *Transl Psychiatry* 2018, 8: 234.
- Kraeuter AK, Guest PC, Sarnyai Z. The elevated plus maze test for measuring anxiety-like behavior in rodents. *Methods Mol Biol* 2019, 1916: 69–74.
- Walf AA, Frye CA. The use of the elevated plus maze as an assay of anxiety-related behavior in rodents. *Nat Protoc* 2007, 2: 322–328.
- Komada M, Takao K, Miyakawa T. Elevated plus maze for mice. *J Vis Exp* 2008: 1088.
- Rein B, Ma KJ, Yan Z. A standardized social preference protocol for measuring social deficits in mouse models of autism. *Nat Protoc* 2020, 15: 3464–3477.
- Peñagarikano O, Lázaro MT, Lu XH, Gordon A, Dong HM, Lam HA, *et al.* Exogenous and evoked oxytocin restores social behavior in the *Cntnap2* mouse model of autism. *Sci Transl Med* 2015, 7: 271ra8.
- Silverman JL, Yang M, Lord C, Crawley JN. Behavioural phenotyping assays for mouse models of autism. *Nat Rev Neurosci* 2010, 11: 490–502.
- Pernicova I, Korbonits M. Metformin—mode of action and clinical implications for diabetes and cancer. *Nat Rev Endocrinol* 2014, 10: 143–156.
- Montvida O, Shaw J, Atherton JJ, Stringer F, Paul SK. Long-term trends in antidiabetes drug usage in the US: Real-world evidence in patients newly diagnosed with type 2 diabetes. *Diabetes Care* 2018, 41: 69–78.
- Golubeva AV, Joyce SA, Moloney G, Burokas A, Sherwin E, Arboleya S, *et al.* Microbiota-related changes in bile acid &

- tryptophan metabolism are associated with gastrointestinal dysfunction in a mouse model of autism. *EBioMedicine* 2017, 24: 166–178.
36. Chelakkot C, Ghim J, Ryu SH. Mechanisms regulating intestinal barrier integrity and its pathological implications. *Exp Mol Med* 2018, 50: 1–9.
 37. Dziedzic A, Saluk-Bijak J, Miller E, Bijak M. Metformin as a potential agent in the treatment of multiple sclerosis. *Int J Mol Sci* 2020, 21: E5957.
 38. Ke HR, Li F, Deng WL, Li ZT, Wang SQ, Lv PJ, *et al.* Metformin exerts anti-inflammatory and mucus barrier protective effects by enriching *Akkermansia muciniphila* in mice with ulcerative colitis. *Front Pharmacol* 2021, 12: 726707.
 39. Saewanee N, Praputittaya T, Malaiwong N, Chalorak P, Meemon K. Neuroprotective effect of metformin on dopaminergic neurodegeneration and α -synuclein aggregation in *C. elegans* model of Parkinson's disease. *Neurosci Res* 2021, 162: 13–21.
 40. Du MR, Gao QY, Liu CL, Bai LY, Li T, Wei FL. Exploring the pharmacological potential of metformin for neurodegenerative diseases. *Front Aging Neurosci* 2022, 14: 838173.
 41. Sportelli C, Urso D, Jenner P, Chaudhuri KR. Metformin as a potential neuroprotective agent in prodromal Parkinson's disease-viewpoint. *Front Neurol* 2020, 11: 556.
 42. Belovicova K, Bogi E, Csatosova K, Dubovicky M. Animal tests for anxiety-like and depression-like behavior in rats. *Interdiscip Toxicol* 2017, 10: 40–43.
 43. Deng J, Zeng LS, Lai XY, Li J, Liu L, Lin QY, *et al.* Metformin protects against intestinal barrier dysfunction via AMPK α 1-dependent inhibition of JNK signalling activation. *J Cell Mol Med* 2018, 22: 546–557.
 44. Moy SS, Nadler JJ, Young NB, Perez A, Holloway LP, Barbaro RP, *et al.* Mouse behavioral tasks relevant to autism: Phenotypes of 10 inbred strains. *Behav Brain Res* 2007, 176: 4–20.
 45. Brown GC. The endotoxin hypothesis of neurodegeneration. *J Neuroinflammation* 2019, 16: 180.
 46. Emanuele E, Orsi P, Boso M, Brogna D, Brondino N, Barale F, *et al.* Low-grade endotoxemia in patients with severe autism. *Neurosci Lett* 2010, 471: 162–165.
 47. McElhanon BO, McCracken C, Karpen S, Sharp WG. Gastrointestinal symptoms in autism spectrum disorder: A meta-analysis. *Pediatrics* 2014, 133: 872–883.
 48. Kanner. History and Development of Autism Spectrum Disorders. In: *Assessment and Treatment of Child Psychopathology and Developmental Disabilities*. 1st ed. Elsevier Ltd. 2006: 1–22.
 49. Israelyan N, Margolis KG. Serotonin as a link between the gut-brain-microbiome axis in autism spectrum disorders. *Pharmacol Res* 2018, 132: 1–6.
 50. El-Ansary A, Al-Ayadhi L. Relative abundance of short chain and polyunsaturated fatty acids in propionic acid-induced autistic features in rat pups as potential markers in autism. *Lipids Health Dis* 2014, 13: 140.
 51. Lucchina L, Depino AM. Altered peripheral and central inflammatory responses in a mouse model of autism. *Autism Res* 2014, 7: 273–289.
 52. Jyonouchi H, Sun SN, Itokazu N. Innate immunity associated with inflammatory responses and cytokine production against common dietary proteins in patients with autism spectrum disorder. *Neuropsychobiology* 2002, 46: 76–84.
 53. Fowlie G, Cohen N, Ming X. The perturbation of microbiome and gut-brain axis in autism spectrum disorders. *Int J Mol Sci* 2018, 19: 2251.
 54. Esnafoglu E, Cırık S, Ayyıldız SN, Erdil A, Ertürk EY, Dağlı A, *et al.* Increased serum zonulin levels as an intestinal permeability marker in autistic subjects. *J Pediatr* 2017, 188: 240–244.
 55. Guo M, Mi J, Jiang QM, Xu JM, Tang YY, Tian G, *et al.* Metformin may produce antidepressant effects through improvement of cognitive function among depressed patients with diabetes mellitus. *Clin Exp Pharmacol Physiol* 2014, 41: 650–656.
 56. Ou ZR, Kong XJ, Sun XD, He XS, Zhang L, Gong Z, *et al.* Metformin treatment prevents amyloid plaque deposition and memory impairment in APP/PS1 mice. *Brain Behav Immun* 2018, 69: 351–363.
 57. DiBona VL, Shah MK, Krause KJ, Zhu WX, Voglewede MM, Smith DM, *et al.* Metformin reduces neuroinflammation and improves cognitive functions after traumatic brain injury. *Neurosci Res* 2021, 172: 99–109.
 58. Gin H, Messerschmitt C, Brottier E, Aubertin J. Metformin improved insulin resistance in type I, insulin-dependent, diabetic patients. *Metabolism* 1985, 34: 923–925.
 59. de Magistris L, Picardi A, Sapone A, Cariello R, Siniscalco D, Bravaccio C, *et al.* Intestinal barrier in autism. *Comprehensive Guide to Autism*. New York, NY: Springer New York, 2014: 2047–2060.
 60. Harrop C, McConachie H, Emsley R, Leadbitter K, Green J, Consortium PACT. Restricted and repetitive behaviors in autism spectrum disorders and typical development: Cross-sectional and longitudinal comparisons. *J Autism Dev Disord* 2014, 44: 1207–1219.
 61. Kelly JR, Kennedy PJ, Cryan JF, Dinan TG, Clarke G, Hyland NP. Breaking down the barriers: The gut microbiome, intestinal permeability and stress-related psychiatric disorders. *Front Cell Neurosci* 2015, 9: 392.
 62. Al-Ayadhi L, Zayed N, Bhat RS, Moubayed NMS, Al-Muammar MN, El-Ansary A. The use of biomarkers associated with leaky gut as a diagnostic tool for early intervention in autism spectrum disorder: A systematic review. *Gut Pathog* 2021, 13: 54.
 63. Santocchi E, Guiducci L, Fulceri F, Billeci L, Buzzigoli E, Apicella F, *et al.* Gut to brain interaction in Autism Spectrum Disorders: A randomized controlled trial on the role of probiotics on clinical, biochemical and neurophysiological parameters. *BMC Psychiatry* 2016, 16: 183.
 64. Xiao L, Yan JY, Feng D, Ye SS, Yang T, Wei H, *et al.* Critical role of TLR4 on the microglia activation induced by maternal LPS exposure leading to ASD-like behavior of offspring. *Front Cell Dev Biol* 2021, 9: 634837.
 65. Płóciennikowska A, Hromada-Judycka A, Borzęcka K, Kwiatkowska K. Co-operation of TLR4 and raft proteins in LPS-induced pro-inflammatory signaling. *Cell Mol Life Sci* 2015, 72: 557–581.
 66. Theoharides TC, Asadi S, Patel AB. Focal brain inflammation and autism. *J Neuroinflammation* 2013, 10: 46.
 67. Theoharides TC, Kavaloti M, Tsilioni I. Mast cells, stress, fear and autism spectrum disorder. *Int J Mol Sci* 2019, 20: E3611.
 68. Nadeem A, Ahmad SF, Bakheet SA, Al-Harbi NO, Al-Ayadhi LY, Attia SM, *et al.* Toll-like receptor 4 signaling is associated with upregulated NADPH oxidase expression in peripheral T cells of children with autism. *Brain Behav Immun* 2017, 61: 146–154.
 69. Deng WL, Li F, Ke HR, Wang SQ, Li ZT, Lv PJ, *et al.* Effect of metformin in autistic BTBR T + Itpr3tf/J mice administered a high-fat diet. *Brain Res Bull* 2022, 183: 172–183.
 70. Matta SM, Hill-Yardin EL, Crack PJ. The influence of neuroinflammation in autism spectrum disorder. *Brain Behav Immun* 2019, 79: 75–90.
 71. El-Ansary A, Al-Ayadhi L. Neuroinflammation in autism spectrum disorders. *J Neuroinflammation* 2012, 9: 265.
 72. Greene RK, Walsh E, Mosner MG, Dichter GS. A potential mechanistic role for neuroinflammation in reward processing impairments in autism spectrum disorder. *Biol Psychol* 2019, 142: 1–12.

REEP1 Preserves Motor Function in SOD1^{G93A} Mice by Improving Mitochondrial Function via Interaction with NDUFA4

Siyue Qin¹ · Pan You¹ · Hui Yu¹ · Bo Su¹ 

Received: 11 May 2022 / Accepted: 25 September 2022 / Published online: 15 December 2022

© Center for Excellence in Brain Science and Intelligence Technology, Chinese Academy of Sciences 2022

Abstract A decline in the activities of oxidative phosphorylation (OXPHOS) complexes has been consistently reported in amyotrophic lateral sclerosis (ALS) patients and animal models of ALS, although the underlying molecular mechanisms are still elusive. Here, we report that receptor expression enhancing protein 1 (REEP1) acts as an important regulator of complex IV assembly, which is pivotal to preserving motor neurons in SOD1^{G93A} mice. We found the expression of REEP1 was greatly reduced in transgenic SOD1^{G93A} mice with ALS. Moreover, forced expression of REEP1 in the spinal cord extended the lifespan, decelerated symptom progression, and improved the motor performance of SOD1^{G93A} mice. The neuromuscular synaptic loss, gliosis, and even motor neuron loss in SOD1^{G93A} mice were alleviated by increased REEP1 through augmentation of mitochondrial function. Mechanistically, REEP1 associates with NDUFA4, and plays an important role in preserving the integrity of mitochondrial complex IV. Our findings offer insights into the pathogenic mechanism of REEP1 deficiency in neurodegenerative diseases and suggest a new therapeutic target for ALS.

Keywords REEP1 · Amyotrophic lateral sclerosis · Mitochondria · Complex IV assembly · NDUFA4

Supplementary Information The online version contains supplementary material available at <https://doi.org/10.1007/s12264-022-00995-7>.

✉ Bo Su
bxs103@sdu.edu.cn

¹ Department of Cell Biology, Shandong Provincial Key Laboratory of Mental Disorders, School of Basic Medical Sciences, Shandong University, Jinan 250012, China

Introduction

Amyotrophic lateral sclerosis (ALS) is one of the most common motor neuron diseases characterized by progressive degeneration of motor neurons (MNs) in the brainstem and spinal cord. Many ALS cases, referred to as sporadic ALS, are not genetically transmitted and their causes remain enigmatic. Only 5%–10% of ALS cases are familial, most of which are associated with repeat expansions of the *C9ORF72* gene or mutations in genes encoding copper-zinc superoxide dismutase (SOD1), TAR DNA binding protein 43 (TDP-43), or fused in sarcoma (FUS) [1]. The cellular and molecular mechanisms underlying MN loss in both familial and sporadic ALS are still unknown, and effective treatments are extremely limited.

Many ALS-associated genes, including *SOD1*, *TDP-43*, *FUS*, and *C9ORF72*, play roles in mitochondrial functions. Evidence gathered from *in vitro* or *in vivo* disease models and ALS patients, strongly implicates the dysfunction of mitochondria as a core component of ALS. Reductions in cellular respiration and ATP production are well documented in ALS and animal models of ALS. In the post-mortem spinal cord of sporadic ALS patients, the activity of complexes I, II, III, and IV (CI, CII, CIII, and CIV) is reduced [2, 3]. Consistent with this, decreased CI + III, CII + III, and CIV activities also occur in the spinal cord of SOD1^{G93A} transgenic mice (G93A mice) [4]. However, the mechanism underlying the impairments of mitochondrial respiration in ALS remains largely unknown.

Receptor expression enhancing proteins (REEPs), a family of six proteins (REEP1–6), were first identified by their ability to enhance the cell surface expression of olfactory receptors and other G protein-coupled receptors [5, 6]. Later studies revealed that REEPs are localized on the tubular endoplasmic reticulum (ER) membrane to coordinate

ER shaping and microtubule dynamics [7]. Among these REEPs, REEP1 is under intensive investigation because of its close association with hereditary spastic paraplegia (HSP), a rare neurodegenerative disorder characterized by progressive degeneration of corticospinal motor neurons [8]. Given the truncating nature of most genetic mutations of REEP1, it has been suggested that REEP1 mutations cause disease by a loss-of-function mechanism [9, 10]. In addition, REEP1-knockout mice display a gait disorder and axonal degeneration closely resembling those seen in HSP patients [11, 12]. At the molecular level, REEP1 has been reported to control the structural and dynamic changes of intracellular membrane structures, including the ER, trafficking vesicles, and lipid droplets, through a microtubule-associated pathway [11–15]. Also, it has been shown that REEP1 is localized in mitochondria [8], however, its function in mitochondria remains unknown.

In the present study, we investigated the expression of REEPs in the spinal cord of the widely-used ALS mouse model G93A mice. We found that the reduction of REEP1 expression is a distinguishing feature of patients and the mouse model of ALS. Overexpression of REEP1 by an AAV-mediated approach prevents motor neuron neurodegeneration in G93A mice by improving mitochondrial function. Our study connects reduced expression of REEP1 to impaired oxidative phosphorylation (OXPHOS) activity in ALS.

Materials and Methods

Animals

Mouse surgery and procedures were approved and conducted in accordance with the Institutional Animal Care and Use Committee of Shandong University. Transgenic SOD1 G93A mice on the C57BL/6 background (B6.Cg-Tg(SOD1*G93A)1Gur/J, Stock No: 004435) were from the Jackson Laboratory, Bar Harbor, USA.

Lumbar Spinal Cord Injection of AAV

Adeno-associated virus serotype 1 encoding GFP (AAV1-GFP) or human REEP1 with Flag tag (AAV1-hREEP1-Flag) under the neuron-specific promoter eSYN, were purchased from WZ Bioscience, Jinan, China. AAVs were injected as previously described [16]. After anesthesia by isoflurane/oxygen inhalation, the mouse vertebral column was immobilized on a stereotactic frame to expose the lumbar spine. Bupivacaine/lidocaine (1:1 v/v) was injected around a small skin incision in the back of an anesthetized mouse. The L1 vertebra was exposed by removing

the small spinal muscles and ligaments attached to its dorsal surface. Then the dorsal portion of the vertebra was removed to expose the spinal cord. 3 μ L AAV (10^{13} viral particles per mL) was injected into two locations at a depth of 1 mm rostral to the transection through a glass micropipette attached to a Hamilton syringe (Hamilton, Reno, USA). The micropipette was left in place for 5 min before the withdrawal. The skin was sutured, and the mice were placed on a temperature-controlled warm pad for a few hours before being returned to their home cage.

Grip Strength and Footprint Test

A grip strength meter (Bioseb, Pinellas Park, USA) was used to measure hind limb grip strength. Both hind paws were placed on a bar connected to the meter. As a mouse grasped the bar, the pull force in grams was recorded on a digital force transducer. After 5 trials, the single best-recorded value was used for statistical analysis. The grip strength meter was periodically calibrated by the manufacturer. Footprints were analyzed using a customized runway (50 cm long, 5 cm wide, and both sides bordered by walls). The fore and hind paws were first dipped into the purple or orange paint. Each mouse was placed on a runway covered by aluminum foil where they ran toward an enclosed dark box. Stride length was presented as the mean distance of forward movement between each stride. The resulting data were further plotted in GraphPad Prism 8 software (GraphPad Software Inc., San Diego, USA).

Electrophysiological Recordings of Skeletal Muscles

We made electromyographic recordings of the compound muscle action potential (CMAP) evoked in hind limb muscles by supramaximal stimulation of the sciatic nerve using the PowerLab 4/35 data acquisition system, a FE155 Stimulator HC, a FE136 Animal Bio Amp, and needle electrodes from ADInstruments (Colorado Springs, USA) as well as ring surface electrodes from Natus Neurology (Orlando, USA). Mice were anesthetized by isoflurane/oxygen inhalation and immobilized with a piece of tape. Reference and ground needle electrodes were inserted into the sacrum and tail tip. The fur around the hind limb was removed and ring-positive and negative electrodes were placed on the gastrocnemius muscle with contact gel. The stimulating needle electrode was inserted into the muscle near the sciatic nerve. A 1–10 mV stimulus 0.1 ms in duration was applied at a frequency of 10 Hz. The recording data were exported to Excel and maximal CMAP was plotted with GraphPad Prism 8 software.

Cell Culture and Transfection

All the cell culture reagents were from ThermoFisher Scientific (Auburn, USA). Lenti-X 293T cells from Takara Bio (Shiga, Japan) were grown and transfected in Dulbecco' modified Eagle's medium (Sigma Aldrich, St. Louis, USA), supplemented with 10% fetal bovine serum (FBS) (v/v) and 1% penicillin-streptomycin in a 5% CO₂ humid incubator at 37°C. Lenti-X 293T cells were tested and confirmed to be free of mycoplasma contamination. The Lenti-X 293T cells were transfected with TransIT®-293 Transfection Reagent according to the manufacturer's protocol. 24 h before the experiments, 500 ng DNA/well was used to transiently transfect 1 × 10⁵ cells in a 24-well plate. The Lenti-X 293T cell line was used for up to 20 passages. The International Cell Line Authentication Committee does not list the cells used in this study as commonly misidentified cell lines. No authentication was conducted during the experiments.

Plasmids

The original plasmid backbone pcDNA3.1 (+) was from Invitrogen (Waltham, USA). To generate Strep or Strep-Flag tagged plasmids, coding sequences of Strep-tag and Flag tag were synthesized and cloned into pcDNA3.1(+) by Gibson assembly (NEB, Ipswich, USA). All the plasmids used in this study are listed in Table S2.

Generation of REEP1-KO and Rescued Cell Lines

REEP1-KO cells were generated from Lenti-X 293T cells with a CRISPR/Cas9 system designed in our lab. pSpCas9(BB)-2A-Puro (PX459) V2.0 was a gift from Zhang Feng (Addgene, Watertown, USA) [17]. The single guide (sg) RNA targeting sequence was predicted using the online CRISPR design tool (<https://benchling.com>). Lenti-X 293T cells were first transfected with the PX459-gREEP1 vector, which targeted 5'-TCACAGACATCTTCC TTTGT-3' of the *REEP1* gene. After puromycin selection, the cells were diluted and seeded in 96-well plates at 1 cell/well to isolate monoclonal cells without REEP1 expression as determined by western blot analysis. To generate rescue cell lines, REEP1-KO cells were transfected with the pcDNA3.1(+)-Zeo-Strep vector, pcDNA3.1(+)-REEP1-Strep, and pcDNA3.1(+)-REEP1Δ101-110-Strep. Of note, the sequence targeted by sgRNA in wild-type (WT) and mutant REEP1 plasmids was codon optimized to 5'-TTT ACCGACATATTCCTTTGT-3' to resist CRISPR/Cas9 cleavage. After zeocin selection, monoclonal cells were obtained by the method described above.

Cell Proliferation

The proliferation of REEP1-KO and control cells was evaluated by growth curve assays. 10⁵ cells were seeded in each well of a 6-well plate. 12 h after seeding, the cells were harvested and the time point was set as Time 0. Then cells were harvested at the indicated time. After staining with DAPI, images were captured by Celldiscoverer 7 (Zeiss, Oberkochen, Germany), and cell numbers were counted.

Immunocytochemistry and Immunofluorescence

Immunohistochemistry was applied using the peroxidase anti-peroxidase protocol. Paraffin-embedded spinal cord sections were first deparaffinized in xylene, rehydrated in graded ethanols, and incubated in Tris-buffered saline (TBS, 50 mmol/L Tris-HCl, and 150 mmol/L NaCl, pH 7.6) for 10 min before antigen retrieval in 1× immunoDNA retriever with citrate (BSB 0021, Bio SB, Santa Barbara, USA). The sections were rinsed with distilled H₂O, incubated in TBS for 10 min, and blocked with 10% normal goat serum (NGS) in TBS for 30 min at room temperature. The sections were further incubated with primary antibodies in TBS containing 1% NGS overnight at 4°C and immunostained by the peroxidase-anti-peroxidase-based method as we described previously [18].

For immunofluorescence staining, cells cultured on coverslips were washed three times with pre-warmed PBS buffer and fixed with 4% paraformaldehyde for 15 min at room temperature. After washing the coverslips 3 times with PBS, the cells were permeabilized by 0.5% Triton X-100 for 25 min. For tissues, deparaffinization and antigen retrieval processing were as above. Then the cell and tissue samples were blocked with 10% NGS (Sigma Aldrich) in PBS for 30 min at room temperature followed by incubation with primary antibodies in PBS containing 1% NGS at 4°C overnight. The antibodies were washed out with PBS, and cells were incubated with 10% NGS in PBS for 10 min and then with Alexa Fluor-conjugated secondary antibodies (Life Technologies, Carlsbad, USA) (1:250) for 2 h at room temperature protected from light. After that, cells were rinsed three times with PBS and the nuclei were stained with DAPI. Finally, they were again washed three times with PBS and mounted with Fluoromount-G mounting medium (Southern Biotech, Birmingham, USA). The antibodies used in this study are listed in Table S3.

Fluorescence Microscopy

Fluorescent images were captured with a Zeiss automated microscope, Celldiscoverer 7, and Zeiss LSM800 (all microscopes controlled by Zen software, Zeiss). For live-cell time-lapse imaging, Lenti-X 293T cells were seeded in a 24-well plate. 24 h after seeding, the culture plate was placed into the Celldiscoverer 7 system with a stage-top incubator (37°C, 5% CO₂).

Immunoblot Analysis and Blue Native PAGE

For immunoblots, cells or tissues were lysed in cell lysis buffer (Cell Signaling Technology, Danvers, USA), containing 1 mmol/L phenylmethanesulfonyl fluoride (PMSF; Millipore, Burlington, USA), protease inhibitor cocktail (Sigma Aldrich), and phosphatase inhibitor cocktail (Sigma Aldrich). The lysate was centrifuged at 14,000 g for 15 min at 4°C. The protein concentration of the supernatant was measured by BCA assay (ThermoFisher Scientific). Equal amounts of proteins (20 µg) were separated by 10% SDS-PAGE and transferred to a polyvinylidene fluoride (PVDF) membrane (Millipore). The membranes were blocked with 10% non-fat dry milk in TBST and incubated with primary antibodies at 4°C overnight. After rinsing 3 times in TBST, peroxidase-conjugated secondary antibodies were applied for 1 h at room temperature, and the blots were developed with Immobilon Western Chemiluminescent HRP Substrate (Millipore). Images were captured using the ChemiDoc Touch Imager (Bio-Rad, CA, USA). The primary antibodies used in this study are listed in Table S3. The blue-native page was applied according to the user's guide of the Novex® native gel electrophoresis system (Life Technologies). Taken briefly, mitochondrial OXPHOS complexes were extracted in 1× NuPage buffer with digitonin (8 g/g mitochondria ratio). After incubation for 30 min on ice, the lysate was centrifuged at 14,000 g for 15 min at 4°C to remove insoluble debris. The protein concentration was determined, and 50 µg of protein combined with 0.25% G-250 was loaded onto a 4–12% precast Bis-Tris gradient gel (Invitrogen, Carlsbad, USA). After electrophoresis, the complexes were electroblotted onto PVDF membranes and incubated with human Mitochondrial cocktail antibodies against CI–CV subunits.

Immunoprecipitation

Cells were collected 24 h after transfection and lysed with lysis buffer (100 mmol/L Tris-HCl, 150 mmol/L NaCl, 1 mmol/L EDTA, and 1% NP40, pH 8.0) containing 1 mmol/L PMSF (Millipore), protease inhibitor cocktail (Sigma Aldrich), and phosphatase inhibitor cocktail (Sigma Aldrich). The lysate was centrifuged at 14,000 g for 15 min at 4°C. The supernatant was incubated with MagStrep "type3" XT beads (IBA Lifesciences, Göttingen, Germany) overnight at 4°C. The beads were washed three times with lysis buffer and eluted with BXT buffer (IBA Lifesciences). The eluted proteins were subjected to western blot or mass spectrometric analysis.

Subcellular Fractionation

Cells were homogenized in IB-1 solution (in mmol/L: 225 mannitol, 75 sucrose, 0.1 EGTA, 20 HEPES; pH 7.4). The total homogenate was centrifuged twice at 600 g for 5 min at 4°C. Subsequently, the supernatant was collected and

centrifuged at 7,000 g for 10 min at 4°C to obtain an enriched mitochondrial fraction. This fraction was washed in IB-2 solution (in mmol/L: 225 mannitol, 75 sucrose, 20 HEPES; pH 7.4) followed by centrifugation at 9,000g for 10 min. The pellets were suspended in MRB buffer (in mmol/L: 250 mannitol, 0.5 EGTA, 5 HEPES; pH 7.4) to obtain a crude mitochondrial fraction. This fraction was further overlaid on top of 8 mL Percoll medium (225 mmol/L mannitol, 25 mmol/L HEPES, 1 mmol/L EGTA, and 30% Percoll (v/v); pH 7.4) and centrifuged at 95,000 g for 30 min at 4°C in an SW40 Ti rotor. The pellet was suspended in MRB buffer again, followed by centrifugation at 6,300 g for 10 min at 4°C to obtain purified mitochondria. To obtain the ER fraction, the supernatant was centrifuged at 20,000g for 30 min at 4°C. The pellet consisted of a lysosomal fraction also containing plasma-membrane contamination. Further centrifugation of the supernatant (100,000g for 1 h at 4°C) resulted in the isolation of ER (pellet) and a cytosolic fraction (supernatant).

For sub-mitochondrial compartment fractionation, isolated pure mitochondria were suspended in an isolation medium (in mmol/L: 225 mannitol, 75 sucrose, 0.1 EGTA, 20 HEPES; pH 7.4) with digitonin at 0.12 mg digitonin/mg mitochondria and stirred gently on ice for 15 min. Then the digitonin-treated samples were diluted with 3 volumes of isolation medium and centrifuged at 9,000 g for 10 min to get supernatant A. The pellet re-suspended in isolation buffer was sonicated for 30 s on ice and centrifuged at 6,500 g for 10 min followed by centrifugation at 144,000 g for 60 min at 4°C to sediment the inner membrane vesicles. The supernatant was collected as a matrix fraction. Supernatant A was centrifuged at 144,000 g for 60 min at 4°C to sediment outer membrane vesicles as pellets and the supernatant was collected as the inner membrane space fraction.

TMRM Staining

Lenti-X 293T or REEP1-KO cells were grown in 24-well plates at 70% confluence at the time of data collection. Cells were incubated with TMRM (200 nM, ThermoFisher Scientific) in fresh culture medium for 30 min in a CO₂ incubator. After two washes with 100 µL PBS containing 0.2% BSA, the plates were read by CellDiscoverer 7 with the RFP/TRITC filter set at Ex/Em = 548/575 nm. Data were analyzed with Zen software.

ATP Measurement

ATP levels were assessed by an ATP Colorimetric/Fluorometric Assay Kit (Biovision, Waltham, USA). Cells (1×10⁶) were lysed in 100 µL ATP assay buffer on ice. The cell lysate was deproteinized using a 10-kDa spin column. 20 µL of the sample was added to a 96-well plate and the volume was adjusted

to 50 μL /well with ATP Assay Buffer. Enough reagent to generate a reaction mix (ATP assay buffer: ATP probe: ATP converter: Developer, at 11:1:1:1) was mixed for all samples and standards. 50 μL of the reaction mixture was added to each well of the 96-well plate, mixed well, and incubated at room temperature for 30 min, protected from light. The absorbance at 570 nm was measured with a microplate reader (Bio-Rad). To generate a standard curve, 0, 2, 4, 6, 8, and 10 μL ATP standard (1 mmol/L) were added to a series of wells and the volume was adjusted to 50 μL /well with ATP Assay Buffer to generate 0, 2, 4, 6, 8, and 10 nmol/well of ATP Standard. The curve was calculated following the manufacturer's instructions.

Analysis of Mitochondrial Complex IV Activity

Mitochondrial complex IV (cytochrome c oxidase) activity was measured using a cytochrome oxidase activity colorimetric assay kit (Biovision) following the manufacturer's instructions. Briefly, 5 μg of isolated mitochondria in cytochrome oxidase assay buffer was added to each well of a 96-well plate. For negative control, an equal volume of Enzyme Dilution Buffer was added. Then 120 μL of the diluted cytochrome c was added to each sample and the control. The spectrophotometer was set at 550 nm on the kinetic program for 30 min at 30-s intervals. The decrease in optical density (OD) over 30 min was recorded. The rate of the reaction was calculated by changes in OD: $\Delta\text{OD}/\text{min}$ by using the maximum linear rate. The oxidation of cytochrome c by complex IV is a biphasic reaction with an initial fast burst followed by a slower activity.

Quantitative Mass Spectrometry

To identify the specific binding partners of REEP1, we used a proteomic approach according to a previously published protocol [19]. Briefly, the control vector and REEP1-Strep were transfected into Lenti-X 293T cells with TransIT[®]-293 transfection reagent (Mirus, Houston, USA). After immunoprecipitation with MagStrep "type3" XT beads, proteins were eluted with BXT buffer (IBA Lifesciences) and separated by 4%–12% Mini-PROTEAN[®]TGX[™] precast protein gels (Bio-Rad). After running for 10 min, 1 cm of the gel was cut and subjected to in-gel trypsin digestion. Tryptic peptides were labeled with ¹⁶O or ¹⁸O and then mixed for differential isotopic analysis. Labeled peptides were analyzed by LC-MS/MS using an UltiMate 3000 LC system (Dionex, Sunnyvale, USA) interfaced with a Velos Pro Ion Trap/Orbitrap Elite hybrid mass spectrometer (ThermoFisher Scientific). Peptides were identified by comparing the resultant MS/MS spectra against the Swiss-Prot database using Mascot database search software (version 2.4, Matrix Science, Chicago, USA). Strict trypsin specificity was applied with one missed cleavage allowed. The ¹⁸O/¹⁶O ratio of each peptide was calculated using Proteomics Tools

software (available at <https://github.com/shengqh/RCPA-Tools>).

RNA Extraction and Reverse Transcription-Quantitative PCR (RT-qPCR)

Total RNA was extracted from Lenti-X 293T cells using the RNAeasy mini kit (Qiagen, Germantown, USA) according to the manufacturer's protocols. cDNA was synthesized by using High-Capacity cDNA Reverse Transcription Kits (ThermoFisher Scientific) with random primers. Quantitative reverse-transcription PCR (qPCR) was performed using the SYBR Premix Ex Taq kit (Takara Bio) in a CFX96 real-time PCR system (Bio-Rad) following the manufacturer's protocol. The thermocycling conditions were as follows: 95°C for 30 s, followed by 40 cycles of 95°C for 5 s and 60°C for 30 s. The mRNA levels of the targeted protein were normalized to GAPDH using the $2^{-\Delta\Delta\text{Cq}}$ method. The primers used for RT-qPCR are listed in Table S2.

Differentiation of SH-SY5Y Cells

SH-SY5Y cells (ATCC, CRL-2266) were differentiated using a combination of previously reported protocols [20, 21]. Briefly, undifferentiated SH-SY5Y cells were maintained in a growth medium composed of Opti-MEM (#31985070, Gibco, Waltham, USA) supplemented with 5% FBS and 1% penicillin/streptomycin. To induce differentiation, cells were first seeded on an uncoated plate and, on the following day, the medium was changed to a differentiation medium composed of Opti-MEM, 1% FBS, 1% penicillin/streptomycin, and 10 $\mu\text{mol}/\text{L}$ all-trans retinoic acids (R2625, Sigma Aldrich). After 3 days of differentiation, the medium was changed to fresh differentiation medium again and cultured for another 3 days. The cells were then split and seeded on poly-*D*-lysine-treated plates or coverslips. On the following days, the medium was changed to neuronal growth medium composed of Neurobasal medium (#A3582901, Gibco) supplemented with brain-derived neurotrophic factor (50 ng/mL) (#248-BD, Novus Bio/R&D Systems, Minneapolis, USA), KCl (20 mmol/L) (#P5405, Sigma), 2% B27 (#17564-044, Gibco), 1% Glutamax, 1% penicillin/streptomycin, and 10 $\mu\text{mol}/\text{L}$ retinoic acids for an additional three days. Then the medium was exchanged again with fresh neuronal growth medium. After 18 days of differentiation, neuronal cells were fixed for immunofluorescence staining or lysed in cell lysis buffer for immunoblot analysis. For neuronal viability assays, differentiated neurons plated in 96-well plates were exposed to 100 $\mu\text{mol}/\text{L}$ H₂O₂ or 10 $\mu\text{mol}/\text{L}$ Tunicamycin for 24 h. Cell viability was measured using Cell Counting Kit-8 (Dojindo Molecular Technologies, Rockville, USA) following the manufacturer's instructions.

Sholl Analysis

Using images with a single microglial cell or astrocyte in the frame, we applied Sholl analysis using ImageJ (NIH, Bethesda, USA) after adjusting the image threshold accordingly. We used the segmented line tool to determine both the center of the soma and the length of the longest integrated radius. Data were grouped with their respective categories [non-transgenic littermates (NTG), G93A/GFP, G93A/REEP1] At least 5 cells were analyzed per animal with at least 3 animals examined per genotype. The average number of intersections of glial cells from NTG, G93A/GFP, and G93A/REEP1 mice at each radius was plotted.

Image Analysis

Images were analyzed with Zen software or Imaris (Bitplane, Belfast, UK). The acquired images were processed by deconvolution (regularized inverse filter) by ZEN software. All confocal images of mitochondria and neuromuscular junctions (NMJs) were reconstructed using the “easy 3D” module in Imaris. At least 200 NMJs from each mouse were counted. The ER structure was extracted using the SURFACE tools in Imaris following the manufacturer’s instructions. Mitochondrial and ER lengths were calculated from single-plane images using Image-Pro Plus software. The length was defined as the Feret maximum. All immunoblot images were analyzed using ImageJ.

Statistical Analysis

Student’s *t*-test, one-way analysis of variance (ANOVA) followed by Tukey’s multiple comparisons test, and two-way ANOVA followed by Bonferroni multiple comparisons test were applied using GraphPad Prism 8 software (GraphPad Software Inc.). Detailed information about the statistical analysis for each experiment is presented in the figure

legends. Data are the mean \pm SEM. $P < 0.05$ was considered to be statistically significant.

Results

Reduced Expression of REEP1 in ALS Patients and G93A Mice

As increasing evidence suggests that REEPs are involved in neurodegenerative diseases like HSP [22], we explored the relationship between REEPs and the classical motor neuron disease, ALS. Making use of an already published transcriptome dataset of the lumbar spinal cord from sporadic ALS patients and age-matched controls [23], we showed that REEP1 and REEP2, but not other REEPs were greatly reduced in these patients (Fig. S1A and B). Consistent with the findings in sporadic ALS cases, transcriptome analysis of motor neurons (MNs) derived from iPSCs (induced pluripotent stem cells) from familial ALS patients harboring a SOD1 A4V mutation demonstrated that REEP1 expression was significantly lower in SOD1A4V MNs than in their isogenic controls (Fig. S1C). Since the widely-used G93A mice develop phenotypes closely mimicking familial and sporadic ALS patients, we next studied the expression of REEPs in the spinal cord of G93A mice and their NTGs. Compared with NTG mice, the expression of REEP1 in the spinal cord was reduced significantly in 120-day-old G93A mice (Fig. 1A and B). In addition, we evaluated the REEP1 expression in G93A mice before and after the onset of the locomotor phenotype. There was likely a time-dependent reduction of REEP1 in G93A mice. At 30 days old, G93A mice showed a trend of decrease in REEP1 expression. The expression of REEP1 decreased by 40% in 60-day-old G93A mice compared with NTG mice. At 90 days old, a further decrease of 30% in REEP1 expression was noted in G93A mice (Fig. S1D). The above results suggest that the reduction of REEP1 expression is a distinguishing feature of patients and a mouse model of ALS.

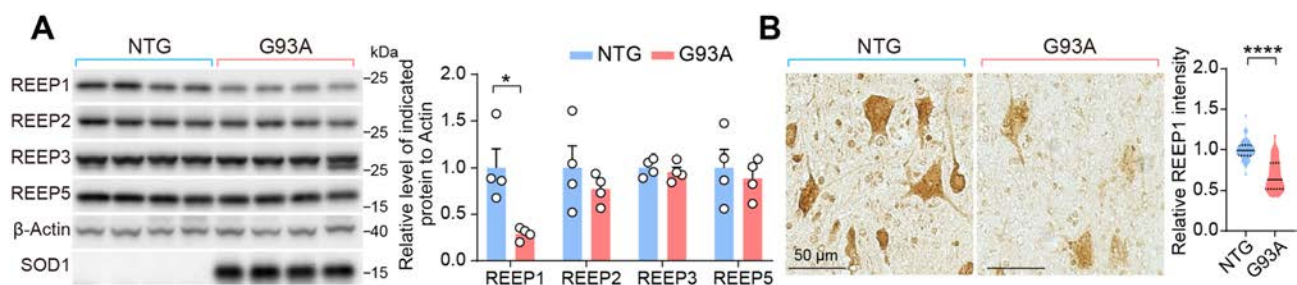


Fig. 1 Reduction of REEP1 in the spinal cord of G93A mice. **A** Representative immunoblots and quantification of REEP expression in the spinal cord of NTG (non-transgenic) and G93A mice ($n = 4$ mice per group). **B** Representative immunohistochemical staining of

REEP1 in the lumbar spinal cord of NTG ($n = 30$ neurons from 3 mice) and G93A mice ($n = 35$ neurons from 3 mice). Scale bars, 50 μ m. Data are the mean \pm SEM. * $P < 0.05$, **** $P < 0.0001$, two-tailed Student’s *t*-test.

Forced Expression of REEP1 Abolishes Skeletal Muscle Atrophy in G93A Mice

We then examined the impact of REEP1 upregulation in spinal motor neurons on behavioral deficits and survival in G93A mice. Since G93A mice have an onset of symptoms at ~60 days and the survival endpoint at ~150 days, we bilaterally injected adeno-associated virus serotype 1 encoding human REEP1 under the neuron-specific promoter eSYN (AAV1-hREEP1-Flag) into the lumbar spinal cord of 45-day-old G93A mice. The motor performance of G93A mice was evaluated by tail suspension, grip strength, and footprint tests after the age of 70 days (Fig. 2A). We first examined the expression of REEP1 in the spinal cord. To explore the cellular distribution of exogenously-expressed REEP1, spinal cord tissue from G93A mice injected with AAV1-hREEP1-Flag (G93A/REEP1) was stained with anti-Flag and anti-NeuN (neuronal nuclear protein) antibodies. As expected, REEP1-Flag was predominantly expressed in NeuN-positive cells, suggesting that REEP1 was successfully expressed in neuronal cells (Fig. S2A). In addition, immunoblot analysis of subcellular fractions further demonstrated that exogenously-expressed REEP1 was present in both ER and mitochondrial fractions, which displayed the same distribution pattern as endogenous REEP1 (Fig. S2B and C). We then compared the expression of REEP1 in AAV-injected G93A mice; immunoblot analysis revealed that G93A/REEP1 mice had a twofold increase of total REEP1 in the lumbar cord of G93A mice compared to GFP-injected G93A mice (G93A/GFP) (Fig. 2B). Surprisingly, the overall life-span of G93A/REEP1 mice was extended when compared with G93A/GFP mice (Fig. 2C), and the motor deficits of G93A mice were remarkably attenuated by REEP1 upregulation (Fig. 2D–F). While G93A/GFP mice showed hind limb folding into the abdomen with an infrequent clasping of their hind limbs, G93A/REEP1 mice exhibited greatly improved performance in tail suspension tests (Fig. 2D, S2D and Video S1). In addition, the declining muscle strength and gait abnormalities in G93A/GFP mice were also alleviated in G93A/REEP1 mice (Figs 2D, E, S2E, and Video S2).

Loss of NMJ integrity due to motor neuron denervation is a prominent feature of G93A mice [24]. Denervation occurs before the symptomatic stage and translates into reduced electrical potential in affected muscles [25]. We then applied electrophysiological tests to measure the CMAP, which is the sum of action potentials in the muscle in response to non-invasive spinal cord electrical stimulation. Decreasing CMAP values in G93A mice reflected NMJ denervation, which was partially restored by REEP1 upregulation (Fig. 2F). Consistent with the improved motor performance, G93A/REEP1 mice displayed well-preserved hindlimb skeletal muscles and alleviated NMJ denervation compared with G93A/GFP mice (Fig. 2G, H). Moreover, we also determined the expression of Agrin, Wnt3, and muscle-specific kinase (MuSK) in muscle tissue from

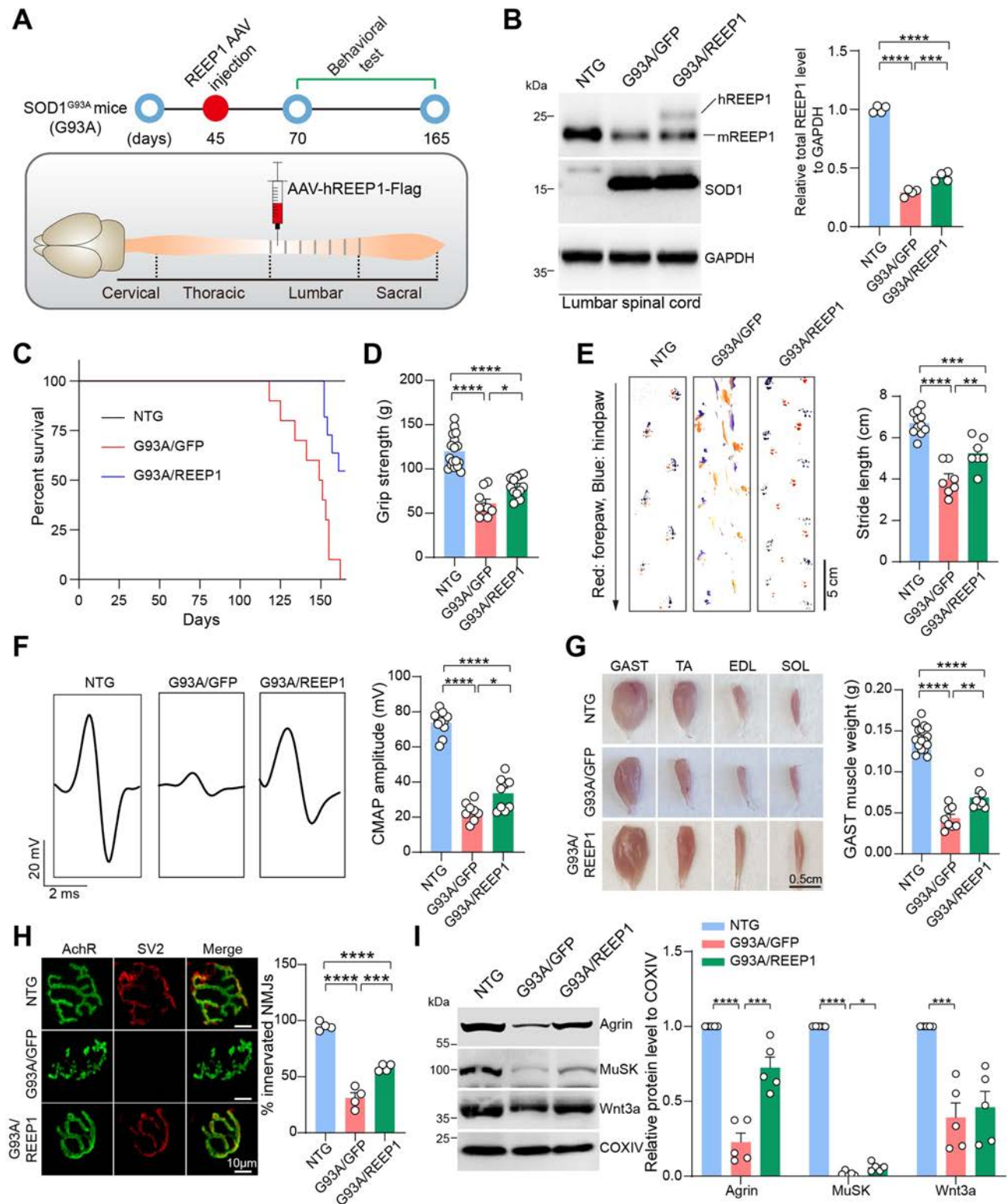
NTG, G93A/GFP, and G93A/REEP1 mice. These three proteins are key regulators of NMJs, in which Agrin and Wnt3 are secreted by motor neurons while MuSK is mainly expressed in skeletal muscle [26]. As expected, G93A/REEP1 mice exhibited stronger expression of Agrin and Musk in skeletal muscles than in G93A/GFP mice (Fig. 2I). There was also a trend of increased levels of Wnt3 in G93A/REEP1 skeletal muscles (Fig. 2I). Therefore, these data strongly support the conclusion that augments expression of REEP1 in neurons in the spinal cord is sufficient to preserve motor function in G93A mice.

Protection Against MN Loss and Gliosis in G93A Mice via REEP1 Upregulation

Since MN numbers significantly decrease in the ventral horn of endpoint G93A mice [27], we next determined the effects of REEP1 overexpression on MN survival in G93A mice. By either Nissl or Choline Acetyltransferase (Chat) staining, we found that the MN numbers in the ventral horn of G93A/REEP1 mice significantly increased when compared to G93A/GFP mice (Fig. 3A, B). Neuroinflammation is a prominent pathological feature of ALS, characterized by the proliferation and activation of microglia and astrocytes, as extensively reported in G93A mice [27]. To assess the extent of gliosis, we immunostained activated microglia and astrocytes in the spinal cord of NTG, G93A/GFP, and G93A/REEP1 mice with specific antibodies against ionizing Ca²⁺-binding adaptor molecule 1 (Iba1) and glial fibrillary acidic protein (GFAP) respectively. Quantification revealed remarkably reduced microgliosis and astrogliosis in the spinal cord of G93A/REEP1 mice (Fig. 3C, D). In addition to the reduced number of microglial cells, we also observed that microglia cells seemed to be more ramified in the spinal cord of G93A/REEP1 mice than G93A/GFP microglial cells. Thus, we then applied Sholl analysis, which is widely used to quantify the complexity of dendritic arbors. The data confirmed that microglial cells display greatly reduced complexity in G93A/GFP mice, and this was partially restored in G93A/REEP1 mice (Fig. S3A). Similarly, astrocytes in G93A/REEP1 mice also demonstrated more ramifications than in G93A/GFP mice (Fig. S3B). Thus, these data support the conclusion that restoring the expression of REEP1 protects against MN loss and gliosis in G93A mice.

Loss of REEP1 Impairs Mitochondrial Function

As REEP1 is closely associated with the ER and mitochondrial function [8, 28], to further unravel the mechanisms of how REEP1 prevents MN loss in G93A mice, we next determined the expression of REEP1 in the ER and mitochondria-enriched fractions from the spinal cord of G93A mice. Immunoblot results demonstrated that REEP1 expression decreased in both ER and mitochondrial fractions (Fig.



S4A), indicating that loss of expression of REEP1 is probably associated with ER and mitochondrial dysfunction in G93A mice. To investigate the effect of REEP1 on mitochondria, we generated REEP1-knockout Lenti-X 293T cells (REEP1-KO) (Fig. 4A) and evaluated mitochondrial function. We first

determined the mitochondrial morphology and distribution in REEP1-KO cells by staining mitochondria with anti-TOM20 antibodies. In >95% of the WT cells, mitochondria with similar sizes were distributed uniformly throughout the cell (Fig. 4B). However, in 41% of REEP1-KO cells mitochondria

Fig. 2 REEP1 upregulation improves the motor performance of G93A mice. **A** Schematic of REEP1 AAV injection and behavioral test timeline. AAV serotype 1 encoding human REEP1 under the neuron-specific promoter eSYN (AAV1-hREEP1-Flag) was injected into the spinal cord at the first lumbar segment (L1) of G93A mice. **B** Representative immunoblots and quantification of REEP1 levels in the lumbar spinal cord of NTG, G93A/GFP, and G93A/REEP1 mice ($n = 4$ mice per group). **C** Kaplan-Meier survival curves of NTG ($n = 16$), G93A/GFP ($n = 10$), and G93A/REEP1 mice ($n = 11$). **D** Hindlimb grip strength of NTG ($n = 17$), G93A/GFP ($n = 9$), and G93A/REEP1 mice ($n = 12$) at 100 days old. **E** Footprint performance and stride length quantification of NTG ($n = 11$), G93A/GFP ($n = 7$), and G93A/REEP1 mice ($n = 7$). The arrow shows the direction of walking. **F** Representative images and quantification of CMAPs evoked by supramaximal stimulation of the sciatic nerve in NTG ($n = 12$), G93A/GFP ($n = 8$), and G93A/REEP1 mice ($n = 9$). **G** Representative images of skeletal muscles and quantification of gastrocnemius muscle weight of NTG ($n = 16$), G93A/GFP ($n = 8$), and G93A/REEP1 mice ($n = 8$). Scale bar, 0.5 cm. **H** Representative images and quantification of NMJ innervation of NTG, G93A/GFP, and G93A/REEP1 mice ($n = 4$ mice per group). Green, acetylcholine receptors (AChR) stained by α -bungarotoxin for motor endplates; red, SV2 for NMJs. Scale bars, 10 μ m. **I** Representative immunoblots and quantification of Agrin, Wnt3a, and MuSK in gastrocnemius muscle of NTG, G93A/GFP, and G93A/REEP1 mice ($n = 5$ mice per group). Data are the mean \pm SEM. * $P < 0.05$, ** $P < 0.01$, *** $P < 0.001$, **** $P < 0.0001$, one-way ANOVA followed by Tukey's multiple comparisons test (**B**, **D**, **E**–**I**).

were aggregated around the perinuclear area, indicating that loss of REEP1 expression induces mitochondrial aggregation (Fig. 4B). Since abnormal distribution is always linked to mitochondrial dysfunction, we further assessed the mitochondrial membrane potential by TMRM staining in live cells, and found that REEP1-KO cells showed a dramatically decreased mitochondrial membrane potential (Fig. 4C). Consistent with this, we also found a reduction of intracellular ATP levels in REEP1-KO cells (Fig. 4D). To study the mechanism underlying the ATP reduction in REEP1-KO cells, we used both native and denaturing electrophoresis to examine mitochondrial OXPHOS assembly. Although no changes were noted in the expression of five complex markers (Fig. S4B), both the assembly and activity of CIV were impaired in REEP1-KO cells (Fig. 4E, F). Similar results were obtained in REEP1-knockout M17 cells, a human neuroblastoma cell line (Fig. S4C). Consistent with this, CIV showed drastically decreased assembly in G93A mice when compared to NTG control (Figs 4G and S4D). Together, these data suggest that REEP1 deficiency suppresses mitochondrial functions.

Meanwhile, the impact of the reduction of REEP1 expression on cell proliferation was also examined. Compared with WT cells, REEP1-KO cells had a significantly decreased proliferation rate (Fig. 4H). As REEP1 is closely associated with not only mitochondrial function but also ER function [8, 28], we hypothesized that the impaired proliferation of REEP1-KO cells may be due to either ER or mitochondrial dysfunction. However, ER structures with an interconnected network of branching tubules in REEP1-KO cells were

almost identical to WT cells (Fig. S4E). In addition, previous studies have shown that REEP1 plays a role in ER stress resistance [29, 30]. We then examined the level of the ER stress signaling marker phosphorylated eIF2 α (p-eIF2 α) in WT and REEP1-KO cells. Immunoblot analysis showed that the p-eIF2 α levels in REEP1-KO cells were comparable to those in WT cells, suggesting there is no ER-stress response ongoing in REEP1-depleted cells (Fig. S4F). Altogether, these data support the conclusion that the decreased proliferation of REEP1-KO cells is likely caused by impaired mitochondrial functions.

REEP1 Interacts with CIV Subunits

Although previous studies have shown that REEP1 is localized in mitochondria [8], the specific localization in mitochondria remains unclear. To address this question, Lenti-X 293T cells were co-transfected with Mito-OMM-GFP and REEP1-Flag, and immunofluorescence staining was applied. After image deconvolution, the immunofluorescent signals from REEP1-Flag co-localized with the co-expressed outer mitochondrial membrane marker Mito-OMM-GFP. Interestingly, part of the REEP1-Flag signal was surrounded by Mito-OMM-GFP, suggesting that REEP1 is also localized inside mitochondria (Fig. S5A). In an attempt to investigate the localization of REEP1 in mitochondria, we prepared sub-mitochondrial compartments by separating the outer mitochondrial membrane (OMM), inner mitochondrial membrane (IMM), mitochondrial intermembrane space (IMS), and matrix from purified mitochondria. Immunoblot analysis revealed that REEP1 was present in both the OMM and IMM fractions (Fig. 5A). Together, these data support the conclusion that REEP1 is localized in the OMM and IMM.

To explore the function of mitochondrial membrane-associated REEP1, a quantitative mass spectrometry (MS)-based approach was used to monitor the dynamics of REEP1-associated protein complexes (Fig. S5B). 82 proteins were found to be enriched in the pull-down samples from the REEP1-Strep-expressing Lenti-X 293T cells (Table. S1). Kyoto Encyclopedia of Genes and Genomes analysis showed that these proteins were enriched in many neurodegenerative diseases, such as Parkinson's disease and Huntington's disease, strongly supporting the idea that these defects in REEP1-regulated pathways could be a common mechanism of neurodegeneration (Fig. S5C). Consistent with the previous study, Gene Oncology analysis revealed that these proteins are mainly localized in membrane structures, including ER and mitochondria (Fig. S5D). Interestingly, we found that these proteins were commonly enriched in Gene Ontology terms largely related to membrane organization and mitochondrial ATP synthesis-coupled proton transport (Figs 5B and S5E). Among these proteins, 5 OXPHOS subunits belonging to CIV and CV were identified: NDUFA4, ATP5A1, ATP5B,

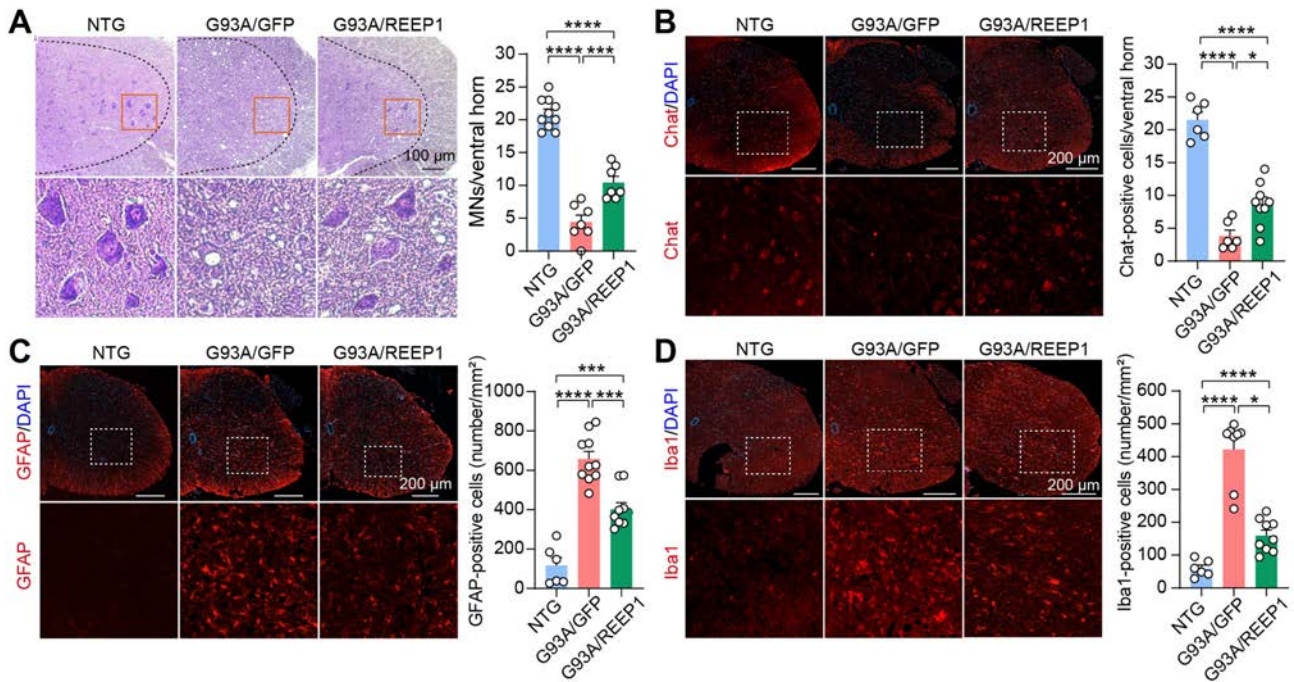


Fig. 3 REEP1 augmentation prevents neuronal loss and gliosis in G93A mice. **A** Representative images and quantification of Nissl staining in the spinal cord of NTG ($n = 10$), G93A/GFP ($n = 7$), and G93A/REEP1 mice ($n = 7$). Scale bar, 100 μm . **B** Representative images and quantification of immunofluorescence staining of Chat in the spinal cord of NTG ($n = 6$), G93A/GFP ($n = 6$), and G93A/REEP1 mice ($n = 9$). Scale bars, 200 μm . **C** Representative images and quantification of immunofluorescence staining of GFAP in the

spinal cord of NTG ($n = 6$), G93A/GFP ($n = 10$), and G93A/REEP1 mice ($n = 9$). Scale bars, 200 μm . **D** Representative images and quantification of immunofluorescence staining of Iba1 in the spinal cord of NTG ($n = 6$), G93A/GFP ($n = 8$), and G93A/REEP1 mice ($n = 9$). Scale bars, 200 μm . Data are the mean \pm SEM. * $P < 0.05$, *** $P < 0.001$, **** $P < 0.0001$, one-way ANOVA followed by Tukey's multiple comparisons test.

ATP5F, and ATP5O. Co-immunoprecipitation (co-IP) analysis further validated the interaction between REEP1 and NDUFA4, ATP5O, and ATP5A1 co-immunoprecipitation between transfected exogenously-expressed NDUFA4-GFP and REEP1 WT/REEP1 Δ 101–110.

To further assess the importance of the REEP1 and NDUFA4 association on CIV assembly, we generated a series of deletion mutations of REEP1 and analyzed their interaction with NDUFA4 (Fig. 5D). We tagged REEP1 at the C-terminus with Strep-tag and co-IP was applied by using cell lysates from NDUFA4-GFP and truncated REEP1-Strep co-transfected Lenti-X 293T cells. A 140 amino-acid (aa) deletion in the N-terminal region of REEP1 abolished the interaction between REEP1 and NDUFA4. On the other hand, deletion of N-terminal 100 aa (Δ N100) remarkably increased the association of REEP1 with NDUFA4 (Fig. 5E). Although further immunofluorescence and subcellular fraction analysis demonstrated that Δ N100 was present in both the ER and mitochondria, more Δ N100 was enriched in the mitochondrial fraction than full-length REEP1 (Fig. S5H, I). This is consistent with a previous study showing that the loss

of the N-terminal domain of REEP1 greatly increased its mitochondrial distribution [31]. We then generated truncated mutations between 100 aa and 140 aa of REEP1. Co-IP analysis showed that the removal of the N-terminal 110 aa (Δ N110) disrupted the interaction between REEP1 and NDUFA4 (Fig. 5F). Like the REEP1 Δ N110 (deletion of the N-terminal 110 aas), the REEP1 Δ 101–110, which lacked the 10 aa residues from 101 to 110, completely abrogated the ability of REEP1 to co-precipitate with NDUFA4 (Fig. 5G). The above results suggest that 101–110 aa of REEP1 is necessary for its binding to NDUFA4.

REEP1 Regulates CIV Assembly Through Interaction with NDUFA4

Based on the identification of the 101–110 motif required for interactions between REEP1 and NDUFA4, we next performed rescue experiments in REEP1-KO cells to validate their functional role in maintaining mitochondrial function. We first explored the subcellular localization of the REEP1 Δ 101–110 by isolation of ER and pure mitochondria

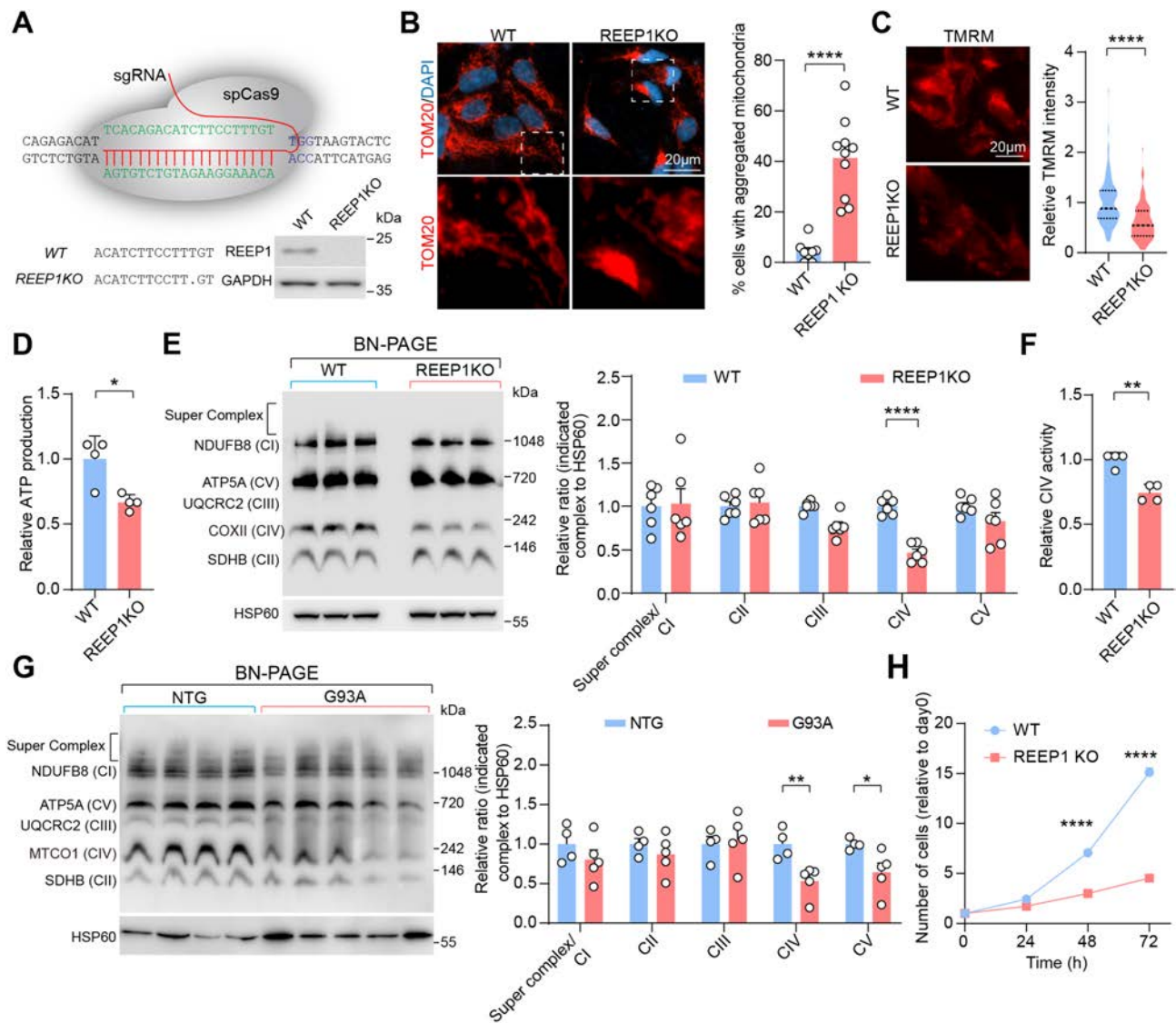


Fig. 4 Loss of REEP1 impairs mitochondrial function. **A** Schematic of CRISPR/Cas9 genome-editing of the REEP1 gene in Lenti-X 293T cells to obtain REEP1-KO cells validated by western blot and DNA sequencing analysis. GAPDH was used as the loading control. **B** Representative images and quantification of aggregated mitochondria in WT ($n = 191$ cells from 3 experiments) and REEP1-KO cells ($n = 178$ cells from 3 experiments). Mitochondria are stained with TOM20. DAPI to visualize nuclei. Scale bar, 20 μm . **C** Quantification of mitochondrial membrane potential staining by TMRM in WT ($n = 101$ cells from three experiments) and REEP1KO cells ($n = 111$ cells from three experiments). Scale bar, 20 μm . **D** Quantification of

ATP levels in WT and REEP1-KO cells ($n = 4$ replicates). **E** Representative immunoblots and quantification of mitochondrial OXPHOS assembly in WT and REEP1-KO cells ($n = 6$ replicates). **F** Quantification of mitochondrial CIV activity in WT and REEP1-KO cells ($n = 4$ replicates). **G** Representative immunoblots and quantification of mitochondrial OXPHOS assembly in 120-day-old NTG ($n = 4$) and G93A mice ($n = 5$). **H** Growth curves for WT and REEP1KO cells over 72 h. Data are the mean \pm SEM. * $P < 0.05$, ** $P < 0.01$, **** $P < 0.0001$, two-tailed Student's *t*-test (**B–G**) and two-way ANOVA followed by Bonferroni multiple comparisons test (**H**).

(Fig. 6A). Similar to WT REEP1, REEP1 Δ 101–110 was present in both ER and mitochondrial fractions, implying that loss of this motif did not change the subcellular localization of REEP1. Then, cell proliferation and mitochondrial function were analyzed to determine whether the loss of the interaction between REEP1 and NDUFA4 could rescue

the phenotype caused by REEP1-knockout. Overexpression of WT REEP1, but not the Δ 101–110 mutations, restored the proliferation deficiency of REEP1-KO cells (Fig. S6A). Unexpectedly, REEP1-KO cells expressing either REEP1 or REEP1 Δ 101–110 showed similar mitochondrial distribution, suggesting that the changes in mitochondrial

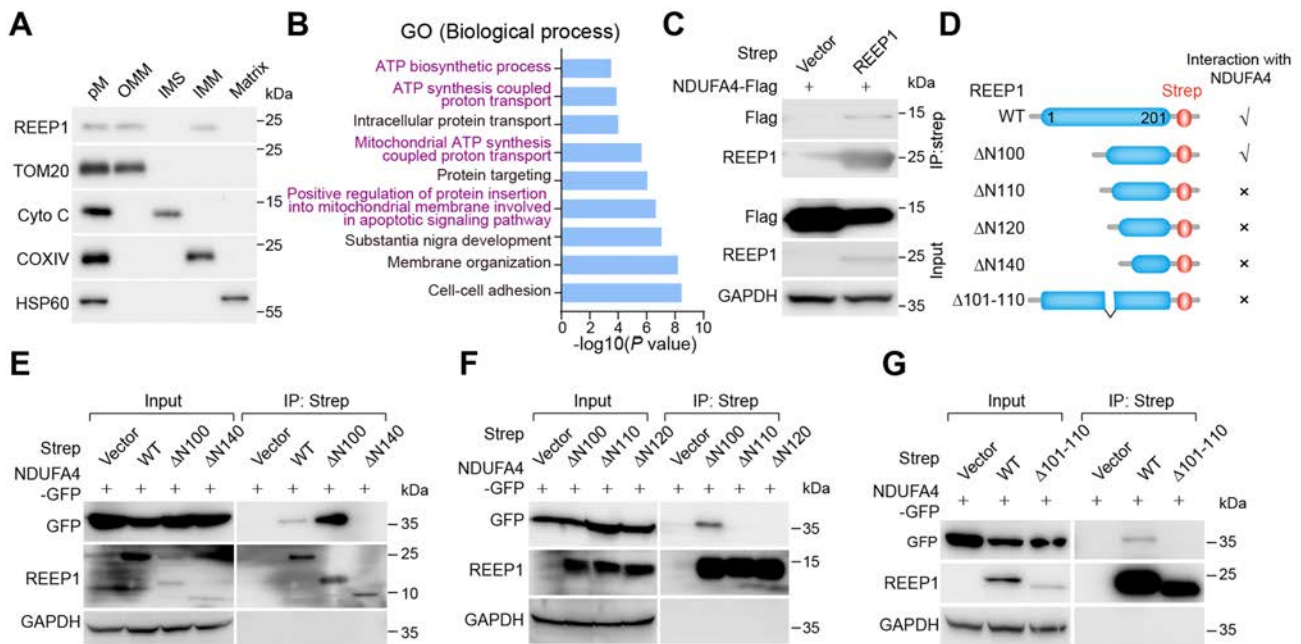


Fig. 5 REEP1 interacts with NDUFA4. **A** Representative immunoblots of REEP1 and markers for sub-mitochondrial fractions from Lenti-X 293T cells: TOM20 for the outer mitochondrial membrane, Cyto C for the inner membrane space of mitochondria, COXIV for the inner mitochondrial membrane, and HSP60 for the mitochondrial matrix. **B** Gene Ontology enrichment analysis of unique interactors of REEP1 according to categories based on biological process. **C** Rep-

resentative immunoblots of co-immunoprecipitation between transfected REEP1-Strep and NDUFA4-Flag in Lenti-X 293T cells. **D** Schematic of REEP1 deletion mutants used for mapping the binding site for NDUFA4. **E, F** Representative immunoblots of co-immunoprecipitation between transfected exogenously-expressed NDUFA4-GFP and REEP1 WT/REEP1 Δ 101–110.

distribution caused by REEP1 loss are not dependent on the interaction between REEP1 and NDUFA4 (Fig. 6B). Moreover, mitochondrial membrane potential and intracellular ATP levels were rescued in REEP1-KO cells expressing REEP1, but not in cells expressing Δ 101–110 (Figs 6C, D and S6B). In addition, CIV assembly and activity were also restored by overexpression of REEP1, but not Δ 101–110 REEP1 (Fig. 6E, F). Therefore, our results strongly suggest that the interaction between REEP1 and NDUFA4 is necessary for maintaining normal mitochondrial function.

As NDUFA4 is essential for CIV assembly and activity, we next studied the expression of NDUFA4 in G93A mice and REEP1-KO cells. Immunoblot analysis revealed that NDUFA4 expression was greatly reduced in the spinal cord of 120-day-old G93A mice compared with age-matched NTG mice (Fig. 6G). Consistent with this, NDUFA4 levels were significantly decreased in REEP1-KO (both Lenti-X 293T cells and M17 cells) (Figs 6H and S6C). While REEP1 completely restored the expression of NDUFA4 in REEP1-KO cells, Δ 101–110 REEP1-expressing REEP1-KO cells revealed levels of NDUFA4 similar to REEP-KO cells (Fig. 6H). As no NDUFA4 mRNA levels change occurred in these cells (Fig. 6I), REEP1 is likely involved in NDUFA4 degradation. Together, these data support the

conclusion that REEP1 is an important regulator of CIV assembly through interaction with NDUFA4.

To further validate these findings in neuronal cells, we generated REEP1-KO SH-SY5Y cells and restored REEP1 expression in these cells by re-expressing WT REEP1 and REEP1 Δ 101–110. These stable cell lines were further differentiated into neurons, which were used for mitochondrial function analysis and neuronal survival assay (Fig. S7A–H). Consistent with the results from Lenti-X 293T cells, re-expressing REEP1 restored NDUFA4 expression and the CIV defects in REEP1-KO neurons. However, neurons expressing REEP1 Δ 101–110 had NDUFA4 levels and CIV defects similar to REEP1-KO neurons, suggesting that the interaction between REEP1 and NDUFA4 is critical for mitochondrial function in neuronal cells (Fig. S7C, D). Although the loss of REEP1 did not affect neuronal survival, REEP1-KO neurons had shorter branches than WT neurons, indicating that REEP1 is essential for neurite outgrowth during neuronal differentiation (Fig. S7E–G). Previous studies have reported that SOD1G93A overexpression induces both oxidative stress and ER stress in neuronal cells, and this potently contributes to neuronal death [32, 33]. To explore the importance of REEP1 for neuronal survival

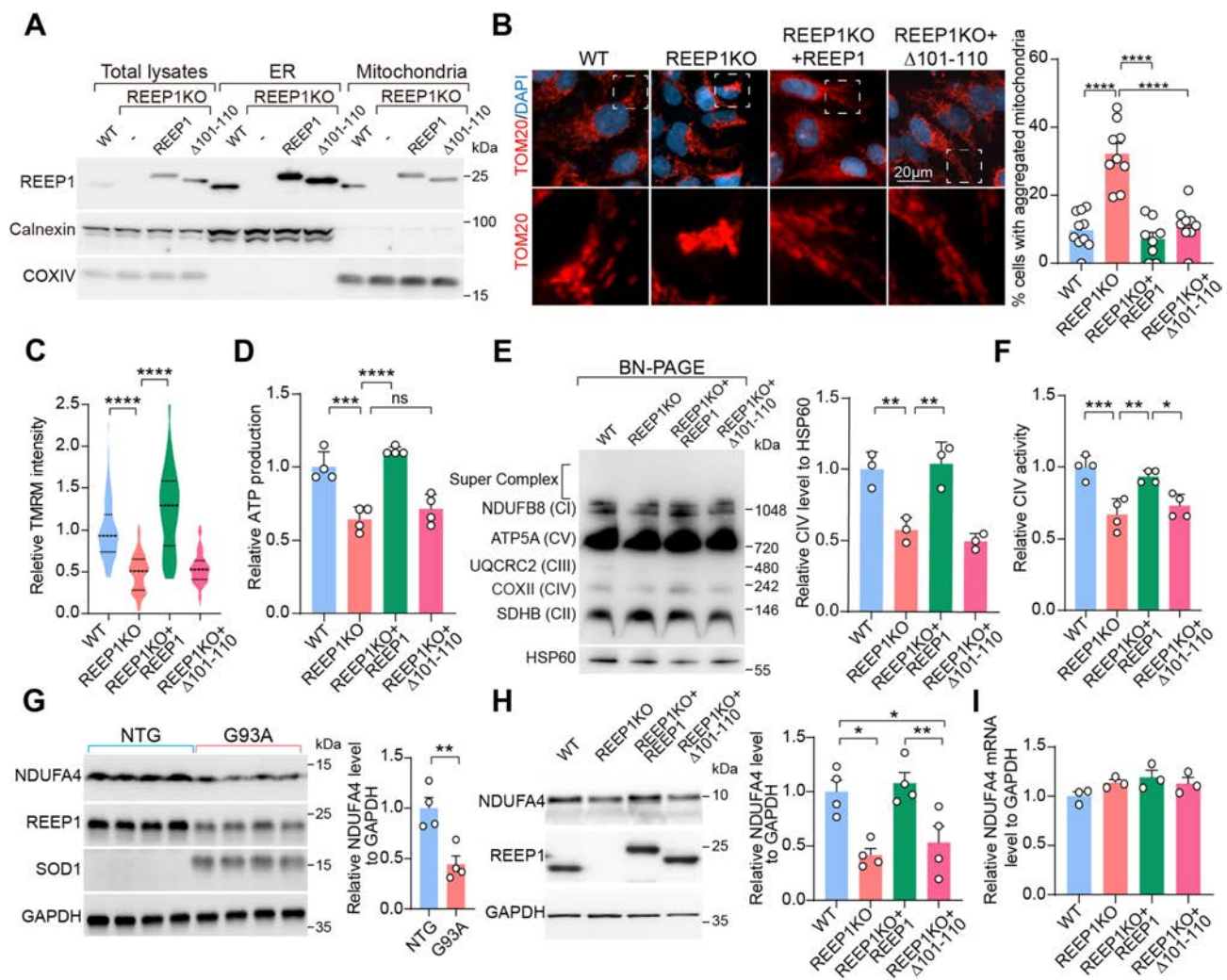


Fig. 6 REEP1 regulates CIV assembly through interaction with NDUFA4. **A** Representative immunoblots of REEP1 in the ER and mitochondrial fractions of indicated cells. Calnexin and COXIV were used as ER and mitochondrial markers, respectively. Overexpressed REEP1 WT and REEP1 Δ 101–110 carrying Strep-tag. **B** Representative images and quantification of aggregated mitochondria in WT ($n = 192$ cells from 3 experiments), REEP1KO ($n = 210$ cells from 3 experiments), REEP1KO+REEP1 ($n = 218$ cells from 3 experiments), and REEP1-KO+ Δ 101–110 cells ($n = 169$ cells from 3 experiments). Mitochondria are stained by TOM20. DAPI is used to visualize nuclei. Scale bar, 20 μ m. **C** Quantification of mitochondrial membrane potential staining by TMRM in WT ($n = 99$ cells from 3 experiments), REEP1-KO ($n = 82$ cells from 3 experiments), REEP1-KO+REEP1 ($n = 94$ cells from 3 experiments), and REEP1-KO+ Δ 101–110 cells ($n = 104$ cells from 3 experiments). **D** Quantification of ATP levels in WT, REEP1-KO, REEP1-KO+REEP1,

and REEP1-KO+ Δ 101–110 cells ($n = 4$ replicates). **E** Representative immunoblots and quantification of mitochondrial OXPHOS assembly in WT, REEP1-KO, REEP1-KO+REEP1, and REEP1-KO+ Δ 101–110 cells ($n = 3$ replicates). **F** Quantification of mitochondrial CIV activity in WT, REEP1-KO, REEP1-KO+REEP1, and REEP1-KO+ Δ 101–110 cells ($n = 4$ replicates). **G** Representative immunoblots and quantification of NDUFA4 expression in the spinal cord from 120-day-old NTG and G93A mice ($n = 4$ mice per group). **H** Representative immunoblots and quantification of NDUFA4 expression in WT, REEP1-KO, REEP1-KO+REEP1, and REEP1-KO+ Δ 101–110 cells ($n = 4$ replicates). **I** Relative mRNA levels of NDUFA4 in WT, REEP1-KO, REEP1-KO+REEP1, and REEP1-KO+ Δ 101–110 cells ($n = 3$ replicates). Data are the mean \pm SEM. * $P < 0.05$, ** $P < 0.01$, *** $P < 0.001$, **** $P < 0.0001$, two-tailed Student's t -test (G) and one-way ANOVA followed by Tukey's multiple comparisons test (B–F, H, and I).

under stress conditions, we treated SH-SY5Y-derived neurons with H_2O_2 and Tunicamycin (TM) to induce oxidative stress and ER stress, respectively (Fig. S7H). Strikingly, loss of REEP1 caused greatly increased sensitivity to oxidative stress in neuronal cells. And re-expressing WT REEP1, but not REEP1 Δ 101–110, fully protected

REEP1-KO cells from oxidative stress compared with WT neurons. Similar phenomena were also found in TM-treated neurons (Fig. S7H). These data together suggest that REEP1 and its interaction with NDUFA4 are critical for neuronal survival under stress conditions.

Mitochondrial Abnormalities in G93A Mice are Restored by REEP1 Upregulation

Next, we determined whether the protective effect mediated by REEP1 augmentation in G93A mice was through mitochondria-associated pathways by analyzing mitochondrial morphology and function in NTG, G93A/GFP, and G93A/REEP1 mice. Although there was a significant upregulation of REEP1 protein levels in lumbar spinal cord extracts from G93A/REEP1 mice compared to G93A/GFP mice, the expression of REEP1 in G93A/REEP1 mice was still lower than that in NTG mice (Fig. 2B). Unexpectedly, immunoblot analysis revealed that reduction of REEP1 expression in the mitochondria of G93A mice was fully restored by AAV1-hREEP1-Flag injection (Fig. 7A). Moreover, the reduced expression of NDUFA4 was partially rescued in lumbar spinal cord extracts from G93A/REEP1 mice (Fig. 7B). Despite that no morphological changes in the ER were noted in these mice, mitochondria in the MNs of G93A mice became fragmented as evidenced by the decrease in mitochondrial length, which was restored by forced expression of REEP1 (Figs. 7C and S8A). Although there were no statistically significant differences, the mitochondrial membrane potential in G93A/REEP1 mice had an increasing trend compared to G93A/GFP mice (Fig. S8B). Activity analysis also demonstrated that CIV deficiencies were rescued by REEP1 upregulation (Fig. 7D). These findings further support the idea that REEP1 protects MNs by improving mitochondrial functions.

Discussion

Here we showed that the expression of REEP1 is significantly reduced in the spinal cord of G93A mice. Augmentation of REEP1 preserved the motor performance of G93A mice by improving mitochondrial function. On the mechanistic level, we demonstrated that REEP1 regulates mitochondrial CIV assembly by association with NDUFA4. These findings partially explain that the mitochondrial CIV dysfunction in ALS and other neurodegenerative diseases might be associated with REEP1 loss-of-function (Fig. 7E).

Morphological alterations of membrane-bound organelles, such as ER, mitochondria, and Golgi have been consistently reported in ALS patients and ALS-associated mouse models [34–39]. As a membrane curvature-inducing protein with various subcellular localizations, our findings suggest that REEP1 deficiency may be responsible for the morphological changes of mitochondria, but not ER structure, in ALS and its experimental models. Since the expression of other REEPs is not altered, REEP1 deficiency is likely specific to ALS. In addition, experimental models

without REEP1 expression demonstrate abnormalities in the ER and mitochondrial morphogenesis [11, 28]. All these studies together suggest that REEP1-mediated dysfunction of organelles might be the cause rather than the consequence of ALS. It is still unclear why mRNA of REEP1 decreases in ALS and it would be interesting to investigate the essential factors regulating REEP1 expression at the transcriptional level.

Regarding the subcellular localization of REEP1, conflicting results have been reported. Although REEP1 was initially identified as a mitochondrial membrane protein [8], later studies showed that endogenous REEP1 is localized to the ER [7, 12, 40]. It is not clear whether this discrepancy is due to the differences in antibody specificity or differences in cell types. Recently, one study has proposed that REEP1 contains subdomains for both mitochondrial and ER localization. The N-terminal domain (aas 1–115) of REEP1 has been shown to facilitate ER localization, whereas the middle domain (aas 116–157) promotes mitochondrial localization [28]. Our findings in this study suggested that REEP1 is located in the inner mitochondrial membrane, forms a protein complex with CIV, and stabilizes the CIV subunit NDUFA4. Of note, no changes were found in CV assembly in REEP1-KO cells, although several subunits have been shown to interact with REEP1, indicating multiple roles of REEP1 in OXPHOS complexes. Further studies are needed to explore the functional consequences of the interactions between REEP1 and CV subunits.

Besides its IMM localization, immunofluorescence staining and subcellular fraction results also showed that REEP1 was present in the OMM (Figs. 5A and S5A). Consistent with this, OMM components associated with REEP1 were also identified by mass spectrometry analysis, including VDAC1, VDAC2, and VDAC3 (Table S1). These data imply that REEP1 may be involved in regulating metabolic and energetic flux across the OMM. More interestingly, the re-expression of REEP1 Δ 101–110 entirely rescued perinuclear mitochondrial aggregation in REEP1-KO cells, suggesting that REEP1 regulates mitochondrial distribution through a pathway distinct from IMM REEP1-mediated CIV assembly. In mammalian cells, mitochondrial distribution is dependent on the microtubule cytoskeleton and a previous study has demonstrated that the REEP1 C-terminal cytoplasmic domain is essential for the interaction with microtubules [7, 41]. Since the microtubule-binding motif is intact in REEP1 Δ 101–110 mutation, OMM-localized REEP1 likely controls mitochondrial distribution in a microtubule-dependent manner. It will be intriguing to explore the role of OMM-REEP1 in the regulation of mitochondrial morphology.

In addition to changes in mitochondrial morphology, respiratory chain deficiency has been extensively reported in patients and animal models of ALS and has been implicated to be directly involved in disease pathogenesis. Among

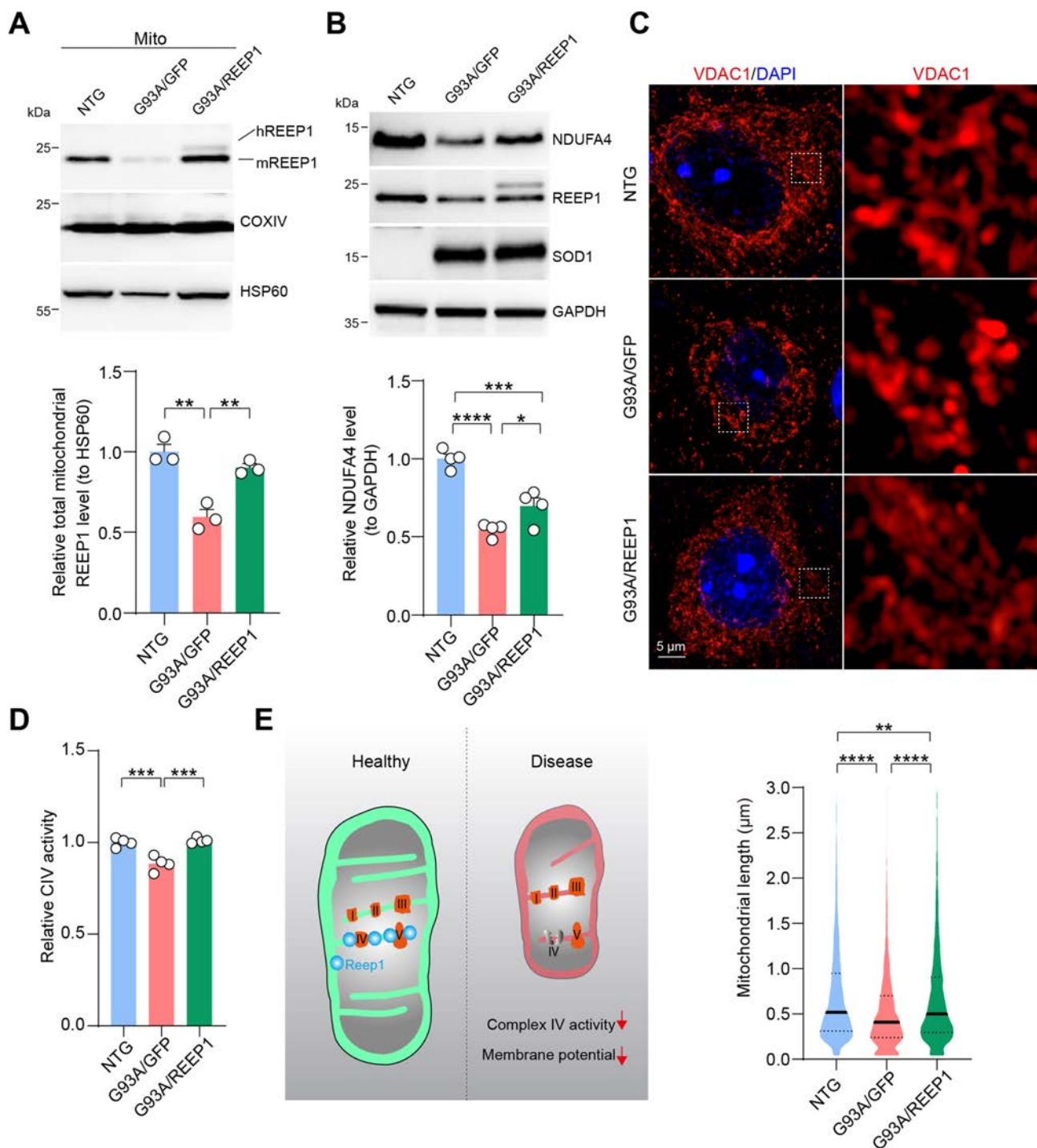


Fig. 7 Impaired mitochondrial function in G93A mice is restored by REEP1 upregulation. **A** Representative immunoblots and quantification of REEP1 levels in mitochondrial fractions from the lumbar spinal cord of NTG, G93A/GFP, and G93A/REEP1 mice ($n = 3$ mice per group). **B** Representative immunoblots and quantification of NDUFA4 levels in the lumbar spinal cord of NTG, G93A/GFP, and G93A/REEP1 mice ($n = 4$ mice per group). **C** Representative images and quantification of the mitochondrial length in motor neurons from NTG, G93A/GFP, and G93A/REEP1 mice ($n = 10$ –15 cells from 3 mice per group). Scale bar, 5 μ m. **D** Quantification of CIV activity of

mitochondria from NTG, G93A/GFP, and G93A/REEP1 mice ($n = 4$ mice per group). **E** Schematic of mitochondrial dysfunction caused by REEP1 deficiency. Under healthy conditions, REEP1 is localized in the outer and inner mitochondrial membranes, where it maintains OXPHOS assembly through interaction with its subunits. In the mitochondria of ALS patients, the reduction of REEP1 expression causes mitochondrial CIV disassembly and membrane potential loss. Data are the mean \pm SEM. * $P < 0.05$, ** $P < 0.01$, *** $P < 0.001$, **** $P < 0.0001$, one-way ANOVA followed by Tukey's multiple comparisons test (**A–D**).

ALS-associated proteins, mutant SOD1 causes not only mitochondrial dynamic changes but also a reduction of OXPHOS assembly and activity [42, 43]. The presence of SOD1G93A in NSC34 cells leads to a significant decrease in the activities of CII and CIV [44]. Consistent with this, in the spinal cord of sporadic ALS cases, CIV activity is markedly reduced [45]. All these data strongly support the idea that CIV deficiency is a distinguishing feature of patients and mouse models of ALS. In this study, we found that overexpression of human REEP1 in G93A mice, which shares 98% similarity with mouse REEP1, improved CIV activity. On the other hand, loss of REEP1 disturbed CIV function, which is essential for cell proliferation in dividing Lenti-X 293T cells. Consistent with this, a reduction of CIV activity was also found in REEP1-KO neurons, suggesting that REEP1 plays a key role in the regulation of CIV function in both dividing and non-dividing cells. Although the loss of REEP1 did not affect neuronal survival under physiological conditions, REEP1-KO neurons demonstrated greatly increased sensitivity to oxidative stress and ER stress. As oxidative stress and mitochondrial dysfunction are detrimental to neuron survival in G93A mice, our data strongly suggest that reduction of REEP1 in the motor neuron may play a central role in motor neuron degeneration in patients and animal models of ALS.

NDUFA4 was first identified as a constituent of NADH dehydrogenase (CI), although later studies revealed that it is a component of CIV and plays a critical role in the assembly and biogenesis of CIV, rather than CI [46, 47]. Our findings revealed that NDUFA4 reduction is a predominant feature of G93A mice. As the mRNA level did not change, the protein level changes of NDUFA4 probably depend on its degradation. The highly heterogeneous lifespans of individual OXPHOS subunits are mainly controlled by the mitochondrial proteolysis system. Mitochondrial proteases facilitate the precise surveillance, removal, and repair of damaged or redundant OXPHOS complexes [48]. The interaction between NDUFA4 and REEP1 might block mitochondrial protease access to the proteolysis sites of NDUFA4. In future studies, the potential proteases for NDUFA4 degradation should be identified, and their role in ALS and other neurodegenerative diseases needs to be explored.

Impaired mitochondrial bioenergetics has been considered to be an important and potential therapeutic target for many neurodegenerative diseases. Many studies have already demonstrated the feasibility of using small molecules to improve mitochondrial OXPHOS activity as a novel approach to prevent neuronal loss and even improve behaviors in experimental models of ALS and Parkinson's disease. For example, one most recent study showed that R13 treatment ameliorates the decline in motor symptoms and associated pathological changes in G93A mice by enhancing the expression level of OXPHOS-related proteins and

accelerating mitochondrial biogenesis [49]. In addition, the small molecule-targeting succinate dehydrogenase subunit B (SDHB) protein of CII blocks dopaminergic neuron death and reverses the behavioral deficits in a rat model of Parkinson's disease [50]. Our data also demonstrated that improvement of mitochondrial CIV assembly and activity greatly alleviated motor neuron death and behavioral deficits in G93A mice. All these studies support the hypothesis that targeting mitochondrial bioenergetics may be a common therapeutic approach to improve mitochondrial and neuronal functions and prevent neurodegeneration.

As discussed above, the REEP1 deficiency described in this study in ALS and ALS mouse models is likely an important mediator of impaired mitochondrial morphology and function in ALS. The REEP1-NDUFA4 axis might be a potential novel therapeutic approach worthy of continued investigation and validation in other experimental models.

Acknowledgements This work was supported by Shandong Key R & D Program Funding (2018GSF118037) and the Shandong Natural Science Foundation (ZR2019JQ24). We thank Translational Medicine Core Facility of Shandong University for consultation and instrument availability that supported this work.

Conflict of interest The authors declare that there are no conflicts of interest.

References

- Hao Z, Wang R, Ren H, Wang G. Role of the *C9ORF72* gene in the pathogenesis of amyotrophic lateral sclerosis and frontotemporal dementia. *Neurosci Bull* 2020, 36: 1057–1070.
- Wiedemann FR, Manfredi G, Mawrin C, Beal MF, Schon EA. Mitochondrial DNA and respiratory chain function in spinal cords of ALS patients. *J Neurochem* 2002, 80: 616–625.
- Borthwick GM, Johnson MA, Ince PG, Shaw PJ, Turnbull DM. Mitochondrial enzyme activity in amyotrophic lateral sclerosis: Implications for the role of mitochondria in neuronal cell death. *Ann Neurol* 1999, 46: 787–790.
- Mattiazzi M, D'Aurelio M, Gajewski CD, Martushova K, Kiaei M, Beal MF. Mutated human SOD1 causes dysfunction of oxidative phosphorylation in mitochondria of transgenic mice. *J Biol Chem* 2002, 277: 29626–29633.
- Saito H, Kubota M, Roberts RW, Chi Q, Matsunami H. RTP family members induce functional expression of mammalian odorant receptors. *Cell* 2004, 119: 679–691.
- Behrens M, Bartelt J, Reichling C, Winnig M, Kuhn C, Meyerhof W. Members of *RTP* and *REEP* gene families influence functional bitter taste receptor expression. *J Biol Chem* 2006, 281: 20650–20659.
- Park SH, Zhu PP, Parker RL, Blackstone C. Hereditary spastic paraplegia proteins REEP1, spastin, and atlastin-1 coordinate microtubule interactions with the tubular ER network. *J Clin Invest* 2010, 120: 1097–1110.
- Züchner S, Wang G, Tran-Viet KN, Nance MA, Gaskell PC, Vance JM, *et al.* Mutations in the novel mitochondrial protein REEP1 cause hereditary spastic paraplegia type 31. *Am J Hum Genet* 2006, 79: 365–369.

9. Beetz C, Schüle R, Deconinck T, Tran-Viet KN, Zhu H, Kremer BPH, *et al.* REEP1 mutation spectrum and genotype/phenotype correlation in hereditary spastic paraplegia type 31. *Brain* 2008, 131: 1078–1086.
10. Goizet C, Depienne C, Benard G, Boukhris A, Mundwiller E, Solé G, *et al.* REEP1 mutations in SPG31: Frequency, mutational spectrum, and potential association with mitochondrial morpho-functional dysfunction. *Hum Mutat* 2011, 32: 1118–1127.
11. Renvoisé B, Malone B, Falgairolle M, Munasinghe J, Stadler J, Sibilla C, *et al.* Reep1 null mice reveal a converging role for hereditary spastic paraplegia proteins in lipid droplet regulation. *Hum Mol Genet* 2016, 25: 5111–5125.
12. Beetz C, Koch N, Khundadze M, Zimmer G, Nietzsche S, Hertel N, *et al.* A spastic paraplegia mouse model reveals REEP1-dependent ER shaping. *J Clin Invest* 2013, 123: 4273–4282.
13. Falk J, Rohde M, Bekhite MM, Neugebauer S, Hemmerich P, Kiehnopf M, *et al.* Functional mutation analysis provides evidence for a role of REEP1 in lipid droplet biology. *Hum Mutat* 2014, 35: 497–504.
14. Klemm RW Jr, Norton JP, Cole RA, Li CS, Park SH, Crane MM, *et al.* A conserved role for atlastin GTPases in regulating lipid droplet size. *Cell Rep* 2013, 3: 1465–1475.
15. Beetz C, Pieber TR, Hertel N, Schabhuhtl M, Fischer C, Trajanoski S, *et al.* Exome sequencing identifies a REEP1 mutation involved in distal hereditary motor neuropathy type V. *Am J Hum Genet* 2012, 91: 139–145.
16. Wang L, Gao J, Liu JY, Siedlak SL, Torres S, Fujioka H, *et al.* Mitofusin 2 regulates axonal transport of calpastatin to prevent neuromuscular synaptic elimination in skeletal muscles. *Cell Metab* 2018, 28: 400–414.e8.
17. Ran FA, Hsu PD, Wright J, Agarwala V, Scott DA, Zhang F. Genome engineering using the CRISPR-Cas9 system. *Nat Protoc* 2013, 8: 2281–2308.
18. Nunomura A, Perry G, Pappolla MA, Wade R, Hirai K, Chiba S, *et al.* RNA oxidation is a prominent feature of vulnerable neurons in Alzheimer's disease. *J Neurosci* 1999, 19: 1959–1964.
19. Kiser JZ, Post M, Wang B, Miyagi M. *Streptomyces erythraeus* trypsin for proteomics applications. *J Proteome Res* 2009, 8: 1810–1817.
20. Dravid A, Raos B, Svirskis D, O'Carroll SJ. Optimised techniques for high-throughput screening of differentiated SH-SY5Y cells and application for neurite outgrowth assays. *Sci Rep* 2021, 11: 23935.
21. Shipley MM, Mangold CA, Szpara ML. Differentiation of the SH-SY5Y human neuroblastoma cell line. *J Vis Exp* 2016: 53193.
22. Fowler PC, Garcia-Pardo ME, Simpson JC, O'Sullivan NC. NeurodegenERation: The central role for ER contacts in neuronal function and axonopathy, lessons from hereditary spastic paraplegias and related diseases. *Front Neurosci* 2019, 13: 1051.
23. D'Erchia AM, Gallo A, Manzari C, Raho S, Horner DS, Chiara M, *et al.* Massive transcriptome sequencing of human spinal cord tissues provides new insights into motor neuron degeneration in ALS. *Sci Rep* 2017, 7: 10046.
24. Vinsant S, Mansfield C, Jimenez-Moreno R, Del Gaizo Moore V, Yoshikawa M, Hampton TG, *et al.* Characterization of early pathogenesis in the SOD1(G93A) mouse model of ALS: Part II, results and discussion. *Brain Behav* 2013, 3: 431–457.
25. Mancuso R, Osta R, Navarro X. Presymptomatic electrophysiological tests predict clinical onset and survival in SOD1(G93A) ALS mice. *Muscle Nerve* 2014, 50: 943–949.
26. Koles K, Budnik V. Wnt signaling in neuromuscular junction development. *Cold Spring Harb Perspect Biol* 2012, 4: a008045.
27. Gurney ME, Pu H, Chiu AY, Dal Canto MC, Polchow CY, Alexander DD, *et al.* Motor neuron degeneration in mice that express a human Cu, Zn superoxide dismutase mutation. *Science* 1994, 264: 1772–1775.
28. Lavie J, Serrat R, Bellance N, Courtand G, Dupuy JW, Tesson C, *et al.* Mitochondrial morphology and cellular distribution are altered in SPG31 patients and are linked to DRP1 hyperphosphorylation. *Hum Mol Genet* 2016, 26: 674–685.
29. Appocher C, Klima R, Feiguin F. Functional screening in *Drosophila* reveals the conserved role of REEP1 in promoting stress resistance and preventing the formation of Tau aggregates. *Hum Mol Genet* 2014, 23: 6762–6772.
30. Wang B, Yu Y, Wei L, Zhang Y. Inhibition of ER stress improves progressive motor deficits in a REEP1-null mouse model of hereditary spastic paraplegia. *Biol Open* 2020, 9: bio054296.
31. Lim Y, Cho IT, Schoel LJ, Cho G, Golden JA. Hereditary spastic paraplegia-linked REEP1 modulates endoplasmic reticulum/mitochondria contacts. *Ann Neurol* 2015, 78: 679–696.
32. Nishitoh H, Kadowaki H, Nagai A, Maruyama T, Yokota T, Fukutomi H, *et al.* ALS-linked mutant SOD1 induces ER stress- and ASK1-dependent motor neuron death by targeting Derlin-1. *Genes Dev* 2008, 22: 1451–1464.
33. An T, Shi P, Duan W, Zhang S, Yuan P, Li Z, *et al.* Oxidative stress and autophagic alteration in brainstem of SOD1-G93A mouse model of ALS. *Mol Neurobiol* 2014, 49: 1435–1448.
34. Lautenschlaeger J, Prell T, Grosskreutz J. Endoplasmic reticulum stress and the ER mitochondria calcium cycle in amyotrophic lateral sclerosis. *Amyotroph Lateral Scler* 2012, 13: 166–177.
35. dal Canto MC, Gurney ME. Neuropathological changes in two lines of mice carrying a transgene for mutant human Cu, Zn SOD, and in mice overexpressing wild type human SOD: A model of familial amyotrophic lateral sclerosis (FALS). *Brain Res* 1995, 676: 25–40.
36. Fujita Y, Okamoto K, Sakurai A, Gonatas NK, Hirano A. Fragmentation of the Golgi apparatus of the anterior horn cells in patients with familial amyotrophic lateral sclerosis with SOD1 mutations and posterior column involvement. *J Neurol Sci* 2000, 174: 137–140.
37. Stieber A, Gonatas JO, Collard J, Meier J, Julien J, Schweitzer P, *et al.* The neuronal Golgi apparatus is fragmented in transgenic mice expressing a mutant human SOD1, but not in mice expressing the human NF-H gene. *J Neurol Sci* 2000, 173: 63–72.
38. Oyanagi K, Yamazaki M, Takahashi H, Watabe K, Wada M, Komori T, *et al.* Spinal anterior horn cells in sporadic amyotrophic lateral sclerosis show ribosomal detachment from, and cisternal distention of the rough endoplasmic reticulum. *Neuropathol Appl Neurobiol* 2008, 34: 650–658.
39. Gao J, Wang L, Liu J, Xie F, Su B, Wang X. Abnormalities of mitochondrial dynamics in neurodegenerative diseases. *Antioxidants (Basel)* 2017, 6: 25.
40. Hurt CM, Bjork S, Ho VK, Gilsbach R, Hein L, Angelotti T. REEP1 and REEP2 proteins are preferentially expressed in neuronal and neuronal-like exocytotic tissues. *Brain Res* 2014, 1545: 12–22.
41. Anesti V, Scorrano L. The relationship between mitochondrial shape and function and the cytoskeleton. *Biochim Biophys Acta BBA Bioenerg* 2006, 1757: 692–699.
42. Magrané J, Hervias I, Henning MS, Damiano M, Kawamata H, Manfredi G. Mutant SOD1 in neuronal mitochondria causes toxicity and mitochondrial dynamics abnormalities. *Hum Mol Genet* 2009, 18: 4552–4564.
43. Tafuri F, Ronchi D, Magri F, Comi GP, Corti S. SOD1 misplacing and mitochondrial dysfunction in amyotrophic lateral sclerosis pathogenesis. *Front Cell Neurosci* 2015, 9: 336.
44. Calabria E, Scambi I, Bonafede R, Schiaffino L, Peroni D, Potrich V, *et al.* ASCs-exosomes recover coupling efficiency and mitochondrial membrane potential in an *in vitro* model of ALS. *Front Neurosci* 2019, 13: 1070.

45. Vielhaber S, Kunz D, Winkler K, Wiedemann FR, Kirches E, Feistner H, *et al.* Mitochondrial DNA abnormalities in skeletal muscle of patients with sporadic amyotrophic lateral sclerosis. *Brain* 2000, 123(Pt 7): 1339–1348.
46. Carroll J, Fearnley IM, Skehel JM, Shannon RJ, Hirst J, Walker JE. Bovine complex I is a complex of 45 different subunits. *J Biol Chem* 2006, 281: 32724–32727.
47. Balsa E, Marco R, Perales-Clemente E, Szklarczyk R, Calvo E, Landázuri MO, *et al.* NDUFA4 is a subunit of complex IV of the mammalian electron transport chain. *Cell Metab* 2012, 16: 378–386.
48. Szczepanowska K, Trifunovic A. Tune instead of destroy: How proteolysis keeps OXPHOS in shape. *Biochim Biophys Acta BBA Bioenerg* 2021, 1862: 148365.
49. Li X, Chen C, Zhan X, Li B, Zhang Z, Li S, *et al.* R13 preserves motor performance in SOD1^{G93A} mice by improving mitochondrial function. *Theranostics* 2021, 11: 7294–7307.
50. Jiang X, Li L, Ying Z, Pan C, Huang S, Li L, *et al.* A small molecule that protects the integrity of the electron transfer chain blocks the mitochondrial apoptotic pathway. *Mol Cell* 2016, 63: 229–239.

Springer Nature or its licensor (e.g. a society or other partner) holds exclusive rights to this article under a publishing agreement with the author(s) or other rightsholder(s); author self-archiving of the accepted manuscript version of this article is solely governed by the terms of such publishing agreement and applicable law.

CircFhit Modulates GABAergic Synaptic Transmission via Regulating the Parental Gene *Fhit* Expression in the Spinal Dorsal Horn in a Rat Model of Neuropathic Pain

Ting Xu^{1,2} · Zhen-Yu Li^{1,2} · Meng Liu³ · Su-Bo Zhang¹ · Huan-Huan Ding⁴ · Jia-Yan Wu^{1,2} · Su-Yan Lin⁵  · Jun Liu⁵ · Jia-You Wei^{1,6} · Xue-Qin Zhang⁷ · Wen-Jun Xin^{1,2,8} 

Received: 26 June 2022 / Accepted: 12 September 2022 / Published online: 13 January 2023

© Center for Excellence in Brain Science and Intelligence Technology, Chinese Academy of Sciences 2023

Abstract Effective treatments for neuropathic pain are lacking due to our limited understanding of the mechanisms. The circRNAs are mainly enriched in the central nervous system. However, their function in various physiological and pathological conditions have yet to be determined. Here, we identified circFhit, an exon-intron circRNA expressed in GABAergic neurons, which reduced the inhibitory synaptic transmission in the spinal dorsal horn to mediate spared nerve injury-induced neuropathic pain. Moreover, we found that circFhit decreased the expression of GAD65 and induced hyperexcitation in NK1R⁺ neurons by promoting the expression of its parental gene *Fhit* in *cis*. Mechanistically,

circFhit was directly bound to the intronic region of *Fhit*, and formed a circFhit/HNRNPK complex to promote Pol II phosphorylation and H2B monoubiquitination by recruiting CDK9 and RNF40 to the *Fhit* intron. In summary, we revealed that the exon-intron circFhit contributes to GABAergic neuron-mediated NK1R⁺ neuronal hyperexcitation and neuropathic pain via regulating *Fhit* in *cis*.

Keywords Chronic pain · Neuropathic pain · CircRNA · Inhibitory transmission · Epigenetic regulation

Introduction

Although many medications such as non-steroidal anti-inflammatory drugs and opioids have been applied to treat neuropathic pain, these drugs are generally ineffective or have severe side effects in patients [1, 2]. Therefore,

Ting Xu, Zhen-Yu Li, and Meng Liu contributed equally to this work.

Supplementary Information The online version contains supplementary material available at <https://doi.org/10.1007/s12264-022-01014-5>.

✉ Su-Yan Lin
linsy33@mail2.sysu.edu.cn

✉ Xue-Qin Zhang
gzzxq2005@126.com

✉ Wen-Jun Xin
xinwj@mail.sysu.edu.cn

¹ Neuroscience Program of Zhongshan School of Medicine and the Fifth Affiliated Hospital, Sun Yat-sen University, Guangzhou 510080, China

² Guangdong Province Key Laboratory of Brain Function and Disease, Sun Yat-sen University, Guangzhou 510120, China

³ Department of Anesthesia and Pain Medicine, Guangzhou First People's Hospital, Guangzhou 510000, China

⁴ Department of Physiology, Xuzhou Medical University, Xuzhou 221004, China

⁵ Department of Neurology, The Second Affiliated Hospital, Guangzhou Medical University, Guangzhou 510000, China

⁶ Guangdong Provincial Engineering Research Center of Molecular Imaging, Guangdong Provincial Key Laboratory of Biomedical Imaging, and Department of Interventional Medicine, The Fifth Affiliated Hospital, Sun Yat-sen University, Zhuhai 519000, China

⁷ The Affiliated Brain Hospital (Guangzhou Huiai Hospital) and School of Health Management, Guangzhou Medical University, Guangzhou 510182, China

⁸ Guangdong-Hong Kong-Macao Greater Bay Area Center for Brain Science and Brain-Inspired Intelligence, Guangzhou 510000, China

seeking new molecular targets and elucidating the mechanism for the treatment of neuropathic pain are urgently needed [3].

Circular RNAs (circRNAs), as new endogenous non-coding RNAs, are widely present in mammals and are highly conserved, stable, and tissue-specific [4, 5]. According to the gene origin, circRNAs are mainly classified into intronic, exonic, and exon-intron circRNAs [6]. Accumulating evidence has shown that exonic circRNAs function as miRNA sponges to suppress the translation of a target gene [7]. By this regulatory method, exonic circRNAs are involved in various nervous system diseases [8, 9]. For example, circRNAs are associated with the development of Parkinson's disease and drug addiction [10, 11]. Recently, our and others' studies have shown that exonic circRNAs such as circAnsk1a regulate the transcription of non-parental target genes *via* changing the activity of transcriptional factors to participate in neuropathic pain [12, 13]. However, whether exon-intron circRNAs participate in neuropathic pain by regulating the transcription of parental genes has not been reported. In normal tissues, *Fhit* (Fragile histidine triad diadenosine triphosphatase) is widely expressed in various epithelial cells and immune cells [14]. Although there is growing evidence that *Fhit* is involved in regulating apoptosis [15], the function of FHIT protein has not been dissected in neurological diseases. In this study, we identified an exon-intron circRNA derived from the *Fhit* gene, circFhit, which is significantly upregulated in the spinal dorsal horn in a neuropathic pain model. Whether and how circFhit regulates the transcription of the *Fhit* gene to contribute to neuropathic pain is largely unclear.

Sensory information is processed by a complex circuit of excitatory and inhibitory interneurons in the spinal dorsal horn. It is transmitted to NK1R (Neurokinin-1 receptor)-positive projection neurons that relay to several brain regions [16]. An essential component of the spinal sensory circuitry is inhibitory interneurons, and loss or reduction of spinal inhibitory interneuron activity is thought to underlie several forms of chronic pain [17, 18]. For example, GABAergic neuronal activity is markedly impaired in the spinal dorsal horn in CCI-model rodents [19]. The impaired GABA synthesis and release enhance the projection neuron excitability to mediate neuropathic pain [20]. Furthermore, our previous data demonstrated that a circRNA directly enhances the excitability of projection neurons in the dorsal horn to contribute to neuropathic pain [13]. Whether circFhit regulates the excitability of GABAergic neurons in the spinal dorsal horn remains unclear in a neuropathic pain model.

In the present study, we first clarified the role of circFhit in SNI-induced neuropathic pain. Further, we explored the mechanism by which circFhit mediates neuropathic pain by regulating its parental gene *Fhit*.

Materials and Methods

Animals

Male Sprague-Dawley rats (180–220 g) were obtained from the Institute of Experimental Animals of Sun Yat-sen University. All the rats were housed individually under controlled conditions, with food and tap water available. All the rats were randomly assigned to different groups. The experimental protocols were approved by the Animal Care and Use Committee of Sun Yat-sen University and were conducted following the National Institutes of Health Guide for the Care and Use of Laboratory Animals. Every effort was made to reduce the number and suffering of animals.

Identification of CircRNA from RNA-seq Analysis

CircRNA-seq was applied following our previous study [13]. The total RNA from spinal dorsal horn tissue was treated with the Epicenter Ribo-Zero rRNA Removal Kit (Illumina) and RNase R (Epicenter) to remove ribosomal RNA and linear RNA. After the preparation of the cDNA library by the NEBNext® Ultra™ RNA Library Prep Kit, the quantity was assessed with Agilent 2200 TapeStation. The sequencing process was carried out on an Illumina HiSeq 3000 instrument. After identifying non-linear fusion junction reads, the sequencing reads were aligned to the rat genome database (Rnor_6.0) by TopHat2. CircRNA expression in different samples was identified with DESeq.

Whole-Genome Expression Analysis from RNA-seq

Total RNA for cDNA libraries was prepared using a cDNA-PCR sequencing kit (SQK-PCS109) according to a protocol provided by Oxford Nanopore Technologies (ONT). The template was reverse-transcribed into full-length cDNA, and defined PCR adapters were added directly to both ends of the cDNA. After cDNA PCR with LongAmp Tag (NEB), PCR products were ligated with T4 DNA ligase (NEB) for ONT adapters. DNA was purified using Agencourt XP beads according to the ONT protocol. The final cDNA library was added to FLO-MIN109 flow cells and ran on the PromethION platform at Biomarker Technologies (Beijing, China).

The raw reads were first filtered, and consensus sequences were mapped to the reference genome using minimap2. The expression level of each group of transcripts was estimated by the number of reads mapped per 10,000 transcripts. Differential expression analysis of the two groups was applied using the edgeR package (3.8.6). The resulting *P* values were adjusted using Benjamini and Hochberg's method to control false discovery rates. Transcripts with *P* values < 0.05 and fold changes ≥ 1.5 found by edgeR were considered differentially expressed.

Quantitative Reverse Transcription PCR (qRT-PCR)

Total RNAs from spinal dorsal horn tissue were extracted with TRIzol (Invitrogen). Norgen's Cytoplasmic and Nuclear RNA Purification Kit (Norgen Biotek) was used to extract nuclear and cytoplasmic RNA. After RNase R treatment and reverse Transcription, SYBR[®] Green Pro Taq HS qPCR was used to quantify the amounts of RNA. The primers used in the study are listed in Table S5.

Spared Nerve Injury (SNI) and Behavioral Tests

The procedure was performed as described [21]. In rats under isoflurane (4%) anesthesia, the tibial and common peroneal branches of the sciatic nerve were ligated and sectioned distal to the ligation, removing 2 mm of the distal nerve stump. In sham-operated rats, the tibial and common peroneal branches of the sciatic nerve were identically exposed without ligation.

To test mechanical allodynia, animals were placed in a plastic box on a metal mesh, and different von Frey filaments were applied alternately to the lateral part of the plantar surface of the hind paw. A nociceptive response was defined as a quick paw withdrawal or paw flinching following von Frey filament application. The 50% paw withdrawal threshold was calculated following a previously validated up-down procedure [22].

Intrathecal Injection of Antisense Oligonucleotides (ASO) or Small Interfering RNA (siRNA)

After rats were anesthetized with isoflurane (4%), polyethylene intrathecal catheters (PE-10, Becton Dickinson) were implanted at the L5 spinal segmental level. The catheter position was confirmed by injection of 2% lidocaine with transient bilateral hind limb paralysis. The cholesterol-conjugated ASO (6 nmol/10 μ L) and siRNA (2 nmol/10 μ L), obtained from RiboBio (specific sequences are listed in Table S6), were intrathecally injected every 3 days after SNI surgery.

Intraspinal Injection of Adeno-Associated Virus (AAV)

To perform intraspinal injection of AAV, the L4–L5 vertebrae were exposed, and the dura was incised to expose the spinal cord. After mounting in a stereotaxic frame, AAV was injected into 4 sites on either side of the spinal dorsal horn (150 nL AAV per site). The micropipette was withdrawn 10 min after the virus injection, and the incision was closed with sutures.

Spinal Cord Slice Preparation

The L4–L6 spinal cord of rats was quickly removed and transferred to an ice-cold sectioning solution bubbled with oxygen (95% O₂ and 5% CO₂) and containing (in mmol/L): 126 NaCl, 3 KCl, 10 D-glucose, 26 NaHCO₃, 1.2 NaH₂PO₄, 0.5 CaCl₂, and 5 MgCl₂. Sections of the L4–L6 spinal cord were cut at 400 μ m on a vibrating microtome (Leica VT-1000 S). The sections were incubated in continuously oxygenated standard artificial cerebrospinal fluid (ACSF) for at least 1 h at 33 °C and then transferred to the recording chamber. Neurons in layers I–II were observed using a 40 \times water-immersion objective on a Nikon microscope (Nikon, Japan).

Whole-Cell Patch Recordings

The recording chamber was continuously filled with pre-warmed 33 °C ACSF at a rate of 2 mL/min. Pipettes (3–6 M Ω , ~2 μ m tip diameter) were drawn on a P-2000G micropipette puller (Sutter Instruments, USA) using borosilicate glass (outer diameter: 1.2 mm, inner diameter: 0.69 mm). An EPC 10 amplifier (HEKA Elektronik, Germany) was used to record data. Patchmaster software (HEKA Elektronik) was used to deliver stimuli and acquire data. Electrophysiological data were processed and analyzed by Clampfit 10.4 (Axon Instruments) and the mini Analysis program (Synaptosoft Corp.).

For spontaneous inhibitory postsynaptic current (sIPSC) recordings, a pipette solution containing (in mmol/L): CsCl 130, NaCl 9, MgCl₂ 1, EGTA 10, and HEPES 10, adjusted to pH 7.3 with CsOH. sIPSCs were recorded at a –70 mV holding potential in a recording buffer containing D-APV (50 μ mol/L) and CNQX (10 μ mol/L). Blue light (473 nm wavelength) was delivered through a 40 \times water-immersion microscope objective (BX51WIF; Olympus) to induce a light-evoked response.

Action potential (AP) recordings were made under current-clamp conditions using a pipette filled with an internal solution containing (in mmol/L): 135 K-gluconate, 0.5 CaCl₂, 2 MgCl₂, 5 EGTA, 5 HEPES, 5 Mg-ATP, and 0.5% Biocytin, pH 7.3). APs were induced by injecting currents every 10 s from –80 to 400 pA in step intervals of 20 pA throughout for 500 ms. Clampfit (Axon Instruments) was used to analyze the relationship between frequency and injected current.

ChIRP (Chromatin Isolation by RNA Purification) for qPCR and Sequencing

ChIRP was applied following our previous study [13]. To capture the complexes containing circFhit and chromatin, we designed probes covering the junction site of circFhit

for use in ChIRP. The rats' L4 and L5 spinal dorsal horn tissues were removed quickly and homogenized into a single-cell suspension in PBS (0.1 mol/L). The suspension was crosslinked with 4% formaldehyde at 25 °C for 30 min, then terminated by adding 1.25 mol/L glycine and incubating for 5 min. After centrifugation, the collected pellet was sonicated, and the DNA was sheared to a length of 100–500 bp. The sonicated samples were centrifuged, and the resulting supernatant was hybridized into probe-bound beads overnight at 37 °C on an end-to-end shaker. Then, the beads were washed five times with 1 mL of pre-warmed wash buffer, each time for 5 min at 37 °C. The beads were retained for qPCR and sequence analysis in the last washing step. The probe sequences are listed in Table S7. The subsequent sequencing was carried out on Illumina NovaSeq 6000. After passing the Solexa Chastity quality filter, the clean reads were aligned to the rat genome using Bowtie software (V2.1.0). Aligned reads were used for peak calling of the ChIRP regions using MACS (V1.4.2). Statistically significant ChIRP-enriched regions (peaks) were identified compared to a Poisson background model, using a *P* value threshold of 10^{-4} . The peaks in samples were annotated by the nearest gene using the UCSC RefSeq database.

RNA-Pulldown and Liquid Chromatography–Tandem Mass Spectrometry (LC–MS/MS)

Rats' L4 and L5 spinal dorsal horn tissues were rapidly removed and homogenized into single-cell suspensions. After cross-linking and centrifugation, the collected pellets were sonicated in an ice water bath. Biotinylated probes with streptavidin beads were mixed with tissue lysate and incubated overnight at 37 °C.

For protein elution, beads were first collected on a magnetic stand. Then the beads were re-suspended in biotin elution buffer and mixed at room temperature for 20 min and 65 °C for 10 min. The supernatants were incubated with 0.1% Sodium deoxycholate (SDC) and 10% trichloroacetic acid (TCA) to precipitate proteins at 4 °C overnight. The next day, proteins were pelleted and then solubilized in 1× Laemmli sample buffer (Invitrogen) and boiled at 95 °C for 30 min with occasional mixing for reverse-crosslinking. After tryptic digestion, the final protein samples were size-separated on bis-tris SDS PAGE gels (Invitrogen) for MS analysis.

RNA-Binding Protein Immunoprecipitation (RIP)

The experiments were performed using the Magna RIP Kit (Millipore). The rats' spinal dorsal horn was collected, homogenized into single-cell suspensions, and lysed. The magnetic beads were incubated at room temperature with antibodies against argonaute (AGO2) (Abcam; ab32381; 5 µg), and heterogeneous nuclear ribonucleoprotein K

(HNRNPK; Proteintech; 11426-1-AP; 5 µg). Tissue lysates were then incubated with bead-antibody complexes at 4 °C overnight. After proteinase K treatment, the immunoprecipitated RNA was extracted and detected by qPCR.

Chromatin Immunoprecipitation (ChIP) Assays

The experiments were performed using the ChIP Kit (CST; 9005). The rats were anesthetized, and the L4–L6 spinal dorsal horn was removed immediately, disaggregated, and fixed. Then, DNA was digested with a micrococcal nuclease. After determining the DNA concentration, 10 µg of digested, cross-linked chromatin was used per immunoprecipitation. The chromatin solution was incubated with antibodies against pSer2-Pol II (Abcam; ab5095; 10 µg), H2Bub1 (CST; 5546; 10 µg), or IgG overnight at 4 °C. The next day, DNA was purified from the immunocomplexes and detected by qPCR.

Co-immunoprecipitation (Co-IP)

The experiments were performed using the Co Immunoprecipitation Kit (Pierce). Dorsal horn tissue was quickly excised and placed in a lysis buffer. After adding Amino Link Plus coupling resin and affinity-purified antibody against HNRNPK (Proteintech; 11426-1-AP; 5 µg), RNF40 (Abcam; ab191309; 5 µg), CDK9 (CST; 2316; 5 µg), or IgG, the complex was incubated on a spinner at room temperature for 90–120 min to ensure immobilization of the antibody. The tissue lysate was added to the appropriate resin column and incubated overnight at 4 °C with gentle shaking. The rotating column was then centrifuged and placed into a new collection tube, the elution buffer was added, and the flow-through liquid was collected by centrifugation. The flow-through immune complexes were analyzed by Western blotting.

Western Blotting

Proteins obtained from spinal dorsal horn tissue were separated by SDS-PAGE and transferred to PVDF membranes. The PVDF membranes were incubated with primary antibodies against HNRNPK (Proteintech; 11426-1-AP; 1:1000), CDK9 (CST; 2316; 1:1000), H2Bub1 (CST; 5546; 1:1000), FHIT (Thermo Fisher; 71–9000; 1:1000), or GAPDH (CST; 2118; 1:1000) overnight at 4 °C. After incubation with secondary antibodies; the immunostained bands were quantified using ImageJ.

Northern Blotting

Digoxin-labeled RNA probes were prepared using the DIG Northern Starter Kit (Roche), and T7 transcription was

performed using the corresponding PCR products as templates. Total RNA was electrophoresed on a 2% agarose gel and transferred to a Hybond-N⁺ membrane (GE Healthcare). After cross-linking with 265-nm UV light, the membranes were pre-hybridized at 62 °C and hybridized to the probe overnight. The membranes were washed twice with 2× SSC and 0.1% SDS at room temperature, and twice more at 62 °C. After washing, the blots were incubated with anti-digoxigenin-AP (Roche) and visualized. The sequences of the probes are listed in Table S7.

Electrophoretic Mobility Shift Assay (EMSA)

The experiment was performed using the Light Shift Chemiluminescent RNA EMSA Kit (Pierce). The biotin-labeled RNA probe was mixed with recombinant HNRNPK protein (Abcam; ab132460; 20 µg) and incubated for 20–30 min at room temperature. Loading buffer was added to the reaction mixture, and samples were loaded onto native acrylamide gels. Electrophoretic separation of RNA-protein complexes was applied at 100 V for 60 min, and images were captured. The sequences of the probes are listed in Table S7.

Fluorescence *In Situ* Hybridization (FISH) and Immunohistochemistry

Rats were anesthetized and cardiac perfusion was performed using 0.9% physiological saline, followed by 4% paraformaldehyde in PBS. Next, L4–L6 spinal cord tissue was removed and post-fixed in the same fixative and then dehydrated with 30% DEPC-sucrose. For RNA-FISH, cryostat sections (25 µm thick) were cut and hybridized at 42 °C overnight with the Digoxin-labeled circFhit probe (1:200, Qiagen). On the next day, after washing with 2× SSC, the sections were incubated at 4 °C overnight with primary antibodies against HNRNPK (Proteintech; 11426-1-AP; 1:1000), NeuN (Millipore; MAB377; 1:200), PAX2 (Invitrogen; 71-6000; 1:500), or Digoxin (Roche; 1:50). After washing three times in 0.01 mol/L PBS, the sections were incubated with Cy3, Alexa 488-conjugated secondary antibody at 37 °C for 60 min. For DNA-FISH, PC-12 cells were incubated with 4% paraformaldehyde at room temperature. After the cells were incubated with proteinase K at 37 °C for 10 min, the mixture of FITC-labeled *Fhit* DNA probe and Digoxin-labeled circ-Fhit probe was added to the PC-12 cells and incubated at 42 °C overnight. The next day, after washing with 2× SSC, the sections were incubated at 4 °C overnight with Digoxin antibodies (Roche; 1:50). For immunohistochemistry, the sections were incubated with primary antibodies against PAX2 (Invitrogen; 71–6000; 1:500), NK1R (Sigma; S8305; 1:1000), and FHIT (Santa Cruz; sc-390481; 1:50) at 4 °C overnight. The next day, the sections were incubated with Cy3, Alexa 488-conjugated secondary antibody

at 37 °C for 60 min. The images of stained sections were captured by a Nikon confocal microscope (C2) equipped with a 40×/NA 0.95 objective lens or by a Nikon Super-Resolution Microscope N-SIM system (3D-SIM, Nikon, Tokyo, Japan) with a 100×/NA 1.49 objective lens. The sequences of the probes are listed in Table S7.

Nuclear Run-On

Nuclear run-on was done as described [23]. Briefly, PC-12 cells were washed three times with cold PBS buffer and lysed in lysis buffer (in mmol/L: 10 NaCl, 3 MgCl₂, 10 Tris-HCl pH 7.4, 0.5% Nonidet P-40). After centrifugation, the pelleted nuclei were washed with 10 mL lysis buffer and re-suspended in 100 µL of freezing buffer (50 mmol/L Tris-HCl pH 8.3, 40% glycerol, 5 mmol/L MgCl₂, and 0.1 mmol/L EDTA). The re-suspended nuclei were mixed with an equal volume of reaction buffer (10 mmol/L Tris-pH 8.0, 5 mmol/L MgCl₂, 1 mmol/L DTT, 300 mmol/L KCl, 20 units of SUPERase-In, 1% Sarkosyl, 500 µmol/L ATP, GTP, and Br-UTP, and 2 µmol/L CTP) and incubated at 30 °C. Next, nuclear RNA was extracted with TRIzol reagent (Invitrogen) and purified through a p-30 RNase-free spin column (BioRad). Following re-suspension with 85 µL of DEPC-water, the RNA was heated in 500 µL binding buffer (0.5× SSPE, 1 mmol/L EDTA, and 0.05% Tween-20) for 1 h at 37 °C. Next, 60 µL of blocked anti-BrdU agarose beads were added to 500 µL of the binding buffer and mixed with heated run-on RNA for 1 h at 4 °C with rotation. After that, the beads were washed once in low salt buffer (0.2× SSPE, 1 mmol/L EDTA, 0.05% Tween-20), twice in high salt buffer (0.5× SSPE, 1 mmol/L EDTA, 0.05% Tween-20, and 150 mmol/L NaCl), and twice in TET buffer (TE pH7.4 and 0.05% Tween-20). BrU-incorporated RNA was eluted with 4× 125 µL elution buffer (20 mmol/L DTT, 300 mmol/L NaCl, 5 mmol/L Tris-HCl pH7.5, 1 mmol/L EDTA, and 0.1% SDS). RNA was then extracted with acidic phenol/chloroform once, and chloroform, and precipitated with ethanol overnight. Real-time quantitative PCR was performed on the sample.

Statistical Analyses

Data were analyzed using SPSS 25.0, and the results are expressed as the mean ± SEM. Normally distributed data were analyzed using a *t* test for two independent samples or one-way ANOVA followed by Dunnett's T3 or Tukey's *post hoc* test. A nonparametric test was used instead when the normality test was not satisfied. The data on pain behavior were analyzed using two-way repeated-measures ANOVA. Correlations were measured by Pearson correlation analysis. The criterion of statistical significance was 0.05.

Results

CircFhit Contributes to Neuropathic Pain Following SNI

Among 603 high-abundance circRNAs obtained by circRNA-sequencing (Table S1), we found that 24 were significantly dysregulated in the spinal dorsal horn on days 7 and 14 following SNI (Fig. 1A). CircFhit (chr15:16547297-16550375), a 289-nt circRNA originating from a part of intron 2 and all of the exons 3 and 4 of the *Fhit* gene (Fig. S1A, B), exhibited the most marked increase following SNI (Table S2, Fig. 1B). The results of northern blotting and qPCR with oligo (dT)₁₈ indicated the circular characteristics of circFhit (Fig. S1C, D). Double staining showed that circFhit was located in the dorsal horn neurons (Fig. 1C) and 82.89% of the circFhit immunosignal was localized in PAX2 (Paired box gene 2, a GABAergic neuronal marker)-positive neurons (Fig. 1D). Structured Illumination Microscopy (SIM) and subcellular fractionation assays demonstrated that circFhit was exclusively expressed in the nuclei of neurons (Figs. 1E and S1E). Next, we found that the knockdown of circFhit in the spinal dorsal horn by intrathecal ASO

injection remarkably ameliorated the mechanical allodynia in SNI rats (Figs. S1F and 1F). Moreover, specific knockdown of circFhit in GABAergic interneurons by intraspinal injection of AAV-mDlx-shRNA(circFhit)-nEF1 α -EGFP had the same effect (Figs. S1G, H and 1G), and overexpression of circFhit in GABAergic neurons by intraspinal injection of AAV-mDlx-circFhit-nEF1 α -EGFP induced marked mechanical allodynia in naïve rats (Figs. S1I and 1H). These results suggested that the upregulated circFhit in the inhibitory interneurons of the spinal dorsal horn contributes to neuropathic pain following SNI.

CircFhit Enhances the Activity of NK1R⁺ Neurons by Reducing GABAergic Synaptic Transmission

To explore whether GABAergic neurons expressing circFhit contributed to SNI-induced neuropathic pain *via* changing inhibitory synaptic transmission, we first characterized the functional connections of the GABAergic neurons to the NK1R⁺ neurons in the spinal dorsal horn. Virus tracing and fluorescence staining showed that the fiber terminals from the GABAergic neurons were located close to NK1R⁺ neurons (Fig. 2A). Brief light stimulation of Chr2-containing

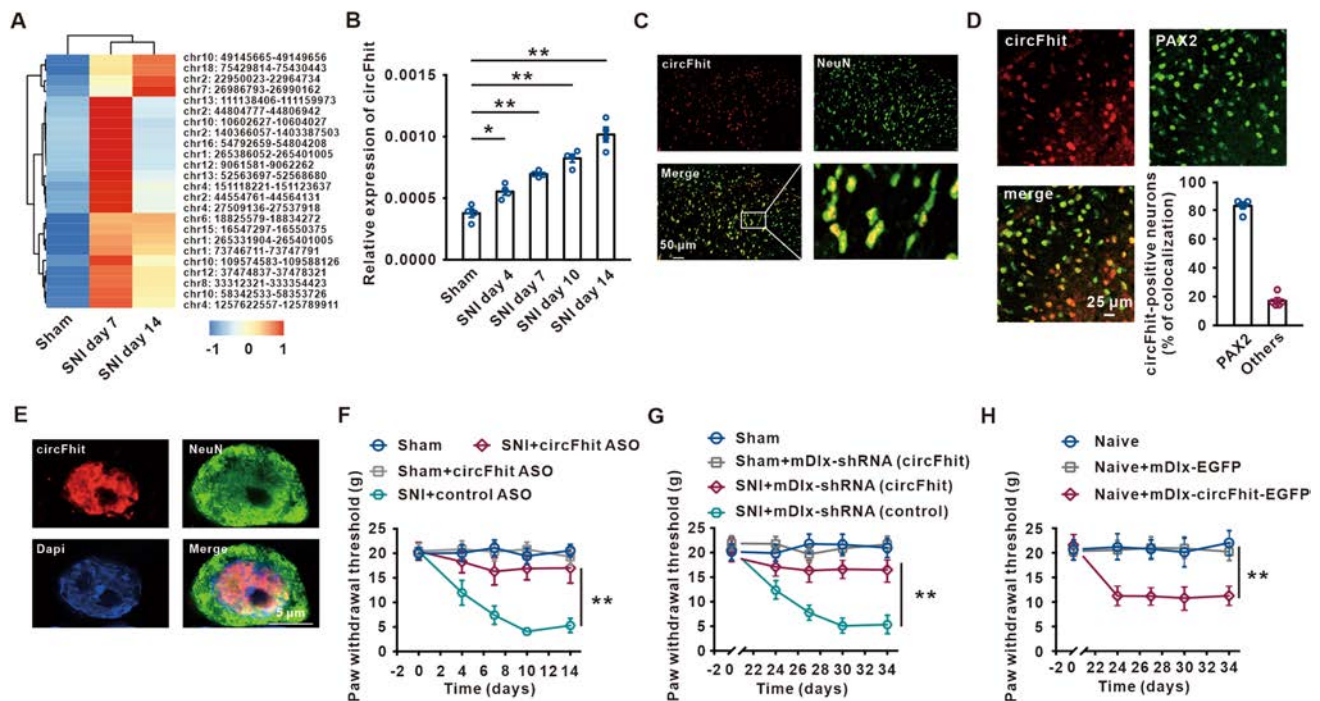


Fig. 1 Identified circFhit contributes to neuropathic pain following SNI. **A** Heat map of the top 24 highly abundant circRNAs on days 7 and 14 following SNI. **B** Relative expression levels of circFhit at different time points after SNI ($n=4$; one-way ANOVA). **C** FISH assay showing that circFhit is expressed in spinal dorsal horn neurons. Scale bar, 50 μ m. **D** Immunohistochemical studies showing the proportion of circFhit expression in spinal PAX2 neurons ($n=5$). Scale bar, 25 μ m. **E** High-resolution images obtained by SIM show

that circFhit is expressed in neuronal nuclei in the spinal dorsal horn (scale bar, 5 μ m). **F** Intrathecal injection of circFhit ASO attenuates the mechanical allodynia induced by SNI ($n=12$; two-way repeated measures). **G** Intraspinal injection of AAV-mDlx-shRNA(circFhit) attenuates the mechanical allodynia induced by SNI ($n=10$; two-way repeated measures). **H** The effect of AAV-mDlx-circFhit-EGFP on withdrawal threshold at 21 days after injection ($n=10$; two-way repeated measures). $**P<0.01$. Data are plotted as the mean \pm SEM.

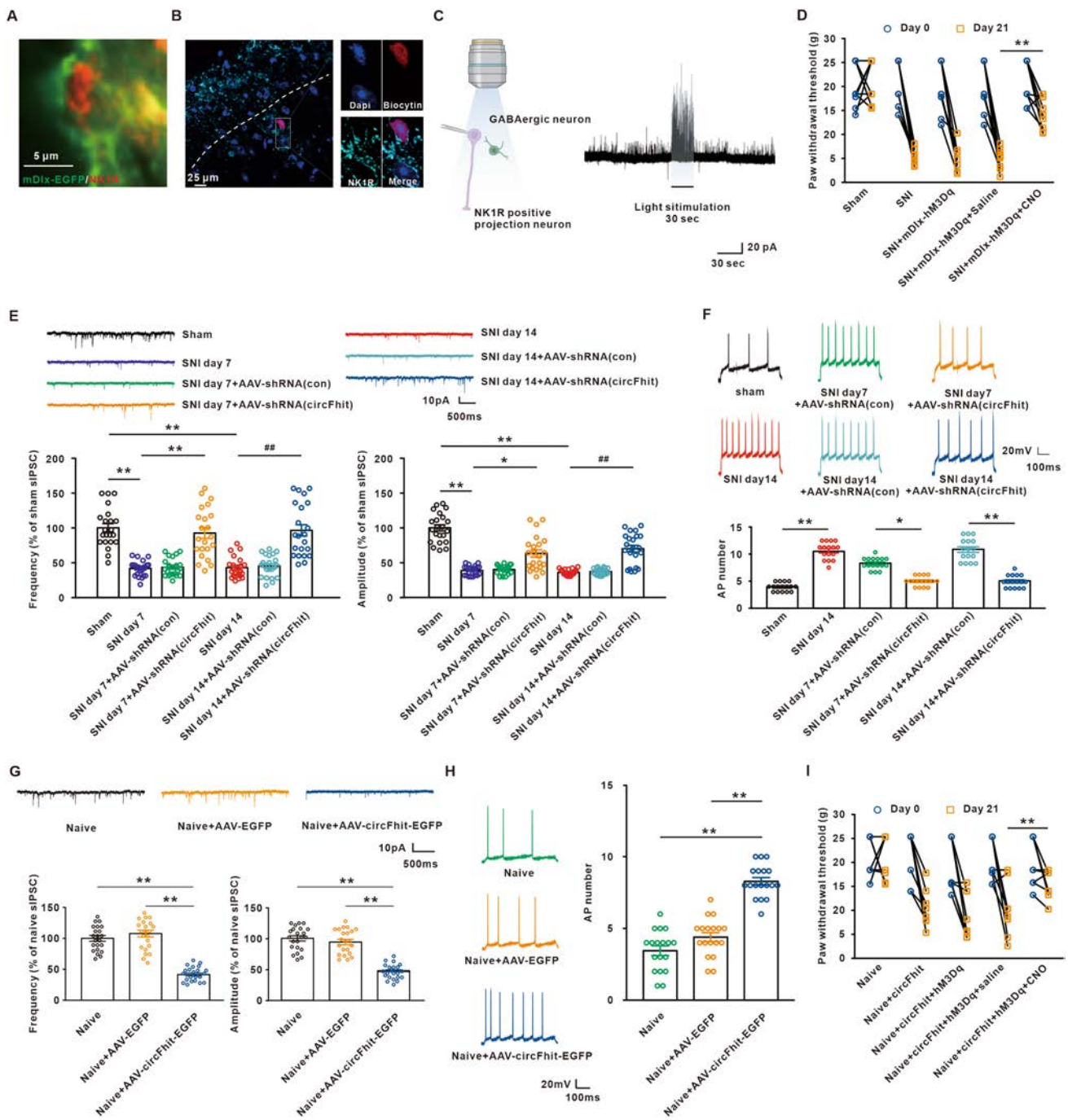


Fig. 2 CircFhit enhances the activity of NK1R⁺ neurons by reducing the excitability of GABAergic neurons. **A** The fibers from the GABAergic neurons (green) are located close to the NK1R⁺ neurons (red; scale bar, 5 μ m). **B** The co-localization of biocytin and NK1R when electrophysiological studies are performed on NK1R⁺ neurons in spinal cord slices (scale bar, 25 μ m). **C** Schematic of the recording configuration in spinal cord slices (left). Representative traces showing IPSCs in NK1R⁺ neurons evoked by light stimulation of GABAergic terminals in the spinal dorsal horn (right). **D** Intraspinal injection of AAV-mDLx-hM3Dq-EGFP and application of CNO attenuate the mechanical allodynia induced by SNI ($n=10$; two-tailed two-sample t -test). **E** Frequency and amplitude of sIPSCs in NK1R⁺ neurons on days 7 and 14 after SNI with or without the injection of AAV-mDLx-shRNA(circFhit) ($n=22$; Kruskal–Wallis nonparametric test). **F** The

number of depolarizing current injection-induced action potentials is increased in dorsal horn neurons following SNI, and this is alleviated by intraspinal injection of AAV-mDLx-shRNA(circFhit) ($n=16$; Kruskal–Wallis nonparametric test). **G** Intraspinal injection of AAV-mDLx-circFhit decreases the frequency and amplitude of sIPSCs ($n=22$; Kruskal–Wallis nonparametric test or one-way ANOVA). **H** The number of depolarizing current injection-induced action potentials is increased in dorsal horn neurons after intraspinal injection of AAV-mDLx-circFhit ($n=18$; Kruskal–Wallis nonparametric test). **I** Intraspinal injection of AAV-mDLx-hM3Dq and application of CNO attenuates the mechanical allodynia induced by overexpression of circFhit ($n=8$; two-tailed two-sample t -test). * $P<0.05$, ** $P<0.01$, ### $P<0.01$. Data are plotted as the mean \pm SEM.

GABAergic neuron terminals in the dorsal horn reliably elicited IPSCs in NK1R⁺ neurons (Fig. 2B, C). Importantly, the activation of GABAergic neurons by using the chemogenetic excitability of hM3Dq and intraperitoneal injection of the clozapine N-oxide (CNO; 2.5 mg/kg) significantly attenuated the mechanical allodynia induced by SNI (Fig. 2D). Next, we explored whether the circFhit in GABAergic neurons modified the excitability of NK1R⁺ projection neurons in SNI. The results showed that intraspinal injection of AAV-mDlx-shRNA(circFhit)-nEF1 α -EGFP prevented the decreased frequency and amplitude of sIPSCs and the increase of action potential number (Fig. 2E, F) following SNI. Overexpression of circFhit significantly reduced the frequency and amplitude of sIPSCs (Fig. 2G) in naïve rats, while the number of action potentials in NK1R⁺ neurons was increased in naïve rats (Fig. 2H). The behavioral test revealed that the activation of GABAergic neurons using the chemogenetic paradigm rescued the circFhit overexpression-induced mechanical allodynia (Fig. 2I). These results suggested that circFhit regulates the microcircuit loop from GABAergic neurons to NK1R⁺ neurons and contributes to neuropathic pain.

After SNI, circFhit Decreases the Expression of GAD65 via Regulating the Parental Gene *Fhit*

Studies have shown that GAD65 and GAD67 are key rate-limiting enzymes mediating GABA synthesis. Western blots showed that the level of GAD65, but not GAD67, was significantly decreased on day 14 following SNI (Fig. 3A), and knockdown of circFhit prevented the SNI-induced downregulation of GAD65 (Fig. 3A). Besides, overexpression of circFhit led to a decrease of GAD65 (Fig. 3B). To investigate the molecular mechanism underlying the regulation of GAD65 expression by circFhit, we applied ChIRP-seq (Fig. S2A). The result that circFhit did not enrich the *Gad65* gene suggested that circFhit regulates GAD65 expression by another mechanism. Next, we integrated the results of ChIRP-seq and mRNA-seq (Fig. S2B) and obtained 66 genes (Fig. 3C, Table S3) that may be directly regulated by circFhit in the setting of neuropathic pain. Of these genes, *Fhit*, the parental gene of circFhit, strongly attracted our interest (Table S3). Following SNI treatment, linear *Fhit* mRNA and protein expression were significantly increased. The time course of mRNA upregulation was consistent and positively correlated with that of circFhit (Figs. 3D, E and S2C). Inhibition of circFhit expression by using AAV-mDlx-shRNA(circFhit) led to a decrease in the upregulated mRNA and protein levels of *Fhit* in SNI rats (Fig. 3F, G). Moreover, overexpression of circFhit increased the *Fhit* mRNA and protein level in naïve rats (Fig. 3H, I).

Next, we explored the relationship between FHIT protein and GAD65 in the development of neuropathic pain.

Double immunofluorescence showed the localization of FHIT in PAX2⁺ inhibitory interneurons (Fig. S2D). Intraspinal injection of AAV-mDlx-shRNA(*Fhit*)-EGFP prevented the decrease of GAD65 expression (Figs. S2E, F and 3J) and frequency/amplitude of sIPSCs in NK1R⁺ neurons (Fig. S2G), and attenuated the withdrawal threshold in SNI rats (Fig. 3K). Overexpression of FHIT in GABAergic neurons significantly reduced the expression of GAD65 (Figs. S2H, I and 3L) and the frequency/amplitude of sIPSCs (Fig. S2J) in NK1R⁺ neurons and induced mechanical allodynia in naïve rats (Fig. 3M). Importantly, the knockdown of FHIT prevented the AAV-mDlx-circFhit-induced GAD65 reduction and the mechanical allodynia in the naïve group (Fig. 3N, O). Taking all the above results together, the upregulated circFhit decreased the GAD65 expression *via* promoting *Fhit* transcription to mediate the neuropathic pain following SNI in rats.

CircFhit Increases Phosphorylated Pol II and Monoubiquitylated H2B on the CircFhit-Binding Region of the *Fhit* Gene Following SNI

To elucidate the mechanism by which *Fhit* transcription is regulated by circFhit, we first performed nuclear run-on experiments in PC-12 cells. The results showed that the overexpression of circFhit by transfected LV-circFhit-EGFP increased the *Fhit* transcription level in the nuclear extract (Fig. 4A). RNA-DNA double FISH further revealed that circFhit was co-localized with the genomic loci of its corresponding parental gene *Fhit* in PC-12 cells (Fig. 4B). By *in silico* analysis and ChIRP-PCR, we found the site of chr15:16333797–16333866 in the *Fhit* gene had the most significant circFhit enrichment following SNI treatment (Fig. S3 and Table S4). The results indicated that circFhit binds to the *Fhit* gene and promotes transcription. Since the Pol II phosphorylation and H2B monoubiquitylation (H2Bub1) play an essential role in the process of gene transcription [24, 25], we examined the enrichment of pSer2-Pol II and H2Bub1 on the circFhit binding site in *Fhit* gene. The ChIP results showed that the pSer2-Pol II enrichment was significantly increased on day 14 following SNI. The application of AAV-mDlx-shRNA(circFhit) significantly decreased the increased enrichment of pSer2-Pol II in SNI-treated rats (Fig. 4C). Overexpression of circFhit increased the enrichment of pSer2-Pol II in the circFhit-binding region in naïve rats (Fig. 4D). In addition, SNI also increased the level of H2Bub1 in the circFhit-binding region, and intraspinal injection of AAV-mDlx-shRNA(circFhit) markedly inhibited the increased enrichment (Fig. 4E). Overexpression of circFhit remarkably increased the monoubiquitylated H2B enrichment in naïve rats (Fig. 4F). These results suggested that circFhit enhances the level of Pol II phosphorylation and

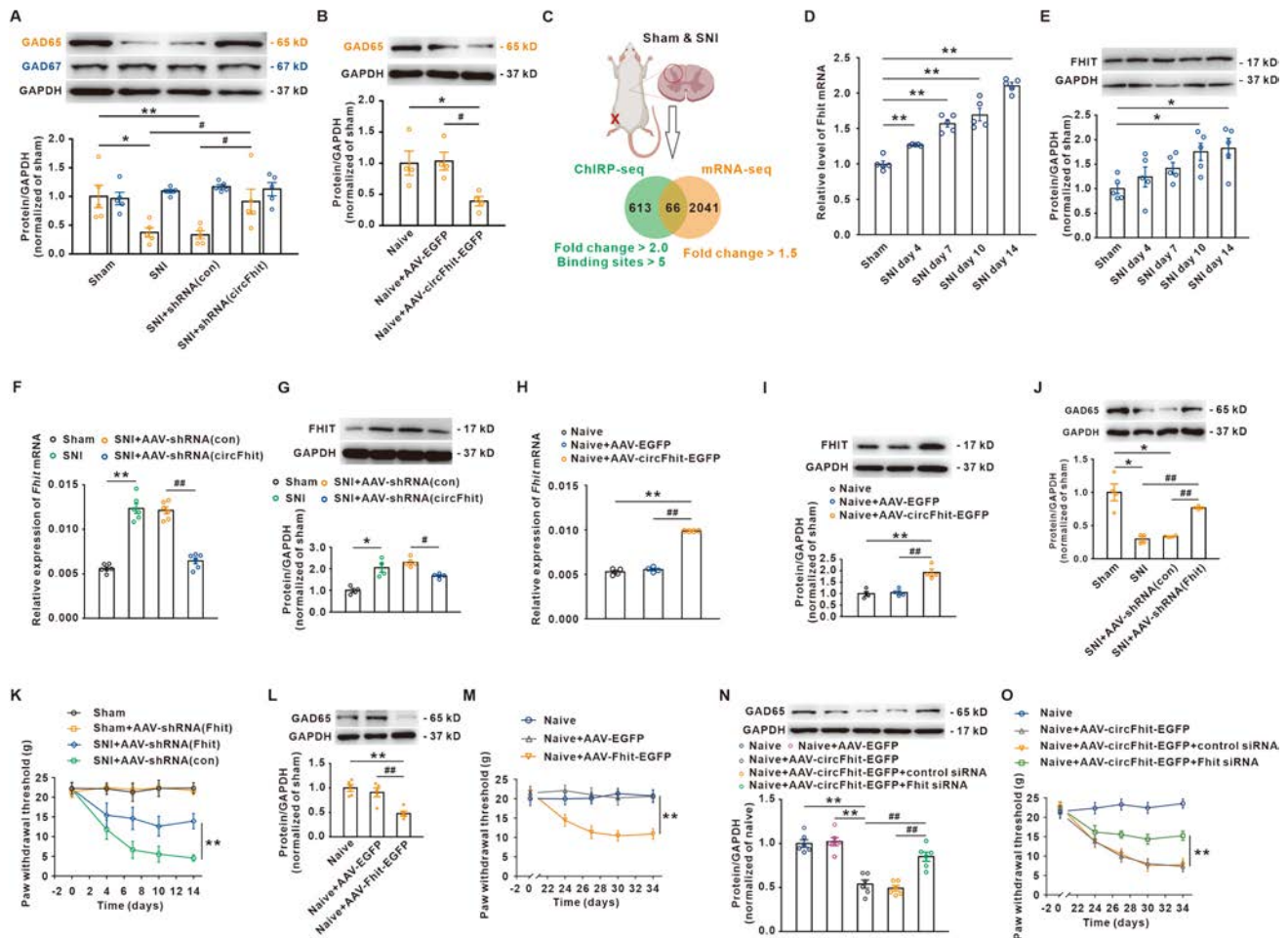


Fig. 3 The circFhit/*Fhit* pathway regulates the expression of GAD65 following SNI. **A** The level of GAD65, but not GAD67, is significantly downregulated in the spinal dorsal horn of SNI-treated rats, and this is reversed by knocking down of circFhit ($n=5$; two-tailed one-way ANOVA). **B** Overexpression of circFhit significantly downregulates the expression of GAD65 ($n=4$; two-tailed one-way ANOVA). **C** Simulated diagram showed the results of ChIRP-seq and mRNA-seq. The Venn diagram shows the overlapping genes between ChIRP-seq and mRNA-seq (green circle, upregulated circFhit-enriched genes in SNI-treated rats; yellow circle, upregulated genes in mRNA-seq after SNI). **D** Relative level of *Fhit* mRNA at different time points after SNI ($n=5$; one-way ANOVA). **E** Relative levels of FHIT protein at different time points after SNI ($n=5$; one-way ANOVA). **F** and **G** Application of AAV-mDlx-shRNA(circFhit) significantly decreases the expression of *Fhit* mRNA ($n=6$; one-way ANOVA) and protein ($n=4$; one-way ANOVA) in SNI-treated rats.

H, I Overexpression of circFhit significantly increases the expression of *Fhit* mRNA ($n=6$; one-way ANOVA) and protein ($n=4$; one-way ANOVA) in naïve rats. **J** Compared with the SNI group, the application of *Fhit* shRNA significantly increases the expression of GAD65 ($n=4$; one-way ANOVA). **K** Application of *Fhit* shRNA significantly increases the withdrawal threshold in SNI-treated rats ($n=12$; two-way repeated measures). **L** Overexpression of FHIT by injection of AAV-Fhit-EGFP decreases the expression of GAD65 ($n=5$; one-way ANOVA). **M** Overexpression of FHIT decreases the withdrawal threshold in naïve rats ($n=10$; two-way repeated measures). **N** Knockdown of FHIT prevents the circFhit-induced GAD65 downregulation in naïve rats ($n=6$; one-way ANOVA). **O** Knockdown of FHIT significantly increases the downregulated mechanical withdrawal threshold induced by overexpression of circFhit ($n=8$; two-way repeated measures). * $P < 0.05$, ** $P < 0.01$, # $P < 0.05$, ### $P < 0.01$. Data are plotted as the mean \pm SEM.

H2B monoubiquitylation in the circFhit-binding region of the *Fhit* gene following SNI.

The CircFhit/HNRNPK Complex Enhances the Enrichment of p-Pol II and H2Bub1 on the *Fhit* Intron Following SNI

To clarify the mechanism underlying circFhit enhancement of p-Pol II and H2Bub1 on the *Fhit* gene, we experimented

with LC-MS/MS and RIP. The results showed that the binding of circFhit and HNRNPK was significantly increased following SNI (Figs. S4A and 5A). High-resolution images obtained by SIM further confirmed that circFhit is bound to HNRNPK in the nucleus (Fig. 5B). Bioinformatics analysis (RBPmap) (Fig. S4B) and EMSA (Fig. S4C) revealed an HNRNPK motif for the binding of circFhit. Moreover, intrathecal injection of HNRNPK siRNA significantly decreased the enrichment of pSer2-Pol II and H2Bub1 in

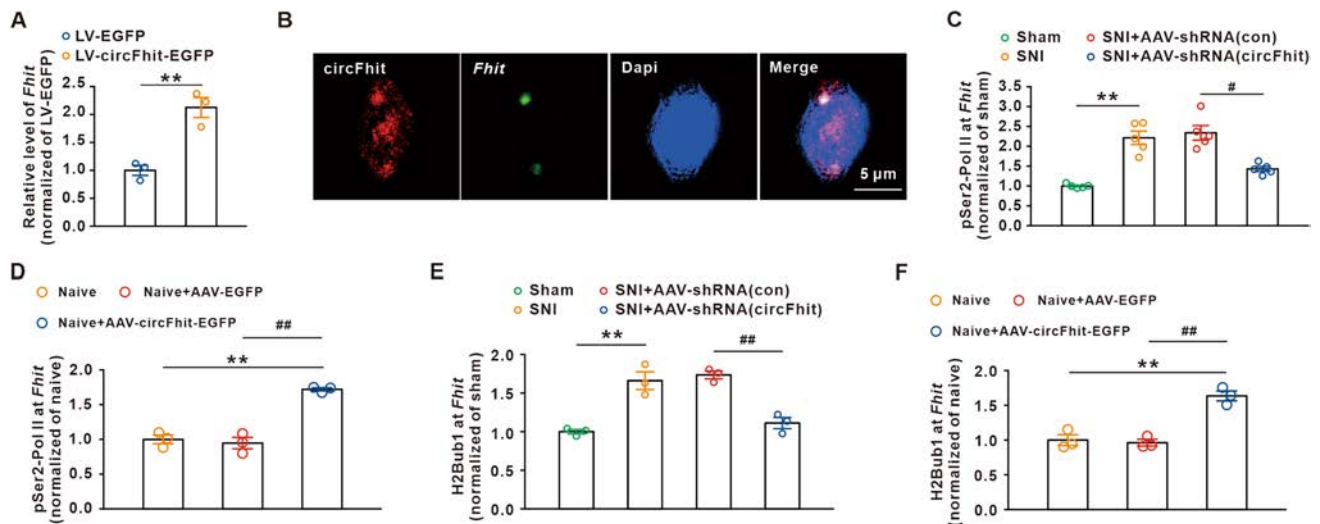


Fig. 4 CircFhit increases the level of phosphorylated-Pol II and monoubiquitylated-H2B on the circFhit-binding region of the *Fhit* gene following SNI. **A** Nuclear run-on experiments showing a specific change in transcription of *Fhit* after circFhit overexpression ($n=3$; two-sample *t*-test). **B** FISH images showing the co-localization of circFhit and the corresponding parental gene locus ($n=3$). Scale bar, 5 μm . **C** ChIP assays reveal that the increased binding of pSer2-Pol II to the *Fhit* gene is significantly decreased after intraspinal injection

of AAV-shRNA(circFhit) following SNI ($n=5$; one-way ANOVA). **D** pSer2-Pol II markedly binds to the *Fhit* gene after overexpression of circFhit ($n=3$; one-way ANOVA). **E** The enrichment of H2Bub1 on the *Fhit* gene is significantly decreased after intraspinal injection of AAV-shRNA(circFhit) in SNI-treated rats ($n=3$; one-way ANOVA). **F** Overexpression of circFhit markedly increases the recruitment of H2Bub1 to the *Fhit* gene ($n=3$; one-way ANOVA). ** $P < 0.01$, # $P < 0.05$, ## $P < 0.01$. Data are plotted as the mean \pm SEM.

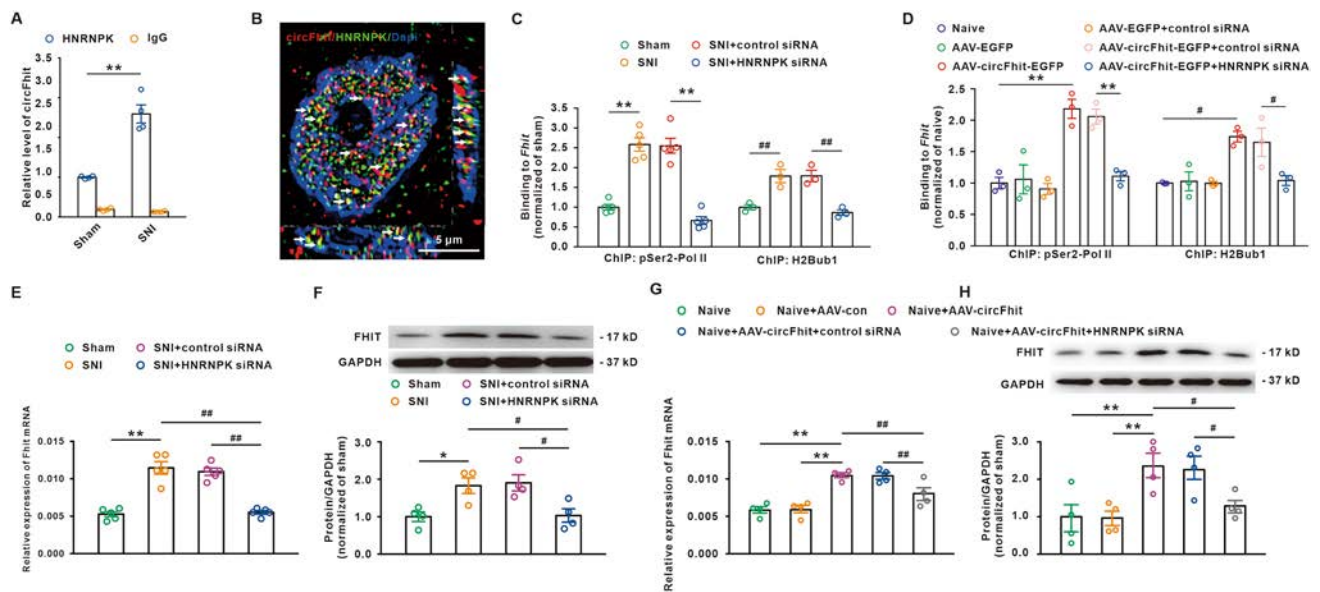


Fig. 5 The circFhit/HNRNPK complex enhances the enrichment of p-Pol II and H2Bub1 on the *Fhit* intron following SNI. **A** The amount of circFhit precipitated by the HNRNPK antibody is increased following SNI ($n=4$; two-sample *t*-test). **B** High-resolution image showing the binding of circFhit and HNRNPK in the nucleus ($n=3$; scale bar, 5 μm ; arrows, co-localization of circFhit and HNRNPK). **C** and **D** HNRNPK siRNA attenuates the increase of pSer2-Pol II and H2Bub1 enrichment on the *Fhit* gene induced by SNI or AAV-circF-

hit-EGFP ($n=5$ or 3; one-way ANOVA). **E** and **F** Intrathecal administration of HNRNPK siRNA ameliorates the upregulation of *Fhit* mRNA and protein induced by SNI ($n=5$ or 4; one-way ANOVA). **G** and **H** Intrathecal administration of HNRNPK siRNA ameliorates the upregulation of *Fhit* mRNA and protein induced by overexpression of circFhit ($n=4$; one-way ANOVA). * $P < 0.05$, ** $P < 0.01$, # $P < 0.05$, ## $P < 0.01$. Data are plotted as the mean \pm SEM.

the *Fhit* intron induced by SNI (Figs. S4D, E and 5C) or the injection of AAV-circFhit-EGFP into naïve rats (Fig. 5D). Importantly, HNRNPK siRNA also reduced the expression of *Fhit* mRNA and protein in SNI rats (Fig. 5E, F), or circFhit-overexpressing rats (Fig. 5G, H).

CircFhit/HNRNPK Recruits CDK9 and RNF40 to Increase p-Pol II and H2Bub1 on the *Fhit* Intron

Evidence has shown that HNRNPK, as an essential RNA-binding protein, regulates gene expression by affecting the functions of other proteins [26], CDK9 (cyclin-dependent kinase 9) plays a vital role in regulating the phosphorylation of pSer2-Pol II in mammalian cell lines [27], and RNF40 (RING finger protein 40), as an essential ubiquitin ligase E3, is critically involved in H2B monoubiquitylation [28]. In the present study, we found a significantly increased amount of CDK9 in the immunocomplex precipitated by the HNRNPK antibody (Fig. 6A) and increased HNRNPK content in the immunocomplex precipitated by the CDK9 antibody (Fig. S5A). Moreover, the interaction between HNRNPK and RNF40 was significantly increased in SNI rats (Figs. 6B and S5B). Intrathecal injection of CDK9 siRNA or RNF40 siRNA significantly downregulated the pSer2-Pol II or H2Bub1, respectively, on the *Fhit* gene in SNI-treated rats (Figs. S5C–F and 6C, D). Moreover, intrathecal injection of CDK9 siRNA or RNF40 siRNA also reduced the expression of *Fhit* mRNA and protein in SNI rats (Fig. S5G–J). Importantly, the knockdown of CDK9 blocked the increases of pSer2-Pol II on the *Fhit* gene and the upregulation of *Fhit* mRNA and protein induced by overexpression of circFhit (Fig. 6E–G). Likewise, the increased H2Bub1 on the *Fhit* gene and *Fhit* mRNA and protein were prevented using RNF40 siRNA following overexpression of circFhit (Fig. 6H–J). Collectively, these results suggested that HNRNPK, as a hub for recruiting CDK9 and RNF40, promotes circFhit-mediated *Fhit* transcription.

Discussion

The exon-intron circRNAs were discovered over a decade ago. However, their function in various physiological and pathological conditions has yet to be determined. In the present study, we, for the first time, elucidated the role of an exon-intron circRNA, circFhit, as well as the novel molecular mechanism involved, to serve as a critical regulator in the pathogenesis of neuropathic pain induced by peripheral nerve injury. The loss and gain of circFhit function demonstrated that the circFhit modulation of FHIT expression contributed to the reduction of GABAergic inhibitory neurotransmitter synthesis and the dorsal horn NK1R⁺ neuronal hyperexcitation and neuropathic pain following SNI.

Mechanistically, we have discovered the direct interaction of exon-intron circFhit and the *Fhit* locus, and the increased binding between circFhit and the intron region of *Fhit* promotes the formation of the circFhit/HNRNPK complex and enhances the CDK9-mediated phosphorylation of Pol II at Ser2 and the RNF40-regulated H2B monoubiquitylation on the circFhit-binding site of the *Fhit* intron, which then facilitates the transcription of the parental *Fhit* gene. Taken together, these findings suggest that the exon-intron circFhit in GABAergic inhibitory neurons regulates the expression of the parental *Fhit* gene in *cis* and subsequently contributes to NK1R⁺ neuronal hyperexcitation and neuropathic pain induced by nerve injury.

Given the low abundance of most circRNAs in mammalian tissues, doubts have been raised regarding any potential biological function for the low abundance circRNAs [29]. In addition, the role of exon-intron circRNAs, as important circRNAs, has not been reported in a pathophysiological setting. In the present study, we screened one highly abundant circFhit, which was upregulated in the nucleus of inhibitory GABAergic neurons in the spinal dorsal horn following SNI. Silencing endogenous circFhit with shRNA significantly increased the frequency of sIPSCs in NK1R⁺ neurons, and reduced the number of action potentials and mechanical allodynia in rats following SNI. Overexpression of circFhit by intraspinal injection of AAV-circFhit-EGFP decreased the frequency of sIPSCs and promoted the projection neurons' excitability and mechanical allodynia. These results indicated that circFhit enhances the NK1R⁺ neurons' excitability by reducing the release of inhibitory GABAergic transmitters, resulting in neuropathic pain. The current data support the hypothesis that circFhit expression is negatively correlated with the expression of GAD65, the rate-limiting enzyme of the GABA neurotransmitter. As projection neurons, the spinal dorsal NK1R⁺ neurons receive information from inhibitory interneurons and excitatory interneurons [30]. The release of the inhibitory GABA neurotransmitter usually causes inhibition of action potentials by hyperpolarizing postsynaptic neurons, including projection neurons, to attenuate mechanical allodynia [31, 32]. Interestingly, the present ChIRP-PCR results showed that circFhit did not directly bind to the *GAD2* gene, but directly interacted with the *Fhit* gene. Furthermore, the expression of circFhit was positively correlated with the level of linear *Fhit* mRNA or protein in the rats with SNI, and FHIT expression regulated NK1R⁺ neuronal excitability in the dorsal horn and pain behavior *via* changing the GAD65 level. *Fhit*, a classical oncogene, has been shown to be an important genome "caretaker" for maintaining DNA stability. Moreover, the expression level of FHIT in neural tissue is altered in various neurological disorders such as depression and autism. Still, no studies have yet explored the specific function of FHIT in neurological disorders. While previous evidence

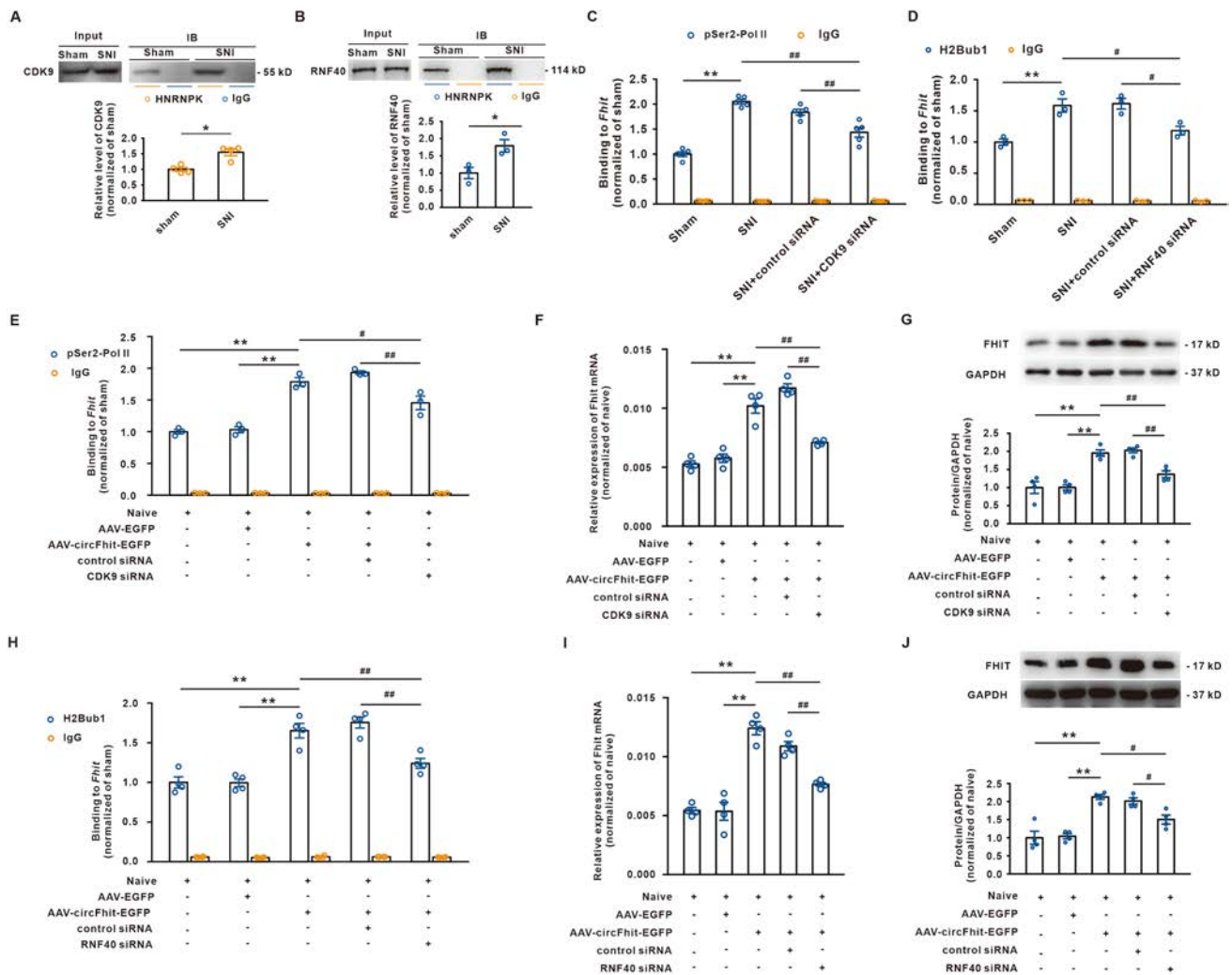


Fig. 6 CircFhit/HNRNPk increases pSer2-Pol II and H2Bub1 on the *Fhit* intron by recruiting CDK9 and RNF40. **A** The interaction between HNRNPk and CDK9 is significantly increased following SNI ($n=4$; two-sample *t*-test). **B** The interaction between HNRNPk and RNF40 is significantly increased following SNI ($n=3$; two-sample *t*-test). **C** Intrathecal administration of CDK9 siRNA decreases the pSer2-Pol II on the *Fhit* gene in the SNI group ($n=5$; one-way ANOVA). **D** Intrathecal administration of RNF40 siRNA decreases the H2Bub1 on the *Fhit* gene in the SNI group ($n=3$; one-way ANOVA). **E** Knockdown of CDK9 decreases the upregulation of

pSer2-Pol II on the *Fhit* gene induced by overexpression of circFhit ($n=3$; one-way ANOVA). **F** and **G** Knockdown of CDK9 decreases the upregulation of *Fhit* mRNA and protein induced by overexpression of circFhit ($n=4$; one-way ANOVA). **H** Knockdown of RNF40 decreases the upregulation of H2Bub1 on the *Fhit* gene induced by overexpression of circFhit ($n=4$; one-way ANOVA). **I** and **J** Knockdown of RNF40 decreases the upregulation of *Fhit* mRNA and protein induced by overexpression of circFhit ($n=4$; one-way ANOVA). * $P < 0.05$, ** $P < 0.01$, # $P < 0.05$, ### $P < 0.01$. Data are plotted as the mean \pm SEM.

has shown the robust expression of FHIT protein in neurons [33], the present study, for the first time, dissected the function of FHIT to regulate the neuronal excitability in the dorsal horn and behavioral hypersensitivity in the setting of neuropathic pain. FHIT regulates the permeability of ion channels, including intra-mitochondrial Ca^{2+} channels [34]. In addition, the study also showed that transfection of *Fhit* increases the susceptibility to TNF- α and IFN in mammalian cell lines [35]. Evidence has shown that increased inflammatory cytokines such as TNF- α and IFN negatively regulate GAD65 expression. So, we speculate that the change of Ca^{2+}

or cytokines may involve GAD65 expression to contribute to the pathogenesis of neuropathic pain.

While previous studies established that gene transcription is fundamentally regulated by long non-coding RNA in mammalian cells [36, 37], the present study provided evidence that the exon-intron circFhit was co-localized with the *Fhit* gene locus, and overexpression of circFhit increased the *Fhit* transcription in the cell nuclei, suggesting that exon-intron circFhit is involved in the transcription of the parental gene in dorsal horn neurons in rodents with nerve injury. However, how circFhit modulates transcription

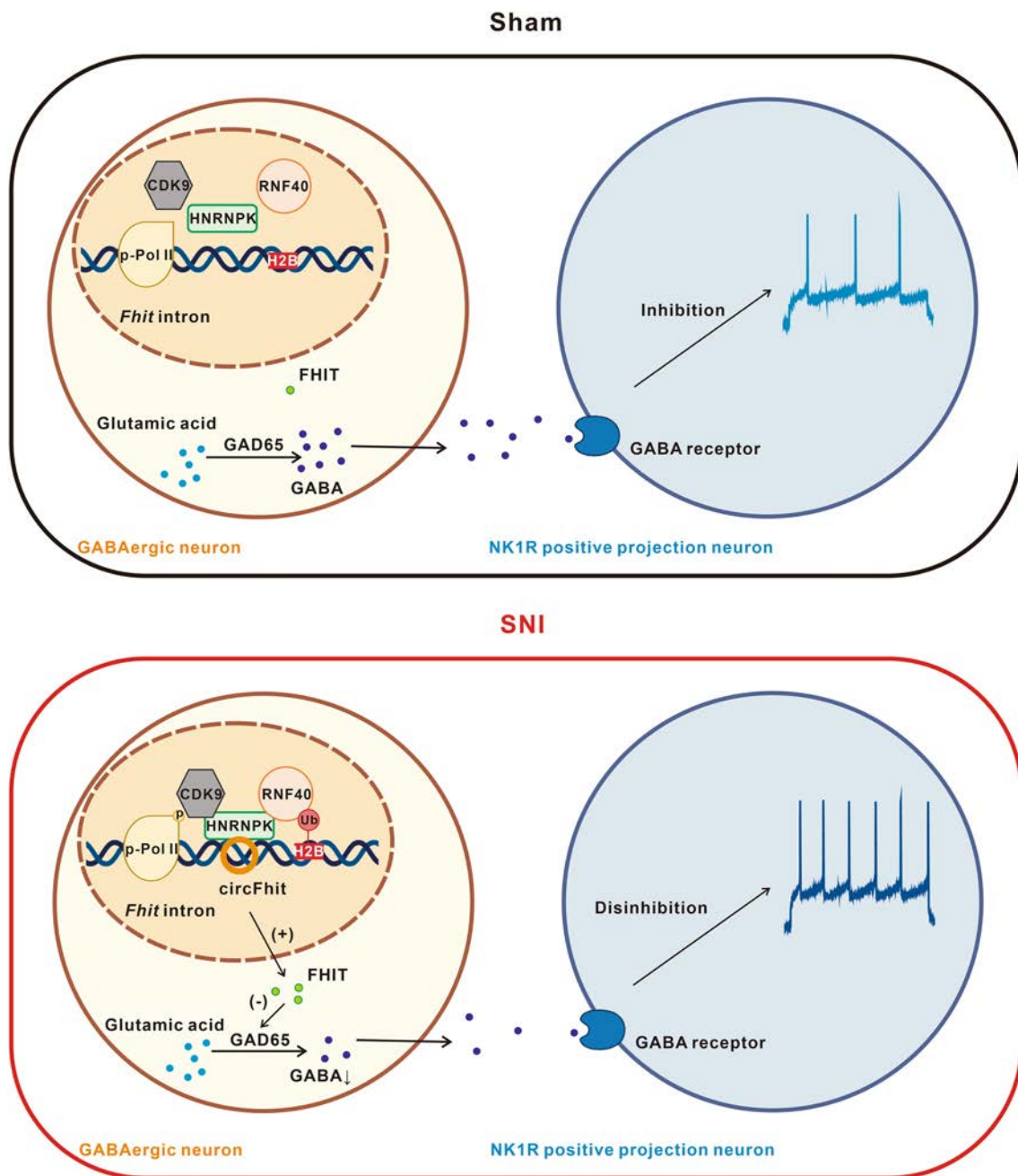


Fig. 7 Summary graph for the hypothesis: the exon-intron circFhit contributes to GABAergic neuron-mediated NK1R⁺ neuronal hyperexcitation and neuropathic pain *via* regulating *Fhit* in *cis*.

of the parental gene *Fhit* is unclear. It is well documented that phosphorylation of pol II plays a critical role in gene transcription [38], and H2B monoubiquitylation regulates gene activation or repression [39]. Our results showed that the increased interaction of circFhit and HNRNPK recruited CDK9/RNF40, which subsequently promoted the phosphorylation of Pol II at Ser2 and the H2B monoubiquitylation on the circFhit-binding site of the *Fhit* intron. These

modifications of transcriptional machinery consequently facilitated the expression of *Fhit* in dorsal horn neurons.

In conclusion, inhibitory GABAergic neurons express exon-intron circFhit *via* recruiting HNRNPK to enhance CDK9/RNF40-mediated transcription of the parental *Fhit* gene, decreases inhibitory synaptic transmission, subsequently enhances the excitability of NK1R⁺ neurons in the dorsal horn, and contributes to the development of mechanical allodynia induced by SNI (Fig. 7).

Acknowledgements This work was supported by the National Natural Science Foundation of China (319700936, 81801103, 81901127, and 82101307), the Science and Technology Program of Guangdong (2018B030334001), the Natural Science Foundation of Guangdong (2019A1515010871, 2019A1515010645, and 2022A1515010414), the Guangzhou Science and Technology Plan Project (201803010006), the Natural Science Foundation of Jiangsu (BK20210904), and the Fundamental Research Funds for the Central Universities (19yky44). We thank Prof. Zhi-Cheng Dong for helping with the experiment on nuclear run-ons.

Conflict of interest The authors declare that there are no conflict of interest.

References

- Hong JT, Kim JH, Kim KS, Lee CS, Shin HC, Kim WK. Pharmacological target therapy of neuropathic pain and patient-reported outcomes in patients with chronic low back pain in Korea: Results from the NLBP Outcomes Research. *Medicine* 2018, 97: e11919.
- Binder A, Baron R. The pharmacological therapy of chronic neuropathic pain. *Dtsch Arztebl Int* 2016, 113: 616–625.
- Ren WJ, Ulrich H, Semyanov A, Illes P, Tang Y. TASK-3: New target for pain-relief. *Neurosci Bull* 2020, 36: 951–954.
- Szabo L, Salzman J. Detecting circular RNAs: Bioinformatic and experimental challenges. *Nat Rev Genet* 2016, 17: 679–692.
- Jia RR, Xiao MS, Li ZG, Shan G, Huang C. Defining an evolutionarily conserved role of GW182 in circular RNA degradation. *Cell Discov* 2019, 5: 45.
- Jeck WR, Sharpless NE. Detecting and characterizing circular RNAs. *Nat Biotechnol* 2014, 32: 453–461.
- Zheng QP, Bao CY, Guo WJ, Li SY, Chen J, Chen B, *et al.* Circular RNA profiling reveals an abundant circHIPK₃ that regulates cell growth by sponging multiple miRNAs. *Nat Commun* 2016, 7: 11215.
- Ebbesen KK, Hansen TB, Kjems J. Insights into circular RNA biology. *RNA Biol* 2017, 14: 1035–1045.
- Ma Y, Liu YX, Jiang ZS. CircRNAs: A new perspective of biomarkers in the nervous system. *Biomed Pharmacother* 2020, 128: 110251.
- Pitcher MH, von Korff M, Bushnell MC, Porter L. Prevalence and profile of high-impact chronic pain in the United States. *J Pain* 2019, 20: 146–160.
- Akhter R. Circular RNA and Alzheimer's disease. *Adv Exp Med Biol* 2018, 1087: 239–243.
- Zheng YL, Guo JB, Song G, Yang Z, Su X, Chen PJ, *et al.* The role of circular RNAs in neuropathic pain. *Neurosci Biobehav Rev* 2022, 132: 968–975.
- Zhang SB, Lin SY, Liu M, Liu CC, Ding HH, Sun Y, *et al.* CircAnks1a in the spinal cord regulates hypersensitivity in a rodent model of neuropathic pain. *Nat Commun* 2019, 10: 4119.
- Kujan O, Abuderman A, Al-Shawaf AZ. Immunohistochemical characterization of FHIT expression in normal human tissues. *Interv Med Appl Sci* 2016, 8: 7–13.
- Trapasso F, Pichiorri F, Gaspari M, Palumbo T, Aqeilan RI, Gaudio E, *et al.* Fhit interaction with ferredoxin reductase triggers generation of reactive oxygen species and apoptosis of cancer cells. *J Biol Chem* 2017, 292: 14279.
- Todd AJ. Neuronal circuitry for pain processing in the dorsal horn. *Nat Rev Neurosci* 2010, 11: 823–836.
- Duan B, Cheng LZ, Ma QF. Spinal circuits transmitting mechanical pain and itch. *Neurosci Bull* 2018, 34: 186–193.
- Peirs C, Seal RP. Neural circuits for pain: Recent advances and current views. *Science* 2016, 354: 578–584.
- Leitner J, Westerholz S, Heinke B, Forsthuber L, Wunderbaldinger G, Jäger T, *et al.* Impaired excitatory drive to spinal GABAergic neurons of neuropathic mice. *PLoS One* 2013, 8: e73370.
- Li CJ, Lei YY, Tian Y, Xu SQ, Shen XF, Wu HB, *et al.* The etiological contribution of GABAergic plasticity to the pathogenesis of neuropathic pain. *Mol Pain* 2019, 15: 1744806919847366.
- Decosterd I, Woolf CJ. Spared nerve injury: An animal model of persistent peripheral neuropathic pain. *Pain* 2000, 87: 149–158.
- Chaplan SR, Bach FW, Pogrel JW, Chung JM, Yaksh TL. Quantitative assessment of tactile allodynia in the rat paw. *J Neurosci Methods* 1994, 53: 55–63.
- Ingolia NT, Ghaemmaghami S, Newman JRS, Weissman JS. Genome-wide analysis *in vivo* of translation with nucleotide resolution using ribosome profiling. *Science* 2009, 324: 218–223.
- Koga M, Hayashi M, Kaida D. Splicing inhibition decreases phosphorylation level of Ser2 in Pol II CTD. *Nucleic Acids Res* 2015, 43: 8258–8267.
- Sansó M, Parua PK, Pinto D, Svensson JP, Pagé V, Bitton DA, *et al.* Cdk9 and H2Bub1 signal to Clr6-Cti/Rpd3S to suppress aberrant antisense transcription. *Nucleic Acids Res* 2020, 48: 7154–7168.
- Xu YJ, Wu W, Han Q, Wang YL, Li CC, Zhang PP, *et al.* New insights into the interplay between non-coding RNAs and RNA-binding protein HnRNPK in regulating cellular functions. *Cells* 2019, 8: 62.
- Cheng JX, Chen L, Li Y, Cloe A, Yue M, Wei JB, *et al.* RNA cytosine methylation and methyltransferases mediate chromatin organization and 5-azacytidine response and resistance in leukaemia. *Nat Commun* 2018, 9: 1163.
- Xie WH, Nagarajan S, Baumgart SJ, Kosinsky RL, Najafova Z, Kari V, *et al.* *RNF40* regulates gene expression in an epigenetic context-dependent manner. *Genome Biol* 2017, 18: 32.
- Lee JT. Epigenetic regulation by long noncoding RNAs. *Science* 2012, 338: 1435–1439.
- Ramírez-Jarquín UN, Tapia R. Excitatory and inhibitory neuronal circuits in the spinal cord and their role in the control of motor neuron function and degeneration. *ACS Chem Neurosci* 2018, 9: 211–216.
- Ramírez-Jarquín UN, Lazo-Gómez R, Tovar-Y-Romo LB, Tapia R. Spinal inhibitory circuits and their role in motor neuron degeneration. *Neuropharmacology* 2014, 82: 101–107.
- Baba H, Ji RR, Kohno T, Moore KA, Ataka T, Wakai A, *et al.* Removal of GABAergic inhibition facilitates polysynaptic A fiber-mediated excitatory transmission to the superficial spinal dorsal horn. *Mol Cell Neurosci* 2003, 24: 818–830.
- Zhao P, Hou N, Lu Y. Fhit protein is preferentially expressed in the nucleus of monocyte-derived cells and its possible biological significance. *Histol Histopathol* 2006, 21: 915–923.
- Rimessi A, Marchi S, Fotino C, Romagnoli A, Huebner K, Croce CM, *et al.* Intramitochondrial calcium regulation by the *FHIT* gene product sensitizes to apoptosis. *Proc Natl Acad Sci U S A* 2009, 106: 12753–12758.
- Pulido M, Chamorro V, Romero I, Algarra I, S-Montalvo A, Collado A, *et al.* Restoration of MHC-I on tumor cells by fhit transfection promotes immune rejection and acts as an individualized immunotherapeutic vaccine. *Cancers* 2020, 12: 1563.
- Goodrich JA, Kugel JF. Non-coding-RNA regulators of RNA polymerase II transcription. *Nat Rev Mol Cell Biol* 2006, 7: 612–616.
- Geisler S, Collier J. RNA in unexpected places: Long non-coding RNA functions in diverse cellular contexts. *Nat Rev Mol Cell Biol* 2013, 14: 699–712.

38. Jonkers I, Lis JT. Getting up to speed with transcription elongation by RNA polymerase II. *Nat Rev Mol Cell Biol* 2015, 16: 167–177.
39. Jung I, Kim SK, Kim M, Han YM, Kim YS, Kim D, *et al.* H2B monoubiquitylation is a 5'-enriched active transcription mark and correlates with exon-intron structure in human cells. *Genome Res* 2012, 22: 1026–1035.

Springer Nature or its licensor (e.g. a society or other partner) holds exclusive rights to this article under a publishing agreement with the author(s) or other rightsholder(s); author self-archiving of the accepted manuscript version of this article is solely governed by the terms of such publishing agreement and applicable law.

Corticostriatal Neurons in the Anterior Auditory Field Regulate Frequency Discrimination Behavior

Zhao-Qun Wang¹ · Hui-Zhong Wen¹ · Tian-Tian Luo¹ · Peng-Hui Chen¹ · Yan-Dong Zhao¹ · Guang-Yan Wu² · Ying Xiong¹

Received: 20 June 2022 / Accepted: 24 September 2022 / Published online: 11 January 2023

© Center for Excellence in Brain Science and Intelligence Technology, Chinese Academy of Sciences 2023

Abstract The anterior auditory field (AAF) is a core region of the auditory cortex and plays a vital role in discrimination tasks. However, the role of the AAF cortico-striatal neurons in frequency discrimination remains unclear. Here, we used c-Fos staining, fiber photometry recording, and pharmacogenetic manipulation to investigate the function of the AAF cortico-striatal neurons in a frequency discrimination task. c-Fos staining and fiber photometry recording revealed that the activity of AAF pyramidal neurons was significantly elevated during the frequency discrimination task. Pharmacogenetic inhibition of AAF pyramidal neurons significantly impaired frequency discrimination. In addition, histological results revealed that AAF pyramidal neurons send strong projections to the striatum. Moreover, pharmacogenetic suppression of the striatal projections from pyramidal neurons in the AAF significantly disrupted the frequency discrimination. Collectively, our findings show that AAF pyramidal neurons, particularly the AAF–striatum projections, play a crucial role in frequency discrimination behavior.

Keywords Anterior auditory field · Cortico-striatal neuron · Frequency discrimination · AAF–striatum projection

Introduction

The anterior auditory field (AAF) and primary auditory cortex (A1) are the major cortical fields in the rodent auditory system [1–4]. Extensive studies have been conducted on the cortical topology, plasticity, cellular response properties, and functional role of A1 [1–5]. Optogenetic manipulations of A1 activity modulate frequency discrimination performance requiring temporal integration [6, 7]. However, little is known about the role of the AAF in auditory information processing, especially in discriminative behavior.

Recently, we found that the AAF plays a key role in the categorization of sound frequency in rats [8]. The results of behavioral experiments also suggested that injecting the γ -aminobutyric acid (GABA) receptor agonist muscimol into the AAF disrupts the frequency discrimination of rats. Moreover, pharmacological inhibition of the AAF activity significantly affects the acquisition of auditory fear behavior [8]. Lomber *et al.* found that inhibition of the bilateral AAF impairs auditory temporal discrimination, whereas inhibition of the posterior auditory cortex area affects the recognition of the sound source's location [9]. These results suggest that the AAF plays an important role in frequency discrimination.

Previous studies on the AAF mainly focused on its projection relationships within the auditory system. The AAF and A1 receive large inputs from different thalamic divisions. For example, the AAF mainly receives projections from the posterior thalamus complex, while A1 mainly receives projections from the ventral medial geniculate body [1, 10]. In

Zhao-Qun Wang and Hui-Zhong Wen contributed equally to this work.

✉ Guang-Yan Wu
wgy009@163.com

✉ Ying Xiong
xiongying2001@163.com

¹ Department of Neurobiology, Chongqing Key Laboratory of Neurobiology, Army Medical University, Chongqing 400038, China

² Experimental Center of Basic Medicine, Army Medical University, Chongqing 400038, China

addition, anatomical and physiological studies have demonstrated that the auditory cortex sends excitatory glutamate projections to the striatum [11], which is involved in the regulation of reward, emotion, motivation, and other higher cognitive functions [12–14]. Thus, the different inputs and projections between AAF and A1 suggest that AAF neurons differ from A1 neurons in physiological properties. Importantly, Song *et al.* also found that there is a strong projection from the AAF to the striatum [13, 15]. Although corticostriatal neurons in A1 are involved in modulating frequency discrimination [16, 17], whether AAF pyramidal neurons and the AAF–striatum pathway are involved in auditory-related discrimination behaviors is unknown.

Thus, in the present study, we used c-Fos staining, fiber photometry recording, and pharmacogenetic manipulation to investigate the function of AAF corticostriatal neurons in a sound discrimination task.

Materials and Methods

Animals

Adult C57BL/6J mice (male, 6–8 weeks, 25–28 g) were provided by the Laboratory Animal Center at the Army Medical University. All experimental procedures were performed in accordance with institutional animal welfare guidelines and were approved by the Army Military Medical University Animal Care and Use Committee. Animals were maintained on a 12-h light/dark cycle with free access to food and water. All efforts were made to minimize animal suffering.

Auditory Frequency Discrimination Behavior

A SuperFcs system (XinRuan, Shanghai, China) was used to generate sound and electricity. Freezing was assessed when no movement (besides respiratory movements) lasted for 0.5 s or more, and the total freezing time during a sound presentation was assessed based on the SuperFcs system.

Training

Mice were placed in a training chamber (28.5 cm × 32 cm × 52.5 cm) and allowed to explore for 100 s for habituation (Fig. 1A, B). After the 100 s baseline period, mice were exposed to 5 pairings composed of a 20-s pure tone (75 dB) and a 2-s footshock (0.6 mA). The tone and the footshock ended at the same time. The tone that was associated with the footshock was the conditioned stimulus (CS). The footshock was the unconditioned stimulus (UCS). The inter-trial interval was 60 ± 20 s at random. Mice were trained to remember one of the two different sound frequencies (a

2- or 12-kHz pure tone) alone. After five trials, animals were transported to their home cage using a transfer cage.

Behavior Test

During paired training, mice were taught to associate a sound with a footshock (Fig. 1C). On the third day, a different cage was used to transfer the testing animals to the testing chamber, which now had a different size (25 cm × 25 cm × 40 cm). To eliminate the effect of sound order on the test results, we established two different testing patterns: 12 kHz or 2 kHz were first used to test the freezing level, then the other frequency was subsequently used to test the mice's freezing level. The mice were allowed to explore the testing chamber for 100 s (baseline), after which the pure tone cue (CS⁺, 75 dB), the same as that used in the training session, was delivered continuously for 100 s. After 30 min, a 100-s pure tone (75 dB) that was not the conditioned stimulus (CS⁻) was delivered in a different, custom-made chamber (30 cm × 20 cm × 40 cm). The other testing pattern used the opposite sound order. Moreover, filter paper or crushed corncob was placed in the bottom of the two testing chambers to increase contextual diversity.

Freezing time was measured when a lack of movement (except respiratory movements) lasted for 0.5 s or more based on detections by the SuperFcs system. The percentage of freezing time was calculated as the ratio between the total freezing time during the sound presentation and the duration of the entire sound presentation. The percentage was assessed based on the behavior of each animal, and the total percentage of freezing time was compared between groups.

Virus and CTB488 Injection

Mice were anesthetized with isoflurane (1%–1.5% isoflurane/oxygen,) and fixed in a stereotaxic apparatus (RWD Life Science, Shenzhen, China) as described previously [11–13]. The viruses or cholera toxin subunit B488 (CTB488, C34775, Invitrogen, Carlsbad, USA) was injected using glass micropipettes (tip diameter, 10–20 μm) at a specific speed (15 nL/min) and volume, controlled by a nanoliter injector (Nanoject III, Drummond Scientific, USA). The micropipette tip was left in place for an additional 5 min after injection, then slowly withdrawn.

To facilitate fiber photometry recording of AAF excitatory neuronal activity during auditory frequency discrimination behavior, mice were microinjected with 50 nL of rAAV2/9-*CaMKIIα-GCaMP6s* [titer: 5.90×10^{12} genome copies (GC)/mL] or rAAV2/9-*CaMKIIα-EGFP* (titer: 4.05×10^{12} GC/mL; Fig. 3B) into the right AAF.

For pharmacogenetic inhibition of AAF pyramidal neuronal activity during auditory frequency discrimination behavior, mice were microinjected with either 50 nL of

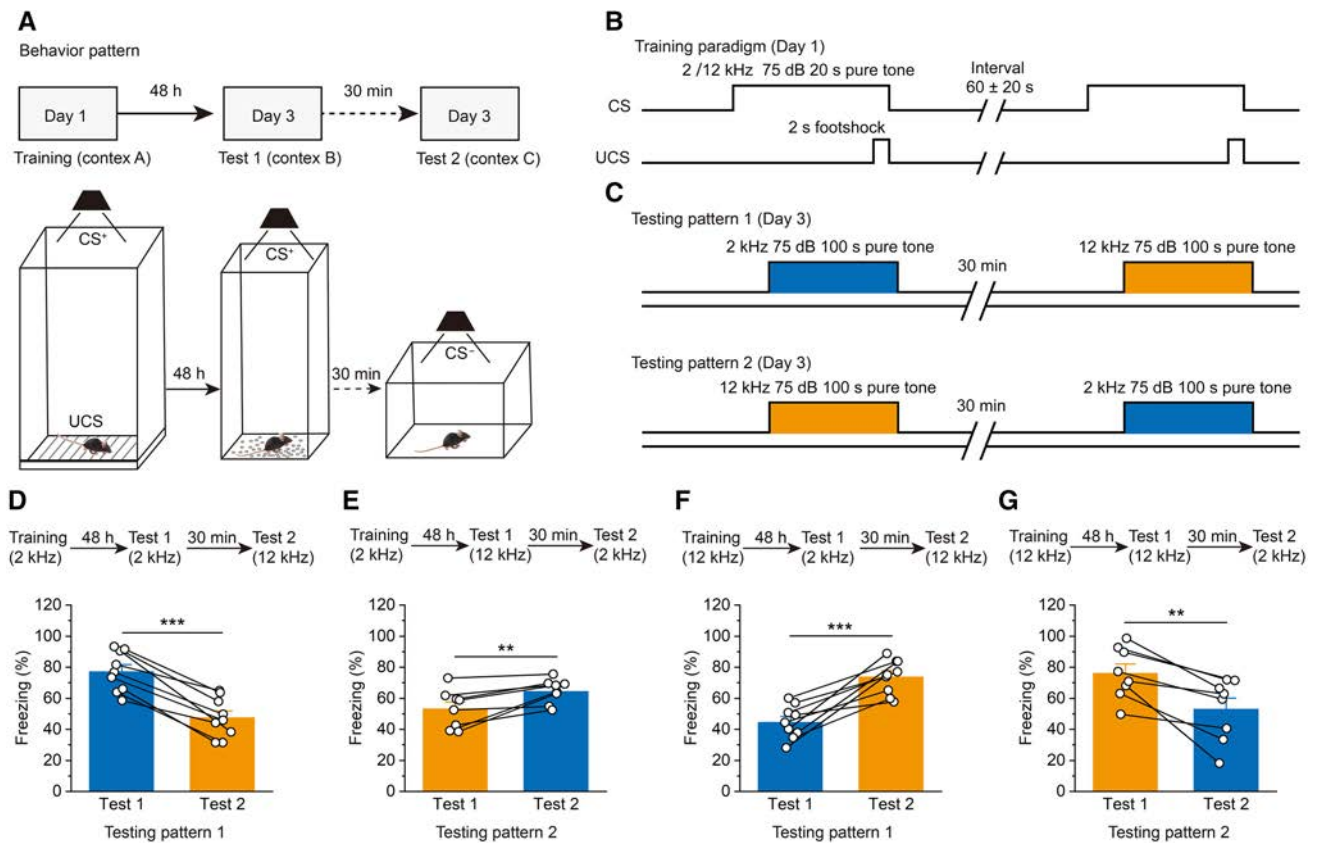


Fig. 1 Mice can differentiate between different tone frequencies in the fear conditioning task. **A** Experimental scheme for the training and fear conditioning tests. **B** Experimental timeline for the training paradigm. **C** Experimental timeline for the testing paradigm. **D**, **E** Freezing levels of the mice in the testing pattern 1 (**D**; $n = 9$) and testing pattern 2 (**E**; $n = 8$) during the 2-kHz training paradigm. **F**, **G**

Freezing levels of the testing pattern 1 (**F**; $n = 9$) and testing pattern 2 (**G**; $n = 8$) during the 12-kHz training paradigm. For **D–G**: all data are shown as the mean \pm SEM; ** $P < 0.01$, *** $P < 0.001$, Paired Student's t -test. CS⁺, conditioned stimulus (the pure tone paired with the footshock); CS⁻, the pure tone not paired with the footshock; UCS, unconditioned stimulus (the footshock).

rAAV2/8-*CaMKII α -hM4Di-mCherry* (titer: 5.89×10^{12} GC/mL) or rAAV2/8-*CaMKII α -mCherry* (titer: 5.04×10^{12} GC/mL) as a control into the bilateral AAF (Fig. 4B).

For anterograde tracing of the AAF–striatum projections, mice were microinjected with 50 nL of rAAV2/8-*CaMKII α -EGFP-P2A-MCS-3FLAG* (titer: 8.21×10^{12} GC/mL) into the right AAF (Fig. 5A).

Mice were microinjected with 150 nL of CTB488 (0.1%, w/v) into the right striatum to allow retrograde tracing of the AAF–striatum projections, and 14 days were allowed for retrograde tracer transport (Fig. 5B).

Mice were microinjected with 50 nL rAAV2/9-*EF1 α -DIO-hM4Di-mCherry* (titer: 2.42×10^{12} GC/mL) to pharmacogenetically inhibit AAF excitatory neuron activity during auditory frequency discrimination behavior or 50 nL rAAV2/9-*EF1 α -DIO-mCherry* (titer: 2.71×10^{12} GC/mL) as a control into the bilateral AAF. The mice were also bilaterally microinjected with 150 nL rAAV2/retro-*CamkII α -Cre* (titer: 6.62×10^{12} GC/mL) into each side of the striatum (Fig. 6B).

All coordinates for viral injection sites are listed as measurements from bregma (in mm). AAF: -2.30 anterior, ± 3.80 lateral, -1.0 ventral; striatum: -1.06 anterior, ± 2.93 lateral, -2.5 ventral.

Pharmacogenetic Manipulations

To attain pharmacogenetic inhibition, mice expressing *hM4Di-mCherry* or *mCherry* (control) were injected intraperitoneally with 2 mg/kg clozapine N-oxide (CNO, HY-17366, MedChemExpress, New Jersey, USA) [diluted with 5% DMSO (D5879, Sigma–Aldrich, Saint Louis, USA) and saline], and the behavioral test was implemented 30 min after CNO injection.

Optical Fiber Implantation

Mice were fixed in a stereotaxic apparatus after being anesthetized with isoflurane (1%–1.5% isoflurane/oxygen). Then, for fiber photometry recording, the optical fibers (ceramic

ferrule: diameter 2.50 mm; optical fiber: 200 μm core diameter, 0.37 NA) were implanted 20 μm above the viral injection site in the right AAF, and two cranial screws were fixed to the skull, while the skull surface was milled with a cranial drill for dental cement fixation. The optical fibers were fixed to the skull with dental cement immediately after the virus injection. The animals were allowed 4 weeks of recovery from the surgery and expression of the virus.

Fiber Photometry

The mice were first trained in a conditioned fear experiment and subjected to an electric shock and a pure tone of 12 kHz (75 dB) using the SuperFcs system (XinRuan, Shanghai, China). Then a fiber photometry recording system (Thinkerbiotech, Nanjing, China) was used to record the fluorescence signals of the AAF. Fluorescence emission was recorded and fluorescence signal excitation was induced using a 470-nm laser. The reference channel used 405-nm excitation light. Moreover, a 405-nm laser was used to exclude movement noise and test the data validity of the Ca^{2+} signal channel.

The mice were placed in a testing chamber and allowed to acclimatize for 5 min after a fiber optic jumper was connected to the ceramic insert on top of the skull. Then the fluorescence signal was recorded during which the mice were exposed to a pure tone (CS^+ : 12 kHz, 75 dB, 200 s). Then, another pure tone (CS^- : 2 kHz, 75 dB, 200 s) was delivered at an interval of ~ 30 min to record the changes in Ca^{2+} signals during the process.

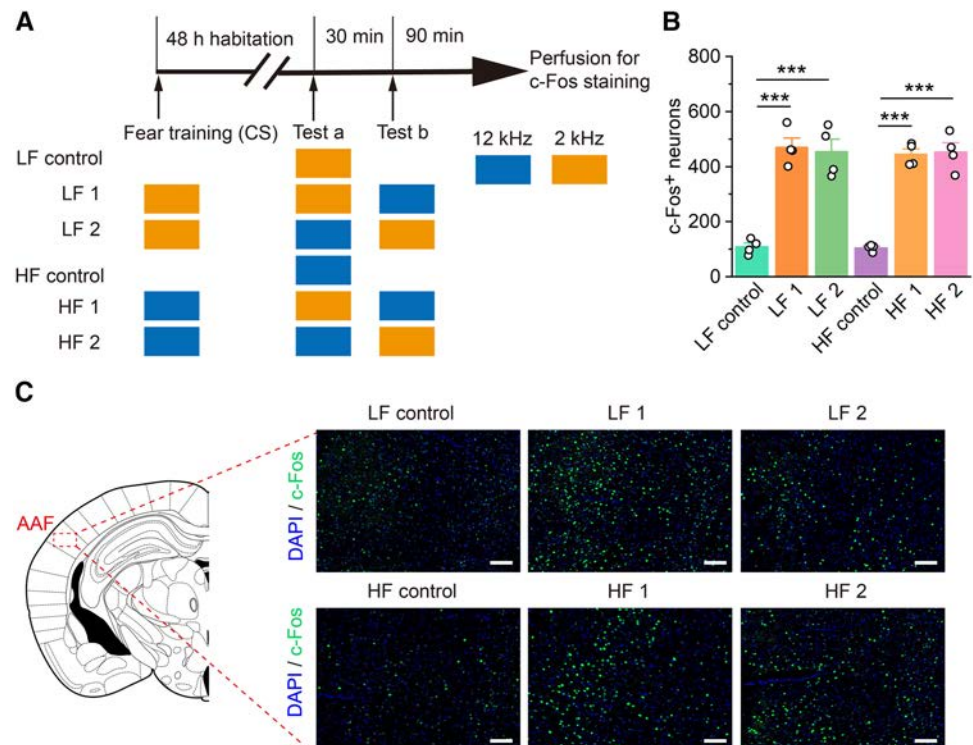
The fiber photometry statistics were analyzed using MatLab 2017b (The MathWorks, Inc., Natick, USA). The change in the fluorescence values ($\Delta F/F_0$) was calculated using $(F - F_0)/F_0$, in which F refers to the fluorescence value at each time point (-2 s to 10 s relative to the pure tone) and F_0 refers to the median of the fluorescence values during the baseline period (-2 s to 0 s relative to the pure tone onset). The $\Delta F/F_0$ values are presented as heatmaps and plots with shaded areas that indicated the SEM to visualize the change in fluorescence. To statistically quantify the change in fluorescence values across the sound testing results, the average amplitude of $\Delta F/F_0$ was defined as the average fluorescence amplitude change from baseline during the peak period (0–4 s relative to the sound test onset) (Fig. 3).

Immunofluorescence

For the assessment of endogenous c-Fos expression induced by auditory frequency discrimination behavior in the AAF, 6 groups of mice received different training and test patterns, and their brains were collected 90 min after testing (Fig. 2A).

The immunofluorescence staining protocol was designed as described below. First, the mice were deeply anesthetized with isoflurane and transcardially perfused with phosphate-buffered saline (PBS, 0.01 mol/L, pH 7.4) followed by 4% paraformaldehyde (PFA). The brains were stored in 4% PFA at 4°C for 24 h and then transferred to a 15% sucrose solution in which they were stored at 4°C for 48 h. The brains

Fig. 2 c-Fos-positive cell numbers are significantly elevated in the AAF after auditory frequency discrimination. **A** Experimental timeline for c-Fos immunofluorescence staining. LF (low frequency), HF (high frequency). **B** c-Fos-positive cell numbers in the AAF are significantly higher after frequency discrimination in the sound training groups ($n = 4$ per group). **C** Representative immunofluorescence images for c-Fos immunofluorescence staining (scale bars, 100 μm). All data are shown as the mean \pm SEM; *** $P < 0.001$, unpaired Student's t -test.



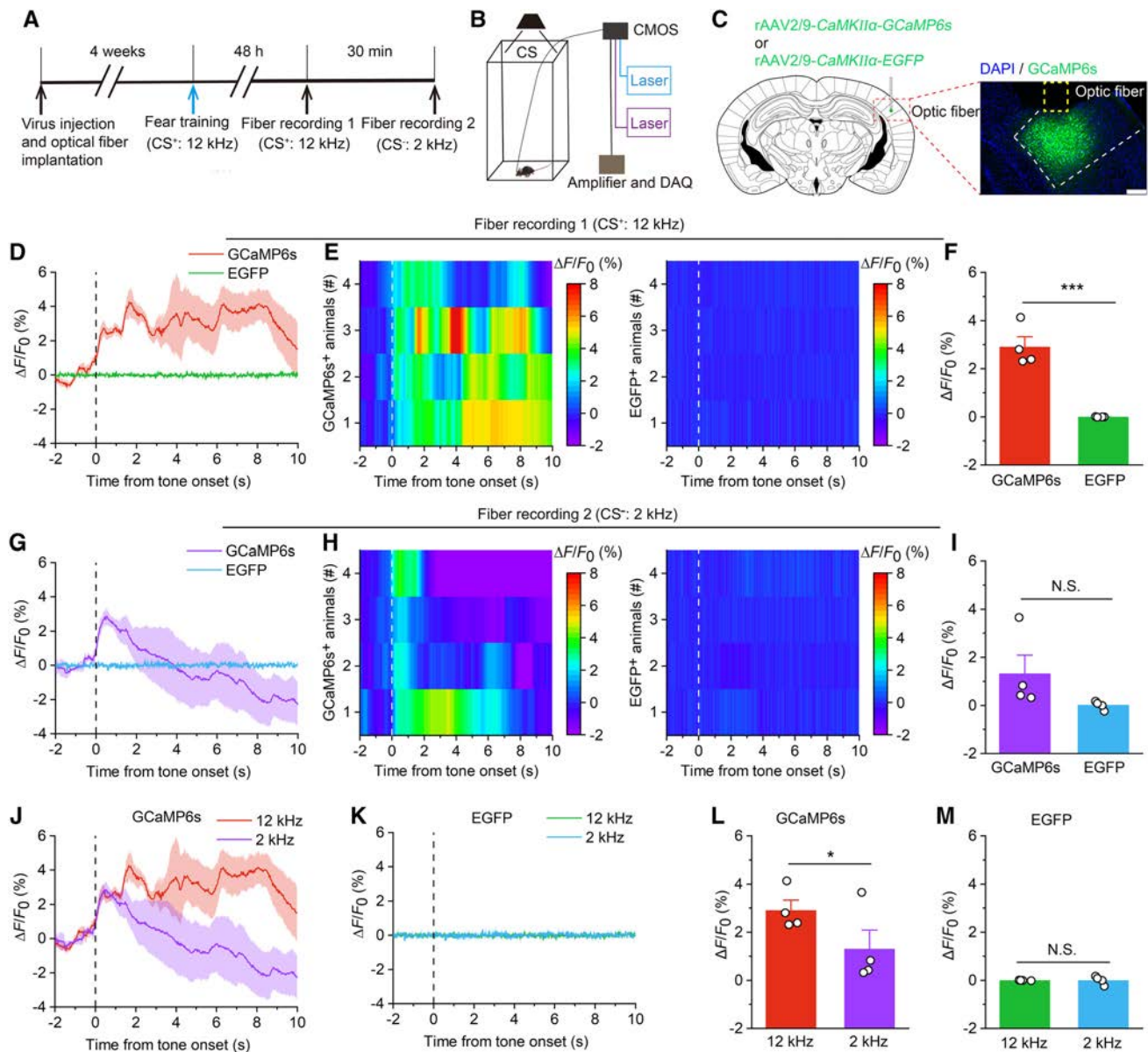


Fig. 3 Activation of pyramidal neurons in the AAF during auditory frequency discrimination. **A** Experimental scheme for virus injection followed by fiber recording. **B** Schematic of synchronized recordings of the fluorescence signal and tone frequency dynamics in animals. CMOS, complementary metal oxide semiconductor; DAQ, data acquisition. **C** Schematic showing virus injection and optical fiber implantation into the right AAF. Scale bar, 200 μm . **D** Average fluorescence change induced by 12-kHz tone (CS⁺) in the GCaMP6s and EGFP groups. **E** Heatmaps showing the average fluorescence change induced by 12-kHz tone in the GCaMP6s and EGFP groups. **F** Mean $\Delta F/F_0$ (0–6 s) induced by 12-kHz tone in the GCaMP6s and EGFP groups ($n = 4$ per group). **G** Average fluorescence change induced by 2-kHz tone (CS⁻) in the GCaMP6s and EGFP groups. **H** Heatmaps

showing the average fluorescence change induced by 2-kHz tone in the GCaMP6s and EGFP groups. **I** Mean $\Delta F/F_0$ (0–6 s) induced by 2-kHz tone in the GCaMP6s and EGFP groups ($n = 4$ per group). **J** Average fluorescence change of GCaMP6s induced by 12-kHz and 2-kHz. **K** Average fluorescence change of EGFP induced by 12-kHz and 2-kHz. **L** Mean $\Delta F/F_0$ (0–6 s) of GCaMP6s induced by 12-kHz and 2-kHz. **M** Mean $\Delta F/F_0$ (0–6 s) of EGFP induced by 12-kHz and 2-kHz. For **D**, **G**, **J**, and **K**, thick lines indicate mean and shaded areas indicate SEM, and the dashed lines indicate the beginning of tone. For **E** and **H**, each row represents one animal. All data are shown as the mean \pm SEM; N.S., no significant difference, * $P < 0.05$, *** $P < 0.001$, unpaired Student's t -test.

were then cut into 30 μm frozen sections (CM1900, Leica, Wetzlar, Germany) that were collected in PBS and rinsed three times in PBS for 15 min at room temperature, incubated in PBST (PBS + 0.1% Triton X-100) with 3% normal

bovine serum albumin for 1 h, and then incubated with primary antibody for 24 h at 4°C (rabbit anti-c-Fos, 1:500, 226003, Synaptic Systems, Goettingen, Germany). The sections then underwent three washing steps for 10 min each

in PBS and were incubated with a secondary antibody for 1 h (goat anti-rabbit conjugated to Alexa Fluor 488, 1:500, Invitrogen, Carlsbad, USA). The sections were washed with PBS (thrice, 10 min) at room temperature, incubated with DAPI (1:2,000, D9542, Sigma–Aldrich, Saint Louis, USA) for 15 min, then subjected to three more washing steps of 10 min each in PBS, followed by mounting and coverslipping on microscope slides. c-Fos expression was verified using a scanning laser microscope (SpinSR, Olympus, Tokyo, Japan). The number of c-Fos-positive neurons was analyzed by ImageJ (1.52a, Bethesda, USA).

Histology

After the behavioral and fiber photometry experiments, brain sections were collected using the methods described above. Sections 30 μm thick were washed with PBS (thrice, 10 min), incubated with DAPI (1:2,000, D9542, Sigma–Aldrich, Saint Louis, USA) for 15 min, and then subjected to an additional 3 wash steps of 10 min each in PBS. Histological verification of virus expression and CTB488 tracing were obtained using a full slide scanning system (VS200, Olympus).

Statistical Analysis

All data are expressed as the mean \pm SEM. Statistical significance was determined using the paired Student's *t*-test, unpaired Student's test, or two-way analysis of variance (ANOVA) with repeated measures, followed by Tukey's *post hoc* test using SPSS software for Windows (v. 25.0; IBM Corp., Armonk, USA). $P < 0.05$ was considered statistically significant.

Results

Mice Differentiate Between Different Tone Frequencies in the Fear Conditioning Task

First, a frequency discrimination behavioral protocol was modified from the classic fear conditioning paradigm (Fig. 1A). When mice were trained with a 2-kHz pure tone at 75 dB (Fig. 1B, C), they showed much more marked freezing to the 2-kHz pure tone than 12-kHz pure tone (Fig. 1D, E). Similarly, when animals were trained with a 12-kHz pure tone at 75 dB (Fig. 1B, C), they showed much more freezing to the 12-kHz pure tone than the 2-kHz pure tone (Fig. 1F, G). Together, these results indicate that mice successfully established frequency discrimination fear conditioning tasks.

The AAF is Activated During the Discrimination of Different Frequencies

Next, to assess the function of the AAF during different tone frequency discrimination behaviors, immunofluorescence was used to investigate the numbers of c-Fos-positive cells (c-Fos⁺) in the AAF of the experimental group, which included the 12- and 2-kHz training groups (Fig. 2A). The results showed that the c-Fos⁺ cell numbers in the AAF increased significantly after the tone test compared with those of the control group (Fig. 2B, C). However, there were no significant differences in c-Fos⁺ cell numbers in the AAF of the 2-kHz and 12-kHz training groups. Therefore, we used a 12-kHz pure tone to train animals in subsequent experiments.

To further confirm AAF neuronal activity during auditory frequency discrimination, we used a fiber photometer to record the intracellular Ca²⁺ signal of these neurons in different tone environments [18, 19] (Fig. 3A, B). Ca²⁺/calmodulin protein kinase II α (CaMKII α) is selectively expressed in numerous pyramidal neurons in the cortex and thalamus [20].

We microinjected recombinant adeno-associated virus (rAAV) expressing a Ca²⁺ indicator (GCaMP6s) or EGFP under the control of the CaMKII α promoter (rAAV2/9-CaMKII α -GCaMP6s, rAAV2/9-CaMKII α -EGFP) into the right AAF and implanted an optical fiber above the injection site (Fig. 3C). Four weeks after virus injection, a photometry recording was made to detect GCaMP6s or EGFP fluorescence changes aligned to frequency discrimination behavior (Fig. 3A). Two different frequency tones (CS⁺: 12 kHz and CS⁻: 2 kHz) that evoked frequency discrimination were delivered to the mice. By aligning the fluorescence signal to the onset of the individual tone test, we found that the fluorescence signal began to increase after the tone test onset in the GCaMP6s group (Fig. 3D, E, G, H). The increase in fluorescence signal was reliably accompanied by tone discrimination behavior and lasted for a few seconds. However, we did not detect a significant increase in the fluorescence signal in the EGFP group (Fig. 3D, E, G, H). Statistical analysis revealed significant differences in the mean $\Delta F/F_0$ induced by 12-kHz tone between the GCaMP6s and EGFP groups (Fig. 3F), whereas the mean $\Delta F/F_0$ induced by 2-kHz tone did not differ significantly (Fig. 3I). Furthermore, the fluorescent signal of GCaMP6s also differed significantly between the 12 kHz and 2 kHz, but not of EGFP (Fig. 3J–M). Mice identified the two different pure tones accurately. Thus, the activity of AAF pyramidal neurons is correlated with auditory frequency discrimination.

Pharmacogenetic Inhibition of the AAF Attenuates Frequency Discrimination

The results of c-Fos staining and fiber photometry showed that AAF pyramidal neurons were activated during auditory frequency discrimination. To further investigate the role of AAF pyramidal neurons in tone processing, a pharmacogenetic approach of designer receptors that are exclusively activated by designer drugs (DREADDs) [21, 22] was applied to evaluate their function. We then microinjected into the AAF recombinant AAV, which encoded the inhibitory DREADD receptor hM4Di (rAAV2/8-CaMKII α -hM4Di-mCherry),

while the control group was microinjected bilaterally with rAAV2/8-CaMKII α -mCherry.

Four weeks later, the frequency discrimination behavioral tests were applied to identify the role of these excitatory neurons (Fig. 4A). In mice expressing the inhibitory hM4Di-mCherry in the AAF pyramidal neurons, CNO injection (2 mg/kg, i.p.) significantly affected the ability of the mice to differentiate between the two frequencies (Fig. 4D, I), while vehicle-injected mice exhibited clear differences in fear behavior associated with auditory frequency discrimination (Fig. 4E, J). Meanwhile, the mice expressing the control mCherry in the pyramidal neurons injected with CNO (2

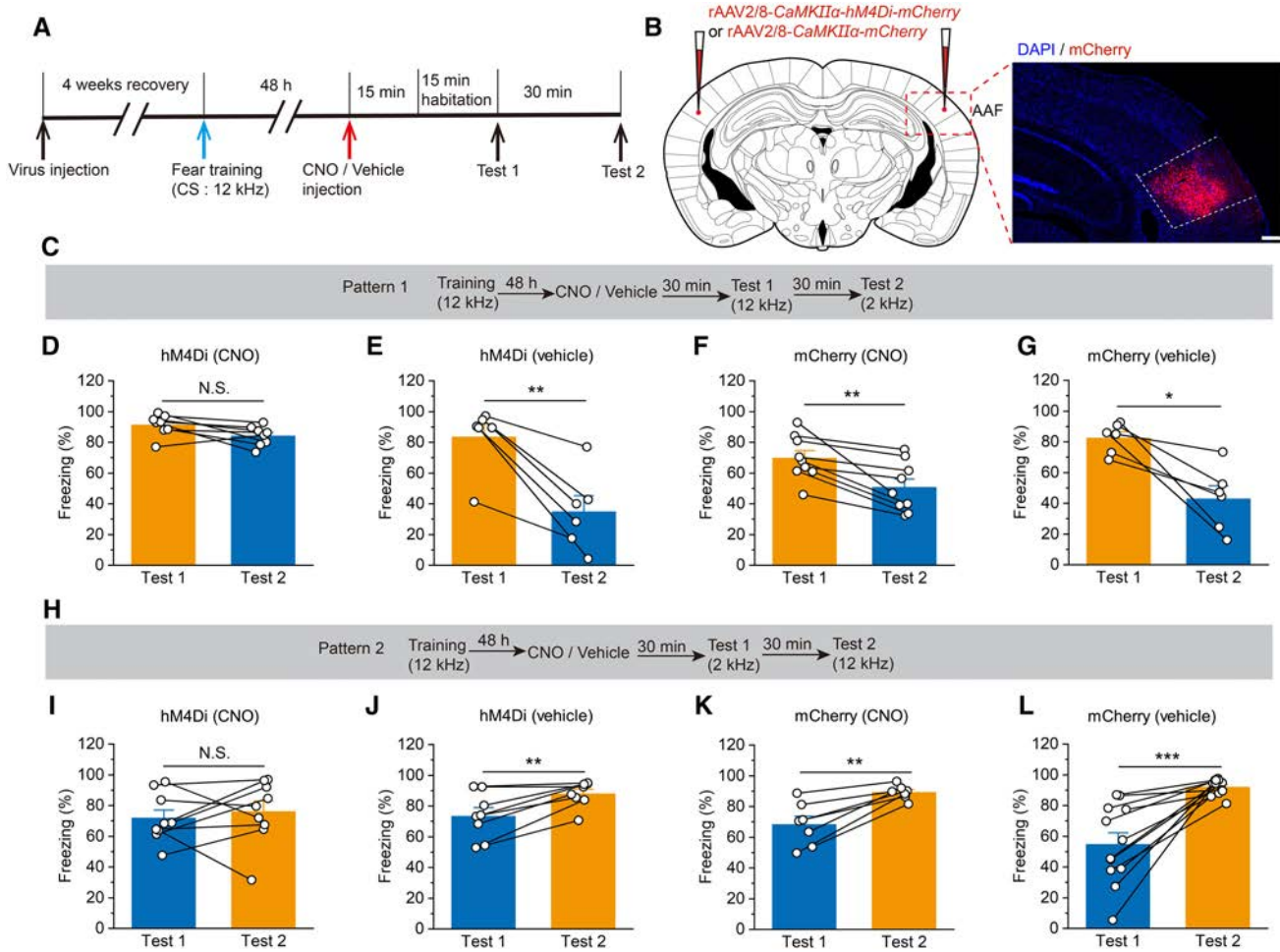


Fig. 4 Significant reduction in auditory frequency discrimination due to pharmacogenetic inhibition of AAF pyramidal neurons. **A** Experimental timeline for virus injection and behavior testing. **B** Schematic showing bilateral injection of virus into the AAF. Scale bar, 200 μ m. **C** Experimental scheme for the training and fear conditioning test of pattern 1. **D** Pharmacogenetic inhibition of hM4Di⁺ pyramidal neurons in the AAF (injected with CNO) significantly disrupts the auditory frequency discrimination behavior ($n = 8$). **E** Vehicle injection does not influence the auditory frequency discrimination behavior of hM4Di-infected animals ($n = 6$). **F, G** The mCherry-infected mice (injected with CNO or vehicle) significantly differentiate the two fre-

quency tones (**F**: $n = 9$; **G**: $n = 6$). **H** Experimental scheme for the training and fear conditioning test of pattern 2. **I** Pharmacogenetic inhibition of pyramidal neurons expressed hM4Di (injected with CNO) significantly disrupts the auditory frequency discrimination behavior ($n = 9$). **J** Vehicle injection does not influence the auditory frequency discrimination behavior of hM4Di-infected animals ($n = 8$). **K, L** The mCherry-infected mice (injected with CNO or vehicle) significantly discriminate the two frequency tones (**K**: $n = 7$; **L**: $n = 12$). All data are shown as the mean \pm SEM, N.S., no significant difference; ** $P < 0.01$, *** $P < 0.001$, paired Student's *t*-test.

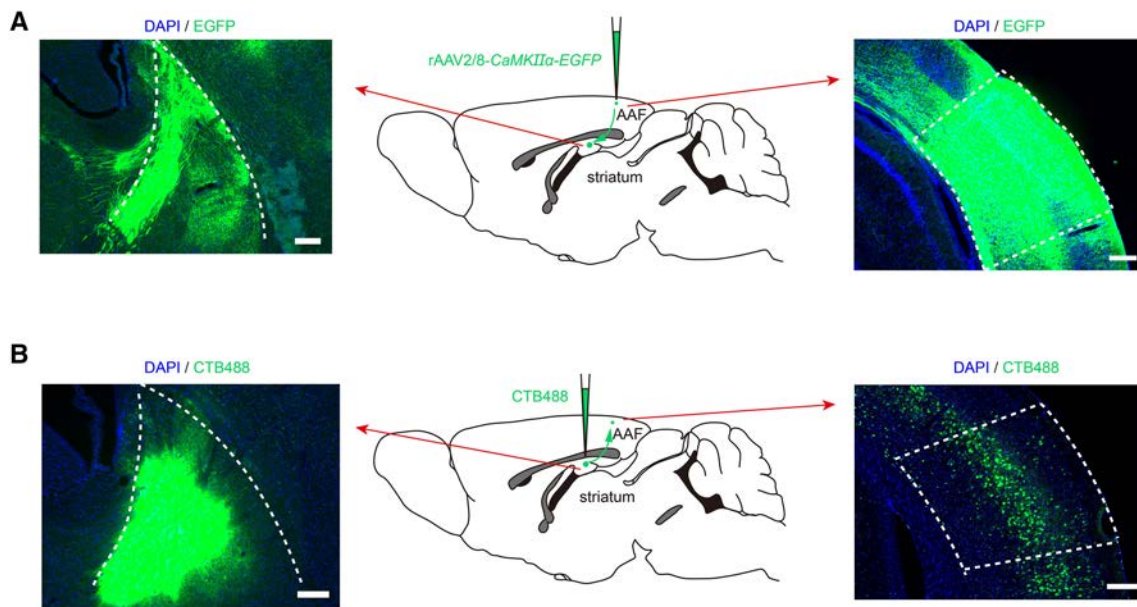


Fig. 5 Neuronal projection from the AAF to the striatum. **A** Neuronal projection from the AAF to the striatum was revealed using EGFP. Middle, EGFP diagram tracing from the AAF to the striatum. Left, EGFP in the striatum. Right, The virus is microinjected into the AAF. Scale bars, 200 μ m. **B** Neuronal projection from the striatum to

the AAF revealed using CTB488. Middle, CTB488 diagram tracing from the striatum to the AAF. Left, CTB488 is microinjected into the striatum. Right, CTB488 signals in the AAF retrogradely filled from the striatum. Scale bars, 200 μ m.

mg/kg, i.p.) or vehicle were able to differentiate between the two frequencies significantly (Fig. 4F, G, K, L). These results suggest that AAF pyramidal neurons play an important role in modulating auditory frequency discrimination.

The AAF–striatum Projections Regulate Auditory Frequency Discrimination

The projections from the auditory cortex to the striatum play an important role in processing sound identity, animal choice, and expected reward size [13, 16, 17, 23]. We found abundant axon terminals labeled with EGFP in the AAF pyramidal neurons present in the striatum of mice microinjected with rAAV2/8-*CaMKII α -EGFP* into the AAF (Fig. 5A). To further determine whether neural projections from the AAF to the striatum are present, the retrograding tracer CTB488 was microinjected into the right striatum. After two weeks, there were many CTB488-labeled neurons in the AAF (Fig. 5B). These results suggested that AAF pyramidal neurons project to the striatum.

We further examined the role of AAF–striatum projections in auditory frequency discrimination by microinjecting a Cre-dependent AAV (rAAV2/9-*EF1 α -DIO-hM4Di-mCherry*) bilaterally into the AAF and a retrograde AAV expressing Cre recombinase (rAAV2/retro-*CaMKII α -Cre*) bilaterally into the striatum (Fig. 6B). hM4Di was expressed selectively in AAF pyramidal neurons projecting to the striatum. Behavioral testing was implemented after 4 weeks

(Fig. 6A), when hM4Di was expressed (Fig. 6B), to verify the function of these neurons in auditory frequency discrimination. The results demonstrated that pharmacogenetic inhibition of pyramidal AAF–striatum projections significantly attenuated auditory frequency discrimination, as indicated by a significant reduction in the freezing level between the two groups (Fig. 6D–G, I–L). Based on these results, we conclude that AAF pyramidal neurons modulate tone frequency discrimination through a descending pathway mediated by the striatum.

Discussion

The AAF is an important area in the auditory cortex, whereas previous studies almost always focused on the role of A1 in auditory-related behaviors. For example, A1 has been reported to be involved in sound-induced freezing [24] and speech discrimination [25]. However, the role of the AAF in sound discrimination remained unclear. Here, we investigated the role of the AAF and AAF–striatum projections in auditory frequency discrimination by using c-Fos staining, fiber photometry, and pharmacogenetics. Our findings established that the AAF pyramidal neurons and the AAF–striatum projection are involved in the regulation of auditory frequency discrimination behavior.

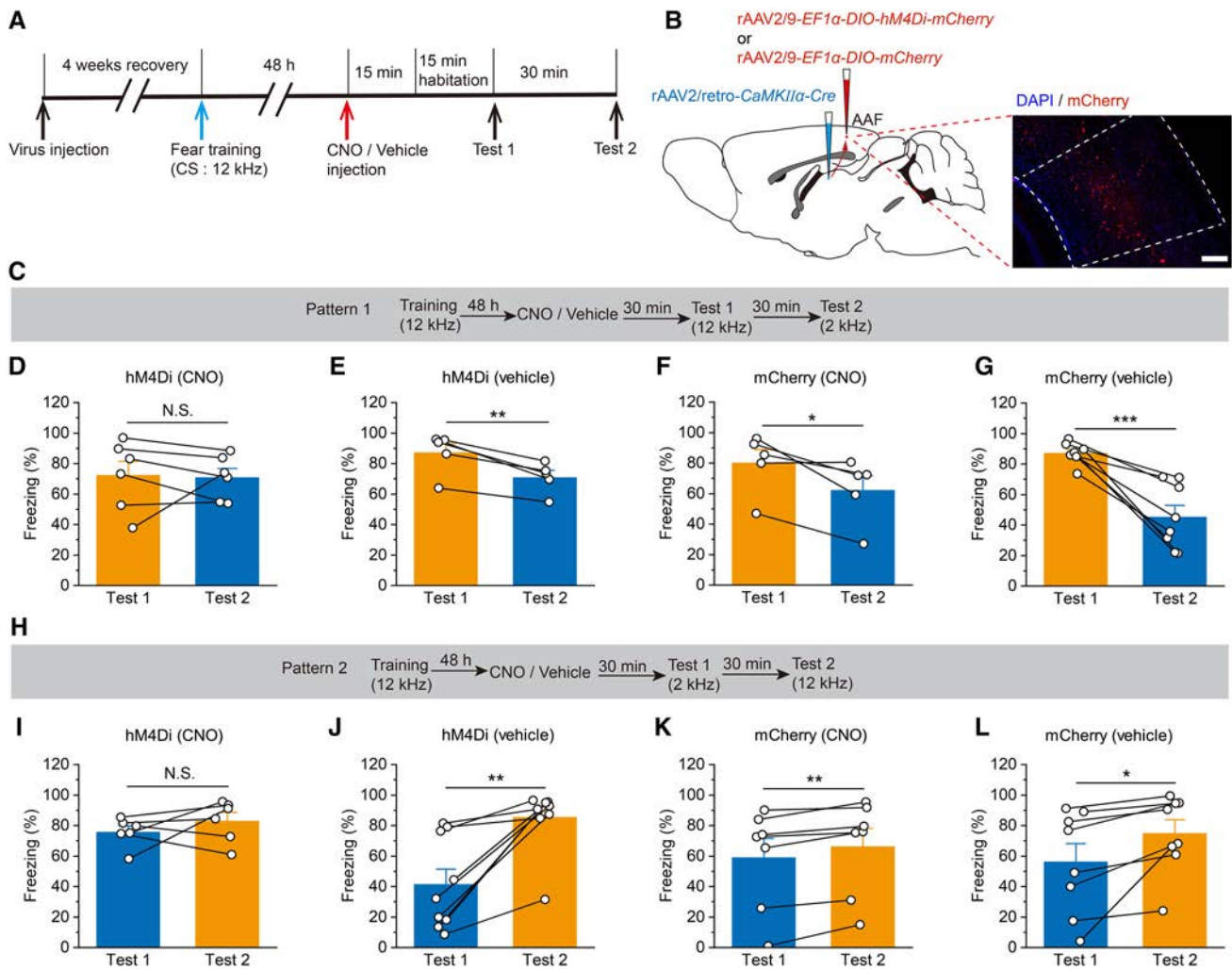


Fig. 6 Pharmacogenetic inhibition of the AAF pyramidal neuron projections to the striatum significantly suppresses the auditory frequency discrimination behavior. **A** Experimental timeline for virus injection and behavior testing. **B** Schematic for viral injection to prevent pyramidal neurons in the AAF from interacting with the striatum and a sample image showing the expression of hM4Di-mCherry in the AAF. Scale bar, 200 μ m. **C** Experimental scheme for the training and fear conditioning test of pattern 1. **D** Pharmacogenetic inhibition of pyramidal neurons expressing hM4Di (injected with CNO) significantly impairs the auditory frequency discrimination behavior ($n = 6$). **E** Vehicle injection does not influence the auditory frequency discrimination behavior of hM4Di-infected animals ($n = 5$). **F, G** The

mCherry-infected mice (injected with CNO or vehicle) significantly discriminate the two frequency tones (**F**: $n = 5$; **G**: $n = 8$). **H** Experimental scheme for the training and fear conditioning test of pattern 2. **I** Pharmacogenetic inhibition of pyramidal neurons expressed hM4Di (injected with CNO) significantly impairs auditory frequency discrimination behavior ($n = 6$). **J** Vehicle injection does not influence the auditory frequency discrimination behavior of hM4Di-infected animals ($n = 9$). **K, L** The mCherry-infected mice (injected with CNO or vehicle) significantly discriminate the two frequency tones (**K**: $n = 7$; **L**: $n = 8$). All data are shown as the mean \pm SEM, N.S., no significant difference, * $P < 0.05$, ** $P < 0.01$, *** $P < 0.001$, paired Student's t -test.

The discrimination of complex sounds is a fundamental function of the auditory system [7, 26]. Based on previous studies [8, 10, 25, 27–31], we developed a frequency discrimination model in which mice recognized one pure tone frequency by measuring freezing (Fig. 1). In fact, frequency discrimination of fear behavior is not inconsistent with fear generalization, in which fear-generalized mice are unable to discriminate between two stimuli [32]. Notably, c-Fos immunofluorescence staining showed that AAF neuronal activity was associated with auditory frequency

discrimination (Fig. 2). Moreover, fiber photometry showed that AAF pyramidal neurons were correlated with auditory frequency discrimination. We found that fluorescent signals began to increase after tone onset (Fig. 3), but they were faint and only lasted for a short time. The reasons for this might be attributable to auditory desensitization due to prolonged sound stimulation [33, 34]. Therefore, we chose a relatively short period (0–6 s after tone onset) for statistical analysis. In addition, pharmacogenetic inhibition of AAF pyramidal neurons significantly impaired frequency discrimination

(Fig. 4). These results suggest that AAF pyramidal neurons play a key role in the modulation of frequency discrimination behavior.

The striatum is known to receive projections from the auditory cortex [24]. The projections from A1 to the striatum have been shown to be prominently involved in reward-motivated auditory discrimination tasks [13, 16, 17]. However, whether there are direct AAF–striatum projections and whether these projections regulate auditory frequency discrimination has remained unclear. In the present study, the existence of direct AAF–striatum projections was confirmed by using both anterograde and retrograde tracing methods (Fig. 5). Moreover, in the present study, pharmacogenetic inhibition of striatum-projecting pyramidal neurons in the AAF resulted in significant attenuation of tone frequency discrimination behavior (Fig. 6), indicating that AAF–striatum projections play a critical role in modulating auditory frequency discrimination.

In addition, other types of projections are also present in the corticostriatal pathway. Anatomical and physiological studies have demonstrated that dorsal striatal neurons receive excitatory glutamate inputs from the auditory cortex, but also receive GABAergic projections from the auditory cortex in mice [12, 13]. However, the role of these GABAergic projections in auditory frequency discrimination is also unclear. Therefore, further studies will be required to uncover whether the GABAergic projections from the auditory cortex to the striatum play a critical role in auditory frequency discrimination.

In conclusion, the results of the present study reveal that the activity of AAF pyramidal neurons is associated with auditory frequency discrimination and AAF–striatum projections are identified as corticostriatal neural pathways involved in the process of auditory frequency discrimination. Our study may help to understand the precise neuronal circuits behind discrimination behavior.

Acknowledgements This work was supported by grants from the National Natural Science Foundation of China (31871075 and 32071015), the Open Project of Chongqing Key Laboratory of Neurobiology (cqsjsw202103 and cqsjsw202101), and the Natural Science Foundation of Chongqing (cstc2020jcyj-msxmX0391).

Conflict of interest The authors claim that there are no conflicts of interest.

References

- Carrasco A, Kok MA, Lomber SG. Effects of core auditory cortex deactivation on neuronal response to simple and complex acoustic signals in the contralateral anterior auditory field. *Cereb Cortex* 2015, 25: 84–96.
- Bizley JK, Cohen YE. The what, where and how of auditory-object perception. *Nat Rev Neurosci* 2013, 14: 693–707.
- Romero S, Hight AE, Clayton KK, Resnik J, Williamson RS, Hancock KE. Cellular and widefield imaging of sound frequency organization in primary and higher order fields of the mouse auditory cortex. *Cereb Cortex* 2020, 30: 1603–1622.
- Solyga M, Barkat TR. Distinct processing of tone offset in two primary auditory cortices. *Sci Rep* 2019, 9: 9581.
- Kim G, Kandler K. Elimination and strengthening of glycinergic/GABAergic connections during tonotopic map formation. *Nat Neurosci* 2003, 6: 282–290.
- Aizenberg M, Mwilambwe-Tshilobo L, Briguglio JJ, Natan RG, Geffen MN. Bidirectional regulation of innate and learned behaviors that rely on frequency discrimination by cortical inhibitory neurons. *PLoS Biol* 2015, 13: e1002308.
- Ceballos S, Piwkowska Z, Bourg J, Daret A, Bathellier B. Targeted cortical manipulation of auditory perception. *Neuron* 2019, 104: 1168–1179.e5.
- Shi Z, Yan S, Ding Y, Zhou C, Qian S, Wang Z, *et al.* Anterior auditory field is needed for sound categorization in fear conditioning task of adult rat. *Front Neurosci* 2019, 13: 1374.
- Lomber SG, Malhotra S. Double dissociation of ‘what’ and ‘where’ processing in auditory cortex. *Nat Neurosci* 2008, 11: 609–616.
- Zhang G, Tao C, Zhou C, Yan S, Wang Z, Zhou Y, *et al.* Excitatory effects of the primary auditory cortex on the sound-evoked responses in the ipsilateral anterior auditory field in rat. *Neuroscience* 2017, 361: 157–166.
- Cox J, Witten IB. Striatal circuits for reward learning and decision-making. *Nat Rev Neurosci* 2019, 20: 482–494.
- Ponvert ND, Jaramillo S. Auditory thalamostriatal and corticostriatal pathways convey complementary information about sound features. *J Neurosci* 2019, 39: 271–280.
- Guo L, Weems JT, Walker WI, Levichev A, Jaramillo S. Choice-selective neurons in the auditory cortex and in its striatal target encode reward expectation. *J Neurosci* 2019, 39: 3687–3697.
- Guo L, Walker WI, Ponvert ND, Penix PL, Jaramillo S. Stable representation of sounds in the posterior striatum during flexible auditory decisions. *Nat Commun* 2018, 9: 1534.
- Nakata S, Takemoto M, Song WJ. Differential cortical and subcortical projection targets of subfields in the core region of mouse auditory cortex. *Hear Res* 2020, 386: 107876.
- Xiong Q, Znamenskiy P, Zador AM. Selective corticostriatal plasticity during acquisition of an auditory discrimination task. *Nature* 2015, 521: 348–351.
- Znamenskiy P, Zador AM. Corticostriatal neurons in auditory cortex drive decisions during auditory discrimination. *Nature* 2013, 497: 482–485.
- Martianova E, Aronson S, Proulx CD. Multi-fiber photometry to record neural activity in freely-moving animals. *J Vis Exp* 2019: e60278.
- Miyamoto D, Murayama M. The fiber-optic imaging and manipulation of neural activity during animal behavior. *Neurosci Res* 2016, 103: 1–9.
- Liu XB, Jones EG. Localization of alpha type II calcium calmodulin-dependent protein kinase at glutamatergic but not gamma-aminobutyric acid (GABAergic) synapses in thalamus and cerebral cortex. *Proc Natl Acad Sci U S A* 1996, 93: 7332–7336.
- Roth BL. DREADDs for neuroscientists. *Neuron* 2016, 89: 683–694.
- Smith KS, Bucci DJ, Luikart BW, Mahler SV. DREADDs: Use and application in behavioral neuroscience. *Behav Neurosci* 2016, 130: 137–155.
- Deutch AY. Extending corticostriatal systems. *JAMA. Psychiatry* 2016, 73: 871–872.
- Li Z, Wei JX, Zhang GW, Huang JJ, Zingg B, Wang X, *et al.* Corticostriatal control of defense behavior in mice induced by auditory looming cues. *Nat Commun* 2021, 12: 1040.

25. O'Sullivan C, Weible AP, Wehr M. Disruption of early or late epochs of auditory cortical activity impairs speech discrimination in mice. *Front Neurosci* 2020, 13: 1394.
26. Allen KM, Salles A, Park S, Elhilali M, Moss CF. Effect of background clutter on neural discrimination in the bat auditory mid-brain. *J Neurophysiol* 2021, 126: 1772–1782.
27. Tao C, Zhang G, Zhou C, Wang L, Yan S, Tao HW, *et al.* Diversity in excitation-inhibition mismatch underlies local functional heterogeneity in the rat auditory cortex. *Cell Rep* 2017, 19: 521–531.
28. Kurt S, Ehret G. Auditory discrimination learning and knowledge transfer in mice depends on task difficulty. *Proc Natl Acad Sci U S A* 2010, 107: 8481–8485.
29. Wang WJ, Wu XH, Li L. The dual-pathway model of auditory signal processing. *Neurosci Bull* 2008, 24: 173–182.
30. He Q, Wang J, Hu H. Illuminating the activated brain: Emerging activity-dependent tools to capture and control functional neural circuits. *Neurosci Bull* 2019, 35: 369–377.
31. O'Sullivan C, Weible AP, Wehr M. Auditory cortex contributes to discrimination of pure tones. *eNeuro* 2019, 6: ENEURO.0340-19.2019.
32. Asim M, Hao B, Yang YH, Fan BF, Xue L, Shi YW, *et al.* Ketamine alleviates fear generalization through GluN2B-BDNF signaling in mice. *Neurosci Bull* 2020, 36: 153–164.
33. Sanjuán Juaristi J, Sanjuán Martínez-Conde M. Auditory fatigue. *Acta Otorrinolaringol Esp* 2015, 66: 36–42.
34. Russell IJ, Kössl M. Sensory transduction and frequency selectivity in the basal turn of the Guinea-pig cochlea. *Philos Trans R Soc Lond B Biol Sci* 1992, 336: 317–324.

Springer Nature or its licensor (e.g. a society or other partner) holds exclusive rights to this article under a publishing agreement with the author(s) or other rightsholder(s); author self-archiving of the accepted manuscript version of this article is solely governed by the terms of such publishing agreement and applicable law.

The Emotion-Regulation Benefits of Implicit Reappraisal in Clinical Depression: Behavioral and Electrophysiological Evidence

Jiajin Yuan¹  · Yueyao Zhang² · Yanli Zhao³ · Kexiang Gao² · Shuping Tan³ · Dandan Zhang^{1,4,5}

Received: 8 May 2022 / Accepted: 16 August 2022 / Published online: 10 November 2022

© Center for Excellence in Brain Science and Intelligence Technology, Chinese Academy of Sciences 2022

Abstract Major depressive disorder (MDD) is characterized by emotion dysregulation. Whether implicit emotion regulation can compensate for this deficit remains unknown. In this study, we recruited 159 subjects who were healthy controls, had subclinical depression, or had MDD, and examined them under baseline, implicit, and explicit reappraisal conditions. Explicit reappraisal led to the most negative feelings and the largest parietal late positive potential (parietal LPP, an index of emotion intensity) in the MDD group compared to the other two groups; the group difference was absent under the other two conditions. MDD patients showed larger regulatory effects in the LPP during implicit than explicit reappraisal, whereas healthy controls showed a reversed pattern. Furthermore, the frontal P3, an index of voluntary cognitive control, showed larger amplitudes in explicit reappraisal compared to baseline in the

healthy and subclinical groups, but not in the MDD group, while implicit reappraisal did not increase P3 across groups. These findings suggest that implicit reappraisal is beneficial for clinical depression.

Keywords Depression · Implicit emotion regulation · Reappraisal · Late positive potential

Introduction

Depression is a common mental disorder characterized by difficulties in emotion regulation [1–3]. The onset of depression is often coupled with frequent use of emotion-focused rumination [4–10], reduced use of adaptive strategies for emotional down-regulation such as cognitive reappraisal [1, 11], and frequent use of a maladaptive strategy that enhances negative thinking [7, 12]. In line with this evidence, it has been reported that depressed individuals are less able to reduce negative affect through instructed reappraisal than healthy controls [13, 14], and this corresponds to hypoactivity in prefrontal regions and hyperactivity in the amygdala [1, 15, 16].

One important mechanism underlying this phenomenon is that depressive symptoms (e.g., sustained depressed mood) deplete cognitive resources, which consequently impair cognitive functions including executive control, memory, and attention in depressive patients [17–22]. However, the intentional use of adaptive strategies for emotional regulation, either initiation or maintenance of a strategy, entails top-down cognitive control mechanisms and the consumption of cognitive resources [23–25], as shown by enhanced activation in the frontoparietal cognitive network [26]. Consistent with this inference, recent studies suggest that the reduced use of reappraisal in depressive patients can be explained, at

Jiajin Yuan, Yueyao Zhang, and Yanli Zhao contributed equally to this work.

Supplementary Information The online version contains supplementary material available at <https://doi.org/10.1007/s12264-022-00973-z>.

✉ Dandan Zhang
zhangdd05@gmail.com

¹ Institute of Brain and Psychological Sciences, Sichuan Normal University, Chengdu 610066, China

² School of Psychology, Shenzhen University, Shenzhen 518060, China

³ Psychiatry Research Center, Beijing Huilongguan Hospital, Beijing 100096, China

⁴ Shenzhen-Hong Kong Institute of Brain Science, Shenzhen 518060, China

⁵ Magnetic Resonance Imaging (MRI) Center, Shenzhen University, Shenzhen 518060, China

least in part, by the fact that intentional strategy use drains their already limited cognitive resources [27]. The inability to regulate negative affect predisposes depressed individuals to sustained negative affect and difficulties in the experience of positive affect, which in turn exacerbate depressive symptoms [1]. Therefore, it is critical to seek an alternative, less resource-costly strategy for the rehabilitation of emotion-regulatory function in depression.

In line with this theme, implicit emotion regulation (also called nonconscious or automatic emotion regulation) is a goal-driven change to one's emotion without explicit instruction or deliberate control or even in the absence of a conscious decision [28]. Previous research has shown that, compared with explicit emotion regulation, implicit emotion regulation works for the reduction of negative emotion at little or no cost of cognitive resources [29–31]. According to previous electrophysiological findings, implicit emotion regulation does not increase the amplitude of frontal P3 (an index of cognitive control) when participants down-regulate their negative emotions [32]. Similarly, neuroimaging evidence has shown that implicit emotion regulation can decrease the activation in the amygdala and insula while it does not increase the activation in the frontoparietal control network [26]. Given that depressive patients are characterized by self-depletion and the resultant deficit in voluntary emotion regulation [27, 33–35], it is possible that implicit emotion regulation, an effortless, resource-saving process, is a more suitable strategy for depressive patients to realize the efficient regulation of depressive emotions. In previous studies, priming techniques have always been used to manipulate implicit regulatory processes [36–40]. For instance, Yuan *et al.* primed acceptance strategy and found implicit emotion regulation reduced emotional experience without enhancing cognitive effort [41]. More relevant to the current study, a recent study on subclinical depression reported that implicit priming of distraction protected depressed individuals from positive affect reduction during frustration, while explicit distraction did not have this effect [34]. As the evidence consistently shows that the implicit method of emotion regulation can reduce negative emotions in healthy and subclinical depressive populations, it is possible that this approach also works in emotion regulation in clinical depression. However, no study has directly tested this possibility to date.

Using behavioral and event-related potential techniques, the current study aimed at exploring the intervention effects of implicit emotion regulation on clinical depression. Three groups of subjects were included, that is, patients diagnosed with major depressive disorder (MDD), participants with subclinical depression, and healthy control participants. The subclinical depression group was included to help depict the trajectory of how emotion-regulatory effects of explicit and implicit reappraisal vary as a function of depression severity. Self-reporting is one of the most-used tools with which to

assess emotion, as it directly reflects one's currently-experienced emotions. However, there is evidence that the validity of self-reports is affected by the expectation of explicit instruction [42–44]. By contrast, event-related potentials (ERPs) are direct measures of brain activity and can be used as objective and sensitive indexes of the emotion regulation effect [45, 46]. Specifically, the late positive potential (LPP) in the parietal scalp region is a reliable measure indicating the emotional intensity and motivational salience of a stimulus [47, 48]. Previous studies have consistently shown that the down-regulation of negative emotion reduces the LPP amplitude [49–52]. Hence, our study applied two indices to measure emotion regulation effects: subjective rating and LPP amplitude. Meanwhile, the frontally-peaking late-positive component during an emotion-regulation task is accepted as an index of resource involvement in effortful control [53–55]. Voluntary inhibition of negative emotion *via* cognitive reappraisal or expressive suppression enhances the LPP amplitude, named either frontal-central P3 [56, 57] or frontal LPP [55, 57]. This control-related frontal component is reported to be more pronounced during explicit *versus* implicit regulation of negative emotion [53]. Therefore, in the current study, we were also interested in how the frontally-peaking late positive component varies across conditions to clarify how cognitive-control processes involved in emotion regulation differ with regulatory methods and depression severity.

We chose cognitive reappraisal as the target strategy as it is considered more reliable in emotion down-regulation than other strategies [58]. Also, reappraisal is a key component in depression-related cognitive therapies such as cognitive-behavioral therapy and dialectical behavioral therapy [59, 60]. Given the fact of insufficient cognitive resources, we speculated that depressive patients may find it difficult to regulate unpleasant emotions *via* intentional reappraisal [27, 33–35]. Instead, due to the automatic, resource-saving characteristics of implicit emotion regulation, we assumed that depressive patients may benefit from the use of implicit reappraisal in terms of emotion regulation. Exploration of this issue may provide a new avenue for the treatment of depression.

Materials and Methods

Participants

Sample size estimation is reported in the Supplementary Material (Part A). Patients were recruited from Beijing Huilongguan Hospital. They were diagnosed with a current major depressive episode according to the Diagnostic and Statistical Manual (DSM-IV) [61]. The diagnosis was based on a structured clinical interview for DSM-IV (SCID-I/P

W/PSY SCREEN) [62]. Exclusion criteria for patients were current or lifetime neurological disorders and any comorbid Axis I disorder. At the time of the experiment, all patients were either untreated with any antidepressant medication, or had undergone a wash-out period of at least two weeks. Subthreshold depression (SD) and control participants were recruited through advertisements in the community around Beijing Huilongguan Hospital. Exclusion criteria for these two groups were neurological disorders and any lifetime Axis I disorders according to the structured clinical interview for DSM-IV Axis I Disorders, Non-Patient edition (SCID-I/NP) [63]. Both patients and SD subjects were additionally required to have a score of ≥ 14 on the Beck Depression Inventory Second Edition (BDI-II) [64], while controls should have a BDI-II score of < 14 . Written informed consent was obtained prior to the experiment. All procedures in this study were in accordance with the 1964 Helsinki declaration and its later amendments or comparable ethical standards. The study was approved by the Ethics Committee of Beijing Huilongguan Hospital (# 2020-0127).

Participants were required to complete four questionnaires on the day of the experiment: (1) the BDI-II, (2) the Trait form of Spielberger’s State-Trait Anxiety Inventory (STAI-T) [65], (3) the cognitive reappraisal dimension of Emotion Regulation Questionnaire (ERQ-R) [66], and (4) the reappraisal subscale of the Thought Control Questionnaire (TCQ-R) [67] (Table 1). Among them, the BDI-II consists of 21 items ranging from 0 to 3, with a higher score indicating more depressive symptoms. The STAI-T consists of 20 items ranging from 1 to 4, with a higher score indicating a higher level of trait anxiety. The ERQ-R assesses 6 items of the tendency to use a cognitive reappraisal strategy

to regulate emotions, ranging from 1 (strongly disagree) to 7 (strongly agree). The TCQ-R is a 6-item scale ranging from 1 to 4, with a higher score indicating a greater extent of use of cognitive reappraisal to control thoughts.

Experimental Design and Procedure

The study had a 3 × 3 mixed design. The within-subject factor was the condition (baseline, implicit and explicit emotion regulation), and the between-subject factor was the group (control, SD, and depressed patient).

The experiment was conducted from 09:00 to 12:00 or 15:00 to 21:00 and the experiment time was matched across the three groups. There were three blocks in the experiment (Fig. 1A), whose order was fixed (i.e., baseline first, then the implicit, followed by the explicit condition) to ensure that the baseline condition was not disturbed by the other two emotion regulation blocks, and the implicit regulation block was not interfered with by the explicit emotion regulation instructions [49]. After the first two blocks, instructions were given to participants to explicitly regulate their emotions using cognitive reappraisal. The three 10-min blocks were separated by two 5-min breaks, resulting in a task time of 40 min. The potential influence of block order was examined in a separate experiment, which revealed a non-significant order effect (Supplementary Material, part B).

In each block, participants performed a word-matching (40 trials per block) and a dot-counting task (50 trials per block). The word-matching task was designed to non-consciously operate emotion regulation goals by priming reappraisal on outcome evaluation [32, 38, 40], while the dot-counting task (rapid dot-counting combined with negative

Table 1 Demographic characteristics of the participants (mean and standard deviation)

Items	Control (C)	Subthreshold (SD)	Patient (P)	Statistics ^a
Sample size	54	52	53	$\chi^2_{(2)} = 0.0, P = 0.981$
Gender (male/female)	24/30	22/30	22/31	$\chi^2_{(2)} = 0.1, P = 0.951$
Age (years)	29.0 (6.5)	28.7 (7.4)	30.8 (6.4)	$F_{(2, 156)} = 1.5, P = 0.218$
Handedness (right/left)	54/0	52/0	53/0	
Education (years)	17.5 (4.2)	16.6 (3.0)	16.2 (2.8)	$F_{(2, 156)} = 2.1, P = 0.126$
BDI-II	2.2 (2.0)	20.0 (5.2)	26.3 (7.8)	$F_{(2, 156)} = 273.4, P < 0.001, C < SD < P$
STAI-T	35.5 (6.5)	53.1 (6.6)	61.4 (7.2)	$F_{(2, 156)} = 205.9, P < 0.001, C < SD < P$
ERQ-R	30.0 (4.7)	26.4 (5.8)	25.4 (5.6)	$F_{(2, 156)} = 11.1, P < 0.001, C > SD/P$
TCQ-R	15.3 (3.3)	13.8 (3.5)	12.3 (3.3)	$F_{(2, 156)} = 10.3, P < 0.001, C > P$
HRSD			21.3 (5.7)	
Age at onset (years)			29.1 (10.1)	
Duration of illness (months)			18.3 (22.2)	
Number of episodes			0.3 (0.8)	

BDI-II, Beck Depression Inventory Second Edition; STAI-T, Trait form of Spielberger’s State-Trait Anxiety Inventory; ERQ-R, the cognitive reappraisal dimension of the Emotion Regulation Questionnaire; TCQ-R, the reappraisal subscale of the Thought Control Questionnaire; HRSD, Hamilton Depression Rating Scale. ^a The χ^2 test was applied to categorical variables. Univariate analysis of variance was applied to continuous variables, with the group as the fixed factor (Bonferroni correction).

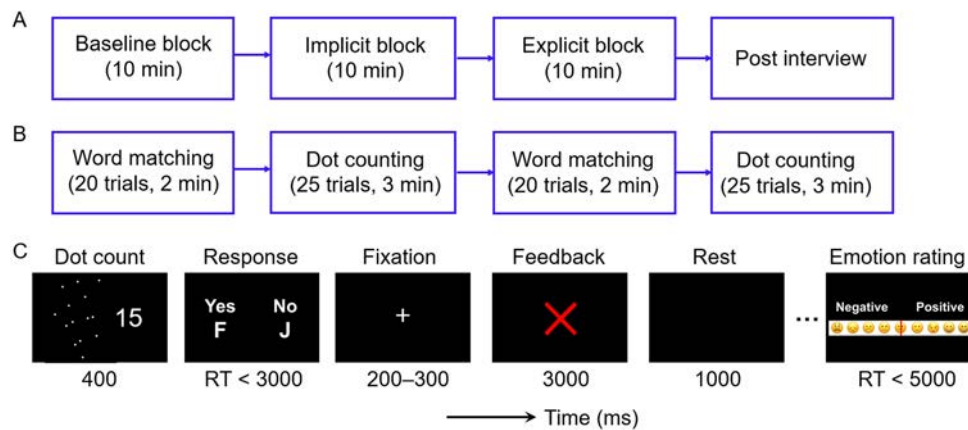


Fig. 1 Experimental procedures. **A** Flowchart of the experiment. The order of the three blocks is fixed to ensure that the baseline condition is not disturbed by the other two emotion regulation blocks, and that the implicit regulation block is not interfered with by the explicit

feedback) was designed to induce depressive emotions in participants [34, 37]. These two tasks were split into four alternately-presented mini-tasks to ensure the effect of priming (Fig. 1B).

In each trial of word-matching, participants chose one out of two optional words and matched its meaning to that of the target word. In the implicit regulation block, the target word and one of the optional words were reappraisal-related items, whereas, in the baseline and explicit regulation blocks, all three words were items unrelated to emotion-regulation. It was hypothesized that the process of matching two reappraisal-related words could activate the goal of regulating the subsequent emotional response through cognitive reappraisal, while matching two words unrelated to emotion-regulation did not influence emotion regulation.

In each trial of dot counting (Fig. 1C), a picture containing randomly-distributed dots was present for 400 ms, and participants were required to judge, within 3 s, whether the number of dots matched a given number presented on the right side of these dots. Then the outcome feedback was presented for 3 s, indicating correct (a green tick) or incorrect responses (a red cross). The outcome feedback was pseudo-randomly produced by the program, including 36 incorrect outcomes (valid trials) and 14 correct ones (fillers) in each block. Furthermore, subjects were also required, in the baseline and implicit reappraisal conditions, to pay close attention to the feedback and experience emotion naturally. In the explicit feedback, subjects were required to reinterpret the meanings of the negative feedback to down-regulate unpleasant emotions, such as “the picture duration and time of answering are both too short, and other people may not answer correctly as well”. To ensure that all participants understood and could follow the instructions without difficulty, they were given enough time to practice reappraising

emotion regulation instructions. **B** Task order in each block. **C** An exemplar trial containing negative feedback in the dot-counting task. The requirement of emotion rating appears every 10 trials and participants report their emotions on a scale of 1–9. RT, response time.

the sample pictures. Also, they were required to explain the explicit instructions before the explicit block. Experimenters reviewed the verbal response of each participant to ensure that they implemented an intended process of cognitive reappraisal.

Lastly, the “emotion rating” requirement was presented in every 10 trials following feedback, during which participants reported their emotions on a 1–9-point scale (1 denotes most unpleasant and 9 denotes most pleasant feelings) by clicking the mouse. There were 5 emotion rating requirements per block, of which 4 followed incorrect (valid) and 1 followed correct feedback (the filler).

A brief interview was conducted after the task to find out how participants felt when they received negative feedback. As a result, 92% (145/159) of participants reported they felt regretful or sad, and the other 8% of participants mentioned that they felt angry besides regretful/sad.

Electroencephalogram (EEG) and emotion rating data were collected during the dot-counting task. We used 20 reappraisal and 70 neutral idioms/phrases in the word-matching task [32, 38, 40]. The reappraisal items had meanings highly related to cognitive reappraisal, while the neutral items did not imply emotion regulation including cognitive reappraisal (Part C of Supplementary Material).

EEG Recording and Analysis

Brain electrical activity was recorded by a 32-channel wireless amplifier with a sampling frequency of 250 Hz (NeuSen. W32, Neuracle, Changzhou, China). Data were recorded on-line referentially against the left mastoid and off-line referenced to the average of the left and right mastoids. The recorded data were then filtered off-line (0.01–20 Hz) and segmented beginning 200 ms prior to outcome presentation

and lasting for 3.5 s. Epochs were baseline-corrected (−200 to 0 ms) followed by averaging in each condition.

This study focused on the frontal P3 and parietal LPP components. The frontal P3 was measured as the average amplitude across the electrode sites at and around FCz (FC1, FC2, Fz, F3, and F4). An *a priori* time window for the P3 amplitude (300–600 ms after outcome onset) was chosen according to previous literature [68, 69]. The parietal LPP was measured as the average amplitude across the electrode sites at and around Pz (P3, P4, Pz, CP1, and CP2). An *a priori* time window for the LPP amplitude was chosen according to previous literature [49, 51, 70]. This window began at the end of the typical P3 time window and lasted for the entire emotional regulation period (500–3000 ms after outcome onset).

Results

Subjective ratings of emotional feelings and the event-related potential (ERP) amplitudes were analyzed only in “incorrect” trials. A full report of results is in Supplementary Material Part D. Here we only report the most important findings.

Emotion Rating

Repeated-measures analyses of variances (ANOVA, Greenhouse-Geisser-corrected) revealed significant main effects of the group [$F_{(2, 156)} = 11.6, P < 0.001, \eta_p^2 = 0.129$; patient < control/SD] and condition [$F_{(2, 312)} = 297.2, P < 0.001, \eta_p^2 = 0.656$; explicit > implicit > baseline] and significant interaction of condition \times group [$F_{(4, 312)} = 26.5, P < 0.001, \eta_p^2 = 0.253$; Fig. 2A]. Simple effect analysis (Bonferroni method) revealed that the emotion rating differed across groups in the explicit regulation condition [$F_{(2, 156)} = 54.1, P < 0.001, \eta_p^2 =$

0.410; patient < SD < control, all pairwise $P < 0.001$]. However, the emotion rating did not show a significant difference across groups in the baseline [$F_{(2, 156)} = 0.6, P = 0.544, \eta_p^2 = 0.008$] and implicit regulation conditions [$F_{(2, 156)} = 1.6, P = 0.205, \eta_p^2 = 0.020$]. Alternatively, we also examined the interaction by testing the condition effect in different groups (Fig. 2B; see Supplementary Materials).

Parietal LPP Amplitude

ANOVA tests showed significant main effects of group [$F_{(2, 156)} = 4.3, P = 0.015, \eta_p^2 = 0.052$; patient > control] and condition [$F_{(2, 312)} = 85.3, P < 0.001, \eta_p^2 = 0.353$; baseline > implicit/explicit] and significant interaction of condition \times group [$F_{(4, 312)} = 13.6, P < 0.001, \eta_p^2 = 0.148$; Fig. 3A]. Simple effect analysis reveals that the LPP amplitudes differed across groups in the explicit regulation condition [$F_{(2, 156)} = 16.0, P < 0.001, \eta_p^2 = 0.170$; patient > SD/control, pairwise $P < 0.001$]. However, the LPP amplitudes did not show a significant difference across groups in the baseline [$F_{(2, 156)} = 1.5, P = 0.230, \eta_p^2 = 0.019$] and implicit regulation conditions [$F_{(2, 156)} = 0.1, P = 0.942, \eta_p^2 = 0.001$]. Alternatively, we also examined the interaction by testing the condition effect in different groups, which indicated that while the healthy group achieved the best emotion regulation effect by explicit reappraisal, the patients had an optimal regulatory effect by implicit reappraisal (Fig. 3B).

Frontal P3 Amplitude

ANOVA tests revealed significant main effect of condition [$F_{(2, 312)} = 19.0, P < 0.001, \eta_p^2 = 0.108$; explicit > baseline/implicit] and interaction of condition \times group [$F_{(4, 312)} = 7.2, P < 0.001, \eta_p^2 = 0.085$; Fig. 4A]. Simple effect analysis revealed that the P3 amplitudes differed across groups in the

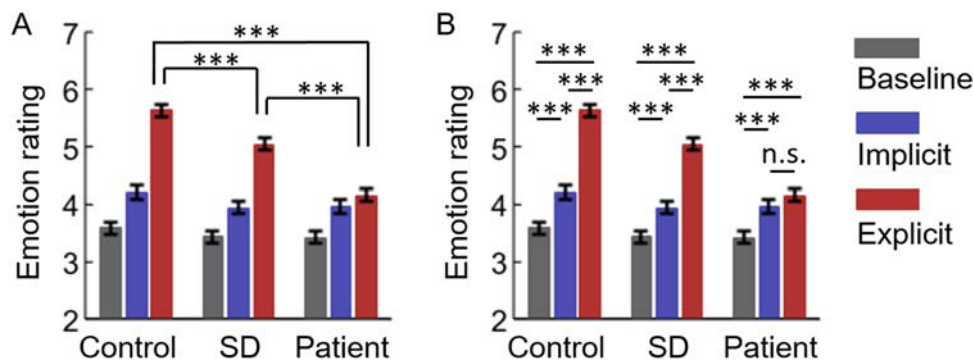
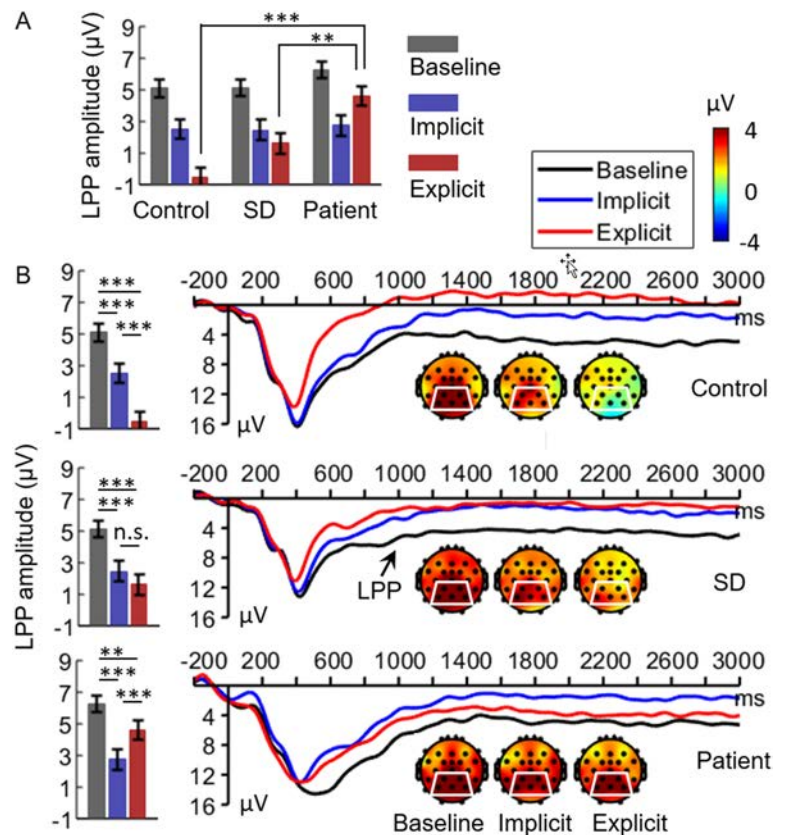


Fig. 2 Subjective emotion ratings. **A** Emotion ratings compared between groups. **B** Emotion ratings within each group. SD, sub-threshold depression; implicit, implicit reappraisal; explicit, explicit reappraisal. Error bars, 2 \times SEM. *** $P < 0.001$; n.s., no significant

difference, Repeated-measures ANOVA tests were applied to the subjective rating, and Greenhouse-Geisser correction for the ANOVA tests was used whenever appropriate ($n = 159$).

Fig. 3 The parietal late positive potential (LPP). **A** Amplitudes of the LPP compared between groups. **B** Waveforms, topographies, and amplitudes of the LPP within each group. ERP waveforms are averaged across electrodes Pz, P3, P4, CP1, and CP2 (white trapezoid). ERP topographies are averaged across a time window of 500–3000 ms after outcome onset. Error bars, $2 \times \text{SEM}$. $**P < 0.01$, $***P < 0.001$; n.s., no significant difference. Repeated-measures ANOVA tests were applied to the parietal LPP, and Greenhouse-Geisser correction for the ANOVA tests was used whenever appropriate ($n = 159$).



explicit regulation condition [$F_{(2, 156)} = 4.8$, $P = 0.009$, $\eta_p^2 = 0.058$; patient < control/SD]. However, the P3 amplitudes did not show a significant difference across groups in the baseline [$F_{(2, 156)} = 0.3$, $P = 0.757$, $\eta_p^2 = 0.004$] and implicit regulation conditions [$F_{(2, 156)} = 0.0$, $P = 0.943$, $\eta_p^2 = 0.001$]. Alternatively, we also examined the interaction by testing the condition effect in different groups, which suggested that the explicit regulation-related enhancement of frontal P3 amplitudes in the control and SD groups was absent in the patients (Fig. 4B).

Correlations

Frontal P3 amplitudes were negatively correlated with parietal LPP amplitudes during explicit reappraisal ($r = -0.226$) but not under baseline or implicit conditions. While emotional ratings negatively predict LPP amplitudes under implicit and baseline conditions, they had limited or no predictive ability for the LPP amplitudes during explicit regulation in depressed individuals (Table 2). The emotion ratings in the explicit regulation condition were negatively correlated with BDI-II ($r = -0.565$) and STAI-T scores ($r = -0.392$), but positively correlated with ERQ-R ($r = 0.280$) and TCQ-R scores ($r = 0.294$). The LPP amplitudes in the explicit regulation condition were positively correlated with

the BDI-II scores ($r = 0.248$). See Supplementary Material for details.

Discussion

Impaired emotion regulation plays a pivotal role in the development and maintenance of depressive disorders [1, 11]. To explore methods that may compensate for the emotion-regulatory deficits in depression, we compared the emotion regulation effects between explicit and implicit reappraisal in healthy, subclinical depression, and MDD populations. The results showed depressive patients had a better emotion regulation effect *via* implicit relative to explicit reappraisal, as shown by the LPP amplitudes in brain potentials, indicating the implicit form of reappraisal is more effective for depressive patients to achieve desirable emotion regulation.

Previous studies have shown that explicit reappraisal of negative events can effectively reduce emotion intensity [58, 71–73]. Consistent with these findings, our results demonstrated that, upon negative feedback, explicit reappraisal produced more positive emotion ratings and reduced LPP amplitudes compared to the baseline condition across the three groups. However, the utility of explicit reappraisal in regulating negative emotion showed a downward change depending on the severity of depression. This pattern was

Fig. 4 The frontal P3. **A** Amplitudes of the P3, compared between groups. **B** Waveforms, topographies, and amplitudes of the P3 within each group. ERP waveforms are averaged across electrodes FCz, FC1, FC2, Fz, F3, and F4 (white trapezoid). ERP topographies are averaged across a time window of 300–600 ms after outcome onset. Error bars, 2× SEM. **P* < 0.05, ***P* < 0.01, ****P* < 0.001. Repeated-measures ANOVA tests were applied to the frontal P3, and Greenhouse-Geisser correction for the ANOVA tests was used whenever appropriate (*n* = 159).

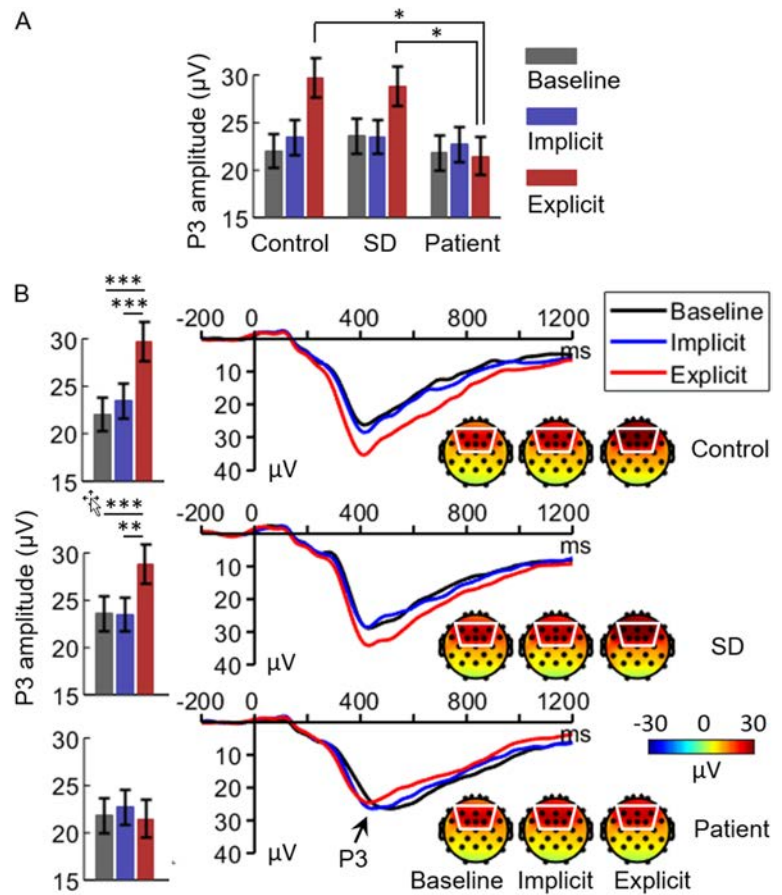


Table 2 Correlation statistics between LPP amplitudes and subjective ratings

Condition	Control (<i>n</i> = 54)			Subthreshold (<i>n</i> = 52)			Patient (<i>n</i> = 53)		
	<i>r</i>	<i>P</i>	<i>P</i> _{cor} ^a	<i>r</i>	<i>P</i>	<i>P</i> _{cor} ^a	<i>r</i>	<i>P</i>	<i>P</i> _{cor} ^a
Baseline	-0.501	<0.001	<0.001	-0.496	<0.001	0.001	-0.492	<0.001	<0.001
Implicit	-0.456	0.001	0.002	-0.523	<0.001	<0.001	-0.501	0.001	<0.001
Explicit	-0.358	0.008	0.024	-0.180	0.201		-0.104	0.459	

^aCorrected using the Holm’s stepwise method.

also evident in the correlations showing the higher the BDI scores, the larger the LPP amplitudes and more negative the emotion rating specific to explicit regulation. These results are in line with earlier findings that cognitive and behavioral correlates of depression do not change qualitatively but differ quantitatively along a continuum of mild, moderate, and severe depression [74, 75]. Also, these results are supported by prior reports that depressed patients have deficits in emotion regulation through the explicit use of regulatory strategies [1, 11, 15].

Many studies have established that explicit emotion regulation relies on a top-down cognitive control mechanism, which entails a substantial involvement of cognitive resources [23–25]. However, depressed patients are known for the depletion of cognitive resources by depressive

symptoms and then for impaired cognitive functions [17–20, 76, 77]. In addition, several functional magnetic resonance imaging (fMRI) studies and meta-analyses have consistently shown that depressed individuals have reduced activation of cognitive-control-related brain regions, resulting in an enhanced amygdala response during explicit reappraisal [1, 2, 15, 16, 78]. Consistent with these findings, our analysis of frontal P3, a component considered to tap into the cognitive control process in emotion regulation [55, 56], showed larger amplitudes in explicit compared to the other two conditions in healthy control and subthreshold groups but not in MDD patients, which confirms the deficits of cognitive control in depression as reported by prior studies [17–22]. The role of the cognitive control deficit in the patients’ reappraisal difficulty was further supported by our finding of a negative

correlation between frontal P3 and parietal LPP amplitudes specific to the explicit reappraisal condition.

Unlike explicit emotion regulation, we found a stable emotion-regulatory effect of implicit reappraisal in LPPs and emotion ratings across the healthy control, subclinical, and patient groups. Many studies have shown that implicit regulation of negative emotion is achieved with little involvement of cognitive control resources [29–31, 79]. Once primed, implicit emotion regulation occurs and functions automatically during the presentation of emotional events, without the need for effortful control [26]. Several fMRI studies have demonstrated that implicit emotion regulation effectively reduces amygdala activation without increased activity in the frontoparietal cognitive control regions [26, 79]. Consistent with these findings, in the current study we did not show any differences between implicit and baseline conditions in frontal P3 amplitudes. Little requirement of effortful control most likely explains our finding that implicit reappraisal significantly reduced subjective emotion and LPP amplitudes, unaffected by the symptoms of depression across the three groups.

It is worth noting that the optimal regulatory method varied significantly with the level of depression, in that explicit emotion regulation generated the largest regulatory effect in the controls but implicit emotion regulation produced the largest regulatory effect in the patients. One explanation is that, unlike depression, controls have intact cognitive control functions for explicit emotion regulation. Indeed, quite a few studies have shown that healthy people tend to use cognitive reappraisal preferentially for the regulation of negative emotions elicited by daily-life stimuli [54, 80]. By contrast, due to cognitive resource depletion, patients are unable to use explicit cognitive reappraisal to effectively regulate negative emotions [1, 76, 77]. However, implicit emotion regulation has the advantage that it does not require the online mobilization of cognitive resources to achieve the goal of emotion regulation [29–31]. More relevant to the current work, a recent study demonstrated that implicit priming of attention distraction is more efficient than explicit attention distraction in regulating frustration-induced emotion in depressed, but not healthy, individuals [34]. Consistent with these studies, our results revealed that implicit reappraisal is more effective for reducing negative emotion in depressed patients than explicit reappraisal as indicated by the LPP amplitudes.

It should be noted that the emotion-regulation effects were inconsistent between emotion ratings and LPP amplitudes in the subclinical and patient groups. Specifically, we found a lower negative emotion rating for explicit compared to implicit conditions, but the two conditions produced a similar emotion regulation effect in LPP amplitudes, in the subclinical group. Meanwhile, the patients showed a similar emotion rating during explicit and implicit regulation (both less negative than baseline), but they exhibited significantly

smaller LPP amplitudes during implicit than explicit reappraisal. Participants received explicit instructions of reappraisal to reduce negative emotion upon negative feedback in the explicit but not the implicit condition. Therefore, emotion ratings in the explicit regulation condition may be susceptible to social desirability or self-anticipation that is absent during the implicit condition [42–44]. Consistent with this inference, the patient and subclinical groups showed significant correlations between LPP amplitudes and emotion ratings in the baseline and implicit conditions but not in the explicit condition (Table 2). Therefore, the electrophysiological index of LPP amplitudes can be considered a more reliable, objective indicator of emotion regulation effects than the emotion ratings.

Finally, it is notable that, in the current study we manipulated a dot counting task with negative feedback to induce negative emotions because this scenario simulated well real frustration in daily life [37] so as to enhance the ecological validity of this study. Unlike our manipulation, many previous studies assessed the effect of implicit emotion regulation using other stimulus types (e.g., affective pictures and film clips) to induce negative emotions such as anger and sadness in participants [39, 81]. Both these studies and the current one consistently demonstrated that various unpleasant feelings can be ameliorated by implicit emotion regulation.

To sum up, in this study we revealed that, compared with healthy subjects, depressed individuals have impaired emotion regulation through explicit reappraisal, and this impairment increases with the severity of depression. More importantly, we further revealed that the implicit form of emotion regulation is reliable and independent of depressive symptoms. This has important clinical implications for the cognitive intervention in depression through implicit emotion-regulation methods, considering the high rate of dropout when a traditional, explicit form of cognitive-behavior therapy is used [82, 83]. However, these conclusions are primarily based on the measurement of LPP amplitudes evoked by immediate frustrating feedback. Also, we used single-session, short-term priming to establish implicit emotion regulation. Therefore, how to translate the current finding into a long-term, sustainable effect of depression intervention needs to be explored in future studies, probably by establishing multiple-session protocols.

Acknowledgments This work was supported by the National Natural Science Foundation of China (31970980 and 31920103009), the Major Project of National Social Science Foundation (20&ZD153), the Shenzhen-Hong Kong Institute of Brain Science (2019SHIBS0003), and the Guangdong Key Project (2018B030335001).

Conflict of interest Authors declare no conflicts of interest in this study.

References

1. Joormann J, Stanton CH. Examining emotion regulation in depression: A review and future directions. *Behav Res Ther* 2016, 86: 35–49.
2. Park C, Rosenblat JD, Lee Y, Pan Z, Cao B, Iacobucci M. The neural systems of emotion regulation and abnormalities in major depressive disorder. *Behav Brain Res* 2019, 367: 181–188.
3. Vanderlind WM, Millgram Y, Baskin-Sommers AR, Clark MS, Joormann J. Understanding positive emotion deficits in depression: From emotion preferences to emotion regulation. *Clin Psychol Rev* 2020, 76: 101826.
4. Aldao A, Nolen-Hoeksema S, Schweizer S. Emotion-regulation strategies across psychopathology: A meta-analytic review. *Clin Psychol Rev* 2010, 30: 217–237.
5. Hamilton JP, Farmer M, Fogelman P, Gotlib IH. Depressive rumination, the default-mode network, and the dark matter of clinical neuroscience. *Biol Psychiatry* 2015, 78: 224–230.
6. Liu DY, Gilbert KE, Thompson RJ. Emotion differentiation moderates the effects of rumination on depression: A longitudinal study. *Emotion* 2020, 20: 1234–1243.
7. Nolen-Hoeksema S, Wisco BE, Lyubomirsky S. Rethinking rumination. *Perspect Psychol Sci* 2008, 3: 400–424.
8. Schäfer JÖ, Naumann E, Holmes EA, Tuschen-Caffier B, Samson AC. Emotion regulation strategies in depressive and anxiety symptoms in youth: A meta-analytic review. *J Youth Adolesc* 2017, 46: 261–276.
9. Sloan E, Hall K, Moulding R, Bryce S, Mildred H, Staiger PK. Emotion regulation as a transdiagnostic treatment construct across anxiety, depression, substance, eating and borderline personality disorders: A systematic review. *Clin Psychol Rev* 2017, 57: 141–163.
10. Zhou HX, Chen X, Shen YQ, Li L, Chen NX, Zhu ZC, *et al.* Rumination and the default mode network: Meta-analysis of brain imaging studies and implications for depression. *Neuroimage* 2020, 206: 116287.
11. Liu DY, Thompson RJ. Selection and implementation of emotion regulation strategies in major depressive disorder: An integrative review. *Clin Psychol Rev* 2017, 57: 183–194.
12. Figueroa CA, DeJong H, Mocking RJT, Fox E, Rive MM, Schene AH, *et al.* Attentional control, rumination and recurrence of depression. *J Affect Disord* 2019, 256: 364–372.
13. He Z, Liu Z, Zhao J, Elliott R, Zhang D. Improving emotion regulation of social exclusion in depression-prone individuals: A tDCS study targeting right VLPFC. *Psychol Med* 2020, 50: 2768–2779.
14. Stephanou K, Davey CG, Kerestes R, Whittle S, Harrison BJ. Hard to look on the bright side: Neural correlates of impaired emotion regulation in depressed youth. *Soc Cogn Affect Neurosci* 2017, 12: 1138–1148.
15. Rive MM, van Rooijen G, Veltman DJ, Phillips ML, Schene AH, Ruhé HG. Neural correlates of dysfunctional emotion regulation in major depressive disorder. A systematic review of neuroimaging studies. *Neurosci Biobehav Rev* 2013, 37: 2529–2553.
16. Zilverstand A, Parvaz MA, Goldstein RZ. Neuroimaging cognitive reappraisal in clinical populations to define neural targets for enhancing emotion regulation. A systematic review. *Neuroimage* 2017, 151: 105–116.
17. Rock PL, Roiser JP, Riedel WJ, Blackwell AD. Cognitive impairment in depression: A systematic review and meta-analysis. *Psychol Med* 2014, 44: 2029–2040.
18. Quinn ME, Stange JP, Jenkins LM, Corwin S, DelDonno SR, Bessette KL, *et al.* Cognitive control and network disruption in remitted depression: A correlate of childhood adversity. *Soc Cogn Affect Neurosci* 2018, 13: 1081–1090.
19. Snyder HR. Major depressive disorder is associated with broad impairments on neuropsychological measures of executive function: A meta-analysis and review. *Psychol Bull* 2013, 139: 81–132.
20. Vilgis V, Silk TJ, Vance A. Executive function and attention in children and adolescents with depressive disorders: A systematic review. *Eur Child Adolesc Psychiatry* 2015, 24: 365–384.
21. Holmes AJ, Pizzagalli DA. Spatiotemporal dynamics of error processing dysfunctions in major depressive disorder. *Arch Gen Psychiatry* 2008, 65: 179–188.
22. Shao R, Liu HL, Huang CM, Chen YL, Gao M, Lee SH, *et al.* Loneliness and depression dissociated on parietal-centered networks in cognitive and resting states. *Psychol Med* 2020, 50: 2691–2701.
23. Morawetz C, Bode S, Baudewig J, Jacobs AM, Heekeren HR. Neural representation of emotion regulation goals. *Hum Brain Mapp* 2016, 37: 600–620.
24. Ochsner KN, Gross JJ. The cognitive control of emotion. *Trends Cogn Sci* 2005, 9: 242–249.
25. Pruessner L, Barnow S, Holt DV, Joormann J, Schulze K. A cognitive control framework for understanding emotion regulation flexibility. *Emotion* 2020, 20: 21–29.
26. Zhang Y, Chen S, Deng Z, Yang J, Yuan J. Benefits of implicit regulation of instructed fear: Evidence from neuroimaging and functional connectivity. *Front Neurosci* 2020, 14: 201.
27. Yoon S, Rottenberg J. Why do people with depression use faulty emotion regulation strategies? *Emot Rev* 2020, 12: 118–128.
28. Etkin A, Büchel C, Gross JJ. The neural bases of emotion regulation. *Nat Rev Neurosci* 2015, 16: 693–700.
29. Gyurak A, Gross JJ, Etkin A. Explicit and implicit emotion regulation: A dual-process framework. *Cogn Emot* 2011, 25: 400–412.
30. Koole SL, Rothermund K. “I feel better but I don’t know why”: The psychology of implicit emotion regulation. *Cogn Emot* 2011, 25: 389–399.
31. Mauss IB, Bunge SA, Gross JJ. Automatic emotion regulation. *Soc Pers Psychol Compass* 2007, 1: 146–167.
32. Yang Q, Tang P, Gu R, Luo W, Luo Y. Implicit emotion regulation affects outcome evaluation. *Soc Cogn Affect Neurosci* 2015, 10: 824–831.
33. Gao W, Chen S, Long Q, Yang J, Yuan J. The progress of emotion regulation methods and paradigms: From voluntary emotion regulation to automatic emotion regulation. *Chin Sci Bull* 2018, 63: 415–424.
34. Li H, Yuan J. The emotion regulation effect of unconscious distraction on the subclinical depression. *Chin Sci Bull* 2018, 63: 2057–2070.
35. Vohs KD, Heatherton TF. Self-regulatory failure: A resource-depletion approach. *Psychol Sci* 2000, 11: 249–254.
36. Braunstein LM, Gross JJ, Ochsner KN. Explicit and implicit emotion regulation: A multi-level framework. *Soc Cogn Affect Neurosci* 2017, 12: 1545–1557.
37. Ding N, Yang J, Liu Y, Yuan J. Paying less but harvesting more: The effect of unconscious acceptance in regulating frustrating emotion. *Sci China Life Sci* 2015, 58: 799–809.
38. Hoid D, Pan DN, Wang Y, Li X. Implicit emotion regulation deficits in individuals with high schizotypal traits: An ERP study. *Sci Rep* 2020, 10: 3882.
39. Mauss IB, Cook CL, Gross JJ. Automatic emotion regulation during anger provocation. *J Exp Soc Psychol* 2007, 43: 698–711.
40. Wang Y, Li X. Temporal course of implicit emotion regulation during a Priming-Identify task: An ERP study. *Sci Rep* 2017, 7: 41941.
41. Yuan J, Long Q, Li X, Deng Z, Ma B, Chen S, *et al.* Regulatory effect of implicit acceptance during outcome evaluation: The temporal dynamics in an event-related potential study. *Int J Psychophysiol* 2019, 141: 37–44.

42. Voudouris NJ, Peck CL, Coleman G. Conditioned response models of placebo phenomena: Further support. *Pain* 1989, 38: 109–116.
43. Montgomery GH, Kirsch I. Classical conditioning and the placebo effect. *Pain* 1997, 72: 107–113.
44. Colagiuri B, Schenk LA, Kessler MD, Dorsey SG, Colloca L. The placebo effect: From concepts to genes. *Neuroscience* 2015, 307: 171–190.
45. Hajcak G, Klawohn J, Meyer A. The utility of event-related potentials in clinical psychology. *Annu Rev Clin Psychol* 2019, 15: 71–95.
46. Helfrich RF, Knight RT. Cognitive neurophysiology: Event-related potentials. *Handb Clin Neurol* 2019, 160: 543–558.
47. Hajcak G, MacNamara A, Olvet DM. Event-related potentials, emotion, and emotion regulation: An integrative review. *Dev Neuropsychol* 2010, 35: 129–155.
48. Liu Y, Huang H, McGinnis-Deweese M, Keil A, Ding M. Neural substrate of the late positive potential in emotional processing. *J Neurosci* 2012, 32: 14563–14572.
49. Zhao J, Mo L, Bi R, He Z, Chen Y, Xu F, *et al.* The VLPFC versus the DLPFC in downregulating social pain using reappraisal and distraction strategies. *J Neurosci* 2021, 41: 1331–1339.
50. He Z, Zhao J, Shen J, Muhlert N, Elliott R, Zhang D. The right VLPFC and downregulation of social pain: A TMS study. *Hum Brain Mapp* 2020, 41: 1362–1371.
51. Schönfelder S, Kanske P, Heissler J, Wessa M. Time course of emotion-related responding during distraction and reappraisal. *Soc Cogn Affect Neurosci* 2014, 9: 1310–1319.
52. Kennedy H, Montreuil TC. The late positive potential as a reliable neural marker of cognitive reappraisal in children and youth: A brief review of the research literature. *Front Psychol* 2021, 11: 608522.
53. Chen S, Yu K, Yang J, Yuan J. Automatic reappraisal-based implementation intention produces early and sustainable emotion regulation effects: Event-related potential evidence. *Front Behav Neurosci* 2020, 14: 89.
54. Shafir R, Schwartz N, Blechert J, Sheppes G. Emotional intensity influences pre-implementation and implementation of distraction and reappraisal. *Soc Cogn Affect Neurosci* 2015, 10: 1329–1337.
55. Moser JS, Hartwig R, Moran TP, Jendrusina AA, Kross E. Neural markers of positive reappraisal and their associations with trait reappraisal and worry. *J Abnorm Psychol* 2014, 123: 91–105.
56. Yuan J, Long Q, Ding N, Lou Y, Liu Y, Yang J. Suppression dampens unpleasant emotion faster than reappraisal: Neural dynamics in a Chinese sample. *Sci China Life Sci* 2015, 58: 480–491.
57. Bernat EM, Cadwallader M, Seo D, Vizueta N, Patrick CJ. Effects of instructed emotion regulation on valence, arousal, and attentional measures of affective processing. *Dev Neuropsychol* 2011, 36: 493–518.
58. Webb TL, Miles E, Sheeran P. Dealing with feeling: A meta-analysis of the effectiveness of strategies derived from the process model of emotion regulation. *Psychol Bull* 2012, 138: 775–808.
59. Beck AT. The current state of cognitive therapy: A 40-year retrospective. *Arch Gen Psychiatry* 2005, 62: 953–959.
60. May JM, Richardi TM, Barth KS. Dialectical behavior therapy as treatment for borderline personality disorder. *Ment Health Clin* 2016, 6: 62–67.
61. American Psychiatric Association. *Diagnostic and Statistical Manual of Mental Disorders—(DSM-IV)*, 4th edn American Psychiatric Publishing Inc, Washington D.C., 1994.
62. First MB, Spitzer RL, Gibbon M, Williams JBW. *Structured Clinical Interview for DSM-IV-TR Axis I Disorders, Research Version, Patient Edition With Psychotic Screen (SCID-I/P W/ PSY SCREEN)*. New York State Psychiatric Institute, New York, 2002.
63. First MB, Spitzer RL, Gibbon M, Williams JBW. *Structured Clinical Interview for DSM-IV-TR Axis I Disorders, Research Version, Non-Patient Edition (SCID-I/NP)*. New York State Psychiatric Institute, New York, 2002.
64. Beck AT, Steer RA, Brown GK. *Manual for the Beck Depression Inventory-II*. Psychological Corporation, San Antonio, TX, 1996.
65. Spielberger CD, Gorsuch RL, Lushene RE, Vagg PR, Jacobs GA. *Manual for the State-Trait Anxiety Inventory (Form Y1–Y2)*. Consulting Psychologist Press, Palo Alto, CA, 1983.
66. Gross JJ, John OP. Individual differences in two emotion regulation processes: Implications for affect, relationships, and well-being. *J Pers Soc Psychol* 2003, 85: 348–362.
67. Wells A, Davies MI. The Thought Control Questionnaire: A measure of individual differences in the control of unwanted thoughts. *Behav Res Ther* 1994, 32: 871–878.
68. Neuhaus AH, Urbanek C, Opgen-Rhein C, Hahn E, Ta TM, Koehler S, *et al.* Event-related potentials associated with attention network test. *Int J Psychophysiol* 2010, 76: 72–79.
69. Munro GES, Dywan J, Harris GT, McKee S, Unsal A, Segalowitz SJ. Response inhibition in psychopathy: The frontal N2 and P3. *Neurosci Lett* 2007, 418: 149–153.
70. Paul S, Simon D, Endrass T, Kathmann N. Altered emotion regulation in obsessive-compulsive disorder as evidenced by the late positive potential. *Psychol Med* 2016, 46: 137–147.
71. Dörfel D, Lamke JP, Hummel F, Wagner U, Erk S, Walter H. Common and differential neural networks of emotion regulation by Detachment, Reinterpretation, Distraction, and Expressive Suppression: A comparative fMRI investigation. *NeuroImage* 2014, 101: 298–309.
72. Gross JJ. Emotion regulation: Current status and future prospects. *Psychol Inq* 2015, 26: 1–26.
73. Troy AS, Shallcross AJ, Brunner A, Friedman R, Jones MC. Cognitive reappraisal and acceptance: Effects on emotion, physiology, and perceived cognitive costs. *Emotion* 2018, 18: 58–74.
74. Bradley BP, Mogg K, Millar N. Implicit memory bias in clinical and non-clinical depression. *Behav Res Ther* 1996, 34: 865–879.
75. Flett GL, Vredenburg K, Krames L. The continuity of depression in clinical and nonclinical samples. *Psychol Bull* 1997, 121: 395–416.
76. Harvey PO, Fossati P, Pochon JB, Levy R, Lebastard G, Léhéricy S, *et al.* Cognitive control and brain resources in major depression: An fMRI study using the n-back task. *Neuroimage* 2005, 26: 860–869.
77. Nebes RD, Butters MA, Mulsant BH, Pollock BG, Zmuda MD, Houck PR, *et al.* Decreased working memory and processing speed mediate cognitive impairment in geriatric depression. *Psychol Med* 2000, 30: 679–691.
78. Picó-Pérez M, Radua J, Steward T, Menchón JM, Soriano-Mas C. Emotion regulation in mood and anxiety disorders: A meta-analysis of fMRI cognitive reappraisal studies. *Prog Neuro Psychopharmacol Biol Psychiatry* 2017, 79: 96–104.
79. Chen S, Ding N, Wang F, Li Z, Qin S, Biswal BB, *et al.* Functional decoupling of emotion coping network subsides automatic emotion regulation by implementation intention. *Neural Plast* 2021, 2021: 6639739.
80. Sheppes G, Scheibe S, Suri G, Gross JJ. Emotion-regulation choice. *Psychol Sci* 2011, 22: 1391–1396.

81. Wyczesany M, Adamczyk AK, Ligeza TS, Bereś A, Marchewka A. Implicit induction of emotional control—a comparative fMRI investigation of self-control and reappraisal goal pursuit. *Emotion* 2021, 21: 1379–1391.
82. Cuijpers P, van Straten A, Andersson G, van Oppen P. Psychotherapy for depression in adults: A meta-analysis of comparative outcome studies. *J Consult Clin Psychol* 2008, 76: 909–922.
83. Weissman MM. Cognitive therapy and interpersonal psychotherapy: 30 years later. *Am J Psychiatry* 2007, 164: 693–696.

Springer Nature or its licensor (e.g. a society or other partner) holds exclusive rights to this article under a publishing agreement with the author(s) or other rightsholder(s); author self-archiving of the accepted manuscript version of this article is solely governed by the terms of such publishing agreement and applicable law.

Different Regional Patterns in Gray Matter-based Age Prediction

Nianming Zuo^{1,2,3,4}  · Tianyu Hu^{1,2,3} · Hao Liu^{1,2,3} ·
Jing Sui^{1,2,3,5} · Yong Liu^{1,2,3,5}  · Tianzi Jiang^{1,2,3,4,5,6,7} 

Received: 16 September 2022 / Accepted: 11 November 2022 / Published online: 13 January 2023

© Center for Excellence in Brain Science and Intelligence Technology, Chinese Academy of Sciences 2023

Dear Editor,

The brain experiences ongoing changes across different ages to support brain development and functional reorganization. During the span of adulthood, although the brain has matured from a neurobiological perspective, it is still continuously shaped by external factors such as living habit, family setting, socioeconomic status, and working environment [1]. In contrast to chronological age (CA), brain (or biological) age (BA) is conceptualized as an important index for characterizing the aging process and neuropsychological state, as well as individual cognitive performance. Growing evidence indicates that BA can be assessed by neuroimaging techniques, including MRIs [2]. Due to their short collection time, stable image features, and (usual) availability during clinical diagnosis, T1-weighted MRIs are considered the first choice for estimating BA, with structural features including

local/global volumes of gray matter (GM) and white matter (WM), geometrical characteristics of the cerebral cortex, and distinctions between GM and WM at the boundary [3].

There are two elusive questions in T1-weighted MRI-based BA prediction. The first question is how to improve prediction accuracy and retain fewer parameters. At present, research is either limited by relatively poor accuracy [4] or by incomplete age-span datasets. So deep learning and lifespan datasets are gradually becoming popular in this field. A clear drawback of current deep learning methodologies is that they are less concerned with model scale and number of parameters. Recent application of a global-local transformer to BA estimation achieved a mean absolute error (MAE) of 2.70 for 8379 subjects (age range 0–97 years), but the number of parameters reached 20.41 million [5]. Too many parameters mean a greater computing burden, lower training efficiency, weaker generalization performance, and considerable memory occupation, making the model less device-friendly. The second question is how to understand the neurobiological principles in age prediction. Although

Nianming Zuo and Tianyu Hu contributed equally to this work.

This study is a corrected version of a retracted article (Zuo N, Hu T, Liu H, Sui J, Liu Y, Jiang T. RETRACTED ARTICLE: Gray matter-based age prediction characterizes different regional patterns. *Neurosci Bull* 2021, 37: 94–98. doi: 10.1007/s12264-020-00558-8).

Supplementary Information The online version contains supplementary material available at <https://doi.org/10.1007/s12264-022-01016-3>.

✉ Nianming Zuo
nmzuo@nlpr.ia.ac.cn

¹ Brainnetome Center, Institute of Automation, Chinese Academy of Sciences, Beijing 100190, China

² National Laboratory of Pattern Recognition, Institute of Automation, Chinese Academy of Sciences, Beijing 100190, China

³ University of Chinese Academy of Sciences, Beijing 100190, China

⁴ Chinese Institute for Brain Research, Beijing 102206, China

⁵ CAS Center for Excellence in Brain Science and Intelligence Technology, Institute of Automation, Chinese Academy of Sciences, Beijing 100190, China

⁶ Key Laboratory for NeuroInformation of the Ministry of Education, School of Life Science and Technology, University of Electronic Science and Technology of China, Chengdu 625014, China

⁷ Queensland Brain Institute, University of Queensland, Brisbane, QLD 4072, Australia

both structural and functional differences between male and female brains are increasingly reported and manifest in the aging trajectory [6] as characterized by MRI T1 images, whether there are gender and age effects of brain regions on age prediction remains less examined.

In this study, we propose an effective and lightweight age prediction model using structural MRI and deep learning, which improves accuracy and achieves an MAE of 3.24 years for a multi-site dataset (18–89 years) with 2.22 million parameters. The whole network structure is shown in Fig. 1. The feature extractor named Fork-SE was inspired by RepVGG [7], given its excellent performance in two-dimensional image tasks. Here, RepVGG was modified by replacing the convolutional blocks with three-dimensional versions and by adding squeeze-and-excitation (SE) blocks. The output of the feature extractor is called the feature vector. The classifier contains a dense neural network layer and

softmax function. The aim of the softmax function is to output a vector of probabilities representing the samples falling into bins of different ages. Therefore, for each sample, the probability vector and soft label can be used to compute Kullback–Leibler divergence loss. The soft label is the result of label smoothing, which means converting the chronological age label to a normal distribution with the mean equal to the scalar value. Using label smoothing, the BA prediction problem is transformed into a classification problem instead of a regression problem, which improves performance. Using label smoothing reduces the search space and guarantees the stability of the convergence, thus reducing the number of parameters required to achieve competitive accuracy.

In addition to the supervised learning paradigm described above, the metric learning paradigm was also

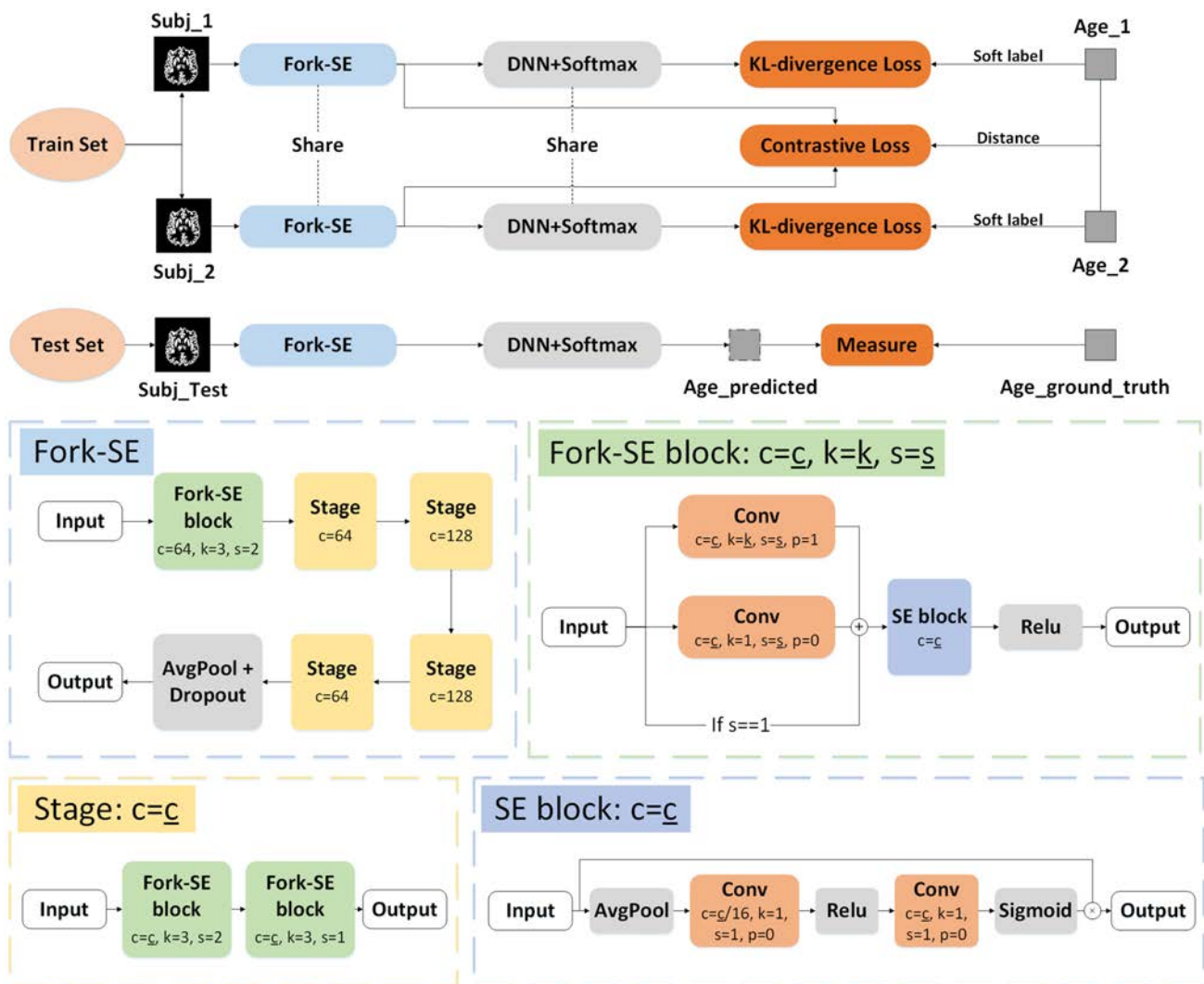


Fig. 1 Network structure of the brain age prediction model proposed in this study.

introduced into the model. See Supplementary Material for calculation details.

A multi-site dataset was used to evaluate the proposed algorithm. It consists of T1-weighted MRI data from 2007 usable participants (after removing unqualified data, including degraded images and those with excessive head motion) with an age range of 18–89 years. The Cam-CAN (Cambridge Centre for Ageing and Neuroscience) dataset [8], containing fluid intelligence records, was used for further analysis of cognitive ability. The prediction error (discrepancy between BA and CA) was estimated to determine its relationship with behavioral performance, i.e. fluid intelligence (abbreviated gF). In the Cam-CAN dataset, gF was assessed by the Cattell test, which contains four subtests of non-verbal puzzles involving series completion, classification, matrices, and conditions. Those participants scoring < 12 were designated as non-engaging and were thus removed (as suggested in the Cam-CAN data package). Therefore, 603 out of the 620 participants had valid gF records, where age = 52.72 ± 18.19 years and gF score = 32.35 ± 6.59 .

To demonstrate the effectiveness of the proposed model, a model ensemble was used. For each model, parameters were optimized based on the training set in the training phase. After each training epoch, the accuracy of the model evaluation set was recorded, while model hyperparameters were manually changed by restoring from a training checkpoint. When the accuracy of the previous model evaluation set could not be improved, a random seed was re-initialized to start training the next model. The above steps were repeated with GM and WM volumes as inputs to obtain five models based on GM volumes and five models based on WM volumes. Using a model ensemble, the testing set results of the 10 models were averaged. Results based on the multi-site dataset showed that the MAE for age prediction was 3.24 years *via* model ensemble (Fig. 2A, B and Table S2).

Furthermore, the prediction error (CA–BA) was significantly correlated with gF ($r = -0.31$, $P < 0.001$). A histogram of age residual is shown in Fig. S2. These results are in accordance with existing research that higher estimated age signifies greater cognitive processing efficiency [9], but they are not consistent with other studies. Thus, further investigations are needed. In addition, the prediction error should not be exclusively considered as an error caused by the age prediction model or system noise, but also should not be viewed as a biomarker of psychiatric disorders, a characterization of individual cognitive capability [9], or an indicator of neurodevelopmental health. Interestingly, moderation analysis (See Supplemental Materials) shows that prediction error is significantly correlated with gF, and this relationship is mainly from the influence of age prediction error at different age groups (because age itself is significantly correlated with gF; refer to Fig. S1).

Because the GM is the primary area for the execution of brain functions, we then focused on GM differences in different sex and age cohorts. For this, a model fully retrained on GM was constructed. A comparison of related GM-based models can be found in Table S3. Gradient-weighted Class Activation Mapping (Grad-CAM) [10] was used to obtain contribution maps of all samples from the constructed model above. Grad-CAM uses gradient backpropagation of the correct category as the weight to sum feature maps. To obtain more accurate voxel-level contributions, Grad-CAM was applied to the output of the first convolutional layer of the model (i.e., before the first SE block in Fig. 1).

The average contribution map of each GM region to the whole adult lifespan was obtained by averaging the contribution maps of all samples (Fig. 2C). The main contribution areas included the caudate nucleus, the edge of the orbito-frontal cortex, the lower part of the inferior temporal gyrus (ITG), part of the thalamus, and other cortical edges such as the insula. Throughout the adult lifespan, the entire brain region broadly contributed to age prediction (Figs. 2C and S4), whereas cortical areas with broad contributions to prediction were mainly areas of the ITG. Previous studies have shown that GM changes in these regions are relatively large [11]. Furthermore, we also identified the caudate nucleus, thalamus, and insula as important contributing regions.

To determine whether sex contributes to differences in brain development and aging, contributions to age prediction were examined separately by sex. The results of correlation maps are shown in Fig. 2D. Then, in the statistical test results of the comparison between them are shown in Fig. S3, age-related changes in GM were more stable in males than in females. Previous research has suggested that males exhibit more robust whole brain and parallel basal ganglia declines relative to females [12], which supports our findings. In addition, studies have shown that GM growth is significantly greater in females than in males [11], which is consistent with the conclusions drawn in this study. Thus, sex differences in the brain may result from compensatory mechanisms aimed at maintaining similar intellectual capacities across the sexes [13].

Given the heterogeneous patterns of correlations at different ages [14], we divided the 18–89-year age span into three subgroups (young: 18–39 years, middle-age: 44–61 years, and old: 69–89 years) for analysis of the predicted contributing regions (Fig. 2E). The results showed that contributing areas in the cortex gradually expanded with age, perhaps reflecting a decrease in age-related cortical volume [14]. In addition, the correlation between age and contributions to age prediction in the different groups showed that the effect of age-related changes in the whole brain GM was significantly greater in the middle-aged group than in the young and old groups (Fig. S5), which is intuitively consistent with

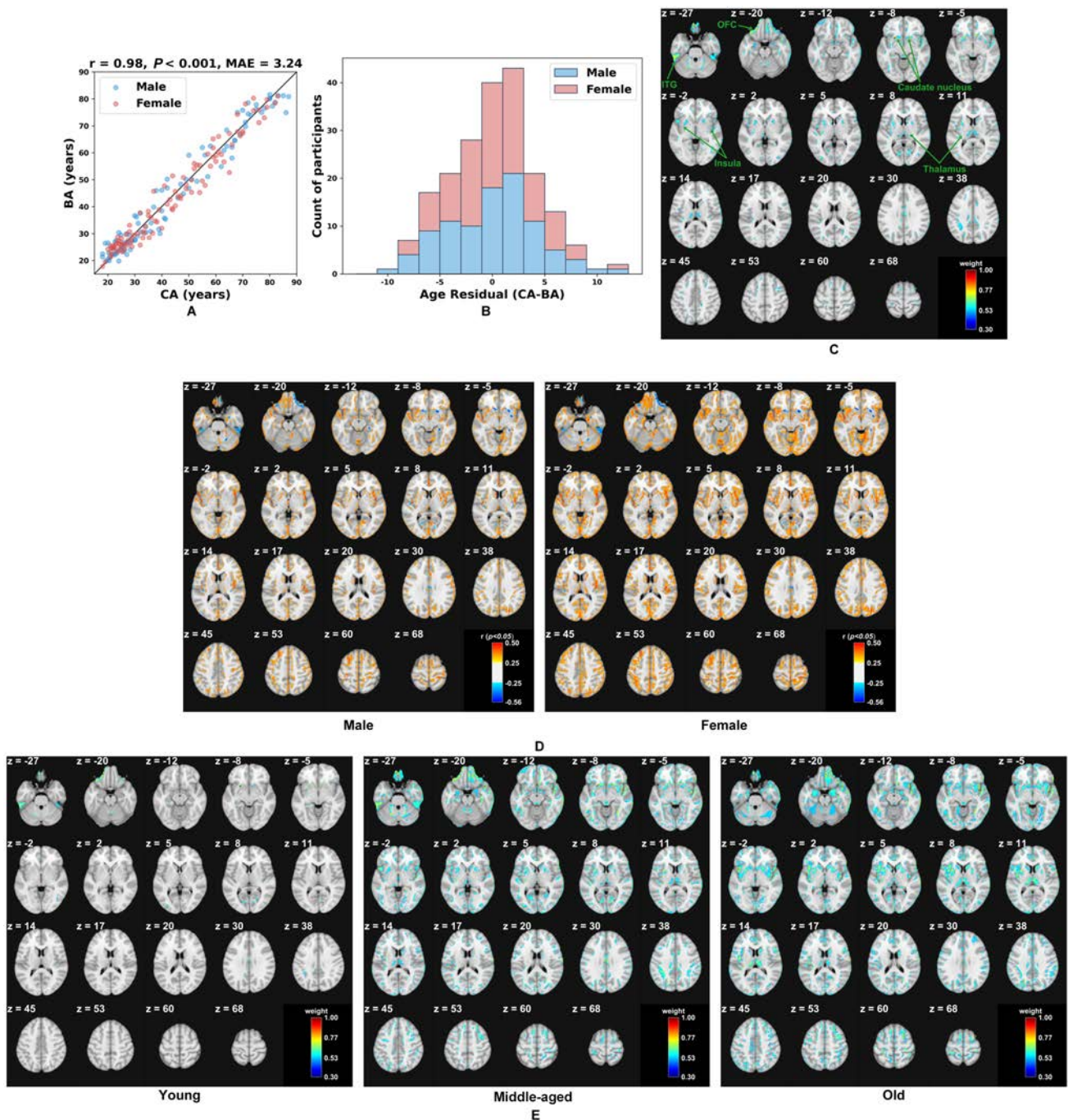


Fig. 2 **A, B** The mean average error for prediction accuracy is 3.24 years. **C** Regions showing the greatest contributions include the caudate nucleus, orbitofrontal cortex, inferior temporal gyrus, thalamus, and insular cortex (z in mm). **D** Correlation maps of contributions at each voxel with age in male and female samples, indicating

that age-related changes in GM are more stable in males than in females (z in mm). **E** Regional contributions to age predictions in the three subgroups: young (18–39 years), middle-aged (44–61 years), and old (69–89 years).

the inverted U-shaped curve characterizing GM volume and age in multiple areas [14].

In summary, we propose a deep learning model that combines supervised and metric learning paradigms for BA prediction, extracting multi-level brain image information

through a multi-branch structure and focusing on key areas through an adaptive attention mechanism, which achieves high precision. We also determined that a higher estimated BA reflects a higher gF. We found that many regions in the brain contribute to age prediction, notably the thalamus,

insula, and caudate nucleus. Age-related regional contributions of GM showed an initial increasing trend in young-to-middle-aged groups, then a decline from the middle-aged-to-old groups. In addition, changes in GM were more stable with age in males than in females. This study is a corrected version of a retracted manuscript. Future work should include additional samples, larger spans, and more balanced data to test the validity of the model.

The T1-weighted image is usually the first choice for MRI scans in clinical diagnosis, so T1-based studies of clinical prediction receive more attention in the literature, and multimodal MRI only provides limited enhancement of prediction accuracy, according to a comprehensive comparison study [3]. The primary anatomical characteristics of brain tissue are extensively used, including the volumes and distinctions between GM and WM. In order to introduce a model that is intuitive and imposes less of a computing burden for clinical application, we did not use more advanced geometrical characteristics of the cortex, such as cortical gyrification and complexities, and our results demonstrate better prediction accuracy than reports using datasets of similar size and age range as in this study. The proposed Fork-SE-based prediction model can be readily extended to larger datasets because the parameters for prediction are entirely determined by the training model (Fig. 1). It should be noted that the current findings are based on a cross-sectional dataset and should be further validated using multi-site and longitudinal datasets.

Acknowledgments This work was supported by the National Natural Science Foundation of China (61971420), Beijing Brain Initiative of the Beijing Municipal Science and Technology Commission (Z181100001518003), Special Projects of Brain Science of the Beijing Municipal Science and Technology Commission (Z161100000216139), and International Cooperation and Exchange of the National Natural Science Foundation of China (31620103905).

Conflict of interest The authors declare that they have no conflict of interest in this work.

References

1. Zuo N, Salami A, Liu H, Yang Z, Jiang T. Functional maintenance in the multiple demand network characterizes superior fluid intelligence in aging. *Neurobiol Aging* 2020, 85: 145–153.

2. Cole JH, Marioni RE, Harris SE, Deary IJ. Brain age and other bodily “ages”: Implications for neuropsychiatry. *Mol Psychiatry* 2019, 24: 266–281.
3. Liem F, Varoquaux G, Kynast J, Beyer F, Kharabian Masouleh S, Huntenburg JM. Predicting brain-age from multimodal imaging data captures cognitive impairment. *NeuroImage* 2017, 148: 179–188.
4. Valizadeh SA, Hänggi J, Mérillat S, Jäncke L. Age prediction on the basis of brain anatomical measures. *Hum Brain Mapp* 2017, 38: 997–1008.
5. He S, Grant PE, Ou Y. Global-local transformer for brain age estimation. *IEEE Trans Med Imaging* 2022, 41: 213–224.
6. Goyal MS, Blazey TM, Su Y, Couture LE, Durbin TJ, Bateman RJ, *et al.* Persistent metabolic youth in the aging female brain. *Proc Natl Acad Sci U S A* 2019, 116: 3251–3255.
7. Ding X, Zhang X, Ma N, Han J, Ding G, Sun J. RepVGG: making VGG-style ConvNets great again. 2021 IEEE/CVF Conference on Computer Vision and Pattern Recognition (CVPR). Nashville, TN, USA. IEEE, pp. 13728–13737.
8. Taylor JR, Williams N, Cusack R, Auer T, Shafto MA, Dixon M, *et al.* The Cambridge Centre for Ageing and Neuroscience (CamCAN) data repository: Structural and functional MRI, MEG, and cognitive data from a cross-sectional adult lifespan sample. *NeuroImage* 2017, 144: 262–269.
9. Erus G, Battapady H, Satterthwaite TD, Hakonarson H, Gur RE, Davatzikos C, *et al.* Imaging patterns of brain development and their relationship to cognition. *Cereb Cortex* 2014, 25: 1676–1684.
10. Selvaraju RR, Cogswell M, Das A, Vedantam R, Parikh D, Batra D. Grad-CAM: Visual explanations from deep networks via gradient-based localization. 2017 IEEE International Conference on Computer Vision. Venice, Italy. IEEE, pp. 618–626.
11. Luders E, Narr K, Thompson PM, Woods RP, Rex DE, Jancke L, *et al.* Mapping cortical gray matter in the young adult brain: Effects of gender. *Neuroimage* 2005, 26: 493–501.
12. Li W, van Tol MJ, Li M, Miao W, Jiao Y, Heinze HJ, *et al.* Regional specificity of sex effects on subcortical volumes across the lifespan in healthy aging. *Hum Brain Mapp* 2014, 35: 238–247.
13. Grabowska A. Sex on the brain: Are gender-dependent structural and functional differences associated with behavior? *J Neurosci Res* 2017, 95: 200–212.
14. Fjell AM, Westlye LT, Grydeland H, Amlien I, Espeseth T, Reinvang I, *et al.* Critical ages in the life course of the adult brain: Nonlinear subcortical aging. *Neurobiol Aging* 2013, 34: 2239–2247.

Springer Nature or its licensor (e.g. a society or other partner) holds exclusive rights to this article under a publishing agreement with the author(s) or other rightsholder(s); author self-archiving of the accepted manuscript version of this article is solely governed by the terms of such publishing agreement and applicable law.

TRPM7 Kinase Domain is Part of the Rac1-SSH2-cofilin Complex Regulating F-actin in the Mouse Nervous System

Junzhuang Chang¹ · Cui Chen¹ · Wei Li¹ ·
Nashat Abumaria¹

Received: 8 August 2022 / Accepted: 19 November 2022 / Published online: 15 March 2023

© Center for Excellence in Brain Science and Intelligence Technology, Chinese Academy of Sciences 2023

Dear Editor,

The ion channel transient receptor potential melastatin-like 7 (TRPM7) has a serine-threonine α -kinase domain (M7CK) on its intracellular C-terminal [1, 2]. In cell lines, M7CK is cleaved and translocated to the nucleus to regulate a variety of cellular processes including cell proliferation and survival [3]. In neuroblastoma cells, M7CK interacts with several cytoskeleton-regulating proteins including cofilin [4]. In the mammalian brain, M7CK regulates synaptic density, plasticity, and learning and memory. Evidence suggests that M7CK protects synaptic and cognitive functions by interacting with, and phosphorylating (inhibiting), cofilin in the brain [5]. It remains unclear how M7CK regulates cofilin activity and whether such regulation might result in changes in actin filaments (F-actin) in neural systems. Ras-related C3 botulinum toxin substrate 1 (Rac1) signaling is a key regulator of cytoskeleton dynamics. Rac1-PAK1 (P21 activated kinase 1)-LIMK1 (LIM domain kinase 1) signaling protects synapse structure/remodeling/plasticity by phosphorylating cofilin, an actin depolymerization factor [6, 7]. Here, we found that M7CK is a key member of a novel protein complex composed of Rac1-M7CK-SSH2 (protein phosphatase

slingshot homolog 2)-cofilin that regulates cofilin activity and dendritic F-actin in the mouse nervous system.

We generated transgenic mice with brain-specific deletion of TRPM7 in CaMKII α -positive glutamatergic neurons (*CaMKII-T7^{-/-}*). By crossing *CaMKII-T7^{-/-}* mice with *Ai3* mice (a Cre-reporter strain, Fig. S1A) and by using immunostaining of TRPM7 using a commercially-available antibody targeting the ion channel part of TRPM7 (see Supplementary Materials and Methods and Fig. S1B for antibody validation), we confirmed that TRPM7 was knocked out in the majority of the glutamatergic neurons (recombination efficiency ~91.5%, Fig. S1A). As a result, quantitative Western blot analysis of TRPM7 protein in homogenized brain tissue using the same antibody showed that the protein was reduced by ~55% in *CaMKII-T7^{-/-}* mice (two-tailed unpaired *t*-test, $t_{(10)} = 5.113$, $P < 0.001$, Fig. 1A, B), which is in line with our previous results [5]. A polyclonal antibody targeting the kinase domain of TRPM7 (amino-acid residues 1300–1539 of mouse TRPM7) was generated (anti-M7CK antibody, see Supplementary Materials and Methods) and validated (Fig. S1C). Using this antibody, we confirmed that M7CK was also significantly reduced in *CaMKII-T7^{-/-}* mice (two-tailed unpaired *t*-test, Welch-corrected $t_{(5,24)} = 2.689$, $P = 0.041$, Fig. 1A, C). Furthermore, we used the co-detected full-length TRPM7 by anti-M7CK antibody to calculate the M7CK/TRPM7 ratio in *Trpm7^{fllox/fllox}* and *CaMKII-T7^{-/-}* mice in order to check if TRPM7 conditional knockout in glutamatergic neurons influenced the cleavage rate of M7CK in the brain. We found no significant differences between *Trpm7^{fllox/fllox}* and *CaMKII-T7^{-/-}* mice (two-tailed unpaired *t*-test, $t_{(10)} = 0.1522$, $P = 0.882$, Fig. 1A, D). Deletion of TRPM7 reduces cofilin phosphorylation by ~80% without changing LIMK1 or PAK1 activity [5]. In line with these findings, we found that cofilin phosphorylation was reduced by ~70% in *CaMKII-T7^{-/-}* mice (Mann-Whitney test, $U = 5$, $P = 0.041$,

Supplementary Information The online version contains supplementary material available at <https://doi.org/10.1007/s12264-023-01045-6>.

✉ Nashat Abumaria
Abumaria@fudan.edu.cn

¹ State Key Laboratory of Medical Neurobiology and MOE Frontiers Center for Brain Science, Department of Laboratory Animal Science, Institutes of Brain Science, Fudan University, Shanghai 200032, China

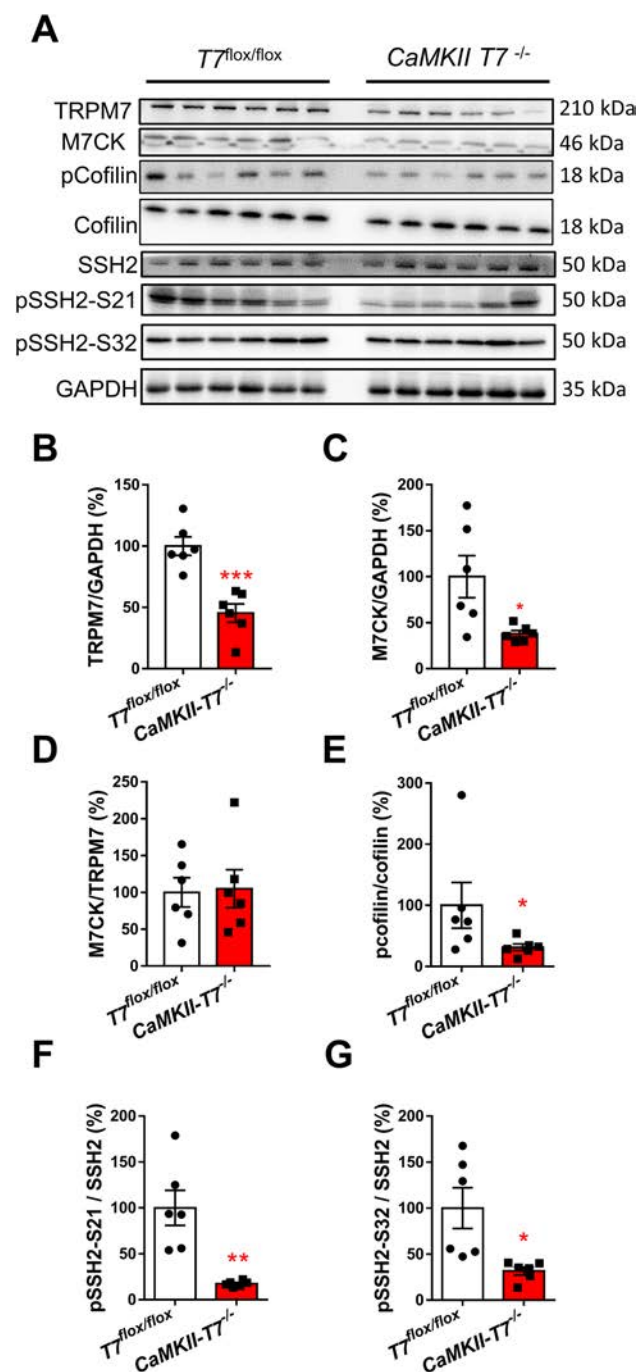
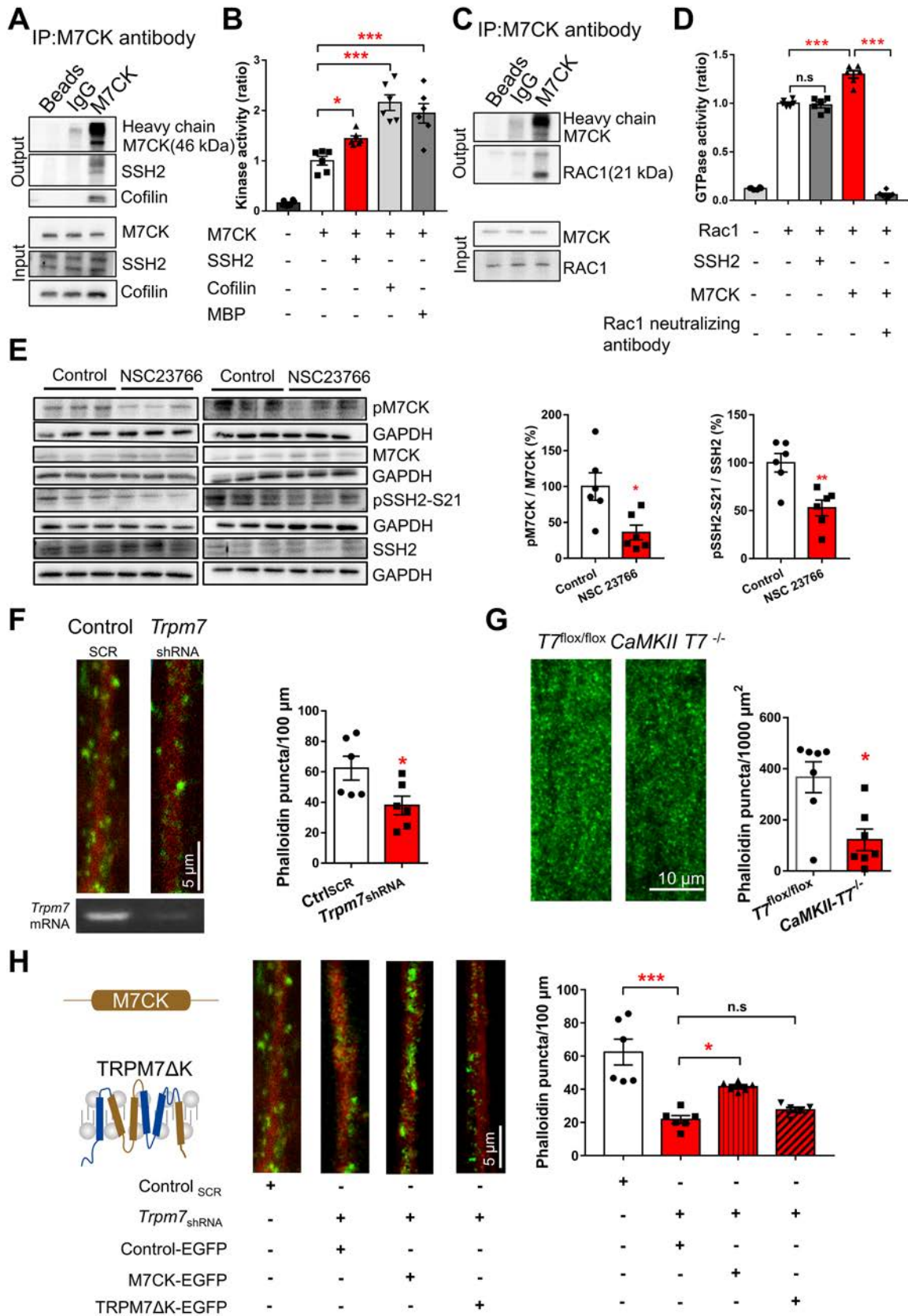


Fig. 1 The phosphorylation levels of cofilin and SSH2 in the hippocampus of TRPM7-knockout mice. **A** Western blot images of protein bands from all the mice that were used for analysis. The following proteins are detected in *TRPM7^{flox/flox}* or *CaMKII-T7^{-/-}* mice: TRPM7, M7CK, cofilin, pCofilin, SSH2, pSSH2-S21, and pSSH2-S32. **B–G** Analysis of the expression levels of TRPM7 (**B**) and M7CK (**C**), the M7CK/TRPM7 ratio (**D**), and the phosphorylation levels of cofilin (**E**), pSSH2-S21 (**F**), and pSSH2-S32 (**G**) calculated as a ratio of the total corresponding protein and presented as percentages of the control *TRPM7^{flox/flox}*. The co-detection of GAPDH bands serves as the loading control. For **B–G**, data are presented as the mean \pm SEM, $n = 6$ per group, two-tailed unpaired *t*-test (**B, C, D, F, G**), Mann-Whitney test (**E**), * $P < 0.05$; ** $P < 0.01$. *** $P < 0.001$.

Fig. 2 M7CK plays a key role in the Rac1-M7CK-SSH2-cofilin signaling pathway. **A** Co-immunoprecipitation of SSH2, cofilin, and M7CK by using an anti-M7CK antibody (targeting the kinase domain). Beads and IgG are loaded and used as control. **B** Analysis of M7CK kinase activity (expressed as the ratio of the control group) without substrate (negative control), or after adding SSH2, cofilin, and/or MBP (serves as a positive control) as substrates. Negative control (no M7CK and no substrate are added) is also presented (but not included in the statistical analysis). $n = 6$ per group. **C** Co-immunoprecipitation of Rac1 and M7CK using anti-M7CK antibody; beads and IgG are loaded and used as control. **D** Analysis of Rac1 activity (expressed as the ratio of the control group) without substrate (negative control), or after adding SSH2 and/or M7CK as substrates. The Rac1 + M7CK reaction activity is diminished by adding the Rac1 activity-neutralizing antibody. Negative control (no Rac1 and no substrate) is also presented (but not included in the statistical analysis). $n = 6$ per group. **E** Left: Western blot images of protein bands from hippocampal neuronal cultures treated with solvent (Control) or NSC23766 (Rac1 inhibitor, $n = 6$ per group). Right: Analysis of the phosphorylation level of M7CK or SSH2 (at serine 21, S21) calculated as a ratio of the total corresponding protein and presented as percentages of the Control. The co-detection of GAPDH bands serves as a loading control. **F** Left: Representative fluorescent images of dendrites stained with phalloidin in primary cell cultures transfected with AAV-Control_{scrambled}-shRNA-*tdTomato* virus (Control_{SCR}) or AAV-*Trpm7*-shRNA-*tdTomato* virus (*Trpm7*_{shRNA}). Below, a representative image of RT-PCR confirms the knockdown of *Trpm7* mRNA. Right: Analysis of dendritic/synaptic phalloidin puncta per 100 μm dendrite. $n = 6$ independent cultures per group. **G** Representative fluorescent images of hippocampal CA1 apical dendrites in the stratum radiatum stained with phalloidin in brain sections from *Trpm7^{flox/flox}* and *CaMKII-T7^{-/-}* mice. Right: Analysis of dendritic phalloidin puncta per 1000 μm^2 area. $n = 7$ per group. **H** Left: Representative fluorescent images of dendrites stained with phalloidin *Trpm7^{shRNA}* transduced cultures following knock-in of EGFP (control), TRPM7 Δ K-EGFP, or M7CK-EGFP. Right: Analysis of dendritic/synaptic phalloidin puncta per 100 μm dendrite showing that the kinase domain, but not the ion channel part, rescues phalloidin puncta in neuronal cultures following knockdown of TRPM7 (the Control_{SCR} group is the same as in **F**; it is presented for comparison purposes). $n = 6$ independent cultures per group. All phalloidin puncta are detected at 647 nm and presented in green for clarity. Data are presented as the mean \pm SEM, one-way ANOVA followed by Bonferroni *post hoc* test (**B, D, H**), two-tailed unpaired *t*-test (**E, F**), Mann-Whitney test (**G**), * $P < 0.05$; ** $P < 0.01$; *** $P < 0.001$.

Fig. 1A, E, see also Fig. S2A). Next, we tested whether the deletion of TRPM7 affected the activity of other proteins known to regulate cofilin activity. The SSH2 regulates actin filament dynamics by dephosphorylating (activating) cofilin [8]. Phosphorylation of SSH2 (pSSH2) at serine residues S21 and S32 inhibits the phosphatase activity of SSH2 [9]. We quantified the phosphorylation level of SSH2 and found that *CaMKII-T7^{-/-}* mice had significantly lower levels of pSSH2 at S21 (two-tailed unpaired *t*-test, Welch-corrected $t_{(5.045)} = 4.311$, $P = 0.007$, Fig. 1A, F, see also Fig. S2B) and S32 (two-tailed unpaired *t*-test, Welch-corrected $t_{(5.359)} = 3.039$, $P = 0.012$, Fig. 1A, G, see also Fig. S2C).

We speculated that M7CK might regulate cofilin activity directly by phosphorylating it and indirectly by preventing its dephosphorylation *via* inhibiting SSH2. If so, then M7CK



should interact with, and phosphorylate both proteins. We used the anti-M7CK antibody to perform all co-immunoprecipitation and Western blotting experiments on the kinase domain of TRPM7. We found that the cleaved kinase domain was co-immunoprecipitated with both cofilin and SSH2 in human embryonic kidney (HEK) cells (Fig. 2A). No actin was detected in this complex (Fig. S3A), suggesting that the M7CK-Cofilin-SSH2 interaction is specific and not indirectly induced by actin-linking. We also tested whether M7CK can be detected in the proximity of cofilin and SSH2 in neuronal cells using co-immunostaining. In hippocampal neuronal cultures, we found that M7CK puncta co-localized with cofilin (Fig. S3B) and SSH2 (Fig. S3C) puncta in different areas within the cytoplasm. We examined whether SSH2 and cofilin could be phosphorylated by M7CK. We conducted an enzymatic kinase activity assay using cofilin and/or SSH2 as substrates for M7CK. Negative controls (no M7CK and/or no substrate was added), as well as a positive control (using myelin basic protein, a well-known substrate detecting M7CK activity [10]), were included in those experiments (Fig. 2B). We found that the signal of kinase activity was significantly increased when myelin basic protein, SSH2, or cofilin was used as the substrate (one-way ANOVA, $F_{(3, 20)} = 14.86$, $P < 0.001$, Fig. 2B). Bonferroni's *post hoc* test showed that the signals in +SSH2 ($P = 0.032$), +cofilin ($P < 0.001$), and +myelin basic protein (MBP, $P < 0.001$) reactions were significantly higher than that in the control reaction containing M7CK but no substrate (Fig. 2B).

Rac1 signaling regulates spine remodeling, synapse density, and plasticity by regulating cofilin activity and F-actin dynamics [6, 11, 12]. We checked if Rac1 interacted with M7CK and whether the kinase might be a phosphorylation target for Rac1. Interestingly, we found that M7CK co-immunoprecipitated with Rac1 in HEK cells (Fig. 2C). Furthermore, enzyme activity assays showed a significant increase in Rac1 activity after adding M7CK but not SSH2 as the substrate (one-way ANOVA: $F_{(3, 20)} = 421.8$, $P < 0.001$; Bonferroni's *post hoc* test, compared with Rac1 with no substrate control group: +SSH2, $P > 0.999$, +M7CK, $P < 0.001$, Fig. 2D). Thus, M7CK appears to be a phosphorylation target of Rac1. When Rac1 activity-neutralizing antibody was added, the activity in the Rac1-M7CK reaction was reduced to levels similar to those measured in the blank negative control (Bonferroni's *post hoc* test, compared with Rac1+M7CK: M7CK+Rac1+Rac1 neutralizing antibody, $P < 0.001$, Fig. 2D) indicating that the activity was due to Rac1 activity and/or the phosphorylation of M7CK by Rac1, not the opposite. We also found that inhibition of Rac1 in neuronal cell cultures resulted in reductions in the phosphorylation levels of M7CK (two-tailed unpaired *t*-test, $t_{(10)} = 2.957$, $P = 0.014$, Fig. 2E) and SSH2 (two-tailed unpaired *t*-test, $t_{(10)} = 3.73$, $P = 0.004$, Fig. 2E).

Finally, to demonstrate the functional effects of this new complex on F-actin, we quantified F-actin puncta within dendritic areas following the suppression and/or deletion of TRPM7 and its kinase *in vitro* and/or *in vivo* (respectively). We used phalloidin staining, a well-known molecule that binds to F-actin colocalized with synaptic proteins in the dendritic spines of excitatory synapses [13]. In hippocampal neuronal cultures, we found that knockdown of TRPM7 by shRNA (*Trpm7*_{shRNA}) resulted in a significant reduction in the numbers of F-actin puncta on the dendrites (two-tailed unpaired *t*-test, $t_{(10)} = 2.472$, $P = 0.033$, Fig. 2F). In brain sections, we found that *CaMKII-T7^{-/-}* mice had a significantly lower density of F-actin puncta in hippocampal CA1 dendritic areas (Mann-Whitney test, $U = 7$, $P = 0.026$, Fig. 2G). Thus, deletion or suppression of TRPM7 (ion channel and the kinase domain) resulted in reductions in F-actin in dendritic areas. To investigate which part of TRPM7 can rescue F-actin puncta, we overexpressed the kinase domain (M7CK-EGFP) or a truncated ion channel (at D1510, TRPM7 Δ K-EGFP that has been shown to be functional [14]) in neuronal cultures following knockdown of TRPM7. We found that expression of the kinase domain, but not the truncated ion channel, was sufficient to significantly increase the F-actin puncta in dendritic areas (one-way ANOVA: $F_{(3, 20)} = 18.67$, $P < 0.001$; Bonferroni's *post hoc* test, in comparison with *TRPM7*_{shRNA} EGFP control: M7CK-EGFP, $P = 0.007$, TRPM7 Δ K-EGFP, $P = 0.678$, Fig. 2H). It is worth noting that complexes of cofilin and actin (known as cofilactin) are prominent in neuronal cells. Such complexes are not easily immunolabeled for cofilin or phalloidin after Triton permeabilization [15, 16]. Thus, we cannot exclude the possibility that changes in cofilactin abundance induced by TRPM7 suppression/deletion might contribute to the decline in phalloidin puncta.

In this study, we discovered a novel signaling pathway; namely Rac1-M7CK-SSH2-cofilin and found that it plays a key role in controlling cofilin activity and regulating F-actin in the nervous system (see schematic illustration, Fig. S4). Furthermore, we found that M7CK is a central component within this novel pathway. Suppression or deletion of the kinase expression critically activated cofilin and reduced F-actin.

The Rac1-cofilin signaling pathway is important for maintaining the normal F-actin dynamics necessary for cell growth, proliferation, and migration. In the mammalian brain, dysfunction in the Rac1-cofilin signaling pathway results in deficits in learning and memory, impairments in synaptic plasticity and remodeling, and reductions in synapse density [11, 12]. These abnormalities are explained by possible impairment in the Rac1-PAK1-LIMK1-cofilin signaling pathway, as it is considered the major pathway controlling cofilin activity and F-actin dynamics [12]. However, PAK1-knockout mice have no reduction in cofilin

phosphorylation [17]. LIMK1-knockout mice have ~50% reduction in cofilin phosphorylation [18]. Meanwhile, Rac1 mutant mice have >70% reduction in cofilin phosphorylation and significant disruption in F-actin dynamics [11]. These studies support the conclusion that Rac1 is a major regulator of cofilin activity and F-actin dynamics, but evidence also suggests that PAK1-LIMK1 might not be the only signaling molecules mediating the effects of Rac1 on cofilin. In the current study, we found that M7CK is a downstream target of Rac1. The kinase inhibits cofilin directly by phosphorylation, and indirectly by preventing its dephosphorylation. Therefore, it is possible that M7CK-SSH2-cofilin is another major signaling pathway used by Rac1 to maintain tight regulation of cofilin activity and F-actin in the nervous system.

Finally, M7CK has been shown to be cleaved from TRPM7 *via* proteolytic mechanisms in different cell lines and tissues [3]. Studies in the mammalian brain have also shown that the kinase domain alone without the ion channel component is sufficient to maintain normal synaptic and cognitive functions [5] indicating that M7CK is also cleaved in the nervous system. The mechanisms underlying the cleavage and translocation of M7CK as well as the signaling pathways interacting with it in the mammalian brain remain to be determined.

Acknowledgements This work was supported by the National Natural Science Foundation of China (31970942 and 81573408), the Shanghai Municipal Science and Technology Major Project (2018SHZDZX01), the ZJ Lab, and Shanghai Center for Brain Science and Brain-Inspired Technology.

Conflict of interest The authors declare no conflict of interest related to this work.

References

1. Abumaria N, Li W, Clarkson AN. Role of the chanzyme TRPM7 in the nervous system in health and disease. *Cell Mol Life Sci* 2019, 76: 3301–3310.
2. Abumaria N, Li W, Liu Y. TRPM7 functions in non-neuronal and neuronal systems: Perspectives on its role in the adult brain. *Behav Brain Res* 2018, 340: 81–86.
3. Krapivinsky G, Krapivinsky L, Manasian Y, Clapham DE. The TRPM7 chanzyme is cleaved to release a chromatin-modifying kinase. *Cell* 2014, 157: 1061–1072.
4. Middelbeek J, Vrenken K, Visser D, Lasonder E, Koster J, Jalink K. The TRPM7 interactome defines a cytoskeletal complex linked to neuroblastoma progression. *Eur J Cell Biol* 2016, 95: 465–474.
5. Liu Y, Chen C, Liu Y, Li W, Wang Z, Sun Q, *et al.* TRPM7 is required for normal synapse density, learning, and memory at different developmental stages. *Cell Rep* 2018, 23: 3480–3491.
6. Li LZ, Yin N, Li XY, Miao Y, Cheng S, Li F, *et al.* Rac1 modulates excitatory synaptic transmission in mouse retinal ganglion cells. *Neurosci Bull* 2019, 35: 673–687.
7. Fan XC, Ma CN, Song JC, Liao ZH, Huang N, Liu X, *et al.* Rac1 signaling in amygdala astrocytes regulates fear memory acquisition and retrieval. *Neurosci Bull* 2021, 37: 947–958.
8. Zhang T, Cheng D, Wu C, Wang X, Ke Q, Lou H, *et al.* Lysosomal hydrolase cathepsin D non-proteolytically modulates dendritic morphology in *Drosophila*. *Neurosci Bull* 2020, 36: 1147–1157.
9. Tang W, Zhang Y, Xu W, Harden TK, Sondek J, Sun L, *et al.* A PLC β /PI3K γ -GSK3 signaling pathway regulates cofilin phosphatase slingshot2 and neutrophil polarization and chemotaxis. *Dev Cell* 2011, 21: 1038–1050.
10. Ryazanova LV, Dorovkov MV, Ansari A, Ryazanov AG. Characterization of the protein kinase activity of TRPM7/ChaK1, a protein kinase fused to the transient receptor potential ion channel. *J Biol Chem* 2004, 279: 3708–3716.
11. Pyronneau A, He Q, Hwang JY, Porch M, Contractor A, Zukin RS. Aberrant Rac1-cofilin signaling mediates defects in dendritic spines, synaptic function, and sensory perception in fragile X syndrome. *Sci Signal* 2017, 10: eaan0852.
12. Lai KO, Ip NY. Structural plasticity of dendritic spines: The underlying mechanisms and its dysregulation in brain disorders. *Biochim Biophys Acta BBA Mol Basis Dis* 2013, 1832: 2257–2263.
13. Park CE, Cho Y, Cho I, Jung H, Kim B, Shin JH, *et al.* Super-resolution three-dimensional imaging of actin filaments in cultured cells and the brain *via* expansion microscopy. *ACS Nano* 2020, 14: 14999–15010.
14. Desai BN, Krapivinsky G, Navarro B, Krapivinsky L, Carter BC, Febvay S, *et al.* Cleavage of TRPM7 releases the kinase domain from the ion channel and regulates its participation in fas-induced apoptosis. *Dev Cell* 2012, 22: 1149–1162.
15. McGough A, Pope B, Chiu W, Weeds A. Cofilin changes the twist of F-actin: Implications for actin filament dynamics and cellular function. *J Cell Biol* 1997, 138: 771–781.
16. Hylton RK, Heebner JE, Grillo MA, Swilius MT. Cofilactin filaments regulate filopodial structure and dynamics in neuronal growth cones. *Nat Commun* 2022, 13: 2439.
17. Asrar S, Meng Y, Zhou Z, Todorovski Z, Huang WW, Jia Z. Regulation of hippocampal long-term potentiation by p21-activated protein kinase 1 (PAK1). *Neuropharmacology* 2009, 56: 73–80.
18. Meng Y, Zhang Y, Tregoubov V, Janus C, Cruz L, Jackson M, *et al.* Abnormal spine morphology and enhanced LTP in LIMK-1 knockout mice. *Neuron* 2002, 35: 121–133.

Publisher's Note Springer Nature remains neutral with regard to jurisdictional claims in published maps and institutional affiliations.

Neural Circuit Mechanisms Involved in Animals' Detection of and Response to Visual Threats

Qiwen Wu^{1,2}  · Yifeng Zhang¹ 

Received: 28 August 2022 / Accepted: 30 October 2022 / Published online: 25 January 2023

© Center for Excellence in Brain Science and Intelligence Technology, Chinese Academy of Sciences 2023

Abstract Evading or escaping from predators is one of the most crucial issues for survival across the animal kingdom. The timely detection of predators and the initiation of appropriate fight-or-flight responses are innate capabilities of the nervous system. Here we review recent progress in our understanding of innate visually-triggered defensive behaviors and the underlying neural circuit mechanisms, and a comparison among vinegar flies, zebrafish, and mice is included. This overview covers the anatomical and functional aspects of the neural circuits involved in this process, including visual threat processing and identification, the selection of appropriate behavioral responses, and the initiation of these innate defensive behaviors. The emphasis of this review is on the early stages of this pathway, namely, threat identification from complex visual inputs and how behavioral choices are influenced by differences in visual threats. We also briefly cover how the innate defensive response is processed centrally. Based on these summaries, we discuss coding strategies for visual threats and propose a common prototypical pathway for rapid innate defensive responses.

Keywords Looming · Innate defensive behavior · Escape · Freezing · Circuit mechanism · Encoding

Introduction

The most important thing for any nervous system is to respond appropriately to external changes. Avoidance of danger is essential for survival and future reproduction. Animals have evolved surprising skills to evade predators. For example, geckos voluntarily sacrifice their tails to distract predators and buy themselves time to escape (Fig. 1A) [1, 2]; possums mislead predators by feigning death from poisoning hence making them unsuitable as food (Fig. 1B) [3]. For most animals, including mice [4, 5], escape or freezing responses are evoked depending on the imminence of the threat (Fig. 1C) [6, 7]. The neural processing of these innate responses to threats forms a closed loop that comprises threat detection, action initiation, action execution, and post-action resetting (preparing for the next threat) [8]. Recent studies have made significant progress toward understanding the neural mechanisms of animals' responses to visual threats. In this review, we summarize the current understanding of the innate defensive responses in insects, zebrafish, and mice; primarily on the neural circuits for the processing and identification of visual threats. After cross-species comparisons, we conclude our overview by proposing a conserved core pathway for the innate response to visual threats.

Visual Threat Processing in Insects

Detection of Looming Objects by the Vinegar Fly

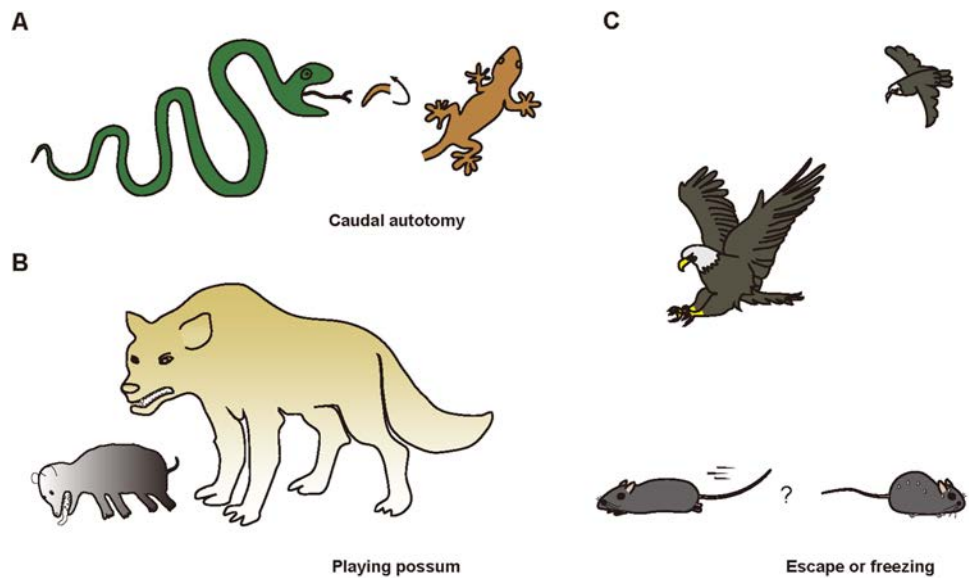
The neural mechanisms of visual threat detection and processing are well-studied in insects [9–13]. The vinegar fly (*Drosophila melanogaster*) has tractable neural circuits that are easier to manipulate compared to vertebrates, thus

✉ Yifeng Zhang
zh.yifeng@gmail.com

¹ Institute of Neuroscience, Center for Excellence in Brain Science and Intelligence Technology, Chinese Academy of Sciences, Shanghai 200031, China

² University of Chinese Academy of Sciences, Beijing 100049, China

Fig. 1 Repertoire of predator avoidance behaviors. **A** A gecko escapes from a snake by forcefully contracting the tail muscle to break its caudal vertebra then shed the still-wriggling tail to distract the snake. **B** A Virginia possum, when confronted by a wolf, pretends to be dead from poisoning, with its tongue sticking out, baring its teeth, its mouth foaming, and a foul smell released from its anal glands. **C** A mouse escapes rapidly to a refuge upon seeing a fast-approaching eagle or freezes to avoid detection if the eagle is just sweeping by.



much of the recent progress has been made in these flies [13, 14]. A dark looming disk is typically used as the visual stimulus to mimic an incoming threat [11, 12]. Sophisticated motor programs for flight take-off can be elicited in flies presented with such a looming stimulus [15, 16]. One neural pathway mediating looming-induced escape behaviors has been mapped for the most part (Fig. 2A). In this pathway, T4/T5 neurons projecting to the lobule plate respond to this looming stimulus in a directionally-selective (DS) manner [17]. Silencing T4/T5 neurons abolishes looming-elicited landing and avoidance behavior, thus they are essential for the detection of looming stimuli [18]. The DS outputs from T4/T5 neurons are then integrated by the lobula plate/lobula columnar type II (LPLC2) visual projection neurons. The primary dendrite of each LPLC2 neuron ramifies in one of four layers innervated by T4/T5 neurons and extends along that layer's preferred motion direction to align with the excitatory DS inputs from T4/T5. Each dendritic branch of the LPLC2 neuron also receives local inhibitory DS inputs for inward motion (i.e., towards the center of the neuron's receptive field). Together, the selectivity of the excitatory and inhibitory inputs form radial motion opponency so that the LPLC2 neuron responds to expanding motion but not to receding motion [19]. Another type of visual projection neuron, lobula columnar subtype 4 (LC4) is also implicated in the detection of a looming stimulus, but the mechanisms underlying its response are not yet understood. The angular velocity of the looming disk is encoded by the LC4 neurons [20], and the size of the looming disk is encoded by the LPLC2 neurons [21]. Combined, information carried by these two types of neurons fully describes the looming disk stimulus at any given moment.

A Common Strategy for Looming Detection in Insects

Other insects seem to share a similar circuit composition for visual threat detection [9, 10]. That is, visual projection neurons convey information on different parameters of the incoming object to downstream neurons. Then the downstream neurons combine this information to decide whether the incoming object is a threat, and direct motor neurons or related interneurons to elicit defensive behaviors if necessary. The lobula giant movement detector (LGMD) neuron and the downstream descending contralateral movement detector (DCMD) neuron found in the locust, for example, are well known for such a composition. Splitting looming information into pathways for size and speed was first described in the context of the LGMD [11]. The LGMD neuron receives inputs from visual neurons conveying information about looming angular speed at its dendritic subfield A and information about looming size at dendritic subfields B and C [11, 22–24]. It combines these inputs nonlinearly to detect visual threats [25, 26]. Then, the DCMD neuron receives this threat information and directs the jumping and flight steering motion in the locust to escape the incoming object [11]. Aside from size and speed, encoding of looming information in the LGMD neuron is also assisted by presynaptic mechanisms that preferentially boost the response to the coherent motion, thereby helping to segregate the looming object from the background [27, 28]. It would be interesting to investigate if similar mechanisms exist in other systems.

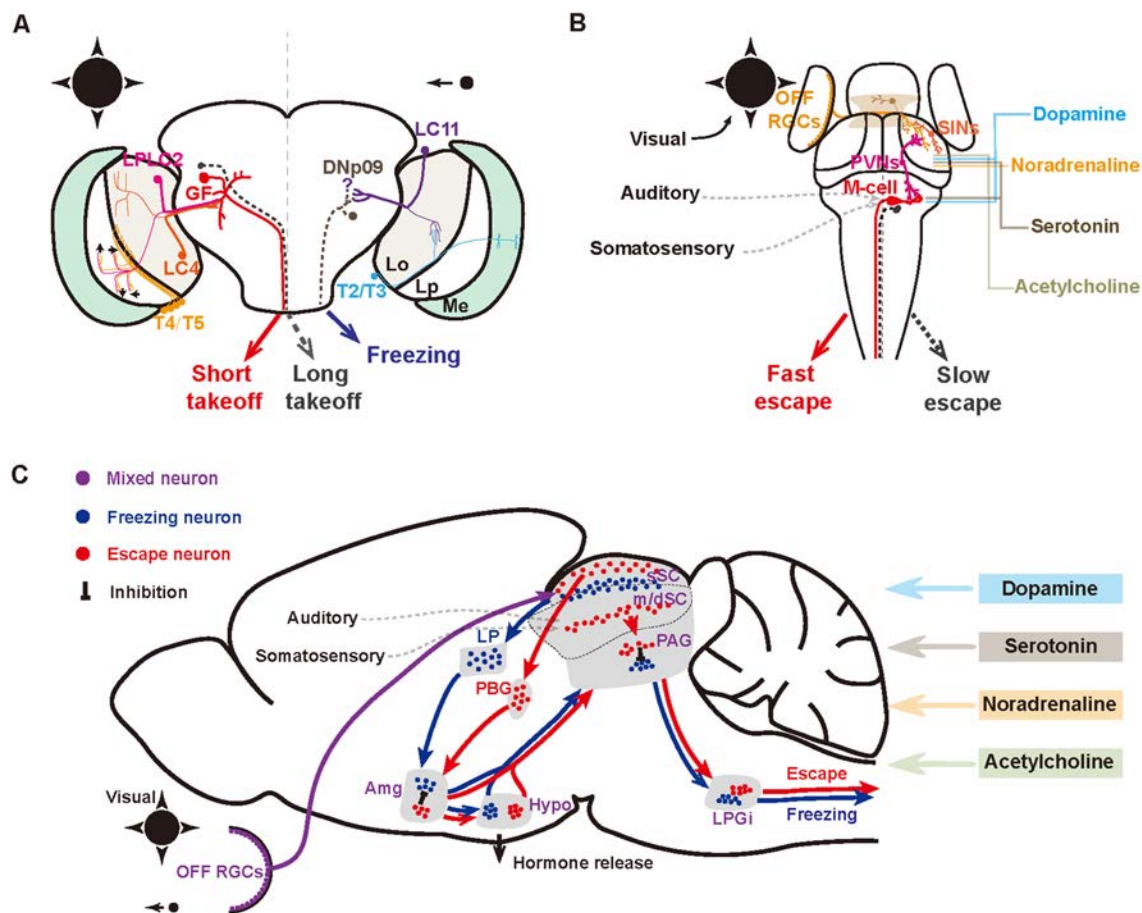


Fig. 2 Neural circuits for visual threat processing and response across species, in *Drosophila* (A), zebrafish (B), and mouse C). **A** Core pathways for escape (left) and freezing (right) in response to visual threats in *Drosophila*. Lo, lobula; Lp, lobula plate; Me, medulla. Dashed line for DNP09: possible connection. The dashed line on the left indicates a non-GF pathway for long take-off. Black arrows in the Lp: the preferred motion directions of T5 neurons. **B** Core escape circuit in zebrafish. Light brown shaded region: thalamus. SINS, superficial inhibitory interneurons; PVNs, periventricular neurons; M-cell, hindbrain Mauthner cell. The dashed line indicates that non-M cells participate in slow escape. Other colored lines indicate modulation of the tectum and M cells. **C** Core pathways for

escape (red) and freezing (blue) in response to visual threats in the mouse. The four modulatory systems are involved in visual threat-evoked innate defensive behaviors, but the scope of their effects and their target brain regions are not fully understood yet. Red/blue: circuit components of the escape/freezing pathway, respectively; purple: participants in both pathways; other colors: modulation of the SC; dotted lines: other sensory inputs. sSC superficial superior colliculus, m/dSC intermediate/deep superior colliculus, LP lateral posterior nucleus, PBG parabrachial nucleus, Amg amygdala, Hypo hypothalamus, PAG periaqueductal grey, LPGi lateral parabrachial nucleus.

Diverse Response Mechanisms to Visual Threats

The outputs from LC4 and LPLC2 neurons are summed nonlinearly in the downstream giant fiber (GF) neuron, a wide-axon descending neuron [13], and the spike timing of the GF determines a fast mode of escape [29]. Direct activation of the GF induces take-off that vinegar flies execute under threat [29–31], and inactivation of the GF abolishes this type of emergency take-off but leaves normal flight take-off unaffected [16, 29, 32]. So, the GF is considered to be an essential part of the neural pathway for threat response in vinegar flies [9, 10, 13].

In addition to the escape pathway *via* GF-mediated fast take-off, there is also a non-GF take-off pathway in the vinegar fly [29, 32, 33]. The *Drosophila* non-GF take-off allows for more controlled motor planning, the same as what occurs in locust escape jumps [15, 16, 29]. The LGMD-mediated escape response in locusts requires > 100 ms of preparation time [11], thus it may resemble more the non-GF response than the GF-mediated response in *Drosophila*. The vinegar flies tend to select the GF pathway when the danger is more imminent, and the GF pathway can even override the non-GF pathway sometimes [29]. But the mechanisms underlying the choice between the two pathways are not yet

understood. The detection of other types of visual threats may involve different visual neurons, with the less urgent threat going through the non-GF pathway or a combination of both pathways [34]. A recent study systematically screened many visual projection neurons and revealed that optogenetic activation of lobula columnar subtype 6 (LC6) and lobula plate/lobula columnar, type I (LPLC1) neurons in the lobula elicit avoidance behaviors [35]. Whether these neurons are important for detecting different types of visual threats remains to be seen.

Freezing is also a behavioral response to visual threats in flies, although the circuit mechanisms are less well studied. Escape can be triggered by looming objects but not by small moving objects, while freezing can be triggered by both [36, 37]. The lobula columnar subtype 11 (LC11) neuron, which receives input from T2/T3 neurons sensitive to small objects, is essential for brief freezing behavior in vinegar flies [36, 38], but not for escape [21]. In addition, silencing T4/T5 neurons, which do not provide inputs to LC11 but are important for the detection of a looming stimulus [18, 19, 38], also significantly weakens freezing behavior [36]. Thus, pathways for processing looming objects and for processing small objects are both implicated in freezing behavior. One may wonder whether the freezing response after seeing small objects is identical to that after seeing a looming stimulus. The former is active freezing to avoid being detected by potential distant predators and the latter is passive freezing to inescapable, imminent danger. How much the neural circuits for freezing under different stimulus conditions differ is a question that needs answering in the future.

Briefly, visual threat detection and response circuits in insects are complex, and much is still unknown. But the pathways detecting imminent danger, simulated by looming disk stimuli, seem to share some common components among different insect species: the encoding of looming size and looming velocity by different visual neurons to represent the visual threat; the nonlinear summation of these two inputs in one neuron to detect the threat; and a direct projection to motor execution neurons for escape responses.

Visual Threat Processing in Zebrafish

Detection of Visual Threats

A dark looming disk elicits a defensive response in almost all the vertebrate species studied, such as fish, amphibians, reptiles, birds, and mammals (including humans) [39–45]. Larval zebrafish have received increasing attention as a useful model in which to study the neural mechanisms underlying behaviors. With the development of better *in vivo* whole-brain functional imaging techniques [46, 47] and single-cell tracing techniques [48, 49], a comprehensive understanding

of single neuron responses to circuit-wide functions, even to whole brain activity during a specific behavior is now feasible in zebrafish [50, 51]. Hence, much progress has been made in larval zebrafish on the mechanisms of visual threat processing and its neural modulation. After retinal projections to the brain stabilize [52], larval zebrafish readily show escape responses to simple looming stimuli [53, 54], animated images [55], robotic predators [56], and live predators [57, 58]. Testing variants of looming stimuli on zebrafish has shown that the expanding motion is necessary to drive the escape behavior, while the luminance change (aka dimming) increases the escape probability [54, 59, 60]. Thus, similar to insects, the encoding and processing of looming stimuli in zebrafish can also be separated into two branches: the expanding/looming motion, which is determined by looming velocity; and the luminance change, which is a function of the size of the looming stimulus.

Although there are light-sensitive neurons in the skin and brain of the zebrafish [61, 62], the detection of visual threats by the retinal ganglion cells (RGCs) is necessary for the innate defensive responses to looming stimuli [54, 63]. There are more than 30 distinct types of RGC in the zebrafish retina [63]. Some RGC types are sensitive to looming motion [54]. Some exhibit sensitivity to stimulus size or changes in luminance [54, 64–66]. Due to the limitation of the Ca^{2+} imaging method used in the functional studies, whether any of these RGCs show encoding capabilities similar to the size-encoding or velocity-encoding neurons in insects remains unknown. Furthermore, a causal connection between any specific RGC type and the visually-triggered defensive responses has not been established yet. Thus, there is still much to be resolved on how visual threat is processed in the zebrafish retina and brain.

RGCs project ten distinct arborization fields in the fish brain, including the optic tectum [52, 67]. Selective ablation of RGC axon bundles in the tectum completely abolishes escape behaviors but does not affect optomotor responses [54]. Further, optogenetic activation of tectal neurons triggers escape behaviors [68, 69]. Thus, the retinotectal connection is critical in visual threat processing. Axons of RGC subtypes terminate in specific layers of the tectum, delivering different aspects of visual information [64, 70–74]. Based on the responses of axon terminals of the RGCs to different variants of the looming stimuli, looming and dimming information are delivered to different parts of the tectum and thus likely processed by different tectal neurons [52, 54, 60, 66, 70, 75]. But whether and how these two channels of information on the same looming stimulus combine in the tectum neurons is still unknown.

A looming (expanding) object on the retina may be either a predator or a potential prey. Zebrafish discriminate between the two mainly based on size information [64]. Looming objects need to surpass a size threshold to elicit

escape behaviors [54, 59, 76, 77]. A similar computation also occurs in the optic tectum: tectal neurons in different layers receive different size-selective RGC inputs, information on smaller objects is sent to superficial layers [78], and information on larger objects is sent to deeper layers [64]. The response of the size-selective tectal neurons is gated by superficial inhibitory interneurons (SINs) [64, 74], which serve as computational modules to separate large predators from small prey [59]. A group of tectal neurons in the innermost layer of the optic tectum, the periventricular neurons, receive inputs from SINs and encode the threshold angular size associated with escape latency [59, 74].

Response Mechanisms to Visual Threats

After the processing of visual threat information in the retina and the tectum, the decision to escape is conveyed by the tectal output neurons to the well-known Mauthner cell (MC) and other reticulospinal neurons in the premotor areas (Fig. 2B) [53, 68, 79]. The MC is a critical element in threat-relevant escape behaviors [42, 53, 73, 76, 80, 81]. Activation of a single MC spike elicits a fast escape response [80–82]; ablation of the MC soma results in a significantly longer escape latency [53, 76, 80, 81, 83–85], while ablation of the MC and its axon abolishes the fast escape behavior [86].

The visually triggered looming pathway can be modulated by many factors. Luminance change information from the thalamus to the tectum helps to direct escape behaviors and likely increases the response probability [60]. Hunger, through serotonergic modulation, alters the neural representation of prey-like stimuli in the tectum, and the behavioral response accordingly [87]. Dopaminergic neurons in the hypothalamus modulate and gate the MC response through hindbrain glycinergic interneurons [53]. Both serotonergic and dopaminergic neurons can be modulated by the habenula [88, 89], and the habenula can also modulate defensive behaviors through the habenula—interpeduncular nucleus—griseum centrale pathway [90–92]. Many other neuromodulatory neurons also respond to a looming stimulus and are thus implicated in the process, such as somatostatin neurons, neuropeptide Y neurons, cocaine- and amphetamine-regulated transcript-positive neurons in the hypothalamus, noradrenergic neurons in the locus coeruleus (LC), and cholinergic neurons in the tegmentum [93–96]. But how these neurons modulate the looming pathway remains largely unknown.

In summary, the detection of looming threats in zebrafish shares some similarities with that in insects, the most significant being the separate processing of looming size and looming motion by different visual neurons. Also worth noting is the shortcut circuit *via* the MC, directly connecting visual detection results to motor outputs [97, 98]. Zebrafish also freeze occasionally under threat [55, 57]. Regrettably, little

is known about the mechanisms underlying this behavior, thus preventing comparison to the insects.

Neural Mechanisms for Visually-Evoked Defensive Behavior in Mice

Mice have evolved two types of innate defensive behavior to evade predators [5]. When the threats are remote, such as an eagle sweeping high above in the sky, mice stop all movements (freeze) and wait for the predator to leave. Freezing helps the mouse avoid being identified as prey at a distance, and is also more energy-efficient than escape. But if the threat is imminent, such as in the case of a fast-approaching predator, escape to a nearby refuge is more likely to ensure survival. In this section, we summarize the current understanding of the neural circuits involved in the generation of visually-triggered freezing and escape behaviors. The contents cover stimulus detection and threat identification in the retina and the superior colliculus (SC), then the circuits in various subcortical regions involved in the decision between freezing and escape responses, and finally the generation of the behaviors in the brainstem.

Visual Threat Detection in the Retina

As the first stage of vision, the retina determines what the brain sees of the outside world, and the detection of visual danger signals starts in the retina. The output neurons of the retina, the RGCs, are responsible for transmitting danger signals to the brain rapidly and correctly as soon as the danger emerges in the visual field. Related to research performed in insects and fish, repeated presentation of a dark expanding disk on an overhead screen is efficient in eliciting a robust defensive response in mice [4], and is often used as a visual threat stimulus, although it is different from the looming stimulus commonly used in insects and fish [11, 12]. An RGC subtype that selectively responds to this dark expanding stimulus was first reported in 2009 [99]. It is a subset of the RGCs labeled by the parvalbumin-Cre transgene (PV-5 RGCs). The morphology and function of the PV-5 RGCs indicate that they are a subtype best known as OFF-transient alpha RGCs (OFFt α RGCs). Alpha RGCs are conserved across mammalian species [100]. They have the largest receptive fields and fastest axonal conductance among all RGC subtypes [101–104]. This makes them ideal for transmitting visual threat signals to the brain. Recently, more evidence emerged that placed the OFFt α RGCs firmly in the center of looming detection in the retina: ablation of either OFFt α RGCs themselves or their input interneurons, vGlut3⁺ amacrine cells, severely diminishes looming-evoked defensive responses [105, 106]; and optogenetic activation of these RGCs in the absence of any visual inputs is sufficient

to induce defensive responses [106]. These results are consistent with OFFt α RGC activation being a necessary and sufficient retinal component of the neural pathway for looming evoked innate defensive responses. It is worth noting that a specific molecular marker, *Kcnip2*, has been identified in the OFFt α RGCs, and a CreER knock-in mouse strain has been created [106]. This will greatly facilitate future targeted functional studies on these RGCs.

In addition to the OFFt α RGCs, other RGC subtypes also play important roles in processing looming stimuli. In one report, the dorsal raphe nucleus (DRN) was shown to modulate looming-evoked defensive responses, and RGCs that project to the DRN are necessary for these responses [107]. In a more recent report, it was found that some RGCs are GABAergic, and ablation of the GABAergic RGCs projecting to the SC diminished looming-induced defensive responses [108]. The subtype identities of these two groups of RGCs, and how they participate in the processing of looming information remain to be explored. Neither OFFt α RGCs nor GABAergic RGCs project to the DRN [106, 108], thus they do not overlap with the DRN-projecting RGCs. But whether a significant proportion of OFFt α RGCs are also GABAergic is unknown, and needs to be clarified in the future.

Interestingly, OFFt α RGCs encode the size of a looming object [106], which is reminiscent of the size coding neuron LPLC2 in vinegar flies [21]. LC4 neurons in the vinegar fly encode looming speed [20]. Together, the activity of LPLC2 and LC neurons fully describes the looming stimulus at any given time. Whether there are RGCs in the mouse retina that encode other parameters of the looming stimulus, such as velocity, would be an intriguing question to investigate.

We have summarized so far how RGCs participate in the detection of looming stimuli. The looming stimuli used in these experiments were dark disks quickly expanding to occupy a large visual angle (typically expanding to 30°–40° in a fraction of a second), thus they are likely perceived as an imminent danger by the animals. Mice respond to imminent danger and remote threats in different ways: escape from imminent danger, but freeze and observe if the threat is from a distance [5, 109]. It is reasonable to infer that there could be another neural pathway to detect and respond to remote dangers, such as a cruising eagle in the sky. This pathway may involve RGCs other than the OFFt α RGCs, as the visual stimulus is different. So far, no clear picture has emerged of how remote danger is detected and processed in the retina. A small and slow-moving disk overhead can be used to mimic a remote threat, and mice freeze when presented with this stimulus [5]. This is also an ideal stimulus for W3-RGCs, an RGC subtype that is selectively activated by slow-moving small objects on a clean background like the sky [110]. Yet no connection between W3-RGCs and freezing behavior has been discovered, due to a lack of molecular tools with which

to study W3-RGCs. More molecular tools to manipulate different RGC subtypes will help to answer whether W3-RGCs are indeed involved in this behavior, or if other RGCs with a similar response profile are responsible.

Recently, RGC inputs to SC neurons that project to either the lateral posterior nucleus (LP) or the parabigeminal nucleus (PBG) have been identified [111]. The LP and PBG are involved in different aspects of innate defensive responses, as we further discuss in the next part. Thus this result provides a more comprehensive picture of RGC subtypes closely connected to visual threat detection. Among these RGC subtypes are the ON-OFF direction-selective RGCs (ooDSGCs) and the OFF-sustained RGCs. The functional similarity (direction selectivity) between ooDSGCs and the T4/T5 neurons in vinegar flies may imply that they play a similar role in looming detection [19]. Meanwhile, OFF sustained α RGCs, being fast-conducting α RGCs that respond to a large moving object, may work synergistically with OFFt α RGCs to signal imminent looming danger. Further examination is needed to fully describe the roles these 14 subtypes of RGC play in visual threat detection and processing.

RGCs may also influence the choice of innate defensive behaviors. The behavioral response of mice to looming stimuli is predominantly escaped, with a small fraction of freezing. One interesting study demonstrated that the loss of *Brn3b* in the retina significantly reduces the escape probability, while keeping freezing intact in response to a looming stimulus, indicating that there are already distinctions between flight and freezing from the retina [112]. Further investigations of which RGC subtypes play roles in it, and how the loss of *Brn3b* impacts their roles, are needed to fully understand this phenotype. In zebrafish, dimming information sent to the tectum through the retino-thalamic pathway helps to determine the direction of escape and increases the response probability [60]. Similarly, some mouse RGCs that encode luminance information indirectly excite SC neurons through neurons in the ventral lateral geniculate nucleus (vLGN) that project to the SC [113, 114]. This retino-thalamo-colliculus pathway may modulate escape behaviors in mice just like in zebrafish.

Threat Identification and Response Choice in the Superior Colliculus

The SC is believed to be critical for the innate defensive response to visual threats [115–118]. It is a laminated mid-brain structure implicated in diverse physiological functions [117, 119–123]. The lamination in the SC is conserved across mammalian species, although the relative thickness of the layers varies [121]. The layers can be roughly divided into two major parts, the superficial SC (sSC) and the intermediate/deep SC (m/dSC), receiving visual and

multisensory inputs, respectively. The anatomical structure [121], functional connectivity [123, 124], and behavioral outputs [115, 117, 119, 120, 122, 125, 126] are different between the sSC and the m/dSC. In this section, we discuss recent findings on neural circuits for the innate defensive behaviors in the sSC and m/dSC separately.

The Superficial SC

The sSC is immediately downstream of the retina and is considered to be a place mostly for visual information processing. Almost all of the RGCs project to the sSC whereas only 20–50% of the RGCs project to the dorsal LGN (dLGN) in rodents [127, 128], thus visual processing in sSC is a critical component of vision-related functions. The processed visual information is then used by the sSC to direct a multitude of innate behaviors.

Neurons in the sSC can be classified into four major types: wide-field (WF) cells, narrow-field (NF) cells, horizontal cells, and stellate cells, each with distinct morphological and electrophysiological properties [129]. Freezing and escape behaviors can be elicited rapidly after optogenetic activation of neurons in the sSC [123, 130–133]. The molecular label for the escape-related neurons is parvalbumin (PV), and they act *via* their projections to the PBG: activation of the PV⁺ neurons projecting to the PBG triggers immediate escape behavior, and the activity of these neurons may be correlated with the time-to-collision with the approaching object [131]. One interesting fact about these neurons is that they are excitatory and not inhibitory, unlike most PV⁺ neurons [134]. PV⁺ neurons in the sSC are heterogeneous based on their morphology, projections, electrophysiological properties, and connections to relevant behaviors [130, 131, 135], but those that project to the PBG may belong to a single type, NF neurons [130, 131]. Although their activation readily triggers escape behavior, it has not been tested whether these PV⁺ neurons that project to the PBG are required for the behavior, thus the participation of other SC neuronal types is still possible. It was first reported that the SC neurons projecting to the LP drive freezing behavior upon optogenetic activation [136], although the report indicated that the neurons were in the m/dSC. Later, neurotensin receptor 1 (Ntsr1) and cerebellin 2 precursors (Cbln2) were found to be potential markers for the sSC neurons that drive freezing behavior [132, 133]. Ntsr1⁺ neurons are WF neurons with large receptive fields [129, 137]. Interestingly, these neurons best respond to small slow-moving objects [129, 137]. This makes Ntsr1⁺ neurons good candidates for alarm neurons that can warn animals of potential predators at a distance. Ntsr1⁺ neurons project exclusively to the LP. Cbln2 expression probably partially overlaps with Ntsr1 expression, and Cbln2⁺ neurons include mostly LP-projecting neurons and a small portion of non-LP-projecting neurons [133]. The exact

relationship between the two markers is not yet clear, but the same subset of freezing-driving neurons is likely labeled by both markers. Ablation or activation experiments with more specificity will help to clarify this.

Thus, two different populations of neurons in the sSC drive the escape and freezing behaviors separately: WF neurons that project to the LP for the freezing behavior and PV⁺ neurons that project to the PBG for the escape behavior. So far, there has been no report of interactions between the two pathways in the sSC; they seem to operate relatively independently (see [130]). Also of note is that the peak response time of WF neurons is correlated with the time-to-collision during a looming stimulus [137], thus they may also contribute to the processing of the looming stimulus, and so interact with the escape pathway. The sSC and the primary visual cortex (V1) have robust information exchange and modulate each other's visual functions. SC neurons in the freezing pathway receive V1 inputs [138], and V1 modulates the magnitude of looming-evoked responses in the SC [139]. Meanwhile, the SC influences the tuning of V1 *via* the tectogeniculate pathway [140]. The tectogeniculate pathway also participates in visual threat processing. Some GABAergic neurons in the sSC project to the dLGN and modulate the choice between freezing and escape through this tectogeniculate pathway [141]. Hence, three out of four outputs of the sSC are connected to visually-evoked defensive behaviors: the sSC-LP pathway for freezing, the sSC-PBG pathway for escape, and the sSC-LGN pathway for modulating the probability of freezing. Whether the sSC-mSC pathway also participates in visually-triggered defensive behaviors remains an interesting question.

Decoding visual information correctly is important for the SC to make appropriate behavioral choices. Visual threat information delivered by the RGCs is not specific enough to use directly as go signals for the behavioral responses. For example, OFFt α RGCs not only respond to dark looming stimuli, but also respond robustly to dark objects appearing or bright objects disappearing inside their receptive fields, yet the latter types of stimuli do not induce defensive behaviors in mice. Therefore, SC circuits downstream of OFFt α RGCs must distinguish the two and only respond when looming stimuli are presented. To understand how sSC neurons further extract and identify visual threat information from the RGC inputs, one needs to first understand how RGCs and sSC neurons are connected. Although efforts have been made to map the connections between the retina and the SC [111], the input RGCs for the Ntsr1⁺ neurons and the PV⁺ neurons, and the circuit mechanisms underlying the processing of RGC inputs by these SC neurons are not yet clear (but see the most recent report [142] while this review was being edited). Nevertheless, we know enough now to form a few hypotheses. For example, activity manipulations of the OFFt α RGCs impact both the escape and the freezing

behaviors [106], thus these RGCs likely make connections with both the Ntsr1⁺ neurons and the PV⁺ neurons. Further, inputs from some other RGCs are likely needed to help these SC neurons to distinguish different stimuli and only respond to those considered potential threats. Similarly, if W3-RGCs are indeed connected to the detection of remote danger, and thus the freezing response, then they should preferentially connect with Ntsr1⁺ neurons. Investigations into these predictions will help to connect the innate defensive-related pathways between the retina and the SC.

Another aspect of visual processing also needs to be investigated to fully understand the role of the SC in visually-triggered innate defensive behaviors: the context-dependent interpretation of the visual information. For example, the same small and slow-moving objects on the retina may signify either a large predator at a distance or a small potential prey close by. How does the SC distinguish the two? Interestingly, it has been demonstrated that WF neurons (aka Ntsr1⁺ neurons), in addition to mediating freezing behavior, are also necessary for prey detection in mice [143]. Incidentally, they also respond robustly to small slow-moving objects [137]. Thus, these neurons receive information from the retina about small and slow-moving objects, identify if it represents a predator or prey, and then trigger completely different behavior outputs based on that identification. One likely method to distinguish predator from prey is to use the location of the object: the prey is present almost exclusively in the lower half of the visual field for the mouse, whereas the predators are mainly located in the upper visual field. Retinotopically, lower and upper visual fields correspond to lateral and medial parts of the SC, respectively. It would be illuminating to test whether activation of Ntsr1⁺ cells at medial and lateral SC locations leads to different behavioral outputs.

The Intermediate and Deep SC (m/dSC)

The m/dSC is one of the most well-studied regions in the brain. It is considered a place for sensory integration and the initiation of motor outputs. It receives inputs from visual, auditory, and somatosensory modules and performs sensory-motor transformation [122, 144, 145]. Here, we mainly focus on the motor output aspect of its functions, more specifically, the circuits involved in the generation of innate defensive behaviors. Unlike the superficial layer, which has limited input and output regions, m/dSC neurons receive inputs from almost the entire brain and part of the spinal cord, and project to multiple thalamic nuclei and the spinal cord [125, 146]. Direct activation of the m/dSC neurons or their axon terminals elicits freezing, escape, orienting, or preying behaviors [116, 133, 136, 147–152]. It is worth noting that activating neurons that project to the ipsilateral brainstem reticular formation (uncrossed pathway) mainly elicit

defensive behaviors while activating neurons that descend to the contralateral brainstem reticular formation (crossed pathway) only induce orienting behaviors [116, 121, 149]. Many studies indicate that neurons in the medial part of the m/dSC are important in defensive behaviors and those in the lateral part are more involved in prey capture [148, 153]. But little is known about the mechanism of divergence between the medial and the lateral parts of the m/dSC. In addition to visual threats, auditory crescendo inputs also evoke defensive behaviors *via* an m/dSC pathway [154]. To generate fast responses to threats, one would expect a direct pathway from the looming-responsive neurons in the sSC to the defensive behavior-related neurons in the m/dSC. Although this has not been tested, with the discovery of more cell-type markers in the SC, we hope this important question will be addressed soon.

Behavior Modulation and Execution: Beyond the SC

Besides the m/dSC, the sSC also projects to the LGN through stellate and horizontal neurons, to the LP through WF neurons, and to the PBG through non-WF neurons [129]. Except for the vLGN, all other targets contain few inhibitory neurons in mice. The vLGN provides important information about changes in luminance to the m/dSC and enhances defensive behaviors [113, 114]. The LP is the lateral posterior part of the thalamus and a homologue of the pulvinar in the primate brain. The LP mediates visually-evoked freezing behavior through projections to the lateral amygdala [130, 136]. The PBG receives inputs from both the sSC and the m/dSC, and forms reciprocal connections with the sSC [155]. The PBG mediates looming-evoked escape behavior [130, 131]. Interestingly, the PBG also projects to the central part of the amygdala [131]. Projections from the m/dSC through the ventral tegmental area (VTA) or ventral midline thalamus (vMT) to the amygdala are also reported to modulate looming-evoked innate defensive responses [147, 156]. Whether connections from the LP, PBG, vMT, and VTA converge or interact in the amygdala remains largely unknown [157–160].

From the amygdala, the pathway likely becomes common for innate defensive responses to threats from all sensory modalities [158, 159, 161–165]. As an aversive stimulus, looming also activates the hypothalamus [166–169], all the way to the periaqueductal grey (PAG) [158, 170–175]. Signals from the m/dSC and the amygdala converge on the dorsal and ventrolateral PAG, respectively [150]. Further downstream, the lateral paraventricular nucleus (LPGi) is the major output nucleus to initiate defensive behaviors. Both the deep SC and the PAG have connections to motor-related midbrain areas such as the cuneiform nucleus and medullary regions such as the LPGi [146, 170, 176, 177]. The LPGi then sends commands to motor neurons in the

spinal cord to generate movements [178, 179]. Freezing and flight responses are mediated by different subsets of neurons in this pathway, but there is also evidence of interactions between the two behavioral options (Fig. 2C) [157, 170].

The entire innate defensive pathway is heavily modulated. The serotonergic DRN, noradrenergic LC, dopaminergic A13, cholinergic PBG, and pedunculopontine tegmental nucleus all provide inputs to the SC [146, 180–182], influence the responses of SC neurons [182, 183], and regulate visually-evoked defensive behaviors [107, 147, 184]. Anatomical data also show that the m/dSC sends projections to dopaminergic systems in the substantia nigra pars compacta and the VTA, the cholinergic system in the pedunculopontine nucleus, and the lateral dorsal tegmental area [146]. Furthermore, the habenula receives visual threat inputs from the hypothalamus and targets almost all midbrain

neuromodulatory systems to modulate escape and freezing behaviors [168, 185, 186]. The mechanisms by which these modulation systems are involved in visually-evoked defensive behaviors and how they interact require further study.

An Evolutionarily Conserved Pathway Across Species

To conclude, we summarize the neural mechanisms involved in visual threat responses, focusing on common features among species. First, there appears to be a common scheme for the identification of looming objects that signal danger. Animals need to identify visual threats quickly and correctly to evade danger in time and at the same time not waste energy on non-threatening objects in the visual field. In

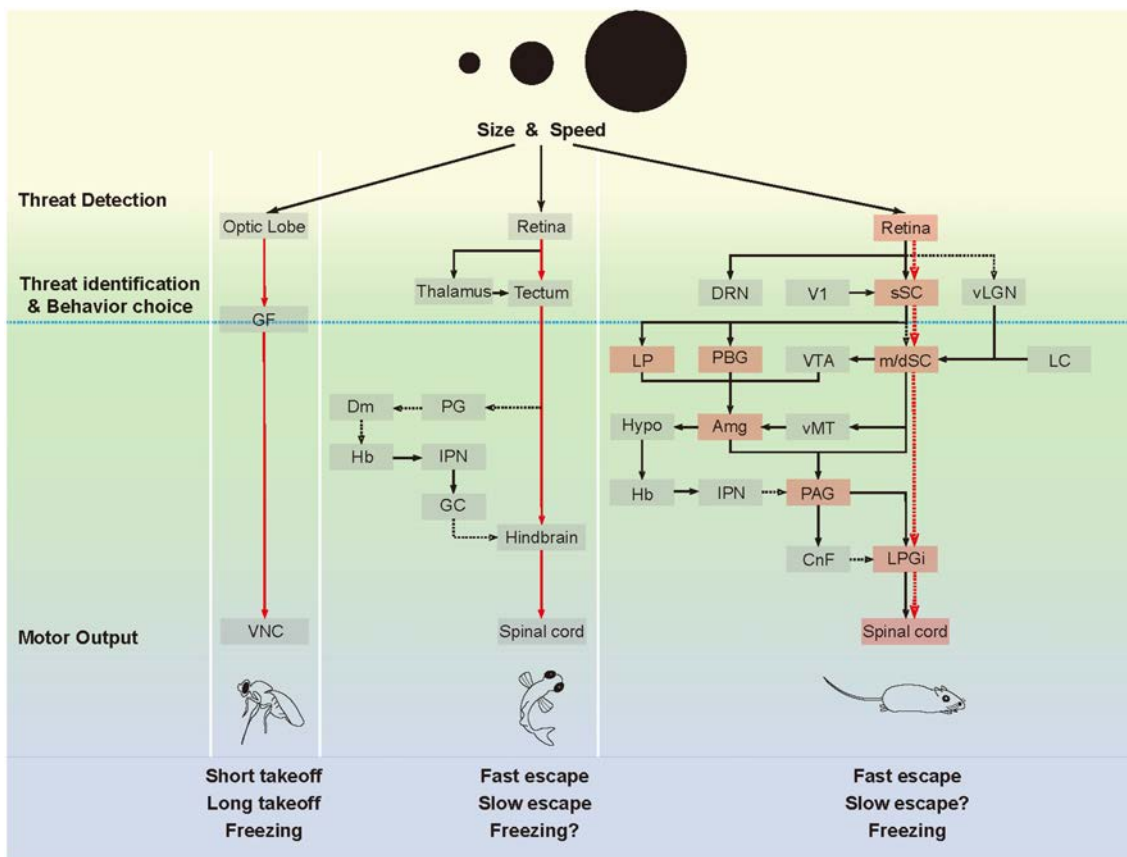


Fig. 3 Schematic overview and cross-species comparison of the neural pathways involved in visual threat processing. Black arrows: known descending connections. Black dashed arrows: suspected descending connections. Red arrows: direct descending pathways in *Drosophila* and zebrafish. Red dashed arrows: hypothesized short-cut pathway in the mouse. Blue dashed line: completion of visual threat processing. Orange areas: brain regions that are indispensable to visual threat responses. *GF* giant fiber, *VNC* ventral nerve cord, *PG* preglomerular nucleus, *Dm* dorsal pallium, *Hb* habenula, *IPN* inter-

peduncular nucleus, *GC* griseum centrale, *V1* primary visual cortex, *vLGN* ventral lateral geniculate nucleus, *sSC* superficial superior colliculus, *DRN* dorsal raphe nucleus, *LP* lateral posterior nucleus, *PBG* parabrachial nucleus, *VTA* ventral tegmental area, *m/dSC* intermediate/deep superior colliculus, *LC* locus coeruleus, *Hypo* hypothalamus, *Amg* amygdala, *vMT* ventral midline thalamus, *PAG* periaqueductal grey, *CnF* cuneiform nucleus, *LPGi* lateral paragigantocellular nucleus.

insects and fish, perhaps also in mice, the same two parameters are used to identify looming objects: object size, and looming speed. The two parameters are encoded in parallel by different sets of visual sensory neurons [21, 25, 106, 112]. In insects, the neurons downstream then combine the size and speed information to correctly identify a looming object, then initiate appropriate behavioral responses [11, 20, 21, 25, 26, 77]. How these two types of information converge in fish and mice is less clear, although the convergence likely also occurs in neurons directly downstream of the size- and speed-encoding RGCs, in the optic tectum (fish) or sSC (mice).

Second, the mechanisms underlying behavior choice show significant similarities. Freezing and escape are two consistent behavioral responses to visual threats across species [187]. Freezing behavior in zebrafish is much less studied, so we can only compare results in insects and mice. In both insects and mice, looming objects induce either escape or freezing [4, 29, 37], while small moving objects induce freezing [5, 36]. Also common to insects and mice, freezing and fleeing are mediated by separate neural circuits, so many manipulations affect only one behavior and not the other [21, 112, 130]. Different visual threats activate the two pathways differently: looming activates both pathways [19, 36, 130, 137]. Small moving objects likely only activate the freezing pathway, although this has not been rigorously tested yet (see [20]). When both pathways are activated, internal states and environmental conditions help bias the behavioral choice toward one or the other [37, 95, 166, 184].

Third, the underlying circuits share a similar overall structure that favors reaction speed. Incoming threats are mainly identified by their size and looming velocity, without consideration of details such as texture or shape. The encoding of size and velocity does not require complex computations; thus, the central process of visual threat identification occurs in two abstracted layers of visual processing (Fig. 3, threat detection layer, threat identification, and behavior choice layer): The first layer encodes looming velocity and object size, and the second layer combines the information and identifies the threat. In vinegar flies and zebrafish, this second layer, GF in vinegar flies and optic tectum neurons in fish, then connects directly to the motor output neurons for behavior execution (Fig. 3). This direct connection ensures a fast response as soon as a threat is identified. In mice, however, such a direct pathway has not been described. This pathway, should it exist, likely connects the visual SC directly to the motor output part of the SC, then to the LPGi in the medulla (Fig. 3, red dashed lines in mouse). Projections and connections between the sSC and the m/dSC are plentiful [129, 146, 188]. In addition, optogenetic activation of Ntsr1⁺ and PV⁺ neurons in the sSC induces responses in m/dSC neurons, indicating functional connections [132]. Further downstream, the m/dSC has projections to the

medulla [146, 189, 190], and activation of m/dSC neurons projecting to the medulla induces defensive behaviors [149], suggesting a direct connection between the m/dSC and the defensive behavior-related medullary structure LPGi. Thus, this sSC-m/dSC-LPGi pathway is anatomically plausible. Based on these, we propose that a retina-to-medulla shortcut pathway exists in mice for visually triggered innate defensive responses (Fig. 3).

Thus, for visually triggered innate defensive responses in different species, although their neural circuits differ drastically in complexity and details, the overall structure and underlying principles appear to be conserved in evolution. Further comparative studies across species may help to better understand the circuit mechanisms underlying visual threat processing and innate defensive responses.

Acknowledgements We thank members of Dr. Yifeng Zhang's and Dr. Jun Yan's lab for their help and support. This review was supported by a general project of the National Natural Science Foundation of China (31871052).

Conflict of interest The authors declare no conflict of interest.

References

1. Clause AR, Capaldi EA. Caudal autotomy and regeneration in lizards. *J Exp Zool A Comp Exp Biol* 2006, 305: 965–973.
2. Higham TE, Russell AP. Flip, flop and fly: Modulated motor control and highly variable movement patterns of autotomized gecko tails. *Biol Lett* 2010, 6: 70–73.
3. Gabrielsen GW, Smith EN. Physiological responses associated with feigned death in the American opossum. *Acta Physiol Scand* 1985, 123: 393–398.
4. Yilmaz M, Meister M. Rapid innate defensive responses of mice to looming visual stimuli. *Curr Biol* 2013, 23: 2011–2015.
5. De Franceschi G, Vivattanasarn T, Saleem AB, Solomon SG. Vision guides selection of freeze or flight defense strategies in mice. *Curr Biol* 2016, 26: 2150–2154.
6. Fanselow MS. Neural organization of the defensive behavior system responsible for fear. *Psychon Bull Rev* 1994, 1: 429–438.
7. Ydenberg RC, Dill LM. The economics of fleeing from predators. *Adv Study Behav* 1986, 16: 229–249.
8. Evans DA, Stempel AV, Vale R, Branco T. Cognitive control of escape behaviour. *Trends Cogn Sci* 2019, 23: 334–348.
9. Card GM. Escape behaviors in insects. *Curr Opin Neurobiol* 2012, 22: 180–186.
10. Herberholz J, Marquart GD. Decision making and behavioral choice during predator avoidance. *Front Neurosci* 2012, 6: 125.
11. Fotowat H, Gabbiani F. Collision detection as a model for sensory-motor integration. *Annu Rev Neurosci* 2011, 34: 1–19.
12. Peek MY, Card GM. Comparative approaches to escape. *Curr Opin Neurobiol* 2016, 41: 167–173.
13. Allen MJ, Godenschwege TA, Tanouye MA, Phelan P. Making an escape: Development and function of the *Drosophila* giant fibre system. *Semin Cell Dev Biol* 2006, 17: 31–41.
14. Modi MN, Shuai Y, Turner GC. The *Drosophila* mushroom body: From architecture to algorithm in a learning circuit. *Annu Rev Neurosci* 2020, 43: 465–484.

15. Card G, Dickinson MH. Visually mediated motor planning in the escape response of *Drosophila*. *Curr Biol* 2008, 18: 1300–1307.
16. Card G, Dickinson M. Performance trade-offs in the flight initiation of *Drosophila*. *J Exp Biol* 2008, 211: 341–353.
17. Maisak MS, Haag J, Ammer G, Serbe E, Meier M, Leonhardt A. A directional tuning map of *Drosophila* elementary motion detectors. *Nature* 2013, 500: 212–216.
18. Schilling T, Borst A. Local motion detectors are required for the computation of expansion flow-fields. *Biol Open* 2015, 4: 1105–1108.
19. Klapoetke NC, Nern A, Peek MY, Rogers EM, Breads P, Rubin GM, *et al.* Ultra-selective looming detection from radial motion opponency. *Nature* 2017, 551: 237–241.
20. von Reyn CR, Nern A, Williamson WR, Breads P, Wu M, Namiki S, *et al.* Feature integration drives probabilistic behavior in the *Drosophila* escape response. *Neuron* 2017, 94: 1190–1204.e6.
21. Ache JM, Polsky J, Alghailani S, Parekh R, Breads P, Peek MY, *et al.* Neural basis for looming size and velocity encoding in the *Drosophila* giant fiber escape pathway. *Curr Biol* 2019, 29: 1073–1081.e4.
22. Krapp HG, Gabbiani F. Spatial distribution of inputs and local receptive field properties of a wide-field, looming sensitive neuron. *J Neurophysiol* 2005, 93: 2240–2253.
23. Gabbiani F, Cohen I, Laurent G. Time-dependent activation of feed-forward inhibition in a looming-sensitive neuron. *J Neurophysiol* 2005, 94: 2150–2161.
24. Wang H, Dewell RB, Zhu Y, Gabbiani F. Feedforward inhibition conveys time-varying stimulus information in a collision detection circuit. *Curr Biol* 2018, 28: 1509–1521.e3.
25. Gabbiani F, Krapp HG, Koch C, Laurent G. Multiplicative computation in a visual neuron sensitive to looming. *Nature* 2002, 420: 320–324.
26. Hatsopoulos N, Gabbiani F, Laurent G. Elementary computation of object approach by wide-field visual neuron. *Science* 1995, 270: 1000–1003.
27. Dewell RB, Gabbiani F. Biophysics of object segmentation in a collision-detecting neuron. *eLife* 2018, 7: e34238.
28. Zhu Y, Dewell RB, Wang H, Gabbiani F. Pre-synaptic muscarinic excitation enhances the discrimination of looming stimuli in a collision-detection neuron. *Cell Rep* 2018, 23: 2365–2378.
29. von Reyn CR, Breads P, Peek MY, Zheng GZ, Williamson WR, Yee AL, *et al.* A spike-timing mechanism for action selection. *Nat Neurosci* 2014, 17: 962–970.
30. Tanouye MA, Wyman RJ. Motor outputs of giant nerve fiber in *Drosophila*. *J Neurophysiol* 1980, 44: 405–421.
31. Lima SQ, Miesenböck G. Remote control of behavior through genetically targeted photostimulation of neurons. *Cell* 2005, 121: 141–152.
32. Fotowat H, Fayyazuddin A, Bellen HJ, Gabbiani F. A novel neuronal pathway for visually guided escape in *Drosophila melanogaster*. *J Neurophysiol* 2009, 102: 875–885.
33. Cheong HS, Siwanowicz I, Card GM. Multi-regional circuits underlying visually guided decision-making in *Drosophila*. *Curr Opin Neurobiol* 2020, 65: 77–87.
34. de Vries SEJ, Clandinin TR. Loom-sensitive neurons link computation to action in the *Drosophila* visual system. *Curr Biol* 2012, 22: 353–362.
35. Wu M, Nern A, Wu M, Morimoto MM, Reiser MB, Card GM, *et al.* Visual projection neurons in the *Drosophila* lobula link feature detection to distinct behavioral programs. *eLife* 2016, 5: e21022.
36. Tanaka R, Clark DA. Object-displacement-sensitive visual neurons drive freezing in *Drosophila*. *Curr Biol* 2020, 30: 2532–2550.e8.
37. Zacarias R, Namiki S, Card GM, Vasconcelos ML, Moita MA. Speed dependent descending control of freezing behavior in *Drosophila melanogaster*. *Nat Commun* 2018, 9: 3697.
38. Keleş MF, Hardcastle BJ, Städele C, Xiao Q, Frye MA. Inhibitory interactions and columnar inputs to an object motion detector in *Drosophila*. *Cell Rep* 2020, 30: 2115–2124.e5.
39. Ball W, Tronick E. Infant responses to impending collision: Optical and real. *Science* 1971, 171: 818–820.
40. Schiff W, Caviness JA, Gibson JJ. Persistent fear responses in rhesus monkeys to the optical stimulus of looming. *Science* 1962, 136: 982–983.
41. Sun H, Frost BJ. Computation of different optical variables of looming objects in pigeon nucleus rotundus neurons. *Nat Neurosci* 1998, 1: 296–303.
42. Preuss T, Osei-Bonsu PE, Weiss SA, Wang C, Faber DS. Neural representation of object approach in a decision-making motor circuit. *J Neurosci* 2006, 26: 3454–3464.
43. Hayes WN, Saiff EI. Visual alarm reactions in turtles. *Animal Behav* 1967, 15: 102–106.
44. Yamamoto K, Nakata M, Nakagawa H. Input and output characteristics of collision avoidance behavior in the frog *Rana catesbeiana*. *Brain Behav Evol* 2003, 62: 201–211.
45. Wang Y, Frost BJ. Time to collision is signalled by neurons in the nucleus rotundus of pigeons. *Nature* 1992, 356: 236–238.
46. Cong L, Wang Z, Chai Y, Hang W, Shang C, Yang W, *et al.* Rapid whole brain imaging of neural activity in freely behaving larval zebrafish (*Danio rerio*). *eLife* 2017, 6: e28158.
47. Kim DH, Kim J, Marques JC, Grama A, Hildebrand DGC, Gu W, *et al.* Pan-neuronal calcium imaging with cellular resolution in freely swimming zebrafish. *Nat Methods* 2017, 14: 1107–1114.
48. Fosque BF, Sun Y, Dana H, Yang CT, Ohyama T, Tadross MR, *et al.* Neural circuits. Labeling of active neural circuits in vivo with designed calcium integrators. *Science* 2015, 347: 755–760.
49. Förster D, Kramer A, Baier H, Kubo F. Optogenetic precision toolkit to reveal form, function and connectivity of single neurons. *Methods* 2018, 150: 42–48.
50. Orger MB. The cellular organization of zebrafish visuomotor circuits. *Curr Biol* 2016, 26: R377–R385.
51. Orger MB, de Polavieja GG. Zebrafish behavior: Opportunities and challenges. *Annu Rev Neurosci* 2017, 40: 125–147.
52. Baier H, Wullimann MF. Anatomy and function of retinorecipient arborization fields in zebrafish. *J Comp Neurol* 2021, 529: 3454–3476.
53. Yao Y, Li X, Zhang B, Yin C, Liu Y, Chen W, *et al.* Visual cue-discriminative dopaminergic control of visuomotor transformation and behavior selection. *Neuron* 2016, 89: 598–612.
54. Temizer I, Donovan JC, Baier H, Semmelhack JL. A visual pathway for looming-evoked escape in larval zebrafish. *Curr Biol* 2015, 25: 1823–1834.
55. Luca RM, Gerlai R. In search of optimal fear inducing stimuli: Differential behavioral responses to computer animated images in zebrafish. *Behav Brain Res* 2012, 226: 66–76.
56. Spinello C, Yang Y, Macrì S, Porfiri M. Zebrafish adjust their behavior in response to an interactive robotic predator. *Front Robot AI* 2019, 6: 38.
57. Bass SLS, Gerlai R. Zebrafish (*Danio rerio*) responds differentially to stimulus fish: The effects of sympatric and allopatric predators and harmless fish. *Behav Brain Res* 2008, 186: 107–117.
58. Ladu F, Bartolini T, Panitz SG, Chiarotti F, Butail S, Macrì S, *et al.* Live predators, robots, and computer-animated images elicit differential avoidance responses in zebrafish. *Zebrafish* 2015, 12: 205–214.
59. Dunn TW, Gebhardt C, Naumann EA, Riegler C, Ahrens MB, Engert F, *et al.* Neural circuits underlying visually evoked escapes in larval zebrafish. *Neuron* 2016, 89: 613–628.

60. Heap LAL, Vanwalleghem G, Thompson AW, Favre-Bulle IA, Scott EK. Luminance changes drive directional startle through a thalamic pathway. *Neuron* 2018, 99: 293–301.e4.
61. Bellingham J, Whitmore D, Philp AR, Wells DJ, Foster RG. Zebrafish melanopsin: Isolation, tissue localisation and phylogenetic position. *Mol Brain Res* 2002, 107: 128–136.
62. Fernandes AM, Fero K, Arrenberg AB, Bergeron SA, Driever W, Burgess HA. Deep brain photoreceptors control light-seeking behavior in zebrafish larvae. *Curr Biol* 2012, 22: 2042–2047.
63. Kölsch Y, Hahn J, Sappington A, Stemmer M, Fernandes AM, Helmbrecht TO, *et al.* Molecular classification of zebrafish retinal ganglion cells links genes to cell types to behavior. *Neuron* 2021, 109: 645–662.e9.
64. Preuss SJ, Trivedi CA, vom Berg-Maurer CM, Ryu S, Bollmann JH. Classification of object size in retinotectal microcircuits. *Curr Biol* 2014, 24: 2376–2385.
65. Robles E, Fields NP, Baier H. The zebrafish visual system transmits dimming information via multiple segregated pathways. *J Comp Neurol* 2021, 529: 539–552.
66. Förster D, Helmbrecht TO, Mearns DS, Jordan L, Mokayes N, Baier H. Retinotectal circuitry of larval zebrafish is adapted to detection and pursuit of prey. *eLife* 2020, 9: e58596.
67. Burrill JD, Easter SS Jr. Development of the retinofugal projections in the embryonic and larval zebrafish (*Brachydanio rerio*). *J Comp Neurol* 1994, 346: 583–600.
68. Helmbrecht TO, dal Maschio M, Donovan JC, Koutsouli S, Baier H. Topography of a visuomotor transformation. *Neuron* 2018, 100: 1429–1445.e4.
69. Fajardo O, Zhu P, Friedrich RW. Control of a specific motor program by a small brain area in zebrafish. *Front Neural Circuits* 2013, 7: 67.
70. Robles E, Laurell E, Baier H. The retinal projectome reveals brain-area-specific visual representations generated by ganglion cell diversity. *Curr Biol* 2014, 24: 2085–2096.
71. Lowe AS, Nikolaou N, Hunter PR, Thompson ID, Meyer MP. A systems-based dissection of retinal inputs to the zebrafish tectum reveals different rules for different functional classes during development. *J Neurosci* 2013, 33: 13946–13956.
72. Nikolaou N, Lowe AS, Walker AS, Abbas F, Hunter PR, Thompson ID, *et al.* Parametric functional maps of visual inputs to the tectum. *Neuron* 2012, 76: 317–324.
73. Marquez-Legorreta E, Piber M, Scott EK (2020) Visual escape in larval zebrafish: Stimuli, circuits, and behavior. In: Gerlai RT (ed) *Behavioral and Neural Genetics of Zebrafish*, Elsevier, Amsterdam, pp 49–71.
74. Del Bene F, Wyart C, Robles E, Tran A, Looger L, Scott EK, *et al.* Filtering of visual information in the tectum by an identified neural circuit. *Science* 2010, 330: 669–673.
75. Bollmann JH. The zebrafish visual system: From circuits to behavior. *Annu Rev Vis Sci* 2019, 5: 269–293.
76. Bhattacharyya K, McLean DL, MacIver MA. Visual threat assessment and reticulospinal encoding of calibrated responses in larval zebrafish. *Curr Biol* 2017, 27: 2751–2762.e6.
77. Fotowat H, Harrison RR, Gabbiani F. Multiplexing of motor information in the discharge of a collision detecting neuron during escape behaviors. *Neuron* 2011, 69: 147–158.
78. Semmelhack JL, Donovan JC, Thiele TR, Kuehn E, Laurell E, Baier H. A dedicated visual pathway for prey detection in larval zebrafish. *eLife* 2014, 3: e04878.
79. Sato T, Hamaoka T, Aizawa H, Hosoya T, Okamoto H. Genetic single-cell mosaic analysis implicates ephrinB2 reverse signaling in projections from the posterior tectum to the hindbrain in zebrafish. *J Neurosci* 2007, 27: 5271–5279.
80. Korn H, Faber DS. The mauthner cell half a century later: A neurobiological model for decision-making? *Neuron* 2005, 47: 13–28.
81. Eaton RC, Lee RKK, Foreman MB. The Mauthner cell and other identified neurons of the brainstem escape network of fish. *Prog Neurobiol* 2001, 63: 467–485.
82. Tabor KM, Bergeron SA, Horstick EJ, Jordan DC, Aho V, Porkka-Heiskanen T, *et al.* Direct activation of the Mauthner cell by electric field pulses drives ultrarapid escape responses. *J Neurophysiol* 2014, 112: 834–844.
83. Kohashi T, Oda Y. Initiation of Mauthner- or non-Mauthner-mediated fast escape evoked by different modes of sensory input. *J Neurosci* 2008, 28: 10641–10653.
84. Liu KS, Fetcho JR. Laser ablations reveal functional relationships of segmental hindbrain neurons in zebrafish. *Neuron* 1999, 23: 325–335.
85. Lacoste AMB, Schoppik D, Robson DN, Haesemeyer M, Portugues R, Li JM, *et al.* A convergent and essential interneuron pathway for mauthner-cell-mediated escapes. *Curr Biol* 2015, 25: 1526–1534.
86. Hecker A, Schulze W, Oster J, Richter DO, Schuster S. Removing a single neuron in a vertebrate brain forever abolishes an essential behavior. *Proc Natl Acad Sci U S A* 2020, 117: 3254–3260.
87. Filosa A, Barker AJ, Dal Maschio M, Baier H. Feeding state modulates behavioral choice and processing of prey stimuli in the zebrafish tectum. *Neuron* 2016, 90: 596–608.
88. Hikosaka O. The habenula: From stress evasion to value-based decision-making. *Nat Rev Neurosci* 2010, 11: 503–513.
89. Suryanarayana SM, Pérez-Fernández J, Robertson B, Grillner S. The lamprey forebrain—Evolutionary implications. *Brain Behav Evol* 2022, 96: 318–333.
90. Agetsuma M, Aizawa H, Aoki T, Nakayama R, Takahoko M, Goto M, *et al.* The habenula is crucial for experience-dependent modification of fear responses in zebrafish. *Nat Neurosci* 2010, 13: 1354–1356.
91. Duboué ER, Hong E, Eldred KC, Halpern ME. Left habenular activity attenuates fear responses in larval zebrafish. *Curr Biol* 2017, 27: 2154–2162.e3.
92. Okamoto H, Agetsuma M, Aizawa H. Genetic dissection of the zebrafish habenula, a possible switching board for selection of behavioral strategy to cope with fear and anxiety. *Dev Neurobiol* 2012, 72: 386–394.
93. Lovett-Barron M, Andalman AS, Allen WE, Vesuna S, Kauvar I, Burns VM, *et al.* Ancestral circuits for the coordinated modulation of brain state. *Cell* 2017, 171: 1411–1423.e17.
94. Feng J, Zhang C, Lischinsky JE, Jing M, Zhou J, Wang H, *et al.* A genetically encoded fluorescent sensor for rapid and specific *in vivo* detection of norepinephrine. *Neuron* 2019, 102: 745–761.e8.
95. Corradi L, Filosa A. Neuromodulation and behavioral flexibility in larval zebrafish: From neurotransmitters to circuits. *Front Mol Neurosci* 2021, 14: 718951.
96. Lovett-Barron M, Chen R, Bradbury S, Andalman AS, Wagle M, Guo S, *et al.* Multiple convergent hypothalamus–brainstem circuits drive defensive behavior. *Nat Neurosci* 2020, 23: 959–967.
97. do Carmo Silva RX, Lima-Maximino MG, Maximino C. The aversive brain system of teleosts: Implications for neuroscience and biological psychiatry. *Neurosci Biobehav Rev* 2018, 95: 123–135.
98. Carr JA. I'll take the low road: The evolutionary underpinnings of visually triggered fear. *Front Neurosci* 2015, 9: 414.
99. Münch TA, da Silveira RA, Siebert S, Viney TJ, Awatramani GB, Roska B. Approach sensitivity in the retina processed by a multifunctional neural circuit. *Nat Neurosci* 2009, 12: 1308–1316.

100. Peichl L. Alpha ganglion cells in mammalian retinae: Common properties, species differences, and some comments on other ganglion cells. *Vis Neurosci* 1991, 7: 155–169.
101. Cleland BG, Levick WR, Wässle H. Physiological identification of a morphological class of cat retinal ganglion cells. *J Physiol* 1975, 248: 151–171.
102. Cleland BG, Levick WR. Brisk and sluggish concentrically organized ganglion cells in the cat's retina. *J Physiol* 1974, 240: 421–456.
103. Krieger B, Qiao M, Rousso DL, Sanes JR, Meister M. Four alpha ganglion cell types in mouse retina: Function, structure, and molecular signatures. *PLoS ONE* 2017, 12: e0180091.
104. Boycott BB, Wässle H. The morphological types of ganglion cells of the domestic cat's retina. *J Physiol* 1974, 240: 397–419.
105. Kim T, Shen N, Hsiang JC, Johnson KP, Kerschensteiner D. Dendritic and parallel processing of visual threats in the retina control defensive responses. *Sci Adv* 2020, 6: eabc9920.
106. Wang F, Li E, De L, Wu Q, Zhang Y. OFF-transient alpha RGCs mediate looming triggered innate defensive response. *Curr Biol* 2021, 31: 2263–2273.e3.
107. Huang L, Yuan T, Tan M, Xi Y, Hu Y, Tao Q, *et al.* A retinoraphe projection regulates serotonergic activity and looming-evoked defensive behaviour. *Nat Commun* 2017, 8: 14908.
108. Cai D, Luo X, Shen K, Shen Y. GABAergic retinal ganglion cells regulate innate defensive responses. *Neuroreport* 2021, 32: 643–649.
109. Yang X, Liu Q, Zhong J, Song R, Zhang L, Wang L. A simple threat-detection strategy in mice. *BMC Biol* 2020, 18: 93.
110. Zhang Y, Kim IJ, Sanes JR, Meister M. The most numerous ganglion cell type of the mouse retina is a selective feature detector. *Proc Natl Acad Sci U S A* 2012, 109: E2391–E2398.
111. Reinhard K, Li C, Do Q, Burke EG, Heynderickx S, Farrow K. A projection specific logic to sampling visual inputs in mouse superior colliculus. *eLife* 2019, 8: e50697.
112. Lees RN, Akbar AF, Badea TC. Retinal ganglion cell defects cause decision shifts in visually evoked defense responses. *J Neurophysiol* 2020, 124: 1530–1549.
113. Salay LD, Huberman AD. Divergent outputs of the ventral lateral geniculate nucleus mediate visually evoked defensive behaviors. *Cell Rep* 2021, 37: 109792.
114. Fratzl A, Koltchev AM, Vissers N, Tan YL, Marques-Smith A, Vanessa Stempel A, *et al.* Flexible inhibitory control of visually evoked defensive behavior by the ventral lateral geniculate nucleus. *Neuron* 2021, 109: 3810–3822.e9.
115. Isa T, Marquez-Legorreta E, Grillner S, Scott EK. The tectum/superior colliculus as the vertebrate solution for spatial sensory integration and action. *Curr Biol* 2021, 31: R741–R762.
116. Dean P, Redgrave P, Westby GWM. Event or emergency? Two response systems in the mammalian superior colliculus. *Trends Neurosci* 1989, 12: 137–147.
117. Oliveira AF, Yonehara K. The mouse superior *Colliculus* as a model system for investigating cell type-based mechanisms of visual motor transformation. *Front Neural Circuits* 2018, 12: 59.
118. Liu X, Huang H, Snutch TP, Cao P, Wang L, Wang F. The superior *Colliculus*: Cell types, connectivity, and behavior. *Neurosci Bull* 2022, 38: 1519–1540.
119. Krauzlis RJ, Lovejoy LP, Zénon A. Superior colliculus and visual spatial attention. *Annu Rev Neurosci* 2013, 36: 165–182.
120. Gandhi NJ, Katnani HA. Motor functions of the superior colliculus. *Annu Rev Neurosci* 2011, 34: 205–231.
121. May PJ. The mammalian superior colliculus: Laminar structure and connections. *Prog Brain Res* 2006, 151: 321–378.
122. Ito S, Feldheim DA. The mouse superior *Colliculus*: An emerging model for studying circuit formation and function. *Front Neural Circuits* 2018, 12: 10.
123. Wheatcroft T, Saleem AB, Solomon SG. Functional organisation of the mouse superior *Colliculus*. *Front Neural Circuits* 2022, 16: 792959.
124. Lee KH, Tran A, Turan Z, Meister M. The sifting of visual information in the superior colliculus. *eLife* 2020, 9: e50678.
125. Basso MA, May PJ. Circuits for action and cognition: A view from the superior *Colliculus*. *Annu Rev Vis Sci* 2017, 3: 197–226.
126. Cang J, Savier E, Barchini J, Liu X. Visual function, organization, and development of the mouse superior *Colliculus*. *Annu Rev Vis Sci* 2018, 4: 239–262.
127. Ellis EM, Gauvain G, Sivyer B, Murphy GJ. Shared and distinct retinal input to the mouse superior colliculus and dorsal lateral geniculate nucleus. *J Neurophysiol* 2016, 116: 602–610.
128. Seabrook TA, Burbridge TJ, Crair MC, Huberman AD. Architecture, function, and assembly of the mouse visual system. *Annu Rev Neurosci* 2017, 40: 499–538.
129. Gale SD, Murphy GJ. Distinct representation and distribution of visual information by specific cell types in mouse superficial superior colliculus. *J Neurosci* 2014, 34: 13458–13471.
130. Shang C, Chen Z, Liu A, Li Y, Zhang J, Qu B, *et al.* Divergent midbrain circuits orchestrate escape and freezing responses to looming stimuli in mice. *Nat Commun* 2018, 9: 1232.
131. Shang C, Liu Z, Chen Z, Shi Y, Wang Q, Liu S, *et al.* BRAIN CIRCUITS. A parvalbumin-positive excitatory visual pathway to trigger fear responses in mice. *Science* 2015, 348: 1472–1477.
132. Sans-Dublanc A, Chrzanowska A, Reinhard K, Lemmon D, Nuttin B, Lambert T, *et al.* Optogenetic fUSI for brain-wide mapping of neural activity mediating collicular-dependent behaviors. *Neuron* 2021, 109: 1888–1905.e10.
133. Xie Z, Wang M, Liu Z, Shang C, Zhang C, Sun L, *et al.* Transcriptomic encoding of sensorimotor transformation in the midbrain. *eLife* 2021, 10: e69825.
134. Wonders CP, Anderson SA. The origin and specification of cortical interneurons. *Nat Rev Neurosci* 2006, 7: 687–696.
135. Villalobos CA, Wu Q, Lee PH, May PJ, Basso MA. Parvalbumin and GABA microcircuits in the mouse superior *Colliculus*. *Front Neural Circuits* 2018, 12: 35.
136. Wei P, Liu N, Zhang Z, Liu X, Tang Y, He X, *et al.* Processing of visually evoked innate fear by a non-canonical thalamic pathway. *Nat Commun* 2015, 6: 6756.
137. Gale SD, Murphy GJ. Active dendritic properties and local inhibitory input enable selectivity for object motion in mouse superior *Colliculus* neurons. *J Neurosci* 2016, 36: 9111–9123.
138. Zingg B, Chou XL, Zhang ZG, Mesik L, Liang F, Tao HW, *et al.* AAV-mediated anterograde transsynaptic tagging: Mapping corticocollicular input-defined neural pathways for defense behaviors. *Neuron* 2017, 93: 33–47.
139. Zhao X, Liu M, Cang J. Visual cortex modulates the magnitude but not the selectivity of looming-evoked responses in the superior *Colliculus* of awake mice. *Neuron* 2014, 84: 202–213.
140. Ahmadlou M, Zweifel LS, Heimel JA. Functional modulation of primary visual cortex by the superior colliculus in the mouse. *Nat Commun* 2018, 9: 3895.
141. Li C, Kühn NK, Alkisar I, Dublanc AS, Zemmouri F, Paesmans S, *et al.* Pathway-specific inputs to the superior colliculus support flexible triggering of innate behaviors. *bioRxiv* 2022, <https://doi.org/10.1101/2022.07.08.499294>.
142. Wu Q, Li E, Zhang Y. A synaptic filtering mechanism in visual threat identification in mouse. *Proc Natl Acad Sci U S A* 2023, 120: e2212786120.
143. Hoy JL, Bishop HI, Niell CM. Defined cell types in superior *Colliculus* make distinct contributions to prey capture behavior in the mouse. *Curr Biol* 2019, 29: 4130–4138.e5.

144. Dräger UC, Hubel DH. Topography of visual and somatosensory projections to mouse superior colliculus. *J Neurophysiol* 1976, 39: 91–101.
145. Holmes NP, Spence C. Multisensory integration: Space, time and superadditivity. *Curr Biol* 2005, 15: R762–R764.
146. Benavidez NL, Bienkowski MS, Zhu M, Garcia LH, Fayzullina M, Gao L, *et al.* Organization of the inputs and outputs of the mouse superior colliculus. *Nat Commun* 2021, 12: 4004.
147. Zhou Z, Liu X, Chen S, Zhang Z, Liu Y, Montardy Q, *et al.* A VTA GABAergic neural circuit mediates visually evoked innate defensive responses. *Neuron* 2019, 103: 473–488.e6.
148. Shang C, Liu A, Li D, Xie Z, Chen Z, Huang M, *et al.* A subcortical excitatory circuit for sensory-triggered predatory hunting in mice. *Nat Neurosci* 2019, 22: 909–920.
149. Isa K, Sooksawate T, Kobayashi K, Kobayashi K, Redgrave P, Isa T. Dissecting the tectal output channels for orienting and defense responses. *eNeuro* 2020, <https://doi.org/10.1523/ENEURO.0271-20.2020>.
150. Evans DA, Stempel AV, Vale R, Ruehle S, Lefler Y, Branco T. A synaptic threshold mechanism for computing escape decisions. *Nature* 2018, 558: 590–594.
151. Stubblefield EA, Costabile JD, Felsen G. Optogenetic investigation of the role of the superior colliculus in orienting movements. *Behav Brain Res* 2013, 255: 55–63.
152. Masullo L, Mariotti L, Alexandre N, Freire-Pritchett P, Boulanger J, Tripodi M. Genetically defined functional modules for spatial orienting in the mouse superior *Colliculus*. *Curr Biol* 2019, 29: 2892–2904.e8.
153. Comoli E, Das Neves Favaro P, Vautrelle N, Leriche M, Overton PG, Redgrave P. Segregated anatomical input to sub-regions of the rodent superior colliculus associated with approach and defense. *Front Neuroanat* 2012, 6: 9.
154. Li Z, Wei JX, Zhang GW, Huang JJ, Zingg B, Wang X, *et al.* Corticostriatal control of defense behavior in mice induced by auditory looming cues. *Nat Commun* 2021, 12: 1040.
155. Tokuoka K, Kasai M, Kobayashi K, Isa T. Anatomical and electrophysiological analysis of cholinergic inputs from the parabigeminal nucleus to the superficial superior colliculus. *J Neurophysiol* 2020, 124: 1968–1985.
156. Salay LD, Ishiko N, Huberman AD. A midline thalamic circuit determines reactions to visual threat. *Nature* 2018, 557: 183–189.
157. Fadok JP, Krabbe S, Markovic M, Courtin J, Xu C, Massi L, *et al.* A competitive inhibitory circuit for selection of active and passive fear responses. *Nature* 2017, 542: 96–100.
158. Gross CT, Canteras NS. The many paths to fear. *Nat Rev Neurosci* 2012, 13: 651–658.
159. Tovote P, Fadok JP, Lüthi A. Neuronal circuits for fear and anxiety. *Nat Rev Neurosci* 2015, 16: 317–331.
160. Liu J, Lin L, Wang DV. Representation of fear of heights by basolateral amygdala neurons. *J Neurosci* 2021, 41: 1080–1091.
161. Silva BA, Gross CT, Gräff J. The neural circuits of innate fear: Detection, integration, action, and memorization. *Learn Mem* 2016, 23: 544–555.
162. Janak PH, Tye KM. From circuits to behaviour in the amygdala. *Nature* 2015, 517: 284–292.
163. LeDoux J. The amygdala. *Curr Biol* 2007, 17: R868–R874.
164. Roozendaal B, McEwen BS, Chattarji S. Stress, memory and the amygdala. *Nat Rev Neurosci* 2009, 10: 423–433.
165. Gothard KM. Multidimensional processing in the amygdala. *Nat Rev Neurosci* 2020, 21: 565–575.
166. Daviu N, Füzesi T, Rosenegger DG, Rasiah NP, Sterley TL, Peringod G, *et al.* Paraventricular nucleus CRH neurons encode stress controllability and regulate defensive behavior selection. *Nat Neurosci* 2020, 23: 398–410.
167. Kim J, Lee S, Fang YY, Shin A, Park S, Hashikawa K, *et al.* Rapid, biphasic CRF neuronal responses encode positive and negative valence. *Nat Neurosci* 2019, 22: 576–585.
168. Lecca S, Meye FJ, Trusel M, Tchenio A, Harris J, Schwarz MK, *et al.* Aversive stimuli drive hypothalamus-to-habenula excitation to promote escape behavior. *eLife* 2017, 6: e30697.
169. Barbano MF, Wang HL, Zhang S, Miranda-Barrientos J, Estrin DJ, Figueroa-González A, *et al.* VTA glutamatergic neurons mediate innate defensive behaviors. *Neuron* 2020, 107: 368–382.e8.
170. Tovote P, Esposito MS, Botta P, Chaudun F, Fadok JP, Markovic M, *et al.* Midbrain circuits for defensive behaviour. *Nature* 2016, 534: 206–212.
171. Silva C, McNaughton N. Are periaqueductal gray and dorsal raphe the foundation of appetitive and aversive control? A comprehensive review. *Prog Neurobiol* 2019, 177: 33–72.
172. Brandão ML, Zanoveli JM, Ruiz-Martinez RC, Oliveira LC, Landeira-Fernandez J. Different patterns of freezing behavior organized in the periaqueductal gray of rats: Association with different types of anxiety. *Behav Brain Res* 2008, 188: 1–13.
173. Misslin R. The defense system of fear: Behavior and neurocircuitry. *Neurophysiol Clin/Clin Neurophysiol* 2003, 33: 55–66.
174. Franklin TB. Recent advancements surrounding the role of the periaqueductal gray in predators and prey. *Front Behav Neurosci* 2019, 13: 60.
175. Lefler Y, Campagner D, Branco T. The role of the periaqueductal gray in escape behavior. *Curr Opin Neurobiol* 2020, 60: 115–121.
176. Esposito MS, Capelli P, Arber S. Brainstem nucleus MdV mediates skilled forelimb motor tasks. *Nature* 2014, 508: 351–356.
177. Capelli P, Pivetta C, Soledad Esposito M, Arber S. Locomotor speed control circuits in the caudal brainstem. *Nature* 2017, 551: 373–377.
178. Ferreira-Pinto MJ, Ruder L, Capelli P, Arber S. Connecting circuits for supraspinal control of locomotion. *Neuron* 2018, 100: 361–374.
179. Ruder L, Arber S. Brainstem circuits controlling action diversification. *Annu Rev Neurosci* 2019, 42: 485–504.
180. Bolton AD, Murata Y, Kirchner R, Kim SY, Young A, Dang T, *et al.* A diencephalic dopamine source provides input to the superior *Colliculus*, where D1 and D2 receptors segregate to distinct functional zones. *Cell Rep* 2015, 13: 1003–1015.
181. Deichler A, Carrasco D, Lopez-Jury L, Vega-Zuniga T, Márquez N, Mpodozis J, *et al.* A specialized reciprocal connectivity suggests a link between the mechanisms by which the superior colliculus and parabigeminal nucleus produce defensive behaviors in rodents. *Sci Rep* 2020, 10: 16220.
182. Stubblefield EA, Thompson JA, Felsen G. Optogenetic cholinergic modulation of the mouse superior colliculus *in vivo*. *J Neurophysiol* 2015, 114: 978–988.
183. Endo T, Yanagawa Y, Obata K, Isa T. Nicotinic acetylcholine receptor subtypes involved in facilitation of GABAergic inhibition in mouse superficial superior colliculus. *J Neurophysiol* 2005, 94: 3893–3902.
184. Li L, Feng X, Zhou Z, Zhang H, Shi Q, Lei Z, *et al.* Stress accelerates defensive responses to looming in mice and involves a locus coeruleus-superior *Colliculus* projection. *Curr Biol* 2018, 28: 859–871.e5.
185. Hu H, Cui Y, Yang Y. Circuits and functions of the lateral habenula in health and in disease. *Nat Rev Neurosci* 2020, 21: 277–295.
186. Lecca S, Nambodiri VMK, Restivo L, Gervasi N, Pillolla G, Stuber GD, *et al.* Heterogeneous habenular neuronal ensembles during selection of defensive behaviors. *Cell Rep* 2020, 31: 107752.

187. Eilam D. Die hard: A blend of freezing and fleeing as a dynamic defense—Implications for the control of defensive behavior. *Neurosci Biobehav Rev* 2005, 29: 1181–1191.
188. Isa T, Hall WC. Exploring the superior colliculus *in vitro*. *J Neurophysiol* 2009, 102: 2581–2593.
189. Redgrave P, Mitchell IJ, Dean P. Further evidence for segregated output channels from superior colliculus in rat: Ipsilateral tecto-pontine and tecto-cuneiform projections have different cells of origin. *Brain Res* 1987, 413: 170–174.
190. Andrezik JA, Chan-Palay V, Palay SL. The nucleus paraventricularis lateralis in the rat. Demonstration of afferents by the retrograde transport of horseradish peroxidase. *Anat Embryol (Berl)* 1981, 161: 373–390.

Springer Nature or its licensor (e.g. a society or other partner) holds exclusive rights to this article under a publishing agreement with the author(s) or other rightsholder(s); author self-archiving of the accepted manuscript version of this article is solely governed by the terms of such publishing agreement and applicable law.

Hippocampus: Molecular, Cellular, and Circuit Features in Anxiety

Hu-Jiang Shi¹ · Shuang Wang¹ · Xin-Ping Wang¹ ·
Rui-Xin Zhang¹ · Li-Juan Zhu^{1,2} 

Received: 10 August 2022 / Accepted: 13 November 2022 / Published online: 21 January 2023

© Center for Excellence in Brain Science and Intelligence Technology, Chinese Academy of Sciences 2023

Abstract Anxiety disorders are currently a major psychiatric and social problem, the mechanisms of which have been only partially elucidated. The hippocampus serves as a major target of stress mediators and is closely related to anxiety modulation. Yet so far, its complex anatomy has been a challenge for research on the mechanisms of anxiety regulation. Recent advances in imaging, virus tracking, and optogenetics/chemogenetics have permitted elucidation of the activity, connectivity, and function of specific cell types within the hippocampus and its connected brain regions, providing mechanistic insights into the elaborate organization of the hippocampal circuitry underlying anxiety. Studies of hippocampal neurotransmitter systems, including glutamatergic, GABAergic, cholinergic, dopaminergic, and serotonergic systems, have contributed to the interpretation of the underlying neural mechanisms of anxiety. Neuropeptides and neuroinflammatory factors are also involved in anxiety modulation. This review comprehensively summarizes the hippocampal mechanisms associated with anxiety modulation, based on molecular, cellular, and circuit properties, to provide tailored targets for future anxiety treatment.

Keywords Anxiety · Hippocampus · Excitatory neurons · Interneurons · Neural circuit

Hu-Jiang Shi and Shuang Wang contributed equally to this review.

✉ Li-Juan Zhu
zhulj@seu.edu.cn

¹ Key Laboratory of Developmental Genes and Human Diseases, MOE, Department of Histology and Embryology, School of Medicine, Southeast University, Nanjing 210009, China

² Shanghai Mental Health Center, Shanghai Jiao Tong University School of Medicine, Shanghai 201108, China

Introduction

The hippocampus is a major target of stress mediators which lead to multiple psychiatric disorders, especially anxiety disorders. Several studies have shown that the hippocampus is structurally and functionally differentiated between the dorsal and ventral portions [1–4]. The ventral hippocampus (vHPC) is closely related to emotion, and its injury particularly impacts anxiety-related functions, whereas the dorsal hippocampus (dHPC) plays a preferred role in learning and spatial memory [1, 5, 6]. Despite many animal and clinical studies suggesting that aberrant hippocampal activity is associated with anxiety disorders, the underlying mechanism is far from being conclusive. Intrahippocampal infusion studies have suggested that different neurotransmitter systems and receptor sub-types are responsible for anxiety or memory functions in the hippocampus [7]. In addition, hippocampal excitatory and inhibitory neurons have been described as targets of anxiety modulation. Many studies using optogenetics and chemogenetics have shown that the connection of neural circuits in the hippocampus and related brain regions is the physiological basis of the regulation of anxiety behavior. Therefore, revealing the molecular, cellular, and neural circuit underpinnings of anxiety would provide answers regarding the functions of the hippocampus in modulating anxiety.

In this review, we summarize the molecular features and cell types of the hippocampal sub-regions, as well as the intra-hippocampus network and connections made by the hippocampus and extra-hippocampus regions, and discuss the recent evidence on the molecular, cellular, and neural circuit mechanisms of anxiety.

Anxiety Disorders

Anxiety arises from a highly alert state in the unambiguous presence of immediate threats and consists of trait and state components [8–10]. Trait anxiety is an individual predisposition that is considered a stable long-term feature in daily life [11–13]. In comparison, state anxiety refers to an acute and transitory response to external stimuli [11, 13], and is usually a context-dependent behavior. State anxiety has evolved as an adaptive avoidance of potential dangers, while extensive and prolonged trait anxiety responses are considered to be pathological phenomena [11]. Anxiety disorders, including generalized anxiety disorder, social phobia, specific phobias, separation anxiety disorder, and panic disorder with or without agoraphobia, are among the most prevalent psychiatric disorders and social problems [14, 15]. The etiology of anxiety disorders is an interaction of genetic vulnerability and psychosocial stress factors, such as adversity in childhood and adolescence, or stressful life events [14–16]. At present, antidepressants are the primary therapeutics for most anxiety disorders, and among these drugs, selective serotonin re-uptake inhibitors and selective serotonin-norepinephrine re-uptake inhibitors are the first-line anxiolytic treatments [17]. However, these agents are not effective in relieving anxiety symptoms for all patients; the harmful side effects and delayed action onset also limit their use. A thorough understanding of the mechanisms underlying anxiety regulation, at the molecular, cellular, and neural circuit levels, will provide a conceptual framework for improving anxiety treatment strategies.

The classic idea that the hippocampus is associated with learning and memory began with the study of Henry Molaison who exhibited severe memory deficits after bilateral medial temporal lobectomy to alleviate drug-resistant seizures [18]. In recent years, the role of the hippocampus in emotion regulation has received more attention, and exciting progress has been made in understanding the mechanism of the hippocampus in anxiety.

Hippocampus

The hippocampus is a complex structure located in the medial temporal lobe, which is implicated in extensive cognitive functions, including declarative memory [19] and spatial navigation [20], as well as emotional responses, such as emotional memory and adaptation [21, 22], and is a model system for structure and function research in animals. Many studies on the anatomy and circuitry of the hippocampus have been done in rodents and primates. Current studies indicate that the extensive role of the hippocampus in cognition and emotion stems from its position in the center of the cerebral cortex and its special internal anatomical structure [23, 24].

Anatomical Features

Anatomically, the rodent hippocampal formation is mainly subdivided into three distinct divisions: the dentate gyrus (DG), the hippocampus (cornu ammonis, CA3, CA2, and CA1), and the subiculum (SUB) [25] (Fig. 1A), which correspond to human hippocampus DG, CA4, CA3, CA2, CA1, and SUB; the human CA4 subregion contains cells within the hilus of the DG [26, 27]. Neuronal somata, dendrites, and axons in all subfields are distributed into specific layers: the stratum pyramidale (SP), alveus, stratum moleculare (SM), stratum oriens (SO), stratum radiatum (SR), and stratum lacunosum (SL) [28].

The DG subdivision is divided into five layers involving the outer SM (SMo), the middle SM (SMm), the inner SM (SMi), the stratum granulosum (SG), and the hilus. The principal glutamatergic neurons are granule cells (GCs) in the SG and mossy cells (MCs) in the hilus. The dendrites and axons of the GCs are located in the SO and hilus, respectively. The two types of glutamatergic neurons have distinct transcriptional characteristics. GCs have specific gene expression including *Prox1*, *Stxbp6*, *Ctip2*, *Maml2*, and *Dock10* [29, 30], while MCs specifically express *Calb2*, *Gria2/3*, *Cntn6*, *Drd2*, *Ociad2*, and *Nmb* [31–33].

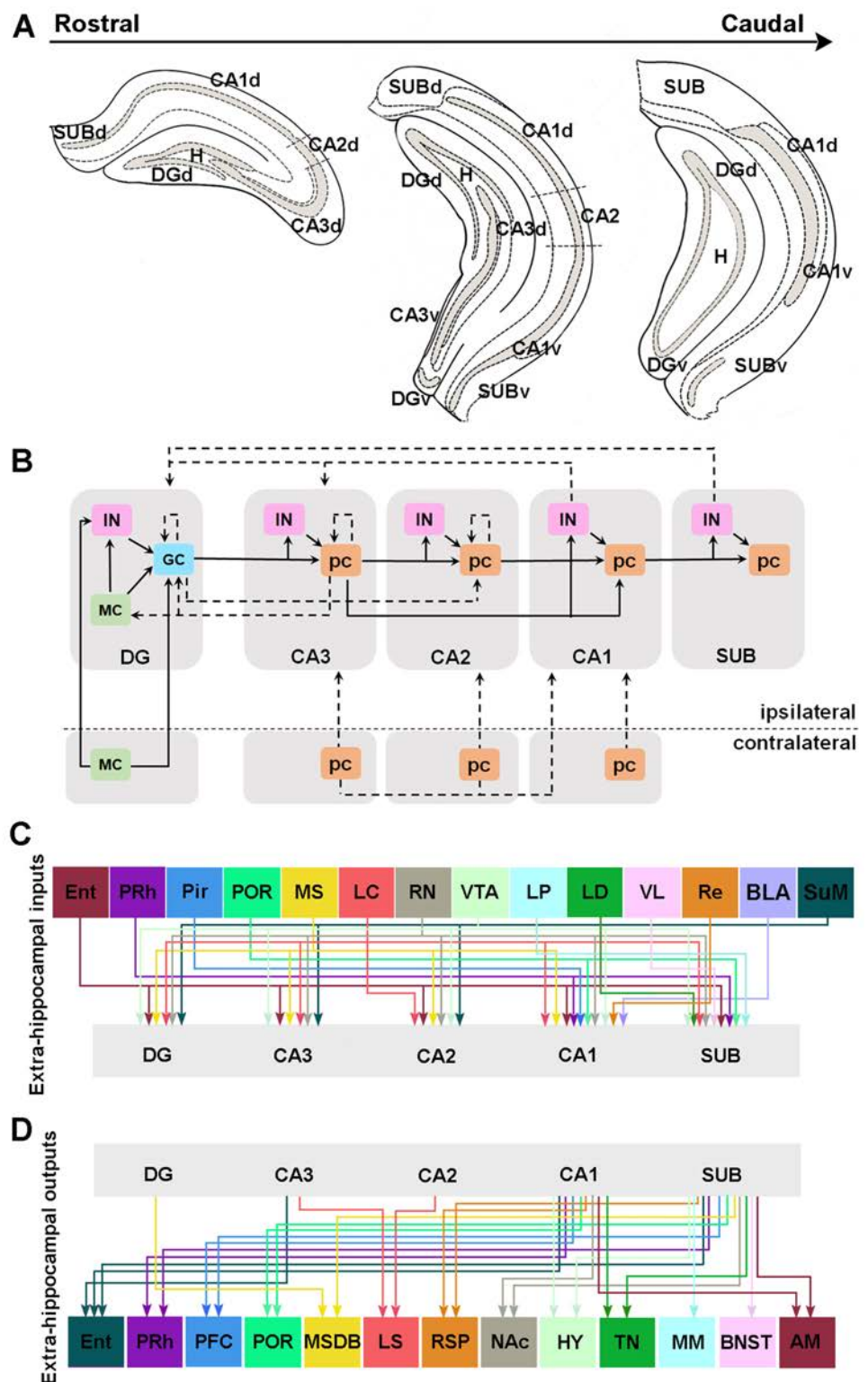
The hippocampus properly refers to three CA fields: CA3, CA2, and CA1. CA3 has a five-layered appearance which comprises the stratum lacunosum moleculare (SLM), SR, SL, SP, and SO. The laminar organization of CA1 and CA2 is similar to that of CA3 except for the absence of SL. The excitatory neurons within CA subdivisions are predominantly pyramidal neurons expressing the broad marker *Sv2b* [33–35]. The apical dendrites of pyramidal neurons are present in the SLM and SR, while their basal dendrites are ramified in the SO, and the axons enter the alveus.

In situ hybridization and next-generation sequencing have demonstrated that CA2 has unique molecular markers (*Rgs14*, *Step*, *Pcp4*, and *Vcan*) [33, 36–40], distinct from those of CA3 (*Socs2*, *Cpne4*, *Tyro3*, *Lyd*, and *Coch*) [33, 41] and those of CA1 (*Satb2* and *Wfs1*) [33, 35].

The inside-to-outside anatomical structure of the SUB comprises three layers: the SM, SP, and polymorphic layer. The SP in the SUB is thicker than in CA3, CA2, and CA1; its principal cell type is pyramidal cells expressing the unique molecular marker *Fnl1* [29]. The SUB receives substantial projections from CA1 and other subfields of the hippocampus [42, 43], and outputs to multiple brain regions. Hence the SUB is the hub of information processing between the hippocampus and other brain regions through this different interconnectivity [44].

All hippocampal subregions have highly heterogeneous inhibitory interneurons, which can be categorized by molecular markers, electrophysiological properties, and morphological characteristics; they are further

Fig. 1 Anatomical features of the hippocampus. **A** Simplified diagram depicting the distribution of different subfields of the dorsal and ventral parts of the hippocampus from rostral to caudal. **B** The projected connections between different neuron types in subregions of the hippocampus, including ipsilateral and contralateral connections. Dashed arrows represent weak projections, solid arrows represent strong projections. **C**, **D** Hippocampal external input (C) and output (D) connectivity networks. DG, dentate gyrus; H, hilus; CA1-3, cornu ammonis 1-3; SUB, subiculum; d, dorsal; v, ventral; i, intermediate; GC, granule cell; MC, mossy cell; pc, pyramidal cell; IN, interneuron; EC, entorhinal cortex; PRh, perirhinal cortex; Pir, piriform cortex; POR, postrhinal cortex; MS, medial septum; LC, locus coeruleus; RN, raphe nuclei; VTA, ventral tegmental area; LP, lateral posterior thalamic nucleus; LD, laterodorsal thalamic nucleus; VL, ventrolateral thalamic nucleus; Re, reuniens nucleus; SuM, supramammillary nucleus; BLA, basolateral amygdala; PFC, prefrontal cortex; DB, diagonal band; LS, lateral septum; RSP, retrosplenial cortex; NAc, nucleus accumbens; HY, hypothalamic nuclei; TN, thalamic nucleus; MM, mammillary bodies; BNST, bed nucleus of stria terminalis; AM, amygdala.



differentiated into at least eight defined GABAergic interneuron populations: positively stained for parvalbumin (PV⁺), neuropeptide Y (NPY⁺), somatostatin

(SOM⁺), calbindin (CB⁺), calretinin (CR⁺), cholecystokinin (CCK⁺), vasoactive intestinal peptide (VIP⁺), and neuronal nitric oxide synthase (nNOS⁺) [28].

Hippocampal Intrinsic Circuitry

The anatomical connectivity of the hippocampus is described as a ‘tri-synaptic loop’. Neurons in the lateral and medial entorhinal cortex (LEC/MEC) provide primary cortical inputs to the dendrites of the GCs in the SMO and SMm of the DG *via* the perforant path, respectively [45]. GCs project to the SL apical dendrites of the CA3 pyramidal cells *via* the mossy fiber (MF) pathway [46]. CA3 pyramidal cells project to the proximal apical dendrites of the CA1 pyramidal cells in the SR *via* the Schaffer collateral (SC) pathway [47, 48]. Finally, CA1 projects to the SUB and back to the deep layers of the EC region, completing a processing loop. Neurons in the DG and CA3 also project to CA2 [49, 50]. In addition to the classical tri-synaptic circuit, the actual microcircuit connections within the hippocampus are quite complex (Fig. 1B).

Commissural systems connect ipsilateral and contralateral structures in the hippocampus. Contralaterally-projecting neurons mainly consist of glutamatergic cells in the dHPC; however, SOM⁺ and PV⁺ GABAergic interneurons also innervate the contralateral hippocampus, but with a lower density [51]. The hilar mossy cells project to the SMi of the contralateral DG [52, 53]. The CA3 pyramidal cells send commissural projections onto synapses in the SO of the contralateral CA3 [54]. CA1 pyramidal neurons receive contralateral CA3 or CA2 inputs in the SR, and contralateral CA1 inputs to the SO *via* commissural projections [40, 55].

In the ipsilateral hippocampus, the DG mainly receives excitatory inputs from MCs and CA3, and inhibitory inputs within the DG, plus a small number of long-distance inhibitory inputs from CA1 and the SUB [53]. In addition, GCs mainly interact indirectly with each other through interneurons or MCs, but there are still a few local direct projections between GCs [53]. Hilar MCs receive a large number of hippocampal inputs, mainly excitatory and inhibitory inputs from the DG and CA3 [56]. GC projections account for 57% of MC inputs. Excitatory inputs of pyramidal neurons from proximal CA3 (CA3c) and intermediate CA3 (CA3b) account for 4.9% and 1.5% of MC inputs [53]. Studies have shown that CA3c indirectly regulates DG GCs through their inputs to MCs [57]. Inhibitory inputs from the DG and CA3 non-pyramidal layers account for 3.7% and 2.5% of MCs presynaptic inputs, respectively [53]. CA3 pyramidal cells (CA3pcs) not only receive EC and DG excitatory inputs but also receives indirect inhibitory inputs from CA3 interneurons and extensive excitatory interconnection between CA3pcs [50, 58, 59]. Recently, retrovirus tracing has shown many direct projections of CA3 pyramidal neurons and inhibitory neurons in DG GCs, where they are distributed in CA3a, CA3b, and CA3c, the distal CA3a input being the strongest [53].

In CA2, the apical dendrites of pyramidal cells receive CA3 Schaffer collateral inputs in the SR [50], while the axons target the basal and apical dendrites of CA1pcs through SO and SR, respectively [60]. Studies have shown that both the basal and apical dendrites of CA2pcs receive projections from ipsilateral CA2 neurons [61] and that DG GCs send functional monosynaptic outputs to pyramidal cells of CA2 through longitudinal projections [37]. CA1 SO has a class of long-distance projection interneurons (“back projection cells”), whose axons project backward through the fissure to other hippocampal subfields, including CA3 and DG [62].

The Extra-hippocampal Connection Network

The hippocampal circuit is mainly modulated by extrinsic inputs, including various cortical areas, the medial septal region, the thalamus, the amygdaloid complex, the supramammillary nucleus, and monoaminergic brainstem nuclei (Fig. 1C).

The EC consists of two subregions with different cytoarchitectures and connectivity (LEC and MEC). The projection is strong to all subfields of the hippocampus, where the superficial cells (layer II) directly project to the DG and CA3, and the deeper cells (layer III) directly project to CA1 and the SUB [63]. There are differences in their direct projections to CA1, as the LEC projects to the region closer to the SUB, whereas the MEC innervates the region closer to CA3 [64]. In addition, hippocampal CA2 receives direct inputs from LEC and MEC [65, 66]. The perirhinal and postrhinal cortices project weakly and only to CA1 and the SUB. The perirhinal cortex preferentially projects to the ventral SUB, whereas the postrhinal cortex targets mainly the dorsal CA1 and SUB [67]. The piriform cortex also weakly contacts vCA1 [68].

The medial septal GABAergic neurons with low-rhythmic firing innervate the DG and CA3, and the connection between these neurons and CA1 regulates contextual memory retrieval [69, 70]. Meanwhile, the septal glutamatergic projections mainly contact interneurons in the alveus/oriens of CA1 [71]. The medial septal nucleus sends cholinergic outputs to CA2 and CA1 [72, 73]. Septo-hippocampal glutamatergic and GABAergic projections terminate predominantly on GABAergic neurons in the hippocampus [74, 75]. Conversely, the septal cholinergic projections primarily target the pyramidal neurons in the hippocampus [75].

The lateral posterior, laterodorsal, and ventrolateral thalamic nuclei send monosynaptic outputs to the SUB [76]. Moreover, the thalamic midline nucleus reunions afferent inputs in the hippocampus modulate CA1 network activity *via* direct excitation and indirect inhibition [77]. Major inputs to the hippocampal formation also come from the amygdala. The basolateral amygdala

(BLA) establishes monosynaptic and glutamatergic outputs to CA1 of the vHPC [78]. Under physiological conditions, the posterior BLA-vCA1 connection is more prominent than the anterior BLA-vCA1 connection [79].

The hippocampal formation also receives inputs from the hypothalamic supramammillary nucleus [80]. This supramammillary projection terminates in all hippocampal subfields *via* the fornix but is more prominent in the DG, CA2, and CA3. The hippocampus also receives projections from brainstem nuclei, including a major noradrenergic input from the locus coeruleus [81, 82], dopaminergic projections from the ventral tegmental area [83, 84], and serotonergic innervation from the raphe nuclei [85, 86] to all subfields of the hippocampus. A study suggests that the locus coeruleus also releases dopamine in the dorsal hippocampus [87].

In addition to the inputs from many regions, the hippocampus forms network connections through outputs to other regions outside the hippocampus, which affects overall brain network activity (Fig 1D). The DG, CA3, and CA2 subregions contribute relatively little to extra-hippocampal outputs; the DG provides GABAergic outputs to the medial septum [88], while CA3 and CA2 mainly project to the dorsolateral septum [89, 90]. Agster and colleagues first found a direct projection from ventral CA3 to the entorhinal cortex [67]. In contrast, the CA1 and SUB regional projections constitute the main network of extra-hippocampal connections. The SUB and CA1 project to the postrhinal, perirhinal, entorhinal, prefrontal, and retrosplenial cortices, as well as to the nucleus accumbens, amygdala, hypothalamic nuclei, and various midline thalamic nuclei [67, 91–95]. The SUB also projects to the septum and diagonal band [89], the bed nucleus of the stria terminalis [96], mammillary bodies, and anterior thalamic nuclei along with the postsubiculum [97].

The Hippocampus in the Pathophysiology of Anxiety

Studies have suggested that the hippocampus is closely involved in cognitive learning and the pathogenesis of mood and anxiety disorders, which may be mediated by the functional heterogeneity of its dorsoventral axis, with the dHPC mediating cognitive learning and the vHPC contributing to emotional regulation, especially in regulating anxiety [5, 98–102]. Moreover, some studies have also shown that dorsal hippocampal neurons are involved in anxiety regulation [103–105]. Here, we review the identified cell types, molecules, and projections in the hippocampus, especially the vHPC, that modulate anxiety-related behaviors.

Cellular Mechanisms of the Hippocampus During Anxiety

The hippocampus is extremely responsive to chronic stress and anxiety-inducing stimuli. In almost all hippocampal subregions, excitatory and inhibitory neurons provide a cellular substrate for anxiety modulation. Chronic stress causes changes in synaptic plasticity, including dendritic shortening and the debranching and spine loss of excitatory neurons, which further impacts excitability in the MF-CA3 and CA3-CA1 synapses. Chronic stress also causes a reduction in dendritic branches and the number of interneurons, thus affecting the excitation-inhibition balance in the hippocampus.

DG Granule Cells in Anxiety In adult rodents and humans, the subgranular zone (SGZ) of the DG continuously generates new GCs [106–109]. Recently, several findings have demonstrated the important role of adult-born and mature GCs in influencing stress response and anxiety regulation. Increased neurogenesis in the DG reduces corticosteroid-induced anxiety-like behaviors [110], whereas inhibition of hippocampal neurogenesis increases anxiety-related behaviors [111]. Several important studies have proposed that adult-born GCs in the vDG, but not in the dDG, are key factors in mediating stress-induced anxiety-related behaviors. In mice, increasing neurogenesis in the vDG prevents the social defeat of stress-induced anxiety-like behaviors by inhibiting the activity of mature GCs [112]. Conversely, chemogenetic silencing of adult-born GCs induces an increased activity in mature GCs, leading to avoidance behavior in the social interaction test and a decrease in center exploration in the open field test [112]. However, another study from the same group found that optogenetic activation of mature vDG GCs contributes to the anxiolytic effects in mice [113]. In addition, chemogenetic activation of tactile experience-induced vDG GCs relieves anxiety [100]. Recently, with the application of single-cell sequencing and transcriptomics, heterogeneous cell populations with different molecular or functional characteristics have been found in different subregions of the hippocampus. Therefore, the above contradictory conclusions may be due to the different functions of GC subsets. In addition, a recent study indicates that activating osteocalcin-positive dDG GCs decreases anxiety-like behaviors by promoting adult DG neurogenesis [103].

GABAergic Interneurons in Anxiety Besides the principal excitatory neurons, the hippocampus is also under the inhibitory control of diverse GABAergic interneurons, which are susceptible to chronic stress and play important roles in modulating anxiety-related behaviors. Disturbances in GABAergic neurotransmission are considered to be the pathological basis of anxiety disorders, as studies in patients and animal models suggest that an imbalance of excitatory

Table 1 Effects of chronic stress on the number and expression of marker protein in hippocampal interneurons.

	Chronic stress response	References
<i>PV-Parvalbumin</i>		
Number	Reduced in vCA1 - Chronic mild stress	[115]
Activity	Loss of PV ⁺ interneurons in vHPC results in anxiety-like behavior in 5xFAD mice	[121]
Expression	Activation of PV ⁺ interneurons in vDG produced significant anxiolytic-like effects	[120]
	Reduced intensity of PV in the vHPC - maternal separation with early weaning	[123]
	Reduced in dHPC - Chronic mild stress	[119]
<i>CR-Calretinin/CB-Calbindin</i>		
Number	Reduced in vCA1 - Chronic mild stress	[115]
Expression	Increased in dCA1 - Maternal separation	[125]
	Increased in CR and CB expression in vDG - Chronic social defeat	[131]
<i>NPY-Neuropeptide Y</i>		
Number	Reduced in vCA1-3 - Chronic mild stress	[115]
Expression	Reduced in dCA1, dCA3 - Chronic restrain stress	[128]
	Reduced in dDG - Chronic mild stress	[127]
<i>SOM - Somatostatin</i>		
Number	Reduced in vDG and vCA1 - Chronic mild stress	[115]
Expression	Reduced in all vHPC - Chronic mild stress	[119]
<i>CCK - Cholecystokinin</i>		
Number	No effects on vHPC - Chronic mild stress	[115]
	No effects on vHPC - Chronic restrain stress	[122]
Expression	Reduced in dCA1-3 - Chronic restrain stress	[133]

dDG, dorsal dentate gyrus; dCA1-3, dorsal cornu ammonis 1-3; dHPC, dorsal hippocampus; vCA1, ventral CA1; vDG, ventral dentate gyrus; dCA3, dorsal CA3; vHPC, ventral hippocampus.

and inhibitory neurotransmitters is the primary cause of anxiety disorders (Table 1).

PV⁺ interneurons are particularly susceptible to chronic stress [114]. Studies indicate that exposure to multiple chronic stress significantly reduces the number of PV⁺ interneurons in vCA1 [115–118], and a decreased expression of PV has been reported in the dorsal hippocampus [119]. Moreover, activation of PV⁺ interneurons in the vDG produces significant anxiolytic-like effects [120], and loss of SST⁺ and PV⁺ interneurons in the vHPC leads to anxiety-like behavior in 5xFAD mice [121]. These changes may also relate to functional deficits like failure to generate the rhythmic spontaneous inhibitory postsynaptic currents recorded after chronic stress [122] and disruption of the balance between excitation and inhibition. Recently, a study has suggested that maternal separation with early weaning reduces the level of parvalbumin (PV) and increases the density of perineuronal nets around PV⁺ interneurons in the vHPC, as well as increasing theta power and enhancing theta-gamma coupling in the vHPC [123]. Contradictory results suggest that no changes in the number or expression of PV occur after chronic unpredictable stress or maternal

separation [124, 125], and may be due to different types of stressors or stress times.

NPY⁺ interneurons, as endogenous ‘stress-resistant molecules’, have marked anxiolytic and anti-epilepsy effects [120, 126]. Evidence suggests that the number of NPY⁺ interneurons decreases in vCA1-3 of the hippocampus after chronic maternal stress (CMS) [115] and that CMS, as well as chronic restraint stress (CRS), reduce NPY expression in the dDG and dCA1-3 respectively [127, 128]. Early life stress events can lead to a reduction in the number of NPY⁺ interneurons in the hilus, which leads to overexcitation of the DG-CA3 circuit [129]. Anxiety-like behaviors induced by predator odor stress are due to reduced NPY release from CA1 NPY⁺ neurons [130]. The impairment of NPY release promotes glutamate release onto the CA1 pyramidal cells, thus increasing synaptic short-term facilitation [130].

CR⁺ interneurons are also reduced in vCA1 after CMS exposure [115], while chronic social defeat increases the CR and CB expression in the vDG [131]. CMS exposure significantly reduces the SOM⁺ interneurons in the vDG and vCA1 [115] and decreases the expression of SOM in the vHPC [119]. The hyperexcitability of SOM⁺ neurons leads

to an enhancement of the inhibitory synaptic output onto the dendrites of CA1 pyramidal neurons and anxiolytic phenotypes [132]. In addition, although chronic stresses have no effect on the number of CCK⁺ interneurons [115, 122], CRS exposure reduces the CCK mRNA [133].

In addition, hippocampal vCA1 oriens-lacunosum moleculare (OLM) interneurons, which specifically express the nicotinic acetylcholine receptor $\alpha 2$ subunit, drive type 2 theta and are associated with increased risk-taking behavior in response to predator odor [98].

Chronic stress leads to changes in the number of inhibitory neurons or the expression of inhibitory neurotransmitters in the hippocampus, and affects the release of glutamate from excitatory neurons, supporting the role of excitation-inhibition imbalance in the pathology of anxiety disorders. Further research into the structural and functional connectivity between glutamatergic and GABAergic neurons in orchestrating hippocampal excitation-inhibition balance may provide a theoretical basis for anxiolytic therapy.

Stress-induced Hippocampal Plasticity in Anxiety The precise pattern of dendrites is the major factor affecting the formation and function of neural circuits, and its morphology also affects the strength of synaptic connections [134]. Stress-induced changes in structural plasticity may lead to the expression of anxiety-related behaviors.

Many studies using magnetic resonance imaging have shown a lower hippocampal volume in patients suffering from anxiety disorders, and antidepressant treatments normalize it [135, 136]. Hippocampal volume loss has also been reported in individuals with adverse life events and chronic glucocorticoid treatment [137–139]. In rodent model studies, exposure to chronic stress and corticosterone also reduces hippocampal volume, which may be due to many cellular changes, including decreased glial number, inhibition of adult neurogenesis, and dendritic atrophy, particularly in the CA3 and CA1 pyramidal cells, as well as DG GCs [136]. Dendritic atrophy is considered to be a reversible loss of the total dendritic length, branching density of apical dendrites, and dendritic spines [140]. For example, it has been shown that CRS causes a significant reduction in branch points and length of the apical and basal dendrites in CA3 [141, 142]. Chronic immobilization stress (CIS) elicits an anxiety response accompanied by a pronounced shortening and debranching of the apical and basal dendrites of the CA3 pyramidal cells and the apical dendrites of CA1 pyramidal cells [143, 144].

Dendritic spines (small protrusions on dendrites) are crucial components in mediating the stress-induced structural plasticity of neurons. Both CRS and maternal separation (MS) stress significantly reduce the mature dendritic spine density of CA1 pyramidal cells [145, 146]. The neurotrophin brain-derived neurotrophic factor (BDNF) promotes

the growth of dendrites and spines [147]. Both CIS and CRS decrease BDNF levels [147, 148], suggesting that BDNF is linked to the stress-induced alterations of dendrites and spines in the hippocampus [149].

Stress-induced abnormal long-term potentiation (LTP) in the MF-CA3 and SC-CA1 synapses is another cellular mechanism that may cause anxiety behaviors [150–152]. A study found that early deprivation induces anxiolytic behaviors by decreasing the threshold of LTP induction in the CA3-CA1 pathway [153]. In contrast, CRS increases anxiogenic behaviors due to the impairment of LTP in the SC-CA1 synapses [154]. These findings reveal that enhanced LTP in the SC synapses may be correlated with anxiolytic-like symptoms. Furthermore, another study showed that MS stress may induce anxiety-like behaviors through decreasing LTP and increasing paired-pulse facilitation ratios in the MF-CA3 pathway [152].

Hippocampus-related Molecular Mechanisms of Anxiety

Mounting evidence reveals that a diversity of molecules in the hippocampus are involved in anxiety modulation: channel proteins, receptors, neurotransmitters, neuropeptides, neuroinflammatory factors, and compounds associated with oxidative stress. These provide significant clues to hippocampus-related molecular mechanisms of anxiety (Table 2).

The hyperpolarization-activated cyclic nucleotide-gated (HCN) channel family governs hippocampal neuronal excitability. Among these, HCN1 is the predominant isoform, while the HCN4 expression level is much lower in CA1 pyramidal neurons [104]. Although both isoforms have been shown to regulate hippocampus-related anxiety-like behaviors, the two proteins exert opposing functions. Knockdown of the HCN1 channel protein in the dCA1 enhances dCA1 activity, upregulates BDNF-mTOR signaling, and produces anxiolytic-like behaviors [105]. Conversely, the shRNA-mediated knockdown of HCN4 in the dHPC generates an anxiogenic effect [104]. A recent study found that HCN channel proteins participate in regulating synaptic transmission and glutamate release [155], suggesting that HCN deficiency might impair glutamatergic transmission.

The glutamatergic and GABAergic systems have crucial roles in the modulation of anxiety [156, 157]. Infusion of N-methyl-D-aspartate receptor (NMDAR) agonists and antagonists into the vHPC induces anxiogenic and anxiolytic responses, respectively [158]. In contrast, the direct injection of gamma amino butyric acid A receptor (GABA_AR) agonists and antagonists into the vHPC have effects opposite to those of NMDAR agonists and antagonists [158]. Moreover, maintaining the excitation-inhibition balance might have a significant effect on regulating glutamate release from hippocampal pyramidal cells.

Table 2 Summary of hippocampal molecules involved in anxiety modulation.

Examples	Subfields	Anxiety-regulating functions	References
<i>Channel protein</i>			
HCN1	dCA1	The anxiolytic effect of HCN1 knockdown.	[105]
HCN4	dHPC	Anxiogenic effect of HCN4 knockdown.	[104]
<i>Neurotransmitter systems</i>			
NMDAR	vHPC	NMDAR agonists increased anxiety. NMDAR antagonists reduced anxiety.	[158]
GABA _A R	vHPC	GABA _A R agonists reduced anxiety. GABA _A R antagonists increased anxiety.	[158]
AChE	vHPC	AChE inhibitor alleviated anxiety.	[160]
	HPC	knockdown of AChE increased anxiety	[161]
D1/D2R	vHPC	The anxiolytic effect of D1/D2R antagonists.	[165]
	vCA3	Anxiogenic effect of D1/D2R antagonists.	[167]
nNOS	HPC	Chronic stress increased the level and activity of hippocampal nNOS Enhancement of nNOS-CAPON coupling is anxiogenic.	[168] [168] [169]
	vHPC	Downregulating of nNOS is anxiolytic.	[171]
AEA /CB1R	HPC	Enhancement of the ECBs signaling is anxiolytic.	[174] [177]
	vHPC	Reduced CB1R in GABAergic neurons and activated CB1R in glutamatergic neurons are anxiolytic	[178]
<i>Neuropeptide systems</i>			
CRH/CRHR1	dHPC	Intervention with CRHR1 is anxiolytic.	[182]
	vHPC	CRHR1 antagonist is anxiolytic.	[183]
NPS	vHPC	The anxiolytic effect of NPS.	[184] [185] [186]
RXFP3	vHPC	Anxiogenic effect of RXFP3 agonists.	[187]
<i>Cytokine</i>			
IL-1 β	DG	Increasing IL-1 β is anxiogenic.	[189]
NLRP3	vHPC	Deletion of NLRP3 is anxiogenic.	[192] [193]
	vHPC	Activation of microglial NLRP3 in CMS.	[194]

HCN, hyperpolarization-activated cyclic-nucleotide-gated channels; NMDAR, N-methyl-D-aspartate receptor; GABA_AR, gamma amino butyric acid A receptor; AChE, acetylcholinesterase; D1/D2R, dopamine D1 and D2 receptor; 5-HT₄R, 5-hydroxytryptamine 4 receptor; 5-HT_{1A}R, 5-HT_{1A} receptor; 5-HT_{2C}R, 5-HT_{2C} receptor; nNOS, neuronal nitric oxide synthase; CAPON, carboxy-terminal PDZ ligand; AEA, arachidonoyl ethanolamide or anandamide; CB1R, cannabinoid 1 receptor; ECB, endocannabinoid; CRH, corticotropin-releasing hormone; CRHR1, corticotropin-releasing hormone receptor 1; NPS, neuropeptide S; RXFP3, relaxin-family peptide 3 receptor; IL-1 β , interleukin-1 β ; NLRP3, nucleotide binding and oligomerization domain-like receptor family pyrin domain-containing 3; HPC, hippocampus; dHPC, dorsal HPC; vHPC, ventral HPC; DG, dentate gyrus; dCA1, dorsal cornu ammonis 1; vCA3, ventral cornu ammonis 3.

The GABA_AR antagonist blocks anxiolytic-like behaviors induced by the infusion of NMDAR antagonists into CA3 [159].

Hyperactivity of cholinergic systems is associated with the processes of hippocampus-modulated anxiety. One study showed that the administration of an acetylcholine esterase (AChE) inhibitor into the vHPC increases cholinergic activity and significantly alleviates anxiety responses [160]. In contrast, another study found that specific knockdown of AChE in the hippocampus promotes anxiety-like behaviors [161].

Dopamine (DA) is one of the neurotransmitters most active in anxiety responses, and its effects can be mediated by both D1 and D2 receptors expressed in the hippocampus [162, 163]. Several studies have revealed that the dopaminergic system modulates anxiety *via* its interaction with the glutamatergic or cholinergic system in the hippocampus. SCH23390, a DA D1 receptor antagonist, has synergistic anxiolytic effects with the NMDAR antagonist MK801 but is ineffective when injected into dCA1 alone [164]. However, the DA D2 receptor antagonist sulpiride suppresses the anxiolytic responses induced by MK801 in dCA1 [164].

Moreover, the D1 and D2 receptor antagonists alleviate the cholinergic anxiogenic effect of nicotine in the vHPC [165, 166]. Nicotine-induced DA release likely promotes anxiety responses, with DA antagonists reversing the anxiogenic effect by blocking D1 and D2 receptors. However, another study suggested that intra-hippocampal injection of SCH23390 or sulpiride into vCA3 blocks cholestasis-induced anxiolytic-like behaviors [167].

The neuronal messenger neuronal nitric oxide synthase (nNOS) is strongly expressed in the hippocampus and is involved in stress responses and anxiety-like behaviors. Chronic stress increases the expression and activity of nNOS in the hippocampus and contributes to stress-induced emotional behaviors [168]. Our previous studies have demonstrated that chronic stress enhances the coupling of nNOS with its carboxy-terminal PDZ ligand (CAPON) and induces anxious phenotypes [168, 169]. Blocking the nNOS-CAPON interaction ameliorates chronic stress-induced anxiety by promoting synaptogenesis [170]. Moreover, short-term running exercise exerts anxiolytic effects by increasing *Nos1* DNA methylation and downregulating the expression of nNOS in the vHPC [171].

Endocannabinoids (ECBs), such as arachidonoyl ethanolamide (anandamide, AEA) and 2-arachidonoyl glycerol (2-AG), are relevant for anxiety regulation and stress responses. AEA and 2-AG levels in the dHPC are altered by diverse chronic stressors [172, 173]; elevation of AEA levels by inhibition of dHPC fatty-acid amide hydrolase and the ECB transporter attenuate anxiety responses [174]. Intra-vHPC injection of an AEA reuptake inhibitor has anxiogenic and anxiolytic effects in the elevated plus maze and the Vogel conflict tests, respectively; this discrepancy may be due to differences in the stress experienced by the subjects prior to the behavioral tests [175]. The hippocampus contains high levels of cannabinoid 1 (CB1) receptors, which are mainly expressed on the axon terminals of CCK⁺ interneurons, but at lower levels in glutamatergic, serotonergic, and cholinergic axon terminals. Evidence suggests that cannabinoid signaling in the hippocampus protects against stress-induced behavioral changes [176]. Injecting Δ^9 -tetrahydrocannabinol, a CB1 receptor agonist, into the vHPC increases the cAMP response element-binding protein (CREB) activation and attenuates anxiety behaviors [177]. Stimulation of the hippocampal CB1 receptors suppresses the release of neurotransmitters and increases BDNF expression [177]. A study has suggested that electroacupuncture exerts an anxiolytic effect *via* downregulating CB1Rs in GABAergic neurons and activating CB1Rs in glutamatergic neurons in the vHPC, thus reducing the release of glutamate and inhibiting the anxiety circuit related to the vHPC [178].

In addition to the diverse neurotransmitter systems, corticotropin-releasing hormone (CRH) acts as a neuropeptide that mediates anxiety and stress-related affective

disorders in the hippocampus. Several studies have found that CRH exerts anxiety-regulating functions by affecting the expression or release of other neurotransmitters or neuropeptides. For instance, injecting CRH into the HPC suppresses the expression of Spexin, which plays an anxiolytic role [179]. CRH receptor type 1 (CRHR1), widely expressed in the hippocampus, has been demonstrated to be a potential drug target for anxiolytics in animals [180, 181]. Studies indicate that predator scent exposure stress increases the level of *Crhr1* mRNA in the dorsal hippocampus, and inhibition of *Crhr1* expression in the hippocampus significantly reverses the anxiety behaviors caused by chronic stress [182]. However, there is little research on whether CRHR1 in the vHPC is involved in the regulation of anxious behavior. Only one study has suggested that intra-vHPC injection of a CRHR1 antagonist increases the time spent in the open arms of an elevated plus maze test [183].

Neuropeptide S (NPS), acting *via* the NPS receptor (NPSR), has been shown to have anxiolytic effects. NPS significantly decreases anxiety-like behaviors when injected into the vHPC, possibly through its potential effects on short-term and long-term synaptic plasticity [184]. For instance, NPS reduces the magnitude of LTP and PPF at the vCA3-vCA1 synapses and induces anxiolytic response not only in normal mice but also in mice with high anxiety-related behavior [185, 186].

Activation of the relaxin family peptide 3 receptor (RXFP3) in the vHPC elicits anxiogenic phenotypes [187]. RXFP3 is mainly expressed in GABAergic SOM⁺ and PV⁺ neurons of all vHPC subregions, and its stimulation might inhibit interneuronal activity [188].

The hippocampus is vulnerable to neuroinflammation and oxidative stress, which are associated with anxiety disorders. Lipopolysaccharide (LPS) induces the downregulation of BDNF and the neuropeptide VGF, and of the neuroinflammatory and oxidative responses in the DG, which are attributable to the elevation of interleukin-1 β (IL-1 β) [189]. Inhibition of IL-1 β activity ameliorates LPS-induced disorders in the DG and results in an anxiolytic effect. Recent studies indicate that IL-1 β inhibits TrkB-mediated BDNF signaling and CREB, which regulate BDNF and VGF expression [190, 191]. Thus, BDNF and VGF downregulation appears to be the anxiogenic mechanisms of IL-1 β . The NLRP3 (nucleotide binding and oligomerization domain-like receptor family pyrin domain-containing 3) inflammasome, is related to the onset and development of a variety of CNS diseases, including anxiety. Deletion of NLRP3 impairs synaptic transduction in vCA3-vCA1 and causes anxiety-like behaviors [192]. However, some studies have indicated that activation of NLRP3 inflammasome in the hippocampus induces anxiety-like behavior [193, 194].

Hippocampal Circuit Plasticity Underlies Anxiety

It is commonly recognized that the hippocampus and multiple brain regions coordinate to regulate anxiety. The vHPC is at the center of the complex neural circuits underlying anxiety regulation [99, 195, 196]. Recently, the application of optogenetics and chemogenetics have provided important insight into the anxiety circuits associated with the hippocampus. Hippocampal input and output nodes play anxiety-regulating roles together with connected upstream nuclei, including the EC, BLA, posterior basolateral amygdala (BLP), median raphe nucleus (MRN), and downstream nuclei, including the medial prefrontal cortex (mPFC), lateral septum (LS), anteromedial part of the bed nucleus of the stria terminalis (amBNST), lateral hypothalamic area (LHA), and amygdala (Fig. 2).

Hippocampal Afferent Circuits Underlie Anxiety *Entorhinal cortex-hippocampus circuits* The EC (including the lateral and medial regions) is one of the major input sources to the hippocampus. However, there are relatively few reports on the relationship between EC and chronic stress or emotional disorders [100, 197, 198], especially anxiety disorders. One study suggested that tactile enrichment induces the activation of neurons in the vDG and increases the pre-synaptic input from the LEC. Chemogenetic activation of the projection reduces anxiety [100]. Therefore, its connec-

tion with the hippocampus in anxiety is not fully understood and needs further exploration.

Amygdala-hippocampus circuits The amygdala receives sensory stimuli associated with threats and plays a role in processing anxiety-associated events [199–201]. In addition, structural BLA and BLP connections to the vHPC have been confirmed [78, 79, 202, 203]. Robust connections and common functions between the amygdala and the vHPC facilitate the elucidation of the neural mechanism underlying anxiety at the circuit level. Felix-Ortiz *et al.* and Pi *et al.* showed that the BLA and BLP provide glutamatergic inputs to pyramidal cells in vCA1, revealing the structural and physiological heterogeneity between BLA-vCA1 and BLP-vCA1 inputs [78, 204].

CRS induces an increase in spine density and glutamatergic signaling in BLA-vHPC, leading to anxiety-like phenotypes in mice [205]. Transient optogenetic activation of the BLA terminals in vCA1 elicits significantly high anxiety behavior. In contrast, optogenetic inhibition of the BLA-vCA1 circuit attenuates the expression of anxiety-like behaviors [78].

By injecting anterograde monosynaptic viral tracers into BLP or BLA in a Calb1-IRES2-Cre-D: Ai9 transgenic mouse, Pi *et al.* found that the BLP and BLA innervate non-overlapping, lamina-specific vCA1 cell populations along the radial axis [204]. Specifically, BLP projects to calbindin1-positive vCA1 cells in the superficial pyramidal layer, and BLA projects to calbindin1-negative vCA1 cells

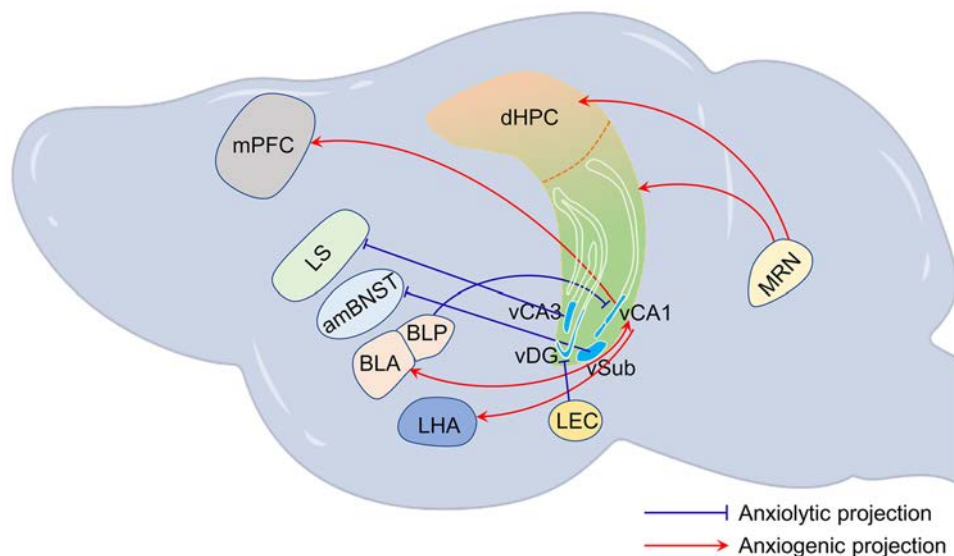


Fig. 2 Upstream and downstream connection networks of the hippocampus that are implicated in anxiety-like behaviors. The sources of inputs into the hippocampus implicated in anxiety are the BLA, BLP, LEC, and MRN. The output regions of the hippocampus implicated in anxiety are the LHA, mPFC, BLA, amBNST, and LS. dHPC, dorsal hippocampus; vCA3, ventral CA3; vCA1, ventral CA1; vSub,

ventral subiculum; amBNST, anteromedial part of the bed nucleus of the stria terminalis; BLA, basolateral amygdala; BLP, posterior basolateral amygdala; LHA, lateral hypothalamic area; LEC, lateral entorhinal cortex; LS, lateral septum; mPFC, medial prefrontal cortex; MRN, median raphe nucleus.

in the deep pyramidal layer. Photoactivation of the BLP-vCA1 inputs elicits an anxiolytic effect, while photoinhibition drives an anxiogenic effect. By contrast, BLA-vCA1 inputs play an opposing role in modulating anxiety-like behaviors compared to the BLP-vCA1 circuit, which is consistent with the studies of Felix-Ortiz *et al.* [78, 204]. Calbindin1 expressed in superficial neurons may be a crucial molecule that contributes to the anxiolytic effect. To confirm the anxiolytic roles of calbindin1-positive vCA1 neurons in the BLP-vCA1 circuit, a Cre-responding ChR2 construct was expressed in the vCA1 of the Calb1-IRES2-Cre-D knock-in mouse and the photoactivation of vCA1^{Calb1+} somata induced an amelioration of anxiety [204].

Raphe nucleus - hippocampus circuits Serotonergic neurons originating in the raphe nuclei mainly project to the hippocampus, where almost all serotonin receptor subtypes are expressed [206, 207]. An *in vivo* microdialysis study found that anxiety-related aversive conditions increase extracellular serotonin within the vHPC [208]. Ohmura *et al.* found that blue light delivered to ChR2 variant-containing serotonergic terminals from the dorsal raphe nucleus and MRN in the vHPC induce serotonergic activation and generate anxiety-related behaviors [209]. Photostimulation of serotonin neurons in the MRN also induces anxiety-like behaviors [210]. However, serotonergic activation in the MRN is unable to induce anxiety-related behaviors in a 5-HT_{2C} receptor knockout line. Thus, serotonergic MRN neurons play anxiogenic roles *via* the 5-HT_{2C} receptors in the vHPC [209].

A recent finding showed that optogenetic manipulation of the serotonergic MRN neurons induces an anxiogenic-like effect in both male and female mice [210]. Another study suggested that the activation of serotonergic MRN neurons facilitates the anxiety response in female mice, partly through its input to the dHPC [211]. The serotonergic receptor underlying anxiety regulation in the dHPC might be the 5-HT_{1A} receptor because the injection of its agonist into the dHPC drives the expression of anxiety behavior [212]. Therefore, the regulation of anxiety by serotonergic signaling in female and male mice may be mediated by different serotonergic receptor subtypes in the dHPC and vHPC.

Hippocampal Efferent Circuits Underlie Anxiety Many studies have shown that glutamatergic projections from the vHPC to several downstream structures are involved in the regulation of anxiety.

vHPC-mPFC The direct single synaptic projection from vHPC to mPFC is a key component of anxiety-related circuits. Mounting evidence shows that the synchronization of the theta-frequency of the vHPC-mPFC circuit transmits anxiety-related information which is correlated with avoidance of the open arms in the elevated plus maze test [213–215]. vHPC-mPFC terminal inhibition using

optogenetic techniques wipes out the theta-frequency synchronization, which is responsible for increased exploration in the open arms [216]. Inhibition of the theta-frequency communication of the vHPC-mPFC by abolishing the disinhibition functions of the mPFC results in open-arm exploration [217]. The anxiogenic role of the vHPC-mPFC circuit was also confirmed by the hM3Dq-mediated activation of the vCA1 neurons projecting to the mPFC, whereas hM4Di-mediated inactivation had the opposite effects [218].

vHPC-LS The glutamatergic vHPC fibers also largely innervate the LS, which is also implicated in anxiety [219, 220]. Disconnecting the ipsilateral input from the vHPC to the LS by an asymmetrical disconnection increases open-arm exploration by rats, suggesting that the vHPC and the LS synergistically regulate anxiety-like behaviors [221]. Moreover, the chemogenetic activation of projections from vHPC to LS suppresses the expression of anxiety-like behaviors, whereas their inhibition has opposite behavioral outcomes [218]. The LS receives dense glutamatergic fiber inputs from the vCA3 pyramidal layer, but few from the vCA1 pyramidal cells.

vHPC-ambNST The ambNST receives strong glutamatergic innervation from the ventral SUB/CA1. High-frequency vSUB/CA1 stimulation elicits NMDAR-mediated LTP in the ambNST, which promotes an anxiolytic effect [222]. Elaboration of the synaptic plasticity in the vSUB/CA1-ambNST circuit will advance our understanding of the role of the vHPC in anxiety regulation.

vHPC-LHA The LHA is implicated as an important brain region in the regulation of anxiety; it receives direct and exclusive outputs from pyramidal neurons in CA1 and the SUB of the vHPC. A recent study has found that a group of vCA1 pyramidal neurons send glutamatergic input into the LHA, and optogenetic activation of these neurons is anxiogenic [223].

vHPC-Amygdala vCA1 neurons make synaptic connections with the basal amygdala (BA) and lateral amygdala (LA) [224, 225]. Studies have shown that the theta frequency synchronization between vCA1 and LA is significantly enhanced in innate anxiety [224], while the synchronization between vCA1-BA and vCA1-mPFC conveys contextual information efficiently, contributing to contextual fear responses [225].

Conclusion

As a key region for information processing in the CNS, the hippocampus receives inputs from subcortical regions and sends outputs to a variety of downstream regions to mediate different behavioral and physiological functions, thus completing the adaptive regulation of the brain to the environment.

Anatomical and pharmacogenetic studies have shown extensive and close connections among the many subregions in the hippocampus and complex interconnections among its various neurons. These results suggest that the accurate regulation of microcircuitry in the hippocampus is an important basis for its physiological function. Most current studies on the hippocampus and anxiety regulation are limited to the connections between the subregions in the hippocampus and extra-hippocampal regions, as well as the regulation of the local inhibitory circuits in the subregions. However, the mechanism of neural networking between the subregions of the hippocampus in anxiety regulation remains unclear. The main challenges are as follows: (1) heterogeneity of the dorsal-ventral structure and gradient connections in the longitudinal axis; (2) complex anatomical connections between the ipsilateral and contralateral hippocampus; and (3) types and projection complexity of principal neurons and interneurons in the hippocampus. These problems make it difficult to dissect the neural networks in the hippocampus that regulate anxiety-related behavior. Recently, with the extensive application of single-cell transcriptomics and other new techniques, it has been shown that the hippocampus is a highly heterogeneous tissue with many cell subpopulations with different functional and connectivity characteristics. Therefore, future studies may focus on the synchronization of activities of hippocampal neural networks between different types of neurons in each subregion, especially the precise neural circuits mediated by different subsets of neurons in the vHPC, to understand the basis of neural circuits underlying different behaviors. This will also provide more accurate and effective targets for the development of new anxiolytic drugs.

In preclinical and clinical anxiety trials, the glutamatergic and GABAergic systems, the neuropeptide systems, and the endocannabinoid systems show positive prospects for future drug development. In the hippocampus of rodents, excitatory and inhibitory neurotransmitter systems, the cholinergic, dopaminergic, and serotonergic systems, have been established as critical components of anxiety-related behaviors. Therefore, these hippocampal molecules will also provide more reference points for the development of new and more effective therapeutic targets.

Acknowledgements This review was supported by the National Natural Science Foundation of China (31970951), the Six Talent Peaks Project of Jiangsu Province (YY-005), the Shanghai Rising-Star Program (21QA1407900), and “Zhong Ying Young Scholar” project of Cyrus Tang Foundation.

Conflict of interest The authors declare no conflict of interest.

References

- Fanselow MS, Dong HW. Are the dorsal and ventral hippocampus functionally distinct structures? *Neuron* 2010, 65: 7–19.
- Bannerman DM, Rawlins JN, McHugh SB, Deacon RM, Yee BK, Bast T. Regional dissociations within the hippocampus—Memory and anxiety. *Neurosci Biobehav Rev* 2004, 28: 273–283.
- Risold PY, Swanson LW. Structural evidence for functional domains in the rat hippocampus. *Science* 1996, 272: 1484–1486.
- Knierim JJ. The hippocampus. *Curr Biol* 2015, 25: R1116–R1121.
- Strange BA, Witter MP, Lein ES, Moser EI. Functional organization of the hippocampal longitudinal axis. *Nat Rev Neurosci* 2014, 15: 655–669.
- Kjelstrup KG, Tuvnes FA, Steffenach HA, Murison R, Moser EI, Moser MB. Reduced fear expression after lesions of the ventral hippocampus. *Proc Natl Acad Sci U S A* 2002, 99: 10825–10830.
- Engin E, Treit D. The role of hippocampus in anxiety: Intracerebral infusion studies. *Behav Pharmacol* 2007, 18: 365–374.
- Davis M, Walker DL, Miles L, Grillon C. Phasic vs sustained fear in rats and humans: Role of the extended amygdala in fear vs anxiety. *Neuropsychopharmacology* 2010, 35: 105–135.
- Crocq MA. A history of anxiety: From Hippocrates to DSM. *Dialogues Clin Neurosci* 2015, 17: 319–325.
- Grupe DW, Nitschke JB. Uncertainty and anticipation in anxiety: An integrated neurobiological and psychological perspective. *Nat Rev Neurosci* 2013, 14: 488–501.
- Endler NS, Kocovski NL. State and trait anxiety revisited. *J Anxiety Disord* 2001, 15: 231–245.
- Zhang M, Ma C, Luo Y, Li J, Li Q, Liu Y, *et al*. Neural basis of uncertain cue processing in trait anxiety. *Sci Rep* 2016, 6: 21298.
- Goes TC, Almeida Souza TH, Marchioro M, Teixeira-Silva F. Excitotoxic lesion of the medial prefrontal cortex in Wistar rats: Effects on trait and state anxiety. *Brain Res Bull* 2018, 142: 313–319.
- Thibaut F. Anxiety disorders: A review of current literature. *Dialogues Clin Neurosci* 2017, 19: 87–88.
- Beesdo K, Knappe S, Pine DS. Anxiety and anxiety disorders in children and adolescents: Developmental issues and implications for DSM-V. *Psychiatr Clin North Am* 2009, 32: 483–524.
- Phillips AC, Carroll D, Der G. Negative life events and symptoms of depression and anxiety: Stress causation and/or stress generation. *Anxiety Stress Coping* 2015, 28: 357–371.
- Murrough JW, Yaqubi S, Sayed S, Charney DS. Emerging drugs for the treatment of anxiety. *Expert Opin Emerg Drugs* 2015, 20: 393–406.
- Scoville WB, Milner B. Loss of recent memory after bilateral hippocampal lesions. *J Neurol Neurosurg Psychiatry* 1957, 20: 11–21.
- Penfield W, Milner B. Memory deficit produced by bilateral lesions in the hippocampal zone. *AMA Arch Neurol Psychiatry* 1958, 79: 475–497.
- Burgess N, Maguire EA, O’Keefe J. The human hippocampus and spatial and episodic memory. *Neuron* 2002, 35: 625–641.
- Phelps EA. Human emotion and memory: Interactions of the amygdala and hippocampal complex. *Curr Opin Neurobiol* 2004, 14: 198–202.
- Franklin TB, Saab BJ, Mansuy IM. Neural mechanisms of stress resilience and vulnerability. *Neuron* 2012, 75: 747–761.
- Moscovitch M, Cabeza R, Winocur G, Nadel L. Episodic memory and beyond: The hippocampus and neocortex in transformation. *Annu Rev Psychol* 2016, 67: 105–134.
- Squire LR, Stark CEL, Clark RE. The medial temporal lobe. *Annu Rev Neurosci* 2004, 27: 279–306.

25. Watson C, Paxinos G, Puelles L (2012) *The Mouse Nervous System*, Elsevier, Amsterdam, pp 783–795.
26. Schultz C, Engelhardt M. Anatomy of the hippocampal formation. *Front Neurol Neurosci* 2014, 34: 6–17.
27. Braak H, Braak E, Yilmazer D, Bohl J. Functional anatomy of human hippocampal formation and related structures. *J Child Neurol* 1996, 11: 265–275.
28. Tribolet NAR, Crossman D. Neary, *Neuroanatomy. An illustrated colour text*. Acta Neurochir 2009, 2010: 152.
29. Ayhan F, Kulkarni A, Berto S, Sivaprakasam K, Douglas C, Lega BC, *et al.* Resolving cellular and molecular diversity along the hippocampal anterior-to-posterior axis in humans. *Neuron* 2021, 109: 2091–2105.e6.
30. Jaeger BN, Linker SB, Parylak SL, Barron JJ, Gallina IS, Saavedra CD, *et al.* A novel environment-evoked transcriptional signature predicts reactivity in single dentate granule neurons. *Nat Commun* 2018, 9: 3084.
31. Volz F, Bock HH, Gierthmuehlen M, Zentner J, Haas CA, Freiman TM. Stereologic estimation of hippocampal GluR2/3- and calretinin-immunoreactive hilar neurons (presumptive mossy cells) in two mouse models of temporal lobe epilepsy. *Epilepsia* 2011, 52: 1579–1589.
32. Scharfman HE, Myers CE. Hilar mossy cells of the dentate gyrus: A historical perspective. *Front Neural Circuits* 2013, 6: 106.
33. Cembrowski MS, Wang L, Sugino K, Shields BC, Spruston N. Hipposeq: A comprehensive RNA-seq database of gene expression in hippocampal principal neurons. *eLife* 2016, 5: e14997.
34. Cembrowski MS, Wang L, Lemire AL, Copeland M, DiLisio SF, Clements J, *et al.* The subiculum is a patchwork of discrete subregions. *eLife* 2018, 7: e37701.
35. Lein ES, Zhao X, Gage FH. Defining a molecular atlas of the hippocampus using DNA microarrays and high-throughput *in situ* hybridization. *J Neurosci* 2004, 24: 3879–3889.
36. Dudek SM, Alexander GM, Farris S. Rediscovering area CA2: Unique properties and functions. *Nat Rev Neurosci* 2016, 17: 89–102.
37. Kohara K, Pignatelli M, Rivest AJ, Jung HY, Kitamura T, Suh J, *et al.* Cell type-specific genetic and optogenetic tools reveal hippocampal CA2 circuits. *Nat Neurosci* 2014, 17: 269–279.
38. Lee SE, Simons SB, Heldt SA, Zhao M, Schroeder JP, Vellano CP, *et al.* RGS14 is a natural suppressor of both synaptic plasticity in CA2 neurons and hippocampal-based learning and memory. *Proc Natl Acad Sci U S A* 2010, 107: 16994–16998.
39. Lein ES, Callaway EM, Albright TD, Gage FH. Redefining the boundaries of the hippocampal CA2 subfield in the mouse using gene expression and 3-dimensional reconstruction. *J Comp Neurol* 2005, 485: 1–10.
40. Shinohara Y, Hosoya A, Yahagi K, Ferecskó AS, Yaguchi K, Sik A, *et al.* Hippocampal CA3 and CA2 have distinct bilateral innervation patterns to CA1 in rodents. *Eur J Neurosci* 2012, 35: 702–710.
41. Basrai HS, Turbic A, Christie KJ, Turnley AM. Suppressor of cytokine signalling 2 (SOCS₂) regulates numbers of mature newborn adult hippocampal neurons and their dendritic spine maturation. *Cell Mol Neurobiol* 2017, 37: 899–909.
42. Naber PA, LopesdaSilva FH, Witter MP. Reciprocal connections between the entorhinal cortex and hippocampal fields CA1 and the subiculum are in register with the projections from CA1 to the subiculum. *Hippocampus* 2001, 11: 99–104.
43. Witter MP, Griffioen AW, Jorritsma-Byham B, Krijnen JL. Entorhinal projections to the hippocampal CA1 region in the rat: An underestimated pathway. *Neurosci Lett* 1988, 85: 193–198.
44. O’Mara SM, Commins S, Anderson M, Gigg J. The subiculum: A review of form, physiology and function. *Prog Neurobiol* 2001, 64: 129–155.
45. van Groen T, Miettinen P, Kadish I. The entorhinal cortex of the mouse: Organization of the projection to the hippocampal formation. *Hippocampus* 2003, 13: 133–149.
46. Nakahara S, Matsumoto M, Ito H, Tajinda K. Ectopic mossy fiber pathfinding in the hippocampus caused the abnormal neuronal transmission in the mouse models of psychiatric disease. *Biol Pharm Bull* 2018, 41: 138–141.
47. Speed HE, Dobrunz LE. Developmental changes in short-term facilitation are opposite at temporoammonic synapses compared to Schaffer collateral synapses onto CA1 pyramidal cells. *Hippocampus* 2009, 19: 187–204.
48. Witter MP. Organization of the entorhinal-hippocampal system: A review of current anatomical data. *Hippocampus* 1993, 3 Spec No: 33–44.
49. Tóth K, Freund TF. Calbindin D_{28k}-containing nonpyramidal cells in the rat hippocampus: Their immunoreactivity for GABA and projection to the medial septum. *Neuroscience* 1992, 49: 793–805.
50. Amaral DG, Witter MP. The three-dimensional organization of the hippocampal formation: A review of anatomical data. *Neuroscience* 1989, 31: 571–591.
51. Eyre MD, Bartos M. Somatostatin-expressing interneurons form axonal projections to the contralateral hippocampus. *Front Neural Circuits* 2019, 13: 56.
52. Scharfman HE. The enigmatic mossy cell of the dentate gyrus. *Nat Rev Neurosci* 2016, 17: 562–575.
53. Sun Y, Grieco SF, Holmes TC, Xu X. Local and long-range circuit connections to hilar mossy cells in the dentate gyrus. *eNeuro* 2017, 4: ENEURO.0097-ENEURO.0017.2017.
54. Queiroz CMT, Mello LE. Synaptic plasticity of the CA3 commissural projection in epileptic rats: An *in vivo* electrophysiological study. *Eur J Neurosci* 2007, 25: 3071–3079.
55. Zhou H, Xiong GJ, Jing L, Song NN, Pu DL, Tang X, *et al.* The interhemispheric CA1 circuit governs rapid generalisation but not fear memory. *Nat Commun* 2017, 8: 2190.
56. Jackson MB, Scharfman HE. Positive feedback from hilar mossy cells to granule cells in the dentate gyrus revealed by voltage-sensitive dye and microelectrode recording. *J Neurophysiol* 1996, 76: 601–616.
57. Scharfman HE. The CA3 “backprojection” to the dentate gyrus. *Prog Brain Res* 2007, 163: 627–637.
58. Rolls ET. An attractor network in the hippocampus: Theory and neurophysiology. *Learn Mem* 2007, 14: 714–731.
59. Lorente De Nó R. Studies on the structure of the cerebral cortex, II, Continuation of the study of the ammonic system. *Journal für Psychologie und Neurologie* 1934, 46: 113–177.
60. Tamamaki N, Abe K, Nojyo Y. Three-dimensional analysis of the whole axonal arbors originating from single CA2 pyramidal neurons in the rat hippocampus with the aid of a computer graphic technique. *Brain Res* 1988, 452: 255–272.
61. Ishizuka N, Weber J, Amaral DG. Organization of intrahippocampal projections originating from CA3 pyramidal cells in the rat. *J Comp Neurol* 1990, 295: 580–623.
62. Sik A, Ylinen A, Penttonen M, Buzsáki G. Inhibitory CA1-CA3-hilar region feedback in the hippocampus. *Science* 1994, 265: 1722–1724.
63. Steward O, Scoville SA. Cells of origin of entorhinal cortical afferents to the hippocampus and fascia dentata of the rat. *J Comp Neurol* 1976, 169: 347–370.
64. Hargreaves EL, Rao G, Lee I, Knierim JJ. Major dissociation between medial and lateral entorhinal input to dorsal hippocampus. *Science* 2005, 308: 1792–1794.
65. Dang R, Zhou Y, Zhang Y, Liu D, Wu M, Liu A, *et al.* Regulation of social memory by lateral entorhinal cortical projection to dorsal hippocampal CA2. *Neurosci Bull* 2022, 38: 318–322.

66. Lopez-Rojas J, de Solis CA, Leroy F, Kandel ER, Siegelbaum SA. A direct lateral entorhinal cortex to hippocampal CA2 circuit conveys social information required for social memory. *Neuron* 2022, 110: 1559–1572.e4.
67. Agster KL, Burwell RD. Hippocampal and subicular efferents and afferents of the perirhinal, postrhinal, and entorhinal cortices of the rat. *Behav Brain Res* 2013, 254: 50–64.
68. Tao S, Wang Y, Peng J, Zhao Y, He X, Yu X, *et al.* Whole-brain mapping the direct inputs of dorsal and ventral CA1 projection neurons. *Front Neural Circuits* 2021, 15: 643230.
69. Salib M, Joshi A, Katona L, Howarth M, Micklem BR, Somogyi P, *et al.* GABAergic medial septal neurons with low-rhythmic firing innervating the dentate gyrus and hippocampal area CA3. *J Neurosci* 2019, 39: 4527–4549.
70. Sans-Dublanç A, Razzauti A, Desikan S, Pascual M, Monyer H, Sindreu C. Septal GABAergic inputs to CA1 govern contextual memory retrieval. *Sci Adv* 2020, 6: eaba5003.
71. Freund TF, Buzsáki G. Interneurons of the hippocampus. *Hippocampus* 1998, 6: 347–470.
72. Pimpinella D, Mastroianni V, Giorgi C, Coemans S, Lecca S, Lalive AL, *et al.* Septal cholinergic input to CA2 hippocampal region controls social novelty discrimination via nicotinic receptor-mediated disinhibition. *eLife* 2021, 10: e65580.
73. Buzsáki G. *Theta* oscillations in the hippocampus. *Neuron* 2002, 33: 325–340.
74. Freund TF, Antal M. GABA-containing neurons in the septum control inhibitory interneurons in the hippocampus. *Nature* 1988, 336: 170–173.
75. Sun Y, Nguyen AQ, Nguyen JP, Le L, Saur D, Choi J, *et al.* Cell-type-specific circuit connectivity of hippocampal CA1 revealed through cre-dependent rabies tracing. *Cell Rep* 2014, 7: 269–280.
76. Bohne P, Schwarz MK, Herlitze S, Mark MD. A new projection from the deep cerebellar nuclei to the hippocampus via the ventrolateral and laterodorsal thalamus in mice. *Front Neural Circuits* 2019, 13: 51.
77. Goswamee P, Leggett E, McQuiston AR. Nucleus reuniens afferents in hippocampus modulate CA1 network function via monosynaptic excitation and polysynaptic inhibition. *Front Cell Neurosci* 2021, 15: 660897.
78. Felix-Ortiz AC, Beyeler A, Seo C, Leppla CA, Wildes CP, Tye KM. BLA to vHPC inputs modulate anxiety-related behaviors. *Neuron* 2013, 79: 658–664.
79. Yang Y, Wang ZH, Jin S, Gao D, Liu N, Chen SP, *et al.* Opposite monosynaptic scaling of BLP-vCA1 inputs governs hopefulness and helplessness-modulated spatial learning and memory. *Nat Commun* 2016, 7: 11935.
80. Amaral DG, Cowan WM. Subcortical afferents to the hippocampal formation in the monkey. *J Comp Neurol* 1980, 189: 573–591.
81. Oleskevich S, Descarries L, Lacaille JC. Quantified distribution of the noradrenaline innervation in the hippocampus of adult rat. *J Neurosci* 1989, 9: 3803–3815.
82. Loy R, Koziell DA, Lindsey JD, Moore RY. Noradrenergic innervation of the adult rat hippocampal formation. *J Comp Neurol* 1980, 189: 699–710.
83. Gasbarri A, Sulli A, Packard MG. The dopaminergic mesencephalic projections to the hippocampal formation in the rat. *Prog Neuro Psychopharmacol Biol Psychiatry* 1997, 21: 1–22.
84. Swanson LW, Sawchenko PE, Cowan WM. Evidence that the commissural, associational and septal projections of the regio inferior of the hippocampus arise from the same neurons. *Brain Res* 1980, 197: 207–212.
85. Luchetti A, Bota A, Weitemier A, Mizuta K, Sato M, Islam T, *et al.* Two functionally distinct serotonergic projections into hippocampus. *J Neurosci* 2020, 40: 4936–4944.
86. Aznar S, Qian ZX, Knudsen GM. Non-serotonergic dorsal and Median raphe projection onto parvalbumin- and calbindin-containing neurons in hippocampus and septum. *Neuroscience* 2004, 124: 573–581.
87. Kempadoo KA, Mosharov EV, Choi SJ, Sulzer D, Kandel ER. Dopamine release from the locus coeruleus to the dorsal hippocampus promotes spatial learning and memory. *Proc Natl Acad Sci U S A* 2016, 113: 14835–14840.
88. Yuan M, Meyer T, Benkowitz C, Savanthrapadian S, Ansel-Bollepalli L, Foggetti A, *et al.* Somatostatin-positive interneurons in the dentate gyrus of mice provide local- and long-range septal synaptic inhibition. *eLife* 2017, 6: e21105.
89. Besnard A, Gao Y, Kim MT, Twarkowski H, Reed AK, Langberg T, *et al.* Dorsolateral septum somatostatin interneurons gate mobility to calibrate context-specific behavioral fear responses. *Nat Neurosci* 2019, 22: 436–446.
90. Leroy F, Park J, Asok A, Brann DH, Meira T, Boyle LM, *et al.* A circuit from hippocampal CA2 to lateral septum disinhibits social aggression. *Nature* 2018, 564: 213–218.
91. Cenquizca LA, Swanson LW. Spatial organization of direct hippocampal field CA1 axonal projections to the rest of the cerebral cortex. *Brain Res Rev* 2007, 56: 1–26.
92. Kloosterman F, Witter MP, Van Haeften T. Topographical and laminar organization of subicular projections to the parahippocampal region of the rat. *J Comp Neurol* 2003, 455: 156–171.
93. Witter MP. Connections of the subiculum of the rat: Topography in relation to columnar and laminar organization. *Behav Brain Res* 2006, 174: 251–264.
94. Witter MP, Naber PA, van Haeften T, Machielsen WC, Rombouts SA, Barkhof F, *et al.* Cortico-hippocampal communication by way of parallel parahippocampal-subicular pathways. *Hippocampus* 2000, 10: 398–410.
95. Fu JY, Yu XD, Zhu Y, Xie SZ, Tang MY, Yu B, *et al.* Whole-brain map of long-range monosynaptic inputs to different cell types in the amygdala of the mouse. *Neurosci Bull* 2020, 36: 1381–1394.
96. Cole AB, Montgomery K, Bale TL, Thompson SM. What the hippocampus tells the HPA axis: Hippocampal output attenuates acute stress responses via disinhibition of CRF+PVN neurons. *Neurobiol Stress* 2022, 20: 100473.
97. Christiansen K, Dillingham CM, Wright NF, Saunders RC, Vann SD, Aggleton JP. Complementary subicular pathways to the anterior thalamic nuclei and mammillary bodies in the rat and macaque monkey brain. *Eur J Neurosci* 2016, 43: 1044–1061.
98. Mikulovic S, Restrepo CE, Siwani S, Bauer P, Pupe S, Tort ABL, *et al.* Ventral hippocampal OLM cells control type 2 theta oscillations and response to predator odor. *Nat Commun* 2018, 9: 3638.
99. Xia F, Kheirbek MA. Circuit-based biomarkers for mood and anxiety disorders. *Trends Neurosci* 2020, 43: 902–915.
100. Wang C, Liu H, Li K, Wu ZZ, Wu C, Yu JY, *et al.* Tactile modulation of memory and anxiety requires dentate granule cells along the dorsoventral axis. *Nat Commun* 2020, 11: 6045.
101. Tovote P, Fadok JP, Lüthi A. Neuronal circuits for fear and anxiety. *Nat Rev Neurosci* 2015, 16: 317–331.
102. Kemp GM, Altissimi HF, Nho Y, Heir R, Klyczek A, Stellwagen D. Sustained TNF signaling is required for the synaptic and anxiety-like behavioral response to acute stress. *Mol Psychiatry* 2022, 27: 4474–4484.
103. Sun D, Milibari L, Pan JX, Ren X, Yao LL, Zhao Y, *et al.* Critical roles of embryonic born dorsal dentate granule neurons for activity-dependent increases in BDNF, adult hippocampal neurogenesis, and antianxiety-like behaviors. *Biol Psychiatry* 2021, 89: 600–614.

104. Günther A, Luczak V, Gruteser N, Abel T, Baumann A. HCN₄ knockdown in dorsal hippocampus promotes anxiety-like behavior in mice. *Genes Brain Behav* 2019, 18: e12550.
105. Kim CS, Chang PY, Johnston D. Enhancement of dorsal hippocampal activity by knockdown of HCN₁ channels leads to anxiolytic- and antidepressant-like behaviors. *Neuron* 2012, 75: 503–516.
106. Cameron HA, McKay RD. Adult neurogenesis produces a large pool of new granule cells in the dentate gyrus. *J Comp Neurol* 2001, 435: 406–417.
107. Song J, Olsen RHJ, Sun J, Ming GL, Song H. Neuronal circuitry mechanisms regulating adult mammalian neurogenesis. *Cold Spring Harb Perspect Biol* 2016, 8: a018937.
108. Boldrini M, Fulmore CA, Tartt AN, Simeon LR, Pavlova I, Poposka V, *et al.* Human hippocampal neurogenesis persists throughout aging. *Cell Stem Cell* 2018, 22: 589–599.e5.
109. Moreno-Jiménez EP, Flor-García M, Terreros-Roncal J, Rábano A, Cafini F, Pallas-Bazarrá N, *et al.* Adult hippocampal neurogenesis is abundant in neurologically healthy subjects and drops sharply in patients with Alzheimer's disease. *Nat Med* 2019, 25: 554–560.
110. Hill AS, Sahay A, Hen R. Increasing adult hippocampal neurogenesis is sufficient to reduce anxiety and depression-like behaviors. *Neuropsychopharmacology* 2015, 40: 2368–2378.
111. Revest JM, Dupret D, Koehl M, Funk-Reiter C, Grosjean N, Piazza PV, *et al.* Adult hippocampal neurogenesis is involved in anxiety-related behaviors. *Mol Psychiatry* 2009, 14: 959–967.
112. Anacker C, Luna VM, Stevens GS, Millette A, Shores R, Jimenez JC, *et al.* Hippocampal neurogenesis confers stress resilience by inhibiting the ventral dentate gyrus. *Nature* 2018, 559: 98–102.
113. Kheirbek MA, Drew LJ, Burghardt NS, Costantini DO, Tannenholz L, Ahmari SE, *et al.* Differential control of learning and anxiety along the dorsoventral axis of the dentate gyrus. *Neuron* 2013, 77: 955–968.
114. Zaletel I, Filipović D, Puškaš N. Chronic stress, hippocampus and parvalbumin-positive interneurons: What do we know so far? *Rev Neurosci* 2016, 27: 397–409.
115. Czéh B, Varga ZK, Henningsen K, Kovács GL, Miseta A, Wiborg O. Chronic stress reduces the number of GABAergic interneurons in the adult rat hippocampus, dorsal-ventral and region-specific differences. *Hippocampus* 2015, 25: 393–405.
116. Filipović D, Zlatković J, Gass P, Inta D. The differential effects of acute vs. chronic stress and their combination on hippocampal parvalbumin and inducible heat shock protein 70 expression. *Neuroscience* 2013, 236: 47–54.
117. Filipović D, Stanisavljević A, Jasnić N, Bernardi RE, Inta D, Perić I, *et al.* Chronic treatment with fluoxetine or clozapine of socially isolated rats prevents subsector-specific reduction of parvalbumin immunoreactive cells in the hippocampus. *Neuroscience* 2018, 371: 384–394.
118. Czeh B, Simon M, van der Hart MG, Schmelting B, Hesselink MB, Fuchs E. Chronic stress decreases the number of parvalbumin-immunoreactive interneurons in the hippocampus: Prevention by treatment with a substance P receptor (NK₁) antagonist. *Neuropsychopharmacology* 2005, 30: 67–79.
119. Rossetti AC, Paladini MS, Colombo M, Gruca P, Lason-Tyburkiewicz M, Tota-Głowczyk K, *et al.* Chronic stress exposure reduces parvalbumin expression in the rat hippocampus through an imbalance of redox mechanisms: Restorative effect of the antipsychotic lurasidone. *Int J Neuropsychopharmacol* 2018, 21: 883–893.
120. Zou D, Chen L, Deng D, Jiang D, Dong F, McSweeney C, *et al.* DREADD in parvalbumin interneurons of the dentate gyrus modulates anxiety, social interaction and memory extinction. *Curr Mol Med* 2016, 16: 91–102.
121. Li H, Zhao J, Lai L, Xia Y, Wan C, Wei S, *et al.* Loss of SST and PV positive interneurons in the ventral hippocampus results in anxiety-like behavior in 5xFAD mice. *Neurobiol Aging* 2022, 117: 165–178.
122. Hu W, Zhang M, Czéh B, Flügge G, Zhang W. Stress impairs GABAergic network function in the hippocampus by activating nongenomic glucocorticoid receptors and affecting the integrity of the parvalbumin-expressing neuronal network. *Neuropsychopharmacology* 2010, 35: 1693–1707.
123. Murthy S, Kane GA, Katchur NJ, Lara Mejia PS, Obiofuma G, Buschman TJ, *et al.* Perineuronal nets, inhibitory interneurons, and anxiety-related ventral hippocampal neuronal oscillations are altered by early life adversity. *Biol Psychiatry* 2019, 85: 1011–1020.
124. Banasr M, Lepack A, Fee C, Duric V, Maldonado-Aviles J, DiLeone R, *et al.* Characterization of GABAergic marker expression in the chronic unpredictable stress model of depression. *Chronic Stress (Thousand Oaks)* 2017, 1: 2470547017720459.
125. Giachino C, Canalia N, Capone F, Fasolo A, Alleva E, Riva MA, *et al.* Maternal deprivation and early handling affect density of calcium binding protein-containing neurons in selected brain regions and emotional behavior in periadolescent rats. *Neuroscience* 2007, 145: 568–578.
126. Heilig M, Zachrisson O, Thorsell A, Ehnvall A, Mottagui-Tabar S, Sjögren M, *et al.* Decreased cerebrospinal fluid neuropeptide Y (NPY) in patients with treatment refractory unipolar major depression: Preliminary evidence for association with preproNPY gene polymorphism. *J Psychiatr Res* 2004, 38: 113–121.
127. Sergeev V, Fetissov S, Mathé AA, Jimenez PA, Bartfai T, Mortas P, *et al.* Neuropeptide expression in rats exposed to chronic mild stresses. *Psychopharmacology* 2005, 178: 115–124.
128. Sweerts BW, Jarrott B, Lawrence AJ. The effect of acute and chronic restraint on the central expression of prepro-neuropeptide Y mRNA in normotensive and hypertensive rats. *J Neuroendocrinol* 2001, 13: 608–617.
129. Alviña K, Farshbaf MJ, Mondal AK. Long term effects of stress on hippocampal function: Emphasis on early life stress paradigms and potential involvement of neuropeptide Y. *J Neurosci Res* 2021, 99: 57–66.
130. Li Q, Bartley AF, Dobrunz LE. Endogenously released neuropeptide Y suppresses hippocampal short-term facilitation and is impaired by stress-induced anxiety. *J Neurosci* 2017, 37: 23–37.
131. LaGamma CT, Tang WW, Morgan AA, McGowan JC, Brachman RA, Denny CA. Antidepressant but not prophylactic ketamine administration alters calretinin and calbindin expression in the ventral hippocampus. *Front Mol Neurosci* 2018, 11: 404.
132. Fuchs T, Jefferson SJ, Hooper A, Yee PH, Maguire J, Luscher B. Disinhibition of somatostatin-positive GABAergic interneurons results in an anxiolytic and antidepressant-like brain state. *Mol Psychiatry* 2017, 22: 920–930.
133. Giardino L, Bettelli C, Pozza M, Calzà L. Regulation of CCK mRNA expression in the rat brain by stress and treatment with sertraline, a selective serotonin re-uptake inhibitor. *Brain Res* 1999, 824: 304–307.
134. Kasai H, Matsuzaki M, Noguchi J, Yasumatsu N, Nakahara H. Structure-stability-function relationships of dendritic spines. *Trends Neurosci* 2003, 26: 360–368.
135. Kitayama N, Vaccarino V, Kutner M, Weiss P, Bremner JD. Magnetic resonance imaging (MRI) measurement of hippocampal volume in posttraumatic stress disorder: A meta-analysis. *J Affect Disord* 2005, 88: 79–86.
136. Schoenfeld TJ, McCausland HC, Morris HD, Padmanaban V, Cameron HA. Stress and loss of adult neurogenesis differentially reduce hippocampal volume. *Biol Psychiatry* 2017, 82: 914–923.
137. Rao U, Chen LA, Bidesi AS, Shad MU, Thomas MA, Hammen CL. Hippocampal changes associated with early-life adversity

- and vulnerability to depression. *Biol Psychiatry* 2010, 67: 357–364.
138. van der Flier WM, Scheltens P. Hippocampal volume loss and Alzheimer disease progression. *Nat Rev Neurol* 2009, 5: 361–362.
 139. Noorlander CW, Tijsseling D, Hessel EVS, de Vries WB, Derks JB, Visser GHA, *et al.* Antenatal glucocorticoid treatment affects hippocampal development in mice. *PLoS One* 2014, 9: e85671.
 140. Sousa N, Lukoyanov NV, Madeira MD, Almeida OF, Paula-Barbosa MM. Reorganization of the morphology of hippocampal neurites and synapses after stress-induced damage correlates with behavioral improvement. *Neuroscience* 2000, 97: 253–266.
 141. McLaughlin KJ, Gomez JL, Baran SE, Conrad CD. The effects of chronic stress on hippocampal morphology and function: An evaluation of chronic restraint paradigms. *Brain Res* 2007, 1161: 56–64.
 142. Orłowski D, Elfving B, Müller HK, Wegener G, Bjarkam CR. Wistar rats subjected to chronic restraint stress display increased hippocampal spine density paralleled by increased expression levels of synaptic scaffolding proteins. *Stress* 2012, 15: 514–523.
 143. Vyas A, Mitra R, Rao BSS, Chattarji S. Chronic stress induces contrasting patterns of dendritic remodeling in hippocampal and amygdaloid neurons. *J Neurosci* 2002, 22: 6810–6818.
 144. Christian KM, Miracle AD, Wellman CL, Nakazawa K. Chronic stress-induced hippocampal dendritic retraction requires CA3 NMDA receptors. *Neuroscience* 2011, 174: 26–36.
 145. Papadakakis A, Sidiropoulou K, Panagis G. Music exposure attenuates anxiety- and depression-like behaviors and increases hippocampal spine density in male rats. *Behav Brain Res* 2019, 372: 112023.
 146. Magariños AM, Li CJ, Gal Toth J, Bath KG, Jing D, Lee FS, *et al.* Effect of brain-derived neurotrophic factor haploinsufficiency on stress-induced remodeling of hippocampal neurons. *Hippocampus* 2011, 21: 253–264.
 147. Bennett MR, Lagopoulos J. Stress and trauma: BDNF control of dendritic-spine formation and regression. *Prog Neurobiol* 2014, 112: 80–99.
 148. Lakshminarasimhan H, Chattarji S. Stress leads to contrasting effects on the levels of brain derived neurotrophic factor in the hippocampus and amygdala. *PLoS One* 2012, 7: e30481.
 149. von Bohlen und Halbach O, von Bohlen und Halbach V. BDNF effects on dendritic spine morphology and hippocampal function. *Cell Tissue Res* 2018, 373: 729–741.
 150. Kumar A. Long-term potentiation at CA3-CA1 hippocampal synapses with special emphasis on aging, disease, and stress. *Front Aging Neurosci* 2011, 3: 7.
 151. Pan E, Puranam RS, McNamara JO. Long-term potentiation of mossy fiber feedforward inhibition of CA3 pyramidal cells maintains E/I balance in epilepsy model. *Neuro* 2022, 9: ENEURO.0375-ENEURO.0321.2021.
 152. Shin SY, Han SH, Woo RS, Jang SH, Min SS. Adolescent mice show anxiety- and aggressive-like behavior and the reduction of long-term potentiation in mossy fiber-CA3 synapses after neonatal maternal separation. *Neuroscience* 2016, 316: 221–231.
 153. Zhang X, Wang B, Jin J, An S, Zeng Q, Duan Y, *et al.* Early deprivation reduced anxiety and enhanced memory in adult male rats. *Brain Res Bull* 2014, 108: 44–50.
 154. Bhagya VR, Srikumar BN, Veena J, Shankaranarayana Rao BS. Short-term exposure to enriched environment rescues chronic stress-induced impaired hippocampal synaptic plasticity, anxiety, and memory deficits. *J Neurosci Res* 2017, 95: 1602–1610.
 155. Neitz A, Mergia E, Imbrosci B, Petrasch-Parwez E, Eysel UT, Koesling D, *et al.* Postsynaptic NO/cGMP increases NMDA receptor currents via hyperpolarization-activated cyclic nucleotide-gated channels in the hippocampus. *Cereb Cortex* 2014, 24: 1923–1936.
 156. Cortese BM, Phan KL. The role of glutamate in anxiety and related disorders. *CNS Spectr* 2005, 10: 820–830.
 157. Lydiard RB. The role of GABA in anxiety disorders. *J Clin Psychiatry* 2003, 64: 21–27.
 158. Rezvanfard M, Zarrindast MR, Bina P. Role of ventral hippocampal GABA(A) and NMDA receptors in the anxiolytic effect of carbamazepine in rats using the elevated plus maze test. *Pharmacology* 2009, 84: 356–366.
 159. Zarrabian S, Farahizadeh M, Nasehi M, Zarrindast MR. The role of CA3 GABAA receptors on anxiolytic-like behaviors and avoidance memory deficit induced by NMDA receptor antagonists. *J Psychopharmacol* 2016, 30: 215–223.
 160. Degroot A, Treit D. Dorsal and ventral hippocampal cholinergic systems modulate anxiety in the plus-maze and shock-probe tests. *Brain Res* 2002, 949: 60–70.
 161. Mineur YS, Obayemi A, Wigstrand MB, Fote GM, Calarco CA, Li AM, *et al.* Cholinergic signaling in the hippocampus regulates social stress resilience and anxiety- and depression-like behavior. *Proc Natl Acad Sci U S A* 2013, 110: 3573–3578.
 162. Köhler C, Ericson H, Radesäter AC. Different laminar distributions of dopamine D₁ and D₂ receptors in the rat hippocampal region. *Neurosci Lett* 1991, 126: 107–109.
 163. Hasbi A, Nguyen T, Rahal H, Manduca JD, Miksys S, Tyndale RF, *et al.* Sex difference in dopamine D1–D2 receptor complex expression and signaling affects depression- and anxiety-like behaviors. *Biol Sex Differ* 2020, 11: 8.
 164. Zarrindast MR, Nasehi M, Pournaghshband M, Yekta BG. Dopaminergic system in CA1 modulates MK-801 induced anxiolytic-like responses. *Pharmacol Biochem Behav* 2012, 103: 102–110.
 165. Zarrindast MR, Naghdi-Sedeh N, Nasehi M, Sahraei H, Bahrami F, Asadi F. The effects of dopaminergic drugs in the ventral hippocampus of rats in the nicotine-induced anxiogenic-like response. *Neurosci Lett* 2010, 475: 156–160.
 166. Nasehi M, Mafi F, Oryan S, Nasri S, Zarrindast MR. The effects of dopaminergic drugs in the dorsal hippocampus of mice in the nicotine-induced anxiogenic-like response. *Pharmacol Biochem Behav* 2011, 98: 468–473.
 167. Nasehi M, Kafi F, Zarrindast MR. Differential mechanisms of opioidergic and dopaminergic systems of the ventral hippocampus (CA₃) in anxiolytic-like behaviors induced by cholestasis in mice. *Eur J Pharmacol* 2013, 714: 352–358.
 168. Zhou QG, Zhu LJ, Chen C, Wu HY, Luo CX, Chang L, *et al.* Hippocampal neuronal nitric oxide synthase mediates the stress-related depressive behaviors of glucocorticoids by downregulating glucocorticoid receptor. *J Neurosci* 2011, 31: 7579–7590.
 169. Zhu LJ, Li TY, Luo CX, Jiang N, Chang L, Lin YH, *et al.* CAPON-nNOS coupling can serve as a target for developing new anxiolytics. *Nat Med* 2014, 20: 1050–1054.
 170. Zhu LJ, Shi HJ, Chang L, Zhang CC, Si M, Li N, *et al.* nNOS-CAPON blockers produce anxiolytic effects by promoting synaptogenesis in chronic stress-induced animal models of anxiety. *Br J Pharmacol* 2020, 177: 3674–3690.
 171. Tomiga Y, Sakai K, Ra SG, Kusano M, Ito A, Uehara Y, *et al.* Short-term running exercise alters DNA methylation patterns in neuronal nitric oxide synthase and brain-derived neurotrophic factor genes in the mouse hippocampus and reduces anxiety-like behaviors. *FASEB J* 2021, 35: e21767.
 172. Dubreucq S, Matias I, Cardinal P, Häring M, Lutz B, Marsicano G, *et al.* Genetic dissection of the role of cannabinoid type-1 receptors in the emotional consequences of repeated social stress in mice. *Neuropsychopharmacology* 2012, 37: 1885–1900.
 173. Zhong P, Wang W, Pan B, Liu X, Zhang Z, Long JZ, *et al.* Monoacylglycerol lipase inhibition blocks chronic stress-induced depressive-like behaviors via activation of mTOR signaling. *Neuropsychopharmacology* 2014, 39: 1763–1776.

174. Lisboa SF, Borges AA, Nejo P, Fassini A, Guimarães FS, Resstel LB. Cannabinoid CB₁ receptors in the dorsal hippocampus and prelimbic medial prefrontal cortex modulate anxiety-like behavior in rats: Additional evidence. *Prog Neuro Psychopharmacol Biol Psychiatry* 2015, 59: 76–83.
175. Campos AC, Ferreira FR, Guimarães FS, Lemos JI. Facilitation of endocannabinoid effects in the ventral hippocampus modulates anxiety-like behaviors depending on previous stress experience. *Neuroscience* 2010, 167: 238–246.
176. Scarante FF, Vila-Verde C, Detoni VL, Ferreira-Junior NC, Guimarães FS, Campos AC. Cannabinoid modulation of the stressed hippocampus. *Front Mol Neurosci* 2017, 10: 411.
177. Rubino T, Guidali C, Vigano D, Realini N, Valenti M, Massi P, *et al.* CB₁ receptor stimulation in specific brain areas differently modulate anxiety-related behaviour. *Neuropharmacology* 2008, 54: 151–160.
178. Hu XF, Zhang H, Yu LL, Ge WQ, Zhan-Mu OY, Li YZ, *et al.* Electroacupuncture reduces anxiety associated with inflammatory bowel disease by acting on cannabinoid CB₁ receptors in the ventral hippocampus in mice. *Front Pharmacol* 2022, 13: 919553.
179. Zhuang M, Lai Q, Yang C, Ma Y, Fan B, Bian Z, *et al.* Spexin as an anxiety regulator in mouse hippocampus: Mechanisms for transcriptional regulation of spexin gene expression by corticotropin releasing factor. *Biochem Biophys Res Commun* 2020, 525: 326–333.
180. Philbert J, Pichat P, Palme R, Belzung C, Griebel G. The CRF₁ receptor antagonist SSR125543 attenuates long-term cognitive deficit induced by acute inescapable stress in mice, independently from the hypothalamic pituitary adrenal axis. *Pharmacol Biochem Behav* 2012, 102: 415–422.
181. Chen Y, Brunson KL, Müller MB, Cariaga W, Baram TZ. Immunocytochemical distribution of corticotropin-releasing hormone receptor type-1 (CRF(1))-like immunoreactivity in the mouse brain: Light microscopy analysis using an antibody directed against the C-terminus. *J Comp Neurol* 2000, 420: 305–323.
182. Kozlovsky N, Zohar J, Kaplan Z, Cohen H. Microinfusion of a corticotrophin-releasing hormone receptor 1 antisense oligodeoxynucleotide into the dorsal hippocampus attenuates stress responses at specific times after stress exposure. *J Neuroendocrinol* 2012, 24: 489–503.
183. Bertagna NB, dos Santos PGC, Queiroz RM, Fernandes GJD, Cruz FC, Miguel TT. Involvement of the ventral, but not dorsal, hippocampus in anxiety-like behaviors in mice exposed to the elevated plus maze: Participation of CRF₁ receptor and PKA pathway. *Pharmacol Rep* 2021, 73: 57–72.
184. Dine J, Ionescu IA, Stepan J, Yen YC, Holsboer F, Landgraf R, *et al.* Identification of a role for the ventral hippocampus in neuropeptide S-elicited anxiolysis. *PLoS One* 2013, 8: e60219.
185. Ionescu IA, Dine J, Yen YC, Buell DR, Herrmann L, Holsboer F, *et al.* Intranasally administered neuropeptide S (NPS) exerts anxiolytic effects following internalization into NPS receptor-expressing neurons. *Neuropsychopharmacology* 2012, 37: 1323–1337.
186. Dine J, Ionescu IA, Avrabos C, Yen YC, Holsboer F, Landgraf R, *et al.* Intranasally applied neuropeptide S shifts a high-anxiety electrophysiological endophenotype in the ventral hippocampus towards a normal-anxiety one. *PLoS One* 2015, 10: e0120272.
187. Rytova V, Ganella DE, Hawkes D, Bathgate RAD, Ma S, Gundlach AL. Chronic activation of the relaxin-3 receptor on GABA neurons in rat ventral hippocampus promotes anxiety and social avoidance. *Hippocampus* 2019, 29: 905–920.
188. Engin E, Stellbrink J, Treit D, Dickson CT. Anxiolytic and antidepressant effects of intracerebroventricularly administered somatostatin: Behavioral and neurophysiological evidence. *Neuroscience* 2008, 157: 666–676.
189. Li M, Li C, Yu H, Cai X, Shen X, Sun X, *et al.* Lentivirus-mediated interleukin-1 β (IL-1 β) knock-down in the hippocampus alleviates lipopolysaccharide (LPS)-induced memory deficits and anxiety- and depression-like behaviors in mice. *J Neuroinflammation* 2017, 14: 190.
190. Rodríguez-Seoane C, Ramos A, Korth C, Requena JR. DISC₁ regulates expression of the neurotrophin VGF through the PI3K/AKT/CREB pathway. *J Neurochem* 2015, 135: 598–605.
191. Guo J, Lin P, Zhao X, Zhang J, Wei X, Wang Q, *et al.* Etazolate abrogates the lipopolysaccharide (LPS)-induced downregulation of the cAMP/pCREB/BDNF signaling, neuroinflammatory response and depressive-like behavior in mice. *Neuroscience* 2014, 263: 1–14.
192. Komleva YK, Lopatina OL, Gorina IV, Shuvaev AN, Chernykh A, Potapenko IV, *et al.* NLRP3 deficiency-induced hippocampal dysfunction and anxiety-like behavior in mice. *Brain Res* 2021, 1752: 147220.
193. Xu Y, Sheng H, Bao Q, Wang Y, Lu J, Ni X. NLRP3 inflammasome activation mediates estrogen deficiency-induced depression- and anxiety-like behavior and hippocampal inflammation in mice. *Brain Behav Immun* 2016, 56: 175–186.
194. Wang YL, Han QQ, Gong WQ, Pan DH, Wang LZ, Hu W, *et al.* Microglial activation mediates chronic mild stress-induced depressive- and anxiety-like behavior in adult rats. *J Neuroinflammation* 2018, 15: 21.
195. Wheeler DW, White CM, Rees CL, Komendantov AO, Hamilton DJ, Ascoli GA. Hippocampome.org: A knowledge base of neuron types in the rodent hippocampus. *Life* 2015, 4: e09960.
196. Calhoon GG, Tye KM. Resolving the neural circuits of anxiety. *Nat Neurosci* 2015, 18: 1394–1404.
197. Avital A, Ram E, Maayan R, Weizman A, Richter-Levin G. Effects of early-life stress on behavior and neurosteroid levels in the rat hypothalamus and entorhinal cortex. *Brain Res Bull* 2006, 68: 419–424.
198. Lu J, Zhang Z, Yin X, Tang Y, Ji R, Chen H, *et al.* An entorhinal-visual cortical circuit regulates depression-like behaviors. *Mol Psychiatry* 2022, 27: 3807–3820.
199. Davidson RJ. Anxiety and affective style: Role of prefrontal cortex and amygdala. *Biol Psychiatry* 2002, 51: 68–80.
200. Tye KM, Prakash R, Kim SY, Fenno LE, Grosenick L, Zarabi H, *et al.* Amygdala circuitry mediating reversible and bidirectional control of anxiety. *Nature* 2011, 471: 358–362.
201. Novaes LS, Dos Santos NB, Batalhote RFP, Malta MB, Camarini R, Scavone C, *et al.* Environmental enrichment protects against stress-induced anxiety: Role of glucocorticoid receptor, ERK, and CREB signaling in the basolateral amygdala. *Neuropharmacology* 2017, 113: 457–466.
202. Pikkarainen M, Rönkkö S, Savander V, Insausti R, Pitkänen A. Projections from the lateral, basal, and accessory basal nuclei of the amygdala to the hippocampal formation in rat. *J Comp Neurol* 1999, 403: 229–260.
203. Pitkänen A, Pikkarainen M, Nurminen N, Ylinen A. Reciprocal connections between the amygdala and the hippocampal formation, perirhinal cortex, and postrhinal cortex in rat. A review. *Ann N Y Acad Sci* 2000, 911: 369–391.
204. Pi G, Gao D, Wu D, Wang Y, Lei H, Zeng W, *et al.* Posterior basolateral amygdala to ventral hippocampal CA1 drives approach behaviour to exert an anxiolytic effect. *Nat Commun* 2020, 11: 183.
205. Zhang JY, Liu TH, He Y, Pan HQ, Zhang WH, Yin XP, *et al.* Chronic stress remodels synapses in an amygdala circuit-specific manner. *Biol Psychiatry* 2019, 85: 189–201.
206. Jacobs BL, Azmitia EC. Structure and function of the brain serotonin system. *Physiol Rev* 1992, 72: 165–229.
207. Berumen LC, Rodríguez A, Miledi R, García-Alcocer G. Serotonin receptors in hippocampus. *Sci World J* 2012, 2012: 823493.

208. Rex A, Voigt JP, Fink H. Anxiety but not arousal increases 5-hydroxytryptamine release in the rat ventral hippocampus *in vivo*. *Eur J Neurosci* 2005, 22: 1185–1189.
209. Ohmura Y, Tsutsui-Kimura I, Sasamori H, Nebuka M, Nishitani N, Tanaka KF, *et al*. Different roles of distinct serotonergic pathways in anxiety-like behavior, antidepressant-like, and anti-impulsive effects. *Neuropharmacology* 2020, 167: 107703.
210. Ohmura Y, Tanaka KF, Tsunematsu T, Yamanaka A, Yoshioka M. Optogenetic activation of serotonergic neurons enhances anxiety-like behaviour in mice. *Int J Neuropsychopharmacol* 2014, 17: 1777–1783.
211. Abela AR, Browne CJ, Sargin D, Prevot TD, Ji XD, Li Z, *et al*. Median raphe serotonin neurons promote anxiety-like behavior via inputs to the dorsal hippocampus. *Neuropharmacology* 2020, 168: 107985.
212. dos Santos L, de Andrade TG, Zangrossi Junior H. 5-HT_{1A} receptors in the dorsal hippocampus mediate the anxiogenic effect induced by the stimulation of 5-HT neurons in the Median raphe nucleus. *Eur Neuropsychopharmacol* 2008, 18: 286–294.
213. Adhikari A, Topiwala MA, Gordon JA. Synchronized activity between the ventral hippocampus and the medial prefrontal cortex during anxiety. *Neuron* 2010, 65: 257–269.
214. Padilla-Coreano N, Canetta S, Mikofsky RM, Alway E, Passecker J, Myroshnychenko MV, *et al*. Hippocampal-prefrontal *Theta* transmission regulates avoidance behavior. *Neuron* 2019, 104: 601-610.e4.
215. Adhikari A, Topiwala MA, Gordon JA. Single units in the medial prefrontal cortex with anxiety-related firing patterns are preferentially influenced by ventral hippocampal activity. *Neuron* 2011, 71: 898–910.
216. Padilla-Coreano N, Bolkan SS, Pierce GM, Blackman DR, Hardin WD, Garcia-Garcia AL, *et al*. Direct ventral hippocampal-prefrontal input is required for anxiety-related neural activity and behavior. *Neuron* 2016, 89: 857–866.
217. Lee AT, Cunniff MM, See JZ, Wilke SA, Luongo FJ, Ellwood IT, *et al*. VIP interneurons contribute to avoidance behavior by regulating information flow across hippocampal-prefrontal networks. *Neuron* 2019, 102: 1223-1234.e4.
218. Parfitt GM, Nguyen R, Bang JY, Aqrabawi AJ, Tran MM, Seo DK, *et al*. Bidirectional control of anxiety-related behaviors in mice: Role of inputs arising from the ventral hippocampus to the lateral septum and medial prefrontal cortex. *Neuropsychopharmacology* 2017, 42: 1715–1728.
219. Zarrindast MR, Valizadegan F, Rostami P, Rezayof A. Histaminergic system of the lateral septum in the modulation of anxiety-like behaviour in rats. *Eur J Pharmacol* 2008, 583: 108–114.
220. Troyano-Rodriguez E, Wirsig-Wiechmann CR, Ahmad M. Neuregulin-2 determines inhibitory synaptic transmission in the lateral septum to optimize stress-induced neuronal activation and avoidance behavior. *Biol Psychiatry* 2019, 85: 1046–1055.
221. Trent NL, Menard JL. The ventral hippocampus and the lateral septum work in tandem to regulate rats' open-arm exploration in the elevated plus-maze. *Physiol Behav* 2010, 101: 141–152.
222. Glangetas C, Massi L, Fois GR, Jalabert M, Girard D, Diana M, *et al*. NMDA-receptor-dependent plasticity in the bed nucleus of the stria terminalis triggers long-term anxiolysis. *Nat Commun* 2017, 8: 14456.
223. Jimenez JC, Su K, Goldberg AR, Luna VM, Biane JS, Ordek G, *et al*. Anxiety cells in a hippocampal-hypothalamic circuit. *Neuron* 2018, 97: 670-683.e6.
224. Lesting J, Narayanan RT, Kluge C, Sangha S, Seidenbecher T, Pape HC. Patterns of coupled theta activity in amygdala-hippocampal-prefrontal cortical circuits during fear extinction. *PLoS One* 2011, 6: e21714.
225. Kim WB, Cho JH. Synaptic targeting of double-projecting ventral CA1 hippocampal neurons to the medial prefrontal cortex and basal amygdala. *J Neurosci* 2017, 37: 4868–4882.

Springer Nature or its licensor (e.g. a society or other partner) holds exclusive rights to this article under a publishing agreement with the author(s) or other rightsholder(s); author self-archiving of the accepted manuscript version of this article is solely governed by the terms of such publishing agreement and applicable law.

Neuronal Mechanisms Govern Glioblastoma Cell Invasion

Xiaowu Lin^{1,2,3,4} · Zhihui Huang^{1,2,3,4} ·
Yongjie Wang^{1,2,3,4} 

Received: 3 August 2022 / Accepted: 18 December 2022 / Published online: 1 February 2023

© Center for Excellence in Brain Science and Intelligence Technology, Chinese Academy of Sciences 2023

Glioblastoma (GBM) remains one of the most aggressive malignancies; it is characterized by genetic heterogeneity and resistance to treatment. One main reason is that GBM cells (GBCs) communicate with other cells in the brain environment to support tumor progression and resist therapy [1]. Tumor-associated astrocytes, for example, have been reported to thwart immunotherapy approaches for GBM by promoting an immunosuppressive environment [2]. Meanwhile, astrocytes surrounding the GBM alter the ability of tumor-associated macrophages to attack the GBM, provide cholesterol to tumor cells, and subsequently promote their survival [3].

Intercellular communication routes include the secretion of cytokines and chemokines or the release of exosomes [4]. Paracrine crosstalk between phenotypic states is critical to reshaping the overall GBM ecosystem, which activates GBCs to transition into stem-like states and promote the tumor process. In addition, direct cell contacts *via* synapses and tumor microtubes (TMs) contribute to tumor growth and

immunity escape. It had been reported that most treatment-resistant GBCs extend long tubular membrane protrusions, which continuously scan the brain microenvironment to invade and colonize the brain. Finally, these GBCs form a multicellular network with other cellular components *via* TMs [5]. However, both in human and mouse diffuse astrocytomas and GBMs, some tumor cells remain isolated from the other cells [6]. This subpopulation of GBCs plays distinct roles in the initiation and invasion of gliomas, but the exact mechanism requires further exploration. As previously reported, chemical synapses can be connected with TMs. These glutamatergic glial synapses may receive signals from neurons to promote glioma growth and invasion [7].

Notably, TM-positive GBCs have been reported to express higher levels of stem cell markers in humans and mice [6]. Furthermore, several pharmacological experiments have demonstrated that TMs and tumor cellular networks are potential therapeutic targets [8]. Thus, a comprehensive understanding of this interrelationship with tumorigenesis and invasion of GBM is critical.

Recently, Professor Winkler's team reported that one of the subpopulations of GBM, which lacks links with other tumor cells and astrocytes, receives synaptic input from neurons. Moreover, the characteristics of this subpopulation are consistent with the neuronal and neural-like tumor cell states both in the mouse model and in humans. Taken together, these findings accentuate that tumor-unconnected GBCs can “hijack” neuronal migration mechanisms to achieve whole-brain invasion and colonization [9].

Firstly, the researchers constructed a patient-derived xenograft [PDX] model and separated GBCs into two groups termed “connected^{TUM/AC}” and “unconnected^{TUM/AC}” *via* SR101 and mGFP labeling. SR101 was taken up minimally by unconnected^{TUM/AC} GBCs but broadly by both astrocytes and connected^{TUM/AC} GBCs. Connected^{TUM/}

✉ Zhihui Huang
huang0069@hznu.edu.cn

✉ Yongjie Wang
wangyongjie@hznu.edu.cn

¹ School of Pharmacy, Hangzhou Normal University, Hangzhou 311121, China

² Key Laboratory of Elemene Class Anti-Cancer Chinese Medicines, Hangzhou Normal University, Hangzhou 311121, China

³ Engineering Laboratory of Development and Application of Traditional Chinese Medicines, Hangzhou Normal University, Hangzhou 311121, China

⁴ Collaborative Innovation Center of Traditional Chinese Medicines of Zhejiang Province, Hangzhou Normal University, Hangzhou 311121, China

^{AC} GBCs exhibited much lower input resistance than unconnected^{TUM/AC} GBCs. They further loaded Rhod 2-AM into the surface of the mouse brain, and the Ca²⁺ events simultaneously recorded in both cell types confirmed that the connections between GBCs and astrocytes are *via* gap junctional coupling.

To identify which subpopulation of GBCs drives the diffuse brain invasion and colonization, the authors then measured the migration speed of connected^{TUM/AC} and unconnected^{TUM/AC} cells. Surprisingly, unconnected^{TUM/AC} GBCs were significantly invasive while connected^{TUM/AC} GBCs remained static, indicating that unconnected^{TUM/AC} GBCs play a key role in GBM invasion.

By combining single-cell RNA sequencing (scRNA-seq) with intravital two-photon microscopy, the researchers sorted the two subpopulations and analyzed their time-dependent expression changes, which revealed that the proportion of unconnected^{TUM/AC} GBCs is greater than connected^{TUM/AC} GBCs at the early stage but decreases over time. Consequently, the unconnected^{TUM/AC} GBCs invade brain regions early on, interact with other GBCs and astrocytes, and eventually transition into connected^{TUM/AC} GBCs.

To probe the molecular and functional cellular states more deeply, the researchers integrated scRNA-seq with intravital imaging. They found that unconnected^{TUM/AC} GBCs mainly displayed neuronal (NEU) and oligodendrocyte precursor-like/neural precursor-like (NPC-like) cell states in all three PDX models, suggesting that GBM may exploit the mechanisms of early neuronal development to attack healthy tissue. Conversely, the connected^{TUM/AC} GBCs showed more mesenchymal (MES) traits. However, the role of the MES-like cellular state of connected^{TUM/AC} GBCs is still unknown.

The authors next explored the correlation between cellular NEU features and brain tumor invasion. They discovered that unconnected^{TUM/AC} GBCs extend two processes and move the soma in the same direction while retracting the trailing process, which was not seen in non-somatokinetic cells. To investigate whether all TMs contribute to invasion, TMs were subclassified into blind-ending or connecting TMs. Blind-ending TMs possessed greater aggressiveness, and these associated small membrane protrusions on a smaller spatial scale could be accessories to invasion. In addition, the motor pattern of blind-ending TMs appeared to resemble neuronal migration during development [10] and these invasive TMs followed a search-efficient mechanism, implying that TM invasion is a search-efficient process.

Then, the authors investigated the dynamic mechanisms of the invasion process. Three major invasion mechanisms were described: branching migration (the highest TM turnover), locomotion, and translocation. They revealed that these invasion mechanisms resemble the migration of NEU progenitor and other neural progenitor cells, which is likely

related to their NEU- and NPC-like transcriptional states. Previous studies have emphasized that neuronal activity fosters the malignant behavior of GBCs and some typical synaptic ultrastructure is located on TMs [7]. Therefore, how do neuroglial synapses impact the formation and growth of TMs and tumor invasion by regulating NEU activity? The authors revealed that NEU activity indeed promotes the TM movement and GBC invasion by dynamic neuroglial synapse-mediated signal input.

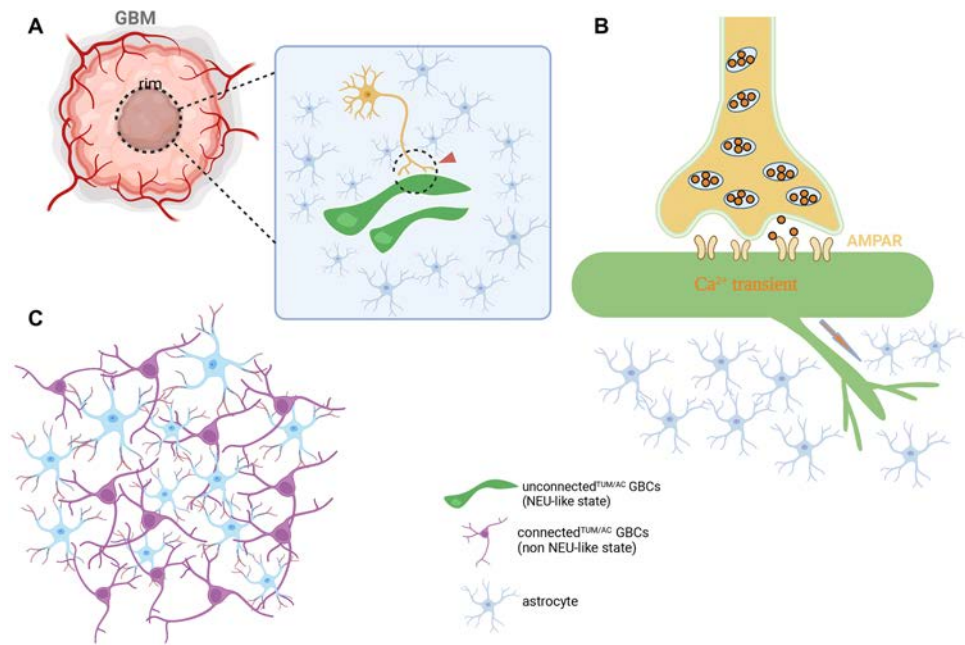
To clarify whether NEU activity is functionally relevant to downstream mechanisms, they used 3D *in vivo* Ca²⁺ imaging to examine the change of Ca²⁺ signals in GBCs. The results showed that neuronal activity increased the Ca²⁺ event area and frequency in GBCs, which was further confirmed by inhibiting Ca²⁺ events. This evidence suggested that neural activation can control TM dynamics and invasion speed *via* Ca²⁺ transients in GBCs and the authors eventually determined that this change in Ca²⁺ signaling caused by neuronal activity is mediated *via* AMPARs (α -amino-3-hydroxy-5-methyl-4-isoxazolepropionic acid receptors).

In summary, this research describes a NEU-/NPC-like subpopulation of GBCs, which receive synaptic input from neurons to promote tumor invasion *via* neuronal migration mechanisms, revealing the relation between tumor heterogeneity and tumor biology.

However, the mechanism of this cellular state is worth further exploration. The authors illustrated that unconnected^{TUM/AC} GBCs evolve into connected^{TUM/AC} GBCs, but the cellular mechanisms underlying this phenomenon are still poorly understood. Besides, the article predominantly confirmed that GBCs not only connected with the tumor cells *via* gap junctions but also established junctions with astrocytes, which extends the concept of a tumor network. The contribution of astrocytes or other types of cells to tumor cellular networks has received little attention, especially in connected^{TUM/AC} GBCs. What happens after unconnected^{TUM/AC} GBCs transform into connected^{TUM/AC} GBCs is still unclear. Furthermore, most unconnected^{TUM/AC} GBCs were found in the tumor rim. So, what influences the distribution of unconnected^{TUM/AC} GBCs and connected^{TUM/AC} GBCs needs further clarification. This different distribution may be related to metabolites associated with tumor metabolism or energy supply [11]. Also, are the neurons that form synapses with unconnected^{TUM/AC} GBCs similarly distributed in specific parts of the brain? This may contribute to solving why gliomas preferentially infiltrate certain brain regions.

As previously reported, contacts between neurons and GBCs occur in three morphological categories, possibly contributing to distinct functional properties [5]. Therefore, whether the molecular structures of the neuroglial synapses found between neurons and unconnected^{TUM/AC} GBCs are different from normal synapses between neurons? The

Fig. 1 The process of unconnected^{TUM/AC} GBC invasion and transformation into connected^{TUM/AC} GBCs. **A** Most of the unconnected^{TUM/AC} GBCs are located at the rim of the tumor and form synapses (indicated by red arrows) with neurons. **B** Activated neurons induce an increase in Ca^{2+} transients in unconnected^{TUM/AC} GBCs via AMPAR-mediated synaptic input, and promote TM-dependent tumor invasion. **C** Unconnected^{TUM/AC} GBCs transform into connected^{TUM/AC} GBCs that connect with astrocytes and form a multicellular tumor network.



authors also noted that the synapses are ephemeral, yet, previous studies have not shed much light on the mechanisms driving the formation and disappearance of these synapses. As to the neurons forming synapses with unconnected^{TUM/AC} GBCs, is there any difference between neurons connecting with unconnected^{TUM/AC} GBCs and neurons connecting with other neurons, and which cell plays a dominant role in the formation of these synapses? Beyond that, which kind of neurons are activated is still unclear.

In addition, a cAMP-response element binding transcription factor is the potential NEU-activity-dependent and Ca^{2+} -regulated target. More bioinformatics analyses are needed to find other differences in gene expression profiles between unconnected^{TUM/AC} GBCs and connected^{TUM/AC} GBCs, such as TGF- β and its downstream mediator thrombospondin 1, which is critical to the TM network in GBM [12], and neuroligin-3, which can induce glioma expression of synaptic genes [13].

In all, this article creatively reveals the essential role of unconnected^{TUM/AC} GBCs in GBM invasion, which differs from most previous theories that the network of communicating tumor cells connected by tumor microtubes regulates the growth of incurable gliomas. Although mounting data have demonstrated that TM-positive GBCs express more stem cell markers, few studies have shown that tumor cells exploit the developmental neural stem cell machinery to invade, following an extraordinarily effective means of spreading. Moreover, Winkler's team emphasized the role of neuronal activity in GBM invasion and established a link between NEU activity, Ca^{2+} signaling, tumor heterogeneity, and TM-dependent tumor invasion (Fig. 1). Their explorations are essential for the novel therapeutic target studies for GBM, as interfering with

these signals may be an effective way to block this invasive mechanism. At the same time, these mechanisms perhaps appear in other solid brain tumors and may even be found in tumors of other tissues.

Therefore, it is crucial to understand how molecular and functional states control behaviors and elucidate the exact downstream mechanisms of how synaptic inputs trigger other tumor biological effects like proliferation and therapy resistance.

References

1. Broekman ML, Maas SLN, Abels ER, Mempel TR, Krichevsky AM, Breakefield XO. Multidimensional communication in the microenvirons of glioblastoma. *Nat Rev Neurol* 2018, 14: 482–495.
2. Henrik Heiland D, Ravi VM, Behringer SP, Frenking JH, Wurm J, Joseph K. Tumor-associated reactive astrocytes aid the evolution of immunosuppressive environment in glioblastoma. *Nat Commun* 2019, 10: 2541.
3. Perelroizen R, Philosof B, Budick-Harmelin N, Chernobylsky T, Ron A, Katzir R, *et al.* Astrocyte immunometabolic regulation of the tumour microenvironment drives glioblastoma pathogenicity. *Brain* 2022, 145: 3288–3307.
4. Roehlecke C, Schmidt MHH. Tunneling nanotubes and tumor microtubes in cancer. *Cancers (Basel)* 2020, 12: 857.
5. Yabo YA, Niclou SP, Golebiewska A. Cancer cell heterogeneity and plasticity: A paradigm shift in glioblastoma. *Neuro-oncology* 2022, 24: 669–682.
6. Xie R, Kessler T, Grosch J, Hai L, Venkataramani V, Huang L, *et al.* Tumor cell network integration in glioma represents a stemness feature. *Neuro-oncology* 2021, 23: 757–769.
7. Venkataramani V, Tanev DI, Strahle C, Studier-Fischer A, Fankhauser L, Kessler T, *et al.* Glutamatergic synaptic input to glioma cells drives brain tumour progression. *Nature* 2019, 573: 532–538.

8. Venkataramani V, Schneider M, Giordano FA, Kuner T, Wick W, Herrlinger U, *et al.* Disconnecting multicellular networks in brain tumours. *Nat Rev Cancer* 2022, 22: 481–491.
9. Venkataramani V, Yang Y, Schubert MC, Reyhan E, Tetzlaff SK, Wißmann N, *et al.* Glioblastoma hijacks neuronal mechanisms for brain invasion. *Cell* 2022, 185: 2899-2917.e31.
10. Yee KT, Simon HH, Tessier-Lavigne M, O’Leary DDM. Extension of long leading processes and neuronal migration in the mammalian brain directed by the chemoattractant netrin-1. *Neuron* 1999, 24: 607–622.
11. Joseph JV, Magaut CR, Storevik S, Geraldo LH, Mathivet T, Latif MA, *et al.* TGF- β promotes microtubule formation in glioblastoma through thrombospondin 1. *Neuro Oncol* 2022, 24: 541–553.
12. Venkatesh HS, Morishita W, Geraghty AC, Silverbush D, Gillespie SM, Arzt M, *et al.* Electrical and synaptic integration of glioma into neural circuits. *Nature* 2019, 573: 539–545.
13. Grillon E, Farion R, Reuveni M, Glidle A, Rémy C, Coles JA. Spatial profiles of markers of glycolysis, mitochondria, and proton pumps in a rat glioma suggest coordinated programming for proliferation. *BMC Res Notes* 2015, 8: 207.

Springer Nature or its licensor (e.g. a society or other partner) holds exclusive rights to this article under a publishing agreement with the author(s) or other rightsholder(s); author self-archiving of the accepted manuscript version of this article is solely governed by the terms of such publishing agreement and applicable law.

Double-Edged Mossy Cells in Temporal Lobe Epilepsy: Evil in the Early Stage Through a BDNF-Dependent Strengthening Dentate Gyrus Circuit

Heming Cheng¹ · Qiuwen Lou¹ · Yi Wang^{1,2} ·
Zhong Chen^{1,3} 

Received: 17 October 2022 / Accepted: 19 November 2022 / Published online: 31 January 2023

© Center for Excellence in Brain Science and Intelligence Technology, Chinese Academy of Sciences 2023

Temporal lobe epilepsy (TLE), one of the most common drug-resistant epilepsies, is characterized by abnormal recurrent excitatory activity originating from the temporal lobe. In the dentate gyrus (DG) of the hippocampus, a common seizure focus of TLE, the glutamatergic mossy cells (MCs) make synaptic connections with the granule cells (GCs) and form recurrent MC-GC-MC excitatory circuits. Cross-layer projections of MCs are able to modulate the excitability of the DG and even the whole hippocampus, and they may be closely involved in TLE. Injury and loss of MCs during chronic seizures have been widely reported in both human patients and animal models of TLE, and the surviving MCs have been disclosed to play an anti-epileptic role [1]. However, the functions and the underlying mechanisms of MCs in the early stage of epileptogenesis remain unclear.

Recently, Nasrallah *et al.* have focused on the connection of the MC-GC excitatory circuit with epilepsy, and revealed that seizure-induced strengthening of the MC-GC circuit plays a detrimental role during the early stage of epileptogenesis [2]. First, by the use of a *Drd2-cre* mouse line

combined with a Cre-recombinase-dependent virus under the CaMKII promoter, they selectively studied the role of MCs in the DG. They verified that chemogenetic silencing of MCs in the DG significantly reduced the amplitude of evoked MC-GC excitatory postsynaptic currents in acute slices from healthy mice, and reduced the susceptibility to seizure stage 3 in mice induced by acute intraperitoneal injection of kainic acid (KA). This is consistent with the results in another acute pilocarpine mouse model reported by Botterill *et al.*, in which inhibiting MCs during epileptogenesis not only reduced the severity of early seizures but also ameliorated the following chronic seizures [3]. Meanwhile, neither of them specifically investigated whether there was any functional difference between the MCs in the dorsal DG and those in the ventral DG during epileptogenesis, given that their axon distributions are heterogeneous and their roles in chronic seizures are distinct [1, 4, 5].

Then Nasrallah *et al.* used two-photon imaging to monitor the activity of the MC-GC circuit *in vivo* and found that both the MCs and GCs are activated after the initial convulsive seizures. More importantly, the enhanced activity of MCs precedes that of GCs, indicating the potential of MCs for driving the activation of GCs. Since the repetitive activity of MCs induced long-term potentiation (LTP) in MC-GC circuits of healthy mice, they further verified that LTP in MC-GC circuits was induced in epileptic mice after an initial stage 3 seizure, the mechanism being enhanced presynaptic MC-GC transmission. In addition, they also found that KA-induced seizures induced LTP in the medial perforant path (MPP)-GC circuit, but mainly through postsynaptic mechanisms. Furthermore, they applied repeated optogenetic activation of MCs to induce LTP in MC-GC circuits in advance and found that this further increased the seizure susceptibility of healthy mice induced by a lower dose of KA (20 mg/kg). Understandably, a lower dose of KA may lower the bar

Heming Cheng and Qiuwen Lou have contributed equally to this article.

✉ Zhong Chen
chenzhong@zju.edu.cn

¹ Key Laboratory of Neuropharmacology and Translational Medicine of Zhejiang Province, School of Pharmaceutical Sciences, Zhejiang Chinese Medical University, Hangzhou 310053, China

² Department of Neurology, The Third Affiliated Hospital of Zhejiang Chinese Medical University, Hangzhou 310053, China

³ Institute of Pharmacology and Toxicology, College of Pharmaceutical Sciences, Zhejiang University, Hangzhou 310058, China

for the MC-GC LTP induction to show an effect. However, whether optogenetically-induced LTP in advance would further aggravate seizure severity induced by a normal dose of KA (30 mg/kg) was not discussed in this article. Above all, these results indicate that enhanced MC-GC synaptic transmission in the early seizure stage promotes epileptogenesis. Further studies could be applied to verify the role of LTP in MPP-GC circuits in seizures and to compare its importance with that of the MC-GC circuits.

It is known that brain-derived neurotrophic factor (BDNF)/tropomyosin receptor kinase B signaling is vital for the formation of LTP. Next, Nasrallah *et al.* further tested in mice in which BDNF was conditional knocked out from GCs, and found that seizure-induced MC-GC and MPP-GC synaptic strengthening required postsynaptic BDNF. Therefore, they further applied genetic removal of BDNF from hippocampal excitatory neurons and found that this reduced the susceptibility to acute seizures. However, considering the inhibitory role in MPP-GC synaptic strengthening by knocking out BDNF from GCs, selectively knocking out BDNF from presynaptic MCs could provide more direct evidence for the role of the MC-GC circuit in early epileptogenesis. It is notable that, just like the paradoxical function of MCs in different periods of seizures, BDNF may play opposite roles in acute and chronic epilepsy [6], since BDNF in the epileptic hippocampus reduces the frequency of spontaneous generalized seizures and improves cognitive performance [7]. Above all, Nasrallah and colleagues found that in the acute stage but not the chronic stage of seizures, the BDNF-dependent LTP in the MC-GC circuit promotes epileptogenesis, and reducing BDNF in the hippocampus would be an effective therapeutic strategy for early epileptogenesis and a potential molecular target for pharmacological treatment of TLE. As for the long way for genetic modulation in clinical therapy, drugs targeting BDNF signals may be further tested for potential translational medicine.

In general, by using chemogenetics, *in vivo* Ca²⁺ imaging, electrophysiology, and a gene-knockout strategy, Nasrallah *et al.* disclosed a detrimental role of MCs in the DG of the hippocampus during early epileptogenesis, with a potential mechanism involving BDNF-dependent synaptic enhancement of MC-GC circuits. Notwithstanding, several further issues remain to be resolved (Fig. 1): (1) MCs in the dorsal and ventral DG have been found to be functionally heterogeneous not only in memory and emotion but also in chronic epileptic seizures [1, 8]. Are the roles and the underlying downstream circuit foundation of the MCs in the dorsal DG consistent with those in the ventral part in acute seizures? This could be further examined by selectively injecting a virus into a particular subregion of the DG or directly expressing the virus under the calretinin promoter, a special marker of MCs in the ventral DG but not the dorsal DG of mice. (2) Apart from the direct input from MCs to

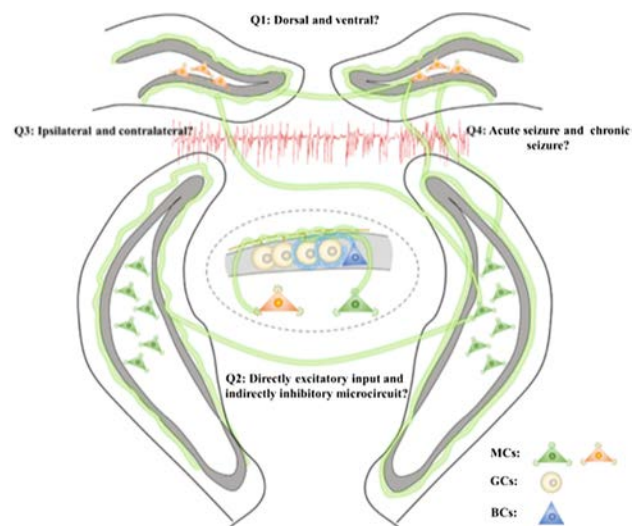


Fig. 1 Further directions to reveal the precise roles of mossy cells in epilepsy. Question 1: Are the roles and the underlying downstream circuit foundation of the MCs in the dorsal DG consistent with those in the ventral part in acute seizures? Question 2: What happens to the MC-BC-GC microcircuits after the initial seizure? Question 3: Is there any functional difference between the MCs ipsilateral and contralateral to the seizure focus? Question 4: How do the MCs change from a detrimental pro-epileptic role during the early stage to a beneficial anti-epileptic role during chronic seizures? Abbreviations: MCs, mossy cells; GCs, granule cells; BCs, basket cells.

GCs, MCs also provide synaptic connections to the basket cells in the hippocampus, thereby forming both a directly excitatory circuit and an indirectly inhibitory microcircuit to modify the balance of the hippocampus [9]. It has been reported that chemogenetic inhibition but not activation of MCs induces an increase in c-fos expression in GC layers under normal physiological conditions [10]. So, what happened to this indirect inhibitory microcircuit after the initial seizure is an important question that deserves further investigation. (3) The MCs play an important role in connecting the bilateral hippocampus in the two cerebral hemispheres by sending both ipsilateral and contralateral projections, and the function of the local connection may be different from that of the remote connection. It is hard for Nasrallah *et al.* and Botterill *et al.* to study the functional difference between the MCs ipsilateral and contralateral to the seizure focus, as they induced seizures by intraperitoneal injection of epileptic drugs. To reveal the role of MCs in the propagation from focal to generalized seizures, further studies could be applied in epileptic models induced unilaterally. (4) Most interestingly and importantly, how did the MCs change from a detrimental pro-epileptic role during the early stage to a beneficial anti-epileptic role during chronic seizures? Are there any characteristic changes or circuit reorganizations that happen to these surviving MCs? These questions deserve further research.

Acknowledgements This work was supported by the National Natural Science Foundation of China (82204353) and the Research Project of Zhejiang Chinese Medical University (2022JKZKTS07).

Conflict of interest The authors declare no conflict of interest.

References

1. Bui AD, Nguyen TM, Limouse C, Kim HK, Szabo GG, Felong S. Dentate gyrus mossy cells control spontaneous convulsive seizures and spatial memory. *Science* 2018, 359: 787–790.
2. Nasrallah K, Frechou MA, Yoon YJ, Persaud S, Gonçalves JT, Castillo PE. Seizure-induced strengthening of a recurrent excitatory circuit in the dentate gyrus is proconvulsant. *Proc Natl Acad Sci U S A* 2022, 119: e2201151119.
3. Botterill JJ, Lu YL, LaFrancois JJ, Bernstein HL, Alcantara-Gonzalez D, Jain S, *et al.* An excitatory and epileptogenic effect of dentate gyrus mossy cells in a mouse model of epilepsy. *Cell Rep* 2019, 29: 2875–2889.e6.
4. Houser CR, Peng Z, Wei X, Huang CS, Mody I. Mossy cells in the dorsal and ventral dentate gyrus differ in their patterns of axonal projections. *J Neurosci* 2021, 41: 991–1004.
5. Botterill JJ, Gerencer KJ, Vinod KY, Alcantara-Gonzalez D, Scharfman HE. Dorsal and ventral mossy cells differ in their axonal projections throughout the dentate gyrus of the mouse hippocampus. *Hippocampus* 2021, 31: 522–539.
6. Liu X, Liu J, Liu J, Liu XL, Jin LY, Fan W, *et al.* BDNF-TrkB signaling pathway is involved in pentylenetetrazole-evoked progression of epileptiform activity in hippocampal neurons in anesthetized rats. *Neurosci Bull* 2013, 29: 565–575.
7. Lin TW, Harward SC, Huang YZ, McNamara JO. Targeting BDNF/TrkB pathways for preventing or suppressing epilepsy. *Neuropharmacology* 2020, 167: 107734.
8. Wang KY, Wu JW, Cheng JK, Chen CC, Wong WY, Averkin RG, *et al.* Elevation of hilar mossy cell activity suppresses hippocampal excitability and avoidance behavior. *Cell Rep* 2021, 36: 109702.
9. Scharfman HE. The enigmatic mossy cell of the dentate gyrus. *Nat Rev Neurosci* 2016, 17: 562–575.
10. Botterill JJ, Vinod KY, Gerencer KJ, Teixeira CM, LaFrancois JJ, Scharfman HE. Bidirectional regulation of cognitive and anxiety-like behaviors by dentate gyrus mossy cells in male and female mice. *J Neurosci* 2021, 41: 2475–2495.

Springer Nature or its licensor (e.g. a society or other partner) holds exclusive rights to this article under a publishing agreement with the author(s) or other rightsholder(s); author self-archiving of the accepted manuscript version of this article is solely governed by the terms of such publishing agreement and applicable law.

RESEARCH HIGHLIGHT

One Small Step for Neurotechnology, One Giant Leap for an In-Depth Understanding of the Brain

Xiaoyun Qiu¹ · Minjuan Sun¹ · Cenglin Xu¹ ·
Yingying Tang² · Zhong Chen¹ 

Received: 26 October 2022 / Accepted: 27 November 2022 / Published online: 31 January 2023

© Center for Excellence in Brain Science and Intelligence Technology, Chinese Academy of Sciences 2023

Is science mostly driven by ideas or by tools? The answers to the everlasting question remain open. But the advances in techniques undoubtedly push forward scientific research to investigate both more in-breadth and in-depth aspects. In neuroscience, the door was opened for recording *in vivo* dynamic neuronal activity through the development of microelectrodes. However, the brain functions through highly interconnected circuits that are composed of numerous distinctly-located neurons [1, 2]. A critical technical issue has been proposed in the field of neurotechnology—how to simultaneously detect multiple neuronal spikes at both wide temporal and spatial scales? In line with this, the latest study published in *Nature Biomedical Engineering* by a joint research group describes ultra-flexible electrode arrays for long-term and far-ranging *in vivo* electrophysiological recordings (Fig. 1), which makes one giant leap in in-depth neural circuitry studies [3].

In this study, based on the previously-developed ultra-flexible and biocompatible nanoelectronic thread electrodes (NETs) [4], the authors further constructed large-scale 3D electrode arrays by fabricating three types of NET modules. The authors claim that these arrays can be implanted at extremely high densities without overmuch occupation of extracellular space and tissue damage. Given that the type I arrays showed a broader volumetric coverage of neural recording, the authors used this design for further

experiments. Using an optimized implantation surgery strategy, the authors achieved desirable high volumetric recording density in a certain region (>1000 electrode contacts per mm³). Then the authors reported that 1.25 sorted single units per contact were detected through an average of 1058 recording contacts per animal, of which, nearly half of the units were deemed to be single units. Given the reliable recording performance of the ultra-flexible electrode arrays, the authors further attempted to electro-physiologically map the visual cortex by implanting 10 types I NET modules into the mouse visual cortex with a spacing of 200 μm. Visual stimuli (drifting gratings at various angles) were further applied to examine the functions of dynamic local neural recordings. About 40% of the 1355 units recorded were modulated by the visual stimuli, and taking advantage of the high-density distribution of the contacts, the authors mapped the spatiotemporal structure of the visual cortical network and resolved local neuron-neuron communications when receiving visual stimuli. Then the authors moved forward to decode the stimulus orientation based on the information derived from the 1355 recorded units through all the stimuli trials. And according to the authors, the decoding errors dramatically decreased as the number of included units increased. So far, ultra-flexible electrode arrays have been demonstrated to be reliable for high-density volumetric recording.

Given that optogenetics has been widely used in neuroscience [5, 6], the authors decided to combine large-scale recording and optical stimulation in Thy1-mhChR2-EYFP transgenic mice. Blue light successfully activated neurons recorded by those contacts adjacent to the optical fiber. And optical stimulation of both long-term potentiation and long-term depression protocols further resulted in the increased coupling of neighboring populations of neurons, highlighting the great compatibility of the arrays with optogenetic

✉ Zhong Chen
chenzhong@zju.edu.cn

¹ Key Laboratory of Neuropharmacology and Translational Medicine of Zhejiang Province, School of Pharmaceutical Science, Zhejiang Chinese Medical University, Hangzhou 310053, China

² Department of Pharmacy, Women's Hospital, School of Medicine, Zhejiang University, Hangzhou 310000, China

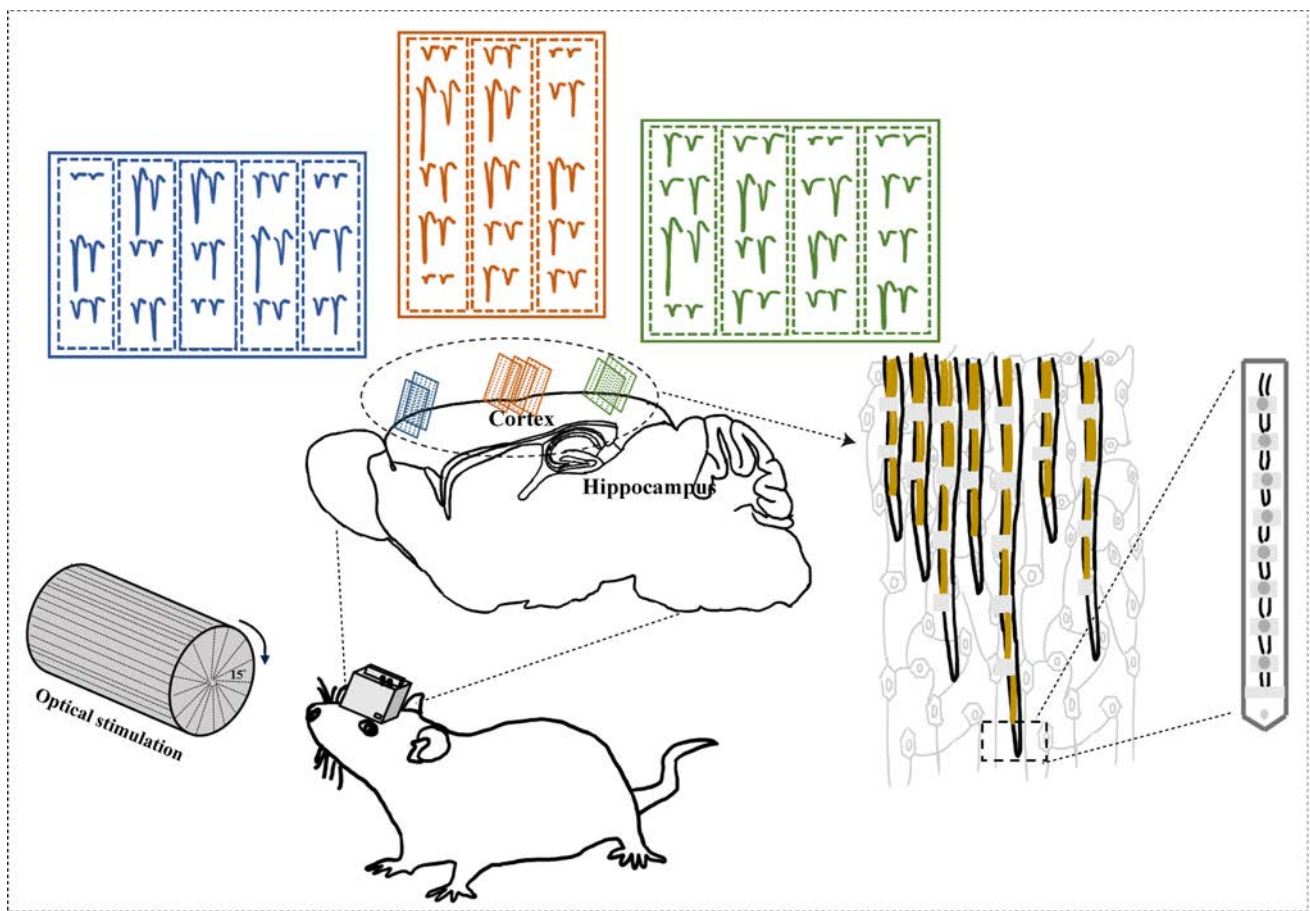


Fig. 1 Diagram of the ultra-flexible electrode arrays for months-long high-density electrophysiological mapping of thousands of neurons in rodents (modified from the original article [3]). Arrays are implanted

into multiple cortical regions, and signals of thousands of neurons are recorded simultaneously during a visual stimulus to map the cortical circuits underlying different behaviors.

tools. Then, the authors implanted multiple NET modules into extensive cortical regions (including motor, sensory, and visual cortices) of both hemispheres. Similarly, the array achieved a high-performance recording capacity across different cortices by yielding 1.32 units per contact. Then, the authors attempted to correlate behavior and neural activity by applying visual stimuli and found that different behaviors were associated with distinct neural activities in corresponding cortical regions. With the assistance of a machine learning long short-term memory regression model, the authors successfully decoded the animal's spontaneous behavioral states from the electrophysiological signals in multiple cortical regions, indicating the great potential of the electrode array for investigating the neural circuitry dynamics of distinct regions. To fulfill the demand for long-term electrophysiological recording, the chronic stability of the arrays was examined. According to the authors, the main recording parameters remained stable for up to 3 months.

Overall, the authors have successfully developed minimal invasive ultra-flexible electrode arrays capable of

stable, months-long, *in vivo* recording of neuronal activity. Although other kinds of electrode arrays have been developed, from the data presented, we are deeply encouraged by the high-density recording capacity, in particular, the accessibility to the simultaneous recording of single units in extensive brain regions. These characteristics, so far, have not been demonstrated in any other previously developed electrode arrays. For neuroscientists or others interested in this field, the importance of this study may not only be in improving the electrophysiological recording qualities but also greatly broadens the dimensions for designing more complex experiments, such as revealing the multilevel neural circuitry basis underlying different behaviors. In our opinion, perhaps further addressing some issues which may be concerning to potential users is somehow beneficial for further popularization and commercialization. Given that deeper regions such as the hippocampus and thalamus play roles as important as the cortices under many physiological and pathological conditions [7, 8], the first question is whether the performance of this electrode array remains excellent in

other deeper areas of the brain. Then, many studies may need to design electrical stimulation or intra-cerebral pharmacology experiments [9, 10]; further testing of the compatibility of this array with stimulating electrodes or cannulas is desirable. Also, with those great improvements compared with currently available electrode arrays, these new arrays may play a vital role in directly analyzing human brain activity, especially in those intractable neurological diseases such as epilepsy and Parkinson's disease [11, 12]. As for achieving a successful clinical translation, performing experiments on non-human primates would be the initial necessary stepping stone.

Acknowledgments This research highlight was supported by Grants from the National Natural Science Foundation of China (82173796) and the Research Project of Zhejiang Chinese Medical University (2022JKJNTZ13).

Conflict of interest The authors declare that they have no competing interest.

References

1. Ying Y, Wang JZ. Illuminating neural circuits in alzheimer's disease. *Neurosci Bull* 2021, 37: 1203–1217.
2. Janak PH, Tye KM. From circuits to behaviour in the amygdala. *Nature* 2015, 517: 284–292.
3. Zhao Z, Zhu H, Li X, Sun L, He F, Chung JE. Ultraflexible electrode arrays for months-long high-density electrophysiological mapping of thousands of neurons in rodents. *Nat Biomed Eng* 2022, <https://doi.org/10.1038/s41551-022-00941-y>.
4. Luan L, Wei X, Zhao Z, Siegel JJ, Potnis O, Tuppen CA, *et al.* Ultraflexible nanoelectronic probes form reliable, glial scar-free neural integration. *Sci Adv* 2017, 3: e1601966.
5. Kim CK, Adhikari A, Deisseroth K. Integration of optogenetics with complementary methodologies in systems neuroscience. *Nat Rev Neurosci* 2017, 18: 222–235.
6. Sun S, Shi J, Wang Y, Cheng J, Huang Z. A temporal precision approach for deep transcranial optogenetics with non-invasive surgery. *Neurosci Bull* 2021, 37: 1260–1263.
7. Xu C, Zhang S, Gong Y, Nao J, Shen Y, Tan B, *et al.* Subicular caspase-1 contributes to pharmacoresistance in temporal lobe epilepsy. *Ann Neurol* 2021, 90: 377–390.
8. Xu L, Lin W, Zheng Y, Chen J, Fang Z, Tan N, *et al.* An H2R-dependent medial septum histaminergic circuit mediates feeding behavior. *Curr Biol* 2022, 32: 1937-1948.e5.
9. Xu C, Wang Y, Zhang S, Nao J, Liu Y, Wang Y, *et al.* Subicular pyramidal neurons gate drug resistance in temporal lobe epilepsy. *Ann Neurol* 2019, 86: 626–640.
10. Ruan Y, Xu C, Lan J, Nao J, Zhang S, Fan F, *et al.* Low-frequency stimulation at the subiculum is anti-convulsant and anti-drug-resistant in a mouse model of lamotrigine-resistant temporal lobe epilepsy. *Neurosci Bull* 2020, 36: 654–658.
11. Xu C, Gong Y, Wang Y, Chen Z. New advances in pharmacoresistant epilepsy towards precise management-from prognosis to treatments. *Pharmacol Ther* 2022, 233: 108026.
12. Li S, Jia C, Li T, Le W. Hot topics in recent parkinson's disease research: Where we are and where we should go. *Neurosci Bull* 2021, 37: 1735–1744.

Springer Nature or its licensor (e.g. a society or other partner) holds exclusive rights to this article under a publishing agreement with the author(s) or other rightsholder(s); author self-archiving of the accepted manuscript version of this article is solely governed by the terms of such publishing agreement and applicable law.

RETRACTION NOTE

Retraction Note to: Gray Matter-Based Age Prediction Characterizes Different Regional Patterns

Nianming Zuo^{1,2,3,4}  · Tianyu Hu^{1,2,3} · Hao Liu^{1,2,3} ·
Jing Sui^{1,2,3,5} · Yong Liu^{1,2,3,5}  · Tianzi Jiang^{1,2,3,4,5,6,7} 

Published online: 13 September 2022

© Center for Excellence in Brain Science and Intelligence Technology, Chinese Academy of Sciences 2022

**Retraction to: *Neurosci. Bull.* January, 2021, 37(1):94–98
<https://doi.org/10.1007/s12264-020-00558-8>**

The authors have retracted this article. After publication we found an error in the implementation code that resulted in data leakage in the age-prediction model training process. We have redesigned the prediction model and tested the mode with an extended dataset (around 2000 subjects, in

contrast to the 600 subjects in this article). Moreover, more investigations have been undertaken based on this model from the perspective of neurobiology for adult brain development. We have prepared a new manuscript for submission to *Neuroscience Bulletin* for peer review. All authors agree with this retraction.

The original article can be found online at <https://doi.org/10.1007/s12264-020-00558-8>.

✉ Nianming Zuo
nmzuo@nlpr.ia.ac.cn

- ¹ Brainnetome Center, Institute of Automation, Chinese Academy of Sciences (CAS), Beijing 100190, China
- ² National Laboratory of Pattern Recognition, Institute of Automation, CAS, Beijing 100190, China
- ³ University of CAS, Beijing 100190, China
- ⁴ Chinese Institute for Brain Research, Beijing 102206, China
- ⁵ Center for Excellence in Brain Science and Intelligence Technology, Institute of Automation, CAS, Beijing 100190, China
- ⁶ Key Laboratory for NeuroInformation of the Ministry of Education, School of Life Science and Technology, University of Electronic Science and Technology of China, Chengdu 625014, China
- ⁷ Queensland Brain Institute, University of Queensland, Brisbane, QLD 4072, Australia

Neuroscience Bulletin

Editors-in-Chief

Shumin Duan, Zhejiang University, Hangzhou, China
Ru-Rong Ji, Duke University, Durham, USA

Deputy Editors

Jiulin Du, Center for Excellence in Brain Science and Intelligence Technology, CAS, Shanghai, China
Zuoren Wang, Center for Excellence in Brain Science and Intelligence Technology, CAS, Shanghai, China

Executive Associate Editors

Iain C. Bruce, Zhejiang University, Hangzhou, China
Guangyin Xu, Institute of Neuroscience, Soochow University, Suzhou, China

Associate Editors

Shiqing Cai, Center for Excellence in Brain Science and Intelligence Technology, CAS, Shanghai, China
Renjie Chai, Southeast University, Nanjing, China
Zhong Chen, Zhejiang University, Hangzhou, China
Yiru Fang, Shanghai Mental Health Center, Shanghai, China
Tianming Gao, South Medical University, Guangzhou, China
Yong-Jing Gao, Nantong University, Nantong, China
Yong Gu, Center for Excellence in Brain Science and Intelligence Technology, CAS, Shanghai, China
Shihui Han, Peking University, Beijing, China
Cheng He, Naval Medical University, Shanghai, China
Tianzi Jiang, Institute of Automation, CAS, Beijing, China
Weidong Le, Sichuan Academy of Medical Science/ Sichuan Provincial Hospital, Chengdu, China
Tao Li, Zhejiang University School of Medicine Affiliated Mental Health Center, Hangzhou, China
Chengyu Li, Center for Excellence in Brain Science and Intelligence Technology, CAS, Shanghai, China
Chun-Feng Liu, Second Affiliated Hospital of Soochow University, Suzhou, China
Minmin Luo, National Institute of Biological Sciences, Beijing, China
Mengsheng Qiu, Hangzhou Normal University, Hangzhou, China
Zilong Qiu, Center for Excellence in Brain Science and Intelligence Technology, CAS, Shanghai, China
Fu-Dong Shi, Tianjin Medical University General Hospital, Tianjin, China
Yangang Sun, Center for Excellence in Brain Science and Intelligence Technology, CAS, Shanghai, China

You Wan, Peking University, Beijing, China
Jian-Zhi Wang, Huazhong University of Science and Technology, Wuhan, China
Kai Wang, Anhui Medical University, Hefei, China
Liping Wang, Shenzhen Institute of Advanced Technology, CAS, Shenzhen, China
Liping Wang, Center for Excellence in Brain Science and Intelligence Technology, CAS, Shanghai, China
Yanjiang Wang, Daping Hospital, Army Medical University, Chongqing, China
Zheng Wang, Peking University School of Psychological and Cognitive Sciences, Beijing, China
Longjun Wu, Mayo Clinic, Rochester, USA
Sheng-Xi Wu, The Fourth Military Medical University, Xi'an, China
Si Wu, Peking University, Beijing, China
Zhi-Ying Wu, The Second Affiliated Hospital Zhejiang University School of Medicine, Hangzhou, China
Ninglong Xu, Center for Excellence in Brain Science and Intelligence Technology, CAS, Shanghai, China
Tianle Xu, Shanghai Jiao Tong University School of Medicine, Shanghai, China
Yun Xu, Nanjing Drum Tower Hospital, Nanjing, China
Tian Xue, University of Science and Technology of China, Hefei, China
Dai Zhang, Peking University, Beijing, China
Hanting Zhang, Qingdao University School of Pharmacy, Qingdao, China
Jie Zhang, Xiamen University, Xiamen, China
Yongqing Zhang, Institute of Genetics and Developmental Biology, CAS, Beijing, China
Chunjiu Zhong, Fudan University, Shanghai, China

Editorial Board

Goran Angelovski, Center for Excellence in Brain Science and Intelligence Technology, CAS, Shanghai, China
George Baillie, Institute of Cardiovascular and Medical Sciences, University of Glasgow, UK
Guo-Qiang Bi, University of Science and Technology of China, Hefei, China

Junli Cao, Xuzhou Medical College, Xuzhou, China
L. Judson Chandler, Medical University of South Carolina, USA
Jun Chen, The Fourth Military Medical University, Xi'an, China
Qing-Hui Chen, Michigan Technological University, Houghton, USA

- Xiaoke Chen**, Stanford University, Stanford, USA
Isaac M. Chiu, Harvard Medical School, Boston, USA
He Cui, Center for Excellence in Brain Science and Intelligence Technology, CAS, Shanghai, China
Jun Ding, Stanford University, Stanford, USA
Zhi-Hua Gao, Zhejiang University School of Medicine, Hangzhou, China
Aaron Gitler, Stanford University, Stanford, USA
Xiaosong Gu, Nantong University, Nantong, China
Junhai Han, Southeast University, Nanjing, China
Gregg E. Homanics, University of Pittsburgh, USA
Ji Hu, ShanghaiTech University, Shanghai, China
Zhi-An Hu, Army Medical University, Chongqing, China
Peter Illes, University of Leipzig, Leipzig, Germany
Pierre Lavenex, University of Fribourg, Fribourg, Switzerland
Juan Lerma, Instituto de Neurociencias de Alicante, Alicante, Spain
Wolfgang Liedtke, Duke University School of Medicine, Durham, USA
Stuart A. Lipton, Sanford-Burnham Medical Research Institute and University of California at San Diego, San Diego, USA
Jingyu Liu, Center for Excellence in Brain Science and Intelligence Technology, CAS, Shanghai, China
Tong Liu, Nantong University, Nantong, China
Lin Lu, Peking University Sixth Hospital, Beijing, China
Benyan Luo, Zhejiang University School of Medicine, Hangzhou, China
Ceng Luo, The Fourth Military Medical University, Xi'an, China
Jian-Hong Luo, Zhejiang University School of Medicine, Hangzhou, China
Zhen-Ge Luo, ShanghaiTech University, Shanghai, China
Lan Ma, Fudan University, Shanghai, China
Qiufu Ma, Dana-Farber Cancer Institute, Boston, USA
Quanhong Ma, Soochow University, Suzhou, China
Robert C. Malenka, Stanford University, Stanford, USA
Manuel S. Malmierca, Universidad de Salamanca, Salamanca, Spain
John H.R. Maunsell, Harvard Medical School, Boston, USA
Earl K. Miller, Massachusetts Institute of Technology, Cambridge, USA
Hideyuki Okano, Keio University, Tokyo, Japan
Vladimir Parpura, University of Alabama at Birmingham, Birmingham, USA
Jos Prickaerts, School for Mental Health and Neuroscience, Maastricht University, The Netherlands
Joshua R. Sanes, Harvard University, Boston, USA
Michael N. Shadlen, Columbia University, New York, USA
Wei Shen, ShanghaiTech University, Shanghai, China
Yousheng Shu, Fudan University, Shanghai, China
Bai-Lu Si, Beijing Normal University, Beijing, China
Sangram S. Sisodia, The University of Chicago, Chicago, USA
Peter Somogyi, University of Oxford, Oxford, UK
Ron Stoop, Lausanne University, Lausanne, Switzerland
Feng-Yan Sun, Fudan University, Shanghai, China
Dick F. Swaab, Netherlands Institute for Neuroscience, Amsterdam, The Netherlands
Yong Tang, Chengdu University of TCM, Chengdu, China
Makoto Tsuda, Kyushu University, Fukuoka, Japan
Alexei Verkhratsky, The University of Manchester, Manchester, UK
Guanghui Wang, Soochow University, Suzhou, China
Yun Wang, Neuroscience Research Institute, Peking University, Beijing, China
Xu-Chu Weng, South China Normal University, Guangzhou, China
William Wisden, Imperial College London, London, UK
Jun-Xia Xie, Qingdao University, Qingdao, China
Zhiqi Xiong, Center for Excellence in Brain Science and Intelligence Technology, CAS, Shanghai, China
Lin Xu, Kunming Institute of Zoology, CAS, Kunming, China
Xiao-Hong Xu, Center for Excellence in Brain Science and Intelligence Technology, CAS, Shanghai, China
Jun Yan, Center for Excellence in Brain Science and Intelligence Technology, CAS, Shanghai, China
Hui Yang, Center for Excellence in Brain Science and Intelligence Technology, CAS, Shanghai, China
Tianming Yang, Center for Excellence in Brain Science and Intelligence Technology, CAS, Shanghai, China
Haishan Yao, Center for Excellence in Brain Science and Intelligence Technology, CAS, Shanghai, China
Shanping Yu, Emory University School of Medicine, Atlanta, USA
Hong Zhang, The Second Affiliated Hospital of Zhejiang University School of Medicine, Hangzhou, China
Xiaohui Zhang, Beijing Normal University, Beijing, China
Xu Zhang, Shanghai Advanced Research Institute, CAS, Shanghai, China
Yong Zhang, Peking University, Beijing, China
Yu-Qiu Zhang, Fudan University, Shanghai, China
Zhi-Jun Zhang, Zhongda Hospital, Southeast University, Nanjing, China
Ping Zheng, Fudan University, Shanghai, China
Jiang-Ning Zhou, University of Science and Technology of China, Hefei, China
Jiawei Zhou, Center for Excellence in Brain Science and Intelligence Technology, CAS, Shanghai, China
Jiangning Zhu, Nanjing University, Nanjing, China

Neuroscience Bulletin

Copyright Information

For Authors

As soon as an article is accepted for publication, authors will be requested to assign copyright of the article (or to grant exclusive publication and dissemination rights) to the publisher (respective the owner if other than Springer Nature). This will ensure the widest possible protection and dissemination of information under copyright laws.

More information about copyright regulations for this journal is available at www.springer.com/12264

For Readers

While the advice and information in this journal is believed to be true and accurate at the date of its publication, neither the authors, the editors, nor the publisher can accept any legal responsibility for any errors or omissions that may have been made. The publisher makes no warranty, express or implied, with respect to the material contained herein.

All articles published in this journal are protected by copyright, which covers the exclusive rights to reproduce and distribute the article (e.g., as offprints), as well as all translation rights. No material published in this journal may be reproduced photographically or stored on microfilm, in electronic data bases, on video disks, etc., without first obtaining written permission from the publisher (respective the copyright owner if other than Springer Nature). The use of general descriptive names, trade names, trademarks, etc., in this publication, even if not specifically identified, does not imply that these names are not protected by the relevant laws and regulations.

Springer Nature has partnered with Copyright Clearance Center's RightsLink service to offer a variety of options for reusing Springer Nature content. For permission to reuse our content please locate the material that you wish to use on link.springer.com or on springerimages.com and click on the permissions link or go to copyright.com and enter the title of the publication that you wish to use. For assistance in placing a permission request, Copyright Clearance Center can be contacted directly via phone: +1-855-239-3415, fax: +1-978-646-8600, or e-mail: info@copyright.com

© Center for Excellence in Brain Science and Intelligence Technology, CAS 2023

Journal Website

www.springer.com/12264

For the actual version of record please always check the online version of the publication.

Subscription Information

Volume 39 (12 issues) will be published in 2023.

ISSN: 1673-7067 print
ISSN: 1995-8218 electronic

For information on subscription rates please contact Springer Nature Customer Service Center: customerservice@springernature.com

The Americas (North, South, Central America and the Caribbean)
Springer Nature Journal Fulfillment,
Harborside Plaza II,
200 Hudson Street, Jersey City,
NJ 07302, USA
Tel. 800-SPRINGER (777-4643);
212-460-1500 (outside
North America)

Outside the Americas

Springer Nature Customer Service
Center GmbH, Tiergartenstr. 15,
69121 Heidelberg, Germany
Tel.: +49-6221-345-4303

Advertisements

E-mail contact: advertising@springer.com or anzeigen@springer.com (Germany)

Disclaimer

Springer Nature publishes advertisements in this journal in reliance upon the responsibility of the advertiser to comply with all legal requirements relating to the marketing and sale of products or services advertised. Springer Nature and the editors are not responsible for claims made in the advertisements published in the journal. The appearance of advertisements in Springer Nature publications does not constitute endorsement, implied or intended, of the product advertised or the claims made for it by the advertiser.

Office of Publication

Springer Nature Singapore Pte Ltd.
152 Beach Road, #21-01/04
Gateway East, Singapore 189721,
Singapore



Impact Factor

5.271

2021 Journal Citation Reports: Q2
(CLARIVATE ANALYTICS, 2022)

NEUROSCIENCE BULLETIN 神经科学通报 (Monthly)

Vol. 39 No. 6 June 15, 2023

Administrated by: Chinese Academy of Sciences

Sponsored by: Center for Excellence in Brain Science and Intelligence Technology, Chinese Academy of Sciences
Chinese Neuroscience Society

Editors-in-Chief: Shunmin Duan, Ru-Rong Ji

Edited by: Editorial Board of *Neuroscience Bulletin*

319 Yueyang Road, Building 8, Room 612, Shanghai 200031, China

Phone: +86-21-64032273; 64170853; 64032696

E-mail: nsb@ion.ac.cn; <http://www.neurosci.cn>

Editors: Bin Wei, Fei Dong, Ting Lyu

Published by: Center for Excellence in Brain Science and Intelligence Technology, Chinese Academy of Sciences

Printed by: Shanghai Shengtong Times Printing Co.,Ltd (A6, No. 2888, Caolang Highway, Jinshan District, Shanghai)

Overseas Distributed by: Springer Nature

Home Distributed by: Local Post Offices

ISSN 1673-7067

CN 31-1975/R

Post Office Code Number: 4-608

Permit of Ad. Number: 3100420130051

Price: ¥ 100.00

ISSN 1673-7067



APEXVIEW

APX 100 一体化智能成像解决方案

持续专注于您的研究
几次点击即可获得出版级质量的图像
快速、高效的数据管理功能



轻松获得高质量图像

一体式封闭显微镜设计

无需暗室也能获取极致荧光图像

“智能样品导航”

助您轻松找到感兴趣区，并立即开始拍摄

全新“Gradient Contrast”观察方式

立体成像即刻呈现

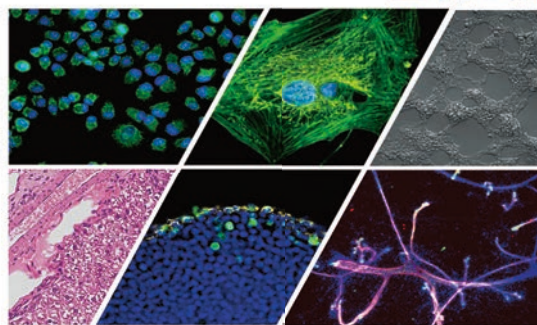
智能“抗漂白模式”

大幅降低光毒性和光漂白，活细胞友好

浩瀚数据的收纳专家

用清晰、统一的索引方式管理您的数据

显而E见



仪景通光学科技(上海)有限公司
EVIDENT (Shanghai) Co. Ltd.

更多详情请咨询: 400-969-0456 / SSBDMarketing@olympus.com.cn



www.olympus-lifescience.com.cn